



Matrix-Free Laser Desorption/Ionisation Mass Spectrometry on Rough or Porous Semiconductor Substrates: Theory and Applications

By

Kai Pong Law, MChem

Thesis submitted to the University of Nottingham
for the degree of Doctor of Philosophy

Dec 2007

The School of Pharmacy
The University of Nottingham

Courage, it would seem, is nothing less than the power to overcome danger, misfortune, fear, injustice, while continuing to affirm inwardly that life with all its sorrows is good; that everything is meaningful even if in a sense beyond our understanding; and that there is always tomorrow.

~ Dorothy Thompson (1893 - 1961)

Abstract

This project aimed to develop a high throughput, laser based, matrix-free, mass spectrometric technique using nanoporous and nanostructured semiconductor substrates for rapid, sensitive, high resolution and accurate mass analytical approach for complex biological matrices.

Laser desorption/ionisation (LDI) based on nanostructured semiconductor surfaces is a novel matrix-free mass spectrometry approach. This novel LDI strategy is closely related to matrix-assisted laser desorption/ionisation (MALDI). However, the functions of the matrix are substituted by an active substrate and the mass spectrum does not suffer matrix interference at the low mass region (m/z below 700). This project aimed to develop this method for pharmaceutical and metabolomic applications, specifically metabolite profiling of complex biological matrices. It was the first time three rival technologies, DIOS, QuickMass and SALDI substrates were evaluated and compared under similar experimental conditions. The study included a comprehensive investigation of the physicochemical properties of these matrix-free LDI substrates, independently from the manufacturers or research group. It also included a comprehensive and detailed mechanistic study and demonstrated the suitability of this novel LDI approach in analysing complex biological mixtures consisting of a hundred or more small biomolecules.

It is believed that the physicochemical properties of the substrate have a strong influence on the LDI efficiency. The nature of the substrates was determined by surface analysis and imaging techniques including secondary ion mass spectrometry (SIMS), X-ray photoelectron spectroscopy (XPS), atomic force microscopy (AFM) and scanning electron microscopy (SEM). Surface properties that govern the LDI processes were identified. It was found that though pores are not strictly required for ion generation, nano-sized porous structure is an important determinant affecting not only the ionisation efficiency, but also the detection mass range and the longevity of the signal. Although a roughened surface is required for the ion generation, the LDI performance does not depend strongly on the surface roughness, but perhaps more on the thickness, dimension, and density of the surface nanostructures. Micron-sized

surface structures do not promote ionisation effectively. Both DIOS and SALDI were found to be silicon based, but the DIOS substrates had been fluoro-silanised. In contrast, the QuickMass substrates were found to be germanium based. The SALDI substrates were found to be oxides passivated. Investigation into surface cleaning technology and chemical modification was carried out on the SALDI substrates. Argon plasma etching followed by fluoro-silane modification was found to be suitable and enhanced the SALDI activity. It was found that fluorine and hydroxyl surface terminations are advantageous. It was proposed that the surface Si-OH moieties are an important proton source and fluorine increases the acidity of the Si-OH moieties.

A wide range of biological and pharmaceutical compounds was analysed to determine the compound classes that were amenable to the method. Compounds analysed include amines, amides, amino acids, peptides, saccharides, steroids, lipids and small organic acids. The chemical properties of the compounds were correlated to the mass spectra generated. Laser induced surface reactions were also investigated by SIMS and XPS chemical imaging. It was found that the ionisation process is not a simple acid-base reaction, but a complicated simultaneous multi-reaction similar to that of MALDI. Laser induces further surface oxidation and produces a reduction potential. It was proposed that the energy transfer mechanism is closely linked to the excitation and relaxation dynamics of the exciton and the special surface state of surfaces' nanocrystallites. It was also proposed that the entropy of the reaction ultimately determines the ions observed and the rate of reaction determines the selectivity. This proposition departed from the conventional view of aqueous basicities and proton affinities dependence.

The analytical characteristics of the DIOS target and MALDI Q-ToF mass spectrometer were investigated. A range of complex biological matrices was analysed, including blood plasma extract, liver extracts, urine extracts, bacterial cells and culture. Extraction methods and the application of principle component analysis (PCA) in the interpretation of the mass spectral data were explored. Suitable extraction methods were found to be important but generally, simplified approaches were sufficient. Even though the RSD value of the ion peaks intensity varied by 10-50%, the application of PCA to the DIOS spectral dataset was still possible.

Acknowledgments

This work would have been impossible without the help of the following people.

I thank my supervisors, Dr. Dave A. Barrett, Dr. Morgan R. Alexander, Professor Michael W. George. I sincerely thank Dr. Barrett for allowing me to have this opportunity and patiently guiding me in thesis writing and his support throughout these three years. I sincerely thank Dr. Alexander for teaching me the detail of SIMS and XPS and other surface analysis techniques, and the feedback for my thesis writing. Many mistakes would have been made without his expertise. I also thank Professor George for his support.

I thank my collaborators, Dr. Sergey N. Nikiforov and Dr. Vladimir A. Karavanskii. I sincerely thank Dr. Nikiforov for taking care of me during my visit to Moscow and the useful discussions and showing me their technological advancement. I thank Dr. Karavanskii for the preparation of SALDI substrates and the discussion. During the thesis writing, I had their works in mind and this thesis is dedicated to them. I hope they will find it very useful in their future work and I hope there will be a chance we meet again.

I thank Dr. Frank Rutten and Dr David Scurr for assistance of the SIMS work, Dr. Emily Smith for assistance of the XPS work, Professor Xinyong Chen for teaching me to use AFM, Mr. Mathew Carlisle for teaching me to use MALDI. I also thank all people in my research group and the School of Pharmacy.

I thank Professor M. Clench of the Sheffield Hallam University for examining this thesis and providing useful feedbacks.

I thank, especially, the RSC/EPSRC for research funding and the University funding for a new MALDI instrument.

List of Abbreviations

| | |
|-------------------|---|
| α -CHCA | α -cyano-4-hydroxycinnamic acid |
| 9AA | 9-aminoacridine |
| <i>ab initio</i> | Latin: from first principles |
| <i>ad libitum</i> | At one's pleasure or desire |
| AC | alternating current |
| ACN | acetonitrile |
| ADME | absorption, distribution, metabolism, excretion |
| AES | Auger electron spectroscopy |
| AFM | atomic force microscopy |
| AHL | <i>N</i> -acyl-L-homoserine lactones |
| AI | autoinducers |
| AQS | alkyl quinolones |
| CE | capillary electrophoresis |
| CNTs | carbon nanotubes |
| CVD | chemical vapour deposition |
| DART | direct analysis in real time |
| <i>de novo</i> | Latin: afresh, anew, beginning again |
| DESI | desorption electrospray ionisation |
| DFA | discriminant function analysis |
| DFT | density functional theory |
| DiMS | direct-injection electrospray mass spectrometry |
| DIOS | desorption/Ionisation on Porous Silicon |
| DQ | design qualification |
| ECR | electron cyclotron resonance |
| EDS | energy dispersive X-ray spectroscopy |
| ESI | electrospray ionisation |
| FDA | food and drug administration |
| FE | field emission |
| FTIR | fourier Transform InfraRed |
| GaN | gallium nitride |
| GB | gas-phase basicity |
| GC | gas chromatography |
| GeNDs | germanium nano-dots |
| GPI | General Physics Institute |
| GTMA | glycidyltrimethyl-ammonium |
| HAQ | 4-hydroxy-2-alkylquinolines |
| HDMS | high definition mass spectrometry |

| | |
|-----------|--|
| HDP | high density plasma |
| HHQ | 4-hydroxy-2-heptylquinoline |
| hk2 | human glandular halikrein 2 |
| hkl | milller indices - Miller Indices are a symbolic vector representation for the orientation of an atomic plane in a crystal lattice and are defined as the reciprocals of the fractional intercepts which the plane makes with the crystallographic axes. <i>e.g.</i> 100, 111 |
| HNQ | 4-hydroxy-2-nonylquinoline |
| HOME-HF | metal-assisted chemical etching in HF/H ₂ O ₂ solution |
| HOPG | high orientated pyrolytic graphite |
| HPLC | high performance liquid chromatography |
| H_{RMS} | height in root mean square |
| HSL | homoserine lactones |
| ICH | International Conference on Harmonisation of Technical Requirements for Registration of Pharmaceuticals for Human Use |
| IE | ionisation energy |
| IUPAC | International Union of Pure and Applied Chemistry |
| IQ | installation qualification |
| LC | liquid chromatography |
| LDI | laser desorption/ionization |
| LDMS | laser desorption/ionisation mass spectrometry |
| LIF | laser induced fluorescence |
| LMIG | liquid metal ion gun |
| LOD | limit of detection |
| LOQ | limit of quantitation |
| LPS | lipopolysaccharides |
| LSD | lysergic acid diethylamide |
| MALDI | matrix-assisted laser desorption-ionisation |
| MBE | molecular beam epitaxy |
| MCP | microchannel plate |
| MS | mass spectrometry |
| MVDA | multivariate data analysis |
| NALDI | Nano-Assisted Laser Desorption/Ionization |
| NIMS | Nanostructure Initiator Mass Spectrometry |
| NIPALS | non-linear iterative partial least squares |
| NMR | nuclear magnetic resonance |
| OQ | operational qualification |
| PA | proton affinity |
| PADI | plasma-assisted desorption/ionization |
| PC | phosphatidylcholine |
| PC | principle component |

| | |
|---------------------|--|
| PCA | principle components analysis |
| PDF | pulsed dynamic focusing |
| pDRE | programmable dynamic range enhancement |
| PECVD | plasma-assisted chemical-vapour-deposition |
| PEG | polyethylene glycol |
| PET | polyethylene terephthalate |
| PI | primary ion |
| PI | propidium iodide |
| PLZT | lead lanthanum zirconate titanate |
| PQ | performance qualification |
| PQS | <i>Pseudomonas</i> quinolone signal |
| PSA | prostate-specific antigen |
| PSi | porous silicon |
| QS | quorum sensing |
| QSI | quorum sensing inhibitors |
| QSSM | quorum sensing signalling molecules |
| RIE | reactive ion etching |
| RSD | relative standard deviation |
| SALDI | surface-assisted laser desorption/ionization |
| SAM | self-assembly monolayer |
| SAM | scanning Auger microscopy |
| SD | standard deviation |
| SEI | scanning electron microscopic image |
| SEM | scanning electron microscope |
| SIMCA | soft independent modelling of class analogy |
| SIMS | secondary ion mass spectrometry |
| <i>sine qua non</i> | Latin: without which it could not be; absolutely essential |
| SiNWs | silicon nanowires |
| SPE | solid-phase extraction |
| STM | scanning tunnelling microscopy |
| TEM | transmission electron microscopy |
| TESP | TappingMode etched silicon probe |
| TFA | trifluoroacetic acid |
| TLC | Thin Layer Chromatography |
| TOF | Time-of-Flight |
| SIMS | secondary ion mass spectrometry |
| UV | ultraviolet (radiation) |
| <i>vide infra</i> | Latin: see below |
| WCA | water contact angle |
| XPS | x-ray photoelectron spectroscopy |

Index

| | |
|---|-----------|
| ABSTRACT | III |
| ACKNOWLEDGMENTS | V |
| LIST OF ABBREVIATIONS | VI |
| INDEX | IX |
| LIST OF FIGURES..... | XIII |
| LIST OF TABLES | XXXIV |
| CHAPTER 1 INTRODUCTION | 1 |
| 1.1 SYSTEMS BIOLOGY: FROM GENOME TO METABOLOME – CHALLENGES OF BIOCHEMICAL PROFILING | 2 |
| 1.2 LASER DESORPTION/IONISATION MASS SPECTROMETRY | 6 |
| 1.3 THE DEVELOPMENT OF SALDI-MS | 8 |
| 1.4 DEVELOPMENT OF DIOS-MS..... | 10 |
| 1.4.1 Preparation and Physicochemical Properties of DIOS Substrates | 11 |
| 1.4.2 Chemical Derivatisation..... | 15 |
| 1.5 THE DEVELOPMENT OF SEMICONDUCTORS NANO-WIRES AND NANO-DOT SURFACES..... | 17 |
| 1.6 DEVELOPMENT OF SALDI SUBSTRATES AND GAS-PHASE SALDI MASS SPECTROMETER AT THE GENERAL PHYSICAL INSTITUTE..... | 20 |
| 1.7 IONISATION MECHANISM | 25 |
| 1.8 APPLICATIONS IN METABOLOMICS..... | 28 |
| 1.9 RESEARCH OBJECTIVES AND SCOPE OF STUDY | 32 |
| 1.10 REFERENCES | 34 |
| CHAPTER 2 METHODOLOGY AND EXPERIMENTAL | 45 |
| 2.1 INTRODUCTION..... | 46 |
| 2.2 CHEMISTRY OF POROUS SILICON..... | 46 |
| 2.3 METHODS OF SURFACE CHARACTERISATION | 54 |
| 2.3.1 Principles of SEM..... | 57 |
| 2.3.2 Principles of AFM | 58 |
| 2.3.3 Principles of ToF-SIMS..... | 60 |
| 2.3.4 Principles of XPS..... | 62 |
| 2.3.5 XPS Imaging (Spectromicroscopy)..... | 63 |
| 2.3.6 Principles of Contact Angle Measurement | 64 |
| 2.4 MATERIALS AND METHODS | 69 |
| 2.4.1 Commercial DIOS Targets | 69 |
| 2.4.2 QuickMass Targets | 69 |
| 2.4.3 SALDI Surfaces..... | 69 |
| 2.4.4 Solvents and Chemicals | 72 |
| 2.4.5 Surface Characterisation..... | 76 |
| 2.4.5.1 SEM | 77 |
| 2.4.5.2 AFM..... | 77 |
| 2.4.5.3 ToF-SIMS | 78 |
| 2.4.5.4 XPS | 78 |
| 2.4.5.5 WCA Measurements | 80 |
| 2.4.5.6 Argon Plasma Etching..... | 81 |
| 2.4.5.7 Fluoro-silane Self-assembly Monolayer (SAM) Modification..... | 81 |
| 2.4.6 LDI Investigations | 83 |
| 2.5 REFERENCES | 86 |
| CHAPTER 3 FROM SUBSTRATES CHARACTERISATION TO LDI PERFORMANCE RELATIONSHIPS | 90 |
| 3.1 INTRODUCTION..... | 91 |
| 3.2 LITERATURE DATA OF SURFACE CHARACTERISTICS AND LDI-MS RELATIONSHIP..... | 97 |
| 3.2.1 Aims of This Chapter | 104 |
| 3.3 RESULTS ON SURFACE CHARACTERISATION | 105 |
| 3.3.1 Surface Morphology of the Matrix-free LDI Substrates by Surface Imaging Techniques..... | 105 |

| | | |
|-------|---|-----|
| 3.3.2 | <i>Commercial DIOS and QuickMass Substrates</i> | 105 |
| 3.3.3 | <i>SALDI Substrates</i> | 107 |
| | Porous Silicon Substrates..... | 107 |
| | Substrates of Void-porous and Dents of Curvatures | 108 |
| | Non-Porous Silicon Substrates Designed for the Gas-Phase SALDI-MS | 109 |
| | Nano-dots and Nano-wells Substrates | 111 |
| | Experimental SALDI Substrates | 111 |
| 3.3.4 | <i>ToF-SIMS Investigation of the LDI Substrates</i> | 115 |
| | 3.3.4.1 DIOS and QuickMass Substrate | 115 |
| | 3.3.4.2 SALDI Substrates..... | 118 |
| | 3.3.4.3 Principle Component Analysis (PCA) of ToF-SIMS Spectral Data of SALDI Substrates (Batch 2005)..... | 118 |
| 3.3.5 | <i>ToF-SIMS Investigation of the Effects of Plasma Etching</i> | 123 |
| 3.3.6 | <i>XPS Investigation of the Effects of Argon Plasma Etching of SALDI Surface</i> | 129 |
| 3.3.7 | <i>XPS Investigation of Fluoro-silane Self Assembly Monolayer (SAM) Modification</i> | 132 |
| 3.3.8 | <i>Plasmon Loss Lines in XPS</i> | 136 |
| 3.3.9 | <i>Water Contact Angle Measurements</i> | 139 |
| 3.4 | SUMMARY AND DISCUSSION OF SURFACE CHARACTERISATION..... | 140 |
| | 3.4.1 <i>Surface Chemistry of the DIOS Targets</i> | 140 |
| | 3.4.2 <i>Surface Chemistry of the QuickMass Targets</i> | 141 |
| | 3.4.3 <i>Surface Chemistry of the Chemically Etched Silicon SALDI Surfaces</i> | 143 |
| | 3.4.4 <i>Surface Cleaning: Argon Plasma Etching of the Silicon SALDI Surfaces</i> | 144 |
| | 3.4.5 <i>Chemical Modification: Fluoro-silane SAM Modification</i> | 145 |
| | 3.4.6 <i>Interfacial Interactions: What Else Has WCA Told Us</i> | 146 |
| 3.5 | SUBSTRATE CHARACTERISTICS AND LDI-MS PERFORMANCE RELATIONSHIP | 149 |
| | 3.5.1 <i>Commercial DIOS and QuickMass Targets: DIOS vs. QuickMass</i> | 149 |
| | 3.5.2 <i>SALDI and DIOS Substrates: SALDI vs. DIOS</i> | 151 |
| | 3.5.3 <i>Inside and Outside of the Etched Spot of SALDI Substrates</i> | 154 |
| | 3.5.4 <i>Plasma Etched and As-received SALDI Substrates</i> | 155 |
| | 3.5.5 <i>SALDI Substrates with Different Surface Roughness and Electro-resistivity</i> | 159 |
| | 3.5.6 <i>Graphite and Sanded Silicon Substrates</i> | 163 |
| | 3.5.7 <i>The LDI Performance of SALDI Substrates Before and After Fluoro-Silane SAM Modification</i> | 164 |
| | 3.5.8 <i>Fluoro-silane SAM Modified SALDI Substrates to As-Received Substrates Prepared by High Etching Current</i> | 165 |
| | 3.5.9 <i>Fluoro-Silane SAM Modified Experimental SALDI Substrates to As-Received Experimental Substrates</i> | 169 |
| 3.6 | SUMMARY AND DISCUSSION OF SURFACE MORPHOLOGY AND CHEMICAL MODIFICATION TO LDI PERFORMANCE..... | 171 |
| 3.7 | CONCLUSIONS | 174 |
| 3.8 | REFERENCES | 176 |

CHAPTER 4 IONIC AND SURFACE REACTIONS ON MATRIX-FREE LDI SUBSTRATES182

| | | |
|-----|--|-----|
| 4.1 | INTRODUCTION..... | 183 |
| | 4.1.1 <i>The DIOS-MS Technique</i> | 183 |
| | 4.1.2 <i>Matrix MALDI Ionisation Reactions</i> | 190 |
| | 4.1.3 <i>Aims of the Chapter</i> | 193 |
| | 4.1.4 <i>Approaches toward Achieving the Objectives:</i> | 194 |
| 4.2 | RESULTS | 195 |
| | 4.2.1 <i>Comparison of MALDI and DIOS</i> | 195 |
| | 4.2.2 <i>Detection of Peptides Using DIOS Technique</i> | 200 |
| | 4.2.3 <i>Detection of Amino Acids</i> | 203 |
| | 4.2.4 <i>Detection of Basic Compounds</i> | 207 |
| | 4.2.5 <i>Detection of Pre-charged Ions and UV Absorbing Compounds</i> | 211 |
| | 4.2.6 <i>Detection of Amides and Saccharides</i> | 212 |
| | 4.2.7 <i>Detection of Acidic Compounds</i> | 214 |
| | 4.2.8 <i>Effect of D₂O and Acidic Buffers on Small Molecules Ionisation</i> | 234 |
| | 4.2.9 <i>Reduction of Metallic Ions</i> | 238 |
| | 4.2.10 <i>Substrate Structural and Chemical Change After LDI Investigation</i> | 239 |
| | 4.2.10.1 Porous Silicon DIOS Substrate | 239 |

| | |
|---|------------|
| 4.2.10.2 XPS and SIMS Imaging To Laser Modification of SALDI Substrate | 241 |
| 4.2.10.3 Observing Native Variation of SALDI Substrate by Using SIMS Imaging | 253 |
| 4.3 SUMMARY AND DISCUSSION | 256 |
| 4.3.1 Proton Affinities and Aqueous Basicities of the Analyte | 256 |
| 4.3.2 Formation of Ions | 257 |
| 4.3.3 Proton Exchange on Silicon Substrates | 259 |
| 4.3.4 Surface Oxides, Halogen and Plasma Etching | 261 |
| 4.3.5 Reducing Power and Electrostatic Field | 262 |
| 4.3.6 Nanocrystalline Silicon Surfaces as Energy Transferring Media | 263 |
| 4.3.7 Possible Roles of the Pores | 269 |
| 4.3.8 Differences to Gas-phase SALDI-MS | 271 |
| 4.4 CONCLUSIONS | 272 |
| 4.5 REFERENCES | 273 |
| CHAPTER 5 ANALYTICAL CHARACTERISATION AND METABOLIC PROFILING USING DIOS-MS ON MALDI Q-TOF PREMIER | 279 |
| 5.1 INTRODUCTION | 280 |
| 5.1.1 Metabolomic Analysis: Emphasis on Biofluids | 280 |
| 5.1.2 Validation Process | 281 |
| 5.1.3 Method Validation | 282 |
| 5.1.4 Literature Data on Method Validation and Application of Biological Samples Using DIOS-MS | 283 |
| 5.1.5 <i>Pseudomonas aeruginosa</i> and Their Secondary Metabolites | 289 |
| 5.1.6 Approaches Used in this Study | 294 |
| 5.1.7 Aims of this Chapter | 295 |
| 5.2 EXPERIMENTAL | 296 |
| 5.2.1 Biological Sample Preparation | 296 |
| 5.2.2 Mass Spectrometry | 299 |
| 5.2.3 Data Analysis by PCA | 300 |
| 5.2.4 Metabolite Databases | 300 |
| 5.3 RESULTS AND DISCUSSION | 301 |
| 5.3.1 Detection Characteristics (Laser Optimisation) | 301 |
| 5.3.2 Dynamic range and Limit of Detection | 306 |
| 5.3.3 Precision and Robustness | 309 |
| 5.3.4 Human Urine | 316 |
| 5.3.5 Human Blood Plasma | 327 |
| 5.3.6 Liver Tissue Extracts | 334 |
| 5.3.7 Detection of Quorum Sensing Signalling Molecules | 360 |
| 5.3.8 Metabolite Profiling of <i>Pseudomonas aeruginosa</i> | 365 |
| 5.4 SUMMARY AND REMARKS | 371 |
| 5.4.1 Method Validation | 371 |
| 5.4.2 Metabolite Profiling of Biological Matrices | 372 |
| 5.4.3 Principle Component Analysis | 375 |
| 5.5 CONCLUSIONS AND FUTURE WORK | 376 |
| 5.6 REFERENCES | 377 |
| CHAPTER 6 CONCLUSIONS AND FUTURE WORK | 385 |
| 6.1 INTRODUCTION | 386 |
| 6.2 MOTIVE OF THE RESEARCH | 386 |
| 6.3 FITNESS FOR PURPOSE: THE STRENGTHS AND THE WEAKNESSES | 387 |
| 6.4 THE DEVELOPMENT AND EVALUATION OF SALDI SUBSTRATES | 389 |
| 6.5 RECOGNITION OF THE IONISATION MECHANISM | 391 |
| 6.6 THE APPLICATION OF COMPLEX BIOLOGICAL MATRICES AND MVDA | 392 |
| 6.7 THE FUTURE DIRECTION | 393 |
| 6.8 FINAL THOUGHT | 395 |
| 6.9 REFERENCES | 396 |
| APPENDICES | I |
| A1: Analytical Performance Parameters | II |
| A2: Conferences and Publications | IV |

| | | |
|-----|-------------------------------------|----|
| A3: | <i>Selected Presentations</i> | IV |
|-----|-------------------------------------|----|

List of Figures

| | |
|--|----|
| Figure 1-1 Classical view of integrated functional genomics. The effects of gene perturbations are evaluated at multiple levels including the transcriptome, proteome and metabolome. A change in the metabolome occurs because of those changes in the transcriptome that result in changes in the levels or catalytic activities. Therefore, metabolomics represents the final step in understanding the gene's function. | 3 |
| Figure 1-2 Strategies for metabolomic investigations. Currently, two complementary approaches are used for metabolomic investigations: metabolic profiling and metabolic fingerprinting. Meta-data refers to specific experimental conditions and protocols used for sample preparations. | 4 |
| Figure 1-3 The principle of MALDI. A MALDI sample is in a state where it is evenly mixed with a matrix. The matrix absorbs the laser energy and converts it into thermal energy. At the same time, a minute amount of the matrix (uppermost surface of the analyte in the diagram) rapidly heats (within several nanoseconds) and vaporises with the sample. | 7 |
| Figure 1-4 The distribution of research or review articles in which the central concept was nanostructured or amorphous semiconductor surface as MALDI substrate in the last 8 years: (A) pie chart showing the international effort and (B) line chart showing the trend of publications each year. Over 75% of literature in total was published in or after 2004. These statistics exclude conference abstracts, patent applications and PhD/Master theses. [Up-to-date Oct 2007] | 10 |
| Figure 1-5 Schematic representation of the DIOS mass spectrometry configuration. DIOS chips are placed on a modified MALDI plate. The analyte is added on the PSi surface and then irradiated UV laser within the MALDI mass spectrometer to induce desorption and ionisation. | 12 |
| Figure 1-6 Photographs of porous silicon emitting light. <i>Left</i> : A 1 cm diameter PSi sample in a Teflon electrochemical cell, under electroluminescence conditions. <i>Right</i> : A 1 cm diameter porous silicon irradiated with UV light which induces photoluminescence emission. | 12 |
| Figure 1-7 Schematic representation of a silicon nanocrystallite. Absorption of a photon with energy higher than the band gap results in promotion of an electron from the valence to the conduction band. Radiative recombination of the excited electron results in emission of a photon of lower energy. | 12 |
| Figure 1-8 The design of the apparatus used to make porous silicon. | 14 |
| Figure 1-9 (<i>Left</i>) A FE-SEM image of an optimal DIOS surface showing nanometer thick porous layer with nanocrystalline structure and photopatterned DIOS target. (<i>Right</i>) The appearance of lithographically etched DIOS target showing an array of sample wells. | 14 |
| Figure 1-10 By using different chemical functionalities, PSi surfaces can be tailored to selectively adsorb and efficiently ionise analytes: (a) trimethylsilane, (b) aminosilane, (c) perfluoroalkylsilane derivatisation and the corresponding DIOS mass spectra of (d) 500 fmol bovine serum albumin (BSA) digest, (e) carbohydrate mixture containing sodiated sucrose ($[M+Na]^+$, m/z 365) and maltotriose ($[M+Na]^+$, m/z 527), and (f) small molecular drugs | |

| | |
|--|----|
| containing midazolam ($[M+H]^+$, m/z 326), propafenone ($[M+H]^+$, m/z 342) and verapamil ($[M+H]^+$, m/z 455)..... | 16 |
| Figure 1-11 (A) Cross-sectional SEM view of a nanostructured column–void Si film grown on a glass substrate showing nanofibres and their aggregates (columns). (B) Plan SEM view of a nanostructured column–void Si film grown on a Si wafer. Process conditions for film growth: 400W, 10 mTorr, 100 °C. The film thickness is close to 600 nm. (C) Cross-sectional SEM view of a nanostructured column–void Si film, where expansion of the columns (fibrous aggregates) occurs with increasing film thickness because of fibrous bifurcation. Process conditions for the film growth: 300W, 20 mTorr, 100 °C. The film was deposited on Si wafer. (E) Mass spectrum of a mixture of peptides spotted on a nanostructured Si film on a plastic substrate (all in the pmol range), including des-arg ¹ -bradykinin (m/z 905), (m/z 1182), angiotensin I (m/z 1297), glu ¹ -fibrinopeptide B (m/z 1571) and neurotensin (m/z 1673)..... | 18 |
| Figure 1-12 Morphology of GeNDs on the GeND chip C. (a) FE-SEM image. (b) AFM image. (c) Three-dimensional image of the same area shown in (b). The size of the nano-dot ~ 200 nm in diameter. | 19 |
| Figure 1-13 SEM images of non-patterned nanowires substrate, before (A) and after (B) laser illumination. | 19 |
| Figure 1-14 AFM images of SALDI substrates, produced by (A) standard anodisation and (B) electrochemical etching in iodine containing electrolyte. Standard etching used 70 mA/cm ² current density and 1 min etching time. Modified etching used 1 mA/cm ² current density and 5 mins etching time. FTIR spectra of SALDI substrates, produced by (C) standard anodisation and by (D) electrochemical etching in iodine containing electrolyte. Tripartite bands at 2100 cm ⁻¹ (labelled 3) and 1000 cm ⁻¹ (labelled 1) are assigned to the stretching and bending modes of SiH moieties respectively. The band at 1100 cm ⁻¹ is assigned to SiO stretching (labelled 2). (E) The intensity of the signal of protonated pyridine obtained from silicon surfaces as a function of the laser fluence, produced by electrochemical etching in iodine containing electrolyte (modified etching) and by standard anodising etching (standard etching). (F) A representative gas-phase SALDI mass spectrum using silicon substrate. | 21 |
| Figure 1-15 (A) Schematic diagram and (B) the setup of a gas-phase SALDI mass spectrometer. A substrate is attached onto an end of a steel rod or a rotating ball platform, which is coupled to a linear time-of-flight mass analyser. Samples are introduced via a GC instrument, or a vapour microflow generator inside the vacuum chamber. Alternatively, the target surface is briefly exposed to a micro airflow locked on a rotating platform. (C) A total ion chromatography (TIC) of a mixture of benzylamine, ethoxyaniline, triethylamine, <i>N</i> -methylphenethylamine and diphenylamine obtained by GC gas-phase SALDI-MS. | 24 |
| Figure 1-16 Adsorption of thermometer molecular ions (TM ⁺ and Cl ⁻) and solvent molecules (S) in derivatised silicon nanopores. Derivatisation is depicted as a dashed line that follows the surface. Pore walls are sufficiently thin to induce quantum confinement of electrons leading to enhanced absorption of laser light. Two possible scenarios exist. The left pore only contains adsorbates and it is used to demonstrate the “dry” desorption mechanism. The right pore shows trapped solvent | |

| | |
|--|----|
| as a result of capillary condensation or inefficient pumping through nanopore (gray area) and exhibits a “wet” desorption mechanism. | 25 |
| Figure 1-17 SEM image of a porous silicon surface after DIOS-MS analysis of a deposited analyte. (A) Normal region of the PSi wafer, identical in morphology to freshly-etched material. (B) Irradiated regions of the surface. | 26 |
| Figure 1-18 Schematic concept diagram illustrating laser desorption/ionization of analyte molecules on nanostructured column/void silicon film. | 27 |
| Figure 1-19 Proposed model of the SALDI multi-staged ionisation reaction. The surface is activated by laser irradiation, followed by the adsorption of neutral analyte and proton donor molecules, the chemical reaction on the surface with proton transfer, production of charged complexes bonded with the surface and finally laser desorption of such preformed protonated or deprotonated ions. | 28 |
| Figure 1-20 Metabolite profiling of <i>Arabidopsis thaliana</i> leaves extract using SALDI-MS. (Left) the mass spectra of water/methanol fraction and (right) chloroform fraction. The wild-type is displaced in black and the transgenic is in red. | 29 |
| Figure 1-21 (A) PC-DFA score plot constructed using the first 60 PCs showing the discrimination of mutants g1 and s4 from the rest of the yeast mutants and the wild type strain. The test set is marked with an asterisk, and the separating clusters encircled for clarification. (B) The first loadings plot of the PC-DFA. Note the prominent peaks at m/z 145 and 146 seen clearly in the expanded portion of the loadings. (C) Mean spectra of g1 (gln3 Δ), g5 (dal80 Δ) and the wild type wh (BY4741) strains showing the differences in the spectra in the region where the prominent discriminatory effect is observed. Note the higher peak intensity at m/z 146 (corresponding to glutamate, [M-H] ⁻) for g1 compared to the rest. (D) Mean spectral response corresponding to glutamine (m/z 147) and glutamate (m/z 148) in the positive-ion direct infusion mass spectra of the three strains as in (C) (error bars represent one standard deviation about the mean). | 30 |
| Figure 1-22 (A) Optical image of human cervical cancer cells, HEK 293, grown on the DIOS substrate; (B) the corresponding fluorescence image of the same cell cluster with nucleuses stained by PI; (C) a typical DIOS MS spectrum collected from HEK 293 cell detection; both PC and PI peaks are labelled with asterisks; (D) the corresponding ion maps of PC (yellow) and PI (orange) fragments overlaid. | 31 |
| Figure 2-1 Schematic representation of PSi production. (A) The reaction is initiated by positive hole generation (h^+), followed by nucleophilic attack of fluoride species with Si and dissolution of SiF_6^{2-} resulting a hydrogen passivated Si surface. (B) Etching cell and control unit. (C) Fabry-Pérot fringes - appearance of colours within the etching solution is a visual indicator for anodisation. The colour changes across the sample and each colour corresponds to a different optical thickness. | 47 |
| Figure 2-2 Representative I-V characteristics of (A) p-type, (B) n-type Si under aqueous electrolyte. Porosification occurs at the regions where $i < i_{ps}$ (highlighted in red). Depending on the etching parameters, four possible porous structure can result: (C) microporous, (D) mesoporous, (E) | |

| | |
|--|----|
| macroporous and (F) damaged pore walls as a result of electrical breakdown. Electropolishing occurs at the region with current densities $i_{ps} < i_{ox}$. | 50 |
| Figure 2-3 Porosity as a function of current densities for (a) lightly doped p-type and (b) highly doped n-type silicon substrate. | 51 |
| Figure 2-4 EPR spectra of PSi (A) before and after O ₂ and H ₂ O adsorption, and (B) after ethanol and C ₂ (CN) ₄ adsorption. | 53 |
| Figure 2-5 Electron-specimen interactions. | 57 |
| Figure 2-6 (A) Schematic of AFM. The deflection of a microfabricated cantilever with a sharp tip is measured by reflecting a laser beam off the backside of the cantilever while it is scanning over the surface of the sample. (B) A SEI of an integrated silicon cantilever. The tips typically have an end radius of curvature 5 to 10 nm. | 59 |
| Figure 2-7 (A) Positive ion yields plotted as a function of ionisation potential. The ion yields are relative to silicon in a silicon matrix with O ₂ ⁺ sputtering. (B) Negative ion yields plotted against electron affinities. The ion yields are relative to silicon for measurements in a silicon matrix with Cs ⁺ ion sputtering. (C) Useful yield of Si in four matrices (Si, SiC, Si ₃ N ₄ , and SiO ₂) obtained in the Si ⁺ mode under three different PI (Cs ⁺ , Ga ⁺ , O ₂ ⁺) bombardments and in the SiCs ⁺ mode. Incorporation of Cs into the material and detecting MCs ⁺ clusters circumvent matrix effect. | 61 |
| Figure 2-8 Schematic of imaging dataset. A stack of images acquired from the same location on the sample over a range of energies. The S/N of each image is relatively poor and many of the images are merely noise. | 63 |
| Figure 2-9 Contact angle, θ_c , at which a liquid/vapour interface meets the solid surface. | 65 |
| Figure 2-10 Infinitesimal displacement of a liquid wedge on a rough surface. | 66 |
| Figure 2-11 The apparent contact angle θ_c as a function of solid surface roughness Γ as described by Wenzel's law. | 67 |
| Figure 2-12 (A) DIOS target and (B) a steel MALDI target coated with QuickMass material. | 69 |
| Figure 2-13 SALDI substrates: (A) standard SALDI substrates and (B) experimental SALDI substrates. | 72 |
| Figure 2-14 Schematic diagrams of Kratos AXIS Ultra XPS system. | 79 |
| Figure 2-15 Fluoro-silane reaction on DIOS target. | 81 |
| Figure 2-16 Custom built reaction vessel for silanisation. | 82 |
| Figure 2-17 Schematic diagram of Micromass M@LDI-MS, provided by the manufacturer. | 84 |
| Figure 2-18 Schematic diagram of Micromass MALDI Q-ToF-MS, provided by the manufacturer. | 84 |
| Figure 2-19 Proposed model of the PDF technique (lines represent ion trajectories): (a) ion trajectories in the case of static electric field and (b) the electric field is switched off 20 ms after the laser pulse. | 85 |
| Figure 3-1 AFM image of PSi substrate produced by galvanostatic anodisation. | 92 |
| Figure 3-2 SEIs of (a) silicon wafer scratched with No. 400 sand paper, (b) stainless steel plate scratched with No. 400 sandpaper, (c) submicrometer groove arrays on silicon, and (d) Au-coated porous alumina. | 93 |

| | |
|---|-----|
| Figure 3-3 Top (left panels) and side (right panels) views of silicon microcolumn arrays produced (A) in ambient air with 1000 laser shots at 1 J/cm ² , (B) in SF ₆ gas at 1 atm. pressure with 1200 laser shots at 0.4 J/cm ² , and (C) in water with 600 laser shots at 0.13 J/cm ² | 95 |
| Figure 3-4 Nanocavity Si surfaces produced by RIE: (<i>top</i>) Top-down FE-SEM images of the surface, etched for (A) 0.5, (B) 1, (C) 1.5, and (D) 5 min, (<i>middle</i>) mass spectra generated by the corresponding surface using a mixture of Val-Met (M ₁) and Ala-Leu-Ala-Leu (M ₂) under similar MS condition, and (<i>bottom</i>) calculated surface parameters of the nanocavity surfaces..... | 96 |
| Figure 3-5 The minimum laser power per pulse required to detect des-pro ³ ,[ala ^{2,6}]-bradykinin for three void-column Si films with different laser coupling, A. A was derived from the reflectance, R, as A = 1-R. The inset represents the control of reflectance (at 337 nm) by varying the deposition power. | 98 |
| Figure 3-6 Absorbance profile of porous and crystalline silicon. × denotes a surface with relatively high surface porosity, ▲ denotes a surface with moderate surface porosity, ■ denotes an oxidised porous silicon surface and ♦ denotes flat silicon..... | 98 |
| Figure 3-7 (A) Photoluminescence images from Pt-patterned p ⁺ - and p ⁻ PSi, with the concave side of the arc corresponding to the Pt-patterned spots. (B) Mass spectra generated from a 1.5-pmol mix of des-Arg ¹ bradykinin (1), α-Bag Cell Peptide ₁₋₈ (2), and angiotensin I (3) on and off areas of luminescence of these same PSi supports indicate that DIOS does not correlate to the luminescence of PSi. | 100 |
| Figure 3-8 (A) Plot showing the change in solvent contact angles for wafers subjected to (○) dry and (▽) methanol storage for 1 day and (□) dry air and (◇) methanol storage for 6 days. Contact angles were measured for ultrapure water containing 0, 25, 50, and 75% methanol on each surface. The lower contact angles for the surfaces subjected to extended storage indicate a more hydrophilic surface as compared to freshly etched surfaces. (B) Mass spectra generated from a 1.5-pmol peptide mix of des-Arg ¹ bradykinin (1), α-Bag Cell Peptide ₁₋₈ (2), and angiotensin I (3) on surfaces under methanol and dry air storage for 6 days indicate that extended storage in methanol preserves the surface integrity as compared to dry storage. | 100 |
| Figure 3-9 Water contact angles on four different surfaces..... | 101 |
| Figure 3-10 FT-IR spectrum of a day old PSi. | 102 |
| Figure 3-11 Auger electron spectrum of a two day old PSi stored in vacuum chamber..... | 102 |
| Figure 3-12 EDS spectra of surface analysed (a) immediate after etching and (b) 24 hours after. | 103 |
| Figure 3-13 (a) SEI and (b) AFM topography of a DIOS substrate from Waters, and (c) SEI and (d) AFM topography of a NanoHorizons QuickMass substrate. These images show that the DIOS substrate is porous whereas the QuickMass substrate has a columnar-void surface morphology. Calculated surface roughness stated is the root mean square by the same AFM image. The images of the QuickMass target were taken on a used target. On the AFM image (d), there appears a line in the middle of the image. Since GeO is dissolvable in water. This line forms a shape of an edge of an aqueous droplet and may be a drying pattern created by dissolved GeO..... | 106 |
| Figure 3-14 SEI (<i>top</i>) and AFM topography (<i>bottom</i>) of the substrate A48-1 and the substrate prepared by vapour-phase etching. | 108 |

| | |
|---|-----|
| Figure 3-15 Surface morphology of the substrate s10 and s11; (a) optical image, (b) SEI and (c) AFM topography. | 109 |
| Figure 3-16 SEI and AFM topography of surfaces designed for the gas-phase SALDI-MS approach. Surfaces s1, was prepared on the non-polished side of a silicon wafer and s2, s4, s5 prepared on the polished side. Consequently, s1 surface has a native roughness, which was not produced by chemical etching. Blanket indicates the measured surface roughness in R.M.S. | 110 |
| Figure 3-17 AFM topography of the nano-dots/wells the SALDI substrates a1 to a5. a4 exhibits a nano-wells structure and a5 exhibits a nano-dots structure. | 112 |
| Figure 3-18 SEI and AFM topography of the experimental substrates e1 to e3. | 113 |
| Figure 3-19 SEI of (A) HOPG, (B) sanded silicon surface. The sanded surface was produced by grinding with diamond powder. | 114 |
| Figure 3-20 (A) Positive and (B) negative ion SIMS spectra of a DIOS substrate (inserts show selected region). Data acquisition was 8 s long on a $100 \times 100 \mu\text{m}^2$ area (for high mass resolution). | 116 |
| Figure 3-21 (A) Positive and (B) negative ion SIMS spectra of a QuickMass substrate (inserts show selected region). The target was first cleaned by DC sputtering using Cs^+ ion gun with 10kV acceleration voltage to remove the surface contaminants, revealing that the surface was made of germanium. The Fe^+ signal originates from the steel plate on which the germanium film was deposited. Data acquisition was 76 s long on a $300 \times 300 \mu\text{m}^2$ area (for high sensitivity). | 117 |
| Figure 3-22 PCA t_1/t_2 score (<i>top</i>) and p_1/p_2 loading plots (<i>bottom</i>) based on the SIMS positive ion dataset. The samples can be classified into three classes: (1) as-received, (2) experimental, and (3) argon plasma etched (100s) in the score plot. The central cluster of the loading plot is mainly composed of hydrocarbon, silicon oxides and metallic ions. | 120 |
| Figure 3-23 PCA t_1/t_2 score (<i>top</i>) and p_1/p_2 loading plots (<i>bottom</i>) based on the SIMS negative ion dataset. The samples can be roughly classified into four classes: (1) as-received, (2) as-received gas-phases etched surface without prior solvent washing, (3) experimental substrates and (4) argon plasma etched (100s) in the score plot. The central cluster of the loading plot contains fluorine, nitrogen, or sulphur-containing species as well as silicon-containing species. | 121 |
| Figure 3-24 Score contribution plots of substrate s10 (<i>top</i>) and s11 (<i>bottom</i>). Data is derived from Figure 3-23. | 122 |
| Figure 3-25 Positive ion SIMS spectra of (A) as-received SALDI surface s3 and (B) after 100s of argon plasma etching. Data was acquired by raster scanning a $500 \times 500 \mu\text{m}^2$ with $5 \times 10^{11} \text{PI}/\text{cm}^2$ | 125 |
| Figure 3-26 Negative ion SIMS spectrum of (A) as-received SALDI surface s3 and (B) after 100s of argon plasma etching. Data was acquired by raster scanning a $500 \times 500 \mu\text{m}^2$ with $5 \times 10^{11} \text{PI}/\text{cm}^2$ | 126 |
| Figure 3-27 Relative changes in the secondary ion intensity (positive): lower mass (<i>top</i>) and higher mass (<i>bottom</i>). Each peak is first normalised with total ion intensity of all selected ions. Relative change is calculated: | 127 |
| Figure 3-28 Relative changes in the secondary ion intensity (negative). The data was treated in the same way as in positive. | 128 |

| | |
|---|-----|
| Figure 3-29 XPS spectra of as-received SALDI surface s3 (solvent washing, no plasma etching). (A) Survey scan, (B) synthetic components of O 1s high resolution scan, the FWHM constant is constrained to be smaller than 1.5, (C) synthetic components of C 1s high resolution scan, and (D) synthetic components of Si 2p high resolution scan. The prominent peaks in the survey spectra are due to silicon, carbon and oxygen. Small amount of fluorine and iodine were also detected. | 130 |
| Figure 3-30 XPS spectra of argon plasma etched SALDI surface s3 (etched 100s). (A) Survey scan, (B) synthetic components of O 1s high-resolution scan, the FWHM constant is constrained to 1.5, (C) synthetic components of C 1s high-resolution scan, and (D) synthetic components of Si 2p high resolution scan. The survey spectrum is dominated by O 1s peak. Peaks due to silicon or carbon are relative minor. A small amount of fluorine, sodium and tin were also detected. | 131 |
| Figure 3-31 XPS spectra of the as-received DIOS surface. (A) Survey scan, (B) synthetic components of O 1s high-resolution scan, (C) synthetic components of C 1s high-resolution scan and (D) synthetic components of Si 2p high resolution scan. The survey spectrum is dominated by fluorine, oxygen, carbon and silicon. The peak width of core-level O 1s scan is narrower than that of SALDI surface. CF ₂ and CF ₃ are also detected in core-level C 1s scan. The Si 2p core-level spectrum is deconvoluted into 4 sets of peaks. X denotes (CH ₂) ₂ (CF ₂) ₇ CF ₃ group. | 134 |
| Figure 3-32 XPS spectra of a silanised DIOS substrate (surface 4). The substrate was first subjected to 60s of plasma etching and then subsequently fluoro-silanised. (A) Survey scan, (B) synthetic components of O 1s high-resolution scan, (C) synthetic components of C 1s high-resolution scan and (D) synthetic components of Si 2p high resolution scan. The survey spectrum is dominated by fluorine, oxygen, carbon and silicon. The peak width of O 1s spectrum is further reduced to 1.3. The peak located at 536.4 eV detected only in silanised surfaces is assigned to oxygen attached to a fluoro-silane group. The Si 2p core-level spectrum is deconvoluted into 4 sets of peaks. X denotes (CH ₂) ₂ (CF ₂) ₇ CF ₃ group. The intensity of oxides, intermediate sub-oxides and elemental silicon is lower relative to as-received surface, and so the core-level O 1s scan. This observation is contributed to relative strong fluoro-carbons attenuation. | 135 |
| Figure 3-33 Si 2s and 2p survey spectra and the plasmon satellite peaks of (A) SALDI surface s3 and (B) DIOS. | 138 |
| Figure 3-34 (A) Wenzel' and (B) Cassie/Baxter's model of a liquid droplet on a rough surface. | 147 |
| Figure 3-35 Mass spectra of lidocaine obtained using DIOS (<i>top</i>) and QuickMass (<i>bottom</i>) target. The spectra are sum of ~1 min scanning, data was acquired manually. Same laser energy setting was used. The protonated ion of lidocaine is located at <i>m/z</i> 235. Peaks located at <i>m/z</i> 257 and <i>m/z</i> 273 are sodium and potassium adducts, respectively. Peak located at <i>m/z</i> 251 may be an oxidised product of lidocaine. Other peaks observed are believed be contamination. | 150 |
| Figure 3-36 The signal of protonated species obtained on DIOS substrate as a function of laser energy setting of the LDI mass spectrometer. | 152 |
| Figure 3-37 The signal of protonated species obtained on the SALDI surface T-1 (as-received) as a function of laser energy setting of the LDI mass spectrometer. | 152 |

| | |
|---|-----|
| Figure 3-38 (A) Positive ion DIOS mass spectra acquired at 40% and 5% laser energy setting using an analyte mixture containing nalidixic acid ($[M+H]^+$ m/z 233), alprenolol ($[M+H]^+$ m/z 250), atenolol ($[M+H]^+$ m/z 250), metoprolol ($[M+H]^+$ m/z 268), nadolol ($[M+H]^+$ m/z 310), timolol ($[M+H]^+$ m/z 317), labetalol (MH^+ m/z 329), angiotensin I ($[M+H]^+$ m/z 1296.5), vitamin B ₁₂ ($[M+H]^+$ m/z 1355.5, fragment m/z 1329.5, and 971.5), folic acid and erythromycin (each 0.1 mM, 2 μ l droplet). Folic acid and erythromycin were not detected as protonated species. (B) Positive ion SALDI mass spectra acquired at 40% and 15% laser energy setting using a mixture of standard compounds as in the case for DIOS. | 153 |
| Figure 3-39 Comparison of etched and non-etched area on SALDI surface s3 using AP-MALDI-QqLIT system. The ions detected on the etched area were sodium adducts of lidocaine and hydrocarbon clusters, because the SALDI surfaces were contaminated. The ion-molecular reaction most probably occurred at the ion-source led to the observed ions. | 154 |
| Figure 3-40 Positive ion mass spectrum of alkyl quinolones obtained on grey non-etched area of SALDI surface. | 155 |
| Figure 3-41 Background mass spectra of SALDI surface s3 that has been argon plasma treated for 18 mins (<i>top</i>) and an as-received surface (<i>bottom</i>). 304 and 326 peaks may be amines that remain after plasma etching. | 157 |
| Figure 3-42 Mass spectra of vitamin B ₁₂ obtained on SALDI surface with argon plasma treatment for 18 mins (<i>top</i>) and as-received (<i>bottom</i>). Data was acquired by scanning the surface for ~1 min and 50% laser energy setting was used to obtain spectra of both Figure 3-41 and Figure 3-42. | 157 |
| Figure 3-43 Positive ion mass spectra of a mixture containing nalidixic acid ($[M+H]^+$ m/z 233), alprenolol ($[M+H]^+$ m/z 250), atenolol ($[M+H]^+$ m/z 250), metoprolol ($[M+H]^+$ m/z 268), nadolol ($[M+H]^+$ m/z 310), timolol ($[M+H]^+$ m/z 317), labetalol ($[M+H]^+$ m/z 329), angiotensin I ($[M+H]^+$ m/z 1296.5), vitamin B ₁₂ ($[M+H]^+$ m/z 1355.5, fragment m/z 972), folic acid and erythromycin (each 0.1 mM, 2 μ l droplet) obtained using SALDI surface T-1. (a) Lower mass region, no plasma etching, laser setting 15%, (b) lower mass region, plasma etched surface, laser setting 80%, (c) higher mass region, no plasma etching, laser setting 15% and (d) higher mass region, plasma etched surface, laser setting 80%. Peak at m/z 116, 158 were surface contaminants and were removed by plasma etching. The mass resolution, particularly the ion peaks at the higher mass region, is improved. | 158 |
| Figure 3-44 Positive ion SALDI mass spectra of 8-hydroxyquinoline, 2-(4-aminophenyl)-6-methylbenzothiazole, alprenolol, atenolol, metoprolol, nadolol, timolol, labetalol, sotalol, glyburide and vitamin B ₁₂ mixture dissolved in ACN/H ₂ O. Spectrum (A) was acquired on SALDI substrate s10 and (B) was acquired on s11. Signals of sotalol and glyburide could not be distinguished from the noise. | 160 |
| Figure 3-45 Positive ion SALDI mass spectra of bradykinin (1 mM, 2 μ l droplet), dissolved in ACN/H ₂ O obtained using substrate s10 and s11. | 161 |
| Figure 3-46 Ion yield of bradykinin on as-received SALDI surface and ion yield of atenolol and metoprolol on plasma etched SALDI surfaces. The substrates used are annotated on the plot. | 162 |

| | |
|--|-----|
| Figure 3-47 Representative positive mass spectra of graphite and sanded silicon surface. The graphite plate was cleaned by using a sharp blade to scrape off the top layers and washed with methanol and water. The sanded surface was sonicated in propan-2-ol before use..... | 163 |
| Figure 3-48 (A) Positive ion mass spectra acquired on an as-received SALDI surface. The high mass region of the spectrum generated by non-modified SALDI substrate is magnified by 10. (B) Spectra acquired on a modified surface. Substrate was first plasma etched for 40 mins and then fluoro-silane modified. The contamination peaks at the lower mass region are removed after the treatment. (C) Spectra acquired on a modified surface as (B), but the laser energy setting was lowered to 5%. Test mixture contained nalidixic acid ($[M+H]^+$ m/z 233), alprenolol ($[M+H]^+$ m/z 250), atenolol ($[M+H]^+$ m/z 250), metoprolol ($[M+H]^+$ m/z 268), nadolol ($[M+H]^+$ m/z 310), timolol ($[M+H]^+$ m/z 317), labetalol ($[M+H]^+$ m/z 329), angiotensin I ($[M+H]^+$ m/z 1296.5), vitamin B ₁₂ ($[M+H]^+$ m/z 1355.5, fragment m/z 972), folic acid and erythromycin (each 0.1 mM, 2 μ l droplet) obtained using SALDI substrate A48-1. Folic acid and erythromycin were not detected as protonated species. | 165 |
| Figure 3-49 Positive ion SALDI mass spectra of the as-received substrates a1 to a5. A “test mix” used as in Figure 3-48 was also applied here. | 167 |
| Figure 3-50 Positive ion SALDI mass spectra of the modified substrates a1 to a5. The substrates were first argon plasma etched for 40 mins and subsequently silanised at ~90°C for 1 hour..... | 168 |
| Figure 3-51 Positive ion SALDI mass spectra generated by the as-received experimental substrates e1 to e3. A “test mix” used as in Figure 3-48 was also applied here. | 170 |
| Figure 3-52 Positive ion SALDI mass spectra generated by the modified experimental substrates e1 to e3. The substrates were first argon plasma etched for 40 mins and subsequently silanised at ~90°C for 1 hour. | 170 |
| Figure 4-1 DIOS mass spectrum of hytrin (Terazosin HCl)..... | 184 |
| Figure 4-2 DIOS mass spectra of pseudoephedrine, codeine, verapamil and vitamin B ₁₂ and their chemical structures..... | 184 |
| Figure 4-3 Negative ion DIOS mass spectrum of the mixture of nonoadeanoic acid (C ₁₉ H ₃₈ O ₂) (M) and heneicosanoic acid (C ₂₁ H ₄₂ O ₂) (M'). The mass spectra of organic contain typically deprotonated species, sodium dimers and potassium trimers..... | 187 |
| Figure 4-4 Plot of A _{monomeric} species/A _{dimeric} species vs. extraction delay. | 187 |
| Figure 4-5 DIOS mass spectra of two compounds in both the positive mode and negative mode: (a) and (b) theophylline (C ₇ H ₈ N ₄ O ₂ , molecular weight 180, structure shown); (c) and (d) a Br-containing caffeine structure analogue (C ₇ H ₇ N ₄ O ₂ Br, molecular weight 259.1, structure unknown). | 188 |
| Figure 4-6 Comparison of internal energy distribution of thermometer ions desorbed from trimethylsilane derivatised DIOS surfaces and from CHCA matrix in MALDI, using nitrogen nanosecond (ns) laser (solid lines) and Nd:YAG picosecond (ps) laser (dashed lines) excitation. MALDI data were obtained at 25.6 and 45.2 mJ/cm ² with the ns and ps laser, respectively. Corresponding fluences for DIOS were 52.4 mJ/cm ² (ns laser) and 55.8 mJ/cm ² (ps laser). Kinetic shifts are not reflected. | 189 |

| | |
|---|-----|
| Figure 4-7 The origin of the two-step model: expansion of the MALDI plume compared to the laser pulse and excited state decay. Density is plotted vs. time for a plume expanding as an adiabatic free jet. A density of 1 is approximately that of a gas at 1 atm. The expansion stops when the gas reaches the environmental background pressure, which may vary in practice from 1 atm to high vacuum. The inset shows the early behaviour, along with a 3 ns N ₂ laser pulse (blue line) and the typical lifetime of matrix excited states (green line). Only during the time when energy and material densities are high can significant ionisation occur. The solid line represents the density if the sample vaporises smoothly. The dashed line represents an explosive phase change for which a well-defined solid-gas boundary may not exist at short times. | 191 |
| Figure 4-8 Unimolecular and bimolecular matrix processes included in the MALDI ionisation model. (A) Pooling of two S ₁ excitations, yielding an iso-energetic system consisting of a S _n and ground-state pair. (B) Pooling of one S ₁ and one S _n excitation, yielding a system consisting of an ion and ground-state pair. The excess energy above the ion state is converted to heat. Eventually, recombination of an ion (with an electron or negative ion) to yield a ground-state neutral. Pooling reactions of matrix excited states are key steps in energy concentration and ionisation. | 192 |
| Figure 4-9 Positive ion mass spectra of ESI tuning mixture: (A) DIOS and (B) MALDI using α-CHCA matrix. The low mass region was obscured by matrix cluster ions. However, ions in the higher mass region are more effectively detected using MALDI. Spectra were acquired on MALDI-ToF system. | 196 |
| Figure 4-10 Negative ion mass spectra of ESI tuning mixture: (A) DIOS and (B) MALDI using α-CHCA matrix. Insert displaces the detected peak in the higher mass region – centroid and background subtracted to highlight the ion peaks. Spectra were acquired on MALDI Q-ToF system. | 196 |
| Figure 4-11 Positive ion mass spectra of peptide sequencing standard (Tyr-Ala-Glu-Gly-Asp-Val-His-Ala-Thr-Ser-Lys-Pro-Ala-Arg-Arg, molecular weight 1657). (A) MALDI using α-CHCA matrix and (B) fluoro-silane modified DIOS. Concentration of the sample was in nM. | 199 |
| Figure 4-12 Positive ion DIOS mass spectrum of 10 μM bradykinin and angiotensin I acquired on MALDI Q-ToF system. | 200 |
| Figure 4-13 Positive ion DIOS mass spectra of synthetic peptides. (A) Ala ₄ (no addition of acidic buffer), and (B) Gly ₄ with addition of 1% acetic acid. Addition of acidic buffer reduces sensitivity. The dominant salt-bridged cationised dimer is in the form of [2M+Na+K-H] ⁺ | 201 |
| Figure 4-14 Positive ion DIOS mass spectrum of leucine enkephalin acquired on AP-MALDI-QqLIT system. | 202 |
| Figure 4-15 Positive ion DIOS mass spectra of leucine enkephalin on DIOS target acquired on ToF system. (A) Without addition of acidic buffer and (B) with addition of 0.1% formic acid. The peptide is weakly detected as protonated species, and the spectra are dominated by its fragment peaks and salt adducts peaks. Addition of acid buffer reduces the relative intensity of [M+H] ⁺ peak. | 202 |
| Figure 4-16 Positive ion DIOS mass spectrum of leucine enkephalin acquired on Q-ToF system. | 203 |

| | |
|---|-----|
| Figure 4-17 Positive ion DIOS mass spectrum of 20 amino acids mixture acquired on MALDI-ToF system. Molecular ion of arginine and histidine dominates the mass spectrum and the remaining 18 amino acids are either not detected as protonated species or difficult to distinguish from the noise. Peaks located at m/z 73, 102 and 130 are common contaminants and are believed originated from the solvent used. Strong “tailing” is observed with all the major ion peaks..... | 204 |
| Figure 4-18 Positive ion DIOS mass spectrum of adenosine. | 207 |
| Figure 4-19 Positive ion DIOS mass spectrum of atenolol..... | 207 |
| Figure 4-20 Positive ion DIOS mass spectrum of metoprolol..... | 208 |
| Figure 4-21 Positive ion DIOS mass spectrum of nadolol and proposed fragmentation pathway. Capture of two additional protons of C-N fragment leads to the peak located at m/z 254. | 208 |
| Figure 4-22 Positive ion DIOS mass spectrum of timolol and proposed fragmentation pathway. Capture of two additional protons of C-N fragment leads to the peak located at m/z 261..... | 208 |
| Figure 4-23 Positive ion DIOS mass spectrum of sotalol and proposed fragmentation pathway. Loss of water leads to the peak located at m/z 255. Fragmentation at C-N bond produces the peak located at m/z 213. | 209 |
| Figure 4-24 Positive ion DIOS spectrum of labetalol and proposed fragmentation pathway. Loss of water leads to the peak located at m/z 311. Loss of two waters lead to the peak located at m/z 294. Capture of two additional protons of C-N fragment leads to the peak located at m/z 163. | 209 |
| Figure 4-25 Positive ion DIOS mass spectrum of procainamide and proposed fragmentation pathway. Fragmentation reactions occur at three possible C-N sites. The molecular peak was located at m/z 236, and three other dominated fragment ions are located at m/z 163, 120 and 100..... | 210 |
| Figure 4-26 Positive ion DIOS mass spectrum of reserpine and proposed fragmentation pathway. Insert shows the magnified region between m/z 600 and 630. The observation of $[M-H]^+$ ions is related to its low ionisation energy. | 210 |
| Figure 4-27 Positive ion DIOS mass spectrum of octadecyl-trimethylammonium bromide acquired on AP-MALDI-QqLIT system..... | 211 |
| Figure 4-28 Positive ion DIOS mass spectrum of 2-(4-aminophenyl)-6-methyl-benzothiazole acquired on AP-MALDI-QqLIT system..... | 211 |
| Figure 4-29 Positive ion DIOS mass spectrum of glyburide on (A) fluoro-silane modified DIOS target with addition of 0.1% formic acid and (B) on as-received DIOS with no addition of acid. Different ionic products were obtained in these cases. | 212 |
| Figure 4-30 Positive ion DIOS mass spectrum of (A) 1 mM raffinose/sodium hydroxide (1:1) mixture and (B) 0.47 mM of β -cyclodextrin/sodium hydroxide (1:4) mixture. Data obtained on MALDI Q-ToF system using recycled DIOS target. The sensitivity significantly improved after the hydrophilicity of the surface is increased. The molar excess of hydroxide used in β -cyclodextrin mixture may account for a serious of hydrolysis products observed. | 213 |
| Figure 4-31 Negative ion DIOS mass spectra of (A) cholic acid (B) diflunisal acquired on MALDI Q-ToF system. Fragmentation of diflunisal occurs via loss of carboxylic acid group. Peak m/z 267 is a phosphate contaminant (determined by MS/MS). | 215 |

| | |
|---|-----|
| Figure 4-32 (A) Positive and (B) negative ion DIOS mass spectrum of flufenamic acid acquired on MALDI Q-ToF system. Fragmentation occurs via loss of H ₂ O (M-OH), <i>m/z</i> 264, and CO ₂ (M-COOH), <i>m/z</i> 236, in carboxylic acid group..... | 215 |
| Figure 4-33 (A) Positive and (B) negative ion DIOS mass spectrum of nalidixic acid acquired on MALDI Q-ToF system. Anti-bacterial agent nalidixic acid is a quinolone acid and it gives both protonated and deprotonated ions and a number of fragment ions under positive and negative mode, respectively. The ion yield of fragments is higher than that of molecular ion. | 216 |
| Figure 4-34 (A) Positive and (B) negative ion DIOS mass spectrum of naproxen acquired on MALDI Q-ToF system. Radical cation was observed in positive ion mode. Fragmentation occurs via loss of a carboxylic acid group. Naproxen is a non-steroidal anti-inflammatory drug..... | 216 |
| Figure 4-35 Proposed fragmentation pathways of nalidixic acid. The positive ions observed are believed due to fragmentation reaction occurs via loss of water and carboxylic acid group. The negative ions observed are believed due to fragmentation at C-N bond. Such a tendency is possibly related to the fragmentation leading to stabilisation by resonance, via the aromatic system and is therefore more energetically favourable. Capturing of two hydrogen atoms was also observed..... | 217 |
| Figure 4-36 Negative ion DIOS mass spectrum of (A) heptadecafluorooctanesulfonic acid (PFOS) potassium salt solution, (B) perfluoroundecanoic acid (PFUnA), and (C) pentadecafluorooctanoic acid (PFOA). Data obtained on MALDI Q-ToF system. | 218 |
| Figure 4-37 (A) positive and (B) negative ion DIOS spectra of 0.1 mM fluorescein. Data obtained on MALDI Q-ToF system. | 219 |
| Figure 4-38 Spectra of verapamil deposited with H ₂ O and D ₂ O on plasma etched SALDI surface. ... | 234 |
| Figure 4-39 DIOS spectra of dopamine with and without addition of acidic modifiers. The spectra are presented normalised to peak <i>m/z</i> 167. Dopamine is an important neurotransmitter. | 235 |
| Figure 4-40 DIOS spectra of adenosine, with or without addition of acidic modifiers. The spectra are presented with the same vertical scale. Adenosine is a nucleoside. | 235 |
| Figure 4-41 DIOS spectra of diphenhydramine, with or without addition of acidic modifiers. The spectra are presented with the same vertical scale. Diphenhydramine is an antihistamine. | 236 |
| Figure 4-42 Proposed fragmentation pathways of diphenhydramine. Protonation occurs at the oxygen, unlike ESI, is energetically unfavourable and leads to fragmentation. | 236 |
| Figure 4-43 DIOS spectra of ornidazole with addition of 1% formic acid and no addition of acidic buffer. Spectra are presented with the same vertical scale. Ornidazole is an anti-protozoan drug, commonly used in poultry industry. | 237 |
| Figure 4-44 (A) Positive ion DIOS spectrum of a copper(II) acetate/sodium chloride mixture acquired on MALDI-ToF system. (B) Negative ion DIOS spectrum of a copper(II) acetate/iron(III) chloride mixture acquired on MALDI Q-ToF system..... | 238 |
| Figure 4-45 Optical images of the surface that has not be used, used for LDI investigation, and damaged by laser..... | 240 |
| Figure 4-46 SEM image of DIOS substrate after use for LDI investigation. The surface had been subsequently washed and stored in propan-2-ol to remove deposited analyte after LDI | |

| | |
|---|-----|
| investigation. The circles highlight the formation of big pores after the substrate was used for LDI investigation. The SEI also shows particles scattered on the surface. | 240 |
| Figure 4-47 SEM images of DIOS substrate after LDI investigation. The surface had not been washed and stored in sealed container in freezer after use. The SEI on the left shows a lower magnification of a sample well. The spiral shape laser “burn mark” was formed as a result of spiral stage movement during data acquisition. Two areas were chosen with high magnification: (A) area that has not been modified by laser and (B) area that has been laser modified..... | 241 |
| Figure 4-48 SEM image of the SALDI substrate s2 after SALDI-MS investigation showing a ring modified by laser etching. The substrate was stored in propan-2-ol until analysis..... | 244 |
| Figure 4-49 XPS imaging of the SALDI surface, s2, showing the ring that has been laser modified. . | 244 |
| Figure 4-50 Reconstructed Si 2p spectra for each pixel generated from multi-spectral datasets summed for the regions that have been laser modified and without defined by reference to the bicolour image..... | 245 |
| Figure 4-51 Reconstructed O 1s spectra for each pixel generated from multi-spectral datasets summed for the regions that has been laser modified and without defined by reference to the bicolour image. The deconvolution of SiO ₂ and SiOH is calculated by constricting the peak width being identical..... | 246 |
| Figure 4-52 2D schematic of (A) smooth and (B) “triangular” rough silicon surface. On a smooth surface, the model of a silicon single-crystal substrate composed of an overlayer of silicon dioxide of thickness d , a contamination layer, and an intermediate oxides layer at the silicon dioxide/silicon interface. The photoelectrons emit at an angle normal to the surface and the thickness of dioxide $d = 3\lambda$, where λ is the attenuation length. On a simplified model of a rough surface, the surface is composed of a number of segments of smooth surface tilted according to the magnitude of the localised roughness, by an off-axis angle, θ , which is the angle between the central axis of the XPS analyser and the surface normal of the sample. Accordingly, the attenuation length measured is larger than the actual thickness of dioxide overlayer..... | 247 |
| Figure 4-53 Optical image of SALDI substrate s1 after SALDI-MS investigation showing an arc caused by laser etching. The green square indicates the area used for SIMS imaging. The substrate was stored in propanol until analysis. | 248 |
| Figure 4-54 ToF-SIMS ion images of laser modified SALDI surface s1. Logarithmic scaling and Poisson correction is used to scale the contrast of the images. | 249 |
| Figure 4-55 SIMS spectra of (A) modified region and (B) non-modified region under positive mode. The spectra are regenerated by summing the spectra collected at the selected region of interest (ROI), insert. Significant differences between the spectra are highlighted by red boxes..... | 251 |
| Figure 4-56 SIMS spectra of (A) modified region and (B) non-modified region under negative mode. The spectra are regenerated by summing the spectra collected at the selected region of interest (ROI), insert. Significant differences between the spectra are highlighted by blue boxes..... | 252 |
| Figure 4-57 Optical image of the as-received SALDI substrate s4. The substrate was stored in propanol until analysis. | 253 |

| | |
|--|-----|
| Figure 4-58 ToF-SIMS ion images of the as-received SALDI surface s4. The images suggest the SALDI substrates are not iodine passivated. Logarithmic scaling and/or Poisson correction is used to scale the contrast of the images. | 254 |
| Figure 4-59 2D schematic of the effects of laser modification to the SALDI surface in SALDI-MS environment. Laser induces oxidation of the surface and leads to formation of Si-OH moiety. | 255 |
| Figure 4-60 Proposed exciton-mediated hydroxylation reaction occurs during SALDI process. $R = H, OH, \text{ or } C_xH_y$. An unbound exciton produced by UV absorption leads to a surface-localised positive charge. This surface charge can then interact with an oxidising agent, or any nucleophile. In this case, where water is the nucleophile, Si-OH is formed. The abstract of an electron from exciton produces the final neutral species observed. | 261 |
| Figure 4-61 Schematic of the band structure of indirect bandgap seiconductors: (A) silicon and (B) germanium. E_g is the bandgap energy. In contrast to direct bandgap semiconductors, the minimum energy in the conduction band is shifted by a k -vector relative to the valence band. The k -vector difference represents a difference in momentum. | 264 |
| Figure 4-62 Schematic illustration of band bending near the surface of n -type semiconductor. (A) illustrates the disequilibrium between the bulk and the surface. (B) shows band at equilibrium. E_C and E_V are the conduction and valence-band edges, E_F the Fermi energy, E_D the energy of the bulk donor (n -type). $Q_{SS} = -Q_{SC}$ are the charges accumulated at the surface and in the space charge layer. $eV_S = eV(z = 0)$ denotes the band bending. (C) Carrier excitation and transport near the surface during photo-excitation that lead to the formation of electron-hole pairs (e^- and h^+). Non-radiative recombination of e^- and h^+ takes place only at the electronic surface state. | 265 |
| Figure 4-63 Proposed reaction profile of protonated ion formation (<i>left</i>) and deprotonated ion and metallic aggregate formation (<i>right</i>). “*” denotes excited state. | 268 |
| Figure 4-64 A proposed model of laser-induced desorption/ionisation on a porous surface. Two-dimension adsorbate on the wall of the pore is excited and desorbed into gas-phase. Unlike the adsorbate on a rough surface, the resulting plume cannot expand into all directions but into one dimension desorbed phase due to the confinement imposed by the porous structure. This generates a pressure gradient and ejects the ions into vacuum. | 270 |
| Figure 5-1 The validation process. | 281 |
| Figure 5-2 Equipment qualification (4Qs). | 282 |
| Figure 5-3 ICH method validation parameters. | 282 |
| Figure 5-4 (A) Well-to-well signal intensity of 360 fmol of ranitidine on 16 wells of a DIOS chip. RSD = 12% (no internal standard). (B) Chip-to-chip average intensities with standard deviation and %RSD. Each colour bar represents an individual DIOS target, three targets per analyte using a M@LDI R, Laser = 15% of maximum, 100 shots. Each chip was spotted 16 times with the desired analyte (0.5 μ L of 250 ng/mL solution except for theophylline which was at 5000 ng/mL due to decreased DIOS performance). Procainamide exhibits detector saturation at 25500 counts. The SDs tend to be lower above 15000 counts. | 284 |

| | |
|--|-----|
| Figure 5-5 DIOS-TOF-MS LSD reproducibility. The sample was applied to 96 wells DIOS plate. 110 data point were collected from those wells. The calculated standard deviation was about $\pm 10\%$ | 285 |
| Figure 5-6 (A) Dynamic range for codeine detection. Insert shows the %RSDs without an internal standard. (B) Codeine response compared to deuterated codeine internal standard. Insert shows the %RSD with internal standard. | 285 |
| Figure 5-7 (A) DIOS-ToF MS standard calibration curve for choline quantification correlating the intensity ratio of choline to the internal standard choline-d ₉ with the concentration of choline. Each data point was run in triplet. (B) LSD calibration curve from 0.05 to 10.00 g/mL using LSD-d ₃ IS and (C) Fentanyl calibration curve from 0.01 to 10.00 g/mL using Fentanyl-d ₅ internal standard. Each data point was run in quadruplet. | 286 |
| Figure 5-8 (A) Calibration curve for sulphated pregnenolone using DIOS-MS and nano-ESI precursor ion scanning. (B and C) DIOS spectra of human urine extracts. The amount of the internal standard (pregnenolone-d ₄) was 316 fmol of pregnenolone. The same amount of the same internal standard was used as in the calibration curve, and samples from males and females were found to contain different amounts of testosterone sulphate. Other conjugated steroids were assigned based upon their known masses or post source decay analysis. | 288 |
| Figure 5-9 Peak intensity versus serum salicylic acid concentration in serum obtained by DIOS-MS measurements after SPE. (n = 5). Y-axis represents the ratio of unlabeled to deuterium-labelled species and x represents the mM concentration of salicylic acid. The curve showed a linear relationship in a serum range of 0.14 to 4.2 mM (20–600 mg/l)..... | 288 |
| Figure 5-10 Chemical structure of (A and B) aeruginosine A and B, (C) pyocyanine, (D) fluorescein/pyoverdine and (E) prochelin..... | 291 |
| Figure 5-11 QSSMs and QSIs. | 293 |
| Figure 5-12 HHQ/PQS dual cell-to-cell communication system. HHQ is synthesised by a bacterial cell and released into the extracellular environment. HHQ is then taken up by neighbouring cells and converted by the action of PqsH into PQS. PQS is exported and used directly as a signal molecule by adjacent cells. | 293 |
| Figure 5-13 Solvent extract procedure. Water extract appears to be blood red, ethyl acetate extract appears to be greenish brown. Other extract are yellow in colour. | 297 |
| Figure 5-14 Extraction of (A) aqueous culture medium and (B) cell pellet by chloroform/methanol and chloroform/butanol. +AF and –AF denotes the bacteria was growth in a medium with the addition of antifoam and without, respectively. | 299 |
| Figure 5-15 Ion intensity of 0.1 mM procainamide versus laser setting. Both the $[M+H]^+$ ion and its fragment at m/z 163 are shown on the plot. Each data point is an average of three replicas. The error bar indicates the highest and the lowest value obtained. | 302 |
| Figure 5-16 DIOS mass spectra of 0.1 mM procainamide at different laser setting: (A) laser setting at 100, (B) 190, (C) 250 and (D) 350. Data was acquired in positive mode with 1 μ l droplet of solution deposited onto each sample well, laser scanned across the well in 1 min. Raw spectra are smoothed, and background subtracted. | 302 |

| | |
|--|-----|
| Figure 5-17 Ion intensity of 0.1 mM cholic acid $[M-H]^-$ versa laser setting. Each data point is an average of three replicas. The error bar indicates the highest and the lowest value obtained. | 303 |
| Figure 5-18 DIOS mass spectra of 0.1 mM cholic acid at different laser setting: (A) laser setting 180, (B) 250 and (C) 350. Data was acquired in negative mode with 2 μ l droplet of solution deposited onto each sample well, laser scanned across the well in 1 min. Raw spectra are smoothed, and background subtracted. Peak at m/z 267 is a phosphate contaminant. | 303 |
| Figure 5-19 Ion intensity of HPLC peptide standard mixture versa laser setting. The peaks corresponding to potassiated methionine and leucine enkephalin and protonated Gly-Tyr and angiotensin II are chosen for plotting. An unknown peak, which is believed to be Val-Tyr-Val, is included. Each data point is the average value of two to eight replicas. The error bar indicates the standard deviation of the laser setting 180 and 200, where $n = 8$ and $n = 4$, respectively. | 305 |
| Figure 5-20 DIOS mass spectra of HPLC peptide standard mixture: (A) laser setting 250 and (B) 350. The concentration of the sample solution was not known. Data was acquired in positive mode with 1 μ l droplet of solution deposited onto each sample well, laser scanned across the well in 1 min. Raw spectra are smoothed, and background subtracted..... | 305 |
| Figure 5-21 Calibration curve of arginine $[M+H]^+$. 1 μ l of solution of concentration from 63 nM to 982 μ M, was deposited onto the target. Data was acquired with 2 min spiral scan at laser setting 220. The LOD was 1.6 fmol. Linearity was 2 orders in magnetite. | 306 |
| Figure 5-22 Calibration curve of metoprolol $[M+H]^+$. 1 μ l of solution of concentration from 6.4 nM to 298 μ M, was deposited onto the target. Data was acquired with 2 min spiral scan at laser setting 220. The LOD was 32 fmol. Linearity was 2 orders in magnetite. | 307 |
| Figure 5-23 Calibration curve of atenolol $[M+H]^+$. 1 μ l of solution of concentration from 12.8 nM to 0.2 mM, was deposited onto the target. Data was acquired with 2 min spiral scan at laser setting 220. The LOD was 64 fmol. Linearity was 2.5 orders in magnetite. | 307 |
| Figure 5-24 Calibration curve of acetylcholine M^+ . 1 μ l of solution of concentration from 12.8 nM to 0.2 mM, was deposited onto the target. Data was acquired with 2 min spiral scan at laser setting 220. The LOD was 12.8 fmol. Linearity was 2 orders in magnetite. The M^+ ion intensity decreased considerably after the concentration of the analyte (acetylcholine chloride) increased over 8 pmol. This was possibly because of the ion-pairing effect due to the increased concentration of chloride ion. | 308 |
| Figure 5-25 Optical micrographs of two spotted DIOS sample wells. The image on the left shows a relatively uniform distribution of the analyte and appears on the image as a circular “water mark” whereas the one on the right shows a non-uniform distribution and the analyte coverage was only ~60%. The white patch in the middle of the image is the laser spot. The images were taken during data acquisition. | 315 |
| Figure 5-26 (A) Positive ion DIOS mass spectrum of human urine and (B) blank (ACN/H ₂ O). Urine was diluted in 1:1 ACN/H ₂ O for 20 times. Data was acquired with 120s spiral scan and the spectra were processed with adaptive background subtraction. | 317 |

| | |
|---|-----|
| Figure 5-27 (A) Negative ion DIOS mass spectrum of human urine and (B) blank (ACN/H ₂ O). Urine was diluted in 1:1 ACN/H ₂ O for 20 times. Data was acquired with 120s spiral scan and the spectra were processed with adaptive background subtraction. | 317 |
| Figure 5-28 (A) Positive and (B) negative ion DIOS mass spectra of human urine donated by the writer. The writer suffers diabetic neuropathy. Glucose was detected as sodium adduct [M+Na] ⁺ at <i>m/z</i> 203. The sample was prepared by diethyl ether/hexane followed by chloroform/butanol. Addition of HCl or NaOH was not required and only suppressed the ion formation. 1 µl of droplet was added onto the sample well. Data was acquired using 120s spiral scan. Laser setting for positive and negative mode was 220 and 200, respectively. Spectra were centroid and processed with adaptive background subtraction. | 319 |
| Figure 5-29 Positive ion DIOS mass spectra of chloroform/butanol extracts. (A) Addition of HCl, (B) addition of NaOH and (C) no addition of modifier. 1 µl of droplet was added onto the sample well. Data was acquired using 120s spiral scan. Laser setting was 220. Spectra were centroid and processed with adaptive background subtraction. | 320 |
| Figure 5-30 Negative ion DIOS mass spectra of chloroform/butanol extracts. (A) Addition of HCl, (B) addition of NaOH and (C) no addition of modifier. 1 µl of droplet was added onto the sample well. Data was acquired using 120s spiral scan. Laser setting was 200. Spectra were centroid and processed with adaptive background subtraction. | 320 |
| Figure 5-31 Positive ion DIOS mass spectra of diethyl ether extracts. (A) Addition of HCl, (B) addition of NaOH and (C) no addition of modifier. 1 µl of droplet was added onto the sample well. Data was acquired using 120s spiral scan. Laser setting was 220, 230 and 210 respectively. Spectra were centroid and processed with adaptive background subtraction. | 321 |
| Figure 5-32 Negative ion DIOS mass spectra of diethyl ether extracts. (A) Addition of HCl, (B) addition of NaOH and (C) no addition of modifier. 1 µl of droplet was added onto the sample well. Data was acquired using 120s spiral scan. Laser setting was 220. Spectra were centroid and processed with adaptive background subtraction. | 321 |
| Figure 5-33 Positive ion DIOS spectra of ethyl acetate extracts. (A) Addition of HCl, (B) addition of NaOH and (C) no addition of modifier. 1 µl of droplet was added onto the sample well. Data was acquired using 120s spiral scan. Laser setting was 220. Spectra were centroid and processed with adaptive background subtraction. | 322 |
| Figure 5-34 Negative ion DIOS spectra of ethyl acetate extracts. (A) Addition of HCl, (B) addition of NaOH and (C) no addition of modifier. 1 µl of droplet was added onto the sample well. Data was acquired using 120s spiral scan. Laser setting was 220. Spectra were centroid and processed with adaptive background subtraction. | 322 |
| Figure 5-35 Negative ion DIOS MS/MS spectra of urine extract with precursor ions <i>m/z</i> 339, 427, 415 and 433. Two major fragment ions at <i>m/z</i> 193 and 209 were obtained. | 323 |
| Figure 5-36 Detection characteristic of the plasma extract. Each data point represents the average value of three replicas. The error bar indicates the highest and the lowest value obtained. | 328 |

| | |
|--|-----|
| Figure 5-37 A representative positive ion DIOS mass spectrum of plasma extract. Data was acquired with 1 min raster scan. Laser setting was 220. The spectrum is smoothed and background subtracted. | 329 |
| Figure 5-38 A representative negative ion DIOS mass spectrum of plasma extract. Data was acquired with 180s spiral scan. Laser setting was 170. The spectrum is smoothed and background subtracted. | 329 |
| Figure 5-39 Positive DIOS MS/MS spectra of plasma exact. Precursor ions m/z 808.6, 780.6, 721.5 and 666.5 were selected and all these ions produce a product ion m/z 147 and 86. Precursor ions m/z 780.6, 721.5 and 666.5 may also be related as common product ions m/z 597.5 or 542.5 are observed. | 330 |
| Figure 5-40 (A) The total ion counts, and (B) the number of ions detected over 5% of the BPI, of nine successive data acquired over nine sample wells, either by spiral scan mode or vertical scan mode. Raw data was first subject to Automatic Peak Detection function of the MassLynx software to remove electronic and chemical noise and the peak lists were then exported to Excel for calculation. Threshold value was set by using Data Threshold function of the MassLynx software to hide data of which the intensity below a set threshold value or in term of percentage scales of the base peak. | 332 |
| Figure 5-41 PCA score plot of (A) PC_1/PC_2 and (B) PC_2/PC_3 . Data was acquired in successively over nine sample wells either by spiral scan mode or by vertical scan mode. PC_1 , 2 and 3 represents 60% of the variability of the dataset. | 333 |
| Figure 5-42 Detection characteristic of liver methanolic extract under positive ion mode. Each data point is the average value of three to five replicas. The error bar indicates the highest and the lowest value obtained. | 334 |
| Figure 5-43 Detection characteristic of liver methanolic extract under negative ion mode. Each data point is the average value of three replicas. The error bar indicates the highest and the lowest value obtained. | 335 |
| Figure 5-44 PCA $t_1/t_2/t_3$ score plot (A) and $p_1/p_2/p_3$ loading plot (B). Dataset was acquired in positive mode. | 337 |
| Figure 5-45 Positive ion DIOS mass spectra of liver extracts. Spectra are arranged in their similarity. Data was acquired with 120s spiral scan and laser setting was 220. The raw spectra are smoothed and background subtracted. | 338 |
| Figure 5-46 PCA $t_1/t_2/t_3$ score plot (A) and $p_1/p_2/p_3$ loading plot (B). Dataset was acquired in negative mode. | 339 |
| Figure 5-47 Negative ion DIOS mass spectra of liver extracts. Spectra are arranged in their similarity. The spectra were acquired with 2 mins spiral scan and laser setting 210. The raw spectra are smoothed and background subtracted. | 340 |
| Figure 5-48 Positive ion DIOS mass spectra of 1:4 (A) methanol/chloroform and (B) methanol/acetonitrile rats' liver tissue extracts. Data was acquired with 120s spiral scan. Laser setting was 230. Raw spectra were centroid and processed with adaptive background subtraction. Region between m/z 300 to 1000 was magnified two times. | 359 |

| | |
|---|-----|
| Figure 5-49 Negative ion DIOS mass spectra of 1:4 (A) methanol/chloroform and (B) methanol/acetonitrile rats' liver tissue extracts. Data was acquired with 120s spiral scan. Laser setting was 200. Raw spectra were centroid and processed with adaptive background subtraction. Region between m/z 400 to 1000 was magnified two times. | 359 |
| Figure 5-50 Positive ion DIOS mass spectra of (A) C ₈ -AHL, (B) 3-oxo-C ₈ -HSL and (C) 3-hydroxyl-C ₈ -HSL. The spectra are dominated by their [M+Na] ⁺ ions. The ions located at m/z 306 and 224 in 3-hydroxyl-C ₈ -HSL spectrum are unknown contaminants from the sample. Inserts displace their structural and chemical formulae. Spectra were acquired by 120s spiral scan at laser setting 210. | 361 |
| Figure 5-51 Negative ion DIOS mass spectra of (A) C ₈ -AHL, (B) 3-oxo-C ₈ -HSL and (C) 3-hydroxyl-C ₈ -HSL. The spectra of C ₈ -HSL and 3-oxo-C ₈ -HSL are dominated by their [M-H] ⁻ ions. Ion peaks located at m/z 168 and 138 are unknown, which could be contaminants or degradation products. The deprotonated species of 3-hydroxyl-C ₈ -HSL is not seen, but the spectrum is dominated by ions located at m/z 122 and 142, which are contaminants from the sample. Inserts displace their structural formulae. Spectra were acquired by 120s spiral scan at laser setting 210. | 362 |
| Figure 5-52 Positive ion DIOS mass spectrum of a mixture of equal molar 3-hydroxyl HSLs. The alkyl chain length of HSLs varies from C4 to C14. Ions detected are sodium adducts. Data was acquired with 120s spiral scan at laser setting 220. | 363 |
| Figure 5-53 Positive ion DIOS mass spectra of (A) a mixture of AQSs and (B) PQS. The molecules are detected as [M+H] ⁺ , dimers and trimers. Data was acquired with 120s spiral scan at laser setting 210. | 364 |
| Figure 5-54 Negative ion DIOS mass spectra of (A) a mixture of AQS and HAQs and (B) PQS. The molecules are detected as [M-H] ⁻ , dimers and trimers. Data was acquired with 60s spiral scan at laser setting 210. | 364 |
| Figure 5-55 Positive ion DIOS mass spectra of bacterial medium and antifoam/NaI mixture..... | 365 |
| Figure 5-56 Positive ion DIOS mass spectra of bacterial culturing medium. (A) As-received (no sample preparation), (B) ETA-chloroform/butanol extract, and (C) ETA-chloroform/methanol extract. The spectra are presented in the same vertical scale. Region of m/z 700-1200 is magnified by 10 times. Data was acquired by 120s spiral scan at laser setting 220. | 367 |
| Figure 5-57 Positive ion DIOS mass spectra of bacterial feeding medium (control). (A) As-received (no sample preparation), (B) ETA-chloroform/butanol extract and (C) ETA-chloroform/methanol extract. The spectra are presented in the same vertical scale as in Figure 5-56. Data was acquired by 120s spiral scan at laser setting 220. | 367 |
| Figure 5-58 Negative ion DIOS mass spectra of bacterial culturing medium. (A) As-received (no sample preparation), (B) ETA-chloroform/butanol extract and (C) ETA-chloroform/methanol extract. The spectra are presented in the same vertical scale. Region of m/z 600-1000 is magnified by 10 times. Data was acquired by 120s spiral scan at laser setting 210. | 368 |
| Figure 5-59 Negative ion DIOS mass spectra of bacterial feeding media. (A) As-received (no sample preparation), (B) ETA-chloroform/butanol extract and (C) ETA-chloroform/methanol extract. | |

| | |
|--|-----|
| The spectra are presented in the same vertical scale as in Figure 5-58. Data was acquired by 120s spiral scan at laser setting 210..... | 368 |
| Figure 5-60 Positive ion DIOS mass spectra of <i>P. aeruginosa</i> bacterial cell pellets extracts: (A) chloroform/methanol and (B) chloroform/butanol. The spectra were acquired with 120s spiral scan at laser setting 220. | 369 |
| Figure 5-61 Negative ion DIOS mass spectra of <i>P. aeruginosa</i> bacterial cell pellets extracts: (A) chloroform/methanol and (B) chloroform/butanol. The spectra were acquired with 120s spiral scan at laser setting 230. The mass region m/z 500-1000 was magnified by 10 times..... | 369 |
| Figure 5-62 Positive and negative ion DIOS mass spectra of <i>P. aeruginosa</i> bacterial cell pellets extracts: (A) and (C) chloroform/methanol, and (B) and (D) chloroform/butanol. The bacterial cell pellet used for chloroform/butanol was cultured without addition of antifoam to the bioreactor whereas the cell pellet for chloroform/methanol was cultured with addition of antifoam and was harvested a day later. The spectra were acquired with 120s spiral scan at laser setting 220 and 210 for positive and negative ion mode, respectively..... | 370 |
| Figure 6-1 Molecular imaging of rat brain tissue by DESI, MALDI and SIMS. | 394 |
| Figure 6-2 Schematic of Waters Synapt™ HDMS™ system, provided by the manufacturer..... | 395 |

List of Tables

| | |
|--|-----|
| Table 1-1 Common analytical protocols used in metabolomics investigations, advantages and disadvantages. | 5 |
| Table 1-2 Common UV-MALDI matrices and their major applications. | 8 |
| Table 2-1 Organic electrolytes used in Si electrochemistry and some of their major properties. | 49 |
| Table 2-2 Comparison of various surface techniques commonly used in characterisation of PSi. | 55 |
| Table 2-3 Etching condition of standard electrochemical etched silicon SALDI surfaces (<i>J</i> is etching current density, <i>t</i> is etching time), HF:EtOH denotes HF/ethanolic solution and HF:EtOH:I ₂ denotes iodine in HF/ethanoic solution, respectively. Some surfaces were etched twice and are denoted by a slash. | 70 |
| Table 2-4 Etching condition of experimental electrochemical etched silicon SALDI surfaces. | 71 |
| Table 2-5 Other surfaces and their preparations. | 71 |
| Table 2-6 List of substances used for mass spectrometric investigation | 72 |
| Table 3-1 Atomic concentration of as-received and plasma etched (100s) SALDI surface s3 determined by XPS survey scan measurement. | 129 |
| Table 3-2 Atomic concentration and surface concentration of carbonaceous species of as-received, as-received then silanised, plasma etched for 60s, and plasma etched for 60s then silanised DIOS surfaces determined by survey scan and high resolution C 1s core scan respectively. (Surface concentration = relative concentration × atomic % concentration of C 1s) | 132 |
| Table 3-3 WCA measurements of DIOS and SALDI surface A48-1. The data presented are the average of at least 3 measurements. The SALDI substrate was stored in propan-2-ol for two months. .. | 139 |
| Table 4-1 Literature and calculated thermochemical values of various compounds. | 186 |
| Table 4-2 List of substances, their chemical formulae and their exact masses in the Agilent ESI tuning mix. | 197 |
| Table 4-3 Expected and detected mass peaks of electrospray calibrant solution using DIOS and MALDI under positive mode, derived from Figure 4-9. | 197 |
| Table 4-4 Expected and detected mass peaks of electrospray calibrant solution using DIOS and MALDI under negative mode, derived from Figure 4-10. | 197 |
| Table 4-5 Aqueous basicities, isoelectric points (pI), proton affinities (PA) and hydrophobicities (log P) of 20 most common amino acids. | 205 |
| Table 4-6 Selected compounds tested using DIOS-MS. Their chemical structures, molecular weights (MW), ionisation energies (IE), proton affinities (PA) and aqueous basicities (pKa values) are presented along with the DIOS spectral responds. The classification is based on the functional group of interest. | 220 |
| Table 4-7 Comparison of the elemental and molecular ions detected by ToF-SIMS at different region of the surface. | 248 |
| Table 4-8 Comparison of the elemental and molecular ions detected by ToF-SIMS at upper and lower region of the surface. | 255 |

| | |
|--|-----|
| Table 5-1 Metabolite databases. | 300 |
| Table 5-2 Target-to-target precision. Three different targets were used and the experiments were carried over in three days. 1 μ solution deposited onto the target. Data was acquired with 2 min spiral scan, laser setting was 220. Six replicas were used for the calculation. | 310 |
| Table 5-3 Precision and robustness. Except naproxen, the data was calculated using the ion intensity of [M+H] ⁺ or [M-H] ⁻ molecular ion. Data was only acquired at suboptimal conditions and was a design of the experiment (<i>i.e.</i> robustness). “Time” refers to acquisition time. | 311 |
| Table 5-4 The precision of ion intensity (IC) of individual peptide in a HPLC peptides standard mixture before and after normalisation to TIC. TIC is summation of all ion counts in the range between m/z 100-1500 in each spectrum. Data was acquired in positive mode, at laser setting 180, raster scan for 60s. Eight replicas are used for the calculation. The normalised values are calculated by $\frac{IC}{TIC} \times 100\%$ and are percentages of TIC. Two decimal points are used because the normalised values are small. SD denotes the standard deviation. | 314 |
| Table 5-5 The precision of ion intensity (IC) of individual substance in a metabonomics test mix. Data was acquired in positive mode, at laser setting 180, raster scan for 60s. 12 replicas were used for the calculation. 4-nitrobenzoic acid, hippuric acid, and theophylline were not detected under positive mode. Data processing is identical to the HPLC peptides standard mixture above. | 314 |
| Table 5-6 Result of the Metline database search for metabolites present in the urine extract derived from the data in Figure 5-28A. The spectrum was first internal “lockmassed” on the sodium adduct of glucose (m/z 203.0532). The name of the proposed metabolites, the formulae, the calculated exact masses and the mass differences (in ppm) are reported in the table. “-” denotes no match has been found within 5 ppm tolerance. | 324 |
| Table 5-7 Result of the Metline database search for metabolites present in the lambs’ liver extracts derived from the data in Figure 5-45. The spectra were first internal “lockmassed” on the fragment ion of phosphocholine (m/z 184.0739). The name of the proposed metabolites, the formulae, the calculated exact masses and the mass differences (in ppm) are reported in the table. “-” denotes no match has been found within 5 ppm tolerance. | 341 |
| Table 5-8 Results of LipidMap search in between the mass range m/z 400-600 for di/triacylglycerols (DG/TG) present in the lambs’ liver extracts derived from the data in Figure 5-45. The spectra were first internal “lockmassed” on the fragment ion of phosphocholine (m/z 184.0739). The formulae, the calculated exact masses and the delta mass (in <i>amu</i>) of the proposed di/triacylglycerols are reported in the table. A maximum delta mass of ± 0.01 <i>amu</i> limit was applied to the search. Only the inputted ions returned a match are listed. C is the number of carbons and DB is the number of double bonds of the proposed di/triacylglycerol. | 345 |
| Table 5-9 Results of LipidMap search in between the mass range m/z 600-1000 for glycerophospholipids present in the lambs’ liver extracts derived from the data in Figure 5-45. The spectra were first internal “lockmassed” on the fragment ion of phosphocholine (m/z 184.0739). The formulae, the calculated exact masses and the delta mass (in <i>amu</i>) of the proposed glycerophospholipids are reported in the table. Only the inputted ions returned a match | |

are listed. A maximum delta mass of ± 0.01 amu limit was applied to the search. C is the number of carbons and DB is the number of double bonds of the proposed glycerophospholipid. Subclasses of glycerophospholipids include phosphocholine (PC), phosphatidylethanolamine (PE), protegrin (PG), phosphatidyl serine (PS), and phosphoinositide (PI).....348

CHAPTER 1 INTRODUCTION

1.1 Systems Biology: From Genome to Metabolome – Challenges of Biochemical Profiling

With the progress of molecular biology projects that accumulate in-depth knowledge of molecular nature of biological systems, the system-level understanding of a biological system has now possibly been grounded on the molecular level. These dramatic technological advances in the life sciences over the past decades have forged a new era of research including the emerging field of systems biology.^{1,2} Systems biology aims at system-level understanding of biological systems, especially the dynamic of an organism's response to a perturbation under the influence of environmental stresses, disease states or genetic mutations. Genomics, transcriptomics, proteomics and metabolomics become integral parts of systems biology. (Figure 1-1) The development of 'omics technologies is also closely linked to the rapid advancement in computer science (bioinformatics), which permits vast amounts of data generated to be analysed, organised and stored. Although the development of systems biology is still in its infancy, it is evident that comprehensive investigations of the 'omics technologies will play a central role in this new science and bring our understanding of biochemical mechanisms in complex systems to the next level.¹

Even with the promise of systems biology, challenges are presented at each of the individual level of 'omics technologies. One major reason is the complexity and diversity of biological systems. For any sequenced organism, there are a vast number of genes. It is estimated that there are 20,000 to 25,000 protein-coding genes in the human genome.³ The genetic factors are very often multifold and interact in the ways that are difficult to understand at the gene level alone.⁴ In elucidating of the gene functions, we may have to rely on proteomics and metabolomics. Proteomics gets us closer to understanding actual changes; nevertheless, it is still not the final answer. The human proteome is at least an order of magnitude larger and more complex than the genome.⁴ Additionally, proteins are much more diverse in structure, function and dynamic range than are genes. Their function also needs to be understood in the context of specific cells and intracellular compartments.

**Printed version includes figure(s) extracted
from the reference source describing
the classical view of systems biology.
Please refer to the cited reference for detail**

Figure 1-1 Classical view of integrated functional genomics. The effects of gene perturbations are evaluated at multiple levels including the transcriptome, proteome and metabolome. A change in the metabolome occurs because of those changes in the transcriptome that result in changes in the levels or catalytic activities. Therefore, metabolomics represents the final step in understanding the gene's function.⁵

There has been a growing interest in metabolomics. This is because the metabolome (the whole set of metabolites in an organism) can be viewed as the end-products of gene expression and define the biochemical phenotype of a cell or tissue. Even so, the development of metabolomics has lagged behind the other 'omics technologies. One of the reasons is the investigation of metabolites is complicated by its enormous complexity and dynamics.^{5,6} The other 'omics approaches are either based on four or five nucleotides or ~20 primary protein-coding amino acids, and it is perceived that they can be handled by a single instrumental platform. The metabolome represents a vast number of components that belong to a disparate class of compounds, such as amino acids, lipids, fatty acids, carbohydrates, small peptides and nucleic acids. These compounds are very diverse in their physical and chemical properties. Metabolite distributions are also subjected to high temporal and spatial variability, such as circadian fluctuations and diet dependence. Consequently, studying the metabolome is a major challenge to analytical chemistry and a metabolomic analysis in its true sense, namely comprehensive quantitative analysis of all metabolites, cannot be achieved with the current instrumentation. This obstacle is being circumvented using selective extraction and parallel analyses using a combination of technologies to obtain the most comprehensive visualisation of the metabolome.⁵ (Figure 1-2)

**Printed version includes figure(s) extracted
from the reference source describing
the targeted approaches and global approaches of metabolomics.
Please refer to the cited reference for detail**

Figure 1-2 Strategies for metabolomic investigations. Currently, two complementary approaches are used for metabolomic investigations: metabolic profiling and metabolic fingerprinting. Meta-data refers to specific experimental conditions and protocols used for sample preparations.¹

Generally, the selection of an analytical approach is a compromise between speed, selectivity, sensitivity, and sometimes, economic factors. The current principal analytical methods for metabolomics are nuclear magnetic resonance (NMR) spectroscopy and mass spectrometry (MS). (Table 1-1) NMR has produced some success but has a relatively low sensitivity. Hyphenated mass spectrometry methods such as GC/MS and LC/MS offer good sensitivity and selectivity, but require a lengthy analysis time. LC also consumes a large volume of solvents and GC requires the analyte to be volatile and thermally stable. Other methods such as capillary electrophoresis coupled to laser induced fluorescence (CE/LIF) detection are highly sensitive, but lack selectivity. Therefore, it is imperative to develop new tools for comprehensive examination of the metabolome and such a platform is not compromised to throughput and sensitivity. The emerged approaches include direct-injection electrospray mass spectrometry (DiMS),⁷ desorption electrospray ionisation (DESI),⁸⁻¹¹ direct analysis in real time (DART),^{12, 13} plasma-assisted desorption/ionization (PADI)¹⁴ and desorption/ionisation on silicon (DIOS).¹⁵

Of all emerging MS technologies, DIOS appears to be a very promising one. DIOS is a laser surface mass spectrometric technique closely related to matrix-assisted laser

desorption/ionisation (MALDI). It does not require a special interface or modification to existing MALDI instruments and is capable of analysing complex biological matrices, but does not suffer signal suppression effect as much as DiMS. Compared to MALDI and other conventional mass spectrometric techniques, DIOS is still in an early stage of development and its true potential is still waiting to be discovered. In this thesis, the method is further developed and optimised, its nature is investigated and potential applications in metabolite profiling are explored.

Table 1-1 Common analytical protocols used in metabolomics investigations, advantages and disadvantages.¹⁶

| | LC/MS | DiMS | GC/MS | NMR |
|----------------------------|-----------------------------------|--|--|---|
| Sample preparation | Extracted into suitable solvent | Extracted into suitable solvent | Extraction and chemical modification | Typically none |
| Chromatographic separation | Medium-resolution separation | No separation | High-resolution separation | No separation |
| Sensitivity | millimolar to nanomolar | millimolar to micromolar | millimolar to nanomolar | millimolar to high micromolar |
| Dynamic range | 10 ⁶ | 10 ⁴ | 10 ⁶ | 10 ³ |
| Speed | slow (5 to 90 min) | rapid (1 to 5 min) | slow (~30 min) | rapid (1 to 5 min) |
| Quantitative accuracy | ± 10% | ± 10% | ± 10% | ± 10% |
| Significant advantages | Soft ionisation; large mass range | Data in one spectrum; Fast | High resolution; EI-MS library available | No sample preparation. Highly reproducible. |
| Significant disadvantages | Speed of analyses | Signal suppression from multiple components. | Significant sample preparation with chemical modification, slow analysis time, harsh ionisation and limited number of molecules can be analysed. | Poor sensitivity and dynamic range; some chemical classes not detected. High instrument cost. |

1.2 Laser Desorption/Ionisation Mass Spectrometry

Although the technique of laser desorption/ionisation mass spectrometry (LDMS) was introduced in the late 1960s,¹⁷⁻¹⁹ the applications of LDMS were very limited until the introduction of light-absorbing compounds called matrices in the late 1980s and hence named matrix-assisted laser desorption/ionisation (MALDI).²⁰ MALDI has since revolutionised biochemical mass spectrometry and is an indispensable tool in proteomics. One of the inventors, Tanaka, was awarded the Noble Prize in Chemistry 2002 for his achievement in developing the MALDI technique.²¹

In a MALDI experiment, analyte molecules are mixed with a large molar excess of the matrix material, the analyte molecules are embedded throughout the matrix and separated from one another, forming analyte-doped matrix crystals after the mixture is dried onto a probe (steel plate) for the irradiation by laser radiation. This solvation effect of the matrix prevents the formation of sample clusters.²² A laser then impinges on the matrix-analyte mixture. The laser energy, instead of causing a thermal spike to the analytes, is absorbed by the matrix and induces rapid heating and excitation of the matrix molecules. The rapid heating causes localised sublimation of the matrix crystal and evaporative ejection of material into the gas phase, entraining intact analyte in the expanding matrix plume. Photo-activated reactions lead to ionisation of both matrix and analyte molecules.²³ (Figure 1-3)

MALDI offers a number of advantages over conventional mass spectrometric approaches.²⁴ Due to the use of pulse laser, data acquisition is fast. MALDI is a soft ionisation technique and high ion yields of the intact analyte molecules with minimal fragmentation are normally obtained. MALDI is very sensitive; typical sample amounts range from 100 fmol to 2 pmol. The use of the matrix increases the efficiency of energy transfer from pulse laser to the analyte, and thus enhances the ionisation efficiency. The desorption of analyte molecules is assisted by the matrix, and analysis of compounds with a molecular weight in excess of 300,000 Da is possible. MALDI also has a higher tolerance to salts and buffers relative to ESI. The operation of a MALDI mass spectrometer is relatively uncomplicated.

**Printed version includes figure(s) extracted
from the reference source describing
the principle of MALDI.
Please refer to the cited reference for detail**

Figure 1-3 The principle of MALDI. A MALDI sample is in a state where it is evenly mixed with a matrix. The matrix absorbs the laser energy and converts it into thermal energy. At the same time, a minute amount of the matrix (uppermost surface of the analyte in the diagram) rapidly heats (within several nanoseconds) and vaporises with the sample.²⁵

Despite the success of MALDI, the technique frequently encounters three major problems associated with the use of organic matrices:

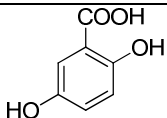
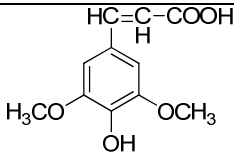
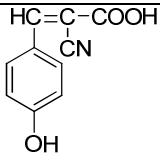
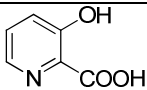
1. matrix optimisation,
2. uneven distribution of analyte, and
3. matrix interferences

The selection of a suitable matrix is complicated but an important step in the optimisation of the MALDI performance (ionisation efficiency, mass resolution, matrix interference, etc). The choice of matrix is based on the laser wavelength used and the class of compound analysed. Some general guidance exists but the procedure is still empirical.²² Numerous matrix candidates have been inspected and their ability to function as a MALDI matrix has been exemplified, but few are found to be good matrices.²² (Table 1-2)

Secondly, the conventional MALDI technique suffers from poor shot-to-shot reproducibility because crystallisation of the matrix often leads to heterogeneous distribution of matrix-analyte deposits. This issue can be partly addressed by different sample preparation techniques, such as the use of liquid matrix,²⁶ spin-coating and electrospray deposition.²⁷

Furthermore, the MALDI mass spectra have a high chemical background due to the formation of clusters of matrix ions or are the degradation products of the matrix. Generally, for organic matrices (Table 1-2), the matrix background occurs at the low mass region (m/z 700 and below) and thus the method is normally applied for macromolecules molecules such as protein and oligonucleotide analysis.

Table 1-2 Common UV-MALDI matrices and their major applications.

| MATRIX | STRUCTURE | WAVELENGTH | MAJOR APPLICATIONS |
|---|---|----------------------|---|
| 2,5-dihydroxybenzoic acid (plus 10% 2-hydroxy-5-methoxybenzoic acid) |  | UV 337 nm, 355 nm | Proteins, peptides, carbohydrates, synthetic polymers |
| Sinapinic acid |  | UV 337 nm, 355 nm | Proteins, peptides |
| α -cyano-4-hydroxy-cinnamic acid |  | UV 337 nm, 355 nm | Peptides |
| 3-hydroxy-picolinic acid |  | UV 337 nm | Nucleic acids |

1.3 The Development of SALDI-MS

In advancing the MALDI technique, approaches that employ a non-conventional matrix have emerged and these methods are generally referred to as surface assisted laser desorption/ionisation (SALDI).²⁸⁻³¹ Examples of materials that can serve as SALDI matrices include graphite,³² activated carbon films,³³ and inorganic metallic particles.³⁴ More recently, nano-materials have been used, examples include carbon nanotubes (CNTs),³⁵ gold nanorods,³⁶ and nano-porous silicon.¹⁵ One of the most important features of SALDI-MS is its absence of matrix interferences in the low mass region where matrix cluster ions suppress the desorption of analyte and obscure the interpretation of MALDI mass spectra in this region. SALDI stands in contrast to

MALDI in this aspect and hence extends the observable mass range to small biomolecules below m/z 700.

The SALDI technique was originally developed by Sunner and Chen at Montana State University (U.S.) as early as 1995.³² Carbon powder glycerol mixture was initially the substrate of choice because carbon was thought to be an inert SALDI matrix and a blackbody in absorbing radiation. This technique was originally inspired by the early work of Tanaka, *et al.*,³⁷ which used cobalt particles in a glycerol matrix. Particles used for SALDI were in the same size range and were constituted by activated carbon powder. Conventional direct laser desorption is less reproducible than SALDI and usually gives rise to fragmentation, which often confuse the mass spectra. Interfacing with thin layer chromatography (TLC) and combining with solid phase extraction (SPE) with SALDI was also investigated.³⁸⁻⁴⁴

In graphite SALDI-MS, cationisation by sodium and potassium is the dominant process in positive mode.⁴⁵ The extent of protonated species is related to the gas-phase thermochemical properties (*e.g.* proton affinity) of the analyte. Graphite SALDI is characterised in practice by a relatively low sensitivity and leads to ion source contamination due to the use of carbon particles. A thin layer of carbon particles was developed in order to avoid such problems. This technique is known as graphite plate laser desorption/ionisation (GPLDI). A low volume of analyte solution is directly deposited onto the surface. To improve peak resolution, an electrical contact between the activated carbon layer and aluminium foil target has to be ensured. Sunner, *et al.*³³ successfully studied different compounds like lysine, caffeine, glucose and bradykinin using this method. These bioorganic compounds appeared mainly as protonated species, and were observed together with a few background ions constituted by alkali cations and various cationised forms of glycerol. Later Kim, *et al.* demonstrated that direct analysis of low molecular weight compounds, like small synthetic polymers,⁴⁶ small macromolecules⁴⁷ and fatty acids⁴⁸ by GPLDI was possible.

Despite SALDI being a promising alternative to MALDI, SALDI did not become a routine research tool for biologists and protein chemists. It has only been a research interest for a small group of scientists in the early 1990s. This was mainly because of a

limited mass range and unsatisfactory detection sensitivity.⁴⁹ Nevertheless, owing to the increasing interest in metabolomics and the successful development of DIOS, SALDI has attracted a lot of attention lately. (Figure 1-4)

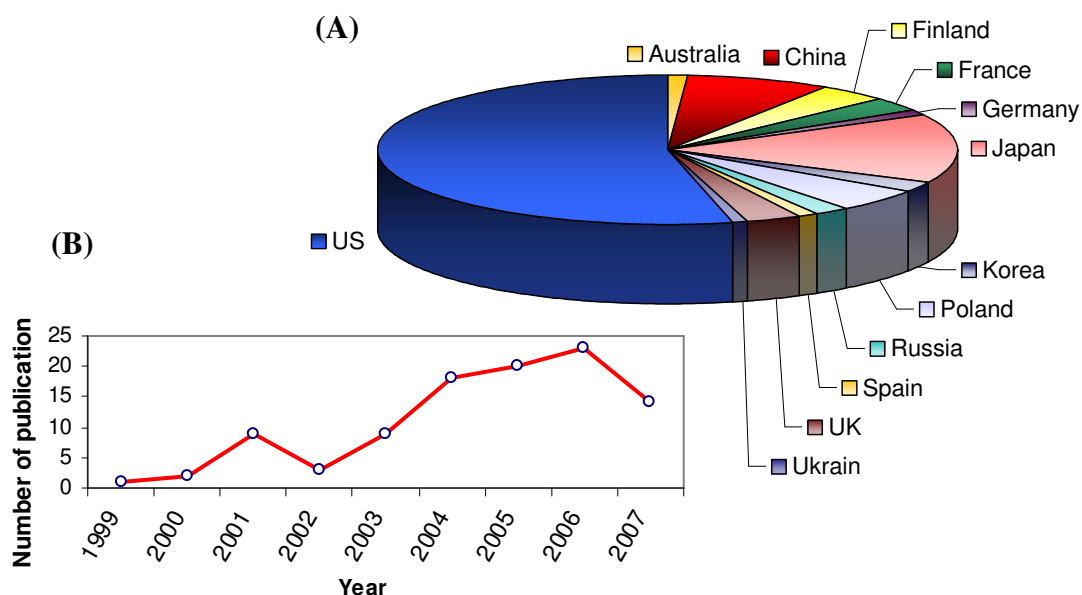


Figure 1-4 The distribution of research or review articles in which the central concept was nanostructured or amorphous semiconductor surface as MALDI substrate in the last 8 years: (A) pie chart showing the international effort and (B) line chart showing the trend of publications each year. Over 75% of literature in total was published in or after 2004. These statistics exclude conference abstracts, patent applications and Ph.D./Master theses. [Up-to-date Oct 2007]

1.4 Development of DIOS-MS

DIOS was first reported by Wei, *et al.* in 1999 and was developed at Scripps Research Institute, US.¹⁵ The method uses pulsed laser desorption/ionisation on porous silicon (PSi) (Figure 1-5) The development of DIOS aims to provide a versatile platform for biomedical applications, principally in proteomics⁵⁰ and metabolomics.⁵¹ Recently, PSi has also been utilised as a solid support for MALDI using conventional matrices.^{52, 53} Comparing porous and non-porous substrates in proteolytic and the MALDI performance, the porous substrates produced improved ion yield and identification of various protein digests, including the prostate cancer biomarker, the prostate-specific antigen (PSA) and the human glandular kallikrein 2 (hk2).

PSi is a UV-absorbing semiconductor comprised of interconnected zero-dimensional nanocrystallites and one-dimensional nanowires produced through galvanostatic (current-controlled) anodisation, electrochemical or photochemical etching of crystalline silicon in the presence of HF.⁵⁴ Depending on the etching conditions and the doping of precursor material, PSi generally has a very complex, anisotropic nanocrystalline architecture of high surface area, ranging from spongy-like morphology typically produced from lightly-doped p-type substrates to a more columnar morphology for n-type precursors.^{54, 55} The size of the pores can vary from a few nanometers to a few microns depending on the conditions of formation and the characteristics of the silicon.

PSi is not a newly discovered material, it was first obtained in around 1956 by Uhlir,⁵⁶ during studies of the electropolishing of Si in HF-based solutions. Although PSi was discovered long ago, its true microstructure (*vide ante*) and remarkable properties (*vide infra*) were not examined until 1990.⁵⁷ Much of the interest in PSi and its morphology derives from its room temperature photoluminescent properties⁵⁸ - visible light emission from high porosity structures arises from quantum confinement effect (Figure 1-6 and Figure 1-7), which make it a useful platform for electronic and optoelectronic devices as well as chemical microsensors. Bulk Si, however, emits light only weakly (<0.001%) in the IR region owing to its indirect band gap.⁵⁵

1.4.1 Preparation and Physicochemical Properties of DIOS Substrates

Shen *et al.*⁵⁹ studied a series of etching parameters in an effort to produce an optimal substrate (judged by qualitative assessments of reproducible S/N levels and the appearance of background ions). Two sets of conditions were found to produce “*fresh*” or “*underivatised*” surfaces suitable for DIOS-MS. One type of surface (*the designated surface*) was prepared from heavily doped n-type silicon wafers (0.008-0.05 $\Omega \cdot \text{cm}$ resistivity), etched at low current densities (4 mA/cm²) for 1 min, under short exposure to moderate white light (50 mW/cm²) in a Teflon cell. (Figure 1-8)

Printed version includes figure(s) extracted
from the reference source describing
the principle of DIOS-MS.
Please refer to the cited reference for detail

Figure 1-5 Schematic representation of the DIOS mass spectrometry configuration. DIOS chips are placed on a modified MALDI plate. The analyte is added on the PSi surface and then irradiated UV laser within the MALDI mass spectrometer to induce desorption and ionisation.¹⁵

Printed version includes figure(s) extracted
from the reference source describing
the electroluminescence and photoluminescence properties of the
chemically functionalised porous silicon.
Please refer to the cited reference for detail

Figure 1-6 Photographs of porous silicon emitting light. *Left:* A 1 cm diameter PSi sample in a Teflon electrochemical cell, under electroluminescence conditions. *Right:* A 1 cm diameter porous silicon irradiated with UV light which induces photoluminescence emission.⁵⁴

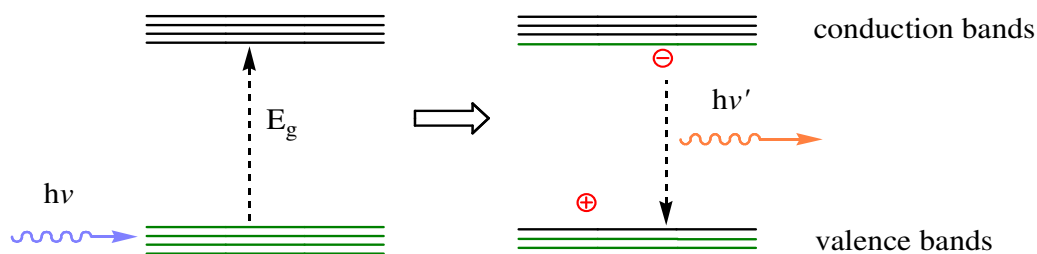


Figure 1-7 Schematic representation of a silicon nanocrystallite. Absorption of a photon with energy higher than the band gap results in promotion of an electron from the valence to the conduction band. Radiative recombination of the excited electron results in emission of a photon of lower energy.

The surface produced had a macro-porous surface morphology. The macrosized pores spaced ~ 100 nm apart. The pore sizes were ~ 70 - 120 nm in diameter with a depth of up to 200 nm. The porosities of these surfaces were $\sim 30\%$ to 40% . Another version, which gave a similar LDI performance, was produced from less heavily doped n-type silicon wafers (0.5 - $2 \text{ } \Omega\cdot\text{cm}$ resistivity), etched at larger current densities (20 mA/cm^2) for 5 minutes under ambient diffuse light ($\sim 0.5 \text{ mW/cm}^2$). The surface morphology was not reported. (See section 2.2) This surface was used for chemical characterisation by diffuse reflectance IR spectroscopy. This is because the designated surface was prepared by a heavily doped silicon wafer, and was opaque to IR radiation.

The authors stressed that these etching parameters produce a surface very different from the surface for photoluminescent applications – relatively, these DIOS-active materials had much larger pores, a much thinner porous layer, and lower overall porosity. On comparing the LDI performance, those surfaces that were effective for photoluminescence were not effective for LDI. It was suggested that the pore size and the overall surface porosity are the most important parameters for DIOS performance.

The study also showed that, silicon crystal orientation *e.g.* 100 , 111 types and altering the concentration of HF from the standard electrolyte mixture (25%) had no significant effect on the DIOS performance. Irreproducible results were associated with the lowering of ethanol below 30% due to considerable H_2 bubbles being generated at the silicon surface at such concentration of ethanol. Photopatterning of the surface could be achieved by two methods: lithographical etching (illuminating n^+ -type silicon through an optical mask), and by covalent derivatisation before etching.

DIOS performance was also found to decrease with oxidation and on long storage in air or brief exposure to oxidising agents. A post-etching procedure, termed double-etching (re-etching of oxidised surface in 5% aqueous HF etching solution for 1 min) could remove the oxides layer and regenerate a hydride surface. The double-etched surfaces showed wider openings and more cylindrical pores, but the pore depths were similar to the single-etched precursors. (Figure 1-9) Although, the double-etched surface required a higher laser threshold, it gave better DIOS performance toward small molecules and tended to have a higher loading capacity than single etched surfaces.

**Printed version includes figure(s) extracted
from the reference source describing
a design of Teflon cell used for making porous silicon.
Please refer to the cited reference for detail**

Figure 1-8 The design of the apparatus used to make porous silicon.⁶⁰

**Printed version includes figure(s) extracted
from the reference source describing
the microscopic morphology and an array of sample spots of the
designed DIOS target.
Please refer to the cited reference for detail**

Figure 1-9 (*Left*) A FE-SEM image of an optimal DIOS surface showing nanometer thick porous layer with nanocrystalline structure and photopatterned DIOS target. (*Right*) The appearance of lithographically etched DIOS target showing an array of sample wells.^{59, 61}

The aforementioned designated DIOS substrate was further optimised after Waters Corp. acquired a license to commercialise the DIOS technology and marketed it for small molecule applications.⁶² The optimised surface morphology for small molecules consists of a 400-700 nm deep pore layer and pore diameters approximately 50-100 nm across. The pore morphology of these substrates is more open than that of a substrate more amenable for peptide analysis. Similar to Shen's observations,⁵⁹ strong etching

procedures result in a fragile deep porous surface and the MS performance is degraded and has more background ions in the mass spectra. The manufacturing process was also further improved (surfactant etching additive) and led to a more reproducible and homogeneous target.

Lee, *et al.*⁶³ have also carried out a detailed study of the DIOS phenomenon and suggested that the LDI process is not only induced by electric perturbations, surface morphology plays an essential role in the process. He found that the pertinent pore size for efficient desorption/ionisation was approximately from 35 to 40 nm but surfaces which had a pore size below 20 nm and low porosity were inefficient surfaces for LDI. Surfaces that had a pore depth of about 800 nm gave the best results. Similarly to Shen and Credo,^{59, 64} increasing the thickness of the porous layer and pores size further did not promote the ionisation efficiently. It was thought that small and shallow pores had low energy trapping performance to necessitate the ionisation and desorption of small molecules. The double-etched surfaces had higher threshold energy for desorption. Tuomikoski *et al.*⁶⁵ have also demonstrated a modified etching cell design, which eliminates the use of the gold Ohmic contact by using backside illumination. It was suggested that this method improves the surface homogeneity. Pore size in the range of 50-200 nm was found to be optimal in that study.

1.4.2 Chemical Derivatisation

Freshly etched PSi produced by chemical anodisation has a high surface concentration of Si-H. However, the Si-H surface slowly reacts with the ambient air.^{54, 55} The oxidation level depends not only on the time elapsed, but also on the storage conditions. Consequently, the chemical composition of a PSi surface and its properties evolve continuously with storage time. The growth of an oxide layer can significantly alter the PSi surface structure and generally leads to impairment of DIOS activity.⁶⁶ One approach to address the instability of PSi is by chemical derivatisation. In fact, the first generation DIOS substrates reported were either hydrogen- or phenethyl-terminated, though it was reported there are not significant differences in the

LDI performance between the derivatised and non-derivatised PSi surfaces.⁵⁴ (see Figure 1-5)

The latest development of DIOS substrate adopts self-assembly of silanes on oxidised DIOS surfaces to enhance surface stability or selectivity (Figure 1-10) and in some cases functionalise the surface for positionally-encoded screening of compounds for reactivity toward catalysts or reagents.⁶⁷⁻⁷¹ A comparison of the DIOS performance of the derivatised surface with a freshly-etched surface revealed that the derivatised surfaces gave S/N values and mass ranges very similar to Si-H surfaces and were far superior to oxidised surfaces. In addition, silanised surfaces showed resistant to oxidation by air and even ozone and have a much longer shelf-life upon storage in air (> 9 months) than underivatised surfaces (< 2 weeks). Furthermore, such a surface afforded a method of on-target sample clean-up.⁶⁷ The outcome is the commercial DIOS target to be studied in this thesis.

**Printed version includes figure(s) extracted
from the reference source describing
three possible chemical modifications of porous silicon that can be used
for laser mass spectrometry and examples of mass spectra acquired
from those substrates.
Please refer to the cited reference for detail**

Figure 1-10 By using different chemical functionalities, PSi surfaces can be tailored to selectively adsorb and efficiently ionise analytes: (a) trimethylsilane, (b) aminosilane, (c) perfluoroalkylsilane derivatisation and the corresponding DIOS mass spectra of (d) 500 fmol bovine serum albumin (BSA) digest, (e) carbohydrate mixture containing sodiated sucrose ($[M+Na]^+$, m/z 365) and maltotriose ($[M+Na]^+$, m/z 527), and (f) small molecular drugs containing midazolam ($[M+H]^+$, m/z 326), propafenone ($[M+H]^+$, m/z 342) and verapamil ($[M+H]^+$, m/z 455).⁷²

1.5 The development of Semiconductors Nano-wires and Nano-dot Surfaces

Several other types of semiconductor nanostructured LDI substrates have also been reported. Methods include thin-film deposition approaches, such as non-porous column/void silicon nano-wires surface produced by plasma-enhanced chemical vapour deposition (PECVD),⁷³ (Figure 1-11) semiconductors nano-wires produced by chemical vapour deposition (CVD)⁷⁴ and germanium nano-dots (GeNDs) deposited on a silicon single-crystal surface by molecular beam epitaxy (MBE).⁷⁵⁻⁷⁸ (Figure 1-12) Currently, germanium columnar/void films prepared by a plasma deposition method are commercially available under the trade name of QuickMass™ from NanoHorizons, Inc. and Shimadzu, Corp.⁷⁹ These films are reported stable under ambient conditions for over one year without observable loss to its LDI-MS activity, providing an archival capability that is comparable to the functionalised DIOS chip.

Another approach is the silicon nanowires (SiNWs) surface.⁶⁸ The nanowires are synthesised using gold nanoclusters (40 nm diameter) as catalysts deposited on a silicon wafer. Nanowires are then grown using silane vapour (SiH₄) as a reactant in a CVD furnace (480°C). To achieve the desired polarity, the surface is oxidised and fluoro-silane derivatised. The optimal SiNWs substrate has nanowires of 10-40 nm in diameter and a few micrometers long with a density of 10-50 wires/μm².⁸⁰ Because of the high surface area, SiNWs surface can act as a TLC plate to perform a chromatographic separation of complex biological matrices and the plate is then analysed according to the location to identify different compounds on the plate.⁶⁸ The SiNWs surface exhibits significantly lower ionisation fluence thresholds than DIOS surface and common MALDI matrices. The mechanistic reason for the lower energy threshold appeared to be related to low laser fluence requirement to reach high surface temperatures and consequently achieve desorption.⁸⁰ SEM images revealed that this layer of nanowires is easily melted and evaporates upon laser irradiation. (Figure 1-13) The SiNWs substrate has also been further optimised and recently commercialised under the trade name of NALDI™ chip from Nanosys, Inc. and Bruker Daltonics, Inc.⁸¹

**Printed version includes figure(s) extracted
from the reference source describing
(A-D) the microscopic morphology of the nanostructured column-void Si
film produced by plasma enhanced chemical vapour deposition and (E)
an example mass spectrum acquired from the substrate.
Please refer to the cited reference for detail**

Figure 1-11 (A) Cross-sectional SEM view of a nanostructured column-void Si film grown on a glass substrate showing nanofibres and their aggregates (columns). (B) Plan SEM view of a nanostructured column-void Si film grown on a Si wafer. Process conditions for film growth: 400W, 10 mTorr, 100 °C. The film thickness is close to 600 nm. (C) Cross-sectional SEM view of a nanostructured column-void Si film, where expansion of the columns (fibrous aggregates) occurs with increasing film thickness because of fibrous bifurcation. Process conditions for the film growth: 300W, 20 mTorr, 100 °C. The film was deposited on Si wafer. (E) Mass spectrum of a mixture of peptides spotted on a nanostructured Si film on a plastic substrate (all in the pmol range), including des-arg¹-bradykinin (m/z 905), (m/z 1182), angiotensin I (m/z 1297), glu¹-fibrinopeptide B (m/z 1571) and neurotensin (m/z 1673).⁸²

**Printed version includes figure(s) extracted
from the reference source describing
the microscopic morphology of the Ge-nano-dots substrates produced
by molecular beam epitaxy.
Please refer to the cited reference for detail**

Figure 1-12 Morphology of GeNDs on the GeND chip C. (a) FE-SEM image. (b) AFM image. (c) Three-dimensional image of the same area shown in (b).⁷⁸ The size of the nano-dot ~ 200 nm in diameter.

**Printed version includes figure(s) extracted
from the reference source describing
the microscopic morphology of the silicon nanowires substrate before
and after laser modification.
Please refer to the cited reference for detail**

Figure 1-13 SEM images of non-patterned nanowires substrate, before (A) and after (B) laser illumination.⁸³

1.6 Development of SALDI Substrates and Gas-phase SALDI Mass Spectrometer at the General Physical Institute

The SALDI substrate development is closely linked to the investigation of ionisation mechanism and gas-phase SALDI mass spectrometer development. Several different substrate materials have been employed, such as graphite and ice,^{84, 85} but semiconductor materials such as silicon, germanium and gallium arsenide have now become the substrate material of choice.⁸⁶⁻⁸⁸ These SALDI substrates and the instrument are designed for the detection of illicit drugs (*e.g.* amphetamines, cocaine and heroine), nerve gases, missile fuels (*e.g.* hydrazines) and explosives (*e.g.* DNT, TNT).^{89, 90}

In the early work, the silicon substrates were prepared by conventional electrochemical etching or anodisation in ethanoic HF solution.^{91, 92} Addition of HCl etching additive was used.⁹³ This preparation method produced a PSi surface that had up to 50 times higher photoluminescence and resistance to oxidation relative to the porous silicon prepared by anodisation. Other additives, such as H₃PO₄ and H₂O₂ were also investigated.⁹⁴⁻⁹⁶

More recently, the substrates have been prepared with iodine-containing electrolyte additives. The iodine additive includes iodine and iodine-containing compounds, which dissociate into *iodine-ions* during chemical etching.⁸⁷ The proportion of HF, ethanol and iodine additive was found to be important. The thickness of the porous layer and porosity depends on the iodine concentration and the etching time. Increasing the concentration of iodine additive generally reduces surface roughness. The addition of iodine greatly influences the process of PSi formation. The surface becomes more chemically homogeneous than those prepared by the standard anodisation method does and the surface structure becomes smaller. Iodine, like bromine, acts as an oxidising agent. Comparatively, iodine is a very weak oxidiser, and consequently the iodine in ethanol solution leads to little direct chemical etching. It is believed that iodine most probably acts as a catalyst. Such preparation also leads to a long-term stabilisation of both the photoluminescent properties and the surface states.^{97, 98} (Figure 1-14)

**Printed version includes figure(s) extracted
from the reference source describing**

(A) and (B) the microscopic morphology of the SALDI substrates, one was prepared by conventional electrochemical of silicon in HF and the other prepared by iodine containing electrolyte in HF, the vertical scale of the AFM images are 35 nm and 13 nm, respectively, (C) and (D) chemical characterisation of these substrates by FTIR, (E) ion intensity of protonated pyridine as a function of laser fluence obtained from these substrates and (F) an example of gas-phase SALDI mass spectrum acquired the modified substrate.

Please refer to the cited reference for detail

Figure 1-14 AFM images of SALDI substrates, produced by (A) standard anodisation and (B) electrochemical etching in iodine containing electrolyte. Standard etching used 70 mA/cm^2 current density and 1 min etching time. Modified etching used 1 mA/cm^2 current density and 5 mins etching time. FTIR spectra of SALDI substrates, produced by (C) standard anodisation and by (D) electrochemical etching in iodine containing electrolyte. Tripartite bands at 2100 cm^{-1} (labelled 3) and 1000 cm^{-1} (labelled 1) are assigned to the stretching and bending modes of SiH moieties respectively. The band at 1100 cm^{-1} is assigned to SiO stretching (labelled 2). (E) The intensity of the signal of protonated pyridine obtained from silicon surfaces as a function of the laser fluence, produced by electrochemical etching in iodine containing electrolyte (modified etching) and by standard anodising etching (standard etching). (F) A representative gas-phase SALDI mass spectrum using silicon substrate.^{87, 99}

The aforementioned preparation methods are called stain-etching. Stain-etching simplifies the preparation procedures by either removing light illumination or electrical bias by adding an oxidising agent into the etching solution. In the methods above, only indoor diffused light is used. It is interesting to note, although addition of iodine-electrolyte into the etchant enhances the photoluminescence efficiency of PSi surface; I_2 , on the other hand, is an effective irreversible photoluminescence quenching agent.¹⁰⁰ Furthermore, there has been a report that iodine matrix additive assists matrix MALDI performance.¹⁰¹

Most recently, to simplify the preparation procedures even further and to remove an electrical contact, the substrates have been prepared using electro-less vapour etching in iodine and HF contained vapours on heavily doped (n^{++} and p^{++} type) silicon.¹⁰² Compared with anodised luminescent porous silicon prepared by standard method, the excitation recombination is two times faster and has higher photoluminescence efficiency for the iodine-contained vapour etched surface.

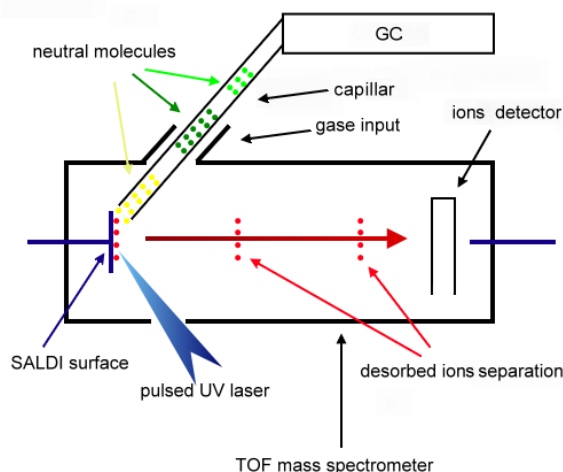
The interface to the mass spectrometer has also been radically altered to permit the use of SALDI-MS as an instantaneous highly selective forensic platform. In conventional SALDI and MALDI approaches, a liquid sample is deposited onto a surface or a probe plate. In the gas phase SALDI approach, the gaseous sample is adsorbed onto the target and this method is specially designed for field applications. The surfaces used normally are roughened and non-porous. Additional roughness can be obtained either using the non-polished side of the silicon wafer or by sanding the wafer with diamond dust before etching. It is suggested that the microscopic roughness of the surface strongly facilitates the adsorption of organic molecules from the gas phase onto the surface and the desorption of the pre-formed analyte ions under pulsed laser irradiation.⁸⁹ It has also been suggested that silicon surfaces with lower porosity are less susceptible to surface contamination under practical laboratory conditions in comparison to silicon surfaces of higher porosity.¹⁰³

The chemically etched surface is not in its final form for SALDI-MS. Further laser treatment is carried out on the target surface under a low pressure inside the mass

spectrometer.⁸⁷ The laser etching procedure partly removes adsorbates that have already been adhered to the surface and alters the surface hydrophilicity. A visual alteration to the surface is notable after the substrate is used. The surface is activated and highly susceptible to gas-phase organic species adsorption and this property is essential for its function here. Sample introduction is then via either a GC instrument or a vapour generator.^{99, 104} Because of the acidic nature (native oxides) of the silicon, compounds that have high aqueous basicities are selectively adsorbed onto the surface. Once the sample is adsorbed onto the surface, it will be ionised and desorbed into gas phase by laser irradiation. The applied electric field pulls the ions toward the detector through the drill tube. (Figure 1-15) Compounds which have high molecular mass cannot be desorbed because of the lack of a matrix to assist the desorption of the analyte into vacuum or since they cannot be introduced in gas-phase by a GC. The signal before and after the sample introduction is then compared (either by computer or operator) and gives either positive or negative result to the target compounds concerned.

The advantages of this design are that it is compact, portable and suitable for field applications. Analytes can be accumulated for an extended time and are effectively pre-concentrated on the surface to improve sensitivity. Coupling to a GC instrument allows a complex mixture to be separated by GC before mass spectrometric analysis. (Figure 1-15C) One of the disadvantages is that the spectra are obscured by relative intense background interferences in the low mass region, though no silicon clusters are observed at the laser energy normally required for analysis. This is circumvented by using the online chromatographic technique. The second issue is signal intensity reproducibility. Gas-phase introduction improved signal intensity precision over the liquid deposition approach, since uneven crystallisation or distribution of the analyte onto surface is avoided. However, the signal intensity variation is still large. Newer gallium arsenide substrates are reported to have improved spot-to-spot signal reproducibility relative to silicon substrates.⁸⁸ The latest development also adopts a rotating platform which was originally developed by Murray, *et al.* to couple CE to MALDI.¹⁰⁵ This design permits the SALDI substrate to be preliminarily exposed to an air-current at atmospheric pressure and is then swiftly brought into the vacuum chamber of the mass spectrometer. To boost the performance even further, a high repetition rate laser (500 Hz) is used.

A



B



C

**Printed version includes an example of TIC acquired
from gas-phase SALDI MS coupled to a GC instrument.
Please refer to the cited reference for detail**

Figure 1-15 (A) Schematic diagram and (B) the setup of a gas-phase SALDI mass spectrometer. A substrate is attached onto an end of a steel rod or a rotating ball platform, which is coupled to a linear time-of-flight mass analyser. Samples are introduced via a GC instrument, or a vapour microflow generator inside the vacuum chamber. Alternatively, the target surface is briefly exposed to a micro airflow locked on a rotating platform. (C) A total ion chromatography (TIC) of a mixture of benzylamine, ethoxyaniline, triethylamine, *N*-methylphenethylamine and diphenylamine obtained by GC gas-phase SALDI-MS.⁸⁸

1.7 Ionisation Mechanism

While the mechanisms of MALDI are a subject of continuing research, a number of models have been already proposed to explain the SALDI or DIOS phenomenon.

Luo, *et al.*¹⁰⁶ noted that energy deposition is very efficient in PSi. The authors proposed that due to limited dissipation through heat conduction in the thin pore walls (quasi-one-dimensional system), the temperature on the wall surfaces of PSi rises more rapidly and to a higher value than at the surface of bulk silicon. This confinement of the deposited energy in the pore walls means that in PSi a particular surface temperature can be achieved at significantly lower laser fluence than in bulk silicon. (Figure 1-16)

**Printed version includes figure(s) extracted
from the reference source describing
the proposed laser desorption/ionisation mechanism
on porous silicon substrates.
Please refer to the cited reference for detail**

Figure 1-16 Adsorption of thermometer molecular ions (TM^+ and Cl^-) and solvent molecules (S) in derivatised silicon nanopores. Derivatisation is depicted as a dashed line that follows the surface. Pore walls are sufficiently thin to induce quantum confinement of electrons leading to enhanced absorption of laser light. Two possible scenarios exist. The left pore only contains adsorbates and it is used to demonstrate the “dry” desorption mechanism. The right pore shows trapped solvent as a result of capillary condensation or inefficient pumping through nanopore (gray area) and exhibits a “wet” desorption mechanism.¹⁰⁶

It is proposed that because of energy deposition by the laser pulse, in the dry pores the rapid heating of the pore walls results in desorption of the adsorbates. In the confined space of the pores, a plume develops that undergoes one-dimensional expansion toward the mouth of the pore. During the expansion, the pressure is kept relatively high due to the confined space. In the wet pores, the rapidly heated trapped solvent reaches the boiling and possibly the spinodal temperature. This gives rise to a high-density solvent

plume expanding with the released adsorbate. Ionisation of the adsorbed molecules can proceed through charged surface states (*e.g.* hydrides) or through ion-molecule reactions in the plume.¹⁰⁶

Supporting evidence includes a SEM image performed on a DIOS surface after analysis. (Figure 1-17) This surface is covalent cleavable linkers modified and the linker is subjected to thermal retro-Diels-Alder fragmentation. The image includes an undisturbed region with its regular pore structure, and irradiated region. The latter areas appear to have melted and bubbled up, perhaps reflecting the release of volatile material trapped in the pores. It is suggested that the 337 nm laser is efficiently absorbed by the silicon substrate beneath the porous layer, resulting in very rapid and localised heating.⁶⁹ Consequently, explosive vaporisation is proposed as a possible mechanism for DIOS.¹⁰⁷ Explosive vaporisation occurs when a liquid is heated so fast that density fluctuations on the liquid become the dominant vaporisation mechanism rather than heterogeneous nucleation. Heterogeneous nucleation takes place when the temperature of the bulk liquid approaches saturation temperature and thus reaches equilibrium with its vapour. In contrast, explosive vaporisation occurs when the liquid approaches a region of intrinsic instability because its temperature rises too close to the superheat limit.¹⁰⁸

**Printed version includes figure(s) extracted
from the reference source
a SEM image supporting the aforementioned proposed mechanism.
Please refer to the cited reference (supplementary document) for detail**

Figure 1-17 SEM image of a porous silicon surface after DIOS-MS analysis of a deposited analyte. (A) Normal region of the PSi wafer, identical in morphology to freshly-etched material. (B) Irradiated regions of the surface.⁶⁹

Another model has been proposed on nano-wires surfaces produced by CVD. It is believed effective optical coupling leads to thermal desorption of the adsorbed analyte.⁸² (Figure 1-18) Furthermore, Choi, *et al.* have also suggested the sharp-end of the nano-wire can generate an extremely high electric field at the front tips upon exposure to laser radiation, which leads to field desorption of the analyte and the generation of high local electric field can accelerate the release of ions. In addition, the front tips of nano-wires can allow the release of electrons when an electric field is applied and this electron release can facilitate the ionisation the analyte.¹⁰⁹

**Printed version includes figure(s) extracted
from the reference source describing
the proposed laser desorption/ionisation mechanism
on nanostructured column-void silicon film produced by PECVD.
Please refer to the cited reference for detail**

Figure 1-18 Schematic concept diagram illustrating laser desorption/ionization of analyte molecules on nanostructured column/void silicon film.⁸²

The SALDI mechanism proposed by Alimpiev, *et al* is based on field enhancement inducing charge separation on the sharp tips at the surface. Adsorbed water plays a vital role of ionisation of basic compounds. Ions are emitted from an active layer and surface porosity is not required.¹⁰³ It is proposed that the ionisation efficiency of organic compounds on SALDI surfaces is strongly dependent on the characteristic size of surface structure irregularities, and the formation of gas-phase ions is initiated on the surface of sharp crystal tips and edges that protrude from the sample surface. It is thought that the electrostatic field is essential in charge separation.¹⁰³ Thus, it was suggested that performance enhancement could be achieved by reducing the characteristic size of surface roughness or irregularities.⁹⁹ The products are the SALDI substrates to be investigated in this study. These SALDI surfaces, perhaps in the absence of porous structure, have a higher laser threshold of silicon surface destruction

(radiation hardness). In addition, it has been proposed that the SALDI surfaces are passivated by hydrogen, fluorine and/or iodine. According to this theory, laser irradiation leads to desorption of this passivated layer and the “activation” of silicon surface bonds. Water is then dissociatively adsorbed and incorporated onto the surface as Si-OH moiety and such reaction requires two adjacent dangling bonds per water molecules.⁹⁹ For organic compounds with high aqueous basicities, proton transfer in a Si-O...H-M complex results in the formation of protonated molecules [M+H]⁺. According to this model, only sufficiently basic molecules will be protonated. and for effective ionisation, the aqueous pKa value of the analyte must be higher than 4.⁹⁹

**Printed version includes figure(s) extracted
from the reference source describing
the proposed laser desorption/ionisation mechanism
on the SALDI substrate (during and after laser etching).
Please refer to the cited reference for detail**

Figure 1-19 Proposed model of the SALDI multi-staged ionisation reaction. The surface is activated by laser irradiation, followed by the adsorption of neutral analyte and proton donor molecules, the chemical reaction on the surface with proton transfer, production of charged complexes bonded with the surface and finally laser desorption of such preformed protonated or deprotonated ions.¹¹⁰

1.8 Applications in Metabolomics

The potential applications of SALDI-MS are extremely wide. Applications in conjunction with nanostructured semiconductor substrates reportedly range from novel pharmaceutical and biomedical applications to the polymer science. A selection of significant examples in metabolic profiling and related areas are discussed below.

Wide varieties of complex biological matrices have been analysed by the method, including urine extract,^{59, 111} human serum and rat plasma extract,^{68, 112, 113} and mouse spinal cord tissue extract.⁶⁸ While those studies aimed to demonstrate the potential and

capability of the method, Finkel, *et al.*¹¹⁴ used an ordered nanocavity SALDI substrates to monitor osmotically induced fluctuation of wide-type and transgenic plants (modified with a human inositol polyphosphate-5-phosphatase enzyme) under an environmental stress (drought). Root, shoot and leaf extracts of *Arabidopsis thaliana* were studied.¹¹⁵ (Figure 1-20) One of the drawbacks of the technique is its poor performance toward quantifying saccharides (albeit they could be detected as salt adducts). These compounds were hence derivatised with glycidyltrimethyl-ammonium (GTMA). Concurrent with previous studies, the result suggested increases in the glucose, fructose and inositol concentration were in response to dehydration.

**Printed version includes figure(s) extracted
from the reference source describing
the principle and examples mass spectra of molecular profiling by
SALDI-MS of *Arabidopsis thaliana* extracts.
Please refer to the cited reference for detail**

Figure 1-20 Metabolite profiling of *Arabidopsis thaliana* leaves extract using SALDI-MS. (Left) the mass spectra of water/methanol fraction and (right) chloroform fraction. The wild-type is displaced in black and the transgenic is in red.¹¹⁵

Vaidyanathan, *et al.*¹¹⁶ have also demonstrated a remarkable study of metabolic footprinting of yeast (*Saccharomyces cerevisiae*) using DIOS-MS. (Figure 1-21) Previously, similar studies have been demonstrated by the same group using DiMS⁷ and a similar approach was also employed therein. In that study, principal components

analysis (PCA) was performed using non-linear iterative partial least squares (NIPALS) algorithm and a selected number of PCs (those contributing to more than 95% of the explained variance) was chosen for discriminant function analysis (DFA). Clustering on the PC-DFA space was then studied. This approach identified the biomarkers that distinguish the wide-types from the mutants. The result could aid the calculation of the genes expression under environmental influence or to speculate the possible metabolic pathway.¹¹⁶ Still, because DIOS is a non-quantitative approach, DiMS was also used at the same time to assist data interpretation.

**Printed version includes figure(s) extracted
from the reference source describing
the analysis of yeast extracts by DIOS-MS.
Please refer to the cited reference for detail**

Figure 1-21 (A) PC-DFA score plot constructed using the first 60 PCs showing the discrimination of mutants g1 and s4 from the rest of the yeast mutants and the wild type strain. The test set is marked with an asterisk, and the separating clusters encircled for clarification. (B) The first loadings plot of the PC-DFA. Note the prominent peaks at m/z 145 and 146 seen clearly in the expanded portion of the loadings. (C) Mean spectra of g1 (gln3 Δ), g5 (dal80 Δ) and the wild type wh (BY4741) strains showing the differences in the spectra in the region where the prominent discriminatory effect is observed. Note the higher peak intensity at m/z 146 (corresponding to glutamate, [M-H]⁻) for g1 compared to the rest. (D) Mean spectral response corresponding to glutamine (m/z 147) and glutamate (m/z 148) in the positive-ion direct infusion mass spectra of the three strains as in (C) (error bars represent one standard deviation about the mean).¹¹⁶

In the studies above, biological compounds are extracted into a solution and deposited onto the substrate prior to mass spectrometric study. Given that SALDI is a surface mass spectrometric technique similar to SIMS and MALDI, direct tissue analysis and ion imaging of small molecules is possible. Kruse *et al.*¹¹⁷ were the first to explore the use of DIOS-MS for direct tissue analysis. Tissue samples of *Aplysia Californica* or cultured invertebrate neurons were directly added onto the PSi. In the study of untreated *Aplysia atrial* gland, the spectra contained membrane lipids in the range of m/z 600-800. A preliminary treatment of methanol-ammonium citrate favoured release and relocation of peptides from tissues into the porous silicon. These methods allowed the observation of known and unknown peptides, and presented a good correlation with the results provided by MALDI-MS. Recently, He, *et al.*¹¹⁸ have applied the DIOS-MS method to two-dimensional ion image of mouse liver tissue and human cervical cancer cells. (Figure 1-22) Similarly to MALDI tissue imaging, the method provides a visual information of spatial distribution of cell membrane and nucleus biomarkers: phosphatidylcholine (PC) and propidium iodide (PI), but also enjoys the benefit of the reduced laser threshold, simpler sample preparation (no matrix) and lower interferences at the low mass region.

**Printed version includes figure(s) extracted
from the reference source describing
the potential ion imaging/mapping by DIOS-MS and
using human cervical cells as an example.
Please refer to the cited reference for detail**

Figure 1-22 (A) Optical image of human cervical cancer cells, HEK 293, grown on the DIOS substrate; (B) the corresponding fluorescence image of the same cell cluster with nucleuses stained by PI; (C) a typical DIOS MS spectrum collected from HEK 293 cell detection; both PC and PI peaks are labelled with asterisks; (D) the corresponding ion maps of PC (yellow) and PI (orange) fragments overlaid.¹¹⁸

1.9 Research Objectives and Scope of Study

Nanostructured semiconductor substrates interfaced with the laser mass spectrometry has immense potential in biomedical research. In particular, without the matrix dependence and interferences as in MALDI using the conventional organic matrix and the possibility of “chip-based” format, this approach permits a robust high-throughput mass analysis of pharmaceutical products and biological related small molecules, in part addressing the challenges in metabolomics. These beneficial factors have attracted the scientific community worldwide. Insofar, about 100 research or review articles have been published. Nevertheless, to make SALDI or DIOS a routine research tool, a lot of work is still needed.

On the other hand, there has also been somewhat of a controversy in the literature over the optimisation of the method, in particular on the structural properties of the substrates and their effects on ionisation efficiency. Furthermore, published data that has actually investigated the surface chemical properties of the substrate are actually rare. In this thesis, a detailed study of this emerging new technology is reported and related to the effects of the physicochemical properties of the substrate to laser desorption/ionisation performance. This project has since developed to bring new evidence or insight to re-examine the propositions and to propose an alternative version of the ionisation mechanism.

According to the provisional recommendation on the Standard Definitions of Terms Relating to Mass Spectrometry (2007) commented to the IUPAC,¹¹⁹ the terminologies SALDI and DIOS were not included in the final draft. The opinion on the nomenclature of the technique remains divided. In this thesis, MALDI is referred to the use of the conventional organic matrices and matrix-free LDI (LDI) is adopted to denote the non-conventional laser mass spectrometry approaches. SALDI is referred to the substrates provided by the Laser Diagnostics Laboratory and their LDI activity. DIOS is referred to the PSi substrates and their LDI activity, and so on.

This project described in this thesis is part of a collaboration with the Laser Diagnostics Laboratory of the General Physics Institute, Moscow to explore the latest development of matrix-free LDI substrates with the aim to develop a sensitive high-throughput laser mass spectrometry approach for metabolomic applications using nanostructured semiconductor substrates. The initial study has been much influenced by the concept developed by the Laser Diagnostics Laboratory and has become the starting point. The scope of study follows the current trend of research in matrix-free LDI approaches and has three essential elements: (1) substrate development, (2) mechanistic elucidation and (3) biological/biomedical application. The subject is developed as follows:

Chapter 1, the introduction (this chapter) reviews the current development of matrix-free LDI technologies and explains the motivation for this research.

Chapter 2, summarise the chemistry of porous silicon (the major material being studied in this study), the basic principles of the surface techniques involved in the study, the materials and the methodologies.

Chapter 3, the rough or porous semiconductor substrates are characterised using a number of surface techniques in order to understand the true natures of these substrates. Their LDI performance is evaluated and compared, to identify the surface features that govern the LDI processes.

Chapter 4, LDI ionic and surface reactions are investigated. A wide range of biological-related and pharmaceutical compounds are analysed in order to determine the capability of this method. Different analytical conditions are also considered. The surface structural and chemical alterations after LDI investigation or laser etching are investigated.

Chapter 5, the feasibility of biomedical applications is studied, including instrumental and method validation, biological sample preparation, and metabolite profiling. MVDA is used in the interpretation of complex mass spectrometric data of complex biological matrices, including human blood plasma, urine, animal liver tissue, and bacterial cell and culture.

1.10 References

1. Dettmer, K., Aronov, P. A. & Hammock, B. D. Mass spectrometry-based metabolomics. *Mass Spectrom. Rev.* 26, 51-78 (2007).
2. Kitano, H. Systems Biology: A Brief Overview. *Science* 295, 1662-1664 (2002).
3. IHGSC. Finishing the euchromatic sequence of the human genome. *Nature* 431, 931-945 (2004).
4. Higgins, A. J. Beyond biochemical profiling for biomarker and target discovery. *Current Drug Discovery*, 21-24 (2004).
5. Summer, L. W., Mendes, P. & Dixon, R. A. Plant metabolomics: large-scale phytochemistry in the functional genomics era. *Phytochemistry* 62, 817-836 (2003).
6. Dunn, W. B. & Ellis, D. I. Metabolomics: Current analytical platforms and methodologies. *Trends in Analytical Chemistry*, 24, 285-294 (2005).
7. Allen, J., Davey, H., Broadhurst, D., Heald, J., Rowland, J., Oliver, S. & Kell, D. High-throughput classification of yeast mutants for functional genomics using metabolic footprinting. *Nat. Biotechnol.* 21, 692-696 (2003).
8. Takáts, Z., Wiseman, J. M., Gologan, B. & Cooks, R. G. Mass Spectrometry Sampling Under Ambient Conditions with Desorption Electrospray Ionization. *Science* 306, 471-473 (2004).
9. Cooks, R. G., Ouyang, Z., Takats, Z. & Wiseman, J. M. Ambient Mass Spectrometry *Science* 311, 1566-1570 (2006).
10. Takáts, Z., Wiseman, J. M. & Cooks, R. G. Ambient mass spectrometry using desorption electrospray ionization (DESI): instrumentation, mechanisms and applications in forensics, chemistry, and biology. *J. Mass Spectrom.* 40, 1261-1275 (2005).
11. Venter, A. & Cooks, R. G. Desorption Electrospray Ionization in a Small Pressure-Tight Enclosure. *Anal. Chem.* 79, 6398-6403 (2007).
12. Cody, R. B., Laramee, J. A. & Durst, H. D. Versatile New Ion Source for the Analysis of Materials in Open Air under Ambient Conditions. *Anal. Chem.* 77, 2297-2302 (2005).

13. Petucci, C., Diffendal, J., Kaufman, D., Mekonnen, B., Terefenko, G. & Musselman, B. Direct Analysis in Real Time for Reaction Monitoring in Drug Discovery. *Anal. Chem.* 79, 5064-5070 (2007).
14. Ratcliffe, L. V., Rutten, F. J. M., Barrett, D. A., Whitmore, T., Seymour, D., Greenwood, C., Aranda-Gonzalvo, Y., Robinson, S. & McCoustra, M. Surface Analysis under Ambient Conditions Using Plasma-Assisted Desorption/Ionization Mass Spectrometry. *Anal. Chem.* 79, 6094-6101 (2007).
15. Wei, J., Buriak, J. & Siuzdak, G. Desorption/ionization mass spectrometry on porous silicon. *Nature* 399, 243-246 (1999).
16. Want, E. J., Cravatt, B. F. & Siuzdak, G. The Expanding Role of Mass Spectrometry in Metabolite Profiling and Characterization. *ChemBioChem* 6, 1941-1951 (2005).
17. Fenner, N. C. & Daly, N. R. Laser Used for Mass Analysis. *Rev. Sci. Instrum.* 37, 1068-1070 (1966).
18. Vastola, F. J. & Pirone, A. J. Ionization of Organic Solids by Laser Irradiation. *Adv. Mass Spectrom.* 4, 107-111 (1968).
19. Vastola, F. J., Mumma, R. O. & Pirone, A. J. Analysis of Organic Salts by Laser Ionization. *Org. Mass Spectrom.* 3, 101-104 (1970).
20. Karas, M. & Hillenkamp, F. Laser desorption ionization of proteins with molecular masses exceeding 10,000 daltons. *Anal. Chem.* 60, 2299-301 (1988).
21. A Nobel Soul, The Nobel Prize in Chemistry 2002. Available at <www1.shimadzu.com/about/nobel/noble/index.html> [accessed 29 Oct 06]
22. de Hoffmann, E. & Stroobant, V. *Mass Spectrometry: Principle and Application* (John Wiley & Sons, LTD., 1999).
23. Griesser, H. J., Kingshott, P., McArthur, S. L., McLean, K. M., Kinsele, G. R. & Timmonse, R. B. Surface-MALDI mass spectrometry in biomaterials research. *Biomaterials* 25, 4861-4875 (2004).

24. Hop, C. E. C. A. & Bakhtiar, R. An introduction to electrospray ionization and matrix-assisted laser desorption/ionization mass spectrometry: Essential tools in a modern biotechnology environment. *Biospectroscopy* 3, 259-280 (1997).
25. MALDI-TOF/MS Principle. Shimadzu Corporation 2004. Available at <www1.shimadzu.com/about/nobel/noble/tec.html> [Accessed 10 Sept 2004]
26. Zenobi, R. & Knochenmuss, R. Ion formation in MALDI mass spectrometry. *Mass Spectrom. Rev.* 17, 337-366 (1998).
27. Hensel, R. R., King, R. C. & Owens, K. G. Electrospray sample preparation for improved quantitation in matrix-assisted laser desorption/ionization time-of-flight mass spectrometry. *Rapid Commun. Mass Spectrom.* 11, 1785-1793 (1997).
28. Afonso, C., Budimir, N., Fournier, F. & Tabet, J.-C. Activated Surfaces for Laser Desorption Mass Spectrometry: Application for Peptide and Protein Analysis *Curr. Pharm. Des.* 11, 2559-2576(18) (2005).
29. Dattelbaum, A. M. & Iyer, S. Surface-assisted laser desorption/ionization mass spectrometry. *Expert Rev. Proteomics* 3, 153-161 (2006).
30. Peterson, D. S. Matrix-free methods for laser desorption/ionization mass spectrometry. *Mass Spectrom. Rev.* 26, 19-34 (2007).
31. Najam-ul-Haq, M., Rainer, M., Szabó, Z., Vallant, R., Huck, C. W. & Bonn, G. K. Role of carbon nano-materials in the analysis of biological materials by laser desorption/ionization-mass spectrometry. *J. Biochem. Biophys. Methods* 70, 319-328 (2007).
32. Sunner, J., Dratz, E. & Chen, Y.-C. Graphite surface-assisted laser desorption/ionization time-of-flight mass spectrometry of peptides and proteins from liquid solutions. *Anal. Chem.* 67, 4335 - 4342 (1995).
33. Han, M. & Sunner, J. An activated carbon substrate surface for laser desorption mass spectrometry. *J. Am. Soc. Mass Spectrom.* 11 (2000).
34. Kinumi, T., Saisu, T., Takayama, M. & Niwa, H. Matrix-assisted laser desorption/ionization time-of-flight mass spectrometry using an inorganic particle matrix for small molecule analysis. *J. Mass Spectrom.* 35, 417-422 (2000).

35. Chen, W.-Y., Wang, L.-S., Chiu, H.-T., Chen, Y.-C. & Lee, C.-Y. Carbon nanotubes as affinity probes for peptides and proteins in MALDI MS analysis. *J. Am. Soc. Mass Spectrom.* 15, 1629-1635 (2004).
36. Chen, L. C., Ueda, T., Sagisaka, M., Hori, H. & Hiraoka, K. Visible Laser Desorption/Ionization Mass Spectrometry Using Gold Nanorods. *J. Phys. Chem. C* 111, 2409-2415 (2007).
37. Tanaka, K., Waki, H., Ido, Y., Akita, S., Yoshida, Y. & Yoshida, T. Protein and polymer analyses up to m/z 100,000 by laser ionization time-of-flight mass spectrometry. *Rapid Commun. Mass Spectrom.* 2, 151-153 (1988).
38. Chen, Y.-C., Shiea, J. & Sunner, J. Thin-layer chromatography-mass spectrometry using activated carbon, surface-assisted laser desorption/ionization. *J. Chromatogr. A* 826, 77-86 (1998).
39. Chen, Y.-C. & Wu, J.-Y. Analysis of small organics on planar silica surfaces using surface-assisted laser desorption/ionization mass spectrometry. *Rapid Commun. Mass Spectrom.* 15, 1899-1903 (2001).
40. Wu, J.-Y. & Chen, Y.-C. A novel approach of combining thin-layer chromatography with surface-assisted laser desorption/ionization (SALDI) time-of-flight mass spectrometry. *J. Mass Spectrom.* 37, 85-90 (2002).
41. Chen, Y.-C. In situ determination of organic reaction products by combining thin layer chromatography with surface-assisted laser desorption/ionization time-of-flight mass spectrometry. *Rapid Commun. Mass Spectrom.* 13, 821-825 (1999).
42. Chen, Y.-C., Shiea, J. & Sunner, J. Rapid determination of trace nitrophenolic organics in water by combining solid-phase extraction with surface-assisted laser desorption/ionization time-of-flight mass spectrometry. *Rapid Commun. Mass Spectrom.* 14, 86-90 (2000).
43. Chen, Y.-C. & Sun, M.-C. Determination of trace quaternary ammonium surfactants in water by combining solid-phase extraction with surface-assisted laser desorption/ionization mass spectrometry. *Rapid Commun. Mass Spectrom.* 15, 2521-2525 (2001).
44. Chen, Y.-C. & Sun, M.-C. Qualitative determination of trace quantities of nonyl phenyl polyethylene glycol ether in water based on solid-phase microextraction combined with

- surface-assisted laser desorption/ionization mass spectrometry. *Rapid Commun. Mass Spectrom.* 16, 1243-1247 (2002).
45. Dale, M. J., Knochenmuss, R. & Zenobi, R. Graphite/Liquid Mixed Matrices for Laser Desorption/Ionization Mass Spectrometry. *Anal. Chem.* 68, 3321-3329 (1996).
 46. Kim, H.-J., Lee, J.-K., Park, S.-J., Ro, H. W., Yoo, D. Y. & Yoon, D. Y. Observation of low molecular weight poly(methylsilsesquioxane)s by graphite plate laser desorption/ionization time-of-flight mass spectrometry. *Anal. Chem.* 72, 5673-5678 (2000).
 47. Kim, J., Paek, K. & Kang, W. Visible surface-assisted laser desorption/ionization mass spectrometry of small macromolecules deposited on the graphite plate. *Bull. Korean Chem. Soc.* 23, 315-319 (2002).
 48. Park, K.-H. & Kim, H.-J. Analysis of fatty acids by graphite plate laser desorption/ionization time-of-flight mass spectrometry. *Rapid Commun. Mass Spectrom.* 15, 1494-1499 (2001).
 49. Guo, Z., Ganawi, A., Liu, Q. & He, L. Nanomaterials in mass spectrometry ionization and prospects for biological application. *Anal. Bioanal. Chem.* 384, 584-592 (2006).
 50. Thomas, J. J., Shen, Z., Crowell, J. E., Finn, M. G. & Siuzdak, G. Desorption/ionization on silicon (DIOS): A diverse mass spectrometry platform for protein characterization. In *Proc. Natl. Acad. Sci. USA.* , (2001). 98, 4932-4937.
 51. Shen, Z., Go, E. P., Gamez, A., Apon, J. V., Fokin, V., Greig, M., Ventura, M., Crowell, J. E., Blixt, O., Paulson, J. C., Stevens, R., Finn, M. G. & Siuzdak, G. A mass spectrometry plate reader: Monitoring enzyme and inhibitor activity with desorption/Ionization on silicon (DIOS) mass spectrometry. *ChemBioChem* 5, 921-927 (2004).
 52. Mengistu, T. Z., DeSouzaab, L. & Morin, S. Functionalized porous silicon surfaces as MALDI-MS substrates for protein identification studies. *Chem. Commun.*, 5659-5661 (2005).
 53. Finnskog, D., Jaras, K., Ressine, A., Malm, J., Marko-Varga, G., Lilja, H. & Laurell, T. High-speed biomarker identification utilizing porous silicon nanovial arrays and MALDI-TOF mass spectrometry. *Electrophoresis* 27, 1093-1103 (2006).
 54. Stewart, M. P. & Buriak, J. M. Chemical and Biological Applications of Porous Silicon Technology. *Adv. Mater.* 12, 859-869 (2000).

55. Schmeltzer, J. M. & Buriak, J. M. in *The Chemistry of Nanomaterials: Synthesis, Properties and Applications, Volume 2* (eds. Rao, C. N. R., Müller, A. & Cheetham, A. K.) 518-550 (John Wiley and Sons, 2004).
56. Uhler, A. Electrolytic shaping of germanium and silicon. *Bell System Tech. J.* 35, 333-347 (1956).
57. Cullis, A. G., Canham, L. T. & Calcott, P. D. J. The structural and luminescence properties of porous silicon. *J. Appl. Phys.* 82, 909-965 (1997).
58. Canham, L. T. Silicon quantum wire array fabrication by electrochemical and chemical dissolution of wafers. *Appl. Phys. Lett.* 57, 1046-1048 (1990).
59. Shen, Z., Thomas, J. J., Averbuj, C., Broo, K. M., Engelhard, M., Crowell, J. E., Finn, M. G. & Siuzdak, G. Porous silicon as a versatile platform for laser desorption/ionization mass spectrometry. *Anal. Chem.* 73, 612-619 (2001).
60. Lewis, W., Shen, Z., Finn, M. G. & Siuzdak, G. Desorption/ionization on silicon (DIOS) mass spectrometry: background and applications. *Int. J. Mass Spectrom.* 226, 107-116 (2003).
61. Want, E. J., Greig, M., Compton, B. J., Bolaños, B. & Siuzdak, G. Mass Spectrometry in High Throughput Analysis. *Spectroscopy* 17, 663-680 (2003).
62. Credo, G. M., Hewitson, H. B., Fountain, K. J., Gilar, M., Finch, J. W., Stumpf, C. L., Benevides, C. C., Bouvier, E. S. P., Compton, B. J., Shen, Z. & Siuzdak, G. Desorption/ionization on silicon mass spectrometry (DIOS MS) of small molecules and peptide: sample handling, preparation and storage effects on performance. 51th Annual Conf. ASMS Montreal, Canada, 8-12 June, (2003).
63. Lee, C.-S., Kim, E.-M., Lee, S.-H., Kim, M.-S., Kim, Y.-K. & Kim, B.-G. Enhancement of analyte ionization in desorption/ionization on porous silicon (DIOS)-mass spectrometry (MS). *Biotechnol. Bioprocess Eng.* 10, 212-217 (2005).
64. Credo, G. M., Hewitson, H., Benevides, C. & Bouvier, E. S. P. Development of a Porous Silicon Product for Small Molecule Mass Spectrometry. In *Mat. Res. Soc. Symp. Proc.*, (2004). Materials Research Society, 808, 471-476.

65. Tuomikoski, S., Huikko, K., Grigoras, K., Ostman, P., Kostiainen, R., Baumann, M., Abian, J., Kotiaho, T. & Franssila, S. Preparation of porous n-type silicon sample plates for desorption/ionization on silicon mass spectrometry (DIOS-MS). *Lab Chip* 2, 247-253 (2002).
66. Go, E. P., Apon, J. V., Uritboonthai, W., Compton, B. J., Bouvier, E. S. P., Finn, M. G., Shen, Z. & Siuzdak, G. Silyl Chemical Modification for Desorption/Ionization on Silicon Mass Spectrometry (DIOS-MS): Application to Surface Stability and Analyte Specificity. 52nd ASMS Conference on Mass Spectrometry and Allied Topics Nashville, Tennessee, May 23 - 27, 2004, (2004).
67. Trauger, S. A., Go, E. P., Shen, Z., Apon, J. V., Compton, B. J., Bouvier, E. S. P., Finn, M. G. & Siuzdak, G. High sensitivity and analyte capture with desorption/ionization mass spectrometry on silylated porous silicon. *Anal. Chem.* 76, 4484 - 4489 (2004).
68. Go, E. P., Apon, J. V., Luo, G., Saghatelian, A., Daniels, R. H., Sahi, V., Dubrow, R., Cravatt, B. F., Vertes, A. & Siuzdak, G. Desorption/ionization on silicon nanowires. *Anal. Chem.* 77, 1641-1646 (2005).
69. Meng, J.-C., Averbuj, C., Lewis, W. G., Siuzdak, G. & Finn, M. G. Cleavable Linkers for Porous Silicon-Based Mass Spectrometry. *Angew. Chem. Int. Ed.* 43, 1255-1260 (2004).
70. Meng, J.-C., Siuzdak, G. & Finn, M. G. Affinity mass spectrometry from a tailored porous silicon surface. *Chem. Commun.* 21, 2108-2109 (2004).
71. Lee, J.-C., Wu, C.-Y., Apon, J. V., Siuzdak, G. & Wong, C.-H. Reactivity-Based One-Pot Synthesis of the Tumor-Associated Antigen N3 Minor Octasaccharide for the Development of a Photocleavable DIOS-MS Sugar Array. *Angew. Chem. Int. Ed.* 45, 2753-2757 (2006).
72. Cohen, L., Go, E. P. & Siuzdak, G. *Small Molecule Desorption/Ionization Mass Analysis* (eds. Hillenkamp, F. & Peter-Katalinic, J.) (Wiley, 2007).
73. Kalkan, A. K., Bae, S., Li, H., Hayes, D. J. & Fonash, S. J. Nanocrystalline Si thin films with arrayed void-column network deposited by high density plasma. *J. Appl. Phys.* 88, 555-561 (2000).
74. Kang, M.-J., Pyun, J.-C., Lee, J.-C., Choi, Y.-J., Park, J.-H., Park, J.-G., Lee, J.-G. & Choi, H.-J. Nanowire-assisted laser desorption and ionization mass spectrometry for quantitative analysis of small molecules. *Rapid Commun. Mass Spectrom.* 19, 3166-3170 (2005).

75. Sato, H., Seino, T., Torimura, M., Yamamoto, A. & Tao, H. Development of a novel ionization plate for soft laser desorption/ionization-mass spectrometry using nanodot structures International Chemical Congress of Pacific Basin Societies (Pacifichem) Hawaii, 17th December, (2005).
76. Sato, H., Seino, T., Yamamoto, A., Torimura, M. & Tao, H. A Novel Soft Laser Desorption/Ionization-Mass Spectrometry Using a Germanium Nanodot Chip as an Ionization Platform. 17th International Mass Spectrometry Conference, Prague, Czech Republic, 29 Aug, 2006 (2006).
77. Sato, H., Yamamoto, A., Seino, T., Torimura, M. & Tao, H. National Institute of Advanced Industrial Science and Technology. Ionization plate for mass spectrometry and mass spectrometer (2006). *US 20060255262*.
78. Seino, T., Sato, H., Yamamoto, A., Nemoto, A., Torimura, M. & Tao, H. Matrix-Free Laser Desorption/Ionization-Mass Spectrometry Using Self-Assembled Germanium Nanodots. *Anal. Chem.* (2007).
79. Press release: NanoHorizons™ Awarded Patent on QuickMass™ Technology, State College, PA, February 9, 2005. Available at <www.nanohorizons.com/PR02092005.shtml> [Accessed Feb 2005]
80. Luo, G., Chen, Y., Daniels, H., Dubrow, R. & Vertes, A. Internal Energy Transfer in Laser Desorption/Ionization from Silicon Nanowires. *J. Phys. Chem. B* 110, 13381-13386 (2006).
81. Daniels, H. & Dikler, S. Analyzing small molecule drug compounds by NALDI mass spectrometry. Bruker Daltonics Technical Note TN-22. (2007).
82. Kalkan, A., Henry, M. R., Li, H., Cuiffi, J. D., JHayes, D., Palmer, C. & Fonash, S. J. Biomedical/analytical applications of deposited nanostructured Si films. *Nanotechnology* 16, 1383–1391 (2005).
83. Chen, Y., Luo, G., Siuzdak, G., Dubrow, R. & Vertes, A. Surface Morphology Effects in Laser Desorption/Ionization 53rd Annual Conf. ASMS, San Antonio, June 5-9, (2005).
84. Belov, M. E., Alimpiev, S. S., Mlynsky, V. V., Nikiforov, S. M. & Derrick, P. J. Laser Ablation of Organic Molecules from Frozen Matrices. *Rapid Commun. Mass Spectrom.* 9, 1431-1436 (1995).

85. Kraft, P., Alimpiev, S., Dratz, E. & Sunner, J. Infrared, surface-assisted laser desorption ionization mass spectrometry on frozen aqueous solutions of proteins and peptides using suspensions of organic solids. *J. Am. Soc. Mass. Spectrom.* 9, 912-924 (1998).
86. Sunner, J., Alimpiev, S. & Nikiforov, S. Morgan Lewis & Bockius LLP. Method and apparatus to produce gas phase analyte ions (2002). *US 20020121595*.
87. Alimpiev, S. S., Nikiforov, S. M., Grechnikov, A. A., Karavanskii, V. A. & Sunner, J. A. Method of forming of rough surface of silicon substrates and electrolyte for anode etching of silicon substrate. (2003). *RU 2003-101425*. RU 2217840.
88. Alimpiev, S. S., Nikiforov, S. M., Grechnikov, A. A., Karavanskii, V. A. & Simanovskii, Y. O. Desorption/ionization of chemical compounds for their mass-spectrometric determination. . (2006). *RU 20050141027 20051228* RU 2285253
89. Alimpiev, S. Novel Technique for Ultra High Sensitive Detection of Drugs. 1st Annual Chemical Science and Commercialization Conference, Moscow, Russia, Sept. 27-29, (2004).
90. ISCT Project no. 2551. A Novel Method for Trace Detection of Narcotics, Explosives and Proteins. Available at <www.istc.ru/ISTC/sc.nsf/html/projects.htm?open&id=2551>
91. Cojocar, I., Pasat, V., Karavanskii, V. & Chumash, V. Optical Hysteresis in free-standing porous silicon films. *J. Optoelectron. Adv. M.* 3, 133-135 (2001).
92. Bykovskii, Y., Karavanskii, V., Kotkovskii, G., Kuznetsov, M., Chistyakov, A., Lomov, A. & Gavrilov, S. Photophysical processes stimulated in nanoporous silicon by high-power laser radiation. *J. Exp. Theor. Phys.* 90, 121-128 (2000).
93. Belogorokhov, A. I., Enderlein, R., Tabata, A., Leite, J. R., Karavanskii, V. A. & Belogorokhova, L. I. Enhanced photoluminescence from porous silicon formed by nonstandard preparation. *Phys. Rev. B* 56, 10276-10282 (1997).
94. Kartopu, G., Bayliss, S. C., Karavanskii, V. A., Curry, R. J., Turan, R. & Sapelkin, A. V. On the origin of the 2.2–2.3 eV photoluminescence from chemically etched germanium *J. Lumin.* 101, 275-283 (2003).
95. Karavanskii, V. A., Lomov, A. A., Sutyurin, A. G., Bushuev, V. A., Loikho, N. N., Melnik, N. N., Zavaritskaya, T. N. & Bayliss, S. Raman and X-ray studies of nanocrystals in porous stain-etched germanium *Thin Solid Films* 437, 290-296 (2003).

96. Kartopu, G., Karavanskii, V. A., Serincan, U., Turan, R., Hummel, R. E., Ekinci, Y., Gunnæs, A. & Finstad, T. G. Can chemically etched germanium or germanium nanocrystals emit visible photoluminescence? *physica status solidi (a)* 202, 1472-1476 (2005).
97. Voloshina, T. V., Zavaritskaya, T. N., Kavetskaya, I. V., Karavanskii, V. A. & Romashov, D. A. Formation and photoluminescence properties of porous silicon produced in iodine-containing electrolytes. *J. Appl. Spectrosc.* 69, 275-278 (2002).
98. Voloshina, T. V., Kavetskaya, I. V. & Karavanskii, V. A. Influence of iodine-containing solutions on the condition of a porous silicon surface and its photoluminescent properties. *J. Appl. Spectrosc.* 71, 89-93 (2004).
99. Alimpiev, S. S., Nikiforov, S. M., Karavansky, V. A., Grechnikov, A. A. & Sunner, J. A. Laser desorption of ions from microscopically rough surfaces: novel technique for ultrahigh sensitivity detection of organic and bioorganic compounds. In Libenson, M. N. *Proc. SPIE*, (2004). 5506 95-106.
100. Karavanskii, V. A., Chistyakov, A. A., Kotkovskii, G. E., Kuznetsov, M. B. & Zakharchenko, K. V. Resonant radiationless excitation transfer in pores of porous silicon. *Phys. Stat. Sol. (a)* 197, 403-408 (2003).
101. Bashir, S., Burkitt, W. I., Derrick, P. J. & Giannakopoulos, A. E. Iodine-assisted matrix-assisted laser desorption/ionisation. *Int. J. Mass Spectrom.* 219, 697-701 (2002).
102. Karavanskii, V., Gillin, W., Sapelkin, A., Melnik, N. N. & Zavaritskaya, T. N. Photoluminescence relaxation kinetics in vapor etched porous silicon. In *Proc. SPIE Int. Conf. Advanced Laser Technologies*, Tianjin, China, Jun. 10, 2006, (2005). 6344 (2006), 286-292
103. Alimpiev, S., Nikiforov, S., Karavanskii, V., Miton, T. & Sunner, J. On the mechanism of laser-induced desorption-ionisation of organic compounds from etched silicon and carbon surfaces. *J. Chem. Phys.* 115, 1891-1901 (2001).
104. Grechnikov, A. A., Mogilevskii, A. N., Alimpiev, S. S. & Nikiforov, S. M. Generator of a vapor microflow for the calibration of gas analyzers. (2006). *RU 2005-113964*.
105. Musyimi, H. K., Narcisse, D. A., Zhang, X., Stryjewski, W., Soper, S. A. & Murray, K. K. Online CE-MALDI-TOF MS Using a Rotating Ball Interface. *Anal. Chem.* 76, 5968-5973 (2004).

106. Luo, G., Chen, Y., Siuzdak, G. & A., V. Surface Modification and Laser Pulse Length Effects on Internal Energy Transfer in DIOS. *J. Phys. Chem. B* 109, 24450-24456 (2005).
107. Nordstrom, A., Apon, J. V., Uritboonthai, W., Go, E. P. & Siuzdak, G. Surfactant-Enhanced Desorption/Ionization on Silicon Mass Spectrometry. *Anal. Chem.* 78, 272-278 (2006).
108. Gloria, R., Lichtenberg, J., Hierlemann, A. & Poulikakos, D. Micro Platform for Investigation of Explosive Vaporization in Micro Enclosures. 9th International Conference on Miniaturized Systems for Chemistry and Life Sciences (μ TAS), Boston, Massachusetts, USA, 9-13th October, (2005).
109. Choi, H.-J. & Pyun, J.-C. Korea Inst. Science Technology. Nanowire Assisted Laser Desorption/Ionization Mass Spectrometric Analysis. (2005). *WO 2005KR00738 2005315*.
110. Alimpiev, S., Nikiforov, S., Karavanski, V., Grechnikov, A. & Sunner, J. Laser desorption of ions from microscopically rough surfaces. Novel approaches for ultrahigh sensitivity detection of organic and bioorganic compounds. The International Symposium Intensive Laser Action & Technological Applications, Saint-Petersburg-Pushkin, Russia, June 29 - July 3, (2003).
111. Anderson, D. F. Mechanism and Application of Desorption/Ionization on Porous Silicon (DIOS). Ph.D. thesis, University of Florida, (2003).
112. Okuno, S. & Wada, Y. Measurement of serum salicylate levels by solid-phase extraction and desorption/ionization on silicon mass spectrometry. *J. Mass Spectrom.* 40, 1000-1004 (2005).
113. Steenwyk, R. C., Hutzler, J. M., Sams, J., Shen, Z. & Siuzdak, G. Atmospheric pressure desorption/ionization on silicon ion trap mass spectrometry applied to the quantitation of midazolam in rat plasma and determination of midazolam 1'-hydroxylation kinetics in human liver microsomes. *Rapid Commun. Mass Spectrom.* 20, 3717-3722 (2006).
114. Finkel, N. H., Prevo, B. G., Velez, O. D. & He, L. Ordered silicon nanocavity arrays in surface-assisted desorption/ionization mass spectrometry. *Anal. Chem.* 77, 1088-1095 (2005).
115. Finkel, N. H. Surface-Assisted Laser Desorption/Ionization-Mass Spectrometry (SALDI-MS) of Controlled Nanofeatures and the Associated Thermal Properties. MSci. thesis, North Carolina State University, (2005).

116. Vaidyanathan, S., Jones, D. G., Ellis, J., Jenkins, T. E., Dunn, W., Hayes, A., Burton, N., Oliver, S., Kell, D. B. & Goodacre, R. A laser desorption ionisation mass spectrometry approach for high throughput metabolomics. *Metabolomics* 1, 1-8 (2005).
117. Kruse, R. A., Rubakhin, S. S., Romanova, E. V., Bohn, P. W. & Sweedler, J. V. Direct assay of Aplysia tissues and cells with laser desorption/ionization mass spectrometry on porous silicon. *J. Mass Spectrom.* 36, 1317-1322 (2001).
118. Liu, Q., Guo, Z. & He, L. Mass Spectrometry Imaging of Small Molecules Using Desorption/Ionization on Silicon (DIOS). *Anal. Chem.* 79, 3535-3541 (2007).
119. Murray, K. K., Boyd, R. K., Eberlin, M. N., Langley, G. J., Li, L. & Naito, Y. Provisional Recommendations on the Standard Definitions of Terms Relating to Mass Spectrometry. 31st January, 2007.

CHAPTER 2 METHODOLOGY AND EXPERIMENTAL

2.1 Introduction

The aims of this chapter are a preparation to the study of surface characterisation of the matrix-free LDI substrates, including the methodologies and instrumental aspect. Some of the physicochemical properties of matrix-free LDI substrates have been discussed in Chapter 1. In this chapter, a detailed description of the chemistry of porous silicon (the major material used in this study) is provided. Experimental design ensures the success of a comprehensive scientific study. The common surface techniques used in characterisation of structured silicon surface are reviewed and suitable approaches for this study are selected. The principles of the selected surface techniques are discussed. Detailed description of materials, chemical modification of the LDI substrates, instrumental design and experimental parameters are provided in this chapter.

2.2 Chemistry of Porous Silicon

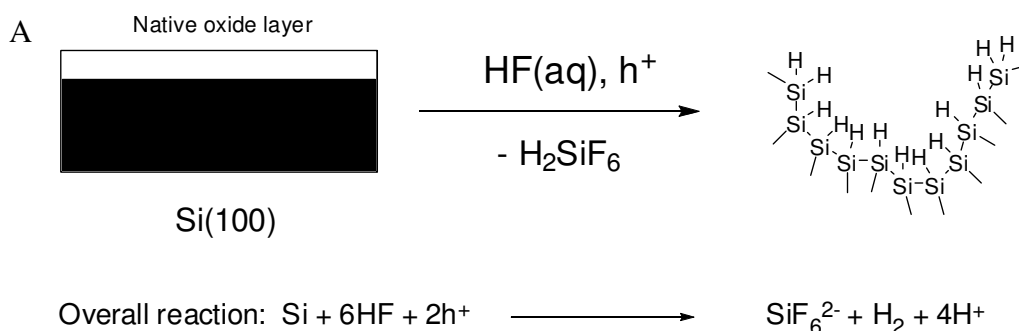
Electrochemical etching of silicon under controlled conditions leads to the formation of nanocrystalline silicon where quantum confinement of photoexcited carriers yields to a band gap opening and an increased radiative transition[‡] rate.¹ The resulting material is named porous silicon (PSi) due to its morphology composed by a disordered web of pores entering into Si. Its structure is like a sponge where quantum effects play a fundamental role. These features, being a quantum system and a sponge are keys both to the success and failure of PSi.¹ In fact, many possible applications exploit the quantum confinement (*e.g.* in light emitting diodes) or the high reactivity of its surface (*e.g.* sensor applications), but to apply PSi to a practical use, one has to master its quantum sponge nature and the methods of investigation.

Dissolution Chemistries:

PSi is formed by an electrochemical etching of Si in an HF solution. Following an electrochemical reaction occurring at the Si surface a partial dissolution of Si settles

[‡] The electronic transition between valance and conduction band, in exchanging photon energy.

in. The exact dissolution chemistries of Si are still in question and different mechanisms have been proposed. It is generally believed that several different reactions are occurring simultaneously during the anodic etching. The reaction ultimately leads to oxidation and dissolution of the surface to silicon hexafluoride.² (Figure 2-1) Under these conditions, Si-Si bonds are electrochemically activated and react with fluoride ions to form soluble, molecular perfluoro species. Solvation of these silicon fluorides by the etching medium yields a physically irregular, high area PSi matrix.² The surface of freshly etched PSi is hydride-terminated (with > 99% of surface silicon atoms capped with 1-3 hydrogen) and not oxide-terminated, resulting in a hydrophobic and chemically homogeneous interface.



**Printed version includes figure(s) extracted
from the reference source describing
a Teflon etching cell and etching process.
Please refer to the cited reference for detail**

Figure 2-1 Schematic representation of PSi production. (A) The reaction is initiated by positive hole generation (h^+), followed by nucleophilic attack of fluoride species with Si and dissolution of SiF_6^{2-} resulting a hydrogen passivated Si surface. (B) Etching cell and control unit. (C) Fabry-Pérot fringes - appearance of colours within the etching solution is a visual indicator for anodisation. The colour changes across the sample and each colour corresponds to a different optical thickness.^{2, 3, 4}

The etching process is controlled by a number of factors, including the composition of the etching solution (electrolyte), the anodic current and potential, wafer type and

resistivity, anodisation duration, illumination (n-type mainly), temperature, etching time and the design of the etching cell. Although substrate fabrication is not involved in this study, the etching parameters directly affect the physicochemical properties of the substrates, the significance of which will be seen in Chapter 3.

Electrolyte:

HF is available commercially as an aqueous solution with up to 50% of HF. As for its uses for PSi production, it is diluted in deionised or ultra-pure water. Absolute ethanol (exceeding 15%) is usually added to the aqueous solution. Adjusting the pH by adding acetic acid is also possible. HF/ethanol mixtures are termed aqueous electrolyte. The function of ethanol is to reduce the surface tension and hence increase the wettability of the PSi surface, ensuring the infiltration of HF solutions within the pores. This is very important for the lateral homogeneity and the uniformity of the PSi layer in depth. In addition, during the reaction hydrogen evolution occurs. Bubbles form and stick on the Si surface in pure aqueous solutions, whereas they are promptly removed if ethanol (or some other surfactant) is present.¹ Moreover, the temperature and electrolyte viscosity also has an influence on the lateral inhomogeneity and surface roughness of the PSi produced.⁵

Addition of an oxidising agent into aqueous HF electrolyte leads to an oxidising electrolyte.⁵ This method is also called stain etching. Nitric acid is an oxidising agent commonly used. Other examples include 0.01-0.1 M H_3PO_4 mixed with 0.001-0.01 M HF,⁶ and diluted HF with some CrO_4 .⁷ Stain-etching is useful if one needs to produce a very thin PSi film. In the formula of $\text{H}_3\text{PO}_4/\text{HF}$, the mechanism of oxide detachment is thought to occur, an anodisation process due to the formation of a thin (50-90) nm oxide layer at the sample surface and its subsequent lifting off.⁶

It is possible to say, the use of aqueous electrolyte and oxidising electrolyte ascribes one of the major differences between the DIOS and SALDI substrates in this study.

Apart from aqueous electrolyte of HF, mixing HF with an organic solvent is also possible and is termed organic electrolyte.⁵ Common organic solvents are listed in Table 2-1.

Table 2-1 Organic electrolytes used in Si electrochemistry and some of their major properties.⁵

**Printed version includes a table extracted
from the reference source describing
various organic electrolytes used for
electrochemical etching of porous silicon.
Please refer to the cited reference for detail**

Current-Voltage (I-V) Characteristics:

Typical *I-V* relationships of the electrochemical cell are shown in Figure 2-2 A and B. For p-type silicon in aqueous diluted HF solution, the diode like behaviour of the Si/HF contact is described by the terms "forward" direction (anodic) and "reverse" direction (cathodic) where only a small leakage is flowing. In the forward region, P_{Si} is formed only below the current peak i_{PS} . (Morphology C and D) Above this region, electro-polishing occurs.

For n-type silicon, the situation is reversed. The cathodic region is the forward biased region. The reverse region is anodic and only a small leakage current flows. In order to generate the same current voltage behaviour as for p-type Si on n-type samples, the electrode has to be illuminated with a high light intensity to generate positive hole. The current voltage curve shows exactly the same behaviour under these conditions except for a cathodic voltage shift of about 500 mV, which is due to the differences in Fermi energies of the different material. P_{Si} is formed below the current peak i_{PS} . Pore

morphology depends on the etching potential. (Morphology C, D and E) However, one can still obtain PSi in n-type Si in the dark, at a large etching potential. While this surface has a similar appearance to n^+ -mesopores, the pore wall of the PSi is damaged (called “break through” pores). (Morphology F) In the discussion of the physicochemical properties of DIOS substrate in the section 1.4.1, Shen, *et al.*⁸ prepared an alternative version of substrate in the dark, but the surface morphology was not presented. According to the etching parameters, that surface should have a porous morphology similar to F.

**Printed version includes figure(s) extracted
from the reference source describing
the current-voltage characteristics of electrochemical etching
of p and n-type silicon under aqueous electrolyte
and the resulting microscopic surface morphology.
Please refer to the cited reference for detail**

Figure 2-2 Representative I-V characteristics of (A) p-type, (B) n-type Si under aqueous electrolyte. Porosification occurs at the regions where $i < i_{ps}$ (highlighted in red). Depending on the etching parameters, four possible porous structure can result: (C) microporous, (D) mesoporous, (E) macroporous and (F) damaged pore walls as a result of electrical breakdown. Electropolishing occurs at the region with current densities $i_{ps} < i_{ox}$.⁹

Effects of Current Density:

For p-type substrates, and for a given HF concentration, the porosity increases with increasing current density. However, for a fixed current density, the porosity decreases with HF concentration.¹ (Figure 2-3a)

For heavily doped n-type Si, the porosity as a function of current density is quite different from the corresponding curves obtained for p-type doped substrates. The porosity exhibits a sharp minimum around 20 mA/cm². (Figure 2-3b) For higher current densities, the behaviour is similar to the p-type doped substrates, but for lower current densities the porosity increases sharply.¹ This large increase in porosity is not explained simply by chemical dissolution but is due to a difference in microstructure. In n-type doped Si, the layers obtained at low current density have a finer structure.¹ On the other hand, the reference source did not mention any increase or decrease in porosity with respect to the HF concentration. It is because the resulting porosity of the substrate does not depend on the concentration of the HF.

**Printed version includes figure(s) extracted
from the reference source describing
the porosity as a function of etching current density
for p and n-type silicon substrate.
Please refer to the cited reference for detail**

Figure 2-3 Porosity as a function of current densities for (a) lightly doped p-type and (b) highly doped n-type silicon substrate.¹⁰

Classification of Morphology:

Figure 2-2 presents four possible porous morphologies. According to IUPAC, the size of the pores is classified into three categories: 1) micropores – with pore diameters and pore distances (or geometries) < 10 nm, mesopores – with geometries in the 10-50 nm region and macropores – with geometries > 50 nm. However, such classification of the geometry of pores does not contain much information about the microscopic information on the morphology of the PSi layer. Terminology such as porous, nano-dot, or nano-well are used to describe the surface morphology in this study.

Chemical Composition of As-prepared PSi:

The internal surface of a PSi layer is very large. Such a large surface contains an enormous quantity of impurities coming from the electrolyte used for electrochemical etching and from the ambient air. Even the vessels in which the samples are stored could contribute to the sample contamination. It is necessary to know the chemical composition of PSi because its properties depend on impurity content and surface passivation.

The original impurity, which is always found in PSi layers, is hydrogen. Freshly etched PSi is almost totally covered by SiH_x groups. ($x = 1, 2, 3$). After formation and drying, the Si-H_x groups are still present on the inner surface for weeks and even months.¹ Hydrogen desorption occurs during annealing. Hydrogen desorbs from SiH_3 groups between 300 and 400°C, while desorption from SiH_2 occurs at 400°C and from SiH around 500°C.¹¹

The second original impurity found in PSi is fluorine. The form in which fluorine is present in PSi is still in question. Desorption experiments demonstrated that SiF_3 groups desorb at the same temperature as SiH_3 , indicating that SiF_3 groups are present on the pore walls.¹¹ The content of fluorine decreases with time. It has been proposed that SiF bonds are progressively replaced by Si-OH bonds through hydrolysis reaction with water vapour in air. On the other hand, only HF and SiF_6^{2-} could be detected by

^{19}F NMR.¹² According to these results, fluorine comes only from residual electrolyte in the pores.

Other impurities are usually incorporated after the anodisation process. These impurities include carbon and oxygen. The source of carbon is atmospheric. The carbon comes from hydrocarbon molecules present in the ambient air and often also in the residual gas in analysis chambers used for SIMS, IR, XPS, etc. Oxygen is normally adsorbed in a few minutes after drying in ambient air. The amount of oxygen can be as high as 1% after 15 min of air exposure and increases to very high percentage values with aging. Dangling bonds are another important feature of PSi. They are the paramagnetic defect at the Si/SiO₂ interface (Pb centres) and have a $\cdot\text{Si}\equiv\text{Si}_3$ structure. Another relevant paramagnetic centre is the $\cdot\text{Si}\equiv\text{SO}_3$ defect (E' centre), which is formed especially in hydrogen depleted oxide layers. The presence of dangling bonds are characterised by electron parametric resonance (EPR) and the concentration of dangling bonds decreases after water and ethanol adsorption.^{13, 14} (Figure 2-4)

**Printed version includes figure(s) extracted
from the reference source describing
the EPR spectra of porous silicon before and after
oxygen, water vapour, ethanol vapour and C₂(CH)₄ adsorption.
Please refer to the cited reference for detail**

Figure 2-4 EPR spectra of PSi (A) before and after O₂ and H₂O adsorption, and (B) after ethanol and C₂(CN)₄ adsorption.¹⁴

Aging and Surface Modification:

The native hydrides terminated surface is metastable and will oxidise in ambient air. This process is referred as aging. While surface oxides passivate the nanocrystalline silicon and stabilise the surface, the electrically insulating and structural defective character of the oxide layer is normally unwanted.² Furthermore, excessive or uncontrolled oxidation may deleteriously and irreversibly alter the useful, inherent properties of nanocrystallites, compromising their integrity and drastically limiting their utility.² Research has been focused on developing methods for the preparation of chemically functional interfaces that protect the underlying silicon nanocrystallites from degradation without changing or annihilating their intrinsic behaviour and for greater control over the interfacial properties.

Two general approaches have been taken. The first involves oxidation of the PSi surface and subsequent reaction with alkoxy- or chlorosilanes. A second approach utilises the native chemical functionalities on the surface of freshly etched material through a series of reactions developed on PSi surfaces. Not only can surface hydrides be used as chemical handles through which derivatisation can take place, but the weaker Si-Si bonds have also proven themselves to be reactive.¹⁵ PSi passivated with organic moieties has higher resistance to oxidation and gives some regulation over the stability of this material. Additionally, the well-documented silane chemistry opens many possibilities in targeted surface tailoring or manipulation, allows the synthesis of derivatised surfaces exhibiting distinct chemical activities or increased sensitivity toward specific analytes.

2.3 Methods of Surface Characterisation

The physical and chemical properties of PSi can be characterised by a variety of analytical techniques. Commonly used methods and their advantages and disadvantages are listed in Table 2-2. Not every technique will be employed, but they are included for reference. The selection depends on availability and suitability. The basic principles of the chosen methods are described in the next section.

Table 2-2 Comparison of various surface techniques commonly used in characterisation of PSi.^{1,2}

| Technique | Advantages | Limitations |
|--|---|--|
| <i>A. Imaging techniques to acquire information about the structural elements of the silicon matrix, such as size, shape, and orientation of the nanocrystalline</i> | | |
| Scanning electron microscopy (SEM) | Provide a pseudo-three-dimensional perspective of the surface topography and reveal details about the size and extent of the porous layer. | For the imaging with SEM, ordinarily an ultra-thin layer of carbon or gold is used to ensure strong contrast and minimise specimen charging. Can cause radiation damage to the sample. |
| Transmission electron microscopy (TEM) | Provide a cross-section image of the porous layer. Particularly suitable to investigation multilayer stack composition prepared by periodic variation of the etching parameters. | Relative to SEM, more specimen preparation is needed. Imaging with TEM requires exceptional caution in the preparation of microscopy samples. Ion milling is the most successful means of preparing exceptional thin specimens without inflicting significant damage to the nanocrystalline structure. |
| Atomic force microscopy (AFM), and scanning tunnelling microscopy (STM) | Both AFM and STM can be used to image PSi surface to atomic scale lateral resolution. Three-dimensional surface profile. Can be operated in ambient air or even a liquid environment. | The dimensions of the scanning probe tip often exceeded those of the porous matrix, resulting in distortion of the vertical scale. AFM does not allow to image deep pores and only the top end of the pores is imaged. STM is limited by the high resistivity of the material. |
| <i>B. To identify the chemical nature or probe the surface chemical composition</i> | | |
| Energy dispersive X-ray spectroscopy (EDS) | Provides rapid qualitative analysis of elemental composition. Combinable with SEM instrument. | Quantitative analysis requires adequate standards |

| | | |
|--|--|---|
| Fourier Transform InfraRed (FTIR) | FTIR signal in PSi is larger relative to the bulk silicon due to much larger specific area. | High concentration of dopant is opaque to IR radiation and obscures the analysis. |
| Secondary ion mass spectrometry (SIMS) | High sensitivity. Elemental and chemical mapping on a sub-micron scale. Able to carry out depth profiling. | Non-quantitative (semi-quantitative at best). Destructive method. Matrix effects. Charging may be a problem in some samples. |
| X-ray photoelectron spectroscopy (XPS) | Quantitative, including chemical state differences between samples. Able to carry out depth profiling with an aid of ion gun and oxide thickness measurements. | Detection limits typically ~ 0.1 at%. The quantitative accuracy for the weak XPS signals is poor. Limited specific organic information. Long analysis time. Sample degradation during analysis. |

C. Measurements on porosity, the specific surface area and interfacial interaction

| | | |
|---------------------------|--|---|
| Weight measurement | Porosity is defined as the fraction of void within the PSi layer and can be determined by weight measurements (before and after anodisation) | No |
| Gas absorption | An approximation of the specific surface area of PSi can be achieved through Brunauer-Emmett-Teller (BET) analysis. Information regarding to the pore size distribution can also obtain. | Very time consuming. Becomes complicated when a mixture of pores co-exist in the same sample. |
| Contact angle measurement | Provide information regarding to the interfacial interaction with the deposited liquid. Low cost and fast. | Surface roughness, surface heterogeneity, adsorption of contamination, vapour and surfactants, all effect to the accurate measurement |

2.3.1 Principles of SEM

SEM is a type of electron microscopy which produces images by detecting low energy secondary electrons (< 50 eV) and so only those formed within the first few nanometers of the sample surface have enough energy to escape and be detected. In the SEM instrument used in this study, an electron beam is first created by thermal excitation of a tungsten hairpin filament and is accelerated toward an anode.¹⁶ Alternatively, electrons can be emitted via field emission and is termed field emission scanning electron microscope (FE-SEM). FE-SEM provides an improved spatial resolution over conventional SEM. The electron beam is focused by magnetic condenser lenses to a very fine beam. The beam then passes through objective lens, which deflect the beam so that it scans in a raster fashion over the sample surface. When the electrons strike the sample, a variety of signals are generated, including X-ray, auger electrons, backscattered electrons and secondary electrons. (Figure 2-5) The detection of secondary electrons, produced by multiple inelastic scattering processes, generates a secondary electron image (SEI) and the contrast in the image is determined by the sample topography (with millimetres depth of field).¹⁷

**Printed version includes figure(s) extracted
from the reference source describing
the electron-specimen interactions.
Please refer to the cited reference for detail**

Figure 2-5 Electron-specimen interactions.¹⁸

Other specific signals originated from different regions of the sample surface can also provide useful information. The emitted X-ray has an energy characteristic of the parent element. Detection and measurement of the X-ray energy permits elemental analysis and this technique is called EDS. Sampling depth of EDS is 1-2 micrometers. Furthermore, the incident primary electrons cause ionisation of atoms. Subsequent relaxation of the ionised atoms leads to the emission of Auger electrons characteristic of the elements present on the sample surface and is the basis of Auger electron spectroscopy (AES) and scanning Auger microscopy (SAM). The technique is surface sensitive (within a few nanometres deep in the surface). For direct band gap semiconductors, such as GaAs and GaN, the SEM electron beam injection induces cathodoluminescence. Cathodoluminescence is a very powerful probe of the optoelectronic behaviour of semiconductors, particularly for studying nanoscaled features and defects.^{16, 17, 19, 20}

2.3.2 Principles of AFM

The AFM is one of the foremost tools for imaging, measuring and manipulating matter at the nanoscale. By using AFM, one cannot only image the surface in atomic resolution but also measure the force at nano-newton scale.

In a typical AFM experiment, a sample surface is placed on a piezoelectric stage, where an AFM probe is brought into close proximity of a sample surface. An AFM probe, typically made of silicon or silicon nitride, consists of a cantilever with a sharp tip, of which the radius of curvature is in the order of nanometers. A laser beam is directed to the upper end of the cantilever and is reflected to the photodiode detector. The weak physical forces, usually less than 10^{-9} N, between the tip and the sample surface lead to an extremely small deflection of cantilever. The deflection is measured, via the reflected laser spot, by an array of photodiodes. The physical forces include Van der Waals forces, mechanical contact force, capillary forces, electrostatic forces, magnetic forces and even chemical forces between the tip and the sample. A constant mean distance (to obtain force information) or force (to obtain height information) between the tip and the surface is maintained by a feedback mechanism, which triggers the z direction movement of the piezoelectric stage. The piezoelectric stage is

also responsible for the x and y direction movement, allowing scanning over the sample along a continuous sequence of raster lines. Recording this movement forms the topographical image.¹⁷ (Figure 2-6)

**Printed version includes figure(s) extracted
from the reference source describing
the principle of AFM and
contain a SEM image of a silicon integrated cantilever.
Please refer to the cited reference for detail**

Figure 2-6 (A) Schematic of AFM. The deflection of a microfabricated cantilever with a sharp tip is measured by reflecting a laser beam off the backside of the cantilever while it is scanning over the surface of the sample. (B) A SEM image of an integrated silicon cantilever. The tips typically have an end radius of curvature 5 to 10 nm.²¹

Modern AFM instruments can be operated in a number of modes, depending on the application, such as imaging with contact, non-contact and tapping mode and force-distance measurements. Only tapping mode for imaging is used in this study and hence will be focused upon in this section.

In the tapping mode, the cantilever is driven to oscillate at or slightly below its resonance frequency using a piezoelectric crystal. However, the cantilever is oscillated in a way that the tip lightly touches or “taps” the surface briefly in each oscillation cycle, and then enough restoring force is provided by the cantilever spring to detach the tip from the sample. As the oscillating cantilever begins to contact the surface intermittently, the oscillation amplitude or phase is modulated by tip-sample interactions and such changes provide the feedback signal for imaging. The changes in the phase of oscillation can also be used to discriminate between different types of

materials on the surface. This technique allows imaging of sample surfaces that are easily damaged, loosely held to their substrate or otherwise difficult to image by other conventional AFM techniques because it overcomes major problems associated with friction, adhesion, electrostatic forces, and other tip-sample related difficulties that can plague other AFM scanning methods.^{17, 21, 22}

2.3.3 Principles of ToF-SIMS

Time-of-Flight Secondary Ion Mass Spectroscopy (ToF-SIMS) uses a pulsed ion beam (usually Cs^+ or Ga^+) of a few keV to sputter molecules from the uppermost atomic layers of the sample surface. Most of the emitted species are neutral, but a small proportion of the emitted species are ionised (secondary ions). These particles are then accelerated into a time-of-flight mass analyser and their mass-to-charge ratio is determined by measuring the exact time at which they reach the detector. SIMS is the most sensitive of all the commonly employed surface analytical techniques. This is because of the inherent sensitivity associated with mass spectrometric-based techniques. Analysing the secondary ions with a mass spectrometer provides information about the elemental, isotopic and molecular composition of the surface.²³

Four operational modes are available using ToF-SIMS:²⁴

- | | |
|--|--|
| 1. Surface spectroscopy (static SIMS): | Used for sub-monolayer chemical analysis, where the applied primary ions dose density is low enough ($< 10^{13} \text{ cm}^{-2}$) to keep the surface quasi non-destructive. |
| 2. Depth profiling (dynamic SIMS) | SIMS is destructive in nature because particles are removed from the surface. This can be used to erode the solid in a controlled manner to obtain in-depth profiles of elements. |
| 3. Ion imaging | By rastering a fine-focussed ion beam over the surface, spatially resolved secondary ion images (chemical maps) can be obtained. |
| 4. 3D analysis | A variant of combining dynamic and imaging SIMS to produce a visualisation of 3D sample structures. Rate of erosion is subjected to different chemical composition on the surface. |

SIMS has several important characteristics:

- SIMS is a surface specific technique because the emitted particles originate from the uppermost one or two monolayers.
- The ionisation efficiency of elemental species is dependent on the ionisation potential (for positive ions) and electron affinity (for negative ions) of the element. (Figure 2-7A and B)
- The secondary ion yields will vary greatly according to the sputtering conditions (primary beam effects) and the chemical environment (matrix effects) of the surface. (Figure 2-7C) For example, significant enhancement in positive ion yields is observed in the presence of highly electronegative elements such as oxygen and fluorine in the sample,^{25, 26} whereas suppression can occur in the presence of an analyte of high gas phase basicity.²⁷ This is one of the major problems with quantification using SIMS and the technique is considered largely qualitative.

**Printed version includes figure(s) extracted
from the reference source describing
the relative ion yield of various elements as a function of their (A)
ionisation potential, (B) electron affinity and (C) the matrix effect of the
substrate.
Please refer to the cited reference for detail**

Figure 2-7 (A) Positive ion yields plotted as a function of ionisation potential. The ion yields are relative to silicon in a silicon matrix with O_2^+ sputtering. (B) Negative ion yields plotted against electron affinities. The ion yields are relative to silicon for measurements in a silicon matrix with Cs^+ ion sputtering.²⁸ (C) Useful yield of Si in four matrices (Si, SiC, Si_3N_4 , and SiO_2) obtained in the Si^+ mode under three different PI (Cs^+ , Ga^+ , O_2^+) bombardments and in the $SiCs^+$ mode. Incorporation of Cs into the material and detecting MCs^+ clusters circumvent matrix effect.²⁹

2.3.4 Principles of XPS

XPS is a surface sensitive (typical detection depth ~10 nm), quantitative chemical analysis technique capable of determining the elemental composition, chemical state and electronic state of the elements on the surface of a material. XPS is a Nobel Prize winning technology. (Physics 1981) The technique relies on irradiation of a material with soft X-rays, which leads to expulsion of the inner shell, or lowest energy electrons. This photoelectric phenomenon was outlined by Einstein in 1905 in equation (0.1).

$$E_B = h\nu - E_K - \Phi \quad (0.1)$$

Where

E_B is the binding energy (the energy required to release an electron from its atomic or molecular orbital, conventionally measured with respect to the Fermi-level of the solid);

$h\nu$ is the energy of photons impinge upon the surface;

E_K is the kinetic energy of the ejected electron, and

Φ is the work function - the energy requires to remove an electron from Fermi-level to vacuum level. Fermi-level is the highest occupied energy level.

In an XPS experiment, a sample is irradiated with monochromatic X-rays of a characteristic energy. The photoelectrons of different kinetic energy are resolved with a spherical mirror analyser and the flux of electrons leaving the surface is measured. By using equation (0.1), the binding energies of the electrons can thus be determined. This is because the binding energies are characteristic of each element and can be used for elemental identification. Furthermore, there is also a slight variation (chemical shift) in the electron binding energies depending on the chemical environment of the atom, providing information about the oxidation state and/or electronic state of an atom.

2.3.5 XPS Imaging (Spectromicroscopy)

Modern XPS instruments are not limited to spectroscopy but also capable of chemical imaging because of improved detector and instrument design leading to enhancement in spatial resolution and sensitivity. The method employs pulse-counting methods, which give high lateral resolution XPS images with quantitative intensities. However, in the image processing, the procedures usually involve a complicated mathematical calculation. A multivariate analysis of an extremely large dataset is carried out to provide chemical state information from the set of images. The PCA procedure can be applied either in the spatial domain or in the energy domain. Further detail can be seen at the CaseXPS help file and reference³⁰ and ³¹. A brief summary is given below.

The first step is to acquire a sequence of images with equal energy steps (typically at 0.2 to 0.5 eV step sizes) over a predetermined energy range. In the example below, the binding energy range over 110 – 95 eV corresponding to the Si 2p region was acquired. (Figure 2-8)

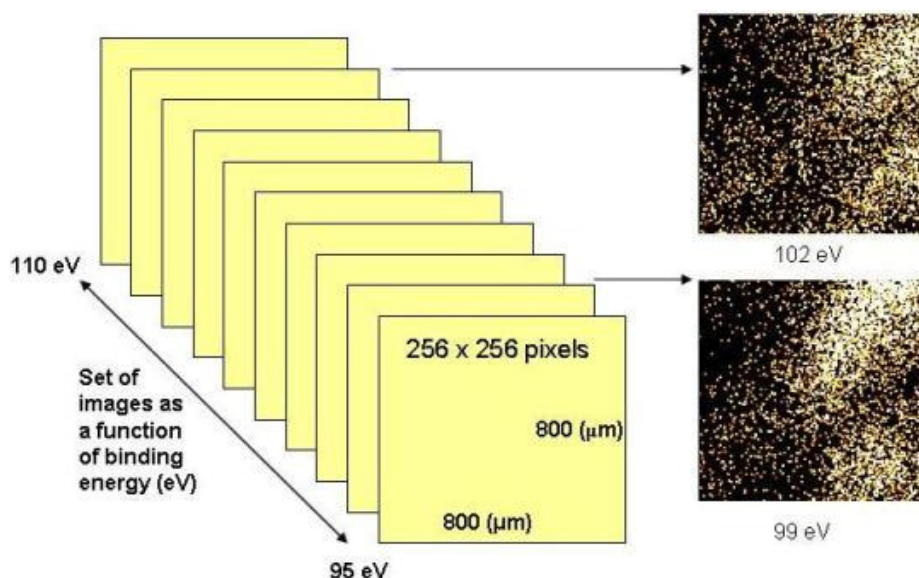


Figure 2-8 Schematic of imaging dataset. A stack of images acquired from the same location on the sample over a range of energies. The S/N of each image is relative poor and many of the images are merely noise.

Each image was acquired for 2 minutes, giving a total acquisition time of 2.5 hours for Si 2p region. Data acquisition was actually carried out along with C 1s and O 1s

regions, meaning that such a procedure is an overnight process. Although a very long experimental time is required, each experimental dataset actually contains 256×256 (65,536) spectra, the acquisition time for a spectrum-at-a-pixel is actually ~ 0.5 s and the S/N for each spectrum is poor. The Sp 2p image dataset actually contains $256 \times 256 \times 75$ channel spectra, which is an extremely large group of data. The data processing therefore requires multivariate statistical analysis approach to identify the chemically significant components of the dataset. Principal component analysis (PCA) and a reduced PCA sort are applied to the dataset to create an orthogonal set of vectors ordered by information content. Once identified the dataset may be reconstructed using only these components, removing the 'noise' components.

The PCA maintains orthogonality during its operation on the dataset. This constraint leads to intensive calculations. In order to reduce the calculation time, singular value decomposition (SVD) is performed to 'sort' the principle components of the large dataset before performing the PCA.³² The performing of SVD sort before PCA on the image data thus reduces the calculation time. The result of the PCA is a set of abstract factors (AF) with the first AF showing the average of all the images and the second AF showing the main deviation from the average and so on. Higher AF's are due to noise. The final image is calculated by a linear combination of the first few abstract factors, essentially removing the noise from the image.

2.3.6 Principles of Contact Angle Measurement

Contact angles are used as a quantitative measure of the wetting interaction between a liquid and a solid. It is defined geometrically as the angle formed by a liquid at the three-phase boundary where a liquid, gas and solid intersect. (Figure 2-9) It can be seen from the figure that if the angle θ_c is less than 90, the liquid spreads and is said to wet the solid. If it is greater than 90, it is said to be non-wetting. A zero contact angle is possible and represents complete wetting. Two different approaches are commonly used to measure contact angles of surfaces: goniometry and tensiometry. Goniometry involves the observation of a sessile drop of test liquid on a solid substrate. Tensiometry involves measuring the forces of interaction as a solid is contacted with a test liquid. Pure water is one of the most important test liquids.³³

■ Solid ■ Liquid □ Gas

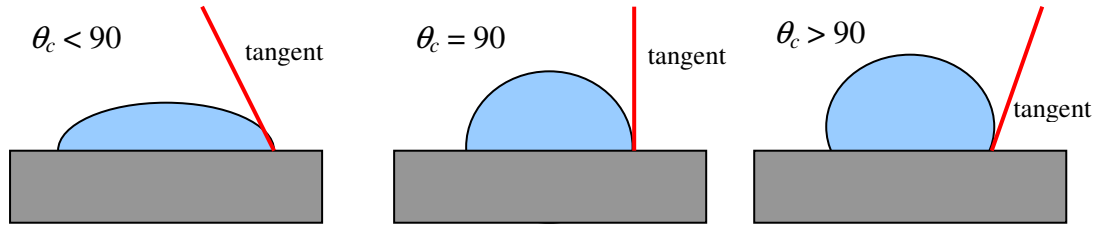
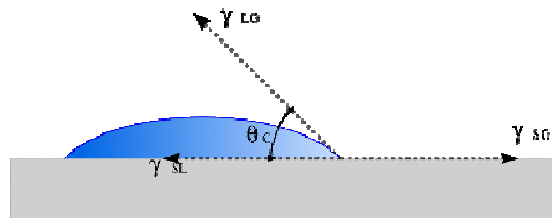


Figure 2-9 Contact angle, θ_c , at which a liquid/vapour interface meets the solid surface.

The basic elements of a goniometer include a light source, sample stage, lens and image capture. Contact angle can be assessed directly by measuring the angle formed between the solid and the tangent to the drop surface. Only the goniometer is used in this study.

The origin of the contact angle can be traced to the balance of forces at the line of contact between the liquid and the solid. If the solid/gas, solid/liquid, and liquid/gas surface tensions (the interfacial free energies) are denoted γ_{SG} , γ_{SL} and γ_{LG} respectively,



then the forces are in balance (*i.e.* chemical equilibrium) if

$$\gamma_{SG} = \gamma_{SL} + \gamma_{LG} \cos \theta_c \quad (\text{Young's equation})^{\S} \quad (0.2)$$

This expression solves to

[§] Young's equation is only valid in “dry wetting” condition. It also ignores the effects of gravitational distortion of the liquid droplet. However, for this study, the surface is dry and only a very small drop of water (less than 5 μl) is used, the gravitational effect can be ignored.

$$\cos \theta_c = \frac{\gamma_{SG} - \gamma_{SL}}{\gamma_{LG}} \quad (0.3)$$

If $0 < \theta_c < 90^\circ$ (which occurs when $\gamma_{SL} < \gamma_{SG}$), then the liquid “wet” the surface fully. In this case, no work is needed to create the solid/liquid interface. If $\theta_c > 90^\circ$ the cohesive forces of the liquid dominate over the adhesive forces between the liquid/solid interface (*e.g.* mercury on glass). If $\theta_c \approx 180^\circ$ (which occurs when $\gamma_{SG} = 0$), no work is needed to prepare the gas/solid interface, and a drop of liquid on the surface of a solid remains separated from it by a thin film of vapour. Measurement of contact angles therefore produces data reflecting the thermodynamics of a liquid/solid interaction.

Having said that contact angle is a result of thermodynamic equilibrium, lowering the excess surface energy by introducing proper roughness (and chemical termination, *e.g.* via fluoro-chemistry or polymer chemistry) on the surface may yield a high water contact angle.

A model to characterise the effect of the surface roughness on the wettability of a solid was first proposed by Wenzel.³⁴ In that model, the contact angle, θ_c , on a rough surface can be evaluated by considering a small displacement of the contact line parallel to the surface. (Figure 2-10)

**Printed version includes figure(s) extracted
from the reference source describing
the thermodynamic principle of contact angle on a rough surface
Please refer to the cited reference for detail**

Figure 2-10 Infinitesimal displacement of a liquid wedge on a rough surface.³⁵

The surface energies per unit contact line are modified by quantity dF , which is given as:

$$dF = -r(\gamma_{SG} - \gamma_{SL})dx + \gamma_{LG} dx \cos \theta_c \quad (0.4)$$

where r is the surface roughness, defined as the ratio of the real area of a rough surface to the geometric projected area. The equilibrium is given by the minimum of F , which results in Wenzel's law:

$$\cos \theta_c = r \cos \theta \quad (0.5)$$

where θ the contact angle on the projected surface.

Since the ratio between the real surface and the projected ones is always greater than one (*i.e.* $r > 1$), the wettability increases for a hydrophilic situation and decreases for a hydrophobic one. (Figure 2-11)

**Printed version includes figure(s) extracted
from the reference source describing
the apparent contact angle as a function of the surface roughness.
Please refer to the cited reference for detail**

Figure 2-11 The apparent contact angle θ_c as a function of solid surface roughness Γ as described by Wenzel's law.³⁵

This theory is only valid on the condition that the droplet has complete contact with the surface over their mutual interface. Wenzel's theory has to be refined when the geometry of the surface is made in such a way that this requirement is not met. An example for such a surface is porous, or a very rough surface. In this case, the droplet

has interfaces with the air being in the pores of the surface, because the droplet sits on the peaks of the surface feature and so bridges the gaps. For this, Cassie and Baxter have modified the Wenzel's equation, considering the solid-air interface of the droplet with the air in the pores. The droplet is therefore laid on a composite surface, composed of solid and air.³⁶ The equation (0.4) becomes:

$$dF = -f_s (\gamma_{SG} - \gamma_{SL}) dx + (1-f_s) \gamma_{LG} dx + \gamma_{LG} dx \cos \theta_c \quad (0.6)$$

where f_s is the fraction of fluid area in contact with the surface, and $(1-f_s)$ is the fraction of the fluid area in contact with air (assuming total contact area = 100%). At equilibrium, F is minimum and Eq. (0.6) results in:

$$\cos \theta_c = f_s \cos \theta + (1-f_s) \cos \theta \quad (0.7)$$

Assuming the water contact angle for air to be 180°, the second term becomes -1, the equation is reduced to:

$$\cos \theta_c = f_s (\cos \theta + 1) - 1 \quad (0.8)$$

The Cassie's law implies that with a small f_s and a large θ it is possible to create surfaces with a very large contact angle.

If the substrate is in the Wenzel's system during the contact with a liquid, the surface may exhibit a low contact angle. It indicates that a hydrophobic surface is not achieved. However, it is possible to reach a transition from the Wenzel to the Cassie/Baxter's system if an optimum roughness introduced to a hydrophobic substrate is optimised. These optimised surface structures can trap air, and has a very small contact area with the liquid water (*e.g.* increasing porosity, and nanowires), the surface will then exhibit super- or even ultra-hydrophobic properties necessary to achieve the lotus effect.³⁷ The significance of which will be discussed in the subsequent chapters.

2.4 Materials and Methods

2.4.1 Commercial DIOS Targets

The DIOS targets and holder were purchased from Waters Corp. (Manchester, UK). The targets were shipped in a sealed argon-filled anti-electrostatic pouch. (Figure 2-12 A) The chip and holder were engineered to the same dimensions for Micromass MALDI systems.

2.4.2 QuickMass Targets

QuickMass targets, with special coating on a steel target, were obtained from NanoHorizons Inc. (Pennsylvania, US) (Figure 2-12 B) and were shipped in a sealed container. Detailed information regarding to the surface preparation was not provided by the manufacturer.

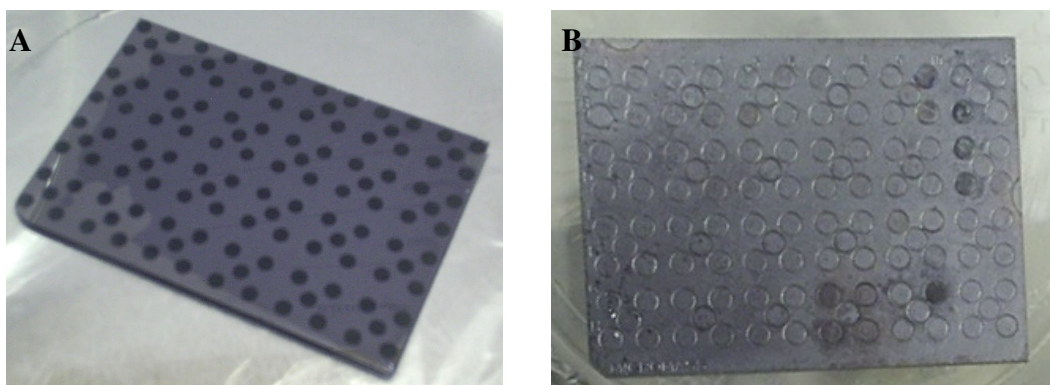


Figure 2-12 (A) DIOS target and (B) a steel MALDI target coated with QuickMass material.

2.4.3 SALDI Surfaces

The SALDI substrates were provided by the Laboratory for Laser Diagnostics for these investigations. The samples were classified according to their nature and preparation methods, *i.e.* standard (patented) and experimental (Figure 2-13). The

etching conditions of these SALDI substrates are listed in Table 2-3 and Table 2-4. Other non-etched roughened substrates were also studied. (Table 2-5)

1. Standard Silicon SALDI surface

Table 2-3 Etching condition of standard electrochemical etched silicon SALDI surfaces (J is etching current density, t is etching time), HF:EtOH denotes HF/ethanolic solution and HF:EtOH:I₂ denotes iodine in HF/ethanoic solution, respectively. Some surfaces were etched twice and are denoted by a slash.

| Batch Oct 2005 (5% iodine etching electrolyte) | | | | | | | |
|---|------------------------------------|---|---------------------------|-------------------------------|------------------------------------|--------------------------------------|--------------------------------|
| <i>Sample</i> | <i>Etching solution</i> | <i>I / mA</i> <i>cm⁻²</i> | <i>t /</i> <i>mins</i> | <i>Silicon</i> <i>type</i> | <i>Resistivity/</i> <i>Ω·cm</i> | <i>Crystal</i> <i>orientation</i> | <i>Polished</i> <i>side</i> |
| s1 | HF:EtOH:I ₂ | 1 | 5 | n ⁺⁺ | 0.010 | 100 | No |
| s2 | HF:EtOH:I ₂ | 1 | 7 | n ⁺⁺ | 0.010 | 100 | Yes |
| s3 | HF:EtOH:I ₂ | 1 | 7 | n ⁺⁺ | 0.010 | 100 | No |
| s4 | HF:EtOH:I ₂ | 1 | 5 | p ⁺ | 0.100 | 111 | Yes |
| s5 | HF:EtOH:I ₂ | 1 | 5 | n ⁺⁺ | 0.010 | 100 | Yes |
| Batch Aug 2006 (0.5% iodine etching electrolyte) | | | | | | | |
| <i>Sample</i> | <i>Etching solution</i> | <i>I / mA</i> <i>cm⁻²</i> | <i>t /</i> <i>mins</i> | <i>Silicon</i> <i>type</i> | <i>Resistivity/</i> <i>Ω·cm</i> | <i>Crystal</i> <i>orientation</i> | <i>Polished</i> <i>side</i> |
| a1 | HF:EtOH/ HF:EtOH:I ₂ | 20/ 1 | 2/ 5 | n ⁺⁺ | 0.010 | 100 | Yes |
| a2 | HF:EtOH | 20 | 2 | n ⁺⁺ | 0.010 | 100 | Yes |
| a3/ a6 | HF:EtOH/ HF:EtOH:I ₂ | 5/ 5 | 1/ 1 | n ⁺⁺ | 0.010 | 100 | Yes |
| a4/ a7 / a8 | HF:EtOH:I ₂ | 5 | 1 | n ⁺⁺ | 0.100 | 100 | Yes |
| a5 | HF:EtOH | 5 | 1 | n ⁺⁺ | 0.010 | 100 | Yes |
| A47-1/ A48-1 | HF:EtOH:I ₂ | 1 | 5 | n ⁺⁺ | 0.010 | 111 | Yes |
| T-1 | HF:EtOH:I ₂ | 1 | 5 | n ⁺⁺ | 0.010 | 100 | Yes |

2. Experimental Silicon SALDI Surface

Table 2-4 Etching condition of experimental electrochemical etched silicon SALDI surfaces.

| Batch Oct 2005 | | | | | |
|--|--|---|------------------------|----------------------------|----------|
| Sample | Substrate | Preparation method | | | |
| s10 | Silicon type: p ⁺⁺ Resistivity: 0.005 Ω·cm Crystal orientation: 111 Polished side | Substrate was first strain etched using HNO ₃ and then subsequently re-etched with HF:EtOH:I ₂ solution. Etching conditions have not been disclosed. | | | |
| s11 | Silicon type: p ⁺ Resistivity: 0.100 Ω·cm Crystal orientation: 111 Non-polished side | Substrate was first roughened by sanding and then subsequently electrochemical etched and oxidised by H ₂ O ₂ and then dipped into HF:EtOH/I ₂ solution. Etching conditions have not been disclosed. | | | |
| vefib-2 | No information has not been provided. | Vapour-phase etched surfaces, prepared by suspending a silicon substrate in a saturated vapour of HF/water (1:1) and I ₂ solution in a stealed container for 1 hour at room temperature. | | | |
| | | | | | |
| Batch Aug 2006 (0.5% iodine etching electrolyte) | | | | | |
| Sample | Substrate | Preparation method | Etching solution | I / mA cm ⁻² | t / mins |
| e1 | All substrates are | The substrate was first | HF:EtOH:I ₂ | 1 | 10 |
| e2 | p ⁺⁺ type silicon | preliminarily etched by | HF:EtOH | 1 | 10 |
| e3 | with resistivity 0.005 Ω·cm, cut at 111 orientation. | stain-etching using HNO ₃ and then subsequently re-etched. | HF:EtOH:I ₂ | 20 | 2 |

3. Other Substrates

Table 2-5 Other surfaces and their preparations.

| <i>Sample</i> | <i>Treatment or description</i> |
|------------------|-----------------------------------|
| Sanded surface | Sanded with diamond dust and bush |
| Graphite surface | Pyrolytic graphite |

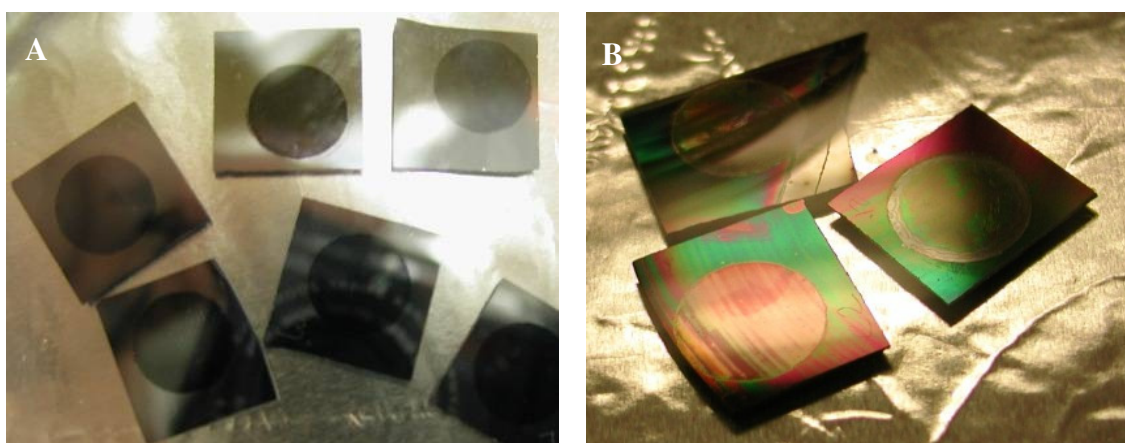


Figure 2-13 SALDI substrates: (A) standard SALDI substrates and (B) experimental SALDI substrates.

2.4.4 Solvents and Chemicals

Solvents and acids: Deionised water (18 MΩ) was generated by USF ELGA MAXIMA water system. Gradient grade acetonitrile, HPLC grade methanol, isopropanol, formic acid and trifluoroacetic acid were all purchased from Fisher. Table 2-6 lists the compounds used in this study. All were used without further purification.

Table 2-6 List of substances used for mass spectrometric investigation

| Substances | Additional information | Manufacturer |
|---|------------------------|--------------|
| [Glu ¹]-Fibrinopeptide B | | Sigma |
| 2-(4-aminophenyl)-6-methylbenzothiazole | | Aldrich |
| 2-Phenylglycine | | Aldrich |
| 3-Hydroxytyramine (Dopamine) | Hydrochloride | Sigma |
| 3,4-Dihydroxy-2-heptylquinoline (PQS) | | |
| 4-Bromobiphenyl | | Aldrich |
| 4-Hydroxyphenylglycine | | Acros |
| 4-Hydroxy-2-heptylquinoline (HHQ) | | |
| 4-Hydroxy-2-nonylquinoline (HNQ) | | |
| 4-Nitroimidazole | | Sigma |

| | | |
|---|--|-------------------|
| 8-Hydroxyquinoline | | |
| Acetylcholine chloride | | Sigma |
| Adenosine | | Sigma |
| Alprenolol | Hydrochloride | Sigma |
| Angiotensin I | Human | Calbiochem |
| Atenolol | | MP Biomedicals |
| Benzamide | | Aldrich |
| Bradykinin | Acetate salt | Sigma |
| Caesium iodide | | Sigma |
| Caffeine | | Aldrich |
| Cefadroxil | H ₂ O content 1.0 mol/mol | Sigma |
| Caesium iodide | | Sigma |
| Cholic acid | | Sigma |
| Cinoxacin | | Sigma |
| Copper II acetate monohydrate | | Aldrich |
| Di flunisal | | Sigma |
| Diphenhydramine | Hydrochloride | Sigma |
| D-Raffinose | Pentahydrate | Aldrich |
| Erythromycin | H ₂ O content 4.2% | Sigma |
| ES Tuning mix | | Agilent |
| Ethylenediamine | | Sigma |
| Flufenamic acid | MP 132-135 °C | Sigma |
| Flumequine | | Sigma |
| Fluorescein [C.I. 45350; Acid yellow 73] | Sodium Salt H ₂ O content 7.5% | Sigma |
| Folinic acid | Calcium salt H ₂ O content 11% Ethanol content 2.6% | Sigma |
| Furfurylamine | | Aldrich |
| Glyburide | | Calbiochem |
| Glycine | | Sigma |
| Heptadecafluorooctanesulfonic acid | Potassium salt | Fluka |
| Heptafluorobutyric acid | Liquid | Aldrich |

| | | |
|-------------------------------|--|-----------------|
| Homovanillic acid | | Acros |
| HPLC peptide standard mixture | | Sigma |
| Hydroquinone | | Aldrich |
| Imidazole | | Aldrich |
| Insulin (Bovine pancreases) | | Sigma-Aldrich |
| Iron III chloride | | Aldrich |
| Ketorolac (Toradol) | Tris salt | Sigma |
| Labetalol | Hydrochloride | Sigma |
| Lactic acid | Li salt | Sigma |
| L-Alanine | | Sigma |
| L-Arginine | Hydrochloride | Sigma |
| L-Ascorbic acid (Vitamin C) | | Sigma Fisher |
| L-Asparagine | MP 235 °C | Sigma |
| L-Aspartic acid | | Sigma |
| L-Cysteine | | Sigma |
| Leucine enkephalin | Peptide content 88% H ₂ O content 2 mol/mol Acetate content 0.5mol/mol | Sigma |
| L-Glutamic acid | | Sigma |
| L-Glutamine | | Sigma |
| L-Histidine | | Sigma |
| Lidocaine | Hydrochloride | Sigma |
| L-Isoleucine | | Sigma |
| L-Leucine | | Sigma |
| L-Lysine | | Sigma |
| L-Methionine | | Sigma |
| L-Phenylalanine | | Sigma |
| L-Proline | | Sigma |
| L-Serine | | Sigma |
| L-Threonine | | Sigma |
| L-Tryptophan | | Sigma |
| L-Tyrosine | | Sigma |
| L-Valine | | Sigma |

| | | |
|--|--------------------|-----------------------|
| Magnesium chloride | | Sigma |
| Malic acid | | Sigma |
| Metoprolol | Tartrate salt | Sigma |
| N-(2-Hydroxyethyl)piperazine-1-ethanesulfonic acid; (HEPES) | pKa = 7.5 at 25 °C | Sigma |
| N,N-Dimethylhexylamine | | Acro |
| Nadolol | | Sigma |
| Nalidixic acid | | Sigma |
| Naproxen | | Sigma |
| n-Decanoic acid | | BOH |
| N-Dodecylmethylamine | | Lancaster |
| Octadecylamine | | Sigma |
| Octadecyl-trimethylammonium bromide | | Aldrich |
| Ornidazole | | Sigma |
| Pentadecafluorooctanoic acid | | Aldrich |
| Pentafluoropropionic acid | Liquid | Aldrich |
| Peptide sequencing standard | | Sigma |
| Perfluoroundecanoic acid | | Aldrich |
| Phenethicillin | | Sigma |
| Phenyltrimethylammonium chloride | | Aldrich |
| Polyalanines Ala-Ala Ala-Ala-Ala Ala-Ala-Ala-Ala Ala-Ala-Ala-Ala-Ala | | Sigma |
| Polyethylene glycol (PEG) - 200 - 600 - 1000 | | Sigma BDH Sigma |
| Polyglycines - Gly-Gly - Gly-Gly-Gly - Gly-Gly-Gly-Gly- - Gly-Gly-Gly-Gly-Gly - Gly-Gly-Gly-Gly-Gly-Gly | | Sigma |

| | | |
|--|------------------------------|------------|
| Polyphenylalanine | | Sigma |
| - Phe-Phe | | |
| - Phe-Phe-Phe | | |
| - Phe-Phe-Phe-Phe | | |
| - Phe-Phe-Phe-Phe-Phe-Phe | | |
| Procainamide | Hydrochloride | Sigma |
| Reserpine | | Sigma |
| Rubidium iodide | | Acros |
| Sodium iodide | | Sigma |
| Sotalol | Hydrochloride | Sigma |
| Stearic acid | | Aldrich |
| Tertahexylammonium bromide | | Aldrich |
| Tetrabutylammonium hydrogen sulfate | | Fluka |
| Tetrabutylammonium phosphate monobasic | | Fluka |
| Timolol | Maleate salt | Sigma |
| Tinidazole | | Sigma |
| Tolmetin | Sodium salt dehydrate | Sigma |
| Tridecafluoroheptanoic acid | | Aldrich |
| Tris(hydroxymethyl)-methylamine | | Fisher |
| Verapamil | Hydrochloride (USP) | Acros |
| Vitamin B ₁₂ | | Biochemika |
| α -hydroxyisovaleric acid | | Sigma |
| β -Cyclodextrin | H ₂ O content 11% | Sigma |
| β -phenyllacetic acid | | Sigma |
| γ -Amino-n-butyric acid (GABA) | | Sigma |

2.4.5 Surface Characterisation

Surface analysis and imaging techniques such as Time-of-Flight secondary ion mass spectrometry (ToF-SIMS), X-ray photoelectron spectroscopy (XPS), scanning electron microscopy (SEM) and atomic force microscopy (AFM), are the methods of choice in surface chemistry investigation. Both AFM and SEM provided complementary information to the surface morphology. Because SIMS is surface specific (1 nm depth) and qualitative, XPS was employed to provide complementary

information to that generated by SIMS and provided surface sensitive (~10 nm depth) quantitative data. Water contact angle (WCA) was also used to evaluate the interfacial interactions of the substrates with liquid water.

2.4.5.1 SEM

SEM analysis was carried out in high vacuum mode using a JEOL JSM-6060LV SEM instrument. Accelerating voltage was 15-20kV and the objective lens distance was ~10 mm. The samples were first cleaved into a suitable size and mounted on a steel holder prior to SEM analysis. No gold coating was required for the analysis.

2.4.5.2 AFM

AFM investigation was carried out on a MultiMode AFM or Dimension 3100 Scanning Probe Microscope (SPM) (Veeco, Santa Barbara, CA, USA) operated using a single laser beam under tapping-mode with an etched silicon probe tip (TESP). The driving frequency was ~300 kHz. The silicon samples were cleaved into a suitable size and mounted on a steel plate using double-sided carbon tape before insertion into the AFM instrument. Acquired images were analysed using ImageMetrology SPIP version 4.

The surface roughness was indicated by the H_{RMS} value, which was calculated using equation (0.9) and (1.0).

$$\bar{H} = \frac{\left(\sum_{i=1}^N H_i \right)}{N} \quad (0.9)$$

$$H_{RMS} = \frac{\sqrt{\sum_{i=1}^N (H_i - \bar{H})^2}}{N} \quad (1.0)$$

Where \bar{H} is the average height and H the relative height and N is the number of points.

2.4.5.3 ToF-SIMS

The silicon samples were stored in HPLC grade isopropanol or were argon plasma etched before analysis. Samples were cleaved to suitable size and mounted under a cleaned molybdenum grid before insertion into the vacuum chamber.

ToF-SIMS data acquisition was carried out on an ION-TOF GmbH (Münster, Germany) TOF-SIMS IV instrument equipped with a reflectron mass analyser and microchannel plate (MCP) detector. The instrument employed a 15 keV $^{69}\text{Ga}^+$ and 10 keV $^{133}\text{Cs}^+$ liquid metal ion gun (LMIG) with 10kV post-acceleration. The AC primary ion (PI) beam was pulsed at 10 kHz frequency using a current between from 1.06 and 1.17 pA for Ga^+ LMIG and 0.95 pA for Cs^+ LMIG, bombarding an area $100 \times 100 \mu\text{m}^2$ (for high mass resolution), $300 \times 300 \mu\text{m}^2$, or $500 \times 500 \mu\text{m}^2$ (for high sensitivity and imaging) using a 256×256 raster. Both positive and negative ion spectra were acquired for each analysis area, with an ion dose of 5×10^{11} PI/cm² per polarity. The pressure of the main chamber was kept between 10^{-7} and 10^{-9} Torr (1 Torr = 133.3 Pa). Optical images were taken at the same time.

Calibration of the mass spectra in the positive detection mode was based on the following peaks, CH_2^+ (14.0157 amu), C_2H_2^+ (26.0157 amu), C_3H_2^+ (38.0157 amu), and C_4H_3^+ (51.0235 amu); and in negative detection mode on CH_2^- (14.0157 amu), C_2^- (24.0000 amu), C_3^- (36.0000 amu), C_4H^- (49.0078 amu). Data acquisition and post-processing analyses were performed using the IonSpec Version 4.010 and IonImage Version 4.0 supplied by the instrument manufacturer.

2.4.5.4 XPS

Samples were either stored in HPLC grade isopropanol or methanol, or argon plasma etched before analysis. Samples were cleaved into a suitable size and mounted on a steel bar using double-sided tape prior to insertion into vacuum chamber.

XPS data was acquired on a Kratos AXIS Ultra instrument, equipped with a delay-line detector (DLD) with a monochromatic Al K α X-ray source (1486.6 eV), operated at 15 mA emission current and 10 kV anode potential. Survey scan spectra were taken using the hemispherical analyser. Fixed analyser transmission (FAT) mode was used, with pass energy of 80 eV for survey scans and pass energy 20 eV for high resolution scans. The magnetic immersion lens system allowed the area of analysis for to be defined by apertures, a 'slot' aperture of 300 \times 700 μm^2 for survey and high resolution scans. The magnetic lens also utilises *magnetic confinement* to minimise charge broadening and improves spatial resolution. The photoelectron images were taken using the spherical mirror analyser from an area of 800 \times 800 μm^2 with 256 \times 256 pixels, the multi-spectral datasets being acquired at 40 eV pass energy, with field of view at 1, image aperture at 1 and stepping through the chosen energy regions at 0.2 eV intervals (count time 2 mins). The take off angle for the photoelectron analyser was 90°. A charge neutraliser filament above the sample surface gave a flux of low energy electrons providing uniform charge neutralisation. A schematic diagram of spectroscopy and imaging mode is shown at Figure 2-14. Datafiles were collected using the instrument Vision 2 software, converted to the VAMAS format, and processed using CasaXPS version 2.3.1.2 with Kratos sensitivity factors and core-level high-resolution scans were charge corrected using CH peak to 285 eV.

**Printed version includes figure(s) extracted
from the reference source describing
the operation of Kratos AXIS Ultra XPS system under spectroscopy
mode and imaging mode.
Please refer to the cited reference for detail**

Figure 2-14 Schematic diagrams of Kratos AXIS Ultra XPS system.³⁸

The SiO₂ thickness was determined using the equation (1.1):³⁹

$$d_{oxides} = \lambda_{SiO_2} \sin \theta \ln(1 + R_{\text{expt}} / R_0) \quad (1.1)$$

Where λ_{SiO_2} is the attenuation length of the Si 2p photoelectrons in SiO₂, θ is the angle between the sample surface plane and the entrance to the electron analyser.

$$\text{And } R_{\text{expt}} = I_{SiO_2} / I_{Si} \text{ and } R_0 = I_{SiO_2}^{\infty} / I_{Si}^{\infty} \quad (1.2)$$

Where I_{SiO_2} and I_{Si} are intensities of the Si 2p peak area in the oxide and metallic states respectively of unknown film, and $I_{SiO_2}^{\infty}$ and I_{Si}^{∞} are the equivalent intensities for the pure bulk materials (“infinitely thick”, >30 nm). Unfortunately, there has been considerable disagreement in the XPS literature in the two sample-dependent constants: λ_{SiO_2} and R_0 . Reported λ_{SiO_2} values vary from 2.4-3.8 nm, while R_0 varies from 0.6-1.01. For this reason, an attenuation length of 3.488 nm was used for the calculation. R_0 was 0.833, a value chosen for the closest type of sample, *i.e.* HF etched Si sample.⁴⁰

2.4.5.5 WCA Measurements

WCA measurements were carried out using a KSV CAM 200 system equipped with manual liquid dispenser, and a high-speed digital CCD fire-wire camera and LED based stroboscope. Data acquisition and analysis was carried out on the software package supplied by the manufacturer, CAM version 2.98. Images were acquired at a predefined rate and a predefined period of time. The acquired images were then stored in a controlling PC. Once images had been acquired, curve fitting was performed automatically using the Young/Laplace equation for contact angle measurements. Accuracy of contact angle measurement is within $\pm 0.5^\circ$.

2.4.5.6 Argon Plasma Etching

Plasma etching was carried out in a Bio-Rad RF Plasma Barrel Etcher PT7100 operated using auto reflected power mode. Samples were stored in isopropanol and dried on a Perish dish before placing into the etching chamber. Etching was carried out using ~3 Pa Argon gas, forward power was ~40 W and reflected power ~3 W. Etching time was varied. Samples were immersed immediately in isopropanol after etching and stored until analysis.

2.4.5.7 Fluoro-silane Self-assembly Monolayer (SAM) Modification

A target was first cleaned and oxidised using argon plasma etching. Immediately after plasma treatment, the target was placed inside a custom built reaction vessel and was allowed to react with 2% w/v of 1H,1H,2H,2H-perfluorodecyldimethylchlorosilane (Lancaster, Lot #: LF003528) in analytical reagent grade toluene (Fisher) at 90-110°C for an hour (Figure 2-15 and Figure 2-16). Afterwards the target was taken out, while still hot, rinsed with methanol, and stored in methanol until analysis. Mixing the perfluorodecyldimethylchlorosilane reagent with toluene leads to a cloudy solution owing to micelle formation but causes no harm to the reaction. The reaction is exothermic and the reaction starts once the temperature reaches 90°C. This method differs from the method adopted by Norstrom, *et al.* where ozone was used to oxidise the silicon surface, 50-100 µl of the reagent was applied onto the oxidised surface, and was incubated in an oven for 15-60 min in a glass Petri dish.^{41, 42}

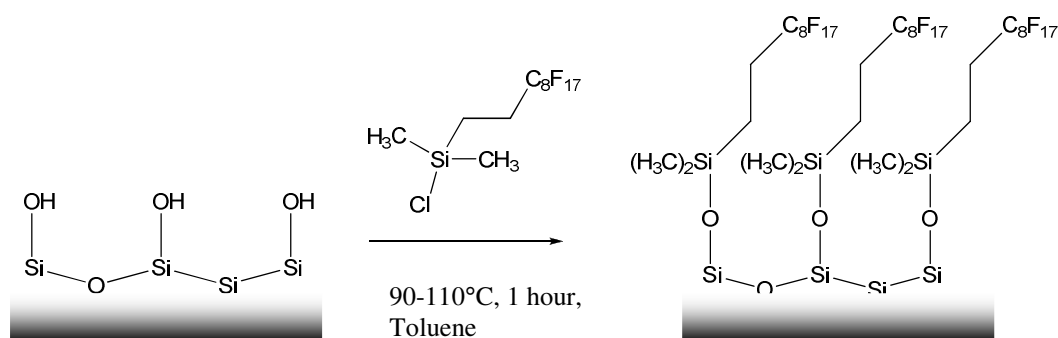


Figure 2-15 Fluoro-silane reaction on DIOS target.

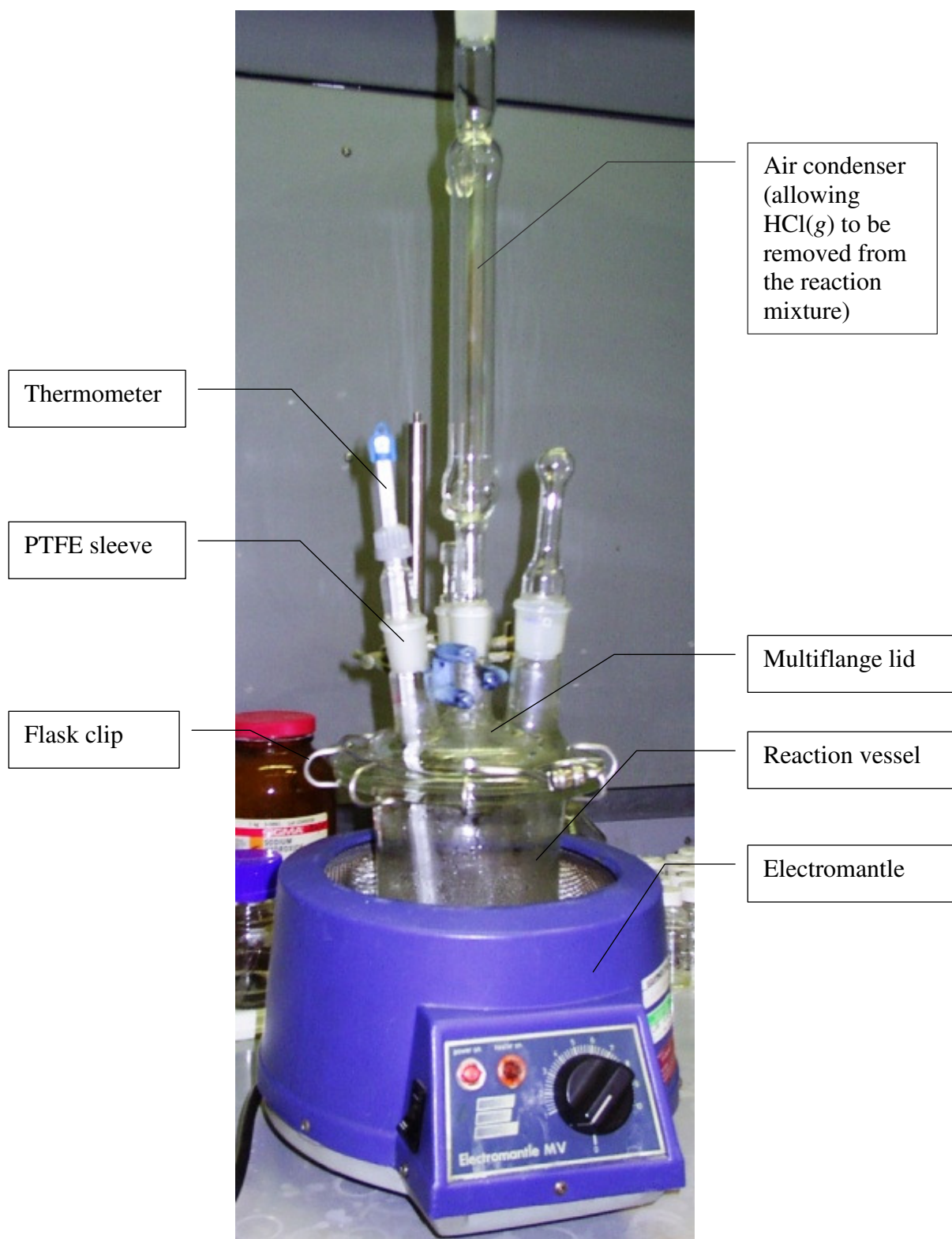


Figure 2-16 Custom built reaction vessel for silanisation.

2.4.6 LDI Investigations

Surface handling was normally carried out in a laminar flow-hood to minimise atmospheric contamination. DIOS target plates were installed on a modified steel plate as instructed by the manufacturer. SALDI substrates were cleaved to suitable size and mounted onto a modified steel plate using double-sided conductive tape. Analyte solution was deposited onto the target surface using a pipette (without matrix). The target surfaces were stored in acetonitrile/propan-2-ol before analysis. QuickMass targets were used directly from their package.

Positive ion mass spectra were acquired using a Micromass M@LDI-TOF (Manchester, UK) mass spectrometer equipped with dual micro-channel plate MCP detector, operating in reflectron mode. (Figure 2-17) The MCP voltage was 1800 V and the pulse voltage was 3500 V. Delay time extraction was 500 ns. The laser energy was set to a constant value. Spectra were acquired at 5 Hz using a nitrogen laser (337 nm). Laser energy was attenuated by a motorised iris equipped for automated laser control. The laser was set to raster a predefined area during data acquisition. Data acquisition and post-processing analyses were performed using the MassLynx version 4.0. The instrument was first mass-calibrated using NaRbCsI/PEGs solution. Standard compounds were dissolved in ACN/H₂O or with addition of acidic buffer. Unless stated otherwise, 1 µL of solution was added on each well and air-dried.

Positive and negative ion mass spectra were also acquired using a Micromass Q-ToF Premier (Manchester, UK) mass spectrometer, fitted with a MALDI ion source in place of the standard API source. The source housing incorporated a nitrogen laser (337 nm). A lens was included in the optical path to focus the laser beam on the target plate surface to a spot approximately 25 µm in diameter. The laser was operated at 20 Hz and was attenuated by a neutral density filter. Samples were introduced on a target plate mounted on a probe that was introduced into the ion source via a vacuum lock and driven by a stepper motor. The ion source housing also equipped with a capillary line and adjustable needle valve to introduce gas into the source to provide collisional cooling of the ion beam to the thermal levels in the hexapole ion guide and improve ion transferring efficiency. A travelling-wave stacked ring ion guide (SRIG) system

propels ions to the collision cell and to the mass analyser.⁴³ Argon was used as collision gas. ToF mass analyser equipped with dual micro-channel plate MCP detector, operated in “V” (single focusing) or “W” (double focusing) mode. (Figure 2-18) The MCP voltage was optimised, typical values varied from 1800 V to 2100 V. Mass resolution was ~8000 in V mode and ~14000 in W mode. Data acquisition and post-processing analyses were performed using the MassLynx version 4.1.

**Printed version includes figure(s) extracted
from the operator instructions manual describing
the design and ion optic of the Micromass M@LDI reflector ToF mass
spectrometer.**

Figure 2-17 Schematic diagram of Micromass M@LDI-MS, provided by the manufacturer.

**Printed version includes figure(s) extracted
from the operator instructions manual describing
the design and ion optic of the Micromass MALDI Q-ToF mass
spectrometer.**

Figure 2-18 Schematic diagram of Micromass MALDI Q-ToF-MS, provided by the manufacturer.

Part of the data was collected using an atmospheric pressure AP-MALDI ion source equipped with pulsed dynamic focusing (PDF) (Mass Tech Inc., Burtonsville, MD, USA) coupled to Applied Biosystems quadrupole linear ion trap system (qLIT) (4000 Q TRAP™ LC/MS/MS, Foster City, CA 94404, USA). PDF functions by guiding ions into the mass spectrometer by aerodynamic flow by switching off the extraction field for a very short period of time (20 μ s) and relies on the suction created by the mass spectrometer orifice to enhance ion transmission efficiency. (Figure 2-19) An extended capillary of 825 μ m i.d. was installed on the mass spectrometer inlet. The target was attached onto a modified steel plate using conductive double-sided tape. The ion source was equipped with a nitrogen laser (337 nm), operating at 10 Hz at room temperature. The laser was transmitted from the laser source via an optical cable to the ion source and the laser intensity could be attenuated by altering the focus of the laser beam onto the receiving end (the end connected to the laser source) of the optical cable. The ion source was controlled by Target™ version 5. Data acquisition and post-processing analyses were carried out using Analyst™ version 1.41. Mass spectrometer settings were optimised before analysis.

**Printed version includes figure(s) extracted
from the reference source describing
the principle of pulsed dynamic focusing of Mass Tech AP-MALDI ion
source.**

Please refer to the cited reference for detail

Figure 2-19 Proposed model of the PDF technique (lines represent ion trajectories): (a) ion trajectories in the case of static electric field and (b) the electric field is switched off 20 ms after the laser pulse.⁴⁴

2.5 References

1. Bisi, O., Ossicini, S. & Pavesi, L. Porous silicon: a quantum sponge structure for silicon based optoelectronics. *Surf. Sci. Rep.* 38, 1-126 (2000).
2. Schmeltzer, J. M. & Buriak, J. M. in *The Chemistry of Nanomaterials: Synthesis, Properties and Applications, Volume 2* (eds. Rao, C. N. R., Müller, A. & Cheetham, A. K.) 518-550 (John Wiley and Sons, 2004).
3. Gómez, D., Fernández, J. A., Astigarraga, E., Marcaide, A. & Azcárate, S. Porous silicon surfaces for metabonomics: Detection and identification of nucleotides without matrix interference. *Phys. Stat. Sol. (c)* 4, 2185-2189 (2007).
4. Porous silicon formation, Department of Electrical and Computer Engineering, University of Rochester. Available at <www.ece.rochester.edu/~weiss/Porous_silicon.html> [Accessed 23 Oct 2005]
5. Föll, H., Christophersen, M., Carstensen, J. & Hasse, G. Formation and application of porous silicon. *Mat. Sci. Eng. R.* 39, 93-141 (2002).
6. Parkhutika, V. P. & Matveeva, E. Observation of New Oscillatory Phenomena during the Electrochemical Anodization of Silicon. *Electrochem. Solid-State Lett.* 2, 371-374 (1999).
7. Christophersen, M., Carstensen, J. & Föll, H. Macropore Formation on Highly Doped n-Type Silicon. *Phys. Stat. Sol. (a)* 182, 45-50 (2000).
8. Shen, Z., Thomas, J. J., Averbuj, C., Broo, K. M., Engelhard, M., Crowell, J. E., Finn, M. G. & Siuzdak, G. Porous silicon as a versatile platform for laser desorption/ionization mass spectrometry. *Anal. Chem.* 73, 612-619 (2001).
9. Stefan Ottow. Classification of Porous Silicon. TECHNISCHE FAKULTÄT DER CHRISTIAN-ALBRECHTS-UNIVERSITÄT ZU KIEL. Available at <www.techfak.uni-kiel.de/matwis/amat/poren/poreover.html> [Accessed at 23 Oct 05]
10. A. Halimaoui, in: L.T. Canham (Ed.), *Properties of Porous Silicon*, IEE INSPEC, The Institution of Electrical Engineers, London, 1997, p. 12.

11. Zoubir, N. H., Vergnat, M., Delatour, T., Burneau, A. & Donato, P. d. Interpretation of the luminescence quenching in chemically etched porous silicon by the desorption of SiH₃ species. *Appl. Phys. Lett.* 65, 82-84 (1994).
12. Petit, D., Chazalviel, J.-N., Ozanam, F. & Devreux, F. Porous silicon structure studied by nuclear magnetic resonance. *Appl. Phys. Lett.* 70, 191-193 (1997).
13. Nickel, N. H. & Schiff, E. A. Direct observation of dangling bond motion in disordered silicon. *Phy. Rev. B* 58, 1114-1117 (1998).
14. Konstantinova, E. A., Dittrich, T., Timoshenko, V. Y. & Kashkarov, P. K. Adsorption-induced modification of spin and recombination centers in porous silicon. *Thin Solid Films* 276, 265-267 (1996).
15. Stewart, M. P. & Buriak, J. M. Chemical and Biological Applications of Porous Silicon Technology. *Adv. Mater.* 12, 859-869 (2000).
16. Reimer, L. Scanning Electron Microscopy: Physics of Image Formation and Microanalysis, Second Edition (Springer, Berlin, 2000).
17. Russell, P., Batchelor, D. & Thornton, J. Scanning Electron Microscopy (SEM) and Atomic Force Microscopy (AFM): Complementary Techniques for High Resolution Surface Investigations Veeco Application Notes (AN46). . (2001).
18. Auger Electron Spectroscopy (AES). Physical Electronic, Inc. Available at www.phi.com/techniques/aes.html [accessed 13 Oct 2007]
19. SEM/EDS: Scanning Electron Microscopy with X-ray microanalysis. South Campus Instrument Center, University at Buffalo. Available at www.sdm.buffalo.edu/scic/sem-eds.html [Access 01 Oct 07]
20. Roger M. Nix. Electron Microscopy - SEM & SAM. Queen Mary University, London. Available at www.chem.qmul.ac.uk/surfaces/scc/ [Accessed 01 Oct 07]
21. Prater, C. B., Maivald, P. G., Kjoller, K. J. & Heaton, M. G. TappingMode Imaging Applications and Technology. Veeco Application Notes (AN04). (2004).
22. Babcock, K. L. & Prater, C. B. Phase Imaging: Beyond Topography Veeco Application Notes (AN11). (2004).

23. Vickerman, J. C. & Briggs, D. ToF-SIMS - An overview (IM Publications, Chichester, West Sussex, 2001).
24. ION-TOF GmbH, Technique. Available at <www.ion-tof.com/technique-IONTOF-TOF-SIMS-TIME-OF-FLIGHT-SURFACE-ANALYSIS.htm> [Accessed 05 Oct 2007]
25. Mann, K. & Yu, M. L. Effect of chemical bonding on positive secondary-ion yields in sputtering *Phy. Rev. B* 35, 6043-6050 (1987).
26. Ottolini, L., Camara, F., Hawthorne, F. C. & Stirling, J. SIMS matrix effects in the analysis of light elements in silicate minerals: Comparison with SREF and EMPA data. *American Mineralogist* 87, 1477-1485 (2002).
27. Jones, E. A., Lockyer, N. P., Kordys, J. & Vickerman, J. C. Suppression and Enhancement of Secondary Ion Formation Due to the Chemical Environment in Static-Secondary Ion Mass Spectrometry. *J. Am. Soc. Mass Spectrom.* 18, 1559-1567 (2007).
28. SIMS Theory: Secondary Ion Yields - Elemental Effects. Available at <www.eaglabs.com/training/tutorials/sims_theory_tutorial/elemeff.php> [Accessed 14 July 2007]
29. Wirtz, T. & Migeon, H.-N. Cation mass spectrometry: toward an optimisation of SIMS analyses performed in the MCs_x^+ mode. *Spectroscopy Europe* 15, 16-22 (2003).
30. Smith, E. F., Briggs, D. & Fairley, N. Further developments in quantitative X-ray photoelectron spectromicroscopy: preliminary results from the study of germanium corrosion. *Surf. Interface Anal.* 38, 69-75 (2006).
31. Piao, H., Tarte, L. L., Hennessy, W. A. & Fairley, N. Understanding delamination in microelectronic devices using AES, XPS and chemometrics. *Surf. Interface Anal.* 39, 493-500 (2007).
32. Walton, J. & Fairley, N. Noise reduction in X-ray photoelectron spectromicroscopy by a singular value decomposition sorting procedure. *Electron Spectrosc. Relat. Phenom.* 148, 29-40 (2005).
33. Contact Angle Measurement: Basic Concepts. Application Note 102. KSV Instruments. Available at <www.ksvinc.com/contact_angle.htm> [Accessed 01 Aug 2006]

34. Wendel, R. N. Resistance Of Solid Surfaces To Wetting By Water. *J. Ind. Eng. Chem.* 28, 988-994 (1936).
35. Uelzen, T. & Muller, J. Wettability enhancement by rough surfaces generated by thin film technology. *Thin Solid Films* 434, 311-315 (2003).
36. Cassie, A. B. D. & Baxter, S. Wettability of porous surfaces. *Trans. Faraday Soc.* 40, 546-551 (1944).
37. Coffinier, Y., Janel, S., Addad, A., Blossey, R., Gengembre, L., Payen, E. & Boukherroub, R. Preparation of Superhydrophobic Silicon Oxide Nanowire Surfaces. *Langmuir* 23, 1608-1611 (2007).
38. High Performance Imaging XPS: The Spherical Mirror Analyser. Kratos Analytical. Available at <www.kratos.com/Agem/SMA.html> [Accessed 17 Aug 2006]
39. D.F. Mitchell, K.B. Clark, J.A. Bardwell, W.N. Leonard, G.R. Massoumi, I.V. Mitchell, Film thickness measurements of SiO₂ by XPS, in Surface and Interface Analysis, vol. 21, 1994, page 44-50.
40. Seah, M. P. & Spencer, S. J. Ultrathin SiO₂ on Si II. Issues in quantification of the oxide thickness. *Surf. Interface Anal.* 33, 640-652 (2002).
41. Nordstrom, A., Apon, J. V., Uritboonthai, W., Go, E. P. & Siuzdak, G. Surfactant-Enhanced Desorption/Ionization on Silicon Mass Spectrometry. *Anal. Chem.* 78, 272-278 (2006).
42. Nordstrom, A., He, L. & G., S. in Encyclopedia of Mass Spectrometry Vol. 6: Ionization Methods (eds. Gross, M. L. & Caprioli, R. M.) 676-683 (Elsevier Science 2007).
43. Giles, K., Pringle, S. D., Worthington, K. R., Little, D., Wildgoose, J. L. & Bateman, R. H. Applications of a travelling wave-based radio-frequency-only stacked ring ion guide. *Rapid Commun. Mass Spectrom.* 18, 2401-2414 (2004).
44. Berkout, V. D., Kryuchkov, S. I. & Doroshenko, V. M. Modeling of ion processes in atmospheric pressure matrix-assisted laser desorption/ionisation. *Rapid Commun. Mass Spectrom.* 21, 2046-2050 (2007).

CHAPTER 3 FROM SUBSTRATES
CHARACTERISATION TO LDI PERFORMANCE
RELATIONSHIPS

3.1 Introduction

Porous silicon (PSi) has been a focus of research since the discovery of its photoluminescent properties in the early 1990s.¹ Moreover, the use of the material in electronic devices has accumulated a large amount of knowledge in this area. Applications of PSi ranges from solar cells to micro-reactors to biosensors.^{2, 3} The surface chemistry of PSi prepared by electrochemical etching in fluorine containing electrolyte and methods for its characterisation have been discussed in Chapter 2.

As for its application in laser induced desorption/ionisation mass spectrometry (LDI-MS), the physicochemical properties of PSi surfaces are crucial to their LDI-MS performance.^{4, 5} Although silicon is not a conventional matrix as in MALDI, it is believed that the porous structure provides a scaffold for trapping the analyte, and the unique optical activity of these nanostructured silicon substrates affords an effective mean of transferring the laser energy to the adsorbate.⁴

However, the published data in relation to the surface characteristics of the substrates that are actually used for LDI applications is primarily on surface morphology using scanning electron microscopy (SEM) or atomic force microscopy (AFM) and comparison of substrates prepared by different bulk materials.

For instance, one of the works of Alimpiev, *et al.* compared nanostructured silicon substrates prepared by hyperthermal fluorine atoms etching and PSi substrates prepared by galvanostic anodisation in an effort to develop a suitable SALDI substrate.⁶ Hyperthermal oxygen atoms etched (O-etched) high orientated pyrolytic graphite (HOPG) was also used. The PSi substrate used has a porous layer over 100 nm thick whereas the F-etched silicon has a non-porous roughened layer less than 10 nm. Figure 3-1 shows an AFM image of the PSi surface. No data related to the surface morphology of HOPG was presented. The authors concluded that the surface must be *rough* to obtain an ion signal and does not need to be *porous*. The authors considered that because surface roughness was the common feature among these three substrates investigated and only the polished silicon surface did not produced a mass spectrum. Given that though, the mass spectrum of diethylamine obtained from the PSi substrate,

which has a thick porous layer, was 50 times more intense than the spectrum obtained from F-etched silicon. PSi was the most effective ion emitter in this study, even compared to O-etched HOPG. This observation concluded that the porous structure plays an important role in re-supplying the surface with analyte after each pulse of laser, supporting the unique retaining capability of porous substrates.

**Printed version includes figure(s) extracted
from the reference source describing
an AFM image of a porous silicon that has been found effective for
SALDI application. The vertical scale of the image is 148.2 nm.
Please refer to the cited reference for detail**

Figure 3-1 AFM image of PSi substrate produced by galvanostic anodisation.⁶

Okuno, *et al.* have also carried out a thorough investigation regarding the requirements for LDI on submicrometer structures.⁷ It was found that silicon and stainless steel surfaces, which had roughened structures introduced by sanding, required lower laser energy to generate ions of synthetic polymers relative to the respective flat surface. (Figure 3-2a and b) It was concluded that the roughness produced by submicrometer irregularities assists direct UV LDI irrespective of the materials. This observation was in part consistent with the results of Alimpiev, *et al.*⁶ The authors suggested that the scratching gives expansion of the surface area and probably renders refraction of laser light, enhancing LDI. Furthermore, the exploitation of silicon substrates etched with an array of grooves (Figure 3-2c) also revealed that grooves of 200 nm and 300 nm generate more intense signals than 100 nm grooved substrates. The orientation between the laser light and groove structures was also found significant to both the ion yield and the background signals. The

authors suggested that macro-sized structure rather than meso- or micro-sized structure is essential for desorption/ionisation on nanofabricated structures. Investigation of porous alumina was also carried out. (Figure 3-2d) When porous alumina or polyethylene was coated with Au or Pt, the analysis of small molecules was improved. Since a porous alumina surface, coated or not, does not have a dangling bond (see section 1.7), siloxene-like molecules nor is it photoactive, this indicates that the surface electro-conductivity plays a key role for direct laser-induced desorption/ionisation and argues against the results of previous studies.[†] Subsequent investigation also revealed that the metallic coating melts during LDI and hence may serve an additional role.⁸

**Printed version includes figure(s) extracted
from the reference source describing
the microscopic surface morphology of the surfaces.
Please refer to the cited reference for detail**

Figure 3-2 SEIs of (a) silicon wafer scratched with No. 400 sand paper, (b) stainless steel plate scratched with No. 400 sandpaper, (c) submicrometer groove arrays on silicon, and (d) Au-coated porous alumina.⁷

Sato, *et al.* have also demonstrated that pyroelectric ceramics, such as lead lanthanum zirconate titanate (PLZT), can also be used as a matrix-free soft LDI substrate.⁹ Substances such as angiotensin I, metallic ion-cyclodextrins complex and synthetic polymers have been shown to be detectable by using this substrate. The PLZT plate employed was an essentially flat surface of which roughness is less than a few

[†] The authors did not specify which studies they were arguing against, but perhaps referring an omission in several studies carried out by Siuzdak's group or Alimpiev's group that surface electro-conductivity is an important factor.

nanometers. PLZT is also a known pyroelectric material, which absorbs UV radiation effectively and generates a strong electric field - a phenomenon known as the photo-pyroelectric effect. The use of PLZT substrate as an ionisation platform without submicro-sized structure implies that the radiation induced polarisation of the substrate is fundamental to LDI. However, this single-crystal flat substrate does not produce satisfactory results because of its small specific surface area.¹⁰ Then again, another pyroelectric material, *porous* gallium nitride (PGaN), was not an effective LDI substrate and could only generate Ga and related cluster ions.¹¹

While the studies presented above were evaluating the suitability of substrate prepared by different bulk material for matrix-free LDI, surface morphology also plays a vital role in LDI-MS.

Chen, *et al.* used different silicon substrates prepared by laser etching, either in ambient air, in SF₆ gas or in liquid water.¹² (Figure 3-3) Substrate prepared in water was the most effective and in air was the least effective for LDI-MS. It was concluded the LDI threshold fluence and efficiency are strongly dependent on the surface morphology though investigation of the surface chemistry was needed.

Finkel, *et al.*¹³ used reactive ion etching (RIE) to prepare a series of nanocavity silicon substrates of different cavity geometries to examine the possible correlation of surface nanocavity features to the observed MS signals. (Figure 3-4) The data suggested that there was a general tendency to increased ion yield in LDI-MS correlating with increasing surface cavity sizes. Nevertheless, the background noise also became more pronounced. The ionisation efficiency on the substrate that had a less than 50 nm thin porous layer (surface A) was poor, whereas the substrate, which had a fragile Si skeleton, network (surface D), the LDI spectra were severely complicated by the background interferences. Relatively, only the substrates (surface B and C) of moderate pore size (~100-150 nm) and porosity (~20-40%) produce a good quality mass spectrum. Indeed, in their subsequent investigations,¹⁴ only the substrates of which porosity was over 20% could be effectively used for LDI-MS. The laser threshold for LDI of glucose was decreased exponentially with increasing porosity. The author contributed the observation that this was a consequence of the reduced thermal conductivity because of increasing porosity.

**Printed version includes figure(s) extracted
from the reference source describing
the microscopic surface morphology of the surfaces.
Please refer to the cited reference for detail**

Figure 3-3 Top (left panels) and side (right panels) views of silicon microcolumn arrays produced (A) in ambient air with 1000 laser shots at 1 J/cm^2 , (B) in SF_6 gas at 1 atm. pressure with 1200 laser shots at 0.4 J/cm^2 , and (C) in water with 600 laser shots at 0.13 J/cm^2 .¹²

Printed version includes figure(s) extracted
from the reference source describing
the microscopic surface morphology of four different nanocavity silicon
surfaces produced by reactive ion etching and example mass spectra
acquired from those substrates.
Please refer to the cited reference for detail

| Surface | Etching time (mins) | Pore width, d (nm) | Pore depth, h (nm) | % porosity | % increased surface area |
|---------|------------------------|-----------------------|-----------------------|------------|-----------------------------|
| A | 0.5 | 53.8 ± 9.7 | 48.9 ± 8.9 | 4.2 | 6.7 |
| B | 1 | 104 ± 9 | 102 ± 21 | 15.6 | 27.9 |
| C | 1.5 | 157 ± 9 | 124 ± 12 | 35.6 | 43.2 |
| D | 5 | 180 ± 24 | 218 ± 53 | 46.8 | 116.8 |

Figure 3-4 Nanocavity Si surfaces produced by RIE: (*top*) Top-down FE-SEM images of the surface, etched for (A) 0.5, (B) 1, (C) 1.5, and (D) 5 min, (*middle*) mass spectra generated by the corresponding surface using a mixture of Val-Met (M₁) and Ala-Leu-Ala-Leu (M₂) under similar MS condition, and (*bottom*) calculated surface parameters of the nanocavity surfaces.¹³

Insofar as the data in the literature shows that enhanced surface area promotes LDI activity, irrespective of the bulk material, and yet the properties of the material itself are influential. Surface morphology plays a critical role. The roughened or porous layer should not be too thin (≤ 50 nm), where the ionisation efficiency is low. The skeleton of nanostructures should not be too fragile, which leads to background interferences complicating the mass spectra.

Although the data on relating surface morphology, or bulk material and LDI performance is available, rarely do those studies extend to the chemical nature of the surface using surface techniques and correlating that to the LDI performance. The purpose of this chapter is dedicated to answering these questions. On the other hand, where other surface techniques are employed, the data are rarely presented. For instance, Shen, *et al.* employed both secondary ion mass spectrometry (SIMS) and X-ray photoelectron spectrometry (XPS) in analysing a series of PSi substrates in an effort to find optimised systems that are suitable for LDI applications and yet no SIMS or XPS data was reported.⁴ Published information relating the surface chemistry of the substrates to the LDI activity has rarely been reported. Reported data is only seen in two Ph.D. theses^{15, 16} from the University of Florida, US and from Tuomikoski, *et al.*¹⁷ The lack of such information encouraged us to undertake a detailed study in relating the surface characteristics to the LDI performance.

3.2 Literature Data of Surface Characteristics and LDI-MS Relationship

One of the early works in this subject was carried out by Cuiffi, *et al.* using silicon columnar/void-network substrate prepared by plasma enhanced chemical vapour deposition (PECVD).¹⁸ Silicon was deposited on either glass or poly(ethylene terephthalate) (PET). Varying the thickness of oxides of the surface and relating that to the laser energy required for LDI led to a conclusion that laser coupling efficiency is an important factor for LDI-MS using this deposited nanostructured silicon film. (Figure 3-5)

**Printed version includes figure(s) extracted
from the reference source describing
the optical coupling efficiency of three different void-column silicon film
in terms of their LDI effectiveness and reflectance.
Please refer to the cited reference for detail**

Figure 3-5 The minimum laser power per pulse required to detect des-pro³,[ala^{2,6}]-bradykinin for three void-column Si films with different laser coupling, A. A was derived from the reflectance, R, as $A = 1 - R$. The inset represents the control of reflectance (at 337 nm) by varying the deposition power.^{18, 19}

Anderson also studied the optical properties of the silicon substrates and related them to the surface morphology and the level of oxides on the surface. The substrates were prepared by H₂O₂-metal-HF (HOME-HF) etching. It was found a high optical absorbance occurs on a substrate of high porosity. The substrate of low porosity exhibits lower optical absorbance. The oxidised substrate exhibits absorbance similar to that of a flat silicon surface.¹⁵ (Figure 3-6)

**Printed version includes figure(s) extracted
from the reference source describing
the optical absorbance profile of four different silicon substrates.
Please refer to the cited reference for detail**

Figure 3-6 Absorbance profile of porous and crystalline silicon. × denotes a surface with relatively high surface porosity, ▲ denotes a surface with moderate surface porosity, ■ denotes an oxidised porous silicon surface and ♦ denotes flat silicon.¹⁵

Given that the optical absorbance (or effectively the laser coupling or energy deposition efficiency) is an important factor for LDI, photoluminescence of PSi is not a relevant surface characteristic for LDI. Kruse, *et al.* used silicon substrates prepared by H₂O₂-metal-HF (HOME-HF) etching to demonstrate that both luminescent and non-luminescent areas can both generate analyte signals in DIOS-MS.¹¹ (Figure 3-7) Although the photoluminescence of PSi is not a relevant factor, when varying laser wavelength from 266, 337 to 532 nm, the mass spectral quality was consistent. It was suggested that the lack of wavelength dependent signal generation is because in MALDI, the excitation laser must match a strong absorption from the matrix, whereas in DIOS, the PSi only needs to absorb a photon that exceeds the band gap of crystalline silicon (1.1 eV). Given that the photon energy used has not only exceeded the band gap energy and it has also exceeded the energy of the luminescence band observed (590 nm), the authors concluded that though there is not any correlation between the DIOS activity to the photoluminescence of the PSi, a common optical absorption event is necessary for both processes.

In the same report, contact angle measurement was employed to study the storage solvent effect and the effects of surface aging.¹¹ (Figure 3-8) The surfaces subjected to extended storage were significantly more hydrophilic than the days-old surfaces, as indicated by smaller contact angles with ultrapure water. However, though the water contact angle was not significantly different for the surfaces stored in dry air and in menthol for six days (highlighted in a red square in Figure 3-8A), only limited signal could be obtained from the surface stored in dry air for six days. (Figure 3-8B) The authors considered that post-etching solvent storage was necessary in preserving the DIOS activity of the etched PSi surface. Since oxidation by oxygen was likely in dry air storage and the oxidation interposed a thin SiO_x layer between the adsorbed analyte and the Si. Because the phonon density of states, which ultimately determines the thermal conductivity, is drastically altered in silicon oxide, and the transfer of thermal energy is hence affected by the surface oxidation. Given this observation, the authors suggested that the thermal contact has to be an important property determining the efficacy of the DIOS ion generation process.

**Printed version includes figure(s) extracted
from the reference source describing
the relationship of photoluminescent properties of the porous silicon
and the usefulness as a DIOS substrate. No direct relationship was
found.**

Please refer to the cited reference for detail

Figure 3-7 (A) Photoluminescence images from Pt-patterned p^+ - and p^- -PSi, with the concave side of the arc corresponding to the Pt-patterned spots. (B) Mass spectra generated from a 1.5-pmol mix of des-Arg¹ bradykinin (1), α -Bag Cell Peptide₁₋₈ (2), and angiotensin I (3) on and off areas of luminescence of these same PSi supports indicate that DIOS does not correlate to the luminescence of PSi.¹¹

**Printed version includes figure(s) extracted
from the reference source describing
the results of contact angle measurement and example mass spectra.
The writer highlights that the water contact angle was essential identical
for the substrates stored either in air or in method for 6 days, however,
the LDI efficiency was significantly different and thus he has an
interpretation to the results differs from the original authors.**

Please refer to the cited reference for detail

Figure 3-8 (A) Plot showing the change in solvent contact angles for wafers subjected to (○) dry and (▽) methanol storage for 1 day and (□) dry air and (◇) methanol storage for 6 days. Contact angles were measured for ultrapure water containing 0, 25, 50, and 75% methanol on each surface. The lower contact angles for the surfaces subjected to extended storage indicate a more hydrophilic surface as compared to freshly etched surfaces. (B) Mass spectra generated from a 1.5-pmol peptide mix of des-Arg¹ bradykinin (1), α -Bag Cell Peptide₁₋₈ (2), and angiotensin I (3) on surfaces under methanol and dry air storage for 6 days indicate that extended storage in methanol preserves the surface integrity as compared to dry storage.¹¹

Li has also used water contact angle measurement in the study of PSi substrate prepared by HOME-HF etching.¹⁶ Crystalline silicon (c-Si), freshly etched PSi, aged PSi (in air 24 hours), and re-etched PSi were investigated. (Figure 3-9) All PSi surfaces were found to have a lower wettability than crystalline silicon. Similar to that observed by Kruse, *et al.*, the PSi surface becomes more wettable when aged. However, the wettability decreases after re-etching. Li explained that the hydrophilicity of the PSi surface increased not only due to the formation of the oxidised layer but also the adsorbed contaminants. Re-etching removes such an effect. However, there is no satisfactory explanation for the fact that the re-etched surface exhibited even lower wettability than the freshly etched PSi. In contrast to Kruse, *et al.*, Li suggested that the apparent increased hydrophobicity of PSi compared to crystalline silicon has to be a combined effect of the surface chemical composition as well as the surface roughness.¹⁶

**Printed version includes figure(s) extracted
from the reference source describing
the results of water contact angle measurement after storing the
substrates at different conditions.
Please refer to the cited reference for detail**

Figure 3-9 Water contact angles on four different surfaces.¹⁶

In the same study, FT-IR and Auger electron spectroscopy (AES) were also used to study the surface composition.¹⁶ In the IR spectrum, (Figure 3-10) the band around 3000-3500 cm^{-1} is assigned to SiO-H stretch, and 1100-1000 cm^{-1} to Si-OH stretch. Although the fresh surface was suggested to be silicon hydride, the Si-H stretch at 2080-2200 cm^{-1} was not observed. (Figure 3-10) Other peaks were assigned due to carbon dioxide adsorbed, and residual water and ethanol remained on the surface: 3800-3500 cm^{-1} ($\nu_{\text{O-H}}$ of H_2O , $\nu_{\text{O-H}}$ of ethanol); 2900 cm^{-1} ($\nu_{\text{C-H}}$ of ethanol); 2370 cm^{-1} ($\nu_{\text{C=O}}$ of CO_2); 1500 cm^{-1} , 1600 cm^{-1} ($\delta_{\text{O-H}}$ of H_2O); 1400, 1200, 1080 cm^{-1} ($\delta_{\text{O-H}}$ of ethanol). In the Auger electron spectrum, (Figure 3-11) Si, C and O were detected. The oxygen signal was contributed to rapid oxidation of the surface, carbon as the main contaminant or trapped solvent (ethanol). In addition, potassium was also detected.¹⁶

**Printed version includes figure(s) extracted
from the reference source describing
a FTIR spectrum of a day old porous silicon.
Please refer to the cited reference for detail**

Figure 3-10 FT-IR spectrum of a day old PSi.¹⁶

**Printed version includes figure(s) extracted
from the reference source describing
a AES spectrum of a two days old porous silicon stored a in vacuum
chamber.
Please refer to the cited reference for detail**

Figure 3-11 Auger electron spectrum of a two day old PSi stored in vacuum chamber.¹⁶

Similarly, Anderson used energy dispersive X-ray spectrometry (EDS) to study the surface composition and the effect of surface aging.¹⁵ EDS spectra obtained immediately after surface preparation showed a high level of fluorine and low level of oxides. Nevertheless, just after a day, the level of fluorine was significantly decreased and the level of oxygen was significantly increased. Storage of freshly prepared PSi in nitrogen preserved the level of fluorine. It was concluded that the surface was quickly oxidised in air.¹⁵ (Figure 3-12)

**Printed version includes figure(s) extracted
from the reference source describing
EDS spectra of a porous silicon immediately after etching and after a
day stored in air, illustrating the rapid process of surface aging.
Please refer to the cited reference for detail**

Figure 3-12 EDS spectra of surface analysed (a) immediate after etching and (b) 24 hours after.

Although limited data from the literature is presented above and largely on the silicon substrate prepared by HOME-HF etching, these data do suggest that the rough or porous silicon substrates used for the matrix-free LDI approach follow the same trend of the general chemistry and possibly the drawbacks of PSi. In this thesis, a range of modified substrates has been studied. The true nature of the commercial products remains a trade secret. On the other hand, the silicon SALDI substrates have only been poorly characterised. These justify our investigation to understand the chemical composition of these semiconductor LDI substrates.

3.2.1 Aims of This Chapter

In this chapter, the commercial DIOS targets from Waters Corp., the QuickMass targets from NanoHorizons, and various SALDI substrates prepared by galvanostic anodisation with iodine etching additive manufactured by the Lab. for Laser Diagnostics, General Physics Institute (GPI) are studied. Surface imaging techniques such as SEM and AFM, surface analysis techniques such as ToF-SIMS and XPS as well as water contact angle (WAC) are used. Argon plasma etching and fluoro-silane self-assembly monolayer (SAM) modification to the SALDI substrates is carried out. This treatment alters the surface chemistry of the substrate and the effects on the LDI performance are investigated. The LDI performance of the substrates is examined by a reflector ToF instrument. The surface chemistry on these surfaces suitable for matrix-free LDI application and any correlation between surface physicochemical properties and the LDI performance is to be studied and are the purposes of this chapter.

3.3 Results on Surface Characterisation

The application of multiple surface analysis techniques in PSi investigation has been rarely reported in literature. There has only been one paper from Feng, *et al.* more than 10 years ago.²⁰ XPS, SIMS, AES, FTIR, photoluminescence (PL) and Raman scattering were used in that study to determine the chemical nature of the PSi surface prepared by electrochemical etching in fluorine containing electrolyte. The same philosophy applies here, but in this case, the chemical nature and surface characteristics of the LDI substrates are studied.

3.3.1 Surface Morphology of the Matrix-free LDI Substrates by Surface Imaging Techniques

To investigate the surface morphology of the LDI substrates available, either from the commercial sources or provided by the Lab. for Laser Diagnostics, GPI, SEM and AFM were employed. These two techniques provide complementary information and the data are presented under the same section. Correlation between the surface morphology of the substrates and the LDI performance are presented later in this chapter.

3.3.2 Commercial DIOS and QuickMass Substrates

Figure 3-13 (a) and (b) show the SEM and AFM images of the commercial DIOS substrates. The images show that the DIOS substrates have pore openings varying from 20 to 200 nm. Considering that the tip curvature is ~30 nm, the AFM image also indicates that a significant number of the pores are smaller than the size of the tip curvature. The image of the pores with lateral features comparable to the tip curvature appears as a convolution of the tip and pore entrance shapes. The vertical scale of the AFM image is larger than 200-250 nm. Given the size of the opening of the pores relative to the size of the tip, the thickness of the porous layer may actually be larger

than the measured value. The significances behind this porous morphology are to be discussed later.

Figure 3-13 (c) and (d) show the SEM and AFM images of the QuickMass substrates. In contrast, the QuickMass substrates have a low surface porosity and have columnar-void surface morphology. The vertical scale of AFM image is about 100 nm. Limited information was available on the QuickMass substrates. How these structural differences from porous morphology relate to the LDI performance is to be investigated. The elemental and molecular nature of the substrate material is to be investigated by SIMS.

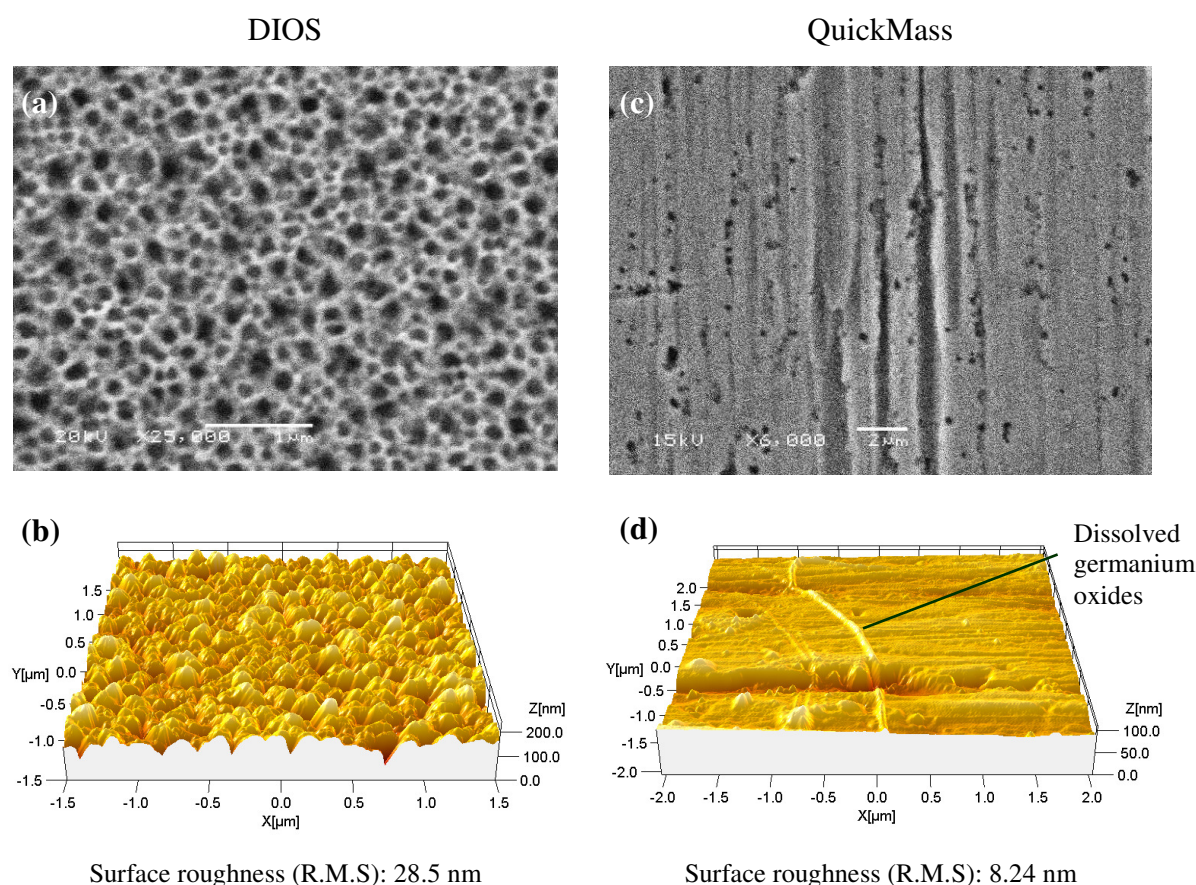


Figure 3-13 (a) SEI and (b) AFM topography of a DIOS substrate from Waters, and (c) SEI and (d) AFM topography of a NanoHorizons QuickMass substrate. These images show that the DIOS substrate is porous whereas the QuickMass substrate has a columnar-void surface morphology. Calculated surface roughness stated is the root mean square by the same AFM image. The images of the QuickMass target were taken on a used target. On the AFM image (d), there appears a line in the middle of the image. Since GeO is dissolvable in water. This line forms a shape of an edge of an aqueous droplet and may be a drying pattern created by dissolved GeO.

3.3.3 SALDI Substrates

The SALDI substrates prepared at the GPI had a wide range of surface morphologies, varying from porous, void-porous, dents of curvatures, roughened, nano-tips and nano-dots/wells. Some surfaces were roughened by sanding and some were etched on the non-polished side of a silicon wafer to obtain additional surface roughness. Different materials such as graphite and silicon were used. Some silicon substrates were prepared by chemical etching with addition of iodine etching additive and some without. The concentration of iodine-additive also varies from 5% to 0.5%. Different etching parameters, such as etching time and current density were used also. Substrate electro-resistivity, type of silicon (n-type, p-type) and crystal orientation were varied at the same time. Background information of the SALDI substrate and gas-phase SALDI-MS development has been given at section 1.6 and 2.2. Etching parameters used in surface preparation can be found at section 2.4.3. Given that variety, the investigation was very complex and presented a challenge. How those variations effect to the LDI performance is to be investigated.

For the ease of presentation and simplicity, different substrates are classified according to their surface morphologies or preparation methods, and representative samples are presented.

Porous Silicon Substrates

Some of the silicon SALDI surfaces are porous. Figure 3-14 (a) and (b) show the SEM and AFM images of substrate A48-1. A48-1 was prepared by electrochemical etching with addition of 0.5% w/v iodine electrolyte additive. The pore size measured is about 10-20 nm. The vertical scale of the AFM image is 150-160 nm. As mentioned previously, AFM only has limited ability in depth profiling and the actual thickness of the porous layer is expected to be higher. SEM and AFM images show that the substrate looks similar to the DIOS substrate, with the exception that the measured surface roughness is only 9.74 nm as oppose to 28.9 nm in DIOS. The average porous size is also smaller than that of DIOS.

Figure 3-14 (c) and (d) show the SEM and AFM images of the substrate prepared by vapour-phase etching in the presence of iodine etching additive. The vertical scale of the AFM image is 200-250 nm but the substrate surface morphology is not as uniform as A48-1. The roughness calculated varies from 27.7 nm to 37.5 nm.

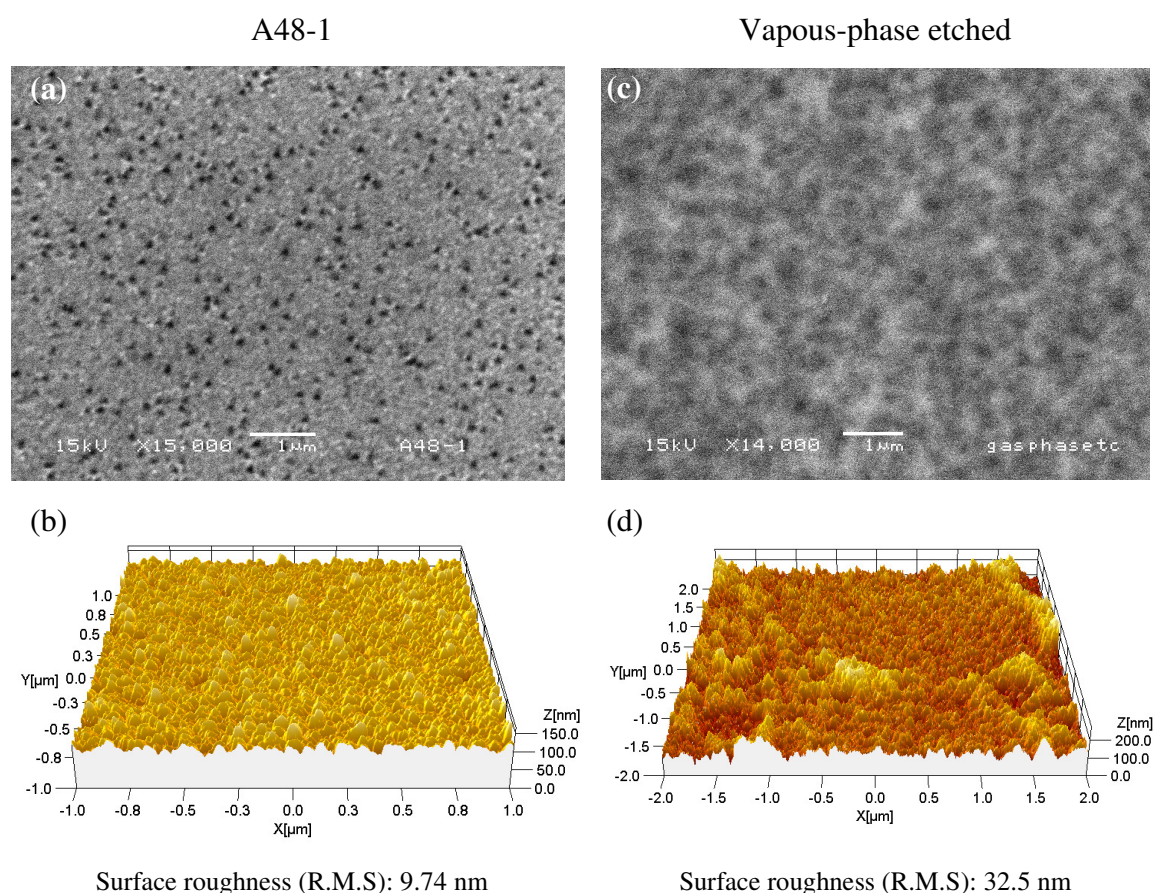


Figure 3-14 SEI (*top*) and AFM topography (*bottom*) of the substrate A48-1 and the substrate prepared by vapour-phase etching.

Substrates of Void-porous and Dents of Curvatures

Figure 3-15 shows the SEM and AFM images of substrate s10 and s11. These silicon substrates exhibited a non-conventional surface morphology. Additional optical images are presented to illustrate the surface morphology at different magnification. Substrate s10 was prepared by first stain-etching in HNO_3 and then subsequently re-etched, whereas s11 was prepared by electrochemical etching on the non-polished side of a silicon wafer and was oxidised in H_2O_2 . The etching parameters were not disclosed. s10 has dents of curvatures whereas s11 has a porous/voids layer.

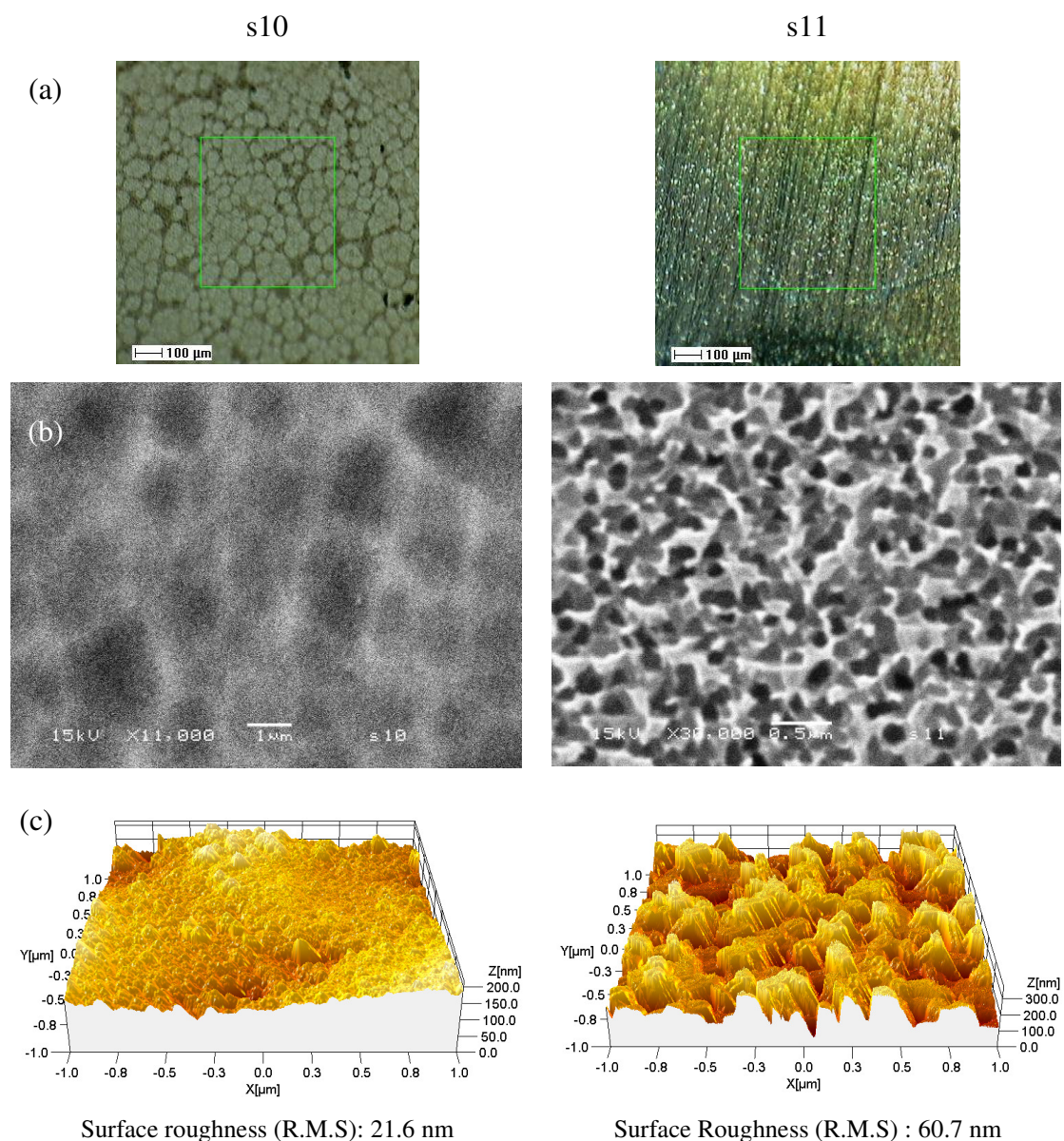


Figure 3-15 Surface morphology of the substrate s10 and s11; (a) optical image, (b) SEI and (c) AFM topography.

Non-Porous Silicon Substrates Designed for the Gas-Phase SALDI-MS

Figure 3-16 shows the substrates designed for the gas-phase SALDI-MS approach. These substrates were prepared by electrochemical etching with 5% w/v iodine etching additive and a low etching current (1 mA/cm^2). Consequently, these substrates only have a thin nano-structured layer ranging from 10 nm to 50 nm thick. The surface roughness measured was in order of few nm. Most of the research effort in the SALDI surface chemical analysis was carried out on this type of substrate. The effects of this surface morphology and their LDI activities will be discussed.

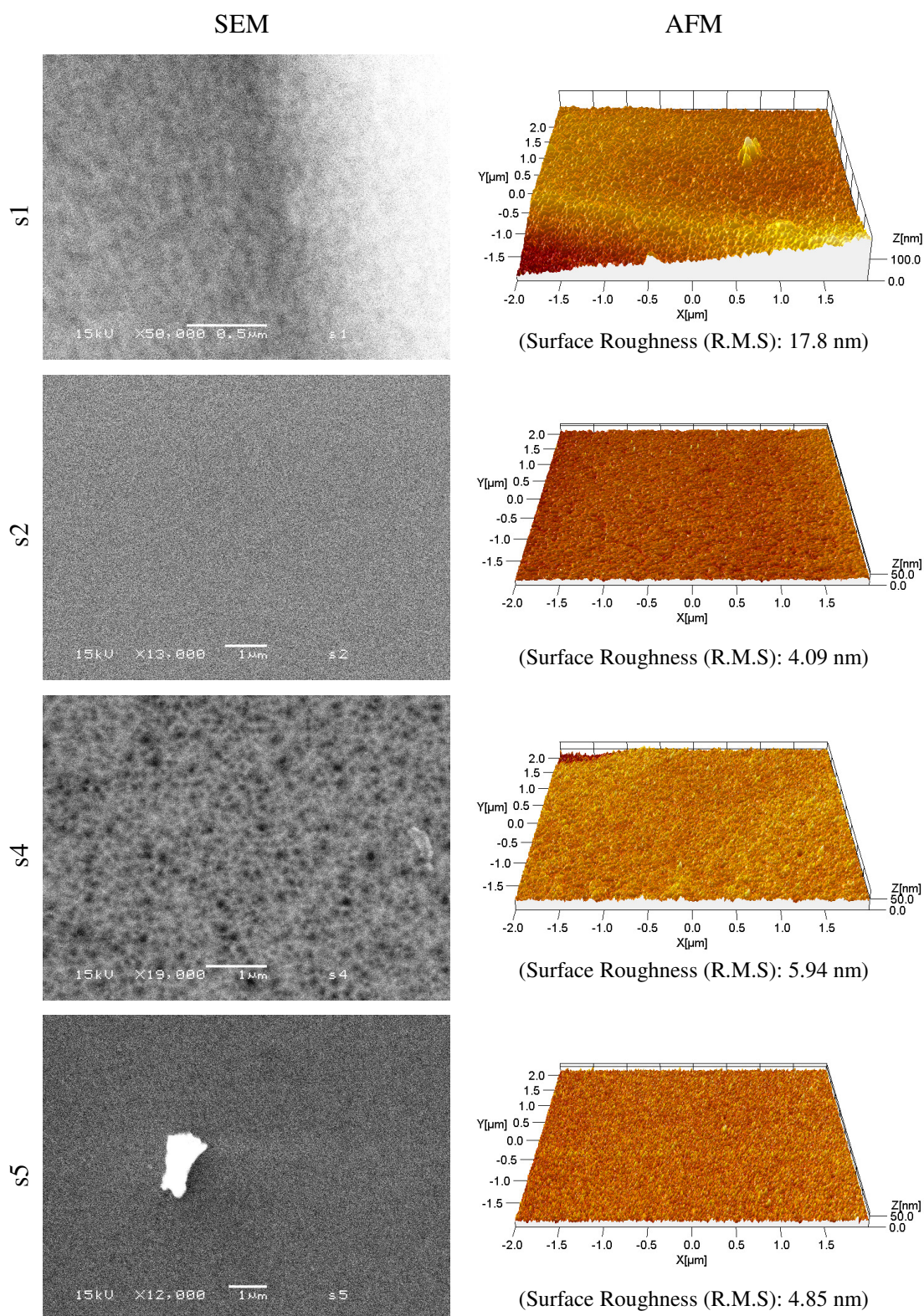


Figure 3-16 SEI and AFM topography of surfaces designed for the gas-phase SALDI-MS approach. Surfaces s1, was prepared on the non-polished side of a silicon wafer and s2, s4, s5 prepared on the polished side. Consequently, s1 surface has a native roughness, which was not produced by chemical etching. Blanket indicates the measured surface roughness in R.M.S.

Nano-dots and Nano-wells Substrates

Substrates a1 to a5 were prepared by a high etching current densities (5 or 20 mA/cm²) using low resistivity n-type silicon wafer and 0.5% w/v iodine etching additive. a1 and a3 were also re-etched. Etching time was short (1, 2 or 5 mins). The relationship of etching current densities and the porosity has been depicted in Chapter 2, figure 2-2 and 2-3(b). These etching parameters produced no pores but a very thin and fragile nano-structured layer. As a result, nano-dots, nano-wells and electro-polished surfaces were obtained. (Figure 3-17) Only the AFM images of the substrates are presented. This was because these surfaces are relatively smooth and the SEM instrument used could not reveal the surface features.

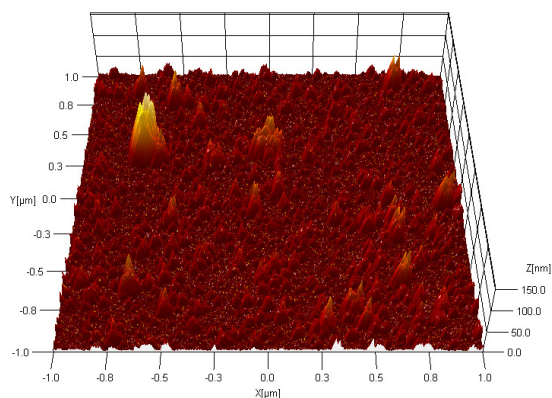
Experimental SALDI Substrates

The experimental SALDI substrates, e1 to e3, were prepared by first stain-etching with HNO₃ and then subsequently re-etched with and without addition of iodine etching additive. Figure 3-18 shows the AFM and SEM images of substrate e1 to e3. Substrate e1 has a thick fragile spongy porous structure and the vertical scale of the AFM image is over 300 nm, substrate e2 has nano-dot structure, and e3 has dents of curvatures. Substrate e1 and e2 were both re-etched for 10 minutes using a low etching current but with a different content in etching electrolyte. In the absence of light illumination and an oxidising electrolyte in the preparation of e2, very little etching occurred. Substrate e2 is thus smoother than e1. In the preparation of e3, the etching current used led to non-selective etching and produced a smooth surface.

HOPG Substrate and Sanded Silicon Substrate

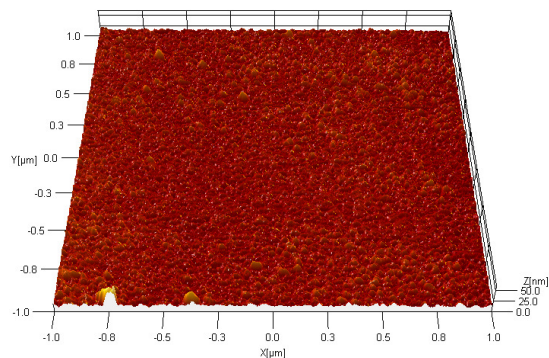
Figure 3-19 shows the SEM images of a HOPG and a sanded silicon surface. The sanded surfaces were roughened by sanding a crystal surface with diamond dusts. The surface structure is in micron size. The relatively large surface structures made AFM characterisation difficult and only the SEM images are shown.

Substrate a1



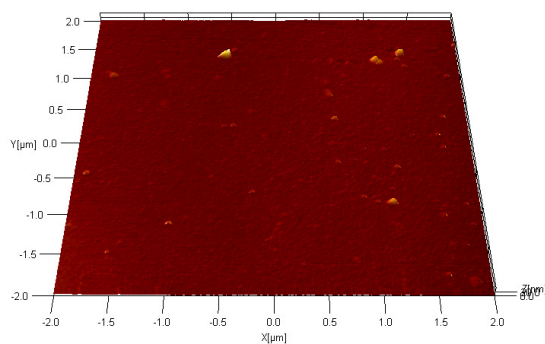
Surface roughness (R.M.S): 9.41 nm

Substrate a2



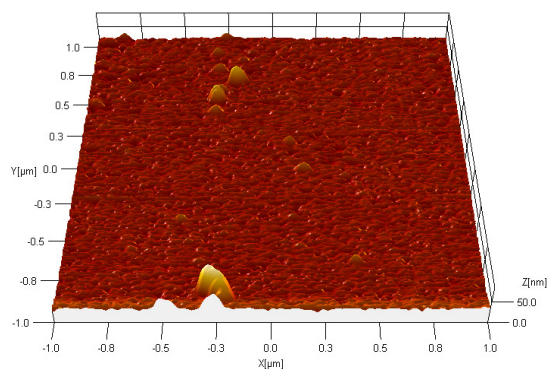
Surface roughness (R.M.S): 2.67 nm

Substrate a3



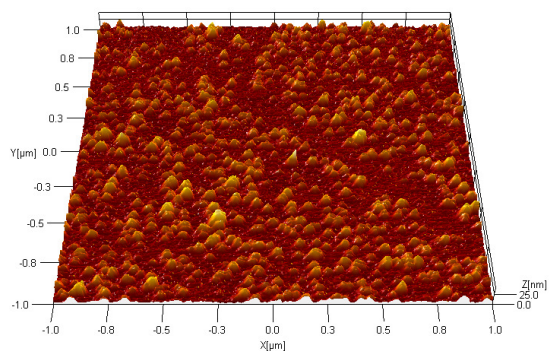
Surface roughness (R.M.S): 1.34 nm

Substrate a4



Surface roughness (R.M.S): 3.67 nm

Substrate a5



Surface roughness (R.M.S): 4.57 nm

Figure 3-17 AFM topography of the nano-dots/wells the SALDI substrates a1 to a5. a4 exhibits a nano-wells structure and a5 exhibits a nano-dots structure.

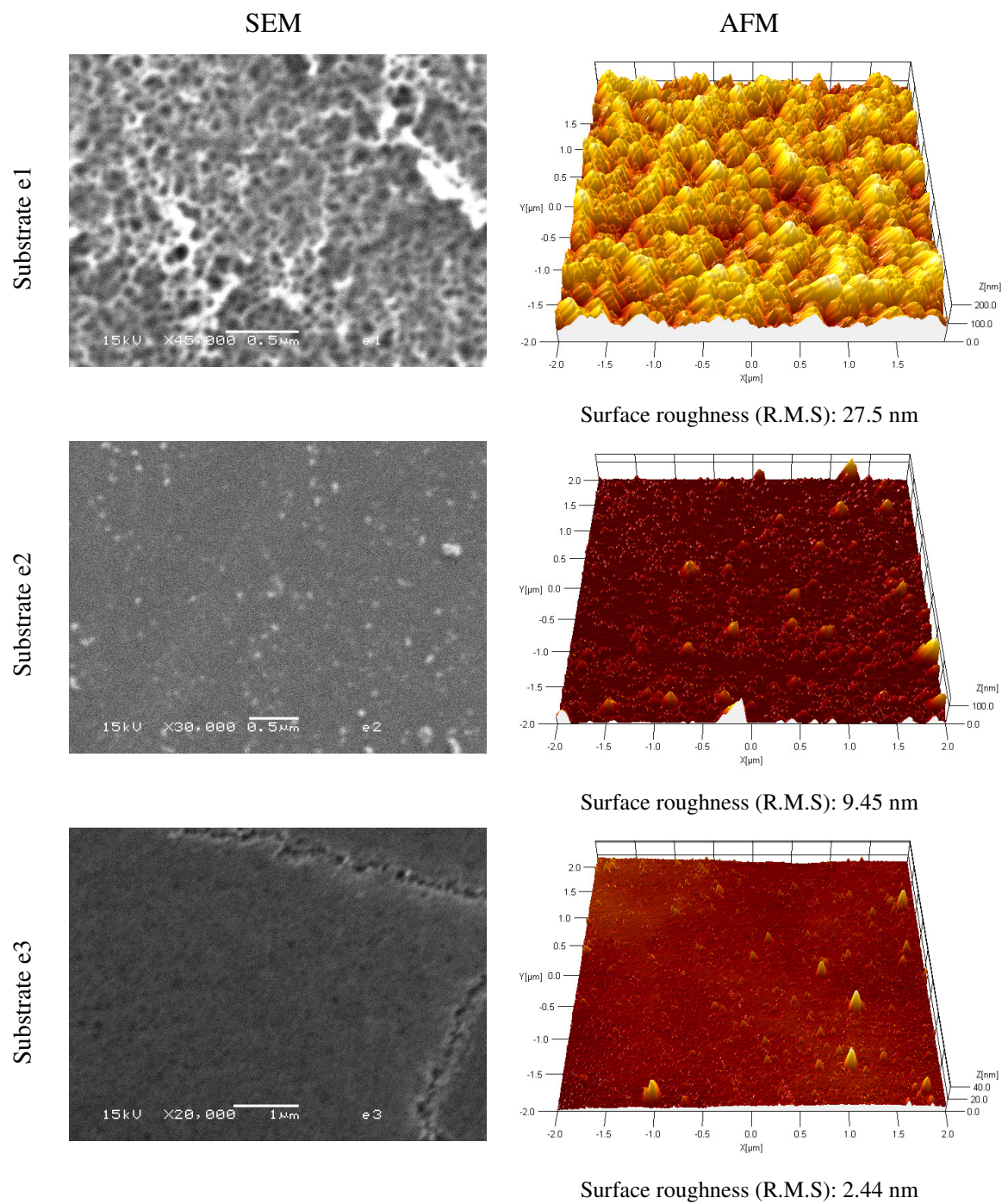
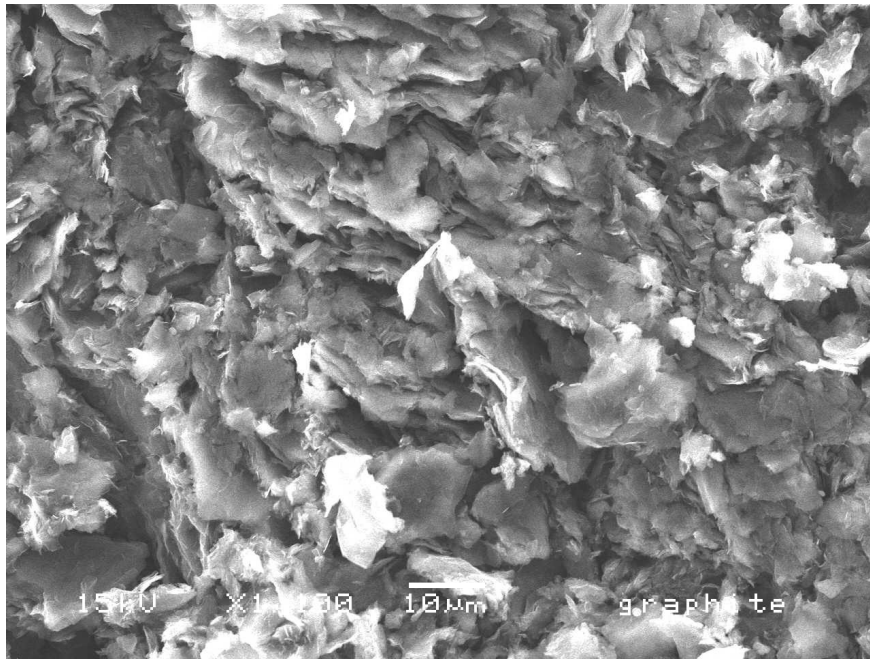


Figure 3-18 SEI and AFM topography of the experimental substrates e1 to e3.

A



B

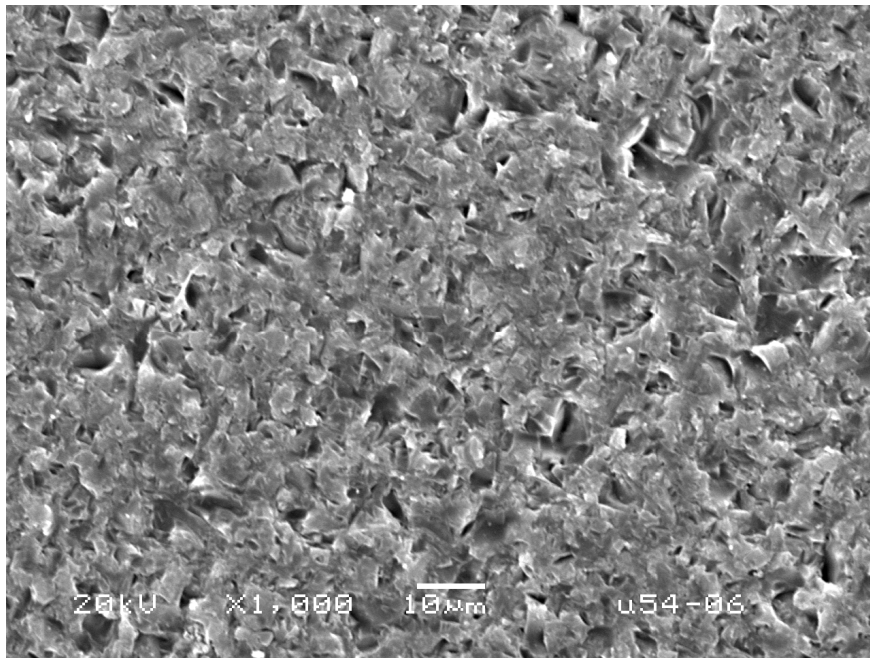


Figure 3-19 SEI of (A) HOPG, (B) sanded silicon surface. The sanded surface was produced by grinding with diamond powder.

3.3.4 ToF-SIMS Investigation of the LDI Substrates

3.3.4.1 DIOS and QuickMass Substrate

Representative SIMS spectra of the DIOS substrates are shown in Figure 3-20. The positive ion SIMS spectrum (Figure 3-20 A) is dominated by Si^+ (m/z , 28) and SiH^+ (m/z , 29), and SiHO^+ (m/z , 45) ion peaks. Na^+ (m/z , 23) and hydrocarbon such as C_3H_3^+ (m/z , 39), C_3H_5^+ (m/z , 41), $\text{C}_2\text{H}_3\text{O}^+$ (m/z , 43) are also observed.

The negative ion SIMS spectrum (Figure 3-20 B) is dominated by H^- (m/z , 1), O^- (m/z , 16) and OH^- (m/z , 17) peaks as well as the halide ions, such as F^- (m/z , 19), and Cl^- (m/z , 35). Various silanol-related clusters were also observed, such as SiHO^- (m/z , 45), SiO_2^- (m/z , 60), SiO_3^- (m/z , 76) SiHO_3^- (m/z , 77) through SiH^- (m/z , 29) and SiH_2^- (m/z , 30) are also seen. PO_2^- (m/z , 63) and PO_3^- (m/z , 79) are also seen. (Note: peak m/z 79 is not assigned to $^{79}\text{Br}^-$ because the $^{81}\text{Br}^-$ is missing and the difference in accurate mass)

On the other hand, the positive ion SIMS spectrum of the QuickMass substrates is dominated by Na^+ (m/z , 23), K^+ (m/z , 39), Fe^+ (m/z , 56) and various Ge^+ isotopes (m/z , 70-76). (Figure 3-21 A) Various germanium-oxide ions are also observed both in positive (m/z , 85-93) and in negative (m/z , 102-109) ion spectrum. (Figure 3-21 B) The negative ion spectrum is also dominated by H^- (m/z , 1), O^- (m/z , 16) and OH^- (m/z , 17) peaks. Other dominant peaks include CN^- (m/z , 24) and CNO^- (m/z , 42). Halide ions, such as F^- (m/z , 19), and Cl^- (m/z , 35) are seen but are relative minor. PO_2^- (m/z , 63) and PO_3^- (m/z , 79) are also seen.

Based on the SIMS spectra of the DIOS and QuickMass substrates, the elemental composition of the QuickMass substrates received is germanium based, whereas the DIOS substrates are silicon based. The detection of Fe^+ on the QuickMass substrates is because of the steel basal support. Various oxide ions are also detected on these two substrates, indicating an oxide-passivated layer is present on the silicon and germanium substrates.

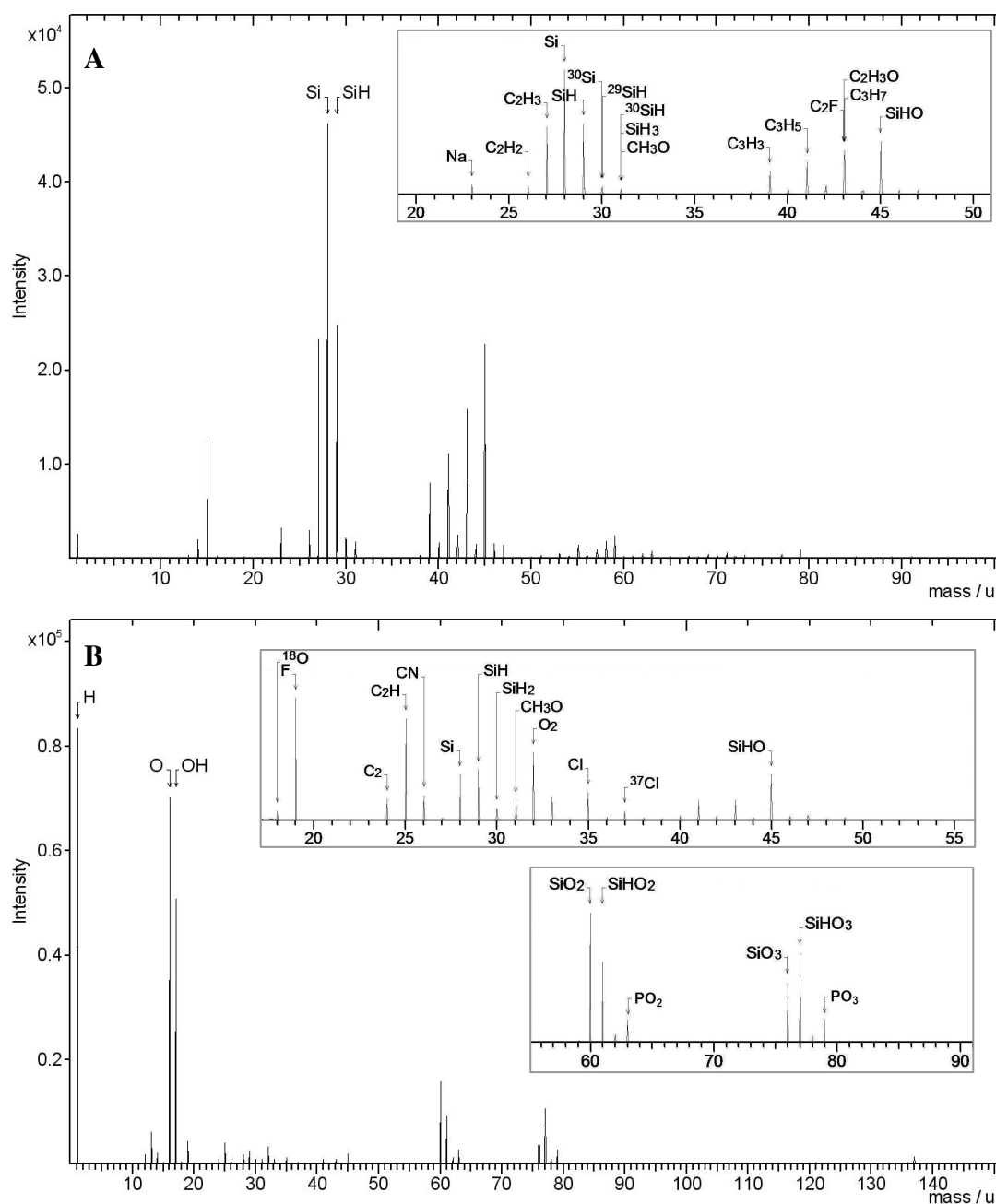


Figure 3-20 (A) Positive and (B) negative ion SIMS spectra of a DIOS substrate (inserts show selected region). Data acquisition was 8 s long on a $100 \times 100 \mu m^2$ area (for high mass resolution).

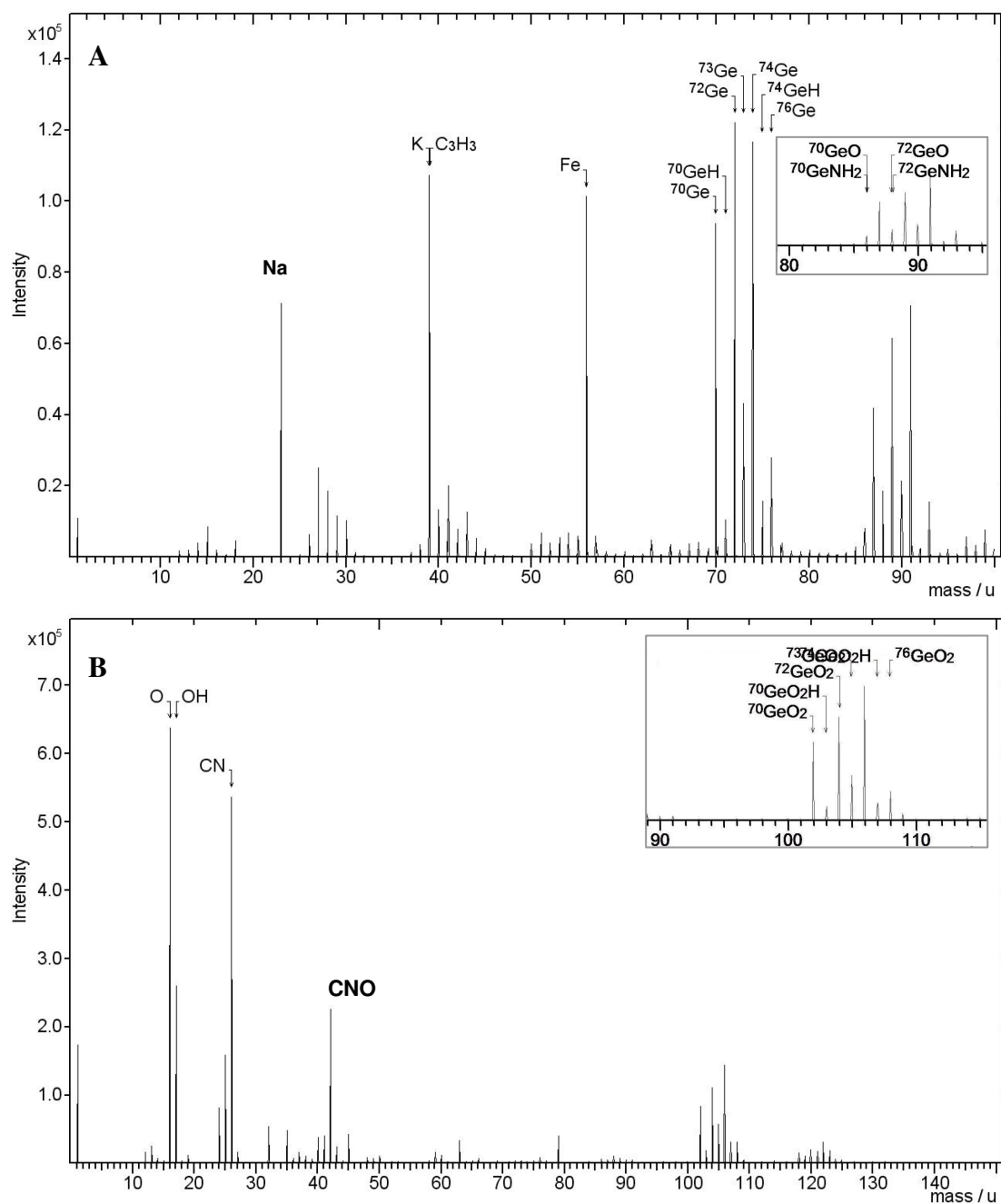


Figure 3-21 (A) Positive and (B) negative ion SIMS spectra of a QuickMass substrate (inserts show selected region). The target was first cleaned by DC sputtering using Cs⁺ ion gun with 10kV acceleration voltage to remove the surface contaminants, revealing that the surface was made of germanium. The Fe⁺ signal originates from the steel plate on which the germanium film was deposited. Data acquisition was 76 s long on a 300 × 300 μm² area (for high sensitivity).

3.3.4.2 SALDI Substrates

The surface of the SALDI substrates contains a wide range of molecular species. The SIMS spectra generally show a high level of hydrocarbon clusters and various silicon hydrides and oxides signals. The results are presented along with our effort to clean these substrates by argon plasma etching.

3.3.4.3 Principle Component Analysis (PCA) of ToF-SIMS Spectral Data of SALDI Substrates (Batch 2005)

It is difficult to interpret the SIMS spectral data manually owing to the complexity of the SIMS spectra, particularly when there are a large number of spectra to consider. Consequently, multivariate data analysis (MVDA) was used. PCA is an important MVDA approach and was employed to distinguish the differences between the SALDI substrates or to classify (pattern recognition) the ToF-SIMS spectral dataset generated by the SALDI substrates here. Except for the vapour-phase etched surface (vefib-2), all surfaces were stored in isopropanol (solvent washing) before the ToF-SIMS analysis. A sanded silicon surface, which has only been roughened, provides a reference here.

One approach to PCA-SIMS is to select a relatively small number of ions of interest from the spectra. In this study, all ions detected in the selected mass range of SIMS spectra were considered. This method is derived from metabolite profiling using NMR. A peak set with the corresponding integrated area was created from all spectra. The areas of these peaks were then calculated for every spectrum and normalised to the total intensity of all peaks in each individual spectrum to correct for differences in total secondary ion yield between spectra. The normalised peak set was then imported to Umetrics SIMCA-P.

PCA is also sensitive to the choice of scaling technique. Scaling to unit variance is a common practice, if there is no prior knowledge about the dataset. Unit scaling implies that the “long” variables are shrunk and the “short” variables are stretched, so

that all variables will rest on an equal footing. However, it is important to note that because of this *non-discriminative* approach, unit variance scaling is to be avoided as this leads to exaggerating the less significant ion peaks to the equal level of important ion peaks and masking the PCA plots. Instead, no scaling and mean-centring was used.

Six PCs are generated on positive ion SIMS dataset and the first two PCs account for 72% of the variability. Four PCs are generated on negative ion SIMS dataset and the first two PCs account 87% of the variability. Figure 3-22 and Figure 3-23 show PCA PC₁/PC₂ score and loading plots of positive and negative SIMS spectral dataset, respectively.

The SALDI substrates tested can be grouped into three major classes in the PCA score plot using the positive ion SIMS dataset (Figure 3-22). The score plot illustrates the plasma etched surface is chemically similar to the sanded surface, whereas the as-received experimental surfaces are distinctive from the rest. However, the score plot also indicates that plasma etching produces a relatively large variation (relative to the as-received substrates) among the three different SALDI surfaces used despite they were plasma etched simultaneously for 100s. The PCA loading plot points out that the signal of Si⁺ and SiHO⁺ in the SIMS spectra accounts the biggest variation of the plasma etched surfaces from other classes of surfaces, whereas SiH⁺ signal accounts for the biggest variation of the as-receive class from the rest of the substrates. Signals of hydrocarbon and silicon oxides ions are common in all the spectra and are located at the centre of the loading plot.

On the evaluation on the negative ion SIMS dataset, the SALDI substrates tested can be grouped into four major classes in the PCA score plot (Figure 3-23). The sanded surface is located in between the as-received and the plasma-etched classes in the loading plot. The PCA loading plot illustrates the difference between the as-received and the plasma-etched surfaces are the OH⁻, O⁻ and various silicon oxides signals. The vapour-phase etched surfaces (vbfib-2) which have not been subjected to solvent washing produce intense signals of halides ions (Cl⁻, F⁻, and I⁻) in the SIMS spectra, and the significance of these ions is highlighted in the loading plot. Other fluorine-related ions, such as SiF⁻, OF⁻ and CNF⁻ are also observed and they are located in the central cluster of the loading plot.

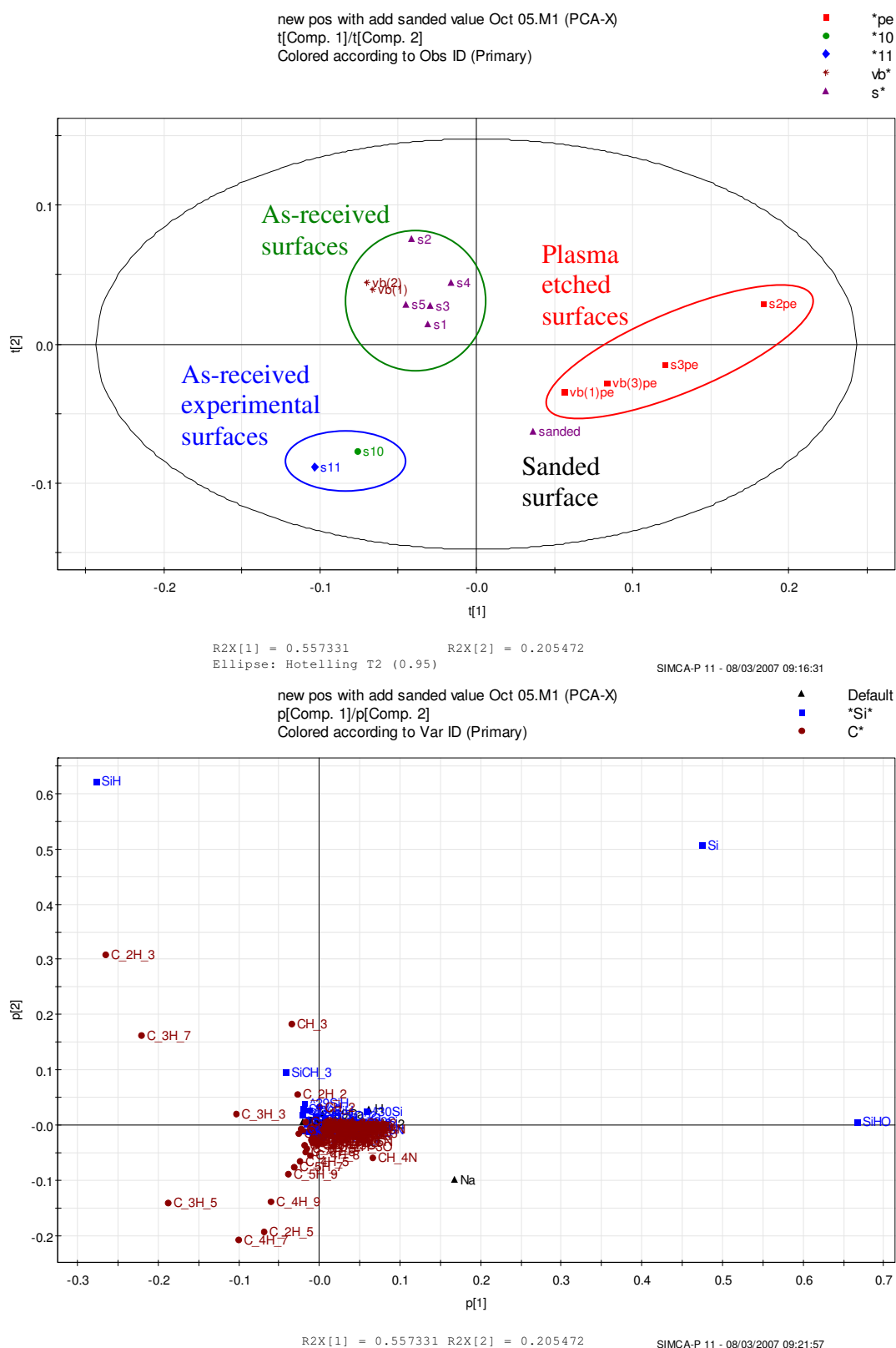


Figure 3-22 PCA t_1/t_2 score (*top*) and p_1/p_2 loading plots (*bottom*) based on the positive ion SIMS dataset. The samples can be classified into three classes: (1) as-received, (2) as-received experimental, and (3) argon plasma etched (100s) in the score plot. The central cluster of the loading plot is mainly composed of hydrocarbon, silicon oxides and metallic ions.

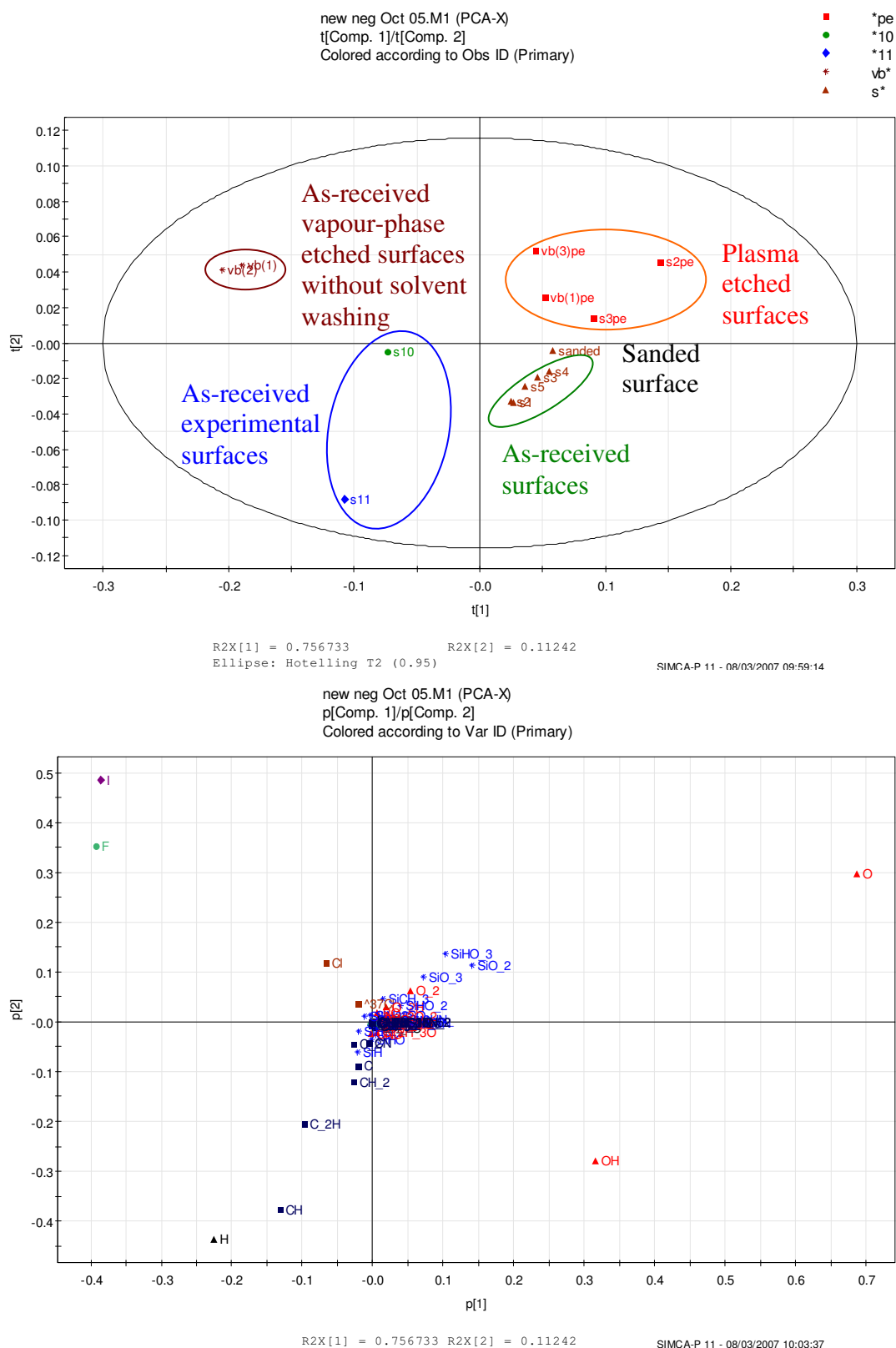


Figure 3-23 PCA t_1/t_2 score (*top*) and p_1/p_2 loading plots (*bottom*) based on the negative ion SIMS dataset. The samples can be classified into four classes: (1) as-received, (2) as-received vapour-phase etched surface without prior solvent washing, (3) as-received experimental substrates and (4) argon plasma etched (100s) in the score plot. The central cluster of the loading plot contains fluorine, nitrogen, or sulphur-containing species as well as silicon-containing species.

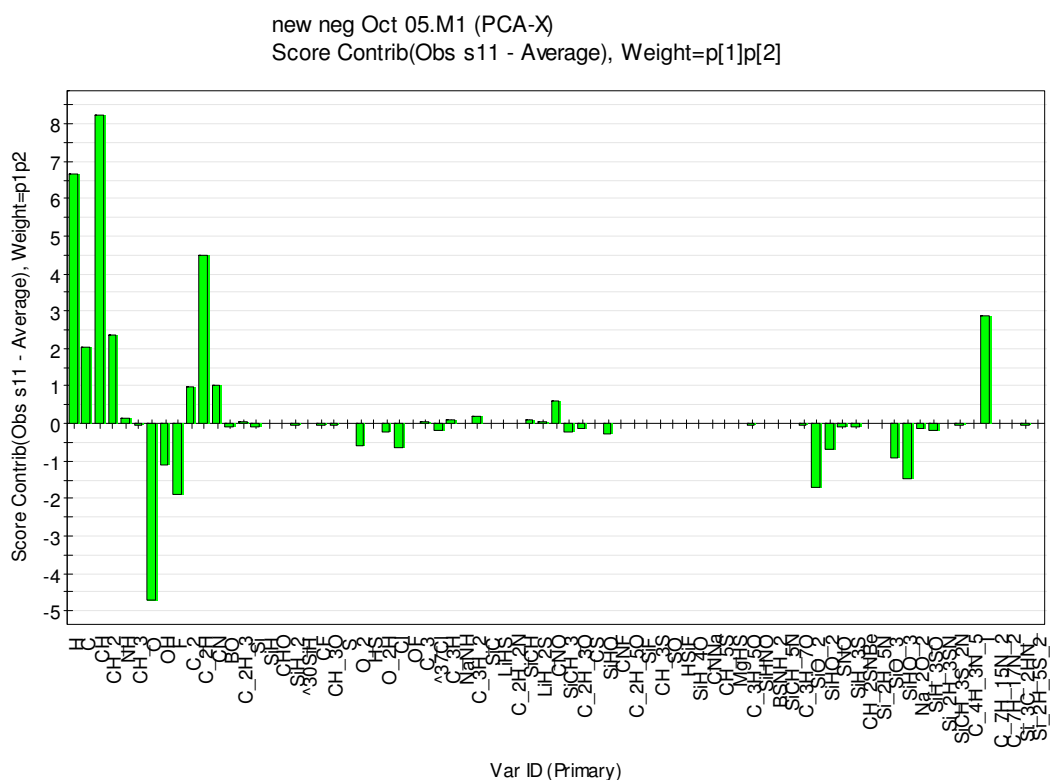
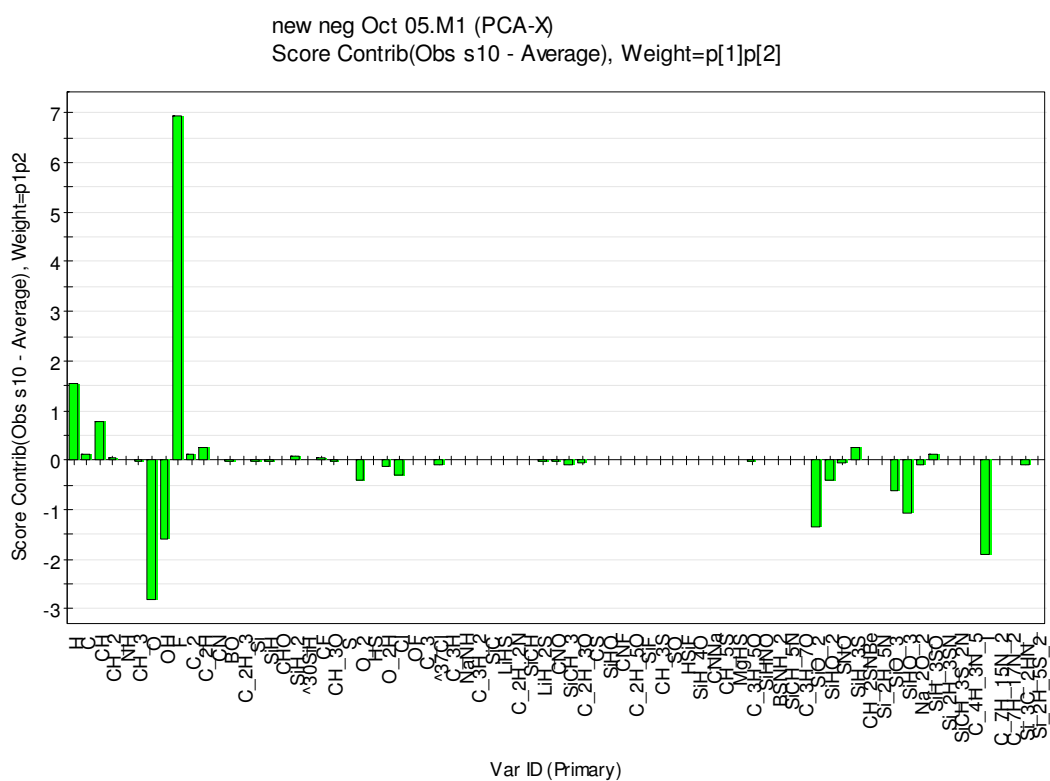


Figure 3-24 Score p_1/p_2 contribution plots of substrate s10 (*top*) and s11 (*bottom*). Data is derived from Figure 3-23.

The as-received experimental substrates also stand out from the rest as shown in the score plot. The differences between s10 and s11 are specified by looking to the contribution plot. (Figure 3-24) While H^- and F^- ions are above average in the spectrum of s10, H^- , C^- , CH^- , C_2H^- and I^- ions are above average in the spectrum of s11. The contribution plots also show that O^- , SiO_2^- , SiHO_2^- , SiO_3^- and SiHO_3^- ions in the spectra of both of these surfaces are less intense than the average of the whole dataset suggesting they have a lower concentration of oxides than the as-received and plasma etched SALDI surfaces.

The classification or cluster analysis presented here is important to our comparison of the LDI performance among different SALDI substrates later in this chapter. Although the investigation was carried out first, cluster analysis by PCA was not necessarily easy to interpret. The realisation of the implications was effective came at last and the results must be subjected to further cross-validation by a subset of sample surfaces using ToF-SIMS and XPS.

3.3.5 ToF-SIMS Investigation of the Effects of Plasma Etching

Plasma etching is central to many manufacturing processes that employ silicon and other thin film devices for electronic, display or related applications.²¹ The uniqueness of plasmas for surface processing is due to the fundamental features of non-equilibrium plasmas. The term “non-equilibrium” here refers to the charged species (electrons and ions) which generally have a much higher average kinetic energy than the neutral species. Non-equilibrium plasmas are unique surface processing environments due to the combination of high fluxes of reactive radicals at low gas temperatures and the effects of ion bombardment at surfaces. The effects of the plasma on surfaces are that the plasma modifies the chemical nature and behaviour of the regions near the surface influenced by ion impact.²¹ Similar arguments apply to plasma deposition of thin films. Furthermore, isotropic and anisotropic silicon microstructures can also be manufactured by plasma etching using reactive plasmas such as SF_6 -base plasmas or halogen containing plasmas, avoiding a wet chemistry etching procedure. This process is termed reactive ion etching (RIE).^{13, 22} Here plasma etching is applied for surface cleaning/processing. Less reactive Ar^+ plasma was used.

Figure 3-25 and Figure 3-26 show the positive and negative ion SIMS spectra of the SALDI surface s3 before and after 100s of argon plasma treatment, respectively. Identical primary ion dose was used to acquire the SIMS spectra. Overall, these spectra are very similar to those obtained from the DIOS substrate. (Figure 3-20) Si^+ (m/z , 28) and O^- (m/z , 16) dominate the positive and the negative spectra, respectively and their intensities increase after the plasma etching. The positive ion spectra also show that the intensity of SiH^+ (m/z , 29) is reduced, and yet the intensity of SiHO^+ (m/z , 45) is increased after the plasma treatment. These suggest the plasma etching procedure has increased the surface concentration or thickness of the oxide layer. On the other hand, the intensity of Na^+ (m/z , 22.99) is higher after the plasma etching. The ion intensities of hydrocarbon species *e.g.* CH_3^+ (m/z , 15) and C_2H_3^+ (m/z , 27) are diminished. In addition, a high intensity of iodide ion (m/z , 127) is observed in the negative spectra but signal of Si-I is not. Initially it was thought the absence of Si-I signal was due to the ion instability. This matter is to be revisited on further examination using XPS.

To evaluate the change in surface chemistry due to argon plasma etching, the raw data is converted to Figure 3-27 and Figure 3-28 which illustrates the relative change of ion intensities in the SIMS spectra before and after argon plasma etching, detected in positive and negative mode, respectively.

Before the treatment, a wide range of hydrocarbon related ions are detected in the positive ion spectra. Nitrogen, sulphur, and iron related ions are also seen. On comparing the positive spectra before and after the plasma treatment, there appears to be two main types of contaminants, one is hydrocarbon in nature and was removed by the plasma treatment and the others seem to be amines in nature and apparently remained after the treatment.²³ Examples include a number of $\text{C}_x\text{H}_y\text{N}_z^+$ ions. It should be noted that though the calculated relative change is large, their signal intensities or surface concentration are not high in the SIMS spectra. These species could have been presented in the deeper layer of the surface and were exposed to the surface, or were subsequently adsorbed after the plasma treatment. The negative ion spectra also show the hydrocarbon and halide ions, such as F^- , Cl^- and I^- were removed after the plasma treatment.

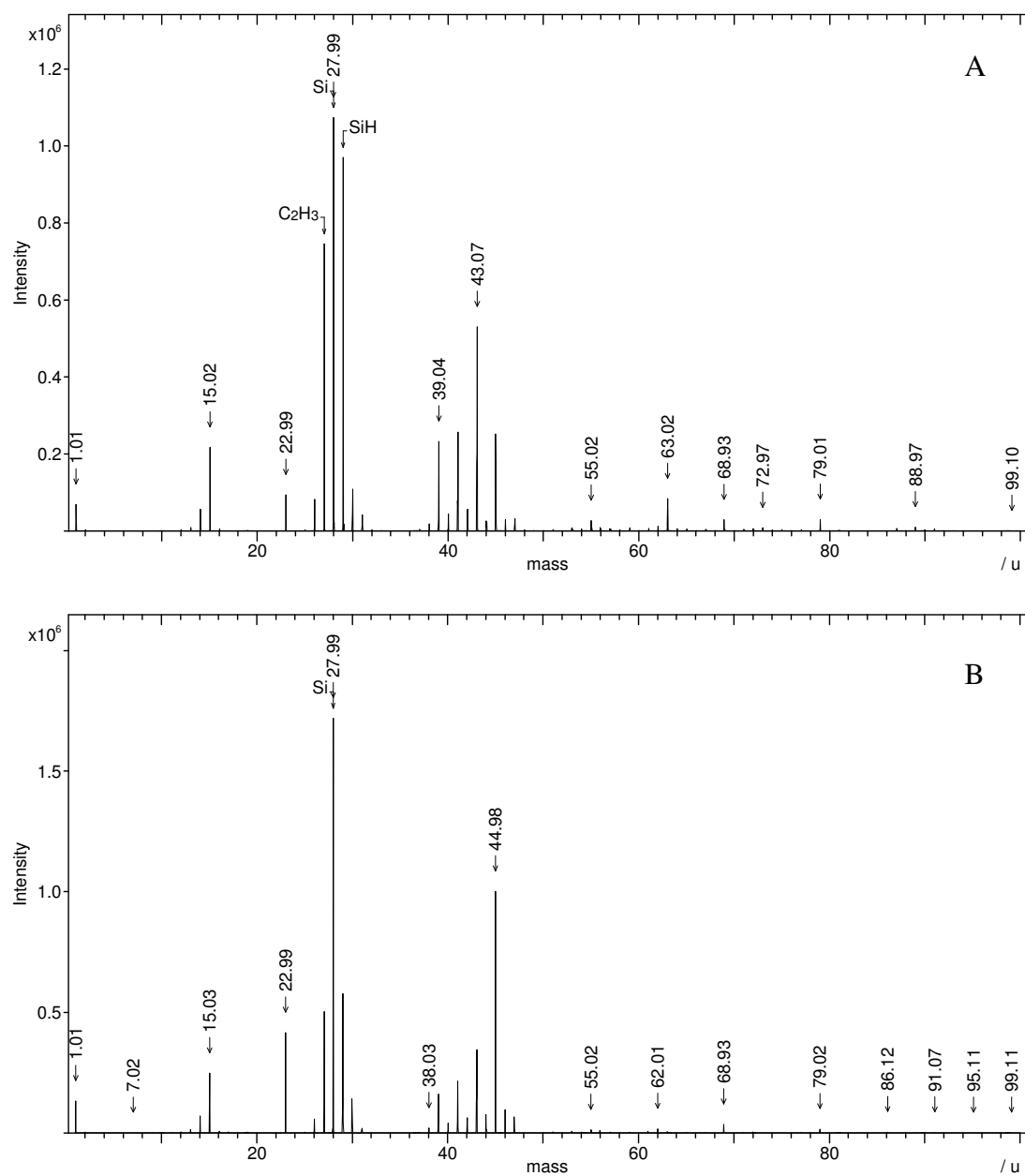


Figure 3-25 Positive ion SIMS spectra of (A) as-received SALDI surface s3 and (B) after 100s of argon plasma etching. Data was acquired by raster scanning a $500 \times 500 \mu\text{m}^2$ with $5 \times 10^{11} \text{ PI/cm}^2$.

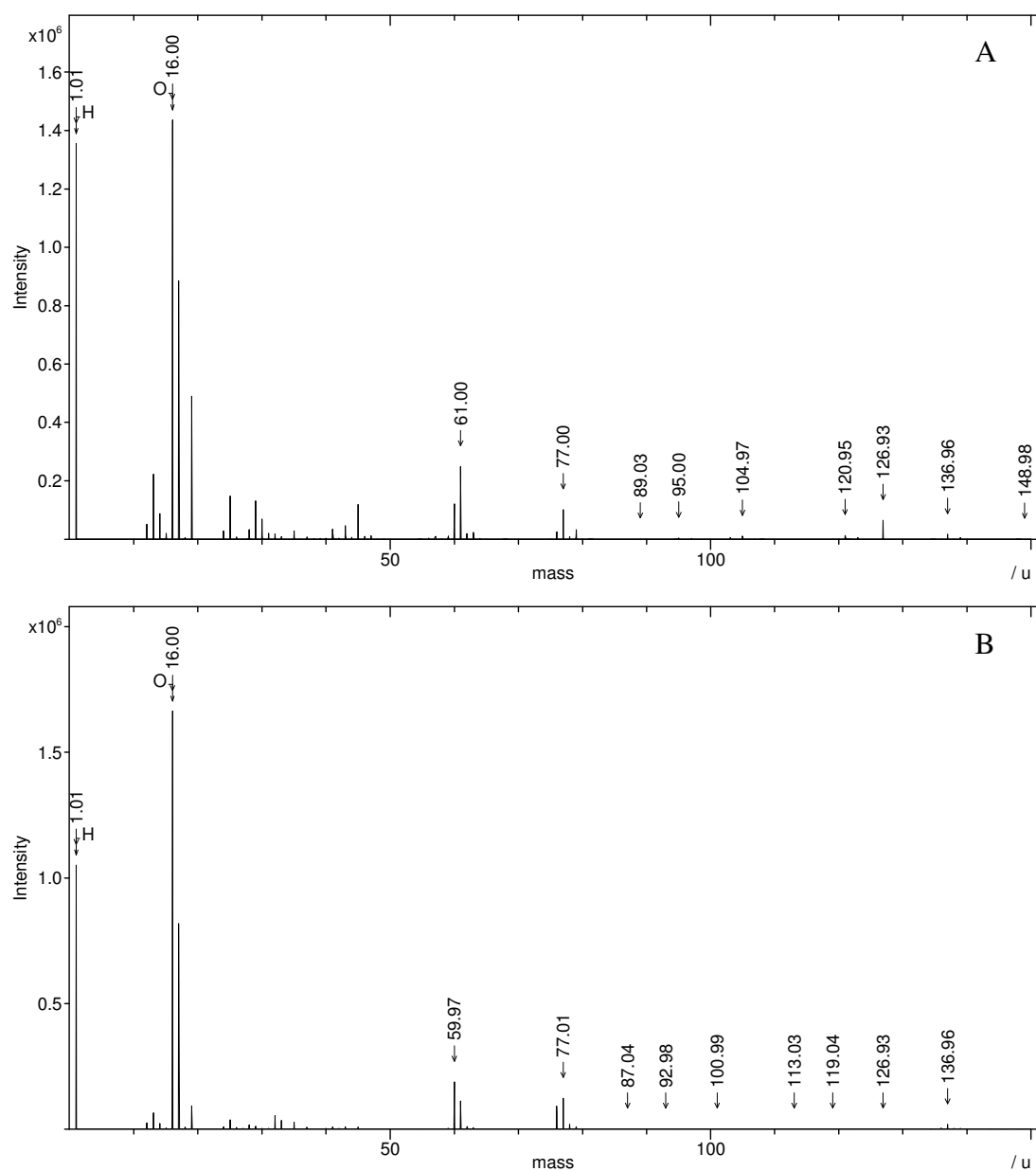


Figure 3-26 Negative ion SIMS spectrum of (A) as-received SALDI surface s3 and (B) after 100s of argon plasma etching. Data was acquired by raster scanning a $500 \times 500 \mu\text{m}^2$ with $5 \times 10^{11} \text{ Pt/cm}^2$.

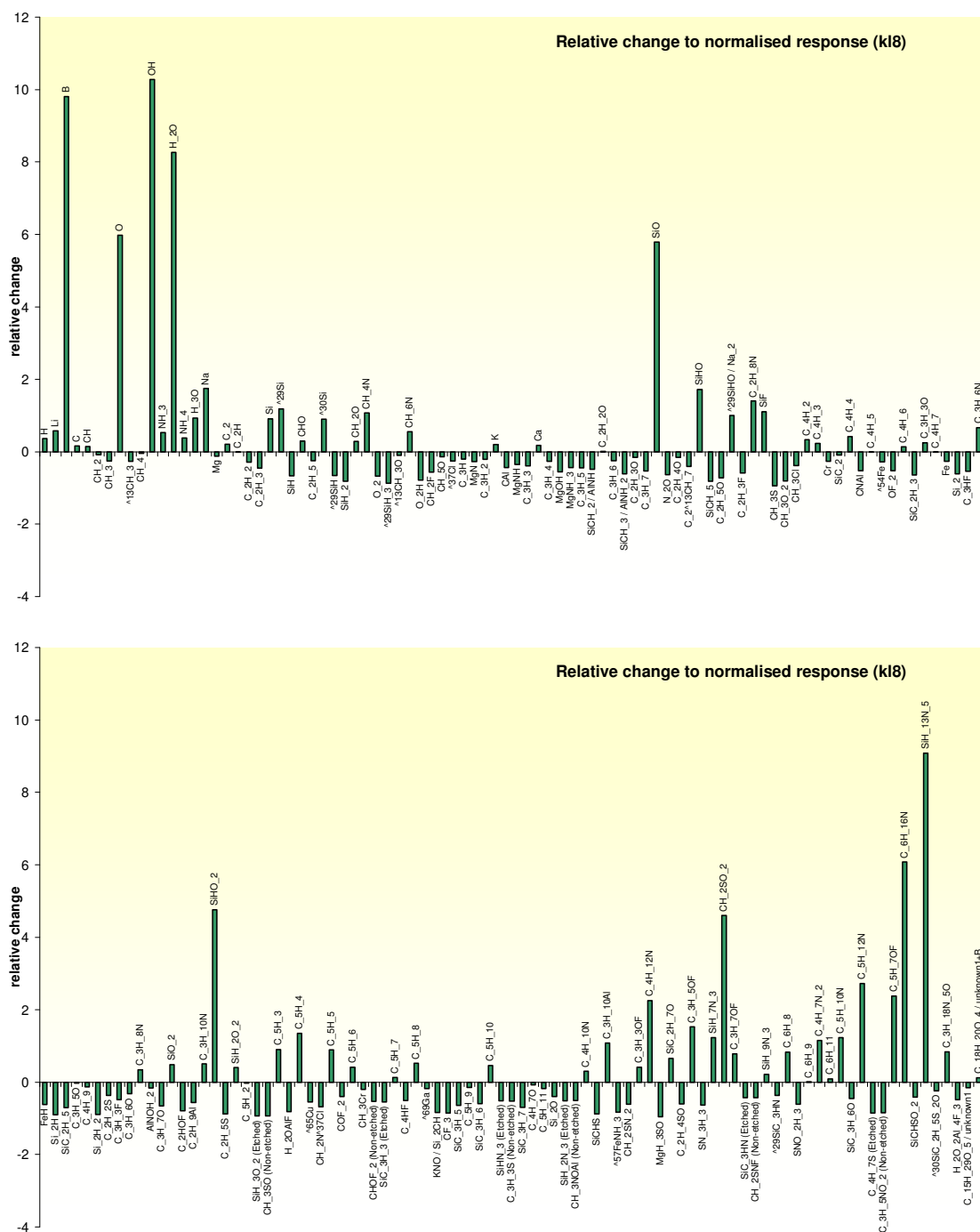


Figure 3-27 Relative changes in the secondary ion intensity (positive): lower mass (*top*) and higher mass (*bottom*). Each peak is first normalised with total ion intensity of all selected ions. Relative change is calculated:

$$\text{Relative change} = \frac{T - N}{N}$$

Where T = Normalised secondary ion intensity of treated surface

N = Normalised secondary ion intensity of untreated surface

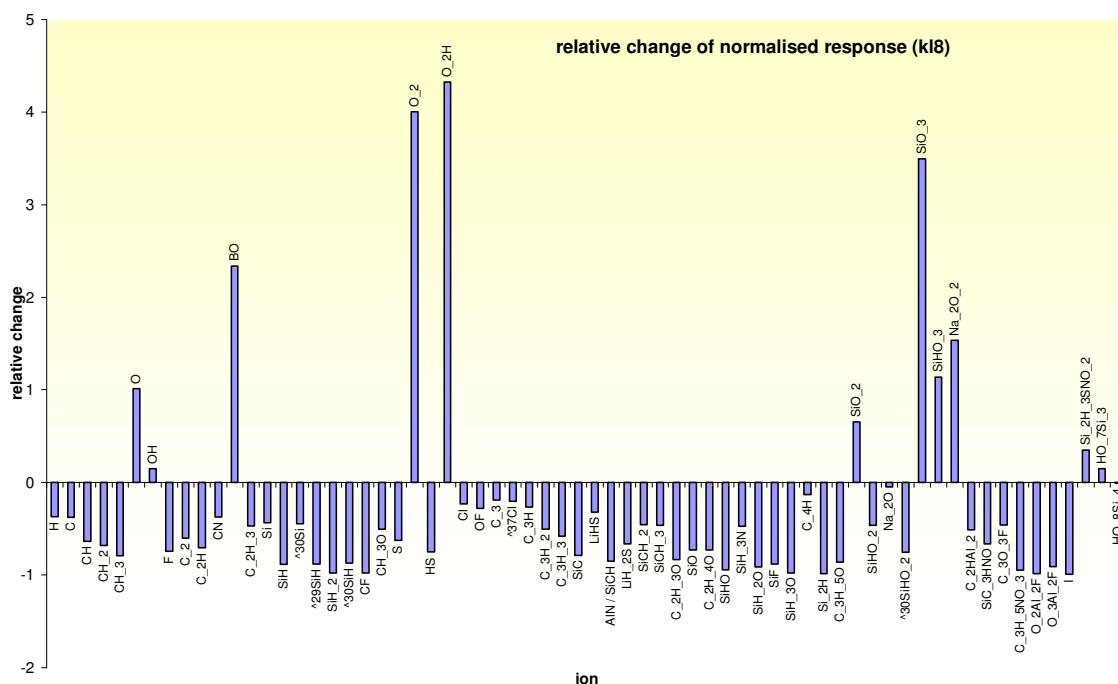


Figure 3-28 Relative changes in the secondary ion intensity (negative). The data was treated in the same way as in positive.

The result shows that the removal of organic species was achievable by argon plasma etching. Furthermore, the surface was oxidised as the secondary ions of various oxides had a relatively higher intensity. Alternatively, this could also be due to the elimination of contamination and thus the oxides, which might have been previously covered by the hydrocarbon, were exposed to the surface after the treatment. This still needs verification by other technique, such as XPS.

Although the SIMS technique provides excellent sensitivity, one of its major limitations lies in quantification. This is because the ionisation yield of a given sputtered species may vary considerably depending on the composition of the matrix in which it is located (known as matrix effect). Secondly, it has also been reported that PSi can effectively adsorb water vapour and hydrocarbon in vacuum, especially under ion beam irradiation, and the concentration of O, C and H can be altered during the analysis.²⁴ For that reason, SIMS can only provide qualitative information. To assign the true nature of these substrates, the questions are revisited using XPS.

3.3.6 XPS Investigation of the Effects of Argon Plasma Etching of SALDI Surface

Figure 3-29 and Figure 3-30 show the XPS spectra of SALDI surface s3 before and after 100s plasma etching, respectively. The prominent peaks are due to silicon, carbon, and oxygen. Small amount of fluorine and iodine are also detected. Table 3-1 summarises the quantification of the elemental species.

Table 3-1 Atomic concentration of as-received and plasma etched (100s) SALDI surface s3 determined by XPS survey scan measurement.

| Si sample | Atomic concentration (at %) on the surface on the SALDI surface determined by XPS survey spectra measurements | | | | | |
|------------------------|---|--------------|------|------|-------|--------|
| | F 1s | I 3d | O 1s | C 1s | Si 2s | Traces |
| As-received surface | 0.9 | > 0.1 | 31.4 | 23.4 | 44.3 | |
| Plasma treated surface | 0.2 | ≥ 0.001 | 54.8 | 6.0 | 38.4 | Na, Sn |

After argon plasma etching, the level of carbon, fluorine, and iodine is significantly reduced. However, the level of oxygen is elevated. Sodium and tin on the SALDI surface become detectable after plasma etching. The core-level O 1s deconvolution suggests both oxides and hydroxides are increased due to plasma etching, but higher proportion of hydroxides than oxides in this case. (Figure 3-29 B and Figure 3-30 B) The core-level C 1s deconvolution (Figure 3-29 C) shows only the peaks of CH and CO. Concurring with the results of SIMS, the carbonaceous species on the surface are effectively removed by plasma etching. (Figure 3-30 C)

Significant changes in the Si 2p spectra are observed on the SALDI surface due to plasma etching. The spectrum shape changes from largely metallic to oxides. (Figure 3-29 D and Figure 3-30 D) The high resolution Si 2p spectra is deconvoluted into three sets of peaks corresponding to elemental silicon, silicon dioxide and sub-oxides. Each pair of peaks corresponds to the lower and the higher spin of a chemical state. The literature value of Si 2p spin orbit splitting is 0.617 eV.²⁵ This model was created taking references to Nesbitt and the references therein.²⁵

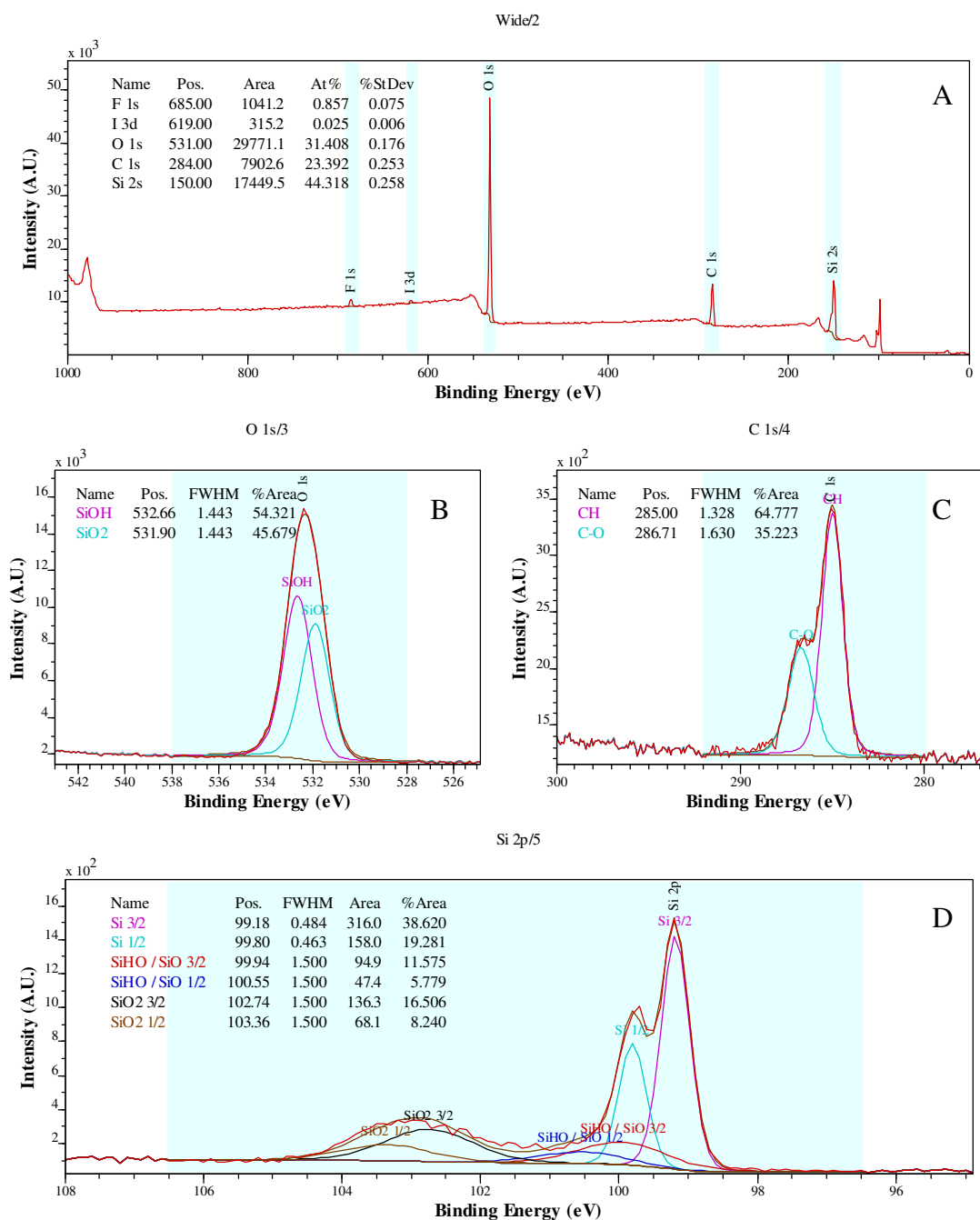


Figure 3-29 XPS spectra of as-received SALDI surface s3 (solvent washing, no plasma etching). (A) Survey scan, (B) synthetic components of O 1s high resolution scan, the FWHM constant is constrained to be smaller than 1.5, (C) synthetic components of C 1s high resolution scan, and (D) synthetic components of Si 2p high resolution scan. The prominent peaks in the survey spectra are due to silicon, carbon and oxygen. Small amount of fluorine and iodine were also detected.

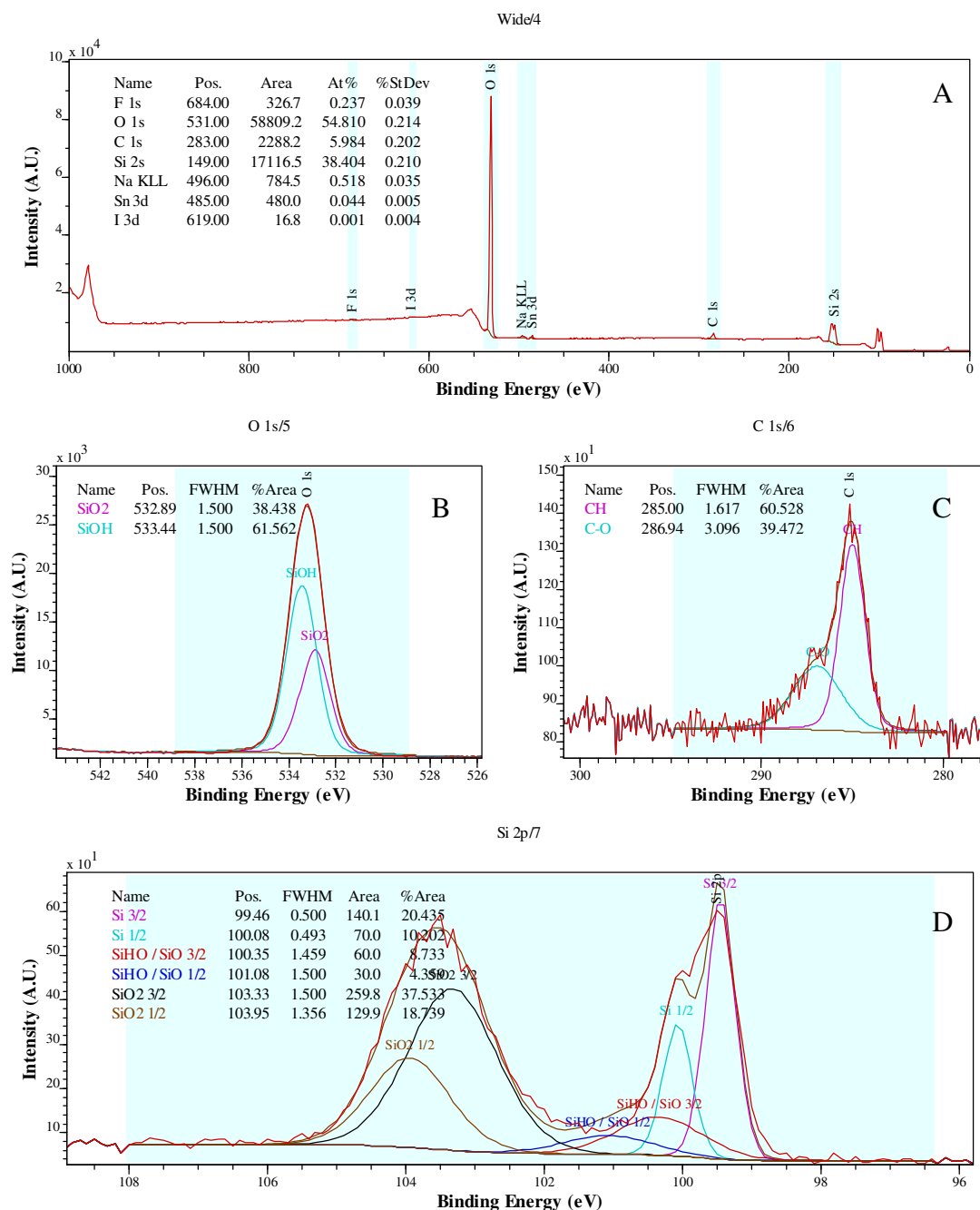


Figure 3-30 XPS spectra of argon plasma etched SALDI surface s3 (etched 100s). (A) Survey scan, (B) synthetic components of O 1s high-resolution scan, the FWHM constant is constrained to 1.5, (C) synthetic components of C 1s high-resolution scan, and (D) synthetic components of Si 2p high resolution scan. The survey spectrum is dominated by O 1s peak. Peaks due to silicon or carbon are relative minor. A small amount of fluorine, sodium and tin were also detected.

3.3.7 XPS Investigation of Fluoro-silane Self Assembly Monolayer (SAM) Modification

As-received DIOS substrate (surface 1), as-received and fluoro-silanised (surface 2), plasma etched for 60s (surface 3), and plasma etched for 60s then fluoro-silanised (surface 4) were chosen for the XPS investigation. Table 3-2 summarises the quantification of surface elemental species and carbonaceous species.

Table 3-2 Atomic concentration and surface concentration of carbonaceous species of as-received, as-received then silanised, plasma etched for 60s, and plasma etched for 60s then silanised DIOS surfaces determined by survey scan and high resolution C 1s core scan respectively. (Surface concentration = relative concentration \times atomic % concentration of C 1s)

| Silicon sample | Atomic concentrations (at.%) on the DIOS surface determined by XPS survey spectra measurements | | | | High-resolution XPS C 1s component fits (% C) | | | |
|---|--|------|------|-------|---|-----------------|-----|-----|
| | F 1s | O 1s | C 1s | Si 2s | CF ₃ | CF ₂ | CO | CH |
| As-received DIOS surface | 18.4 | 38.0 | 19.0 | 24.6 | 1.2 | 5.7 | 6.8 | 5.3 |
| As-received and fluoro-silanised | 41.4 | 18.8 | 27.7 | 12.1 | 2.9 | 15.2 | 5.7 | 3.9 |
| Plasma etched for 60s | 1.5 | 58.7 | 7.8 | 31.9 | 0 | 0.6 | 4.7 | 2.5 |
| Plasma etched for 60s then fluoro-silanised | 51.0 | 11.3 | 30.6 | 7.1 | 3.4 | 19.2 | 4.1 | 3.9 |

The survey scans of all surfaces are dominated by fluorine, oxygen, silicon and carbon. Their peak intensities vary due to different treatment received. No sodium was detected and was verified by Na 1s core-level scan. High concentration of fluorine is observed in the fluoro-silanised surfaces, while the plasma etched surface has a reduced level of fluorine as well as carbon and has an increased level of oxides. Surprisingly, a relative high level of fluorine was also observed on the as-received DIOS surface. The source of the relative high level of fluorine on the as-received surface is revealed when we inspect the high resolution C 1s scan of the as-received DIOS and fluoro-silanised surfaces. (Figure 3-31 C and Figure 3-32 C) On inspecting the spectra of the as-received DIOS surface, in addition to C-O and CH, a similar intensity of CF₃ and CF₂ were also detected. The peak shape is comparable to that of

fluoro-silanised surfaces. The source of these carbonaceous species is not known. The fluorocarbons, whether they are active ingredients or contaminants, might have already been introduced during the manufacturing process.

A monolayer of 1H,1H,2H,2H-perfluorodecyldimethylsilane group covalently linked to the surface was expected on derivatised surfaces. The ratio of $\text{CF}_3\text{:CF}_2\text{:CH}_2$ in XPS C 1s spectra was expected to be in 1:7:4, and yet the ratio of $\text{CF}_3\text{:CF}_2\text{:CH}_2$ roughly 1:5:4 and 1:6:1 were obtained on the two derivatised surfaces, respectively. Firstly, C-O and CH could adsorb from air or were trapped methanol remained on the surface and appeared on all 4 surfaces as contaminants. This led to inaccurate quantification of CH introduced due to the derivatisation procedures. Secondary, the CH groups were buried underneath the CF groups and its signal was attenuated, because the photoelectrons were blocked to reach the detector. This also means the quantification of the surface species might be inaccurate for the derivatised surfaces.

Using the Si 2p core-level scan, we may also be able to model the surface chemistry of the as-received (surface 1) and fluoro-silanised (surface 4) DIOS surfaces in more detail. The model assumes that the DIOS surface had been fluoro-silanised and is taking references to Nesbitt and the references therein.²⁵ The spectra are fitted into 4 sets of peaks, each represents a chemical state. (Figure 3-31 D and Figure 3-32 D) Each pair of peaks is the upper and lower spin of a chemical state. The literature value of Si 2p spin orbit splitting is 0.6 eV²⁵ and the lower and upper spin states of all synthetic components are displaced.

The dominant Si 2p peak is assigned to SiO_2 , the SiO_2 peak is constricted between 102 to 105 eV according to literature data, and all other peaks are constricted relative to SiO_2 . Elemental silicon and intermediate sub-oxides are detected at the lower binding energy relative to SiO_2 peak. The intermediate sub-oxides are assigned to Si-OH and SiO states. The highest chemical state is assigned to the silicon bonded to fluorocarbon and is located at the highest binding energy. On overlapping the Si 2p spectra (result not shown), we can see the overall peak shape shifts to higher binding energy from the plasma etched to the as-received to the fluoro-silanised surfaces. This is very likely due to the fluoro-silane group and therefore the highest energy synthetic peaks are assigned to the fluoro-silane group, *i.e.* $-\text{O}-\text{Si}-(\text{CH}_2)_2(\text{CF}_2)_7\text{CH}_3$.

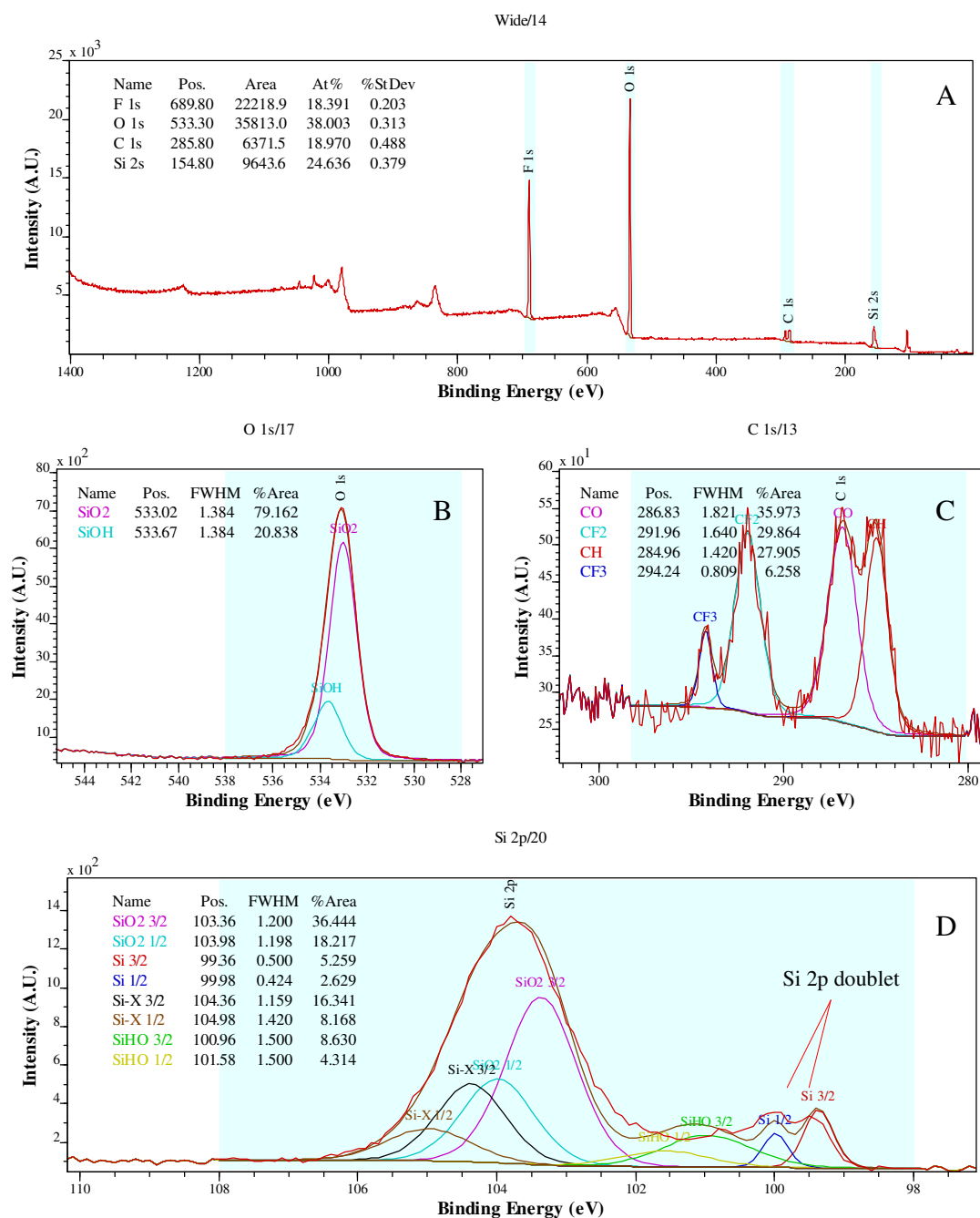


Figure 3-31 XPS spectra of the as-received DIOS surface. (A) Survey scan, (B) synthetic components of O 1s high-resolution scan, (C) synthetic components of C 1s high-resolution scan and (D) synthetic components of Si 2p high resolution scan. The survey spectrum is dominated by fluorine, oxygen, carbon and silicon. The peak width of core-level O 1s scan is narrower than that of SALDI surface. CF₂ and CF₃ are also detected in core-level C 1s scan. The Si 2p core-level spectrum is deconvoluted into 4 sets of peaks. X denotes (CH₂)₂(CF₂)₇CF₃ group.

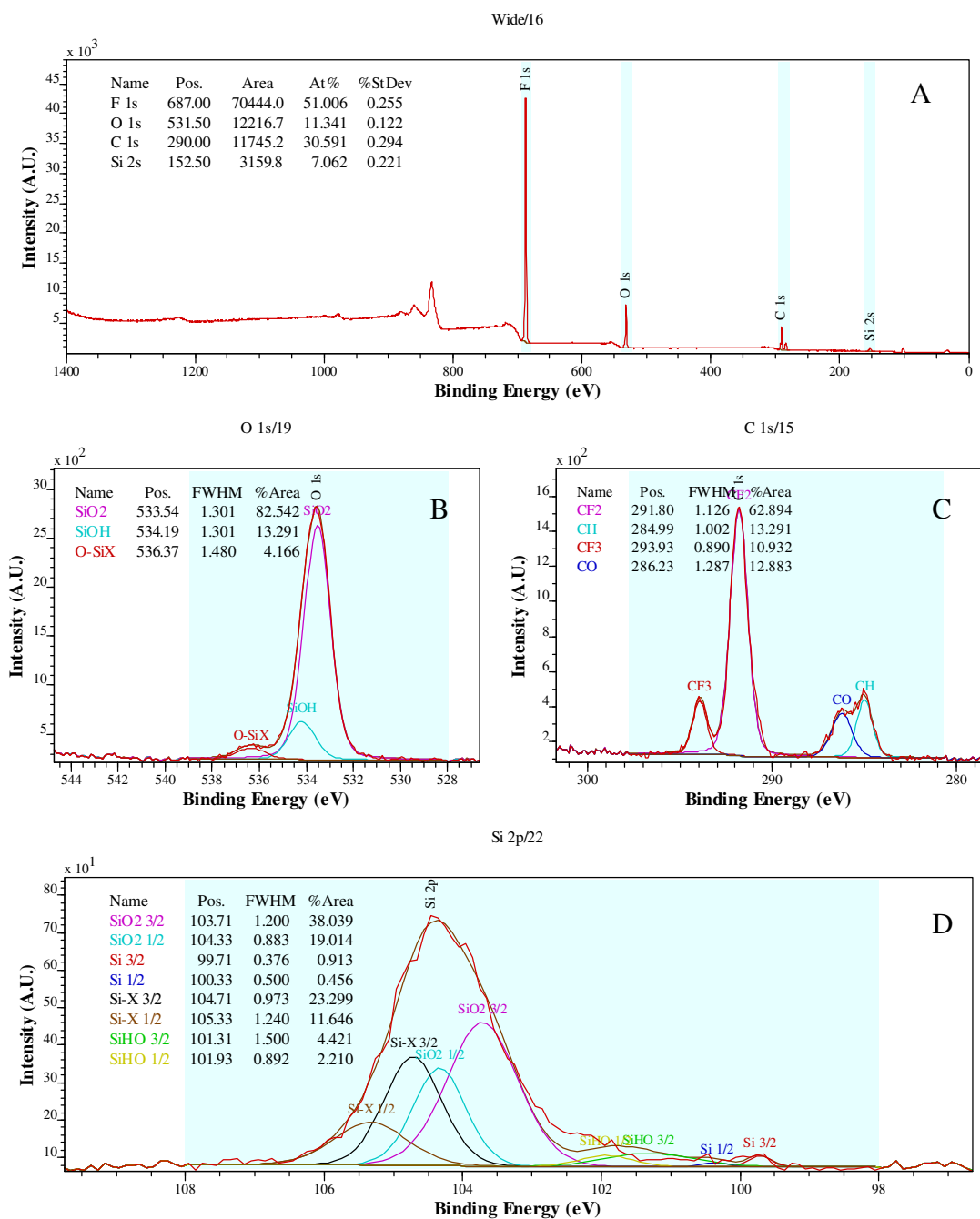


Figure 3-32 XPS spectra of the derivatised DIOS substrate (surface 4). The substrate was first subjected to 60s of plasma etching and then subsequently fluoro-silanised. (A) Survey scan, (B) synthetic components of O 1s high-resolution scan, (C) synthetic components of C 1s high-resolution scan and (D) synthetic components of Si 2p high resolution scan. The survey spectrum is dominated by fluorine, oxygen, carbon and silicon. The peak width of O 1s spectrum is further reduced to 1.3. The peak located at 536.4 eV detected only in silanised surfaces is assigned to oxygen attached to a fluoro-silane group. The Si 2p core-level spectrum is deconvoluted into 4 sets of peaks. X denotes $(\text{CH}_2)_2(\text{CF}_2)_7\text{CF}_3$ group. The intensity of oxides, intermediate sub-oxides and elemental silicon is lower relative to as-received surface, and so the core-level O 1s scan. This observation is contributed to relative strong fluorocarbons attenuation.

3.3.8 Plasmon Loss Lines in XPS

The collection of electrons in a crystal represents plasma of great density. In physics, the quantisation of plasma oscillations is the quantum quasi-particle plasmon.²⁶ In another word, the collective motion of the nearly free electrons in metals and semiconductors give rise to plasmon oscillation. Plasmon energy is associated with the optical, chemical, and structural properties of nanostructures and can be investigated by XPS.^{27, 28} In photoemission spectra, plasmons appear as secondary structures (plasmon loss lines) located at higher binding energy than the corresponding core-level lines. The loss peaks are associated with inelastic energy-loss processes to plasmons when the electrons released from the Si 2s or 2p orbitals. Plasmon loss feature originated from the surface and from the bulk and hence called surface plasmon and bulk plasmon. Bulk is within the depth of inelastic mean free path.

The interest of this study lies on a report that localised surface plasmon resonance is an important factor and possible an energy deposition and transfer pathway in using gold nanorod substrates for LDI.²⁹ By using XPS, we can evaluate whether the plasmon phenomena also applicable to the nano-structured silicon LDI substrates.

Figure 3-33 (A) shows the XPS survey scan of the SALDI substrate, s3. The plasmon loss lines relative to the Si 2s peak are visible at 167 eV, 173 eV and 184 eV. These features are of bulk plasmon characteristic. The peak located at 167 eV is thought to be plasmon-loss electrons from elemental Si in origin and the peak located at 173 eV shouldering to the main plasmon peak is thought to be from silicon oxides in origin. The value of the plasmon excitation energy is ~17.1 eV which is lower than that measured by Sato²⁷ and Mannella²⁸ (17.4 eV). Surface plasmons which are expected at ~12 eV above the main peak for a clean Si surface are less evident.³⁰ It is believed that because the surface is chemically passivated by oxides, the surface plasmon signal was quenched.

After plasma etching, the secondary structures are broadened and slightly shifted to higher binding energy. The signal intensities are also lower after the plasma etching.

These changes could be related to the reduction of surface contamination and metallic properties of the surface after prolonged plasma etching. The presence of strong bulk plasmon loss line indicates that the SALDI surface is largely metallic in nature.

The plasmon satellite feature observed on the DIOS substrate is very much different from what have been observed on the SALDI substrate. Figure 3-33 (B) shows the XPS survey spectra of the Si 2s and 2p of an as-received DIOS and a plasma treated DIOS surface. The plasmon peak is located at 170.9 eV, whereas for the SALDI surface, the peak is located at 167.0 eV. No significant shift to the plasmon loss lines due to plasma treatment.

Additionally, due to the removal the fluorocarbons from the surface after the plasma treatment, higher Si 2s and 2p intensity is observed on the plasma-etched surface. This relates to the reduced attenuation by the fluorocarbons. The Si 2s core line is located at 154.9 eV for DIOS surface and plasma etched DIOS surface. The Si 2s peak has shifted by ~5 eV due to the fact that DIOS surface is oxides/hydroxides surface. The overall low plasmon peaks intensity suggests the DIOS surface is largely non-metallic as opposite to the SALDI surface.

The absence of surface plasmon satellite features in the SALDI and the DIOS substrates suggests that surface plasmon resonance is less likely an important factor in the use of these substrates for LDI application. Furthermore, UV photons have a high penetration depth and the photon energy is unlikely deposited in the near surface region, though an additional analyte layer has to be considered when these substrates are used for LDI applications. Despite bulk plasmon being observed, its influence to the analyte deposited on the surface is relatively remote and the laser photon energy does not match (and in fact quite far away from) the bulk plasmon energy measured. Accordingly, one must question the relevance of plasmon resonance phenomenon as an essential factor in SALDI and DIOS in contrast to gold nanorod substrates. While plasmon lost line features in XPS highlight one of the significant differences between SALDI and DIOS substrates, but for the mechanistic consideration, plasmon or any field desorption phenomenon, is unlikely involved in the ion formation process. (See section 4.3.5)

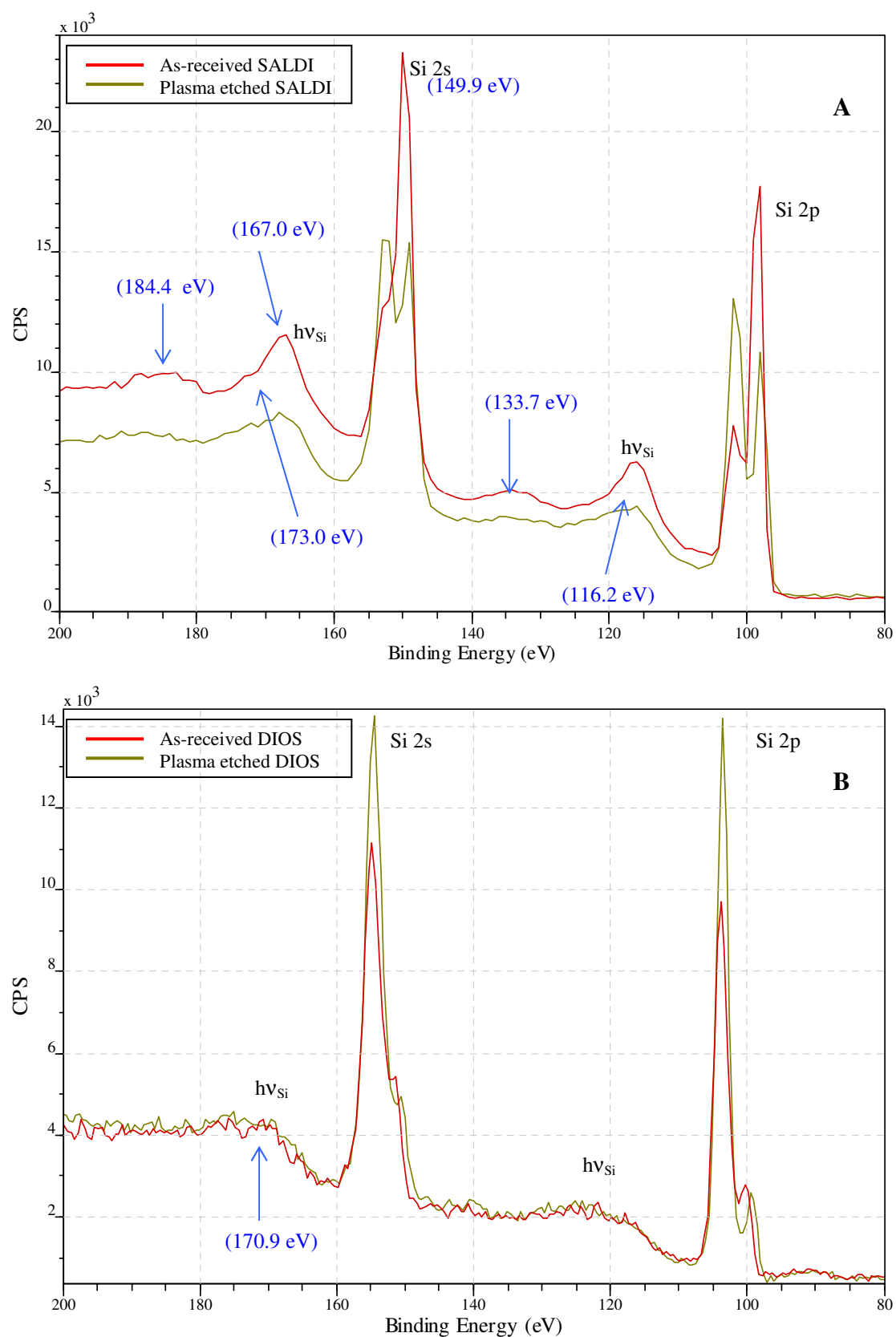


Figure 3-33 XPS Si 2s and 2p survey spectra and the plasmon satellite peaks of (A) SALDI surface s3 and (B) DIOS.

3.3.9 Water Contact Angle Measurements

DIOS substrate has been recognised as hydrophobic based on the observation that aqueous droplets bead up on the surface.⁴ The WCA measurements give information regarding to the wettability of the surface. The surface wettability greatly influences the sample droplet aggregation and distribution, and so to the LDI signals intensity and reproducibility. Understanding the implications of surface wettability also allows us to apply appropriate solvent system for the mass spectrometric analysis. On the other hand, the proposed reduction in the characteristic size of microscopic surface irregularities on the SALDI substrates may has an effect on the interfacial interactions.³¹ Contact angle can also be considered in terms of the thermodynamics of the materials involved and provides information related to the interfacial free energies, which is in turned influenced by the surface morphology and chemistry. The DIOS and SALDI substrates were therefore further characterised using WCA measurement. The results are summarised in Table 3-3. Deionised water was used as the test liquid.

Table 3-3 WCA measurements of DIOS and SALDI surface A48-1. The data presented are the average of at least three measurements. The SALDI substrate was stored in propan-2-ol for two months.

| Silicon sample | DIOS / degree | SALDI / degree |
|---|---------------|----------------|
| As-received | 132.2 ± 0.7 | 25.1 ± 0.8 |
| Plasma etched for 60s | 29.3 ± 2.6 | 14.6 ± 1.4 |
| Plasma etched for 60s then fluoro-silanised | 134.5 ± 1.0 | 92.3 ± 2.0 |

The WCA measurement shows that the as-received DIOS surface has approximately the same WCA with the fluoro-silanised DIOS surfaces, ~132°. This stands in contrast to the as-received SALDI substrate, which only has a WCA ~25°, and fluoro-silanised SALDI surfaces, which has a WCA ~92°. Argon plasma etched surfaces (in both DIOS and SALDI) are highly hydrophilic and water spread out. In another experiment (results not shown) the measured WCA of argon plasma etched surface and plasma etched then fluoro-silanised surfaces did not change significantly by extending the plasma etching time up to 30 mins.

3.4 Summary and Discussion of Surface Characterisation

3.4.1 Surface Chemistry of the DIOS Targets

The DIOS targets have been investigated by SEM, AFM, SIMS and XPS. The SEM and AFM images show that the surface is porous and has a thick porous layer. Pore size measured by SEM varies from ~20 nm to 200 nm. AFM images show the topography of the surface morphology. The surface roughness of the substrate is 28.9 nm (R.M.S.) measured by AFM. The result of the surface morphology study is consistent with the literature data.

However, the XPS results also show that the DIOS surface is passivated by fluorocarbon and this explains a high WCA obtained. Additionally, the porous morphology affects the WCA. A few percent of fluorine is expected for freshly etched porous silicon surface (Figure 3-12) and supposedly in the form of SiF_x ($x = 1-3$). The quantification results show the atomic concentration of fluorine is 18.4%. Core-level C 1s scan suggests 14.9% of the fluorine is in the form of CF_x , indicating only 3.5% of fluorine is in the form of SiF_x , accounting the low intensity of SiF_x peaks in SIMS spectra. These results suggest, the commercial DIOS target might have already been fluoro-silane modified and the silane coverage is ~15%, identical to that stated in a patent application.³²

These results contradict the proposal of Shen and Credo that DIOS is a hydride surface.^{4, 33} Shen did employ XPS in the investigation of DIOS surfaces and only commented that oxidation more readily occurs on the singly etched surface than doubly etched surface. This may suggest the chemistry of the DIOS substrate investigated is not identical to the DIOS substrate developed by Shen. In the case of Shen, oxidised surface was re-etched in 5% HF solution and this procedure is efficient in partially removing the SiO_x species, and restoring the hydrophobicity of an oxidised DIOS surface. The results suggest otherwise. It appears there was a shift in product design or improvement at around 2005 and this is consistent with the time of

the product release and the ongoing development work carrying at the Scripps Research Institute.^{32, 34-36}

The use of fluoro-silanisation accounts for the success of the DIOS surface design. For a high-throughput array format for mass spectrometry analysis, a hydrophobic surface is necessary to prevent the sample droplet spreading or cross-contamination between sample-wells. On the other hand, a hydride surface, though hydrophobic, is unstable for long-term storage. This modification changes a predominantly hydride (or silanol) surface to a fluoro-silane surface and stabilises the surface from further oxidation. (See section 1.4.2 and 2.2) In the absence of the main proton source (Si-OH moiety) on a hydride surface, high LDI performance would not be achievable. The ability to retain both hydrophobicity and the main proton source accounts for the success of the commercial DIOS surface design. Fluorine on the other hand might have another role, such as withdrawing the electron density from the oxygen and stabilises the surface hydroxyl groups, increasing the acidity of the surface.

3.4.2 Surface Chemistry of the QuickMass Targets

The surface morphology and chemistry of the QuickMass target has been investigated by SEM, AFM and SIMS. SEM and AFM results show the QuickMass surface has a very low surface porosity and has columnar-void morphology. The SIMS results suggest the QuickMass surface is germanium based as various Ge-related clusters were detected.

According to the patent applications and the Ph.D. thesis of the developers,³⁷⁻⁴⁰ the QuickMass thin-film is prepared by physical vapour deposition (PVD) and this surface morphology is designed to suppress ambient species adsorption and background interferences. Deposition/evaporation is carried out in by in a Kurt Lesker e-beam evaporator. The precursor material is 99.999% Ge cubes, evaporated from a vitreous carbon crucible. Corning 1737 glass or polished stainless steel substrate materials can be used (in this case, it was steel substrate) and the target thickness is 100 nm. It also appears that this germanium based substrate replaces columnar/void network silicon film material prepared by plasma-enhanced chemical vapour

deposition (PECVD) previously developed by the same group^{18, 41} as the LDI mass spectra below m/z 600 suffers interferences obtained on the silicon thin-film due to due to rapid hydrocarbon adsorption.⁴⁰

Earlier in the AFM surface analysis (Figure 3-13 (d)), a drying pattern was observed. This is thought to be dissolved germanium oxides. The use of germanium is believed to afford a self-cleaning mechanism. For silicon, the thickness of oxides increases during the storage and that has been shown to be detrimental to the LDI performance.⁴ Germanium oxides, on the other hand, are unstable and are dissolvable by water. Once the sample solution is deposited onto the target, a fresh surface is exposed for the analysis and thus unlike the DIOS target, the QuickMass target does not require inert gas sealed packaging and can be stored in air (covered) for a long time.

Furthermore, the patents also suggest that although silicon can absorb UV-radiation effective, it may not work effectively for IR laser sources. The use of germanium will work for the near IR wavelength because of the differences in their optical band-gap structure. This was the first published suggestion relating the optical band gap of the semiconductor substrate to the LDI processes.

On the other hand, post-deposition surface modifications are possible.³⁹ The methods include growth of a thin silicon dioxide layer, light-mediated surface functionalisations with 1-hexyne, 5-hexyn-1-ol, 1-decyne, and 9-decen-1-ol, and most importantly, amino-silanisation.¹⁸ The observation of nitrogen-containing clusters in SIMS spectra may be the products of amino-silanisation. Further examination requires fresh samples and XPS.

In fact, several self assembling silane molecules presenting different terminal functional groups have been used.^{18, 40} These modifications alter the surface hydrophobicity/ hydrophilicity and acidity/ basicity and influence the LDI process by modifying the surface interaction.³⁹ It was suggested, the reduction of van der Waals and hydrogen bonding via surface chemistry may enhance LDI.³⁹

It should be noted that product development is a continual process, and the sample we obtained was coated on a steel plate and may not be identical to the commercial

product from Shimadzu, in which the thin-film is coated on a glass slide. For instance, laser drilling is employed to generate sample spots on glass substrate,⁴⁰ the effect of this pre-treatment on the final surface structure has not been studied. Further manufacturing optimisation is expected since the development of this prototype.

3.4.3 Surface Chemistry of the Chemically Etched Silicon SALDI Surfaces

The SALDI surfaces have also been investigated by SEM, AFM, SIMS and XPS, and modified by argon plasma etching and fluoro-silane. The investigation of SALDI substrates have been challenging and involving a wide range of morphology, types of substrates, surface chemistry and contamination.

In general, the silicon SALDI substrate is a similar product to the DIOS target. Comparatively, the SALDI substrates are not as advanced as the commercial products.

PCA was applied to aid the interpretation of SIMS spectral data and classified different SALDI surfaces in terms of their surface chemistry prepared by different methods and post-etching treatment. The chemistry is dominated by silicon oxides and carbonaceous contamination. It should also be noted though the intensity of I⁻ was high in SIMS spectra, the surface concentration of iodine was close to the detection limit of XPS. Additionally, no Si-I or related ions were detected by SIMS. Passivation by fluorine or iodine as suggested is less evidenced.³¹

It appears that the addition of the mild oxidation agent (the iodine-etching additive), has generated an ultra-thin oxide layer on the surface and the surface is therefore hydrophilic and has low WCA. Rapid surface aging could be an additional effect but could not be determined given the experimental condition. Compare to the DIOS substrate, the SALDI substrates have a higher bulk plasmon activity observed using XPS, indicating that the SALDI substrate, though passivated by a thin layer of oxides, is still largely metallic.

3.4.4 Surface Cleaning: Argon Plasma Etching of the Silicon SALDI Surfaces

There are two main complications in the use of the PSi substrates for small molecular analysis by LDI-MS:

1. Relatively short shelf-life due to surface aging.
2. Accumulation of contamination due to the increased surface area.

These complications are common to all surface techniques because surfaces and interfaces are highly reactive and high surface potential leads to adsorption of ambient species. Previously, Kruse, *et al.*, Zhang, *et al.*, Anderson and Li have all reported the surface contamination entirely diminished the application of DIOS to small molecules analysis.^{11, 15, 16, 42} Apart from storing the surface in pure alcoholic solvent, or use only the freshly prepared surface, there has not been an alternative solution. Re-etched the surface is possible but will alter the surface morphology. Unfortunately, we suffered the same problem in the use of the SALDI substrates.

A suitable method was devised to clean up the SALDI substrates before use. Solvent washing combined with argon plasma etching was adopted. A method inspired by Finkel, *et al.*,¹³ who demonstrated SALDI active substrate could be generated by reactive ion etching (RIE) using a mixture of SF₆ and O₂ as etching gas and then the SiO₂ layer was removed by HF. The difference was that argon gas was used here and the sample was not immersed into HF after plasma etching. This method was a remedy that appeared to be promising to refresh the aged contaminated SALDI surface. Additional advantages of argon plasma etching include preserving the surface structure^{43, 44} and avoiding hazardous chemicals such as Piranha solution, which may result in extensive oxidation of the surface and/or morphological change.

Overall, the SIMS and XPS results show argon plasma etching leads to a clear silanol surface. The thickness of oxide layer is increased after the treatment. This, in addition to the effects of surface roughness of the SALDI substrates, led to a low WCA observed on the plasma-etched surface.

Kostishko, *et al.* have investigated the effect of argon plasma treatment of PSi surface using Auger electron spectroscopy (AES),⁴⁵ and our observations concurred with theirs. They suggested that low level of oxygen remains in the etching chamber. When the surface is sputtered with argon ions, highly reactive Si dangling bonds are formed. Radicals of oxygen and desorbed species will therefore react with the silicon. Because of plasma etching, the chemical environment was altered and the surface concentration of oxides was increased.

Increasing the thickness of oxides generally degrades the LDI performance,⁴⁶ but how this may affect the LDI performance could be investigated. If it was the case, possible future work is to explore different etching gases, such as hydrogen or argon-hydrogen gas, given that hydrogen-plasma etching has been reported to reduce oxidised porous silicon to silanols surface and enhance photoluminescence.⁴⁷

3.4.5 Chemical Modification: Fluoro-silane SAM Modification

PSi obtained by electrochemical etching slowly oxidises over time. An insulating oxide layer leads to degraded LDI performance. The situation is also true for photo-electronic applications of PSi. One of the strategies is chemical derivatisation. This method stabilises the silicon surface and introduces functional groups that may enhance LDI sensitivity or selectivity. The earliest attempt to stabilise DIOS substrate used Lewis acid mediated hydrosilylation of freshly prepared hydrogen-terminated substrate. Phenethyl-modified and ethyl undecenoate-modified DIOS substrate was shown to be promising.^{2, 17, 48} These reactions require freshly-etched H-terminated silicon substrate and are carried out in an inert atmosphere.

Equally, silanisation of the oxidised surface is another attractive approach and has been explored in the QuickMass^{18, 40} and the DIOS⁴⁹ substrates. The simplicity of the reaction and the wide range of reagents available make this method easily accessible and very tempting to exploit in surface modification. Silanisation normally involves a mild chemical oxidation pre-treatment of Si-H surface to form the Si-OH intermediate. Ozone oxidation of freshly prepared porous silicon pre-treatment was previously demonstrated.⁴⁹⁻⁵¹

Following this research direction, fluoro-silane self-assembly monolayer modification to the SALDI substrates was applied. As discussed above, argon plasma etching treatment leads to a cleaner and silanol silicon SALDI surface. It is important to note that clean surface is required for producing a uniform surface and Si-OH intermediate is essential for the reaction. Able to clean the surface at the same time gives an advantage because of the surface contamination complication of the SALDI substrates.

After modification, the surface was hydrophobic ($\text{WCA} > 90^\circ$) and water droplet beaded up on the surface. Qualitative testes also showed that sample droplets, constituted of polar organic solvent systems, such as 50% ACN, 100% ACN, or 100% methanol, did not spread out, and was retained on the surface. In contrast, droplet of the aforementioned organic solvents would spread out on the as-received surface. This has an implication that because some biological extracts, such as phospholipids, do not dissolve well in water and some is more stable in organic solvent for long-term storage. Sample droplet constituted of organic solvent systems can therefore applied directly on modified surface. Conversely, argon plasma etched surfaces have a very small WCA, a water droplet would spread out on the treated surface owing to the surface roughness and oxides termination. Since the SALDI surfaces were not in an array format and were cut into small pieces for use, the spreading did not cause practical problem and might actually help the sample distributed evenly on the surface.

3.4.6 Interfacial Interactions: What Else Has WCA Told Us

A smooth fluoro-silanised Si/SiO₂ modified surface is reported to have a WCA $\sim 109^\circ$,⁵² because of the hydrophobic nature of fluoro-silanised surfaces, and yet $\sim 132^\circ$ was obtained in DIOS substrate, *i.e.* $\sim 23^\circ$ higher. Conversely, fluoro-silane modified SALDI surface had a WCA $\sim 93^\circ$, *i.e.* $\sim 16^\circ$ lower. A question is why the DIOS surface exhibits a positive derivation whereas the SALDI surface exhibits a negative derivation of WCA. Possible reasons have to be related to the surface roughness and surface energy since the surface chemistry of the surfaces after modification should be similar.

Classical works of Wenzel⁵³ and Cassie and Baxter⁵⁴ established the relationship between the roughness and surface energy to the water wettability of rough or porous surface. Their theories have become the theoretical foundation for the development of water resisting and wetting material today. The theories of WCA have been given at section 2.3.6. The Wenzel's and Cassie/Baxter models are depicted in Figure 3-34.

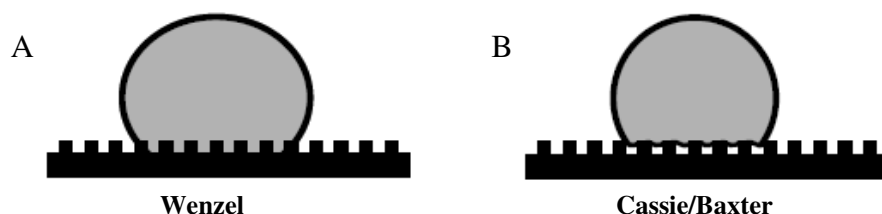


Figure 3-34 (A) Wenzel's and (B) Cassie/Baxter's model of a liquid droplet on a rough surface.

The model proposed by Wenzel describes the water contact angle, θ_c at rough surfaces:

$$\cos \theta_c = r \cos \theta \quad (\text{Wenzel's law}) \quad (0.1)$$

where r is a roughness factor defined as the ratio of the actual area of a rough surface to the geometric projected area and θ is the thermodynamic contact angle on a smooth surface. Since r is always larger than 1, the surface roughness enhances both the hydrophilicity of hydrophilic surfaces, as well as the hydrophobicity of hydrophobic surfaces.

Cassie and Baxter's model differs from Wenzel's in that a porous hydrophobic surface traps air in the hollows of the pores. Cassie and Baxter proposed an equation describing the water contact angle, θ_c at a surface composed of solid and air:

$$\cos \theta_c = f_1 (\cos \theta_1 + 1) - 1 \quad (\text{Cassie's law}) \quad (0.2)$$

where θ_c and θ_1 are the water contact angle of porous surface and smooth surface, respectively, and f_1 and $(1-f_1)$ are the fractions of solid surfaces and air in contact with water, respectively.

Firstly, as shown by XPS that a significant proportion of the surface was still terminated with oxide moieties and the surface was not fully fluoro-silanised.

Secondly, the surface morphology of the SALDI substrate is explained by the Wenzel's model, and thus during the contact with a droplet of water, the surface exhibits a contact angle lower than 109° . However, the porous structure of the DIOS substrate permits air trapping, shifting from Wenzel's to Cassie/Baxter's system, and thus exhibits a contact angle larger than 109° .

By using the Wenzel's law (equation 0.1), and take $\theta_c = 93^\circ$, $\theta_l = 109^\circ$, for the SALDI system, the calculated value of $r = 0.16$. This indicates that the increased surface area (in contact with water) was $\sim 16\%$.

By using the Cassie's law (equation 0.2), and take $\theta_c = 131^\circ$, $\theta_l = 109^\circ$, for the DIOS system, the calculated value of $f_l = 0.51$. This indicates that only $\sim 50\%$ of the projected area was in contact with water.

The thermodynamic implication is that the enhanced surface area (in this case 16%) introduced by the surface roughness in the SALDI system, whether as-received or modified, makes the surface acquire an excess free surface energy and therefore the surface has strong interactions or adhesion to the adsorbate. The proposed reduction to the characteristic size of the surface irregularity for the SALDI surfaces,^{6, 31} actually shifts the system further away from Cassie/Baxter's system to an ideal Wenzel's system. The non-porous roughened morphology therefore increases gaseous adsorption and diffusion efficiency, which leads to increase in ion current in the gas-phase SALDI-MS approach and may not have a direct relationship to the enhancement in electrostatic field as proposed previously. Accordingly, the enhanced adsorption and diffusion apparently is required for the gas-phase SALDI-MS, in which the rate of gaseous adsorption of analyte is a significant determining factor.

In contrast, the porous morphology in the DIOS system actually reduces the free surface energy, and the cohesive force of the water droplet is thus greater than the adhesion force between the droplet and the surface. A water or sample droplet is thus confined into a small area and beads up. For the conventional liquid deposition approach, the liquid confinement effect ensures the enrichment of analyte molecules onto a small area and hence enhances the ion yield in DIOS-MS.

3.5 Substrate Characteristics and LDI-MS Performance Relationship

Following the investigation of the surface morphology and characteristics, the impact of those factors on the LDI performance is now investigated and co-related. In particular, how porous surfaces compare to non-porous surfaces, and how the surface roughness affects the ion yield and the effect of chemical modification of the surface on the LDI performance. The LDI performance is determined by a number of parameters, including ion yield, background interferences, signal-to-noise ratio (S/N), overall quality of mass spectra, laser energy required for optimal performance and sensitivity to detect larger molecules.

3.5.1 Commercial DIOS and QuickMass Targets: DIOS vs. QuickMass

Firstly, the general LDI performance of the DIOS targets as oppose to the QuickMass targets is considered. Further investigation of DIOS performance is presented in the next chapters.

Although their sensitivity and range of detectable compounds differ, both the DIOS and the QuickMass targets can generate good quality mass spectra. (Figure 3-35) However, the low surface-to-volume ratio of the QuickMass targets also leads to lower performance compared to the porous and high specific surface area DIOS targets, and usually the QuickMass targets require a higher concentrated sample for successful application (normally for neutral compounds, ~0.1 mg/ml or ~1 mM).⁵⁵ This possibly explains why there has not been any major publication since the product release. An exceptional high sensitivity occurs on the QuickMass target when the analyte molecules are a pre-charged ion, such as quaternary amines. This is because these molecules have already carry a positive charge and can be desorbed directly from the surface (*i.e.* require no ionisation step).

As previously described, the surface morphology of the DIOS surface is porous, whereas the QuickMass target is largely rough. This implies that the presence of pores is not strictly required for ion generation, but rather affects the ion yield. Moreover, the ion signal diminished relatively rapidly on the QuickMass targets and a constant movement of the laser spot was required because the materials deposited on the surface were quickly consumed or vaporised. However, for DIOS, the ion signal lasts for many shots without relocation of the laser spot. It is proposed that an additional function of the pores is to provide a confined space to retain the analytes and to lower the neutral yield (desorption of analyte molecules by direct vaporisation). This observation may relate to a desorption selectivity due to the porous morphology of the DIOS system. It is because ions are effectively extracted by the extraction field of the mass spectrometer, whereas the neutral molecules are retained on the surface because of a higher desorption potential on the porous surface relative to the non-porous surface and therefore neutral molecules are not desorbed into gas-phase effectively. The proportion of ion yield relative to neutral yield is thus higher on the porous substrates and explains the longevity of the signal and the total ion intensity.

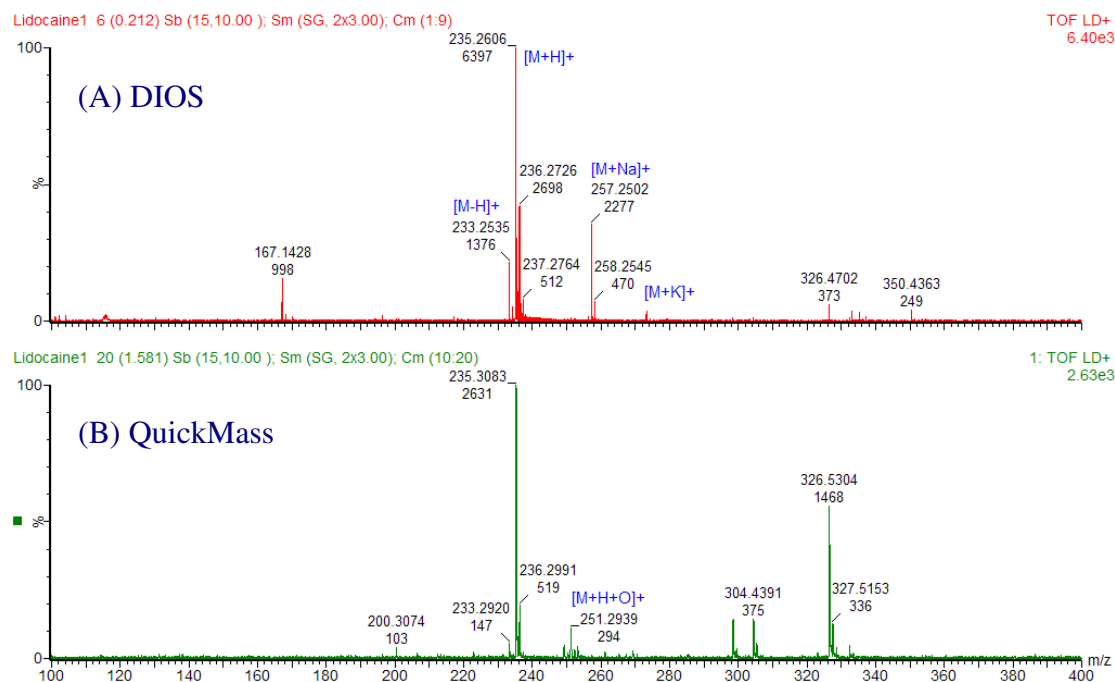


Figure 3-35 Positive ion mass spectra of lidocaine obtained using (A) DIOS and (B) QuickMass target. The spectra are sum of ~1 min scanning, data was acquired manually. Same laser energy setting was used. The protonated ion of lidocaine is located at m/z 235. Peaks located at m/z 257 and 273 are sodium and potassium adducts, respectively. Peak located at m/z 251 may be an oxidised product of lidocaine. Other peaks observed are believed be contamination.

3.5.2 SALDI and DIOS Substrates: SALDI vs. DIOS

In optimising the laser energy for maximal ionisation efficiency, an investigation on how this might effect to the quality of the DIOS and SALDI spectra was carried out. This approach is also suitable approach in comparing the LDI performance of the DIOS and the SALDI substrates because of the non-linear laser-to-ion yield response. The laser energy is controlled by the diameter of an optical iris in the MALDI-ToF mass spectrometer used and effectively this controls the laser spot size as well. A mixture of small molecules (test mix), mimicing a biological matrix, was used in this experiment. The test mix contained a small organic acid, several amines, a peptide and a cobalt organometallic metabolite (vitamin B₁₂).

The variation of the ion counts of the protonated ions with respect to the laser energy setting on DIOS substrate is plotted in Figure 3-36. The result shows that the maximum of ion yield (optimum) is obtained at laser energy settintg about 5% and then the ion yield drops and flucatuates between ~25% and ~40%. The spectra produced by 5% and 40% laser energy settings are consistent. (Figure 3-38 A) The variation of the ion counts of the protonated ions with respect to the laser energy setting obtained using the as-received SALDI substrate T-1 is plotted to Figure 3-37. The study were carried out using the same analyte mixture, ensuring the results are compable to that of the DIOS substrate. Conversely, a maximum of ion yield is obtained at laser energy about 15% and then the ion yield drops and then rises again. Possibily, there is another maximum before the laser threshold of surface destruction. The mass spectra generated at 40% laser energy setting was consistent with those generated at 10 or 15% laser energy. (Figure 3-38 B)

On comparing the Figure 3-36 and Figure 3-37, laser energy required for DIOS for optimal ion yield is lower than that of SALDI, at 5% opposed to 15%, and DIOS produced a relative higher ion yield than SALDI at their these laser setting. At the laser energy of 40%, the LDI performance of these two substrates is similar, with the exception that the peptides are less well detected by using the SALDI substrate. (Figure 3-38) These suggest that the SALDI substrate requires a high laser energy to

achieve LDI efficiently. These differences must be co-related to the surface morphology and the differences in surface chemistry as discussed previously.

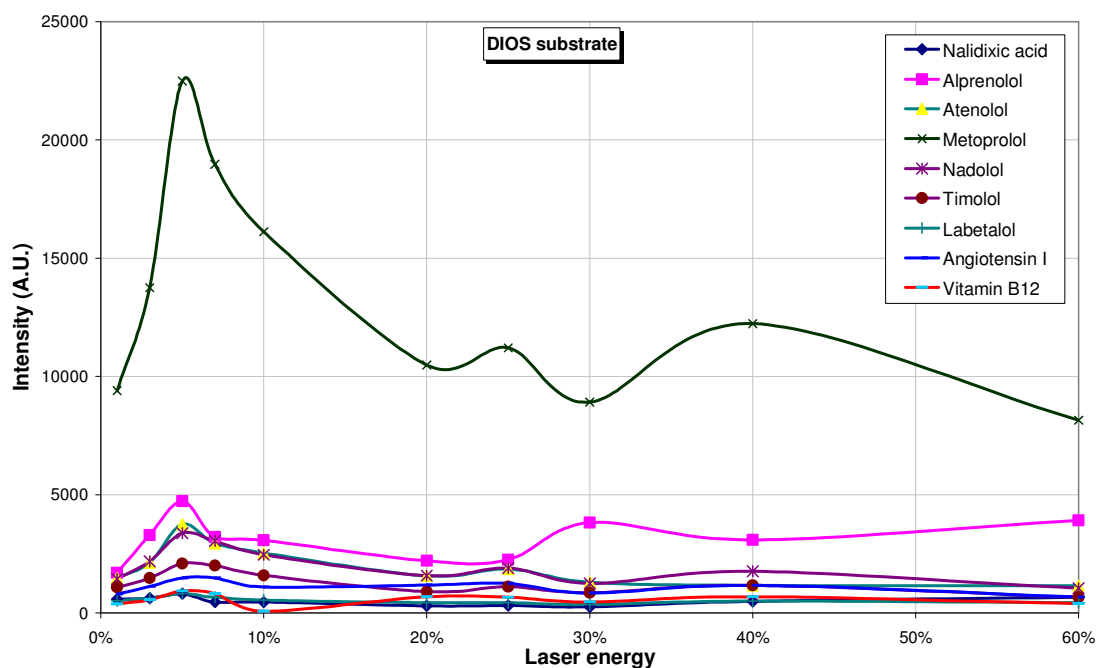


Figure 3-36 The signal of protonated ions obtained on DIOS substrate as a function of laser energy setting of the LDI mass spectrometer.

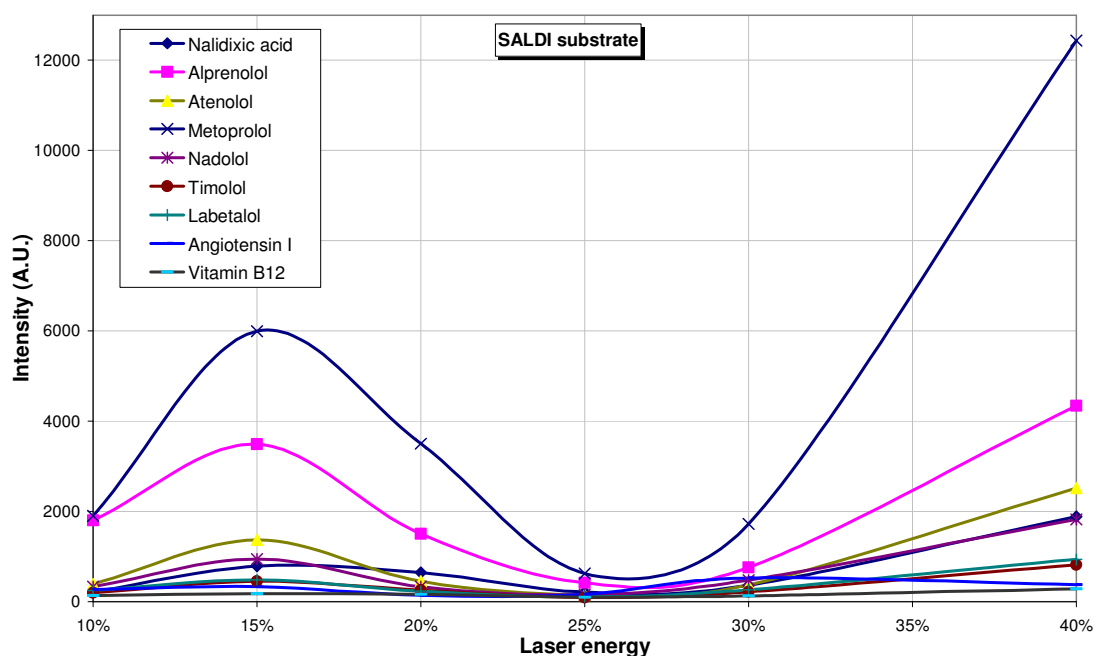


Figure 3-37 The signal of protonated ions obtained on the SALDI surface T-1 (as-received) as a function of laser energy setting of the LDI mass spectrometer.

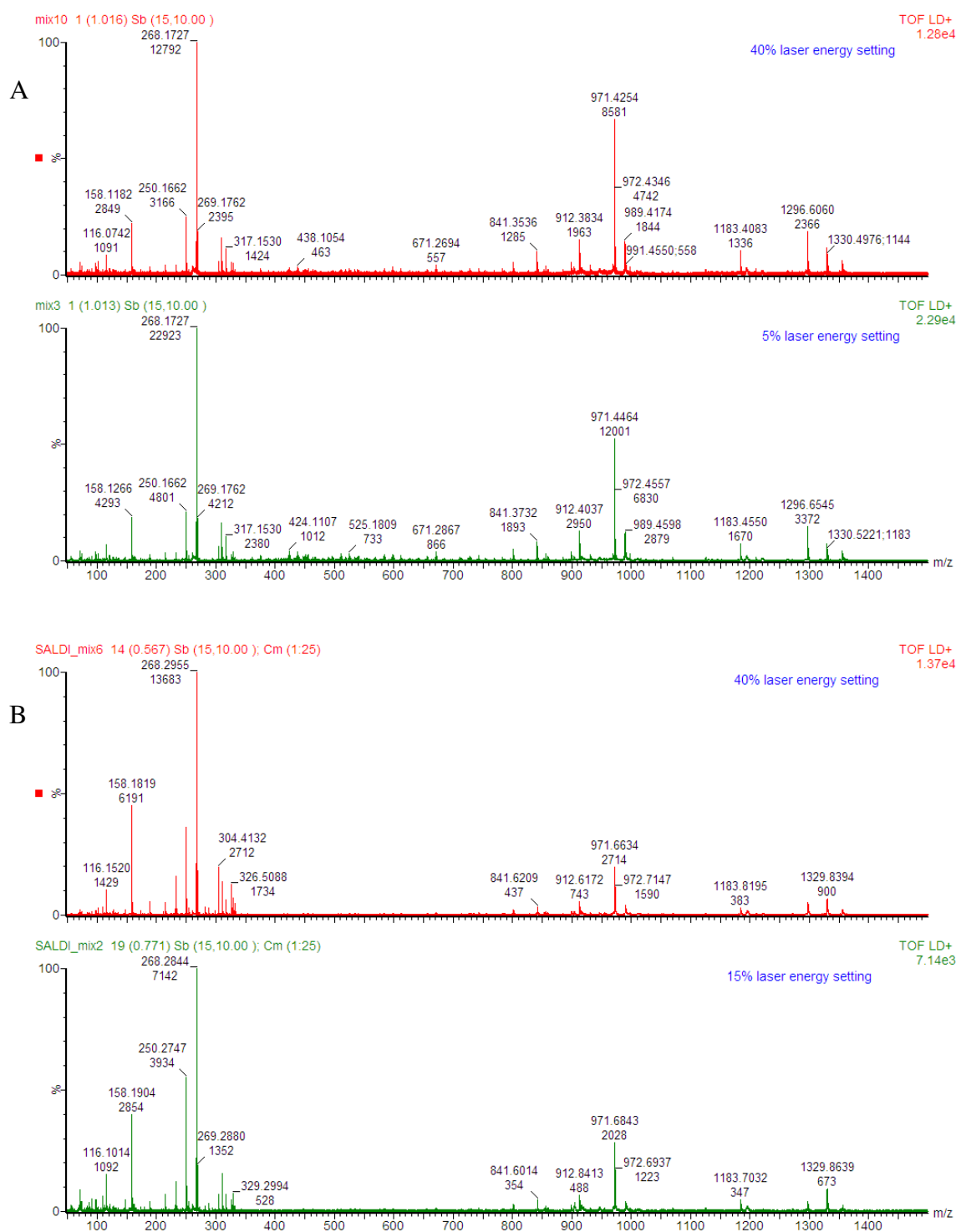


Figure 3-38 (A) Positive ion DIOS mass spectra acquired at 40% and 5% laser energy setting using an analyte mixture containing nalidixic acid ($[M+H]^+$ m/z 233), alprenolol ($[M+H]^+$ m/z 250), atenolol ($[M+H]^+$ m/z 250), metoprolol ($[M+H]^+$ m/z 268), nadolol ($[M+H]^+$ m/z 310), timolol ($[M+H]^+$ m/z 317), labetalol ($[M+H]^+$ m/z 329), angiotensin I ($[M+H]^+$ m/z 1296.5), vitamin B₁₂ ($[M+H]^+$ m/z 1355.5, fragment m/z 1329.5, and 971.5), folic acid and erythromycin (each 0.1 mM, 2 μ l droplet). Folic acid and erythromycin were not detected as protonated ion. (B) Positive ion SALDI mass spectra acquired at 40% and 15% laser energy setting using a mixture of standard compounds as in the case for DIOS.

3.5.3 Inside and Outside of the Etched Spot of SALDI Substrates

A typical SALDI surface received has a chemically etched spot located in the centre of a silicon wafer and appears dark. Outside the etched spot is a grey region, located at the edge of the etched spot. The etched spot is the area normally used in our study. One observation was that the etched area could generate mass spectrum, but on the non-etched area, only scattered ions were obtained. (Figure 3-39)

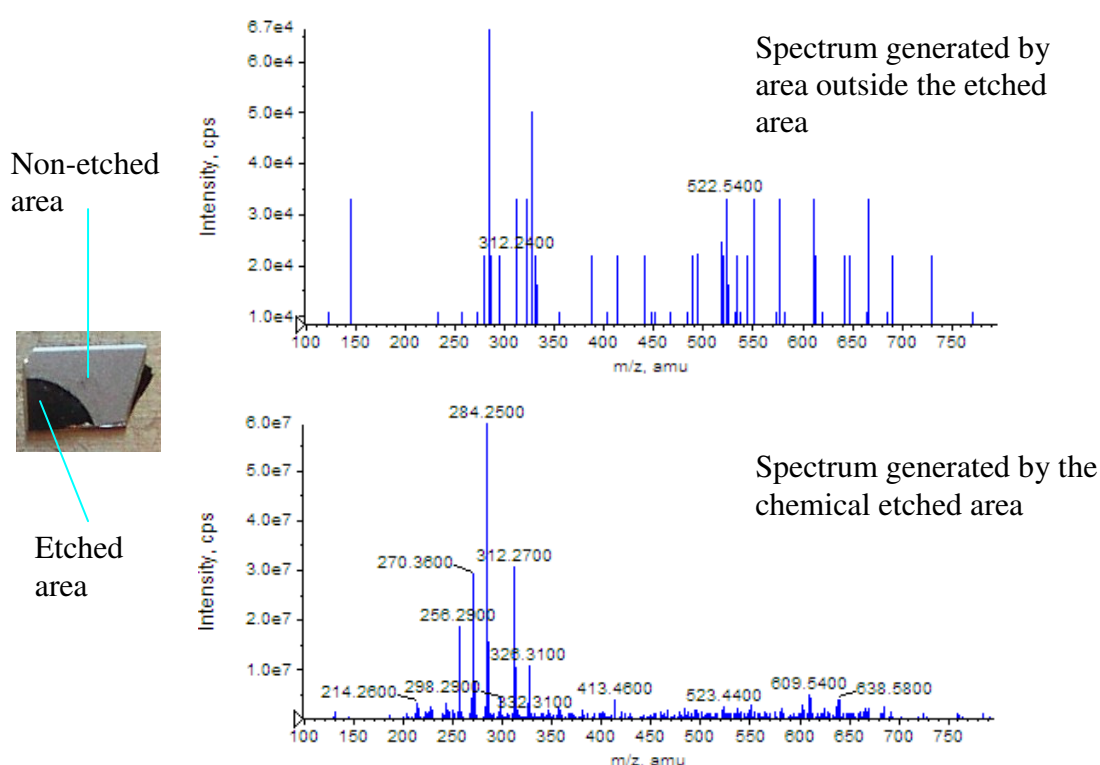


Figure 3-39 Comparison of etched and non-etched area on SALDI surface s3 using AP-MALDI-QqLIT system. The ions detected on the etched area were sodium adducts of lidocaine and hydrocarbon clusters, because the SALDI surfaces were contaminated. The ion-molecular reaction most probably occurred at the ion-source led to the observed ions.

It was still possible to obtain SALDI spectra on the non-etched area. One example is the bacterial signalling molecules, alkyl quinolones. (Figure 3-40) It is known that the quinolones are UV absorbing with the absorption maxima varying from 250 to 350 nm.⁵⁶ This suggests the difference between the two areas is the effectiveness in absorbing UV radiation. The dark area produced by chemical etching acts as an

effective energy receptacle, transferring the photon energy to the analyte and assists ion generation,⁵⁷ whereas on the grey non-etched area, the analyte is needed to be UV absorbing. Hence, an effective energy disposition is probably a major requirement for LDI.

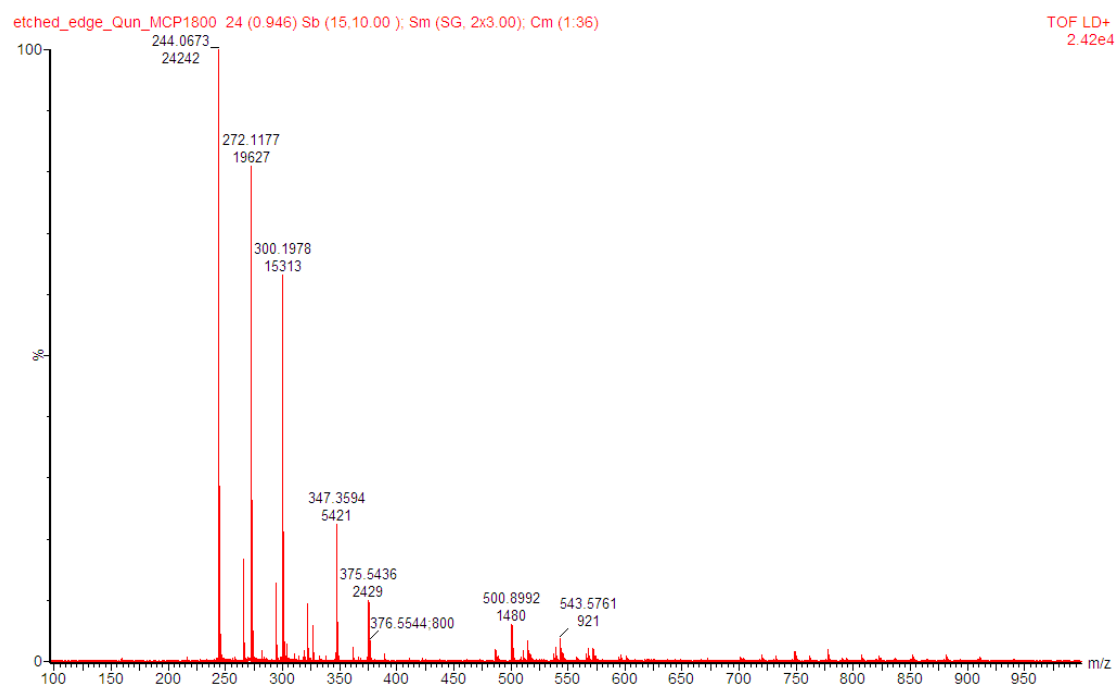


Figure 3-40 Positive ion mass spectrum of alkyl quinolones obtained on grey non-etched area of SALDI surface. (See Chapter 5 for further discussion of quorum-sensing molecules)

3.5.4 Plasma Etched and As-received SALDI Substrates

A plasma etching approach was developed to tackle the surface contamination complications of the SALDI substrates. We have previously seen the changes in surface chemistry of the SALDI substrates induced by plasma etching using SIMS and XPS. Conversely, neither SIMS nor XPS requires plasma etching as a cleaning tool for surface analysis, possibly because sonication and ion sputtering are the methods more suitable for SIMS and XPS and avoid the oxidation induced by the treatment.

In terms of the SALDI spectra, two distinct features were observed using the treated surfaces:

1. The level of background was significantly lower. (Figure 3-41)
2. Mass resolution was improved. (Figure 3-42)

The reason for the higher mass resolution is not clear. It appears the contaminants alter the conductivity of the surface and this causes an inhomogeneous electric field of the acceleration voltage on the different area of the surface, which results in lowering the mass resolution.⁵⁸

However, comparing plasma etched SALDI sample with freshly prepared SALDI surface, much higher laser energy was required for the treated surface to operate, despite the contaminant peaks being removed and the mass resolution being improved. (Figure 3-43)

There are a number of possible reasons. Firstly, after argon plasma etching, the oxide thickness was increased and the surface became more reflective to laser light. Secondly, the sample droplet would also diffuse out covering a larger area on the surface during sample deposition, lowering the surface concentration of the analyte and consequently lowering the ion intensity. As discussed previously, the contact angle represents the work (energy) required to create the liquid/solid interface. The excess surface energy of the liquid/solid interface is a thermodynamic consequence due to a combing effect of surface roughness and the chemical nature of the surface. For the conventional liquid deposition approach, the sample droplet should ideally be confined onto a small area and apparently, in our investigation, a hydrophobic surface is preferred over a hydrophilic one.

Furthermore, a thick oxide layer may hinder the electronic process. However, this may also enhance the thermal processes (by reducing the thermal conductivity) as a counter balancing effect. Consequently, the LDI activity has been maintained or not been significantly degraded at the high laser energy setting.

Then again, from these preliminary results, plasma etching of SALDI surface is therefore required to clean the surface in order to produce an acceptable quality of SALDI mass spectrum because of the contamination issues of the SALDI surfaces.

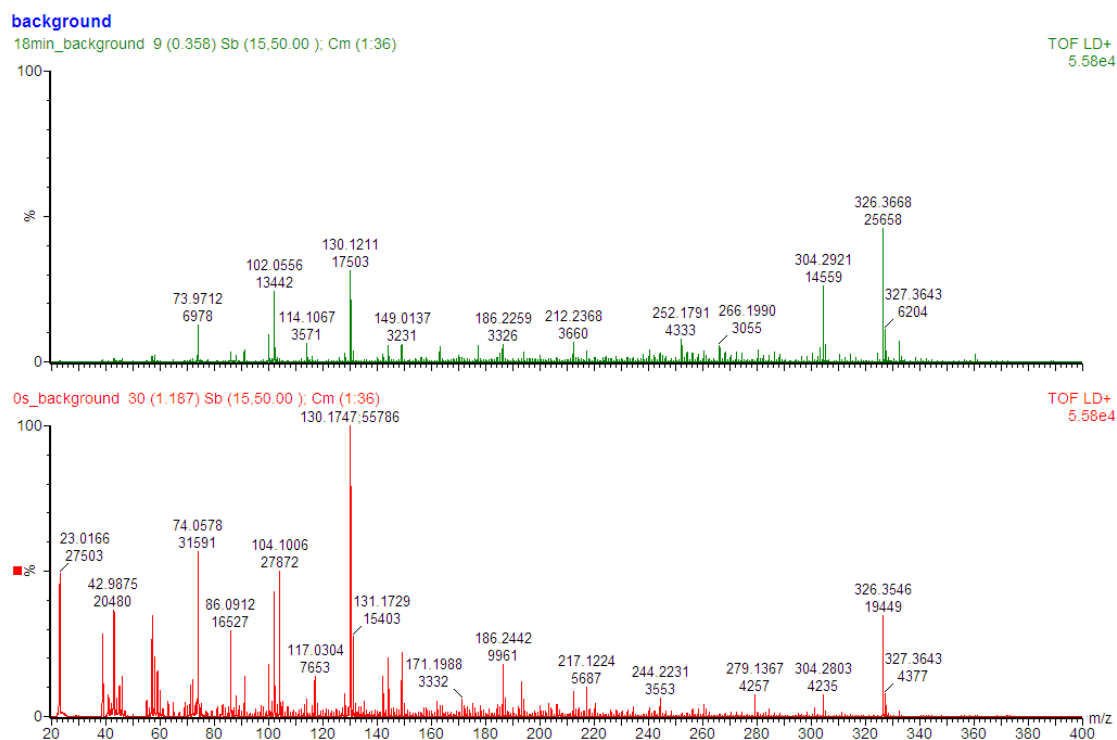


Figure 3-41 Background mass spectra of SALDI surface s3 that has been argon plasma treated for 18 mins (*top*) and an as-received surface (*bottom*).

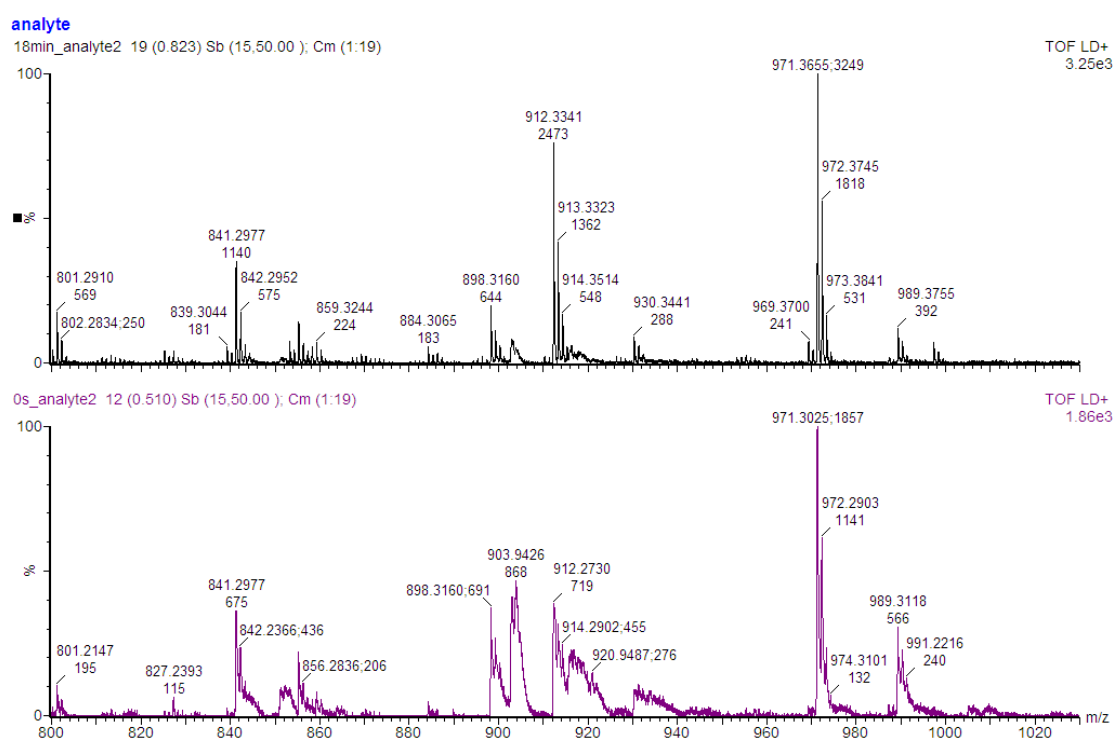


Figure 3-42 Mass spectra of vitamin B₁₂ obtained on SALDI surface with argon plasma treatment for 18 mins (*top*) and as-received (*bottom*). Data was acquired by scanning the surface for ~1 min and 50% laser energy setting was used to obtain spectra of both Figure 3-41 and Figure 3-42.

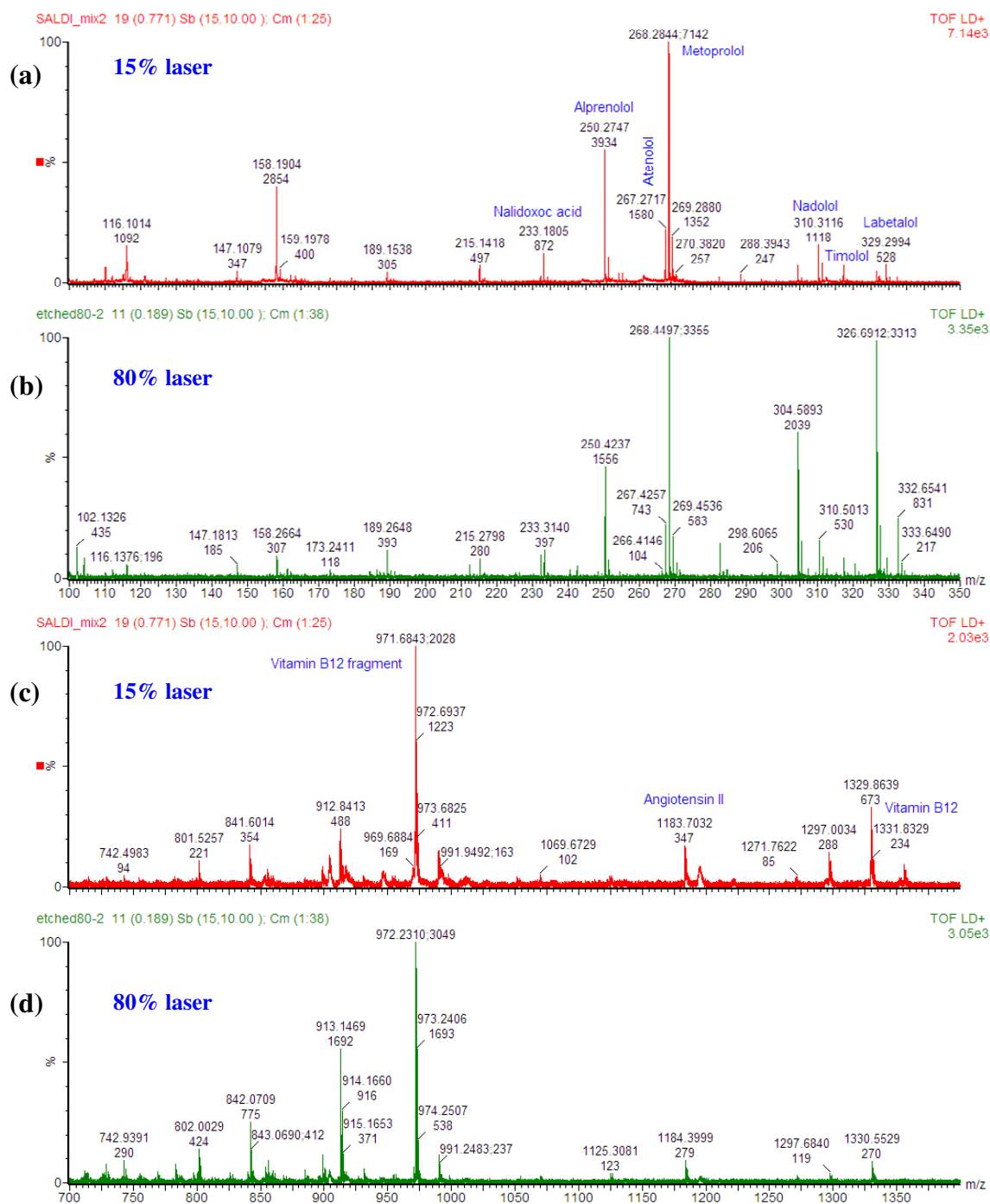


Figure 3-43 Positive ion mass spectra of a mixture containing nalidixic acid ($[M+H]^+$ m/z 233), alprenolol ($[M+H]^+$ m/z 250), atenolol ($[M+H]^+$ m/z 250), metoprolol ($[M+H]^+$ m/z 268), nadolol ($[M+H]^+$ m/z 310), timolol ($[M+H]^+$ m/z 317), labetalol ($[M+H]^+$ m/z 329), angiotensin I ($[M+H]^+$ m/z 1296.5), vitamin B₁₂ ($[M+H]^+$ m/z 1355.5, fragment m/z 972), folinic acid and erythromycin (each 0.1 mM, 2 μ l droplet) obtained using SALDI surface T-1. (a) Lower mass region, no plasma etching, laser setting 15%, (b) lower mass region, plasma etched surface, laser setting 80%, (c) higher mass region, no plasma etching, laser setting 15% and (d) higher mass region, plasma etched surface, laser setting 80%. Peak at m/z 116, 158 were surface contaminants and were removed by plasma etching. The mass resolution, particularly the ion peaks at the higher mass region, is improved.

3.5.5 SALDI Substrates with Different Surface Roughness and Electro-resistivity

It has been proposed that the ion desorption efficiency of SALDI surfaces is strongly dependent on surface roughness.⁶ To investigate how the roughness may effect to the LDI performance at liquid-deposition approach, the LDI performance of SALDI substrates prepared by a number of etching parameters were evaluated. Substrate resistivity is considered at the same time, because the SALDI substrates available are subjected to multiple variables.

Firstly, we shall consider substrates s10 and s11. Both substrates s10 and s11 were prepared using 111 orientated p-type silicon wafers, but s10 (0.005 $\Omega\cdot\text{cm}$) has a higher electro-conductivity than s11 (0.100 $\Omega\cdot\text{cm}$). Surface s10 was prepared by first stain etching and then subsequently re-etched with HF/EtOH. The surface produced is non-porous and has dents of curvatures of which can be observed using optical microscopy. The results ToF-SIMS investigation suggest that this surface has a relatively high concentration of fluorine. s11 was prepared by a method similar to that of the double etched DIOS substrate preparation, with the exception that etching was performed on the non-polished side of a silicon wafer and thus the surface has a very high surface roughness. The etching parameters were not disclosed to us. Both s10 and s11 were briefly sonicated before mass spectrometric analysis. The SEM and AFM images of the surfaces have been presented at Figure 3-15.

Figure 3-44 shows the LDI mass spectra generated by these two surfaces using a mixture of small molecules. The surface s11 generates about 10 times higher ion yield than s10 in this case, and yet s10 produced a much clearer spectrum. Similar observation has been reported by Finkel, *et al.*¹³ (see Figure 3-4) Nevertheless, s11 has a poorer performance toward larger molecules such as vitamin B₁₂ and bradykinin (Figure 3-45). The observed higher ion yield on the SALDI substrate s11 is believed related to increased surface area and/or a 300 nm thick porous layer. The poor performance toward larger molecules is believed related to the surface contamination and/or the substrate conductivity.

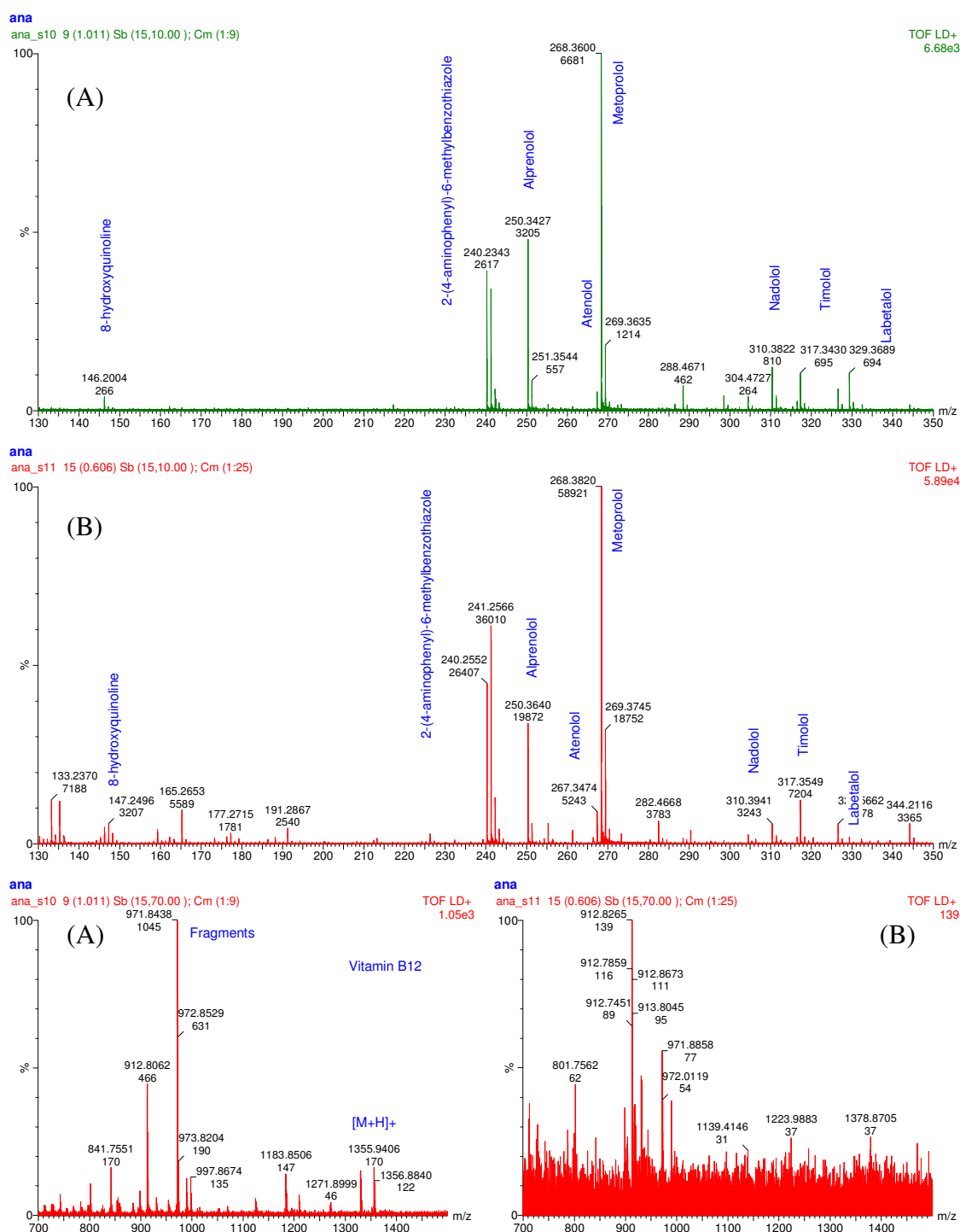


Figure 3-44 Positive ion SALDI mass spectra of 8-hydroxyquinoline, 2-(4-aminophenyl)-6-methylbenzothiazole, alprenolol, atenolol, metoprolol, nadolol, timolol, labetalol, sotalol, glyburide and vitamin B₁₂ mixture dissolved in ACN/H₂O. Spectrum (A) was acquired on SALDI substrate s10 and (B) was acquired on s11. Signals of sotalol and glyburide could not be distinguished from the noise.

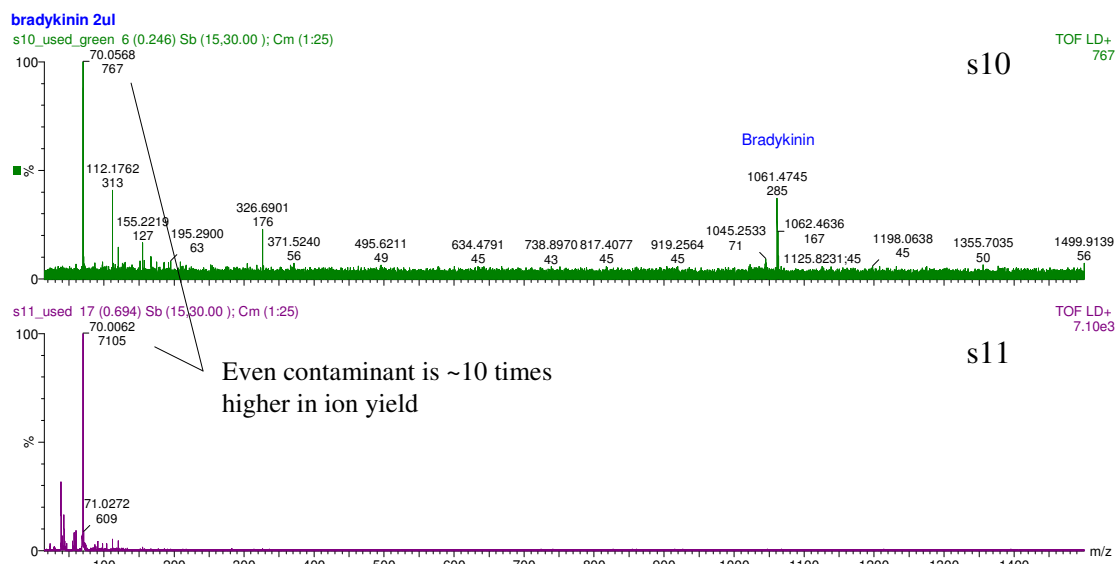


Figure 3-45 Positive ion SALDI mass spectra of bradykinin (1 mM, 2 μ l droplet), dissolved in ACN/H₂O obtained using substrate s10 and s11.

It appears that a roughened or porous surface morphology is able to retain analyte molecules more effectively relative to a smoother surface and enhances the cross-section area relative to the laser spot for the ionisation. A thick porous layer is thought to re-supply the surface with analyte and could generate a pressure gradient relative to the vacuum chamber and assists the ion desorption. We have seen previously that the sensitivity to large molecules is improved after the surface is cleaned by plasma etching. Contamination may also have effects to thermo- and electro-conductivity, as we have seen mass resolution of the LDI spectra is improved after plasma etching. The substrate s11 was porous and was harder to be cleaned by sonication compared to smoother substrate s10 and the spectra were complicated with contamination peaks below m/z 200. It is believed this led to poor sensitivity toward larger molecules. More examples are shown later to verify these observations.

Another set of substrates, s1, s2, s4, s5 and vapour phase-etched surfaces (vefib-2) are now being considered. These substrates differ from the s10 and s11 as they were prepared by single-etching method using HF/EtOH solution or vapour with iodine etching additive and exhibit a different surface chemistry as shown by ToF-SIMS and are therefore considered separately from s10 and s11. Substrate s1, s2, and s5 were prepared using 100 n-type silicon wafer (0.010 Ω -cm), s4 was prepared using 111 p-type silicon wafer (0.100 Ω -cm). Etching current was 1 mA/cm², etching time varied

from 5 to 7 minutes. Etching time for vapour-phase etched surface was 1 hour. This set of surface showed a relative smooth variation of surface roughness. The SEM and AFM images of these surfaces can be found at Figure 3-14 and Figure 3-16.

The ion yield of the protonated ion in the LDI mass spectra is plotted against the surface roughness measured by AFM. (Figure 3-46) 1 mM bradykinin solution (2 μ l droplet, dissolved in ACN/H₂O) was used in this test because the sensitivity was low, as was the QuickMass substrate. Interestingly, substrate s5 stands out from the rest in this set of surfaces. The reason is not clear. The same trend was also observed using small molecules if the surfaces were first subjected to 30 mins of argon plasma etching before analysis. ~1 mM concentration of the analyte was required. The substrate conductivity also has an effect toward the SALDI activity, and as a result, substrate s4 has a particularly poor LDI performance. It is believed, negative charge accumulates on the surface during LDI. Oxides layer or high electro-resistivity substrate will therefore screen off the charge neutralisation between laser pluses and so the ion desorption process. On these preliminary results, the SALDI activity of these substrates does not strongly dependent on the surface roughness but perhaps two optimal morphologies exist.

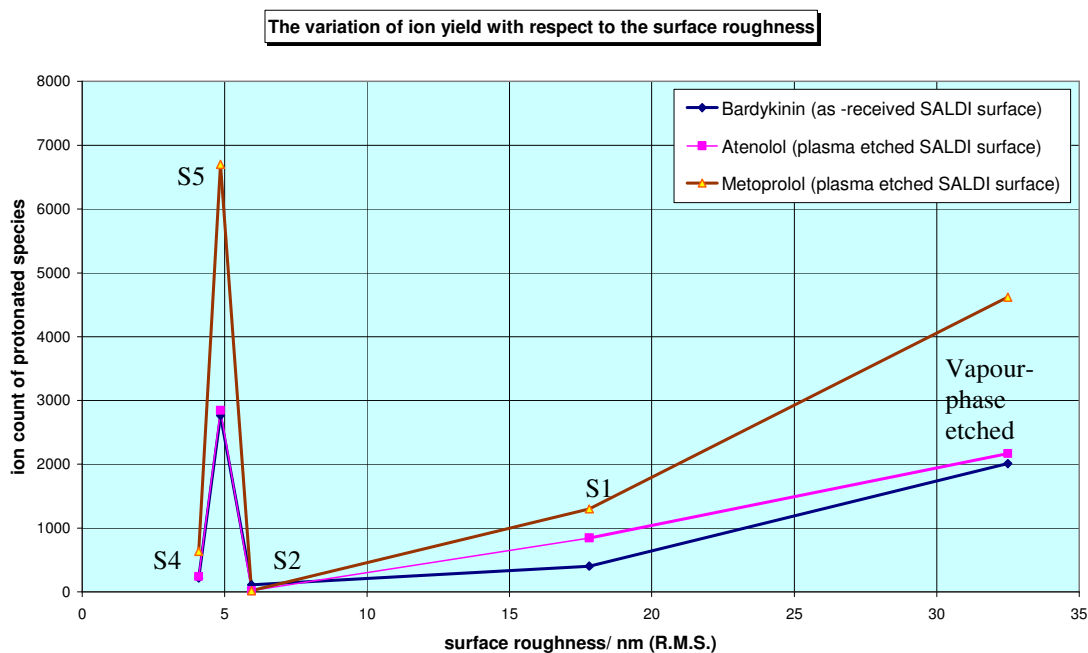


Figure 3-46 Ion yield of bradykinin on as-received SALDI surface and ion yield of atenolol and metoprolol on plasma etched SALDI surfaces. The substrates used are annotated on the plot.

3.5.6 Graphite and Sanded Silicon Substrates

To understand how Alimpiev, *et al.* would have come to the view that SALDI activity is governed by reducing the surface roughness,⁶ we may have to look into their early works in using graphite and other types of substrate. Graphite and sanded silicon, substrates were initially introduced as a control in this study. (Figure 3-19) These surfaces have micron-size structural features and a large surface roughness but are only able to generate low quality mass spectra, or salt adduct ions and the sensitivity of these surfaces is very low for general application. The graphite surface requires relative high laser energy for LDI and no protonated ion was detected because addition of glycerol was not performed (see section 1.3). Comparatively, chemically etched silicon surfaces, which have reduced surface roughness and small surface features, produce a much better result than these highly roughened surfaces. In spite that a roughened structure is helpful and perhaps required for LDI, the writer comes to the view that the overall surface roughness is secondary and is an over generalisation to the SALDI performance.

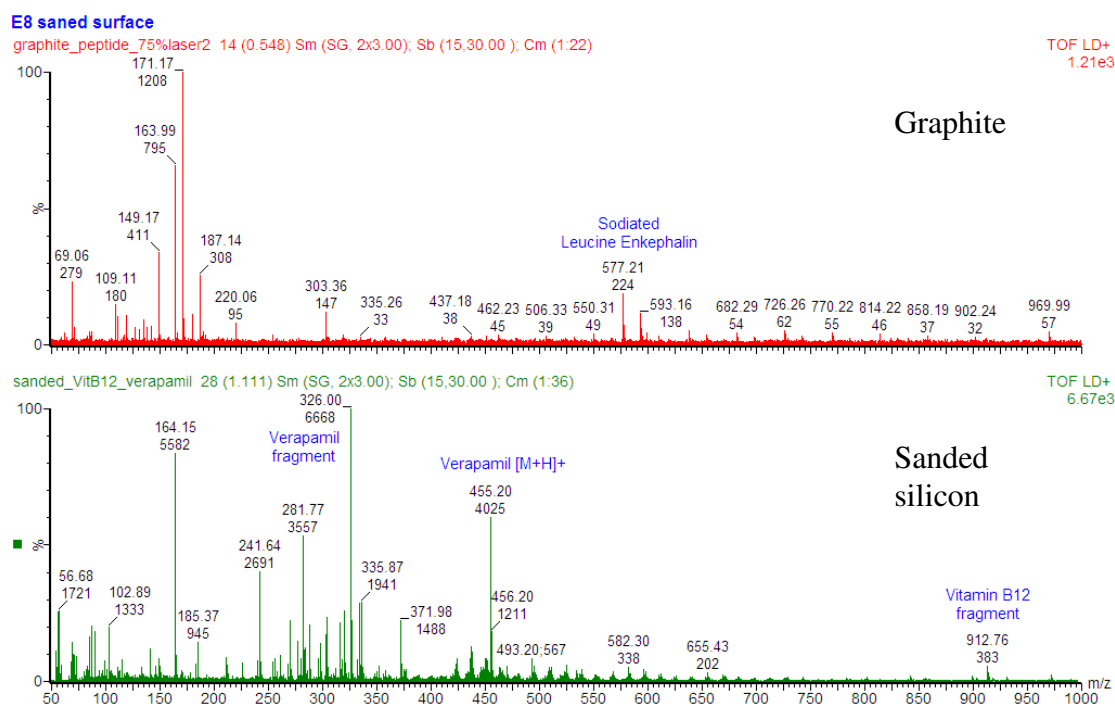


Figure 3-47 Representative positive mass spectra of graphite and sanded silicon surface. The graphite plate was cleaned by using a sharp blade to scrape off the top layers and washed with methanol and water. The sanded surface was sonicated in propan-2-ol before use.

3.5.7 The LDI Performance of SALDI Substrates Before and After Fluoro-Silane SAM Modification

More often than not, the LDI mass spectra generated by the SALDI substrates are complicated with contamination peaks and a cleaning procedure was therefore developed as discussed earlier. In all the SALDI substrates tested, substrate A48-1 seems to give the best performance in all SALDI samples investigated. Figure 3-48A shows the SALDI spectra acquired on the as-received substrate A48-1 using the “test mix”.

The SEM and AFM images of A48-1 have been shown at Figure 3-14. The substrate is porous and has a thick porous layer. The surface morphology looks similar to the DIOS substrate under SEM and AFM with the expectation that the nano-structure is smaller and has lower surface roughness. Pore opening is ~10-50 nm. Enhanced surface area is ~16%, calculated by WCA measurement. The mass spectra generated have a reasonable S/N without the need for the post-etching treatments. It is therefore reasonable to assume that the presence of pores and enhanced surface area are necessary for the best possible SALDI-MS performance. This also relates to the slower gaseous adsorption property of porous surface.

It should also be noted that similar substrate T-1, which was also prepared by the similar etching parameters but has different crystal orientation, has no significant difference in SALDI performance. This is consistent with previous studies that crystal orientation is not a relevant factor in affecting the LDI performance.⁴ Nevertheless, the face of crystal affects the rate of chemical etching and so the thickness of the porous layer.

Given the results of our surface characterisation and modification and knowing that the commercial DIOS substrate is manufactured with fluoro-silanisation,⁵⁰ we applied the method to the SALDI substrates and evaluated the LDI performance. (Figure 3-48 B and C). The result suggests that the modification has not only removed contamination peaks but also enhanced the SALDI performance, lowering the laser energy required for LDI. More examples will be given in the later sections.

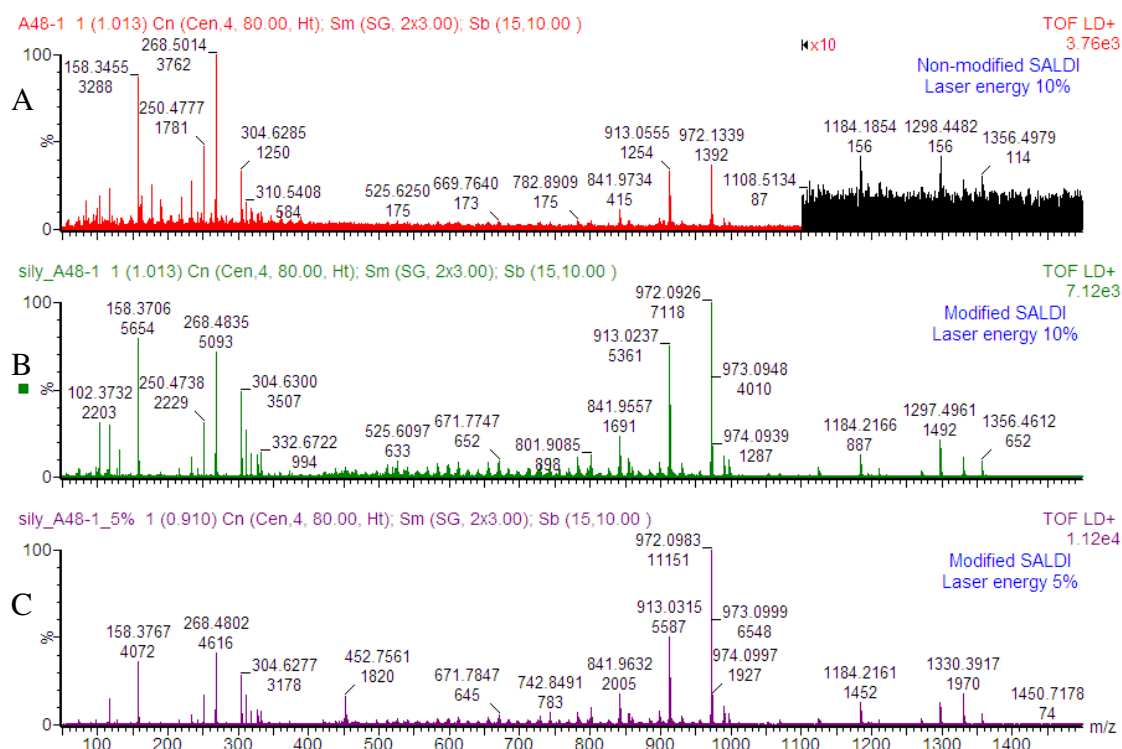


Figure 3-48 (A) Positive ion mass spectra acquired on an as-received SALDI surface. The high mass region of the spectrum generated by non-modified SALDI substrate is magnified by 10. (B) Spectra acquired on a modified surface. Substrate was first plasma etched for 40 mins and then fluoro-silane modified. The contamination peaks at the lower mass region are removed after the treatment. (C) Spectra acquired on a modified surface as (B), but the laser energy setting was lowered to 5%. Test mixture contained nalidixic acid ($[M+H]^+$ m/z 233), alprenolol ($[M+H]^+$ m/z 250), atenolol ($[M+H]^+$ m/z 250), metoprolol ($[M+H]^+$ m/z 268), nadolol ($[M+H]^+$ m/z 310), timolol ($[M+H]^+$ m/z 317), labetalol ($[M+H]^+$ m/z 329), angiotensin I ($[M+H]^+$ m/z 1296.5), vitamin B₁₂ ($[M+H]^+$ m/z 1355.5, fragment m/z 972), folic acid and erythromycin (each 0.1 mM, 2 μ l droplet) obtained using SALDI substrate A48-1. Folic acid and erythromycin were not detected as protonated ion.

3.5.8 Fluoro-silane SAM Modified SALDI Substrates to As-Received Substrates Prepared by High Etching Current

We have seen fluoro-silane modification to the above SALDI surface enhances its LDI activity. All the modified substrates were first subjected to 40 minutes argon plasma etching and then subsequently silanised in toluene at $\sim 90^\circ\text{C}$ for 1 hour. In this test, the same “test mix” of 0.1 mM nalidixic acid, alprenolol, atenolol, metoprolol,

nadolol, timolol, labetalol, folic acid, erythromycin, angiotensin I, and vitamin B₁₂. 2 µl droplet was deposited onto the surface and 10% laser was used.

The SALDI spectra generated before and after modification are shown at Figure 3-49 and Figure 3-50, respectively. The AFM images of the surfaces have been presented at Figure 3-17.

It was dismaying that the spectra generated were full of interferences at the lower mass region and poor performance at the higher mass region before modification. Substrate a1 seems to have the best SALDI performance before the surface modification in this set of surfaces, as it appears this is co-related to the largest structure observed on the surface using AFM in this set of surfaces.

After modification, all substrates showed some degrees of improvement. The larger molecules became detected and the level of interference became lower. The largest improvement was obtained at a4 substrate. It may be because it has some nano-wells.

In fact, if only the intensity of molecular peaks at low mass region is considered, the ion yield is decreased though S/N is improved. It is believed that hydrocarbon contamination was acting as a matrix, and bringing the small molecules into vacuum or even being a weak proton source when they were non-selectively desorbed at the same time. Desorption of contaminant suppressed the LDI of larger molecules and is one of the reasons larger molecules could not be detected before modification. The second reason is after modification, the optimal laser energy decreases from 15% to 5%. Since a fixed laser energy setting was used for comparison, the optimal performance of the modified surface was not shown.

Although ions can be generated on these non-porous surfaces supporting the suggestion that the presence of pores is not strictly required for LDI, none of these results substantiates that reducing roughness or the size of surface irregularities improves the SALDI activity. In fact, it is the opposite. It can be concluded that in the absence of pores and nano-structures of appropriate dimension, the SALDI performance is bound to be poor.

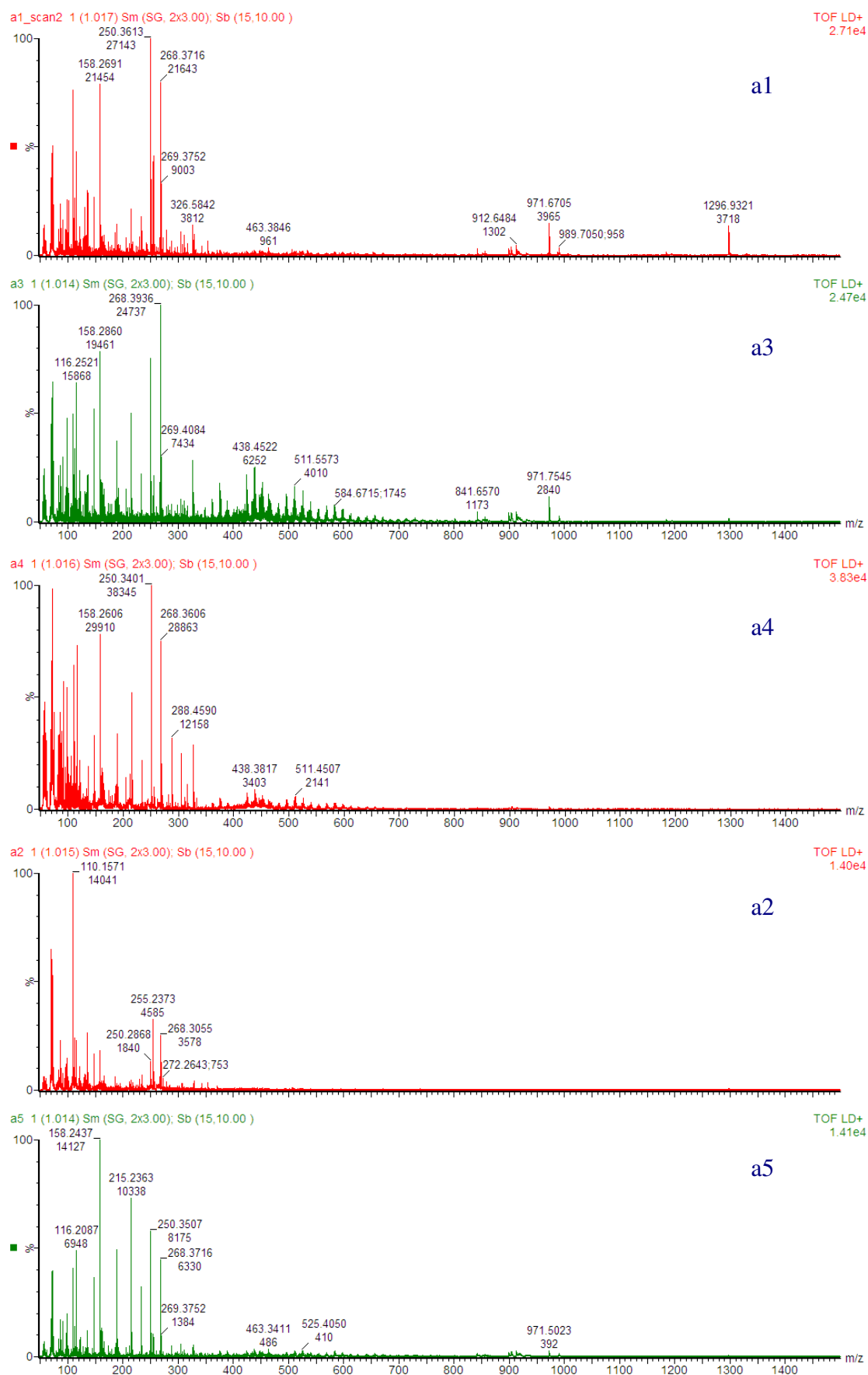


Figure 3-49 Positive ion SALDI mass spectra of the as-received substrates a1 to a5.

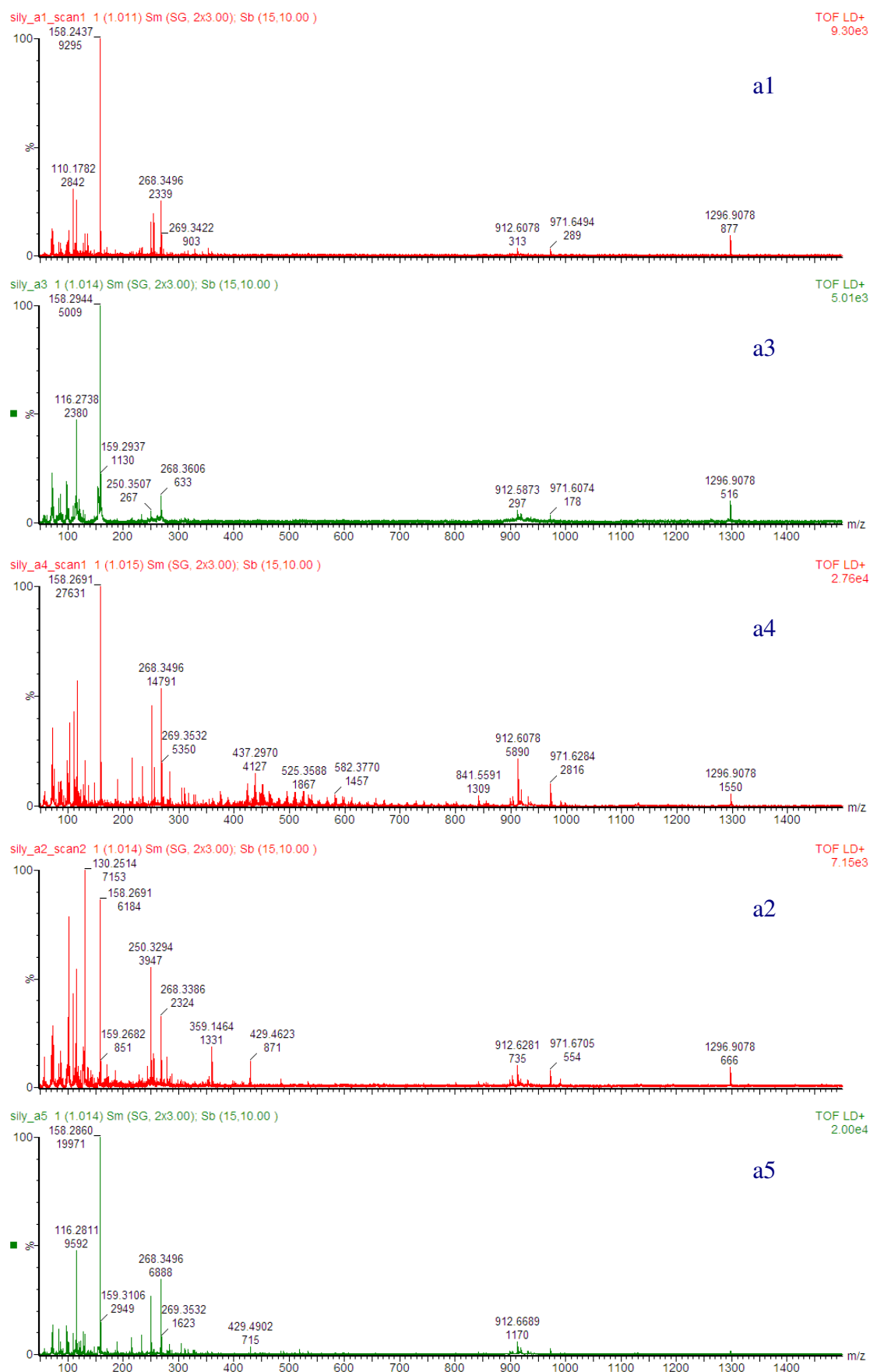


Figure 3-50 Positive ion SALDI mass spectra of the modified substrates a1 to a5. The substrates were first argon plasma etched for 40 mins and subsequently silanised at ~90°C for 1 hour.

3.5.9 Fluoro-Silane SAM Modified Experimental SALDI Substrates to As-Received Experimental Substrates

The experimental SALDI substrates were prepared by first stain-etching with HNO_3 and then subsequently re-etched in HF solution with or without addition of iodine etching additive.

The same experimental conditions were applied to these substrates as in section 3.5.8. Figure 3-51 and Figure 3-52 show mass spectra generated by these substrate before and after modification. The SEM and AFM images of substrate e1 to e3 have been presented at Figure 3-18.

Substrate e1 has a thick porous structure and it could generate spectra with no difficulty. This is consistent with the previous results that thick porous layer and nanostructures are crucial in assisting ion generation. Because of the use of an iodine-etching additive, small and fragile structures were further weakened with thick porous layer and a large number of scratches were observed on the surface even without any modification. It seemed that the nano-structures were too fragile to stand the vigorous post-etching modification (boiling in toluene) and the ion yield was decreased after modification.

Substrates e2 and e3 also suffer contamination problem and the quality of the LDI mass spectra were quite poor before modification. Substrate e2 has nano-dot structure and e3 has dents of curvatures. Both e2 and e3 show improvements after modification. This is also consistent with the previous results. This suggests that as well as nano-pores or nano-tips, although they are not as effective, surface curvatures could assist ion generation.

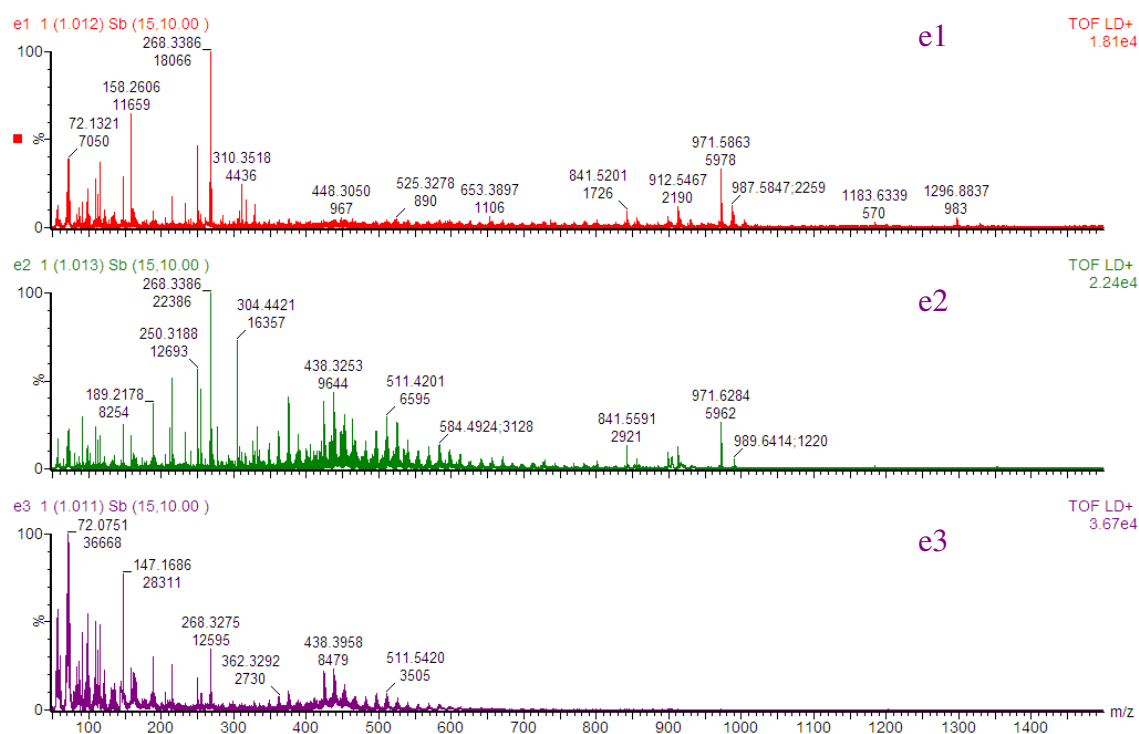


Figure 3-51 Positive ion SALDI mass spectra generated by the as-received experimental substrates e1 to e3.

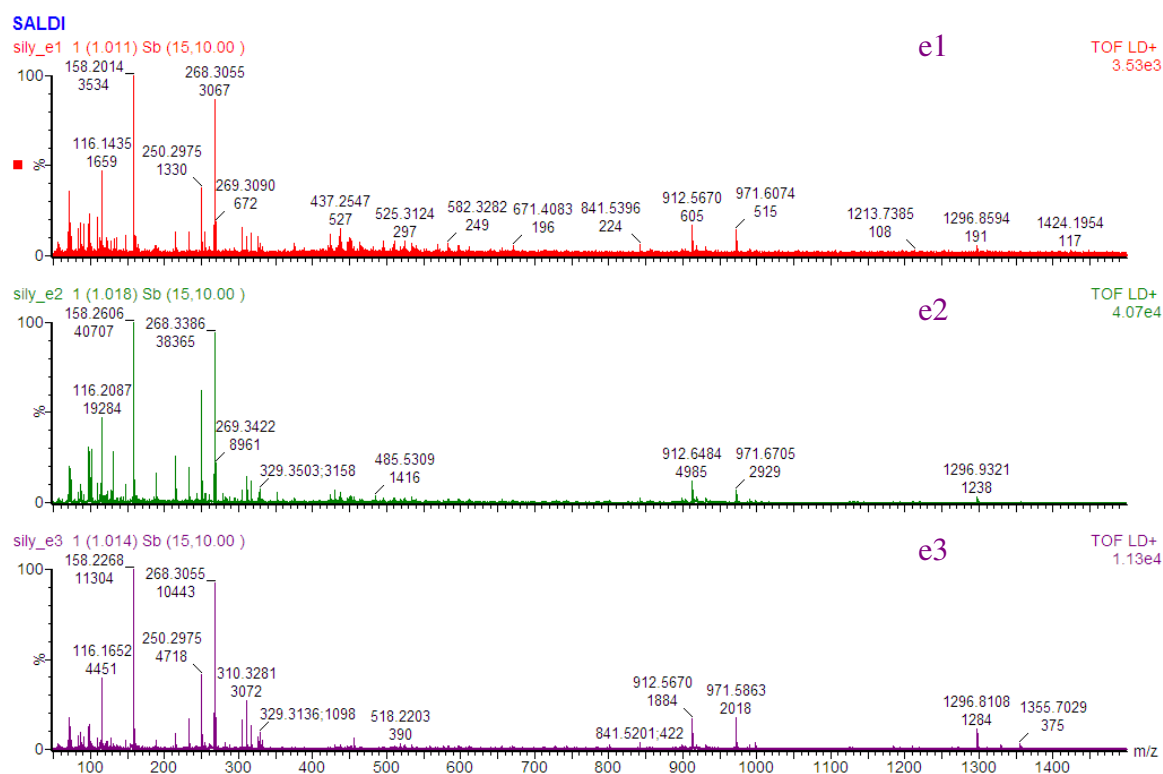


Figure 3-52 Positive ion SALDI mass spectra generated by the modified experimental substrates e1 to e3. The substrates were first argon plasma etched for 40 mins and subsequently silanised at ~90°C for 1 hour.

3.6 Summary and Discussion of Surface Morphology and Chemical Modification to LDI Performance

The order of performance between substrates investigated is that DIOS > porous SALDI > QuickMass > non-porous SALDI. It should also be noted that a great variation of LDI performance was observed among different SALDI substrates and this order is given by impression rating.

From the evidence collected, a roughened surface is generally preferred over a smooth surface. A nano-sized porous surface is preferred over a non-porous surface. Nano-sized pores and tips, which enhance the surface area, can generally assist ion formation. Substrates that have a thick porous layer (200 to 300 nm) generally produce a higher ion yield than substrates that have a thin porous layer (50 nm or less). Substrates of low electro-resistivity are preferred as charge accumulated on the surface can be neutralised more rapidly than substrate of high electro-resistivity.

From the observations as a whole, the LDI performance of PSi substrates does not strongly depend on surface roughness, but perhaps more on the thickness, dimension and density of the surface nanostructures. For the special case of PSi substrates, these factors could be manifested into pore size and/or porosity. Still, this is a complicated multi-factorial issue and a conclusive deduction cannot be made based on the experimental results. Undoubtedly, further reducing the surface irregularities or roughness is unnecessary and does not improve the SALDI activity nor will it generate a higher quality LDI mass spectrum. Even though reducing the surface irregularities from micron-size to sub-micron/nano-size does enhance the SALDI performance, further reducing the surface irregularities is excessive and in fact, reduces the surface area of the substrate required for optical absorption, retaining the analyte and laser induced surface reactions. Although it has been shown that a roughened surface is required for ion generation, surface roughness alone is a poor indicator of the SALDI performance. On the other hand, porous structure can potentially encapsulate air or solvent in the porous volume upon sample deposition.

The expansion of trapped material during LDI may enhance the desorption/ionisation of ions. (See section 4.3.7)

These observations are in fact similar to the general principle laid down by Junner, *et al.*, and have been explained in a patent application.⁵⁹ It stated that an optimised SALDI surface has roughness values greater than 20 nm (average roughness or root mean square roughness) and enhanced surface area (relative to smooth silicon surface before etching) between 20% to 40%. Indeed, substrates which have a thick porous layer larger than 250 nm generate substantially higher ion yield than non-porous or shallow porous substrate and the gaseous adsorption rate is significantly slower.^{6, 59} These were understood to be due to differences in analyte transport and adsorption resulting from the different porosities of the ionisation surfaces.⁵⁹ Although those substrate parameters are preferred for effective SALDI activity, only a small proportion of silicon SALDI samples received fell into this category.

It appears that the recent development of the SALDI substrates has been taking the route to support the novel design of gas-phase sample introduction interface, and thus optimised for gaseous adsorption and benefits to the gas-phase SALDI-MS approach. Although it is unambiguous that porous or rougher surfaces can produce a higher ion yield, non-porous surfaces are actually preferred for gas-phase SALDI-MS. Since the gas-phase SALDI-MS is designed to be an instantaneous, highly selective forensic platform, let alone the low gaseous adsorption rate is non-ideal for its application. In fact, the gas-phase SALDI-MS approach relies on enrichment of the analyte continuously adsorbed onto the surface to achieve high sensitivity. Secondly, such a thin-layer structure (smaller than 50 nm thick) may be more stable for long term storage than highly porous substrate in an unprotected condition.^{19, 60} Thirdly, a porous surface also has a low laser threshold of surface destruction. Other reasons include contamination control because a porous surface is difficult to be cleaned. These issues have been paramount in the gas-phase SALDI-MS development and have over-shadowed the factors actually valid for enhancing LDI activity. However, the non-porous surfaces seem to be highly specific for the gas-phase SALDI-MS approach and explaining why they have not been suitable for the liquid deposition approach. On the other hand, the writer cannot see any disadvantage to store any of

these substrates in a protected condition and extending the shelf-life from months to over a year.

There has been one exception to the general observation. The SALDI substrate s5 has a LDI performance outstanding among the non-porous SALDI substrates. This may be because it has the right structural dimension and other substrate properties that lead to an effective polarisation induced by laser radiation or processes an intrinsic electromagnetic or surface resonance (a wavevector overlapping state with the bulk states)⁶¹ that promotes ion formation. This result is not surprising when we compare this observation to a report that flat pyroelectric ceramic lead lanthanum zirconate titanate (PLZT) can also be used for soft LDI-MS substrate.⁹ This is a matter subjected to further investigation and may this be the exception that Alimpiev's SALDI ionisation theory referred to and a system optimised or balancing for both gaseous adsorption and SALDI-MS.³¹

Then again, because of the use of iodine etching additive, light illumination is not required for the surface preparation and lithographic patterning becomes impracticable. The absence of high throughput array format made these SALDI surfaces an non-ideal high-throughput platform for biomedical applications.

Surface chemistry is vital in affecting the LDI performance. Some improvements of the SALDI mass spectra can be achieved using argon plasma etching. The removal of contaminants enhances the quality of mass spectra and yet a thicker oxide layer degrades the SALDI performance and requires elevated laser energy to operate compared to the freshly etched SALDI surfaces. Combine solvent washing, plasma etching and fluoro-silane modification, the LDI performance of SALDI substrates can be significantly improved and lower the laser required for the ion generation and remove background interferences. Overall, clean hydrophobic surface chemistry generally leads to better quality of SALDI mass spectra. While it have been shown chemical modification led to improvements in LDI performance or reduction in background in LDI mass spectra of SALDI surface, the modification is still needed to be further optimised along with the surface morphology optimisation.

However, whether the silicon surface is porous or not, highly roughened or not, chemically etched or not, some forms of ion could be produced. This indicates that the presence of pores or roughness on the surface is not an absolute requirement for LDI, but rather an enhancement or co-factor that assists ion formation and is preferred. The same principle should therefore apply so as to whether the surface is etched by standard galvanostatic etching or anodisation with addition of iodine etching additive, SALDI using gas-phase approach or liquid-disposition approach.⁵⁹ The minimal requirement here is nanostructures on semiconductor substrate.

This can possibly be rationalised by quantum physics. It is known when a particle has a size approaching or less than 100 nm, it often exhibits quantum properties which would be otherwise not observable on micron-size or larger particles. Presumably, the same principle applies here because PSi is generally described as an assembly of nanocrystallites.⁶² (See section 1.4) It is possible that the nano-sized structures are therefore related to the optical coupling or energy deposition due to its quantum properties and is fundamental to the LDI activity.^{18, 57} Further discussions are summarised into an ionisation mechanism proposed. (See section 4.3.6)

3.7 Conclusions

The DIOS substrate from Waters Corp., the QuickMass germanium thin-films from NanoHorizons Inc., and a range of SALDI substrates from the GPI had been examined. It is the first time that an independent study has been carried out to examine the physicochemical properties of these substrates and evaluate their LDI performance. The surface morphology of the substrates was investigated using SEM and AFM. To investigate the chemical nature of the surface substrates and the effects of plasma etching and fluoro-silane modification, ToF-SIMS, XPS and WCA were employed. Using various surface techniques, we were able to investigate which surface factors govern the DIOS/SALDI activity and produce information that may lead to improved substrate design.

The commercial DIOS substrate is fluoro-silane modified porous silicon. In contrast, the QuickMass substrate is a germanium thin-films prepared by PVD method. The

germanium thin-film is coated on a steel target, and is not identical to the commercial product from Shimadzu, in which the thin-film is coated on a glass slide. The SALDI substrates are passivated by a thin layer of oxides. Chemical passivation by Si-I proposed is less in evidence. It appears that the use of a weak oxidising agent, leads to the formation of an ultra-thin oxide layer. This has been confirmed by XPS and WCA studies. Plasma etching can effectively remove the surface contamination but it also increases the thickness of the oxide layer.

Surface morphology has a great influence on the LDI performance. Porous substrates produce a better ion yield than non-porous surfaces and are the LDI substrate of choice for biological mass spectrometry. Although it is arguable that pores are not directly involve in ion formation, undoubtedly they are required for enhancing the ion yield. Non-porous substrates are not suitable for biological applications.

Surface chemistry is also an important factor in affecting the LDI performance. Fluoro-silane modification and argon plasma pre-treatment to the SALDI surface significantly improves its performance and reduction of background interferences, whether it is porous or non-porous surface. Plasma etching is not required for silanisation. However, plasma etching pre-treatment is recommended for the SALDI surfaces, because plasma etching is a necessary cleaning step for removal of surface contamination before any modification. It is also because after etching, the level of hydroxides is higher as shown by XPS and this leads to a denser and possibly uniform silanisation.

As a whole this study provides vital information on the surface properties and identifies the requirements for successful application of LDI-MS and is *sin qua non* for the subsequent investigations.

3.8 References

1. Canham, L. T. Silicon quantum wire array fabrication by electrochemical and chemical dissolution of wafers. *Appl. Phys. Lett.* 57, 1046-1048 (1990).
2. Stewart, M. P. & Buriak, J. M. Chemical and Biological Applications of Porous Silicon Technology. *Adv. Mater.* 12, 859-869 (2000).
3. Schmeltzer, J. M. & Buriak, J. M. in *The Chemistry of Nanomaterials: Synthesis, Properties and Applications, Volume 2* (eds. Rao, C. N. R., Müller, A. & Cheetham, A. K.) 518-550 (John Wiley and Sons, 2004).
4. Shen, Z., Thomas, J. J., Averbuj, C., Broo, K. M., Engelhard, M., Crowell, J. E., Finn, M. G. & Siuzdak, G. Porous silicon as a versatile platform for laser desorption/ionization mass spectrometry. *Anal. Chem.* 73, 612-619 (2001).
5. Lee, C.-S., Kim, E.-M., Lee, S.-H., Kim, M.-S., Kim, Y.-K. & Kim, B.-G. Enhancement of analyte ionization in desorption/ionization on porous silicon (DIOS)-mass spectrometry (MS). *Biotechnol. Bioprocess Eng.* 10, 212-217 (2005).
6. Alimpiev, S., Nikiforov, S., Karavanskii, V., Miton, T. & Sunner, J. On the mechanism of laser-induced desorption-ionisation of organic compounds from etched silicon and carbon surfaces. *J. Chem. Phys.* 115, 1891-1901 (2001).
7. Okuno, S., Arakawa, R., Okamoto, K., Matsui, Y., Seki, S., Kozawa, T., Tagawa, S. & Wada, Y. Requirements for Laser-Induced Desorption/Ionization on Submicrometer Structures *Anal. Chem.* 77, 5364-5369 (2005).
8. Wada, Y., Yanagishita, T. & Masuda, H. Ordered Porous Alumina Geometries and Surface Metals for Surface-Assisted Laser Desorption/Ionization of Biomolecules: Possible Mechanistic Implications of Metal Surface Melting. *Anal. Chem.* 79, 9122-9127 (2007).
9. Sato, H., Seino, T., Yamamoto, A., Torimura, M. & Tao, H. Soft Laser Desorption/Ionization Mass Spectrometry Using a Pyroelectric Ceramic Plate. *Chem. Lett.* 34, 1178-1179 (2005).
10. Sato, H., Yamamoto, A., Seino, T., Torimura, M. & Tao, H. National Institute of Advanced Industrial Science and Technology. Ionization plate for mass spectrometry and mass spectrometer (2006). *US 20060255262*.

11. Kruse, R. A., Li, X., Bohn, P. W. & Sweedler, J. V. Experimental factor controlling analyte ion generation in laser desorption/ionization mass spectrometry on porous silicon. *Anal. Chem.* 73, 3639-3645 (2001).
12. Chen, Y. & Vertes, A. Adjustable Fragmentation in Laser Desorption/Ionization from Laser-Induced Silicon Microcolumn Arrays. *Anal. Chem.* 78, 5835-5844 (2006).
13. Finkel, N. H., Prevo, B. G., Velez, O. D. & He, L. Ordered silicon nanocavity arrays in surface-assisted desorption/ionization mass spectrometry. *Anal. Chem.* 77, 1088-1095 (2005).
14. Finkel, N. H. Surface-Assisted Laser Desorption/Ionization-Mass Spectrometry (SALDI-MS) of Controlled Nanofeatures and the Associated Thermal Properties. MSci. thesis, North Carolina State University, (2005).
15. Anderson, D. F. Mechanism and Application of Desorption/Ionization on Porous Silicon (DIOS). Ph.D. thesis, University of Florida, (2003).
16. Li, Q. Exploring desorption/ionization on porous silicon mass spectrometry and its applications. Ph.D. thesis, University of Florida, (2005).
17. Tuomikoski, S., Huikko, K., Grigoros, K., Ostman, P., Kostiainen, R., Baumann, M., Abian, J., Kotiaho, T. & Franssila, S. Preparation of porous n-type silicon sample plates for desorption/ionization on silicon mass spectrometry (DIOS-MS). *Lab Chip* 2, 247-253 (2002).
18. Cuiffi, J. D., Hayes, D. J., Fonash, S. J., Brown, K. N. & Jones, A. D. Desorption-ionization mass spectrometry using deposited nanostructured silicon films. *Anal. Chem.* 73, 1292-1295 (2001).
19. Kalkan, A., Henry, M. R., Li, H., Cuiffi, J. D., JHayes, D., Palmer, C. & Fonash, S. J. Biomedical/analytical applications of deposited nanostructured Si films. *Nanotechnology* 16, 1383-1391 (2005).
20. Feng, Z. C., Wee, A. T. S. & Tan, K. L. Surface and optical analyses of porous silicon membranes. *J. Phys. D: Appl. Phys.* 27, 1968-1975 (1994).
21. Graves, D. B. & Humbird, D. Surface chemistry associated with plasma etching processes. *Appl. Surface Sci.* 192, 72-87 (2002).
22. Gorecka-Drzazga, A. Plasma dry etching of monocrystalline silicon for the microsystem technology *Optica Applicata* 32, 339-346 (2002).

23. Nishiki, K., Sasaki, Y., Shimazaki, A., Tamaoki, M. & Yanagi, S. The effect of airborne contaminants in the cleanroom for ULSI manufacturing process In Advanced Semiconductor Manufacturing Conference and Workshop, (1995). ASMC 95 Proceedings,
24. Loni, A., Simons, A. J., Canham, L. T., Phillips, H. J. & Earwaker, L. G. Compositional variations of porous silicon layers prior to and during ion-beam analyses. *J. Appl. Phys.* 76, 2825-2832 (1994).
25. Nesbitt, H. W., Bancroft, G. M., Davidson, R., McLntyre, N. S. & Pratt, A. R. Minimum XPS core-level line widths of insulators, including silicate minerals. *American Mineralogist* 89, 878–882 (2004).
26. Raether, H. in Springer Tracts in Modern Physics 84 (Springer Verlag, Berlin, 1965).
27. Sato, S., Rath, S., Akiyama, S., Nozaki, S. & Morisaki, H. Volume plasmons in porous silicon. *J. Appl. Phys.* 86, 1774-1776 (1999).
28. Mannella, N., Gabetta, G. & Parmigiani, F. Plasmon energy shift in porous silicon measured by x-ray photoelectron spectroscopy. *Appl. Phys. Lett.* 79, 4432-4434 (2001).
29. Chen, L. C., Ueda, T., Sagisaka, M., Hori, H. & Hiraoka, K. Visible Laser Desorption/Ionization Mass Spectrometry Using Gold Nanorods. *J. Phys. Chem. C* 111, 2409-2415 (2007).
30. Zhang, Y. F., Liao, L. S., Chan, W. H., Lee, S. T., Sammynaiken, R. & Sham, T. K. Electronic structure of silicon nanowires: A photoemission and x-ray absorption study. *Phys. Rev. B* 61, 8298-8305 (2000).
31. Alimpiev, S. S., Nikiforov, S. M., Karavansky, V. A., Grechnikov, A. A. & Sunner, J. A. Laser desorption of ions from microscopically rough surfaces: novel technique for ultrahigh sensitivity detection of organic and bioorganic compounds. In Libenson, M. N. Proc. SPIE, (2004). 5506 95-106.
32. Siuzdak, G., Go, E., Shen, Z., Compton, B. & Bouvier, E. Waters Investments Limited. Methods, Compositions and Devices for Performing Ionization Desorption on Silicon Derivatives. (2004). WO 2004US17853 20040604. WO2005001423.
33. Credo, G. M., Hewitson, H. B., Fountain, K. J., Gilar, M., Finch, J. W., Stumpf, C. L., Benevides, C. C., Bouvier, E. S. P., Compton, B. J., Shen, Z. & Siuzdak, G. Desorption/ionization on silicon mass spectrometry (DIOS MS) of small molecules and peptide:

- sample handling, preparation and storage effects on performance. 51th Annual Conf. ASMS Montreal, Canada, 8-12 June, (2003).
34. Wall, D. B. Waters Investments LTD. Improved deposition of dissolved analyte to hydrophobic surfaces by desolvation of organic solvents. (2004). *WO 2003US33677 20031021*. WO 2004038402.
 35. Steenwyk, R. C., Hutzler, J. M., Sams, J., Shen, Z. & Siuzdak, G. Atmospheric pressure desorption/ionization on silicon ion trap mass spectrometry applied to the quantitation of midazolam in rat plasma and determination of midazolam 1'-hydroxylation kinetics in human liver microsomes. *Rapid Commun. Mass Spectrom.* 20, 3717-3722 (2006).
 36. Bovier, E. S. P., Dellarovere, D., Benevides, C. C. & Fadgen, K. Waters Investments Limited. Methods, compositions and devices for performing ionization desorption on silicon derivatives. (2007). *WO 2006-US31932*.
 37. Fonash, S. J., Kalkan, A. K. & Bae, S. The Penn State Research Foundation. Deposited thin film void-column network materials. (2000). WO 0074932.
 38. Fonash, S. J., Bae, S., Hayes, D. J. & Cuiffi, J. The Penn State Research Foundation. Deposited thin films and their use in detection, attachment, and bio-medical applications. (2002). *US 20020048531*.
 39. Fonash, S. J., Kalkan, A. K., Cuiffi, J. & Hayes, D. J. The Penn State Research Foundation. Matrix-free desorption ionization mass spectrometry using tailored morphology layer devices. (2002). *US 20020187312 WO 02093170*.
 40. Hayes, D. J. Micrototal Analysis System For Enzymatic Drug Metabolism and Analysis. Ph.D. thesis, The Pennsylvania State University, (2004).
 41. Kalkan, A. K., Bae, S., Li, H., Hayes, D. J. & Fonash, S. J. Nanocrystalline Si thin films with arrayed void-column network deposited by high density plasma. *J. Appl. Phys.* 88, 555-561 (2000).
 42. Zhang, Q., Zou, H., Guo, Z., Zhang, Q., Chen, X. & Ni, J. Matrix-assisted laser desorption/ionization mass spectrometry using porous silicon and silica gel as matrix. *Rapid Commun. Mass Spectrom.* 15, 217-223 (2001).
 43. Umezu, I., Kohno, K., Aoki, K., Kohama, Y., Sugimura, A. & Inada, M. Effects of argon and hydrogen plasmas on the surface of silicon. *Vacuum* 66, 453-456 (2002).

44. Todorović, D. M., Smiljanić, M., Sarajlić, M., Vasiljević-Radović, D. & Randjelović, D. Investigation of the effects of Ar plasma etching in Si surface by photoacoustic method. *J. Phys. IV France* 125, 451-453 (2005).
45. Kostishko, B. M., Appolonov, S. V. & Kostishko, A. E. Fluorine surface concentration change during the argon-oxygen ion treatment of porous silicon. *Appl. Surface Sci.* 189, 113-118 (2002).
46. Vaidyanathan, S., Jones, D., Ellis, J., Jenkins, T., Chong, C., Anderson, M. & Goodacre, R. Laser desorption/ionization mass spectrometry on porous silicon for metabolome analyses: influence of surface oxidation. *Rapid Commun. Mass Spectrom.* 21, 2157-2166 (2007).
47. Wang, Q., Gu, C. Z., Li, J. J., Wang, Z. L., Shi, C. Y., Xu, P., Zhu, K. & Liu, Y. L. Enhanced photoluminescence from porous silicon by hydrogen-plasma etching. *J. Appl. Phys.* 97, 093501-4 (2005).
48. Buriak, J. M., Stewart, M. P., Geders, T. W., Allen, M. J., Choi, H. C., Smith, J., Raftery, D. & Canham, L. T. Lewis Acid Mediated Hydrosilylation on Porous Silicon Surfaces. *J. Am. Chem. Soc.* 121, 11491-11502 (1999).
49. Trauger, S. A., Go, E. P., Shen, Z., Apon, J. V., Compton, B. J., Bouvier, E. S. P., Finn, M. G. & Siuzdak, G. High sensitivity and analyte capture with desorption/ionization mass spectrometry on silylated porous silicon. *Anal. Chem.* 76, 4484 - 4489 (2004).
50. Nordstrom, A., Apon, J. V., Uritboonthai, W., Go, E. P. & Siuzdak, G. Surfactant-Enhanced Desorption/Ionization on Silicon Mass Spectrometry. *Anal. Chem.* 78, 272-278 (2006).
51. Luo, G., Chen, Y., Siuzdak, G. & A., V. Surface Modification and Laser Pulse Length Effects on Internal Energy Transfer in DIOS. *J. Phys. Chem. B* 109, 24450-24456 (2005).
52. Coffinier, Y., Janel, S., Addad, A., Blossey, R., Gengembre, L., Payen, E. & Boukherroub, R. Preparation of Superhydrophobic Silicon Oxide Nanowire Surfaces. *Langmuir* 23, 1608-1611 (2007).
53. Wendel, R. N. Resistance Of Solid Surfaces To Wetting By Water. *J. Ind. Eng. Chem.* 28, 988-994 (1936).
54. Cassie, A. B. D. & Baxter, S. Wettability of porous surfaces. *Trans. Faraday Soc.* 40, 546-551 (1944).

55. Xiang, F., Cuiffi, J. D., Wang, A. Y. & Hayes, D. J. A New Approach to Small Molecular Analysis using Matrix-Less Laser Desorption and a Hybrid Mass Spectrometer, Potential for Metabonomic Applications 53rd Annual Conf. ASMS, San Antonio, June 5-9, (2005).
56. Park, H.-R., Chung, K.-Y., Lee, H.-C., Lee, J.-K. & Bark, K.-M. Ionization and Divalent Cation Complexation of Quinolone Antibiotics in Aqueous Solution. *Bull. Korean Chem. Soc.* 21, 849-854 (2000).
57. Vertes, A. in Laser Ablation and its Applications (ed. Phipps, C. R.) 505-528 (Springer, 2007).
58. Kinumi, T., Shimomae, Y., Arakawa, R., Tatsu, Y., Shigeri, Y., Yumoto, N. & Niki, E. Effective detection of peptides containing cysteine sulfonic acid using matrix-assisted laser desorption/ionization and laser desorption/ionization on porous silicon mass spectrometry. *J. Mass Spectrom.* 41, 103-112 (2006).
59. Sunner, J., Alimpiev, S. & Nikiforov, S. Morgan Lewis & Bockius LLP. Method and apparatus to produce gas phase analyte ions (2002). *US 20020121595*.
60. Yang, D.-Q., Meunier, M. & Sachera, E. Room temperature air oxidation of nanostructured Si thin films with varying porosities as studied by x-ray photoelectron spectroscopy. *J. Appl. Phys.* 99, 084315-1-6 (2006).
61. Kolasinski, K. Surface science : foundations of catalysis and nanoscience (John Wiley & Sons, Chichester, UK, 2002).
62. Canham, L. Properties of Porous Silicon (ed. Weiss, B. L.) (Institution of Engineering and Technology, Stevenage, 1997).

CHAPTER 4 IONIC AND SURFACE REACTIONS ON MATRIX-FREE LDI SUBSTRATES

4.1 Introduction

4.1.1 The DIOS-MS Technique

The development of DIOS-MS has attracted a lot of attention because it is a versatile LDI-MS platform offering the potential for high-throughput screening of pharmaceutical compounds and metabolites. The uniqueness and attraction of the DIOS technique is the characteristic absence of matrix interference in the low mass region of the mass spectra, and a wide range of low molecular weight compounds that can be detected, (Figure 4-1 and Figure 4-2) while enjoying the robustness and the high throughput of the MALDI-MS environment. Even at the early stages of the DIOS-MS development, it was foreseeable that combining the speed and automation of existing MALDI-MS instrumentation with the DIOS substrate could provide a versatile tool for many different applications, without the matrix interferences normally associated with MALDI in the low-mass region.^{1, 2} The method itself is simple; sample droplets in a suitable solvent system are directly applied onto the substrate and allowed to dry. The DIOS spectra are also uncomplicated, molecular and pseudomolecular ions dominate the mass spectra for a variety of pharmaceutical compounds, in both positive and negative ionisation modes. Good quality spectra can be obtained for a variety of compound classes, over a broad mass range, with minimal fragmentation. Resolution and mass accuracy depends on the specific instrument. The DIOS method also has a higher salt tolerance than ESI, the method requires little to no modifications to the instrumental design and control and data acquisition can be automated.^{1, 2}

The DIOS method has some limitations and the application of the method is not as straight forward as suggested. Background interferences due to surface contaminations and surface aging due to oxidation have been problematical. These problems were discussed in Chapter 3. Additionally, the ionisation reaction is not as soft or simple as ESI and fragmentation and various ionic reactions occur. Built upon the foundation of Chapter 3, a comprehensive assessment of the SALDI/DIOS activities is to be ascertained in this chapter.

**Printed version includes a DIOS mass spectrum of hytrin extracted
from the reference source.**

Please refer to the cited reference for detail

Figure 4-1 DIOS mass spectrum of hytrin (Terazosin HCl).²

**Printed version includes DIOS mass spectra of pseudoephedrine,
codeine, verapamil and vitamin B₁₂ and their chemical structures
extracted from the reference source.**

Please refer to the cited reference for detail

**Figure 4-2 DIOS mass spectra of pseudoephedrine, codeine, verapamil and vitamin B₁₂ and their
chemical structures.³**

The pioneering works in this area include the studies carried out at the University of Helsinki, Finland.^{4, 5} A wide range of pharmaceutical compounds was analysed by AP-DIOS. These studies demonstrated the capability of the method and the sensitivity for various compound classes. They also correlated the chemical properties of the analyte to the ion signals observed in the DIOS mass spectra. For example, it was demonstrated that 1-naphthylmethylamine, instead of forming a protonated molecule, produces $[M+H-2H]^+$ and $[M+H-NH_3]^+$ ions.⁴ It has been proposed this may be due to dissociation of H_2 from the methylamine moiety before ionisation, leading to significant additional resonance stabilisation. On the other hand, paracetamol yields a water-loss ion $[M+H-H_2O]^+$, while ketoprofen loses acetic acid to give $[M+H-CH_3COOH]^+$. A peptide angiotensin II, also yielded sodium adducts $[M+Na]^+$, di-sodium adducts $[M+2Na-H]^+$, and tri-sodium adducts $[M+3Na-2H]^+$.⁴

It has also been established that the sensitivity of DIOS is highly dependent on the proton affinity of the molecule, in particular the presence of amine groups.⁴ To verify this initial observation, Ostman, *et al.*^{5, 6} compared the relative sensitivity of various pharmaceutical compounds and their thermochemical properties detected by the DIOS method under positive ion mode. (Table 4-1) The authors concluded that only compounds with relatively high PA values above a threshold value of 920-950 kJ/mol could be efficiently ionised as protonated molecules and produce very clean mass spectra under AP-DIOS conditions on unmodified PSi substrate. The compounds that could not be detected were typically analytes lacking high PA functional groups. Moreover, the observation of the radical cation for methyl-9-anthracenecarboxylate and the possible radical cation of 9H-carbazole may indicate that if the ionisation energy and PA of a compound is low enough (below about 7.5 eV and about 900 kJ/mol, respectively), formation of the radical cation is possible.⁵ It should be noted that because of the lack of experimental data, the PA values were calculated by *ab initio* and hybrid density functional theory (DFT) calculations.

Conversely, an alternative view proposed by Alimpiev, *et al.* was that the aqueous basicities (pKa-values) of the analyte molecules are to be important,⁷ because they found that the compounds such as acetophenone, dimethylsulfoxide could not be detected, despite the high PA values of these compounds. An exception occurred for the pyrene due to its relatively low ionisation energy.

Table 4-1 Literature and calculated thermochemical values of various compounds.⁵

**Printed version includes a table extracted
from the reference source describing
the relationship of the proton affinity of 20 compounds and their relative
ionisation efficiency.
Please refer to the cited reference for detail**

On the other hand, acidic compounds do not ionise efficiently in positive ion mode, but they can be detected in negative ion mode due to their low proton affinities. Then again, for straight chain fatty acids, instead of forming predominately deprotonated species, metallic aggregates (cationised deprotonated multimers) are seen in the DIOS spectra.⁸ (Figure 4-3) An important aspect of this finding is that the statistical distribution of homo- and heteromultimeric species (dimers and trimers) is in 1:2:1 ratio, reflecting a situation which cannot exist in solution because of the chiral effect of the molecules. Essentially, this observation opposes that which has been proposed previously that ions are pre-formed in a solvated state, and end up being detected.⁷ Furthermore, the relative proportion of deprotonated species and metallic aggregates is dependent on the laser intensity as well as extraction delay time.⁸ (Figure 4-4)

A further observation is that basic compounds like theophylline (a methylxanthine drug used in therapy for respiratory diseases such as chronic obstructive pulmonary disease or asthma, naturally found in black tea and green tea) and caffeine not only can they be detected in positive ion mode, they can also be detected in negative ion mode.⁹ For theophylline in positive mode, $[M+H]^+$, $[M+Na]^+$ and $[M+K]^+$ are detected, however the compound displaces a single peak $[M]^-$ in negative mode. As for the Br-containing caffeine analogue, all analyte signals were suppressed by the background peaks in positive mode, and yet a doublet of the molecular ion located at

m/z 258 and m/z 260 representing the Br isotopic pattern is obtained in negative ion mode.⁹ Fragmentation due to removal of Br leads to a fragment peak located at m/z 180. (Figure 4-5) From all of the above, we may be able to see that the ionisation reactions are not limited to protonation, deprotonation reaction or adduct formation.

Printed version includes a negative ion DIOS mass spectrum of two fatty acids extracted from the reference source highlighting the formation of cationic multimers. Please refer to the cited reference for detail

Figure 4-3 Negative ion DIOS mass spectrum of the mixture of nonadecanoic acid ($C_{19}H_{38}O_2$) (M) and heneicosanoic acid ($C_{21}H_{42}O_2$) (M'). The mass spectra of organic contain typically deprotonated species, sodium dimers and potassium trimers.⁸

Printed version includes figure(s) extracted from the reference source describing the relative ion abundance of the fatty acids cationic multimers with respect to the extraction delay time of the mass spectrometer. Please refer to the cited reference for detail

Figure 4-4 Plot of $A_{\text{monomeric species}}/A_{\text{dimeric species}}$ vs. extraction delay.⁸

**Printed version includes positive and negative ion DIOS mass spectra
of theophylline and Br-containing caffeine extracted
from the reference source.
Please refer to the cited reference for detail**

Figure 4-5 DIOS mass spectra of two compounds in both the positive mode and negative mode: (a) and (b) theophylline ($C_7H_8N_4O_2$, molecular weight 180, structure shown); (c) and (d) a Br-containing caffeine structure analogue ($C_7H_7N_4O_2Br$, molecular weight 259.1, structure unknown).⁹

Several studies have also compared DIOS-MS and MALDI-MS techniques and to examine their similarities and differences.

Luo, *et al.*¹⁰ probed the internal energy (IE) of ions produced in MALDI and DIOS using a number of thermometer molecules and a concept called survival yield. Survival yield is the ratio of total ion intensity of molecular ions to total ion intensity of both molecular ions and fragment ions. Comparing the energy deposition in the desorption process during MALDI and DIOS revealed that DIOS produced ions with higher energy content. (Figure 4-6) The IE depended much less on laser fluence in DIOS than in MALDI and the degree of fragmentation, measured by the survival yield, was remarkably insensitive to laser fluence variations and to surface derivatisation.

**Printed version includes figure(s) extracted
from the reference source describing
the internal energy distribution of thermometer ions generated by DIOS-
MS and MALDI-MS.
Please refer to the cited reference for detail**

Figure 4-6 Comparison of internal energy distribution of thermometer ions desorbed from trimethylsilane derivatised DIOS surfaces and from CHCA matrix in MALDI, using nitrogen nanosecond (ns) laser (solid lines) and Nd:YAG picosecond (ps) laser (dashed lines) excitation. MALDI data were obtained at 25.6 and 45.2 mJ/cm² with the ns and ps laser, respectively. Corresponding fluences for DIOS were 52.4 mJ/cm² (ns laser) and 55.8 mJ/cm² (ps laser). Kinetic shifts are not reflected.¹⁰

Okuno, *et al.*¹¹ used a number of organic dyes, including Methylene Blue, Janus Green B, Crystal Violet and Rhodamin B to investigate redox reactions occur in DIOS and MALDI. In MALDI, these molecules produced M^+ ion peaks whereas in DIOS $(M^\bullet)H^+$ or $(MH^\bullet)^+$ was obtained, corresponding to one-electron reduction product. Then again, Cu(II) was reduced to Cu(I),¹² and, 1,2-diferrocenylethane and *N,N*-dimethylaminomethylferrocene (ferrocene derivatives), are oxidised to M^+ as is the case of MALDI.¹³ It should be noted that the latter compound has an amino group (as well as a Fc center) and it was believed that it can catch a proton easily and yet a protonated ion did not form. The authors believe that the ionisation mechanism of DIOS may differ greatly from that of MALDI,¹³ and may be analogous to SALDI, such that formation of gas-phase ions is initiated on the surface of sharp crystal tips and edges that protrude out of the sample surface. Such sub-micrometer structures of PSi might promote electron transfer.¹¹

4.1.2 Matrix MALDI Ionisation Reactions

Given the close relation of the DIOS and MALDI techniques, understanding of the MALDI ionisation reactions may assist our study. On the current understanding of the MALDI reaction, the locations and processes of ion formation seem to be numerous and cannot be explained by a single process.¹⁴ According to Knochenmuss,¹⁵⁻¹⁷ the current model of UV-MALDI ionisation reactions is a two-step process, primary and secondary ionisation. Initial (primary) ion formation or separation is the first step that occurs during or shortly after the laser pulse (in nanosecond scale). Following the generation of primary ions, secondary ion-molecule reactions the desorption plume (in microsecond scale) converting the primary ions into the most thermodynamically favourable secondary ion products that are those detected. This difference in time scales is the origin of the two-step nature of MALDI reactions.¹⁷ (Figure 4-7)

Consider the ionisation potential of a typical molecule requires 8-9 eV. The photon energy from the 337 nitrogen laser is only 3.68 eV.¹⁵ Direct photoionisation requires two or more photons arriving at the same site at the same time. This is a less likely event and only occurs at the laser intensity beyond that normally required for MALDI-MS and does not generally appear to be a major contributor.

An important concept in MALDI ionisation is photoexcitation and energy pooling. Energy pooling is one of several energy concentration possibilities imagined in early MALDI work. It is a phenomenon in which the electronic excitation energy of two nearby molecules is redistributed and higher energy processes become possible.¹⁷ A pooling event can be considered as when neighbouring molecules are both individually excited to S_1 state, but none has the sufficient energy leading to ionisation. Interaction between excited neighbouring molecules can occur due to wavefunction overlapping. Imagine one of them transmits its energy to its neighbour and while itself is relaxed to the ground state, promoting its neighbour to a S_n state (Figure 4-8A). Sequential event leads to sufficient energy that can lead to ionisation. (Figure 4-8B) This proposition is supported by computation simulation and experimental data using 2,5-dihydroxybenzoic acid (DHB) matrix.

**Printed version includes figure(s) extracted
from the reference source describing
the two-step MALDI model: the primary ionisation and secondary
reaction of the MALDI reaction.
Please refer to the cited reference for detail**

Figure 4-7 The origin of the two-step model: expansion of the MALDI plume compared to the laser pulse and excited state decay. Density is plotted vs. time for a plume expanding as an adiabatic free jet. A density of 1 is approximately that of a gas at 1 atm. The expansion stops when the gas reaches the environmental background pressure, which may vary in practice from 1 atm to high vacuum. The inset shows the early behaviour, along with a 3 ns N₂ laser pulse (blue line) and the typical lifetime of matrix excited states (green line). Only during the time when energy and material densities are high can significant ionisation occur. The solid line represents the density if the sample vaporises smoothly. The dashed line represents an explosive phase change for which a well-defined solid-gas boundary may not exist at short times.¹⁷

**Printed version includes figure(s) extracted
from the reference source describing
the concept of energy pooling in MALDI reaction.
Please refer to the cited reference for detail**

Figure 4-8 Unimolecular and bimolecular matrix processes included in the MALDI ionisation model. (A) Pooling of two S_1 excitations, yielding an iso-energetic system consisting of a S_n and ground-state pair. (B) Pooling of one S_1 and one S_n excitation, yielding a system consisting of an ion and ground-state pair. The excess energy above the ion state is converted to heat. Eventually, recombination of an ion (with an electron or negative ion) to yield a ground-state neutral. Pooling reactions of matrix excited states are key steps in energy concentration and ionisation.^{17, 18}

4.1.3 Aims of the Chapter

In the previous chapter, the commercial DIOS target, the QuickMass target and various rough and smooth SALDI surfaces have been investigated. Their surface morphology, chemical nature and cleaning and modification methods have been discussed. The surface characteristics that are important in affecting or enhancing the LDI activity or performance have been determined. There are still questions that remain unanswered. For example, how does the LDI approach compare to MALDI, what type of compounds can be detected by the matrix-free technique? How are ions formed on these LDI substrates? Do physical and/or chemical changes occur to the surface after the substrates are used for LDI? How is laser energy transferred to the analyte via the substrate and the apparent requirement for nanostructures on a semiconductor surface? Can we find out the possible reasons for the inconsistent reports in literature? This chapter is dedicated to answering these questions. Experiments are designed to verify the propositions reported previously in literature with the aim to make an impartial conclusion.

4.1.4 Approaches toward Achieving the Objectives:

To achieve the objectives, the questions will be approached from three different angles. Typical experimental conditions and instrumental settings have been given in section 2.4.

1. *By Laser Mass Spectrometry*: Unlike previous studies, which focus on a small selection of compound classes, mass spectra are acquired using a wide variety of biological related compounds, including peptides, amino acids, amines, organic acids, polysaccharides, steroids, alkaloids and even inorganic ions. It is the first time in a single study, the detection capability of the DIOS approach and so its ionic reaction is fully evaluated.

2. *At Different Pressures and Ion Optic*: In addition, the matrix-free method is evaluated under three different MALDI systems. Unless stated otherwise, the LDI spectra presented in this chapter are acquired on an ultra-high vacuum (chamber pressure 10^{-7} Torr) MALDI reflector time-of-flight (MALDI-ToF) mass spectrometer and is limited to positive ion mode. A newly acquired MALDI quadrupole time-of-flight (MALDI Q-ToF) system has subsequently replaced the MALDI-ToF position, allowing the investigation to be performed in both positive and negative ion mode. The vacuum chamber of MALDI interface is operated at low vacuum pressure (10^{-2} - 10^{-3} Torr). The third system, atmospheric pressure MALDI quadrupole linear ion trap (AP-MALDI-QqLIT) has also been employed. The investigation assist us to verify whether different MALDI system will lead to different LDI activity, and if so, to determine whether this could a possible cause to the inconsistency reported in literature.

3. *Surface Chemical Imaging Technologies*: For the first time, XPS and SIMS chemical imaging techniques are employed to investigate the chemical change to the SALDI surface due to laser modification or ablation, and for the first time, a complete picture will be revealed.

4.2 Results

4.2.1 Comparison of MALDI and DIOS

One of the disadvantages of the conventional MALDI technique is its poor performance toward molecules smaller than m/z 700 due to the production of a large amount of background interferences from the matrix. The effect of which is demonstrated in Figure 4-9. Matrix ions suppress the ionisation of small molecules and the interferences obscure the detection of small molecules in this region. However, the use of DIOS without the admixture of matrix allows efficient detection of the ion signals in the low mass region.

Secondly, selection of matrix is critical to the analyte of interest. The use of α -CHCA matrix is most commonly used for peptides and proteins analysis in MALDI under positive mode and may be less suitable under negative mode. This is demonstrated in Figure 4-10. The ion signals compared to that of DIOS were relatively weak and the spectrum was dominated by the ion peaks of α -CHCA matrix ($[M-H]^-$ at m/z 188 and $[M-COOH]^-$ at m/z 144) used and a number of matrix clusters.

The above spectra were generated by an electrospray calibrant solution (Agilent Technology), which contains a mixture of trimethylaminoacetic acid (betaine) perfluoroalkylphosphazenes and trifluoroacetic acid ammonium salt. (Table 4-2) The expected (reference masses) and observed mass peaks and their intensities are summarised in Table 4-3 and Table 4-4 under positive and negative mode. The expected peaks are provided by manufacturers based on data acquired using direct injection ESI-MS and has been verified using the Q-ToF system used in this study. Under the ESI condition, trimethylaminoacetic acid was detected as $[M+H]^+$, m/z 118 and trifluoroacetic acid as $[M-H]^-$, m/z 112. Whereas perfluoroalkylphosphazenes form predominately adduct ions with acetate and trifluoroacetate were detected as either mono-acetate adducts and trifluoroacetate-acetate adducts under positive and negative mode, respectively.

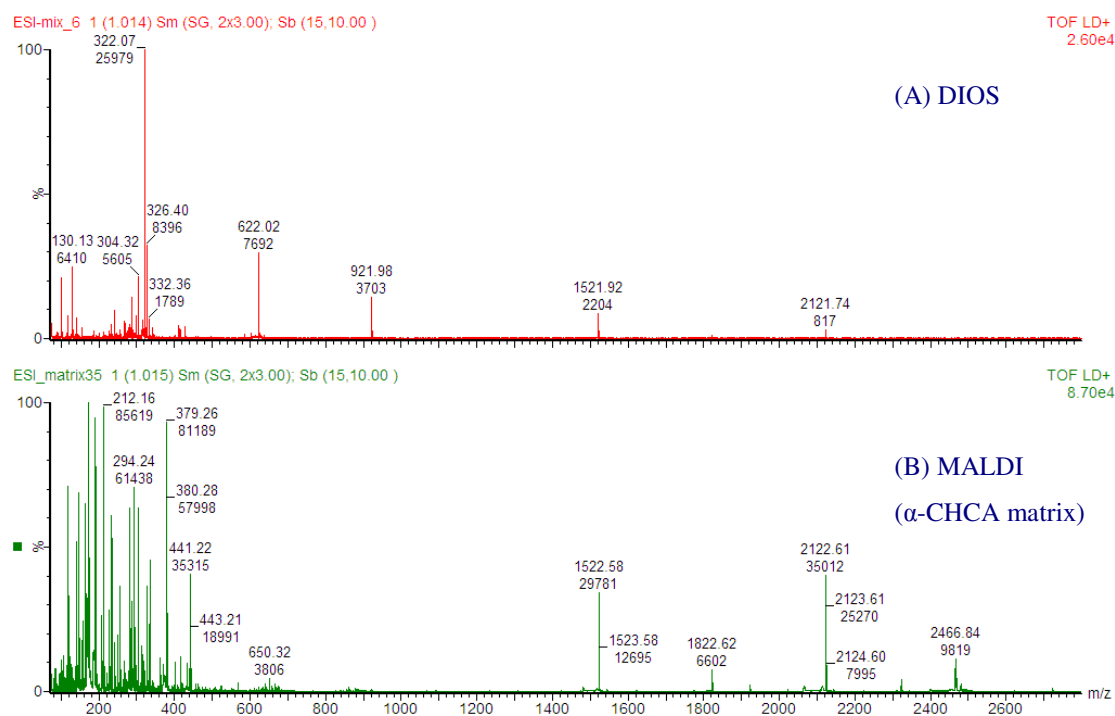


Figure 4-9 Positive ion mass spectra of ESI tuning mixture: (A) DIOS and (B) MALDI using α -CHCA matrix. The low mass region was obscured by matrix cluster ions. However, ions in the higher mass region are more effectively detected using MALDI. Spectra were acquired on MALDI-ToF system.

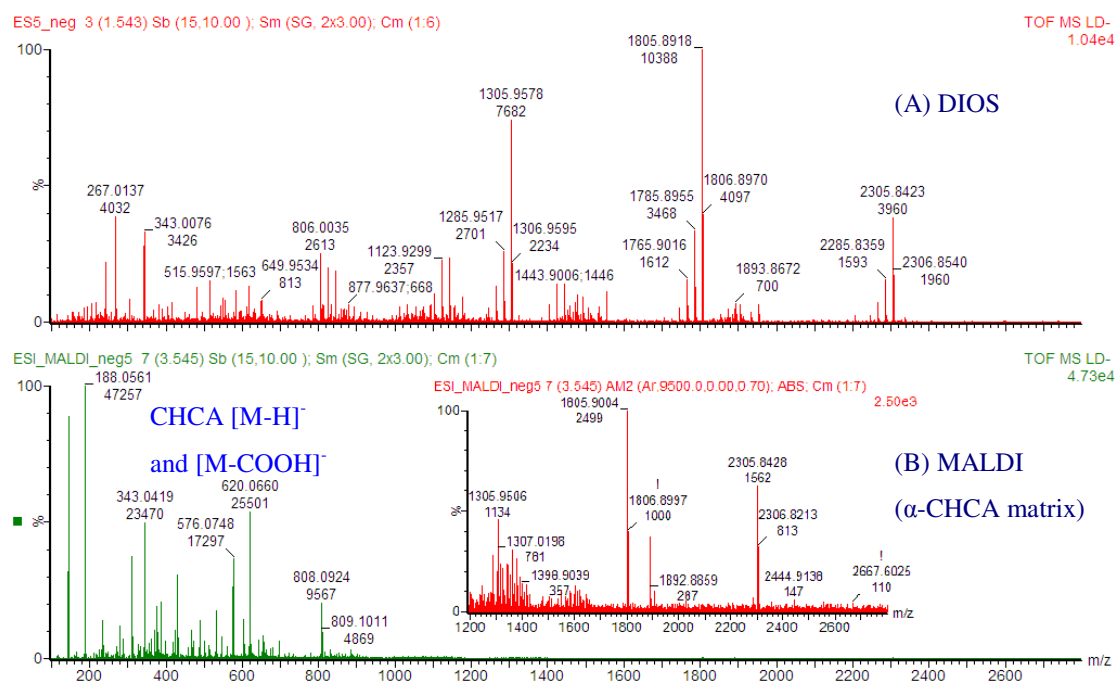


Figure 4-10 Negative ion mass spectra of ESI tuning mixture: (A) DIOS and (B) MALDI using α -CHCA matrix. Insert displaces the detected peak in the higher mass region – centroid and background subtracted to highlight the ion peaks. Spectra were acquired on MALDI Q-ToF system.

Table 4-2 List of substances, their chemical formulae and their exact masses in the Agilent ESI tuning mix.

| <i>Substance</i> | <i>Chemical formula</i> | <i>Exact mass (amu)</i> |
|--|--|-------------------------|
| trifluoroacetic acid | C ₂ HF ₃ O ₂ | 113.9929 |
| betaine | C ₅ H ₁₁ NO ₂ | 117.0790 |
| hexamethoxyphosphazene | C ₆ H ₁₈ NO ₆ P ₂ | 262.0609 |
| hexakis(2,2-difluoroethoxy)phosphazene | C ₁₂ H ₁₈ F ₁₂ NO ₆ P ₂ | 562.0418 |
| Hexakis(1H,1H,3H-tetrafluoropropoxy)phosphazene | C ₁₈ H ₁₈ F ₂₄ NO ₆ P ₂ | 862.0226 |
| hexakis(1H,1H,5H-octafluoropentoxy)phosphazene | C ₃₀ H ₁₈ F ₄₈ NO ₆ P ₂ | 1461.9843 |
| hexakis(1H,1H,7H-dodecafluoroheptoxy)phosphazene | C ₄₂ H ₁₈ F ₇₂ NO ₆ P ₂ | 2061.9460 |
| hexakis(1H,1H,9H-perfluorononyloxy)phosphazene | C ₅₄ H ₁₈ F ₉₆ NO ₆ P ₂ | 2661.9076 |
| tris(heptafluoropropyl)-S-triazine | C ₁₂ F ₂₁ N ₃ | 584.9757 |

Table 4-3 Expected and detected mass peaks of electrospray calibrant solution using DIOS and MALDI under positive mode, derived from Figure 4-9.

| <i>Mass</i> | <i>Expected (ESI) (m/z)</i> | <i>DIOS (m/z)</i> | <i>Count</i> | <i>MALDI (m/z)</i> | <i>Count</i> |
|-------------|-----------------------------|-------------------|--------------|--------------------|--------------|
| 1 | 118.09 | 118.09 | 2005 | 118.19 | 61858 |
| 2 | 322.05 | 322.07 | 25979 | 322.24 | 2581 |
| 3 | 622.03 | 622.02 | 7692 | 622.31 | 1469 |
| 4 | 922.01 | 921.98 | 3703 | 922.39 | 650 |
| 5 | 1521.97 | 1521.92 | 2204 | 1522.58 | 29781 |
| 6 | 2121.93 | 2121.74 | 817 | 2122.61 | 35012 |
| 7 | 2721.89 | × | - | 2722.50 | 823 |

Table 4-4 Expected and detected mass peaks of electrospray calibrant solution using DIOS and MALDI under negative mode, derived from Figure 4-10.

| <i>Mass</i> | <i>Expected (ESI) (m/z)</i> | <i>DIOS</i> | <i>MALDI</i> | <i>Detected in DIOS (m/z)</i> | <i>Detected in MALDI (m/z)</i> |
|-------------|-----------------------------|-------------|--------------|-------------------------------|--------------------------------|
| 1 | 112.99 | ✓ | ✓ | 1305.70 | 1305.69 |
| 2 | 431.98 | × | × | 1805.55 | 1805.54 |
| 3 | 601.98 | × | × | 2305.39 | 2305.38 |
| 4 | 1033.99 | × | × | | |
| 5 | 1633.95 | × | × | | |
| 6 | 2233.91 | × | × | | |
| 7 | 2833.87 | × | × | | |

Under the positive mode (Table 4-3), all the expected ions were obtained both in DIOS and MALDI. The intensities of ion peaks below m/z 1000 observed in DIOS were generally higher relative to that in MALDI (peaks located at m/z 322, 622 and 922). On contrary, opposite was true for the ion peaks larger than m/z 1000 (peaks located at m/z 1521, 2121 and 2721). Furthermore, the ion peaks obtained in MALDI shifted slightly to a higher m/z value when mass calibration was carried out using a DIOS substrate. Similarly, when the mass calibration was carried out using MALDI with matrix, the ion peaks of DIOS was slightly shifted to a lower m/z value. The slightly shift of the m/z value is possibly related to the thickness of the target and this causes a mass shift measured by the ToF mass analyser.

Under the negative mode (Table 4-4), almost a completely different set of ions was detected in DIOS and MALDI relative to the ESI-MS and the ions observed were likely fragment ions. This suggests that in ESI-MS, adduct formation with acetate and trifluoroacetate is favourable, whereas fragmentation seems to be the predominating process in LDI-MS. This observation implies that the DIOS and MALDI mechanism may be more closely similar but is quite different from that of ESI. Peak shifting as drastic as in ToF system was not observed because of the decoupling of the ion source from the mass analyser in Q-ToF system.

To look into this matter further, alternatively we may have a closer look to the ion yield of the peptide in the mid-mass range. The peptide sequencing standard is used as an example here. This peptide is often used for instrument testing and is the largest peptide standard used in this study because we focus our effort into advancing the method into analysing molecules below 1000 Da. Figure 4-11 shows the spectra generated by MALDI using α -CHCA matrix and fluoro-silane modified DIOS target. The S/N measured using DIOS was ~ 30 , whereas in MALDI the S/N was over 100. Without the matrix assistance, similar to the above observations, the S/N obtained in DIOS was lower. The laser used has not been optimised for MALDI and a better S/N was obtained using higher energy (result not shown). Having said that, though DIOS is less sensitive than MALDI in peptides detection, no other matrix-free substrate in this study could actually detect the peptide in this given concentration. In this case, mass calibration was carried using MALDI. Similarly, the mass peak detected in DIOS is also slightly shifted to a lower m/z value.

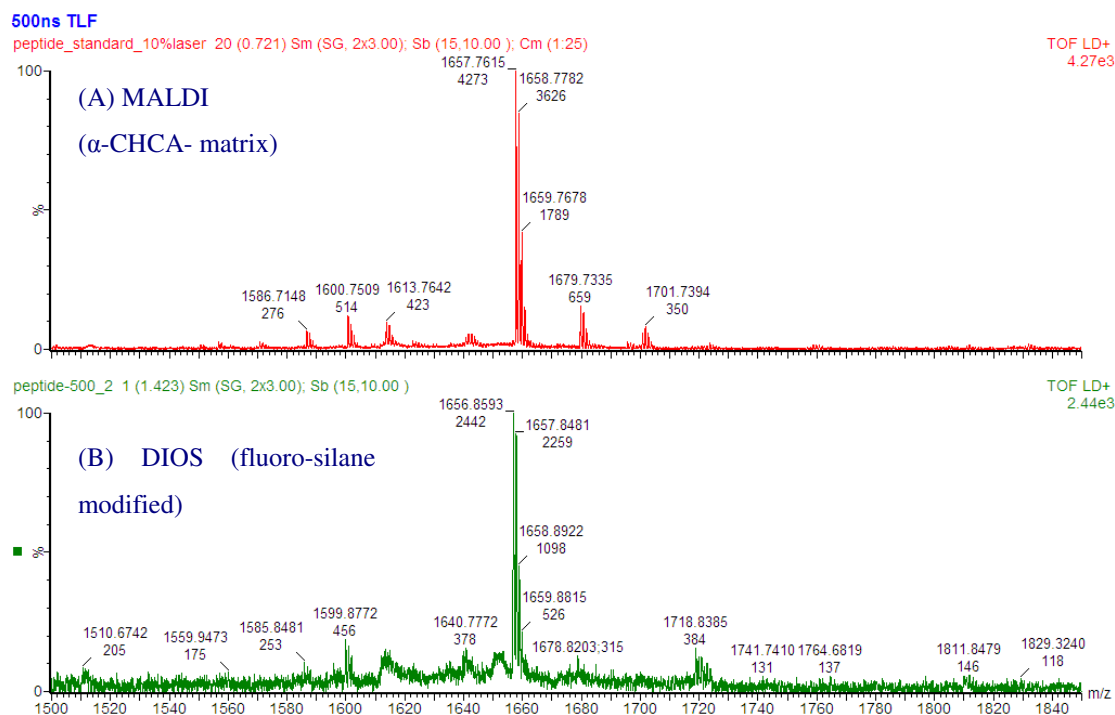


Figure 4-11 Positive ion mass spectra of peptide sequencing standard (Tyr-Ala-Glu-Gly-Asp-Val-His-Ala-Thr-Ser-Lys-Pro-Ala-Arg-Arg, molecular weight 1657). (A) MALDI using α -CHCA matrix and (B) fluoro-silane modified DIOS. Concentration of the sample was in nM.

These observations can be rationalised as follows. The presence of matrix interferences suppressed the detection of ion signal of smaller molecules lower than m/z 1000. Since no matrix was added in DIOS and the ion suppression effect was eliminated and thus the ion peaks intensities were higher in DIOS in this region. However, without the matrix bringing the larger molecules into vacuum, the ion yield in the mass region higher than m/z 1000 was lower compared to MALDI. Although α -CHCA matrix can be used in negative mode, due to its acid nature, its use is not appropriate in the negative ion mode.¹⁹ For comparison purpose, a basic matrix, such as 9-aminoacridine (9AA) could be used instead.^{20, 21}

A reviewer has also pointed out that betaine might have caused an additional suppression effect. In a separated study carried out by LC-ESI-MS, a high concentration of betaine strongly suppresses ion formation of other compounds in a complex biological mixture. The suppression effect is because of the increased liquid conductivity from the charged species in ESI condition. However, increased conductivity would not normally lead to ion suppression in LDI condition, but if it were the case, this might be caused by ion-pairing effect.

4.2.2 Detection of Peptides Using DIOS Technique

A key use of the MALDI technique in biomedical research is the detection of intact proteins or peptides molecules. However, there are some differences in the MALDI spectra due to the instrumental factors in terms of ion yield or sensitivity. Examples reported in literature include vacuum and atmospheric pressure interface,²² laser alignment between MALDI systems,²³ and the design of the detector.¹⁹ MALDI also has strong dependence on the selection of matrix and sample preparation technique used. Since the DIOS technique has been applied in proteomics,^{24, 25} and given that the matrix-free technique is matrix independent, it would be interesting to consider the use of DIOS in detection for peptides in the low mass range, and to determine any significant differences in the DIOS spectra or the LDI performance as a result of different MALDI systems.

For a number of peptides, protonated molecules $[M+H]^+$ normally dominate the DIOS spectra. Peptides such as bradykinin and angiotensin are detected with good sensitivity. (Figure 4-12) However, this does not apply to all peptides studied.

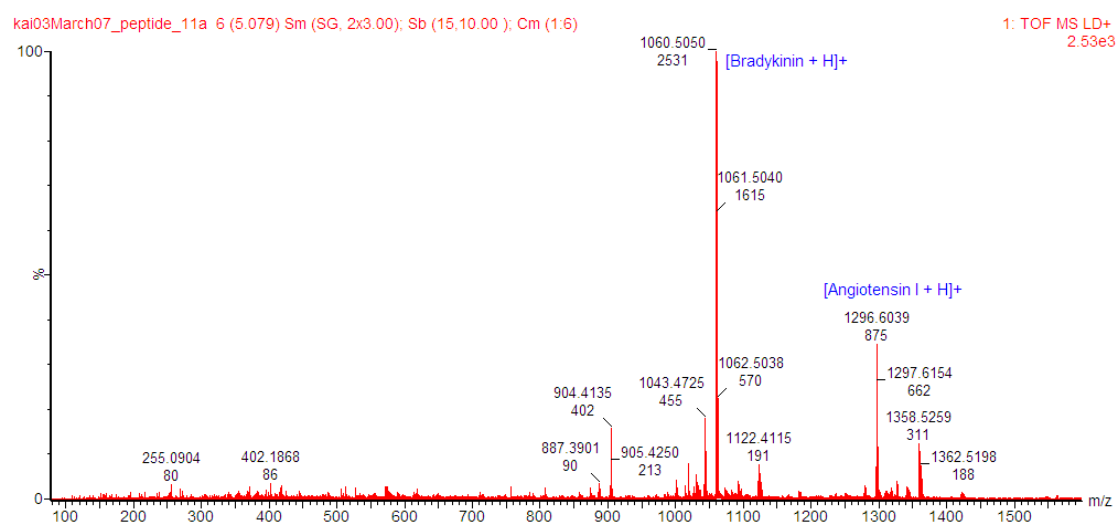


Figure 4-12 Positive ion DIOS mass spectrum of 10 μ M bradykinin and angiotensin I acquired on MALDI Q-ToF system.

The spectra of synthetic peptides, polyglycines, polyalanines and polyphenylalanines, are dominated by their salt adducts and salt-bridged cationised dimers and/or trimers. (Figure 4-13) Additionally, it appears that the increasing chain length has an effect toward the ion yield of protonated species, correlating to the increasing PA value. Addition of acidic modifier, acetic acid, does not improve sensitivity.

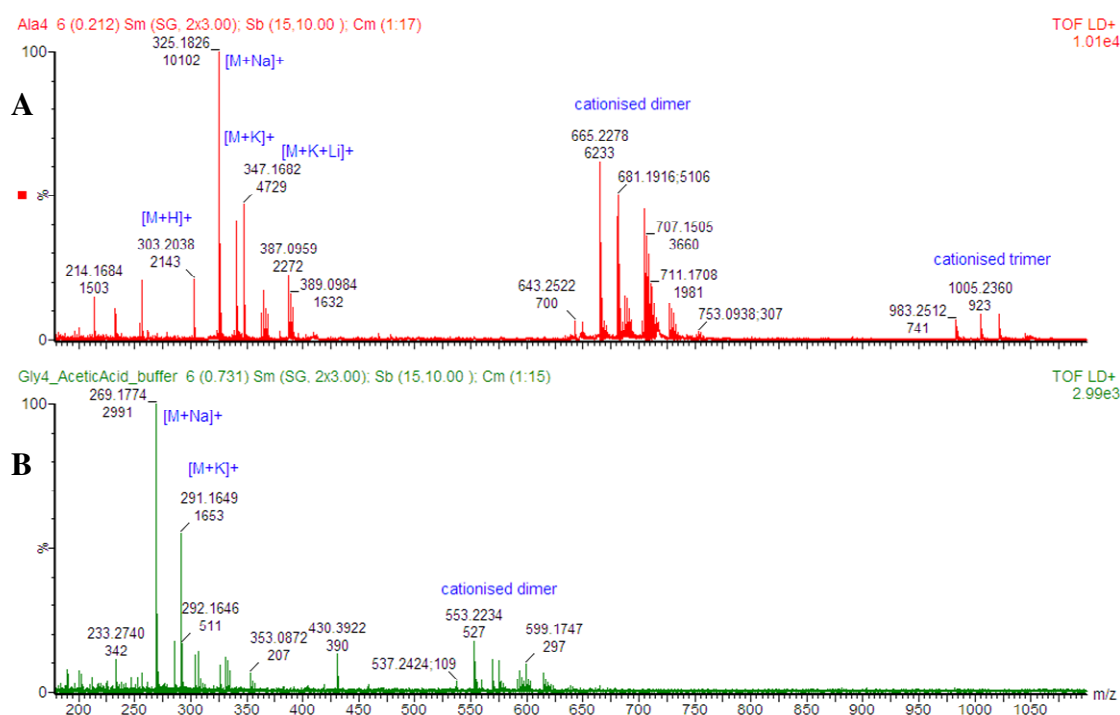


Figure 4-13 Positive ion DIOS mass spectra of synthetic peptides. (A) Ala₄ (no addition of acidic buffer), and (B) Gly₄ with addition of 1% acetic acid. Addition of acidic buffer reduces sensitivity. The dominant salt-bridged cationised dimer is in the form of [2M+Na+K-H]⁺.

The spectra of neuropeptides, leucine enkephalin, are quite interesting. Different responses were observed in the three systems used. The protonated molecules and the fragment ion at m/z 491 dominate the AP-DIOS mass spectrum (Figure 4-14) and the result is similar to that reported previously using gold nanoparticles/CHCA matrix obtained on an AP-MALDI system.²⁶ DIOS-ToF spectra are dominated by fragment ions at m/z 434 and 491. Protonated ion and sodium and potassium adducts are also seen. (Figure 4-15) In Q-ToF DIOS, the spectrum is dominated by fragment ion at m/z 326. (Figure 4-16) In all the vacuum systems, the peak intensity of the protonated molecule is lower than its fragment and its salt adducts. It can be concluded that the instrumental factors can significantly affect the relative intensity and distribution of the ionic species observed.

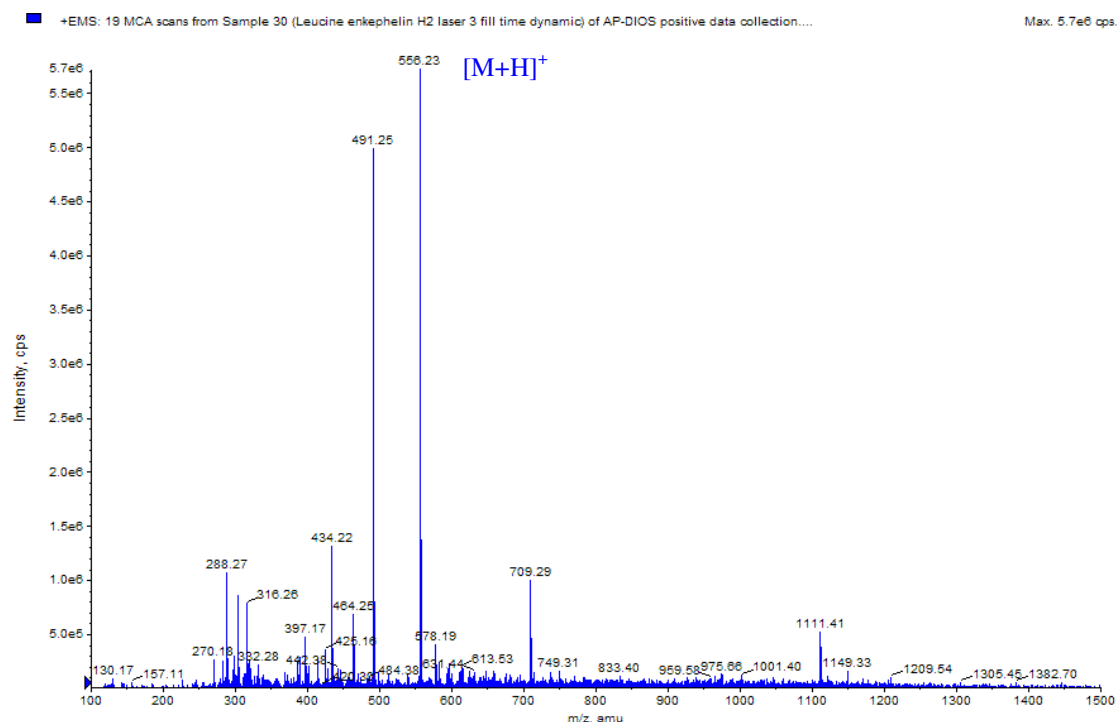


Figure 4-14 Positive ion DIOS mass spectrum of leucine enkephalin acquired on AP-DIOS-QqLIT system.

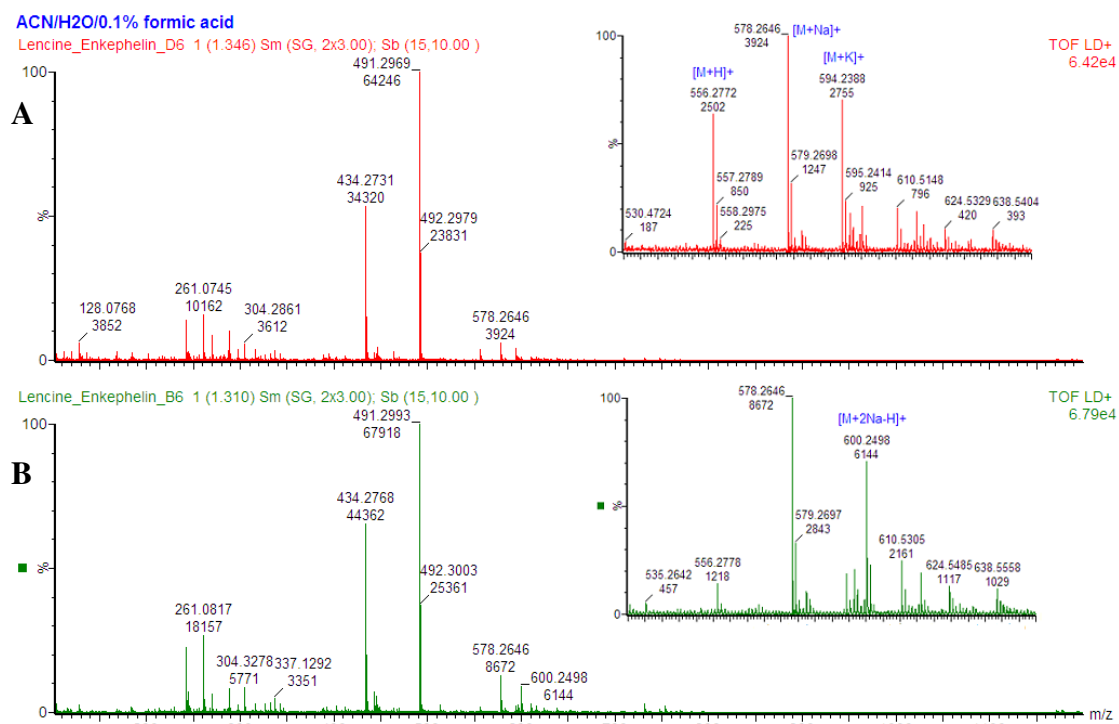


Figure 4-15 Positive ion DIOS mass spectra of leucine enkephalin on DIOS target acquired on ToF system. (A) Without addition of acidic buffer and (B) with addition of 0.1% formic acid. The peptide is weakly detected as protonated species, and the spectra are dominated by its fragment peaks and salt adducts peaks. Addition of acid buffer reduces the relative intensity of $[M+H]^+$ peak.

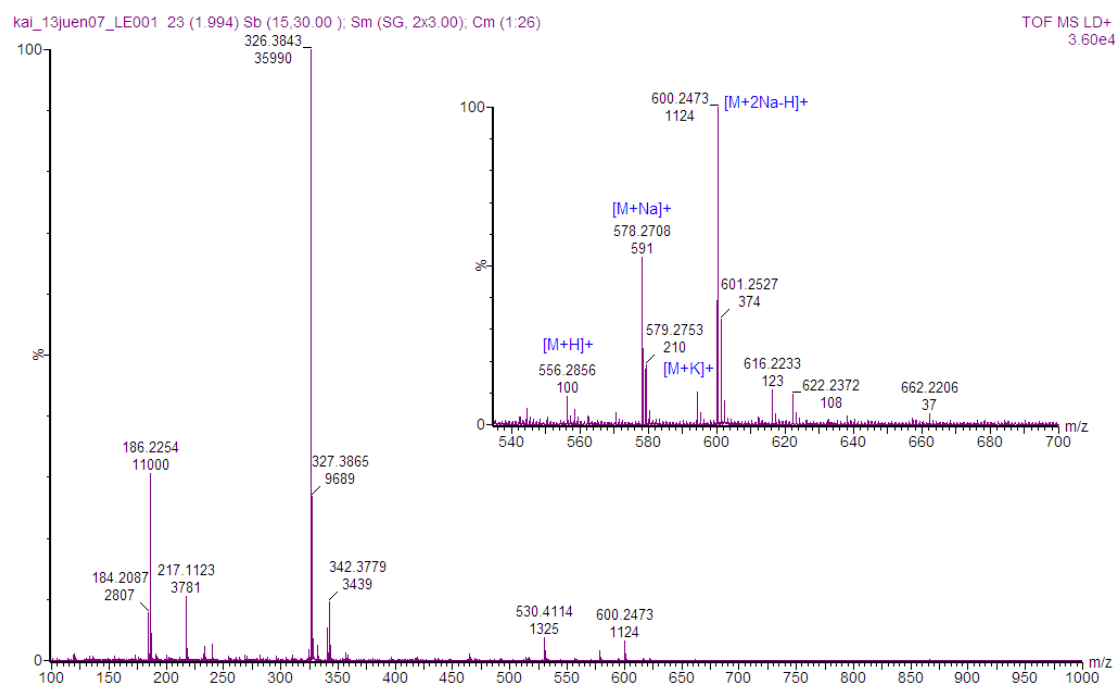


Figure 4-16 Positive ion DIOS mass spectrum of leucine enkephalin acquired on Q-ToF system.

4.2.3 Detection of Amino Acids

Amino acids are well-documented metabolites and their physiochemical properties are readily available. It is therefore possible to relate their physiochemical properties and their DIOS sensitivity to determine which chemical property has the greatest influence on the ion yield. Aqueous basicities (pKa), proton affinities (PA) and hydrophobicities of 20 common amino acids are listed in Table 4-5. The amino acids (all in L-form) were tested both individually and as a mixture under positive ion mode. Figure 4-17 shows a DIOS spectrum of a mixture of equal-molar amino acids dissolved in ACN/H₂O.

As reported by Vaidyanathan, *et al.*,²⁷ molecular ion of arginine and histidine dominated the spectrum and the remaining 18 amino acids were not detected effectively. Lysine, glutamine and phenylalanine could also be detected when they were analysed individually but the sensitivity was very low and could not be distinguished clearly from the background noise. Indeed, the mass region below m/z

200 of the mass spectra is often complicated with noise and this is a practical difficulty for compounds of low sensitivity.

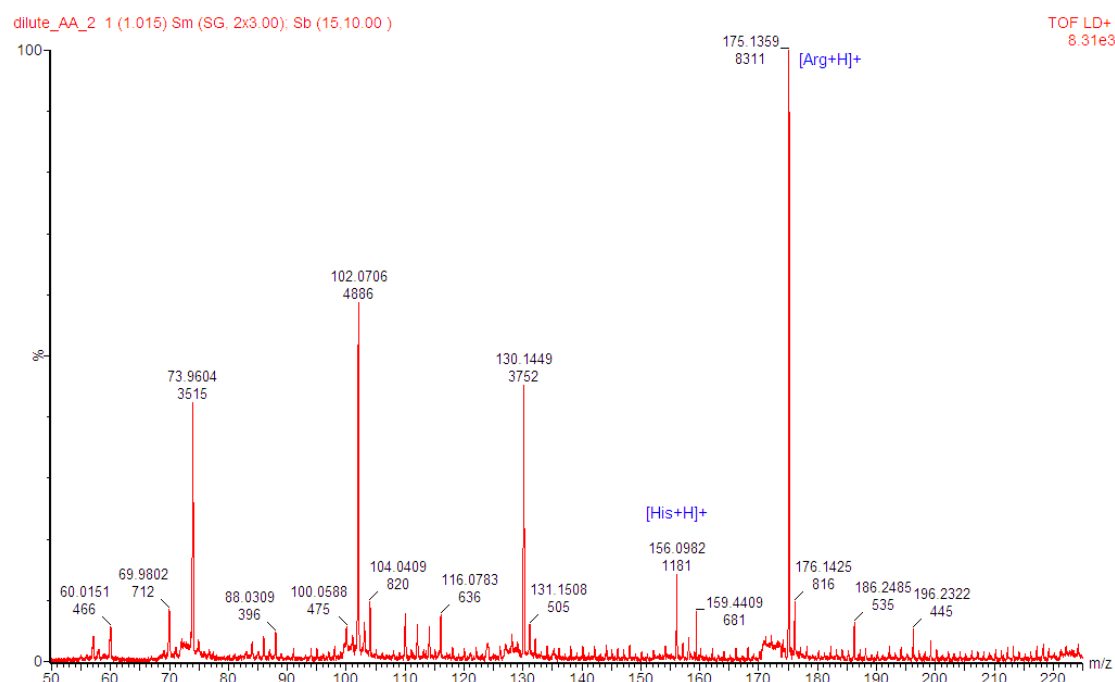


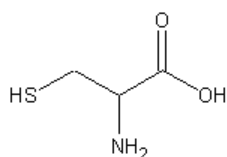
Figure 4-17 Positive ion DIOS mass spectrum of 20 amino acids mixture acquired on MALDI-ToF system. Molecular ion of arginine and histidine dominates the mass spectrum and the remaining 18 amino acids are either not detected as protonated species or difficult to distinguish from the noise. Peaks located at m/z 73, 102 and 130 are common contaminants and are believed originated from the solvent used. Strong “tailing” is observed with all the major ion peaks.

It has been proposed that for detection of protonated species, the pKa value of the analyte has to be larger than 4.⁷ All amino acids have an amino group of which the pKa value is larger than 4 and accordingly all should have been detected. Nevertheless, this does not seem to be applicable. Alternatively, if the pKa value of the side chain of the amino acid is considered, cysteine and tyrosine in addition to lysine, arginine and histidine should be detected in positive ion mode. Then again, this does not appear to be the case. The reason is that, although the side chains of cysteine and tyrosine, have high pKa values, they do not have a protonation site (nitrogen). In fact, it has been reported tyrosine (and phenylalanine) could only be well detected if it was derivatised to its (butyl) ester form²⁸ and cysteine cannot be detected in negative mode either.^{27, 29} This raises a question whether the pKa value is a relevant factor to SALDI or to DIOS.

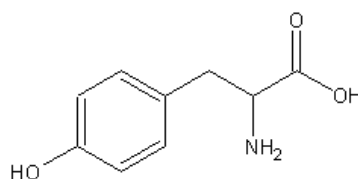
Table 4-5 Aqueous basicities, isoelectric points (pI), proton affinities (PA) and hydrophobicities (log P) of 20 most common amino acids.

| Amino acids | Exact mass | pKa | | | pI | PA/ kJmol ⁻¹ | Log P |
|---------------|------------|------|-----------------|------------|-------|-------------------------|-------|
| | | COOH | NH ₃ | side chain | | | |
| Alanine | 89.0477 | 2.35 | 9.87 | - | 6.00 | 901.6 | 0.616 |
| Arginine | 174.1117 | 2.01 | 9.04 | 12.48 | 10.76 | 1051.0 | 0 |
| Asparagine | 132.0535 | 2.02 | 8.80 | - | 5.41 | 929.0 | 0.236 |
| Aspartic acid | 133.0375 | 2.10 | 9.82 | 3.86 | 2.77 | 908.9 | 0.028 |
| Cysteine | 121.0197 | 2.05 | 10.25 | 8.00 | 5.07 | 903.2 | 0.68 |
| Glutamic acid | 147.0532 | 2.10 | 9.47 | 4.07 | 3.22 | 913.0 | 0.043 |
| Glutamine | 146.0691 | 2.17 | 9.13 | - | 5.65 | 937.8 | 0.251 |
| Glycine | 75.0320 | 2.35 | 9.78 | - | 5.97 | 886.5 | 0.501 |
| Histidine | 155.0695 | 1.77 | 9.18 | 6.10 | 7.59 | 988.0 | 0.165 |
| Isoleucine | 131.0946 | 2.32 | 9.76 | - | 6.02 | 917.4 | 0.943 |
| Leucine | 131.0946 | 2.33 | 9.74 | - | 5.98 | 914.6 | 0.943 |
| Lysine | 146.1055 | 2.18 | 8.95 | 10.53 | 9.74 | 996.0 | 0.283 |
| Methionine | 149.0510 | 2.28 | 9.21 | - | 5.74 | 935.4 | 0.738 |
| Phenylalanine | 165.0790 | 2.58 | 9.24 | - | 5.48 | 922.9 | 1 |
| Proline | 115.0633 | 2.00 | 10.60 | - | 6.30 | 920.5 | 0.711 |
| Serine | 105.0426 | 2.21 | 9.15 | - | 5.68 | 914.6 | 0.359 |
| Threonine | 119.0582 | 2.09 | 9.10 | - | 5.60 | 922.5 | 0.45 |
| Tryptophan | 204.0899 | 2.38 | 9.39 | - | 5.89 | 948.9 | 0.878 |
| Tyrosine | 181.0739 | 2.20 | 9.11 | 10.07 | 5.66 | 926.0 | 0.88 |
| Valine | 117.0790 | 2.29 | 9.72 | - | 5.96 | 910.6 | 0.825 |

- pKa and PI data obtained from the Michigan State University: Amino Acid pKa Values, <<http://www.cem.msu.edu/~cem252/sp97/ch24/ch24aa.html>> and the University of Calgary: Table of pKa and pI values, <<http://www.chem.ucalgary.ca/courses/351/Carey5th/Ch27/ch27-1-4-2.html>>
- PA data obtained from NIST Chemistry WebBook <<http://webbook.nist.gov/>>
- Hydrophobicity data obtained from the University of Texas: Hydrophobicity of the Physiological L-alpha-Amino Acids, <<http://psyche.uthct.edu/shaun/SBlack/aagrase.html>>. The hydrophobicities given are the "scaled" values from computational log (P) determinations by the "Small Fragment Approach". The equation used to scale raw log (P) values to the scaled values given is as follows: Scaled Parameters = (Raw Parameters + 2.061)/4.484.

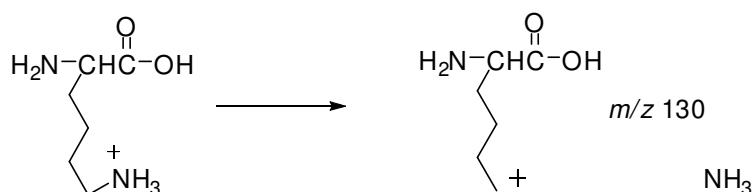


Cysteine



Tyrosine

On considering the PA values and LDI sensitivity of amino acids, PA values of arginine and histidine are high and explain why they were detected as molecular ions. In addition, their ion intensity is reflected by their respective PA value. Then again, lysine has a PA value larger than histidine and its protonated peak was not observed. It is possible that protonated lysine fragments to lose an NH_3 and the fragmented ions overlapped with a major contaminant peak at 130.



The less than satisfactory detection capability of DIOS toward amino acids could be improved by using a linear ToF mass analyser. Chen could detect arginine, tryptophan, histidine, glutamine and glycine (in the order of sensitivity correlating to the PA values of the amino acids) as $[\text{M}+\text{H}]^+$ ion using graphite, PSi substrates as well as smooth silicon wafer cooled to 130K.³⁰

A possible reason is related to the filtering effect of the reflector of the ToF system.³¹ This situation happens when metastable decomposition occurs in between the ion source and the detector. In linear ToF system, the intensity of a molecular ion signal does not reduce because the linear velocity of the fragmenting ion is conserved and the fragments formed are therefore detected at the same flight-time as their intact precursor.

However, if fragmentation occurs between the ion source and the reflector, the ions will be lost by the reflector due to their change in kinetic energy. Only fragments still having kinetic energies close to that of the precursor, such as $[\text{M}+\text{H}-\text{NH}_3]^+$ are transmitted due to the energy tolerance of the reflector and give rise to a “tailing” of the signal. (See Figure 4-17) Should it be the case, it would be an evidence that metastable decomposition of excited ionic species occurs during LDI and the design of the mass spectrometer or the ion optic has a significant influence to the ion distribution of the LDI spectra as discussed previously.

4.2.4 Detection of Basic Compounds

Basic compounds such as amines and nucleosides were analysed under positive ion mode and generally protonated molecules $[M+H]^+$ dominate the spectra. (Figure 4-18 to Figure 4-20). However, fragmentation and ion-molecular reactions are common. (Figure 4-21 to Figure 4-26) For many compounds tested, the fragmentation reaction follows a specific pattern. Fragmentation for amines mostly occurs at C-N bond, whereas loss of H_2O occurs at hydroxyl group. An exception is indole alkaloid, reserpine, which forms quasi-molecular ions $[M-H]^+$ due to its low ionisation energy. (Figure 4-26) The fragmentation and ion-molecular reactions cannot be completely prevented by using lower laser fluence or chemical modification and is consistent with the observation of Luo, *et al.*³²

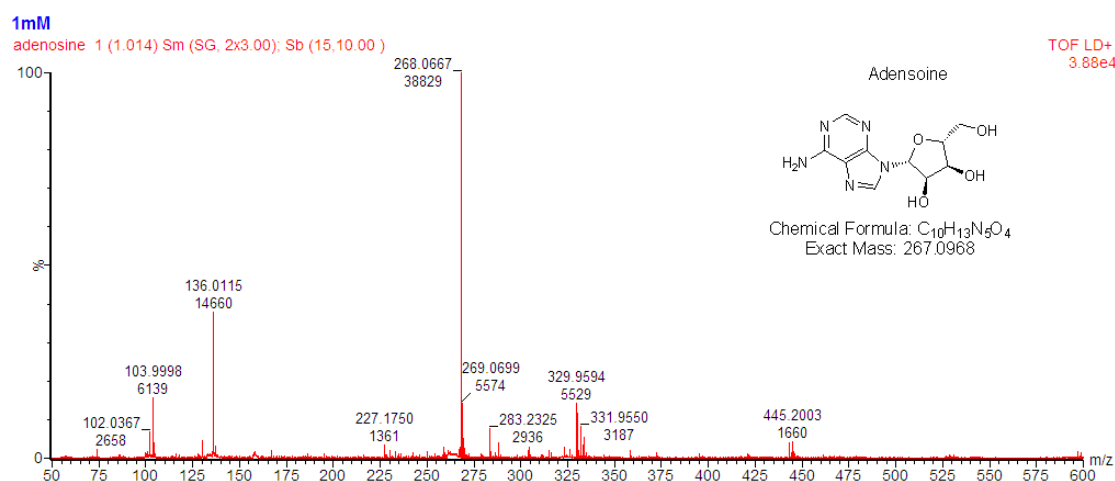


Figure 4-18 Positive ion DIOS mass spectrum of adenosine.

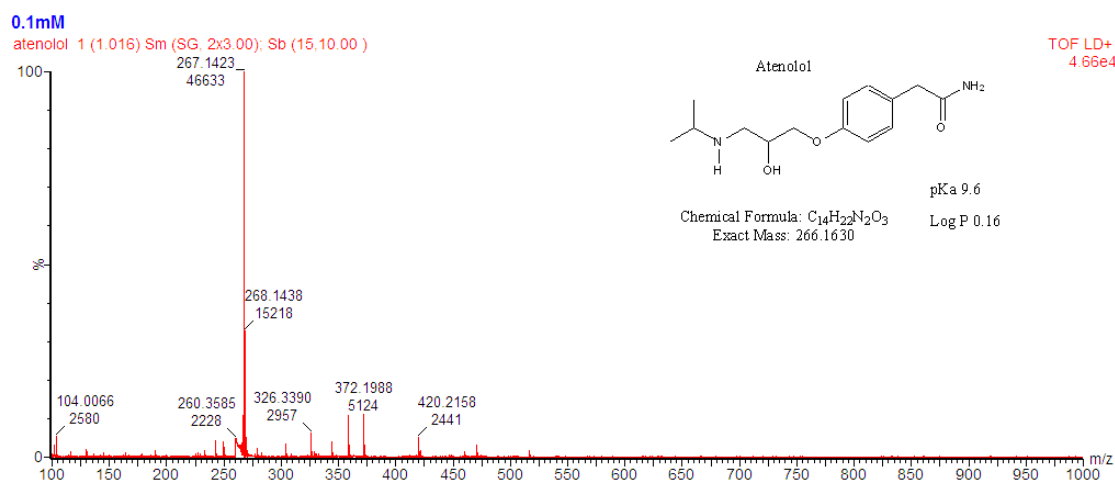


Figure 4-19 Positive ion DIOS mass spectrum of atenolol.

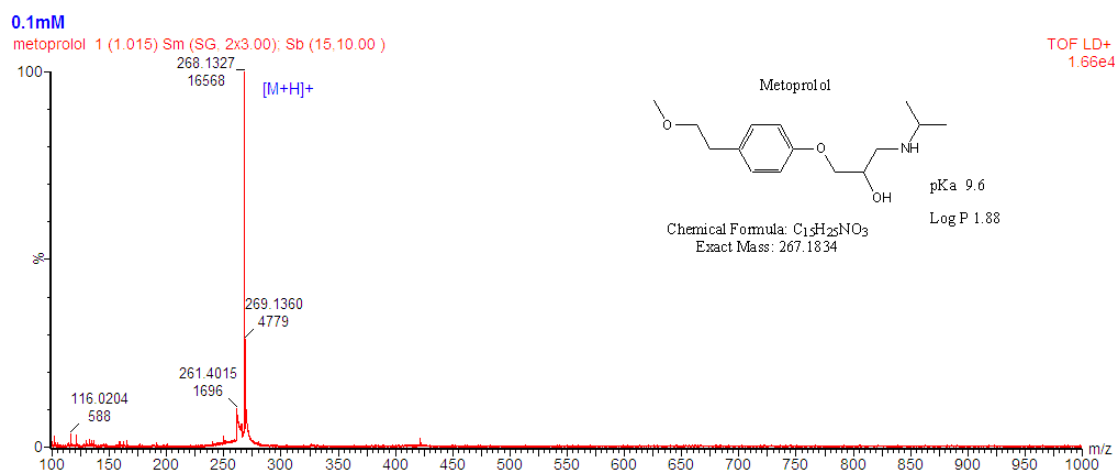


Figure 4-20 Positive ion DIOS mass spectrum of metoprolol.

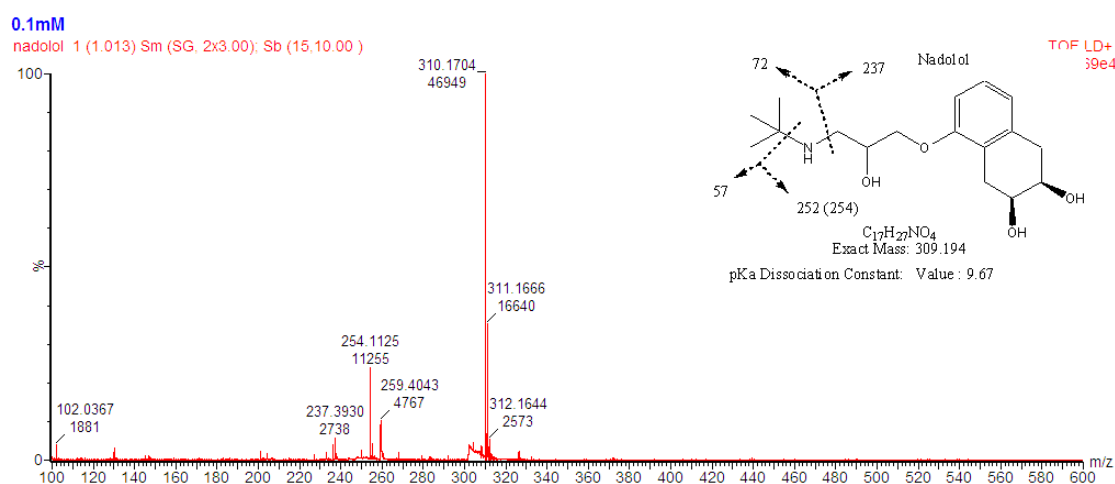


Figure 4-21 Positive ion DIOS mass spectrum of nadolol and proposed fragmentation pathway. Capture of two additional protons of C-N fragment leads to the peak located at m/z 254.

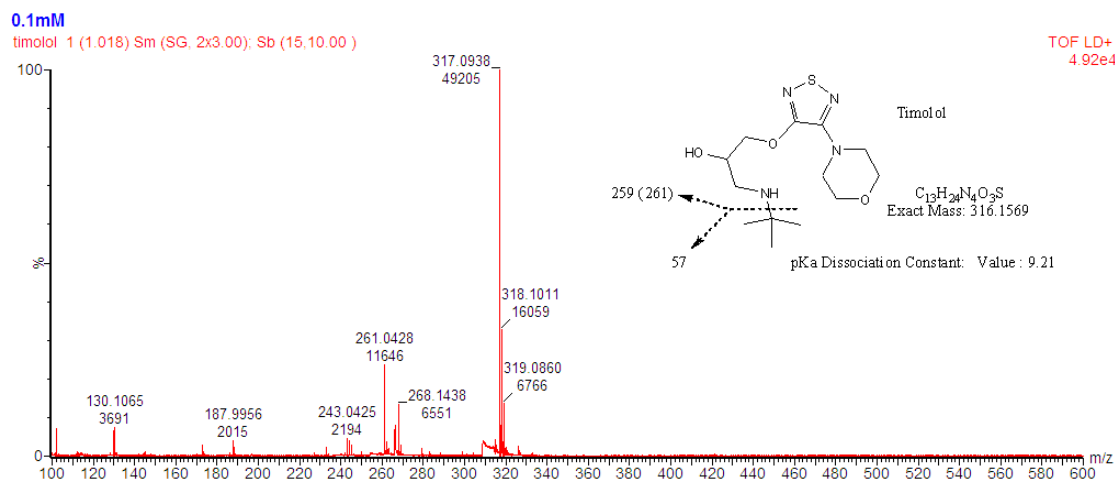


Figure 4-22 Positive ion DIOS mass spectrum of timolol and proposed fragmentation pathway. Capture of two additional protons of C-N fragment leads to the peak located at m/z 261.

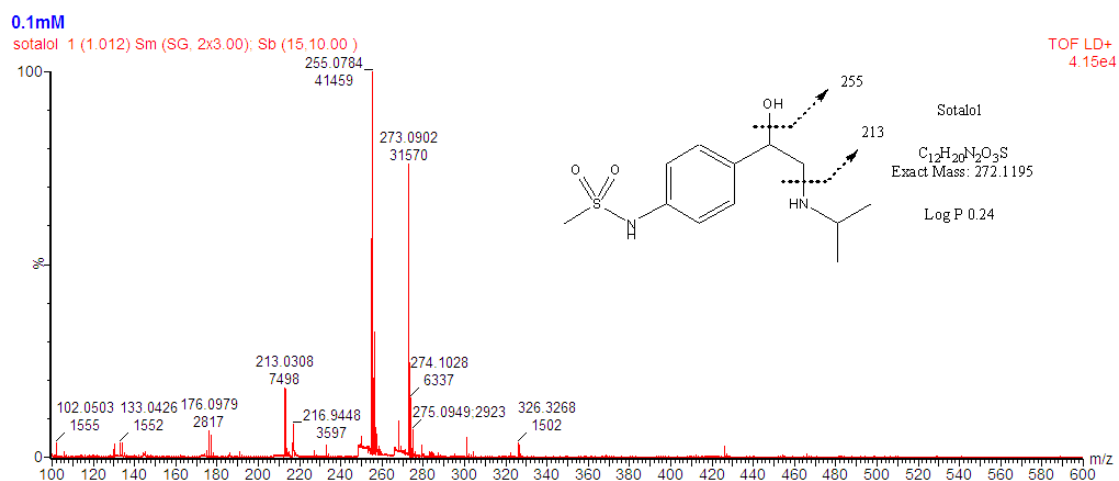


Figure 4-23 Positive ion DIOS mass spectrum of sotalol and proposed fragmentation pathway. Loss of water leads to the peak located at m/z 255. Fragmentation at C-N bond produces the peak located at m/z 213.

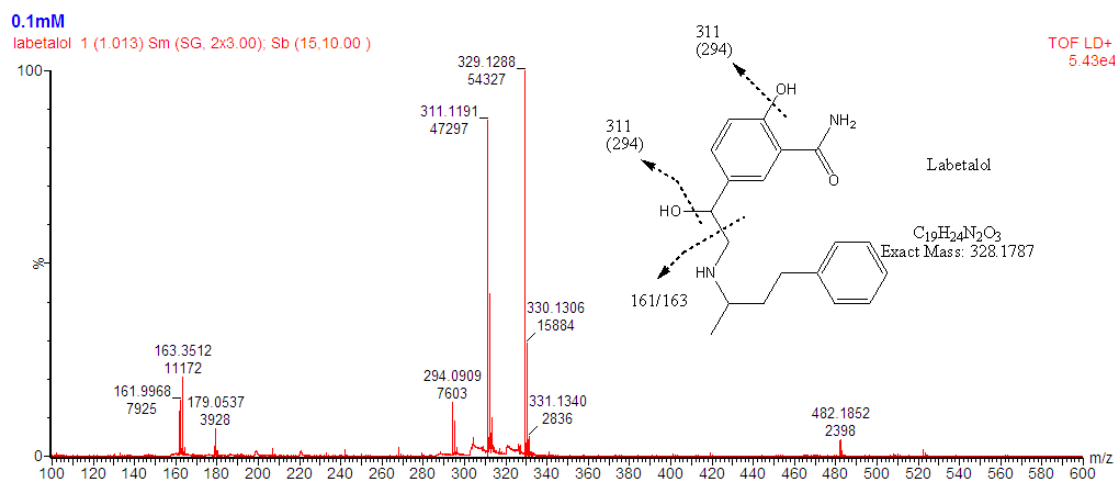


Figure 4-24 Positive ion DIOS spectrum of labetalol and proposed fragmentation pathway. Loss of water leads to the peak located at m/z 311. Loss of two waters lead to the peak located at m/z 294. Capture of two additional protons of C-N fragment leads to the peak located at m/z 163.

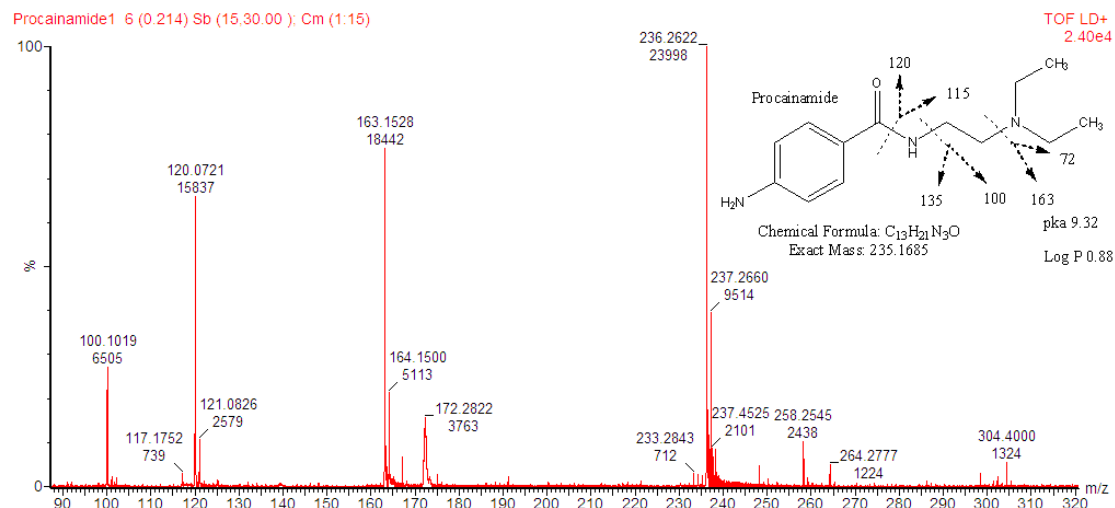


Figure 4-25 Positive ion DIOS mass spectrum of procainamide and proposed fragmentation pathway. Fragmentation reactions occur at three possible C-N sites. The molecular peak was located at m/z 236, and three other dominated fragment ions are located at m/z 163, 120 and 100.

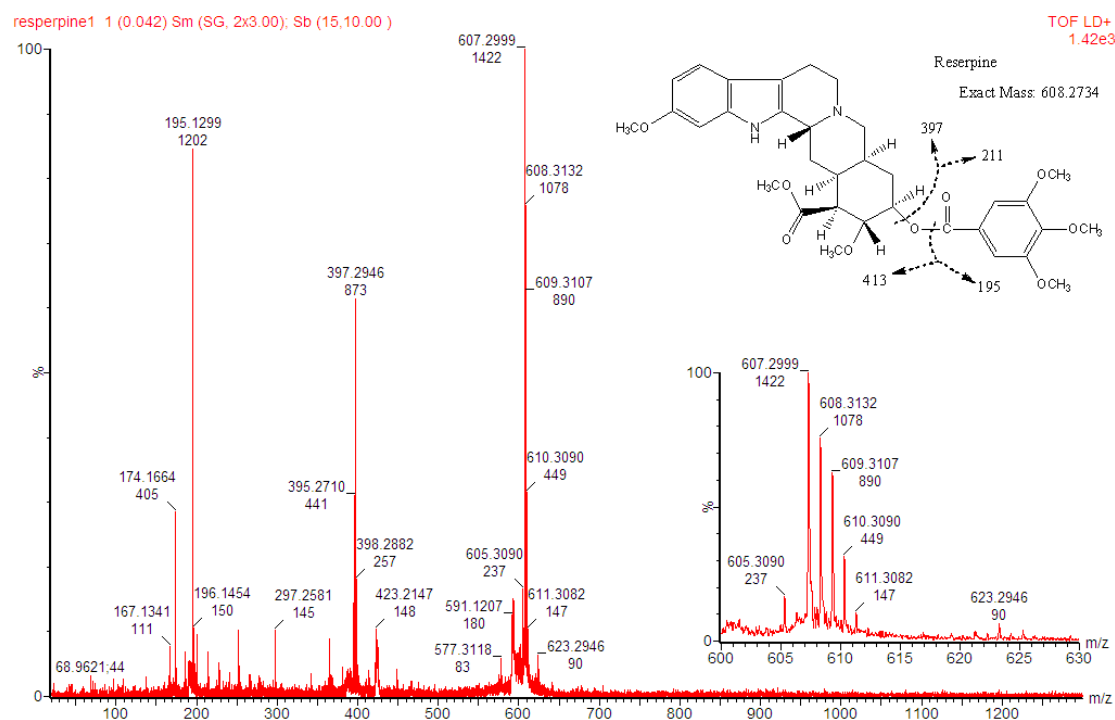


Figure 4-26 Positive ion DIOS mass spectrum of reserpine and proposed fragmentation pathway. Insert shows the magnified region between m/z 600 and 630. The observation of $[M-H]^+$ ions is related to its low ionisation energy.

4.2.5 Detection of Pre-charged Ions and UV Absorbing Compounds

Pre-charged compounds such as quaternary amines or compounds that absorb UV radiation can be directly desorbed or ionised and form M^+ and $[M+H]^+$ ion. (Figure 4-27 and Figure 4-28)

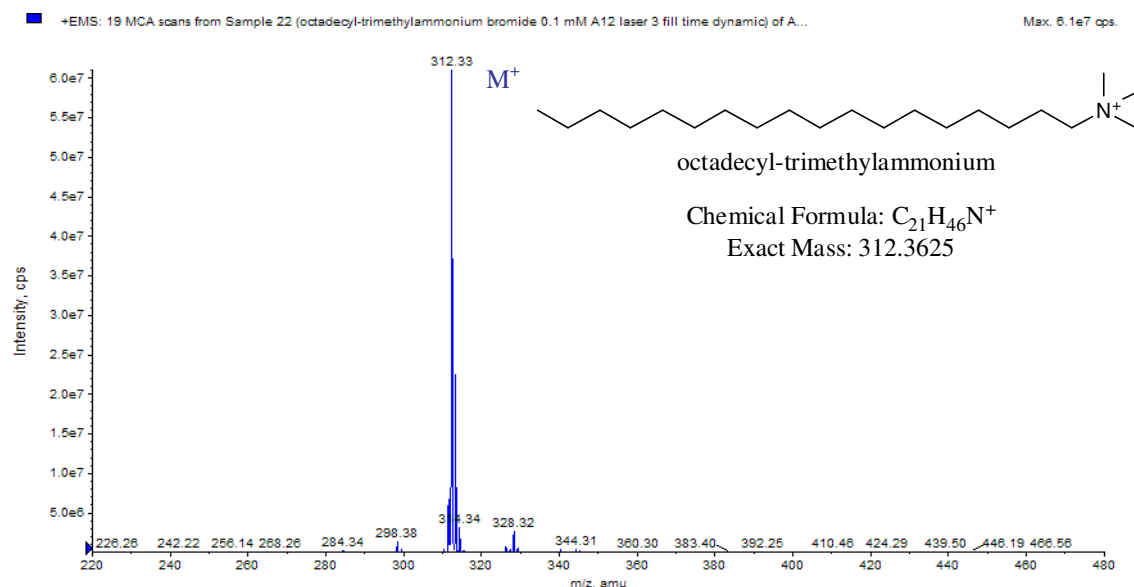


Figure 4-27 Positive ion DIOS mass spectrum of octadecyl-trimethylammonium bromide acquired on AP-MALDI-QqLIT system.

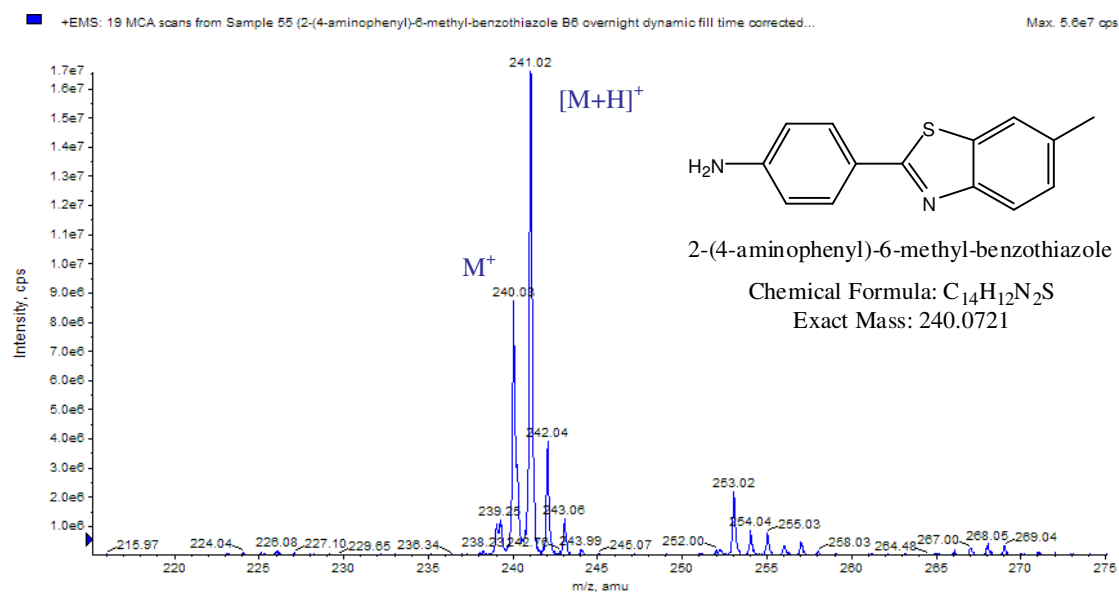


Figure 4-28 Positive ion DIOS mass spectrum of 2-(4-aminophenyl)-6-methyl-benzothiazole acquired on AP-MALDI-QqLIT system.

4.2.6 Detection of Amides and Saccharides

The DIOS spectra of a sulfonylurea drug, glyburide[†] are dominated by its sodium and potassium adducts and a variety of alkylation products. (Figure 4-29) It should be noted that the distribution of ions was irreproducible in this case, where the detection of glyburide relied on adducts formation and the control of salt presence in the sample solution or on the surface was difficult to control.

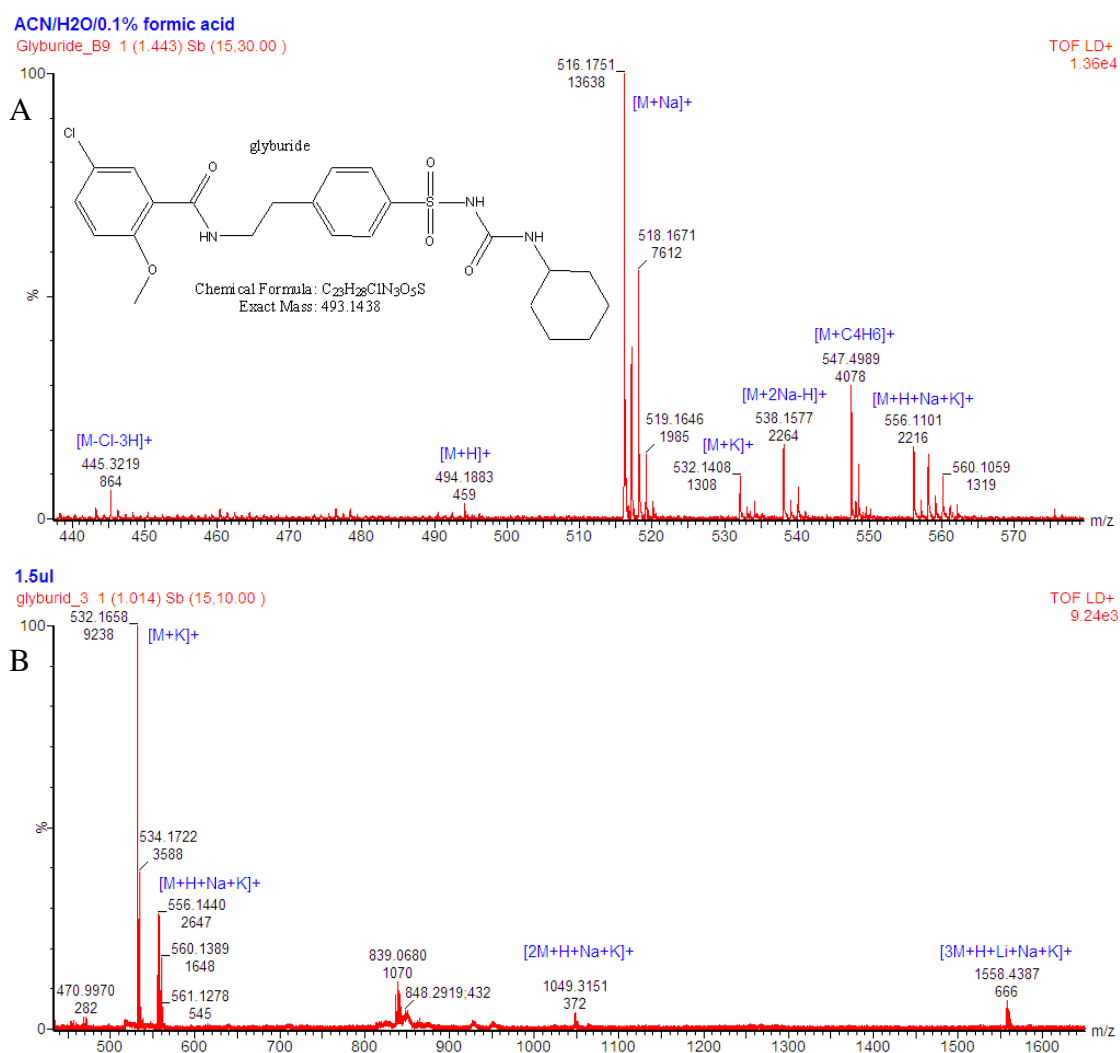


Figure 4-29 Positive ion DIOS mass spectrum of glyburide on (A) fluoro-silane modified DIOS target with addition of 0.1% formic acid and (B) on as-received DIOS with no addition of acid. Different ionic products were obtained in these cases.

[†] Glyburide is a class of compound called sulfonylurea and is used to control hyperglycaemia in type II diabetes mellitus.

Saccharides and oligosaccharides, as in MALDI, are effectively detected as salt adducts in positive mode. (Figure 4-30) Adding diluted sodium iodine solution to a saccharide-containing sample is one of the approaches to enhance adduct formation.³³ In this case, sodium hydroxide solution was added and was aimed to minimise ion suppression effect of salt. Furthermore, this approach also enhanced fragmentation as hydrolysis products (loss of monosaccharide units) and could aid the structural elucidation of polysaccharides.

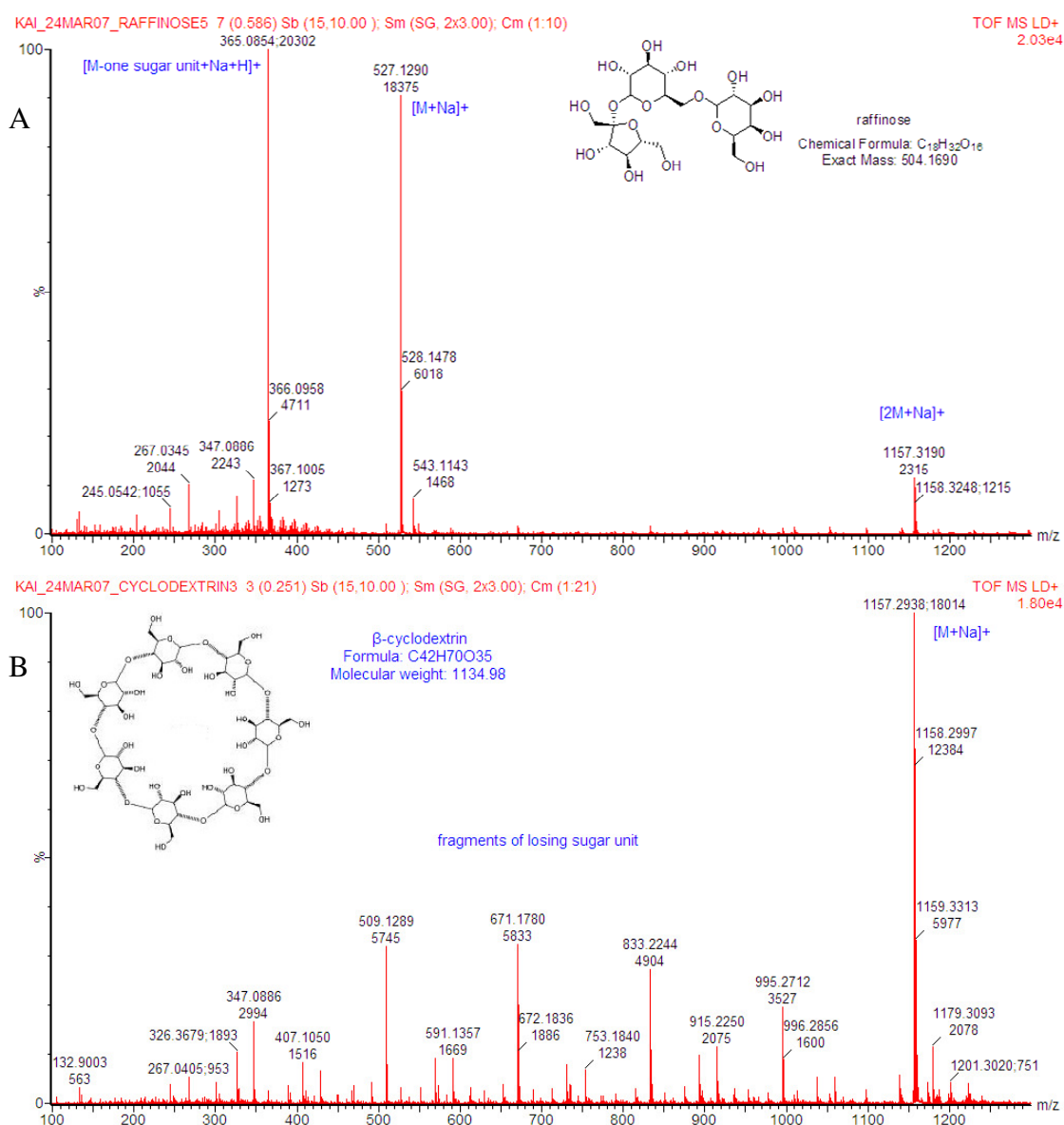


Figure 4-30 Positive ion DIOS mass spectrum of (A) 1 mM raffinose/sodium hydroxide (1:1) mixture and (B) 0.47 mM of β-cyclodextrin/sodium hydroxide (1:4) mixture. Data obtained on MALDI Q-ToF system using recycled DIOS target. The sensitivity significantly improved after the hydrophilicity of the surface is increased. The molar excess of hydroxide used in β-cyclodextrin mixture may account for a series of hydrolysis products observed.

4.2.7 Detection of Acidic Compounds

For small acidic compounds in the negative ion mode, the simplest form of ion is the deprotonated molecules, $[M-H]^-$. (Figure 4-31) The DIOS spectra of cholic acid[‡] and diflunisal have a good S/N and the deprotonated molecules dominate the spectra. However, this situation did not apply to every acidic compounds tested. On many occasions, the investigation of small acidic molecules in negative ion mode was either unsuccessful or the spectra had unsatisfactory S/N. It seems that the small acidic compounds that could be effectively detected as deprotonated molecules in negative ion mode must have a means of stabilising themselves – for instance, cholic acid has a steroid system, and diflunisal has an aromatic system and fluorine functional groups.

Flufenamic acid is an example of this situation. (Figure 4-32) The molecule contains a carboxylic acid, a secondary amine and a trifluoromethyl functional group. The positive spectrum of flufenamic acid is dominated by its fragment ion at m/z 264. The negative spectrum is dominated by the deprotonated molecules and the fragment ion at m/z 236. Cationised dimers were also observed at the higher mass range. The presence of amine group in flufenamic acid does not lead to protonated ion formation, fragment ions and possibly $[M-2H]^+$ ion at m/z 279 were detected in the positive spectrum. The formation of the deprotonated molecules observed in the negative ion spectrum correlates to the stabilisation effect introduced by the aromatic system and the $-CF_3$ group. Loss of a carboxylic acid group leads to the fragment ion observed. Indeed, fragmentation occurring by loss of H_2O ($-OH$) and CO_2 ($-COOH$) groups is quite common.

Nalidixic acid and naproxen are given here as further examples and they can be detected in positive and negative ion mode. (Figure 4-33 and Figure 4-34) Nalidixic acid is more effectively detected in negative mode, whereas the spectra of naproxen are dominated by its fragment ions in either positive or negative. A proposed scheme of the fragmentation pathways of nalidixic acid is given at Figure 4-35.

[‡] Cholic acid is a bile acid, metabolite of cholesterol.

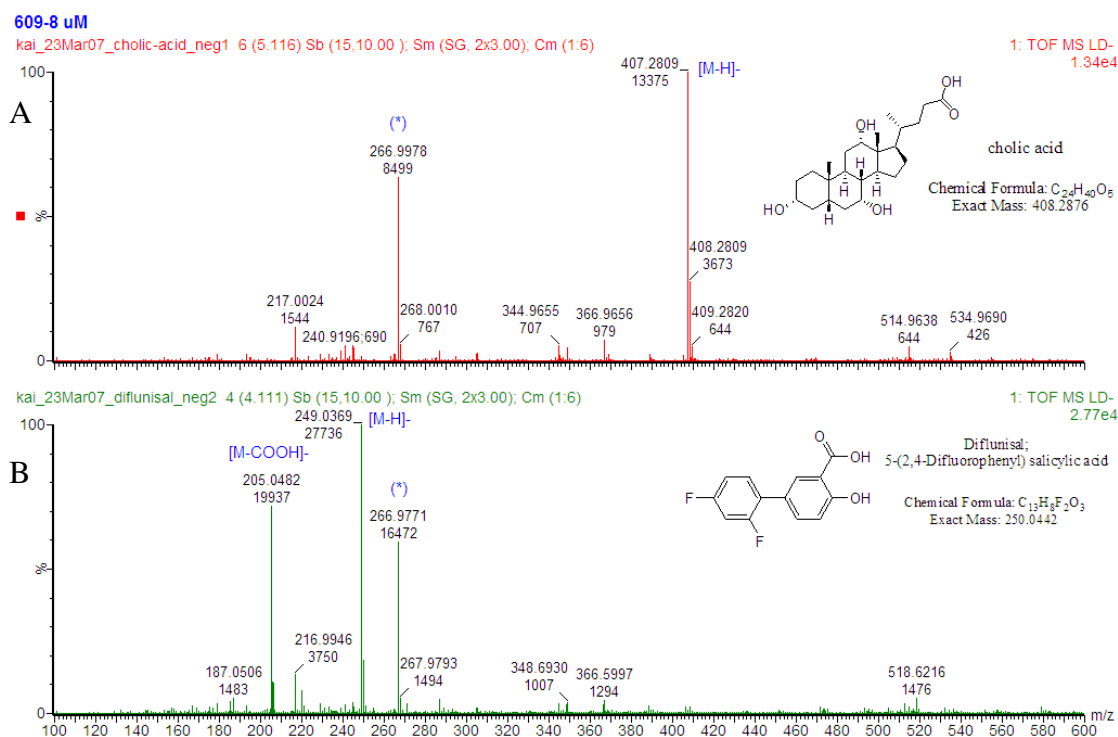


Figure 4-31 Negative ion DIOS mass spectra of (A) cholic acid (B) diflunisal acquired on MALDI Q-ToF system. Fragmentation of diflunisal occurs via loss of carboxylic acid group. Peak m/z 267 is a phosphate contaminant (determined by MS/MS).

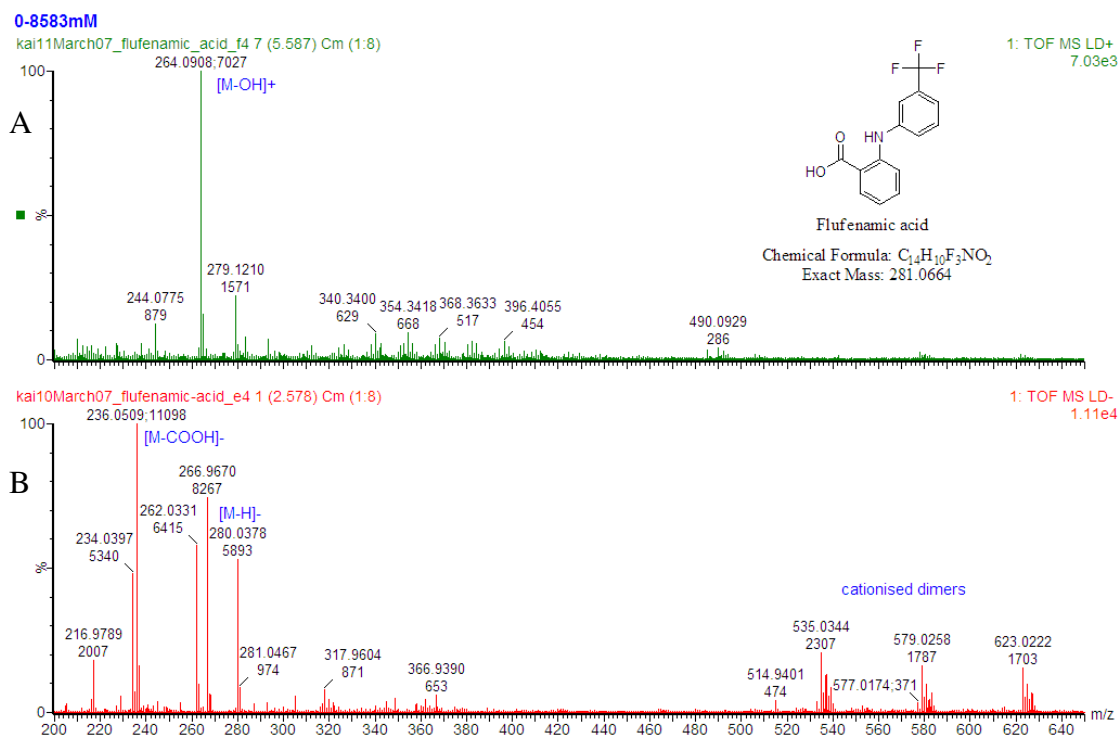


Figure 4-32 (A) Positive and (B) negative ion DIOS mass spectrum of flufenamic acid acquired on MALDI Q-ToF system. Fragmentation occurs via loss of H_2O (M-OH), m/z 264, and CO_2 (M-COOH), m/z 236, in carboxylic acid group.

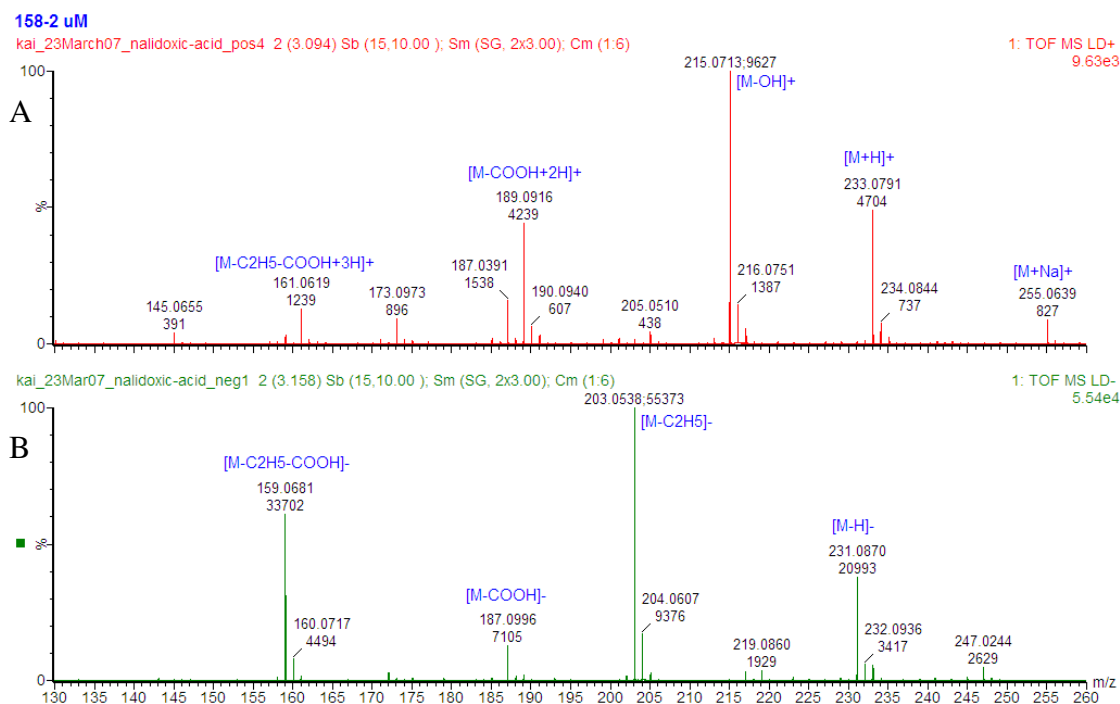


Figure 4-33 (A) Positive and (B) negative ion DIOS mass spectrum of nalidixic acid acquired on MALDI Q-ToF system. Anti-bacterial agent nalidixic acid is a quinolone acid and it gives both protonated and deprotonated ions and a number of fragment ions under positive and negative mode, respectively. The ion yield of fragments is higher than that of molecular ion.

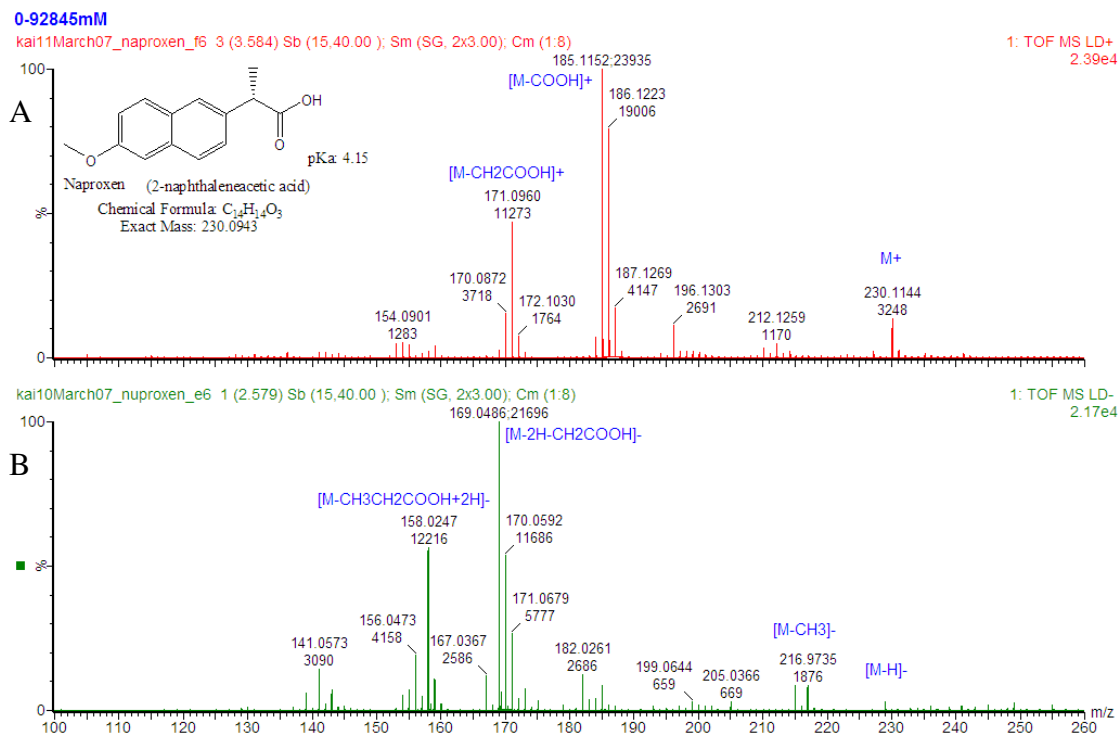


Figure 4-34 (A) Positive and (B) negative ion DIOS mass spectrum of naproxen acquired on MALDI Q-ToF system. Radical cation was observed in positive ion mode. Fragmentation occurs via loss of a carboxylic acid group. Naproxen is a non-steroidal anti-inflammatory drug.

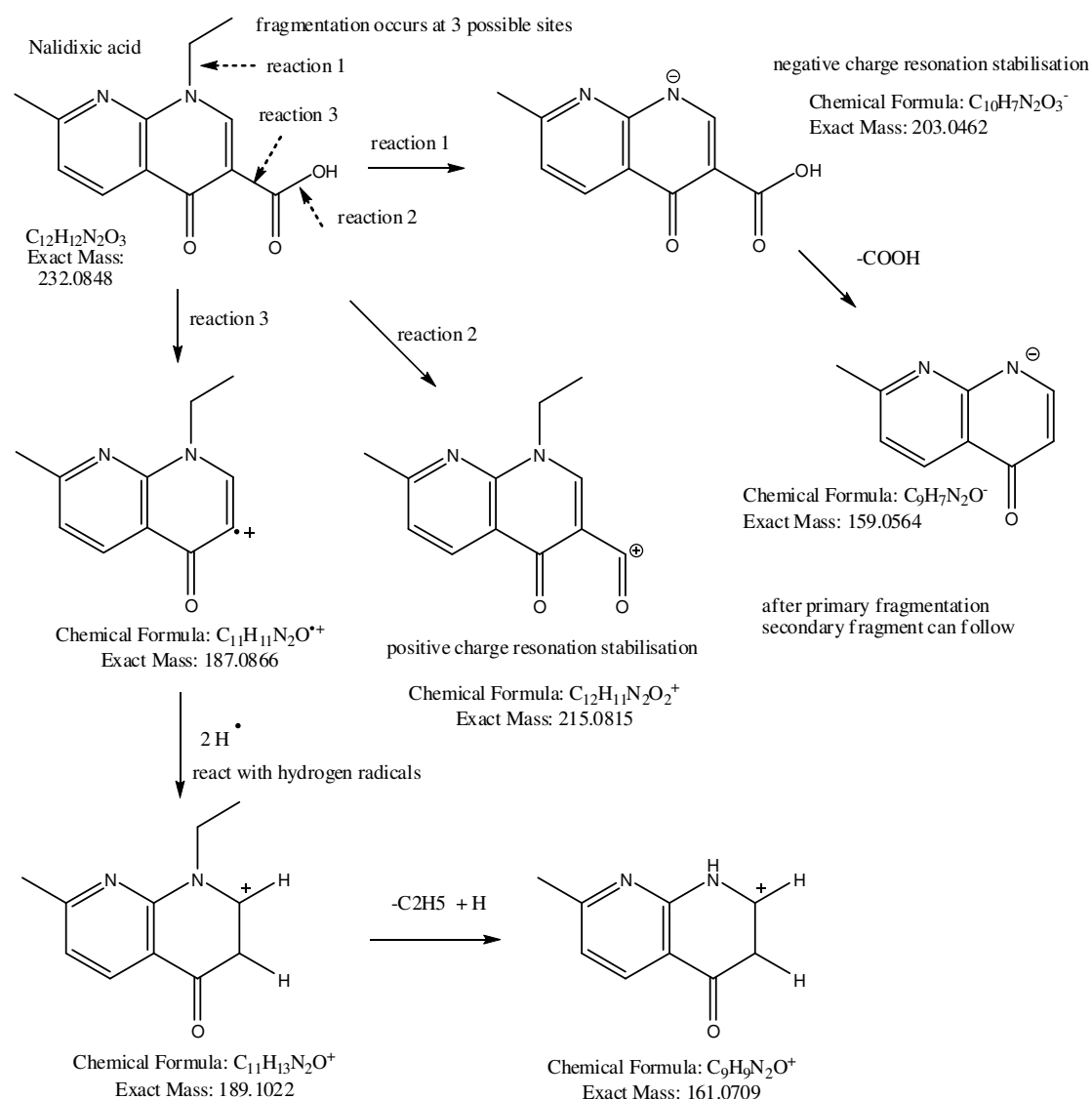


Figure 4-35 Proposed fragmentation pathways of nalidixic acid. The positive ions observed are believed due to fragmentation reaction occurs via loss of water and carboxylic acid group. The negative ions observed are believed due to fragmentation at C-N bond. Such a tendency is possibly related to the fragmentation leading to stabilisation by resonance, via the aromatic system and is therefore more energetically favourable. Capturing of two hydrogen atoms was also observed.

On the other hand, the most likely species observed for small straight chain organic acids tested are metallic aggregates (salt-bridged cationised multimers) rather than deprotonated species. This unique property is demonstrated by several acidic surfactants here. (Figure 4-36) A detailed investigation has been reported by Budimir, *et al.*^{8, 34} and has been discussed in the introduction section. A highlight here is that, the spectrum of fluorosulphonic acidic surfactant is dominated by deprotonated ion,

whereas fluoroacetic acids surfactants are not. Based on these observations, one can reasonably expect that the formation of metallic aggregates observed for small fatty acid-like molecules is highly likely a consequence of the redistribution of electron density to the metallic ion in order to achieve stabilisation.

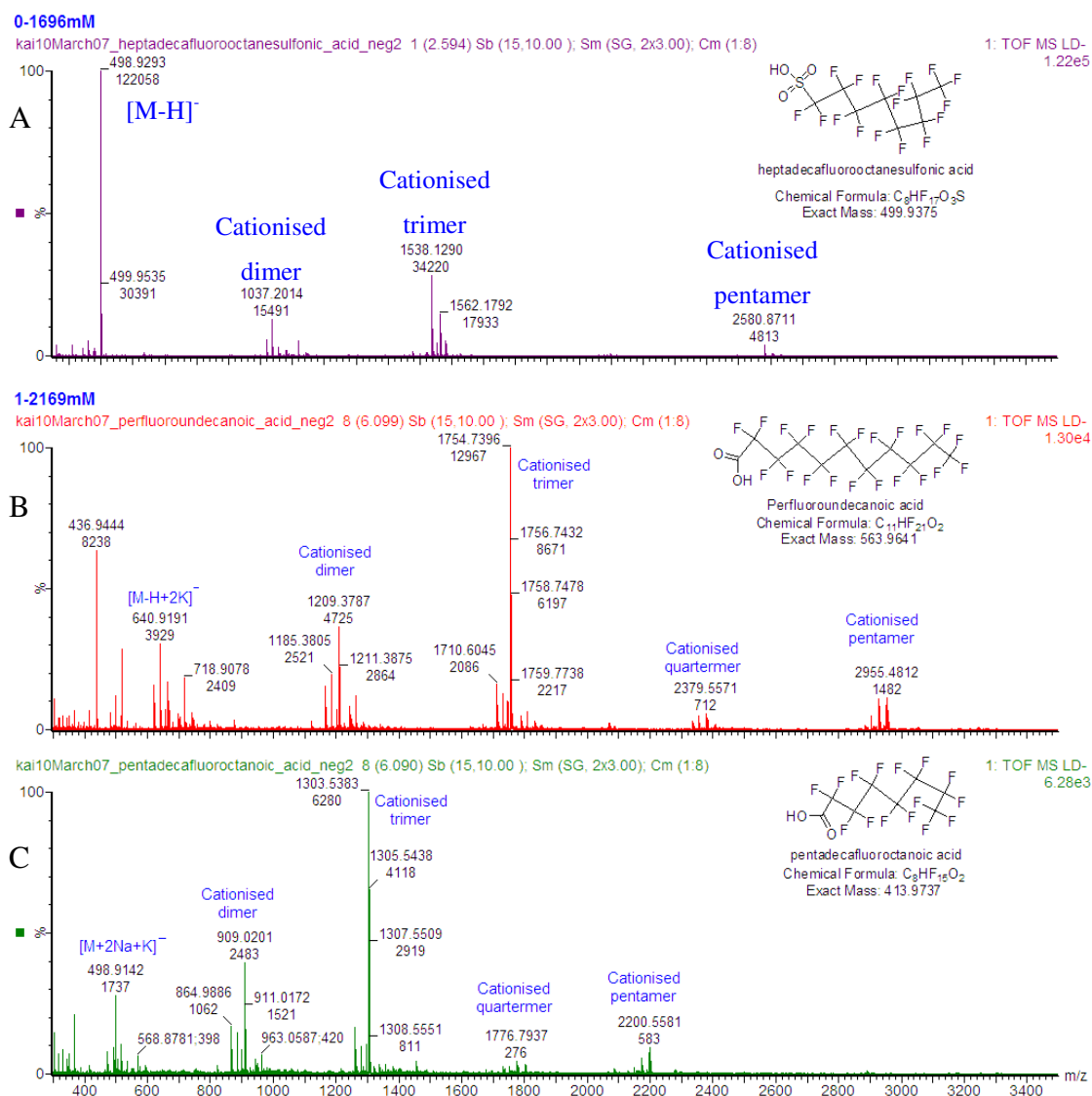


Figure 4-36 Negative ion DIOS mass spectrum of (A) heptadecafluorooctanesulfonic acid (PFOS) potassium salt solution, (B) perfluoroundecanoic acid (PFUnA), and (C) pentadecafluorooctanoic acid (PFOA). Data obtained on MALDI Q-ToF system.

The spectral respond of fluorescein is another interesting example worth highlighting. Fluorescein can be detected under positive and negative ion mode. (Figure 4-37) However, the ion yield of the protonated form is on average 10 times higher than the deprotonated form. It can also be seen from the negative spectrum that the formation of potassium adducts is more favourable than the deprotonated form. Fluorescein is

slightly acidic and has an absorption maximum at 494 nm. It does not have a high pKa value, nor does it have a nitrogen atom, but multiple ionisation equilibria. It is proposed that the protonated and deprotonated ions are preformed and the shift of the equilibria to favour the protonated form is a result of its high PA value. It also appears also that the stabilisation of the deprotonated form is achieved through a redistribution of electron density to the metallic ion.

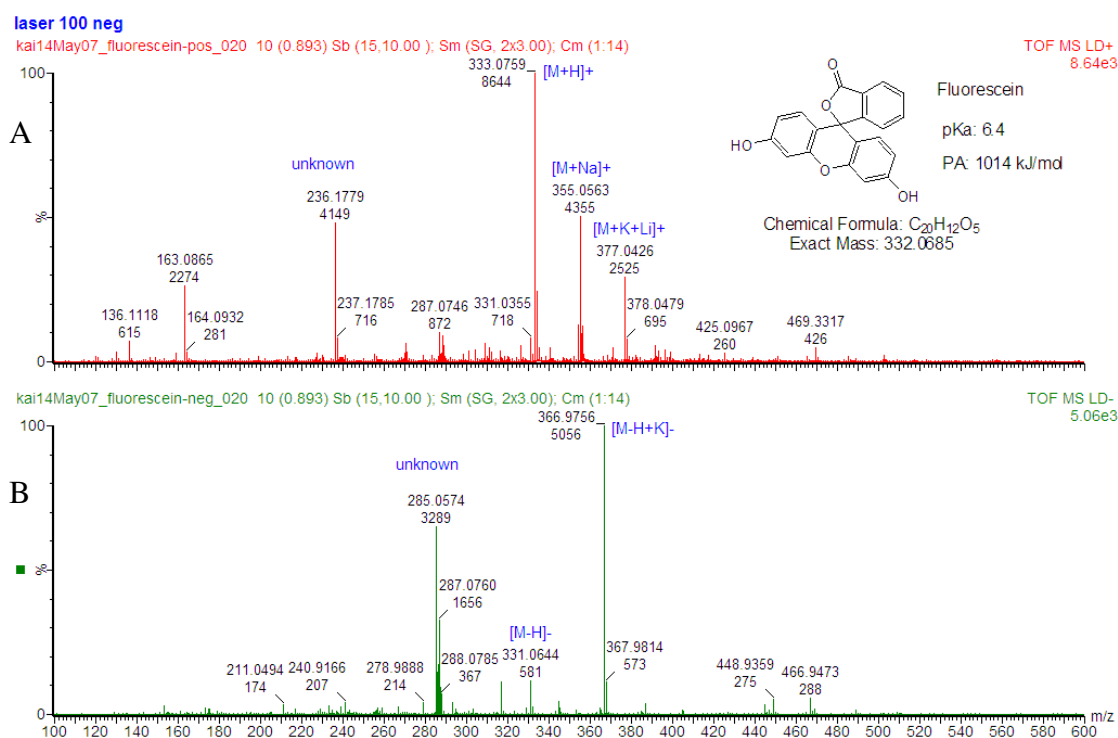
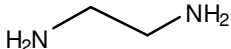
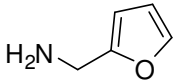
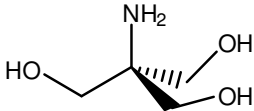
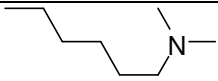
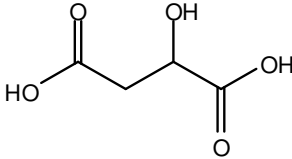
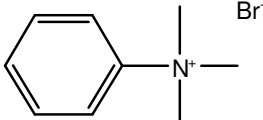
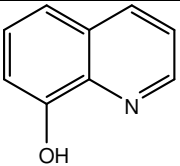
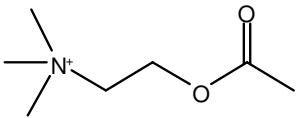
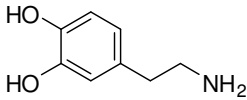
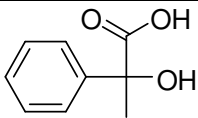
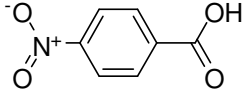


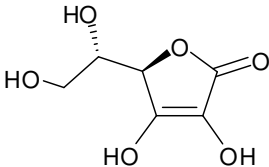
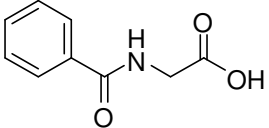
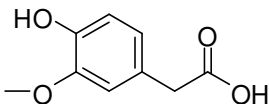
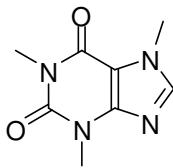
Figure 4-37 (A) positive and (B) negative ion DIOS spectra of 0.1 mM fluorescein. Data obtained on MALDI Q-ToF system.

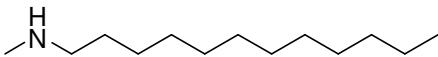
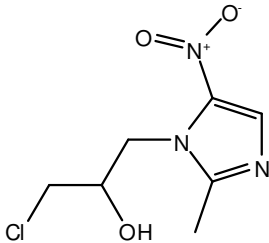
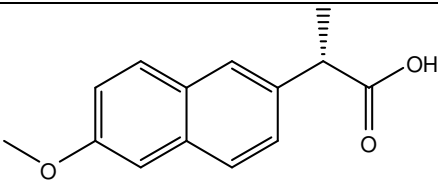
A brief summary: A number of biologically related small molecules have been tested using DIOS-MS and their trend of spectral responds is highlighted according to their chemical nature. Due to limited space, only a selection of spectra has been presented. The data collected is summarised in Table 4-6. A note needs to be added here: the initial study included the investigation using QqLIT-MS under negative ion mode. Unfortunately, the design of the detector is biased toward positive ions detection making the data acquired in negative mode invalid. Additionally, dopamine was effectively detected by MALDI-ToF (see Figure 4-39), but it could not be effectively detected by the MALDI Q-ToF system, implying ion stability is more important than aqueous basicity or proton affinity of the analyte molecule.⁵

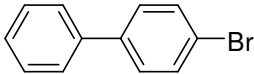
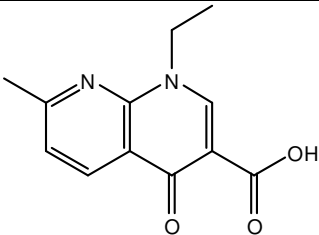
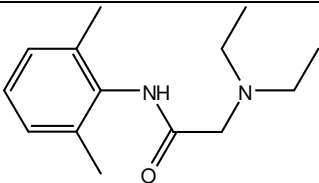
Table 4-6 Selected compounds tested using DIOS-MS. Their chemical structures, molecular weights (MW), ionisation energies (IE), proton affinities (PA) and aqueous basicities (pKa values) are presented along with the DIOS spectral responds. The classification is based on the functional group of interest.

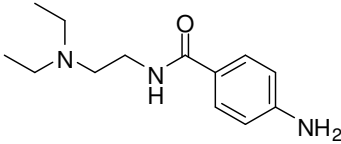
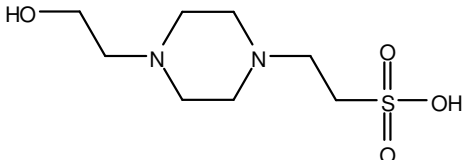
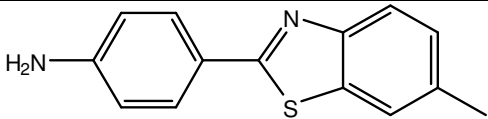
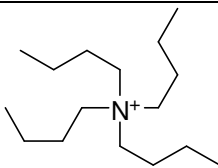
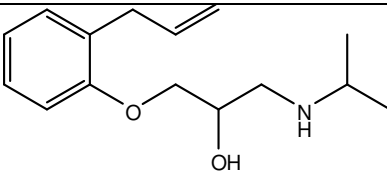
| <i>Classification</i> | <i>Compound</i> | <i>Structure</i> | <i>MW</i> | <i>DIOS Spectral respond (m/z)</i> | <i>Physical properties</i> |
|-----------------------|----------------------------------|--|-----------|---|--|
| Amine | Ethylenediamine |  | 60 | [M+H] ⁺ at 61 Spectra severally complicated with hydrocarbon | IE 8.6-9.25 PA 951.6 kJ/mol pKa 9.92 |
| Amine | Furfurylamine |  | 97 | [M-NH ₂] ⁺ fragment at 81 | pKa 8.89 |
| Amine | Tris(hydroxymethyl)-methyllamine |  | 121 | [M+H] ⁺ at 122 [M-OH] ⁺ at 104 [M+Na] ⁺ at 144 Cationised multimers | |
| Amine | N,N-Dimethylhexylamine |  | 129 | [M+H] ⁺ at 130 | |
| Organic acid | Malic acid |  | 134 | [M-H] ⁻ at 133 (v. weak) and [2M-H+Na] ⁻ at 290 | pKa ₁ 3.40 pKa ₂ 5.05 |
| Amine | Phenyltrimethylammonium bromide |  | 136 | M ⁺ at 136 C-N fragment at 121 C-N fragment and capture of H at 122 | |

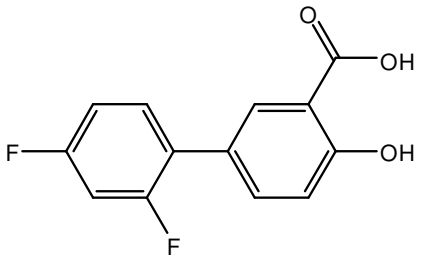
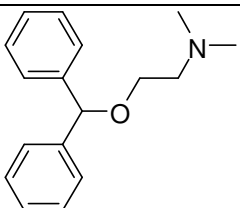
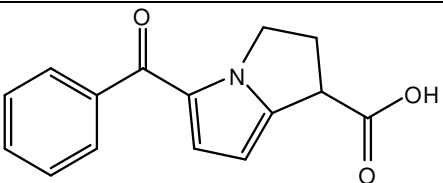
| | | | | | |
|--------------|---------------------|--|-----|---|----------------------------------|
| Quinoline | 8-hydroxyquinoline |  | 145 | $[M+H]^+$ at 146 | Absorb 336 nm UV pKa 5.02 |
| Amine | Acetylcholine |  | 146 | M^+ at 146 C-N fragment at 87 | |
| Amine | Dopamine |  | 153 | MALDI-TOF: $[M+H]^+$ at 154 (weakly) $[M-NH_2]^+$ fragment at 137 Could not be detected by MALDI Q-ToF system | pKa 8.93 |
| Organic acid | Phenyllactic acid |  | 166 | $[M-H]^-$ at 165 (v. weak), $[M-OH-2H]^-$ at 147 in MALDI Q-ToF system | |
| Organic acid | 4-Nitrobenzoic acid |  | 167 | $[M-H]^-$ at 166 $[M-COOH]^-$ at 122 $[2M-2H+Na]^-$ at 355 $[3M-2H+K]^-$ at 537 $[4M-3H+Na+K+Li]^-$ at 733 | pKa 3.44 IE 10.2 ± 0.2 eV |

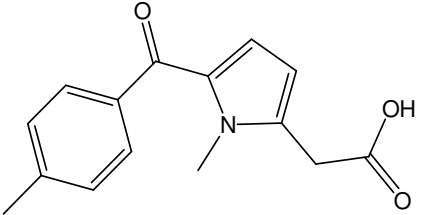
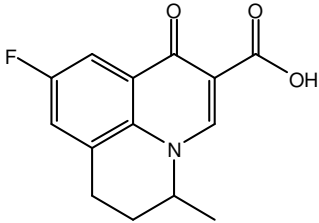
| | | | | | |
|-------------------|-------------------|---|-----|--|---------------------------------------|
| Organic acid | Ascorbic Acid |  | 176 | $[M-H]^-$ at 175 (v. weak) | pK_{a1} 4.10 pK_{a2} 11.79 |
| Organic acid | Hippuric acid |  | 179 | In positive: $[M-H+2Na]^+$ at 224 $[2M-2H+3Na]^+$ at 425 $[2M-4H+5Na]^+$ at 469 In negative: $[M-H]^-$ at 178 $[M-COOH]^-$ at 134 $[2M-2H+Na]^-$ at 379 | |
| Organic acid | Homovanillic acid |  | 182 | Not detected | 4.41 |
| Xanthine alkaloid | Caffeine |  | 194 | In positive Spectra quite noisy $[M+H]^+$ at 195 $[M+Na]^+$ at 217 $[M+H+Na]^+$ at 218 $[M+K]^+$ at 233 | IE 7.95-8.5 eV pK_a 10.4 (40 °C) |

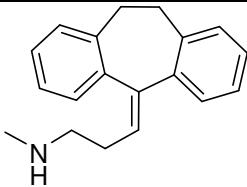
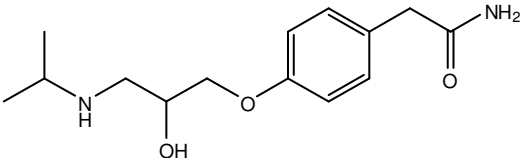
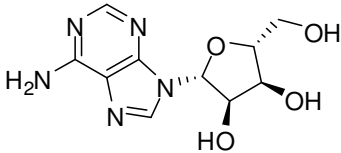
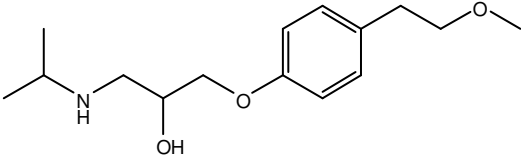
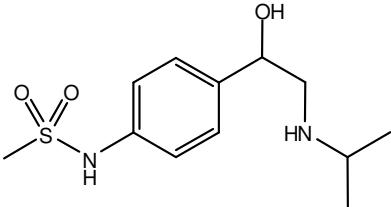
| | | | | | |
|------------------------------|----------------------|---|-----|--|----------|
| | | | | $[M+2Na+K]^+$ at 279 In negative $[M-H]^-$ at 193 C-N fragment at 179 in both positive and negative | |
| Amine | N-dodecylmethylamine |  | 199 | $[M+H]^+$ at 200 A series of alkylation products | |
| Azole | Ornidazole |  | 219 | $[M+H]^+$ at 220 $[M+Na]^+$ at 242 $[M+Na+K]^+$ at 280 Sensitivity improve with addition of formic acid | |
| Organic acid/ naphthalene | Naproxen |  | 230 | In positive: M^+ at 230 $[M-COOH]^+$ at 185 $[M-COOH+H]^+$ at 186 $[M-COOH-CH_3+H]^+$ at 171 In negative: | pKa 4.15 |

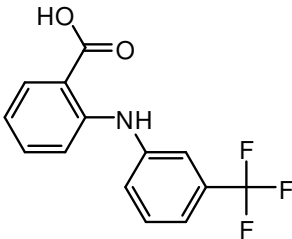
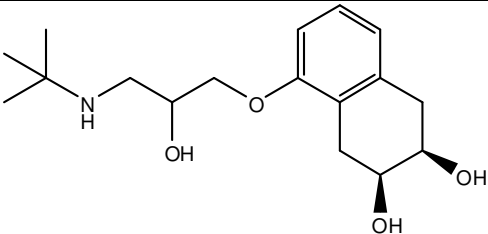
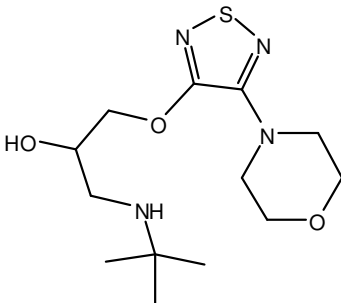
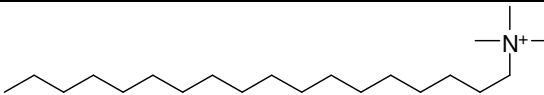
| | | | | | |
|----------------------------|-----------------|--|-----|---|-------------------|
| | | | | [M-H] ⁻ at 229 (weak) [M-CH ₃] ⁻ at 215 (weak) [M-CH ₄ COOH] ⁻ at 169 [M-CH ₃ CH ₂ COOH+2H] ⁻ at 158 | |
| Biphenyl | 4-Bromobiphenyl |  | 232 | [M+H] ⁺ at 233 (weak) [M+Na] ⁺ at 256 (weak) C-Br fragment, at 153 (weak) | IE 8.05 ± 0.02 eV |
| Quinolone/ organic acid | Nalidixic acid |  | 232 | In positive: [M+H] ⁺ at 233 [M-OH] ⁺ at 215 [M-COOH+2H] ⁺ at 189 In negative [M-H] ⁻ at 231 C-N fragment at 203 multimer at 419, 463 and 649 | pKa 8.6 |
| Amine | Lidocaine |  | 234 | [M+H] ⁺ at 235 [M+Na] ⁺ at 257 | pKa 8.01 |

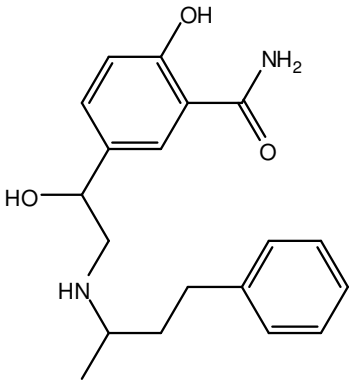
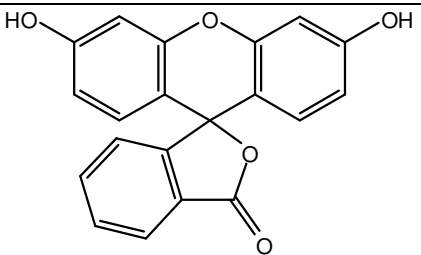
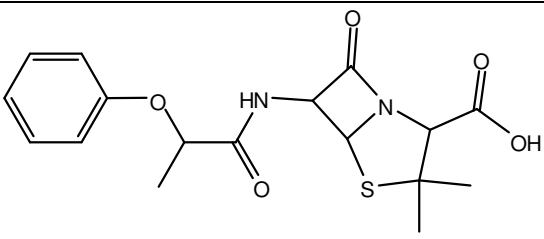
| | | | | | |
|-------------------------|--|--|-----|--|--|
| Amine | Procainamide |  | 235 | [M+H] ⁺ at 236 [M+Na] ⁺ at 258 [M+Na-H+Li] ⁺ 264 C-N fragment at 100, 120, 163 | pKa 9.32 |
| Amine/ sulfonic acid | 4-(2-Hydroxyethyl)-1-piperazineethanesulfonic acid (HEPES) |  | 238 | [M+H] ⁺ at 239 in positive – spectrum complicated with interferences [M-H] ⁻ at 237 in negative | pKa 7.5 (data provided by manufacturer, Sigma) |
| Azole/ amine | 2-(4-aminophenyl)-6-methylbenzothiazole |  | 240 | [M+H] ⁺ at 241 M ⁺ at 240 | |
| Amine | Tetrabutylammonium ion |  | 242 | M ⁺ at 242 | |
| Amine | Alprenolol |  | 249 | [M+H] ⁺ at 250 [M-OH] ⁺ at 232 Dimer at 403, 483 | pKa 9.60 |

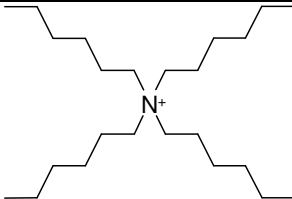
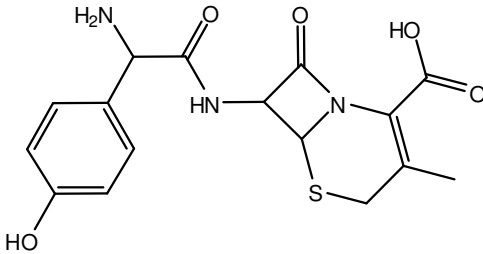
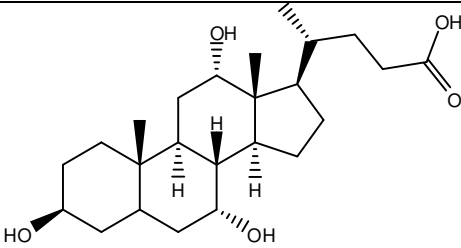
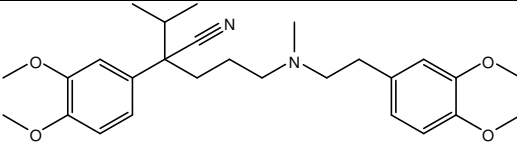
| | | | | | |
|--------------|-----------------|--|-----|---|-----------|
| Organic acid | Diflunisal |  | 250 | <p>[M-H]⁻ at 249 [M-2OH]⁻ at 216 [M-COOH]⁻ at 205</p> | |
| Amine | Diphenhydramine |  | 255 | <p>[M+H]⁺ at 256 [M+Na]⁺ at 278 C-O fragment at 167</p> | pKa 8.98 |
| Organic acid | Ketorolac |  | 255 | <p>In positive: [M+H]⁺ at 258 (v. weak) [M-COOH]⁺ at 210/212 [M-CH₂COOH]⁺ at 196</p> <p>In negative: [M-H]⁻ at 254 [M-COOH]⁻ at 210 [M-COOH-2H]⁻ at 208 C-C fragment at 186</p> | pKa ~4.47 |

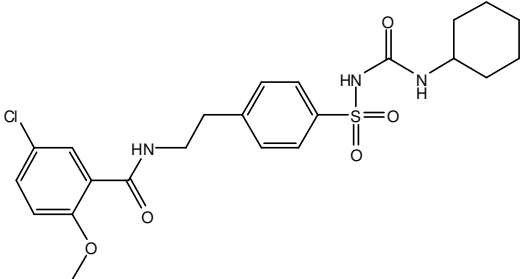
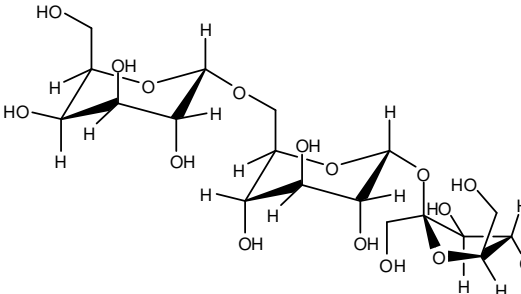
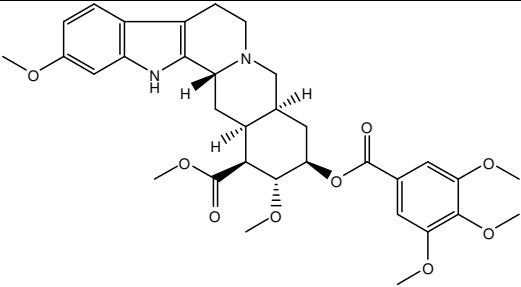
| | | | | | |
|----------------------------|------------|---|-----|---|-----------|
| Organic acid | Tolmetin |  | 257 | <p>In positive:</p> <p>[M+H]⁺ at 258 [M-COOH]⁺ at 212 [M-CH₂COOH] at 198</p> <p>In negative</p> <p>[M-H]⁻ at 256 (weak) [M-COOH]⁻ at 212 [M-COOH-2H]⁻ at 210 [M-CH₂COOH]⁻ at 198 Cationised multimers (in both positive and negative)</p> | pKa ~4.22 |
| Quinolone/ organic acid | Flumequine |  | 261 | <p>in positive</p> <p>[M+H]⁺ at 262 [M-OH]⁺ at 244 [M-COOH+2H]⁺ at 218</p> <p>In negative:</p> <p>[M-H]⁻ at 260 [M-COOH+3H]⁻ at 219 [M-C₃H₂O₃]⁻ at 175</p> | pKa 6.2 |

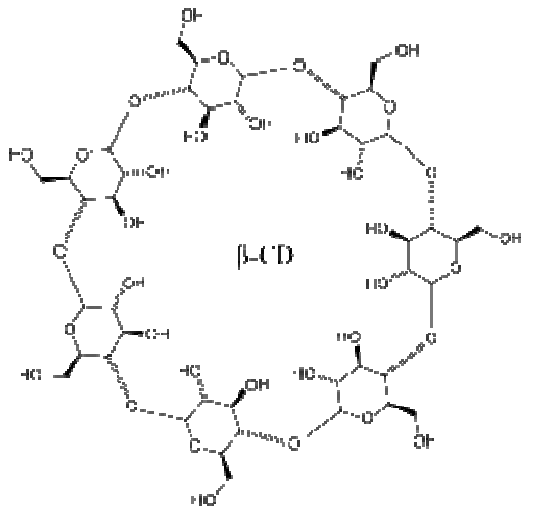
| | | | | | |
|------------|----------------------------------|--|-----|---|------------------------------|
| | | | | Cationised multimers in both positive and negative | |
| Amine | Nortriptyline (Nortriptylene) |  | 263 | [M+H] ⁺ at 264 C-N fragment at 233 C-C fragment at 218, 203 C=C fragment at 191 | IE 8.39 ± 0.11 eV |
| Amine | Atenolol |  | 266 | [M+H] ⁺ at 267 [M-OH] ⁺ at 249 (weakly) | pKa 9.60 |
| Nucleoside | Adenosine |  | 267 | [M+H] ⁺ at 267 [M+Na+K] ⁺ at 329 C-N fragment at 136 | PA 989.3 kJ/mol pKa 12.35 |
| Amine | Metoprolol |  | 267 | [M+H] ⁺ at 268 [M-OH] ⁺ at 250 (weakly) | pKa 9.70 |
| Amine | Sotalol |  | 272 | [M+H] ⁺ at 273 [M-OH] ⁺ at 255 | pKa 9.76 |

| | | | | | |
|------------------------|---------------------------------|--|-----|--|----------|
| Amine/ organic acid | Flufenamic acid |  | 281 | In positive: [M-OH] ⁺ at 264 [M-H] ⁻ at 280 [M-2H-OH] ⁻ at 262 [M-COOH] ⁻ at 236 Cationised dimer | pKa 3.9 |
| Amine | Nadolol |  | 309 | [M+H] ⁺ at 310 [M-OH] ⁺ at 292 (weakly) C-N fragment and capture 2H at 254 C-N fragment at 237 | pKa 9.67 |
| Amine | Timolol |  | 316 | [M+H] ⁺ at 317 C-N fragment at 261 | pKa 9.21 |
| Amine | Octadecyl-trimethylammonium ion |  | 321 | M ⁺ at 347 | |

| | | | | | |
|----------|----------------|---|-----|--|----------|
| Amine | Labetalol |  | 328 | <p>$[M+H]^+$ at 329</p> <p>$[M-OH]^+$ at 311</p> <p>$[M-OH-OH]^+$ at 294</p> <p>C-N fragment at 161/163</p> | pKa 9.40 |
| Aromatic | Fluorescein |  | 332 | <p>$[M+H]^+$ at 333 (in positive)</p> <p>$[M-H]^-$ at 331 (in negative)</p> <p>Salt adducts</p> | pKa 6.4 |
| Amide | Phenethicillin |  | 346 | $[M+H+3Na+Li]^+$ at 441 | pKa 2.7 |

| | | | | | |
|--------------------------|------------------------|--|-----|--|--|
| Amine | Tertahexylammonium ion |  | 354 | M ⁺ at 354 | |
| Amide | Cefadroxil |  | 363 | Not detected | pKa ₁ 2.56 pKa ₂ 7.24 pKa ₃ 9.67 pI 4.90 |
| Steroid/ organic acid | Cholic Acid |  | 408 | [M+Na] ⁺ at 431 [M-H+2Na] ⁺ at 453 [M-H+Na+K] ⁺ at 469 [M-H+2K] ⁺ at 485 [M+2H+acetate] ⁺ at 469 [M-H] ⁻ at 407 | pKa 4.98 |
| Amine | Verapamil |  | 454 | [M+H] ⁺ at 455 C-N fragment at 164 C-C fragment at 303 | pKa 8.92 |

| | | | | | |
|-----------------|-----------|---|-----|--|-----------------------|
| Amide | Glyburide |  | 494 | $[M+Na]^+$ predominate at 615 | pKa 5.3 |
| Saccharine | Raffinose |  | 504 | $[M+Na]^+$ at 527 $[M-C_6H_{11}O_5+Na+H]^+$ at 365 | |
| Indole alkaloid | Resperine |  | 608 | $[M-H]^+$ at 607 in positive C-O fragment at 395, 397, 195 in positive $[M-H]^-$ at 607 in negative (weak) | IE 7.88 eV pKa 6.6 |

| | | | | | |
|------------|-----------------------|--|------|--|--|
| Saccharine | β -Cyclodextrin |  | 1135 | $[M+Na]^+$ at 1157 A series of fragments losing monosaccharide unit | |
|------------|-----------------------|--|------|--|--|

- pka values were taken from various sources include Chemfinder.com and Luan, *et al.*³⁵
- Cefadroxil pka values were obtained from Advanced Analytical Technologies, Inc., available at www.aati-us.com/solutions/pharmaceutical/pka_plmeasurement.html.
- IE and PA data obtained from NIST web book.

4.2.8 Effect of D₂O and Acidic Buffers on Small Molecules Ionisation

It has been suggested that residual solvents such as water or acids are the proton source in DIOS-MS.¹² It has also been reported that introduction of water vapour and acetic acid vapour in the gas-phase SALDI-MS substantially increases the ion yield of protonated species.⁷ To verify whether water or acid has any effect to the spectral quality, mass spectra were acquired using a number of substances prepared with addition of D₂O or acidic modifiers. Verapamil dissolved in D₂O was first compared with verapamil dissolved in ACN/H₂O; using plasma etched SALDI surface, s3. No time was allowed for exchanging hydrogen to take place and the droplet was forced to dry off in 1 to 2 minutes at 70°C. If water was a proton source, there should be a shift of the molecular ion peak by one m/z unit or a significant different in isotopic distribution of the molecular ions. The spectra obtained showed no shift of mass unit nor was there any effect to the isotopic distribution of the molecular ion. (Figure 4-38) Moreover, all solvent systems used in our studies should have no appreciable absorption at 337 nm. It appears, unlike IR-DIOS/MALDI,³⁶ residual solvents are not a main proton source, nor a matrix in the vacuum UV-MALDI experimental condition.

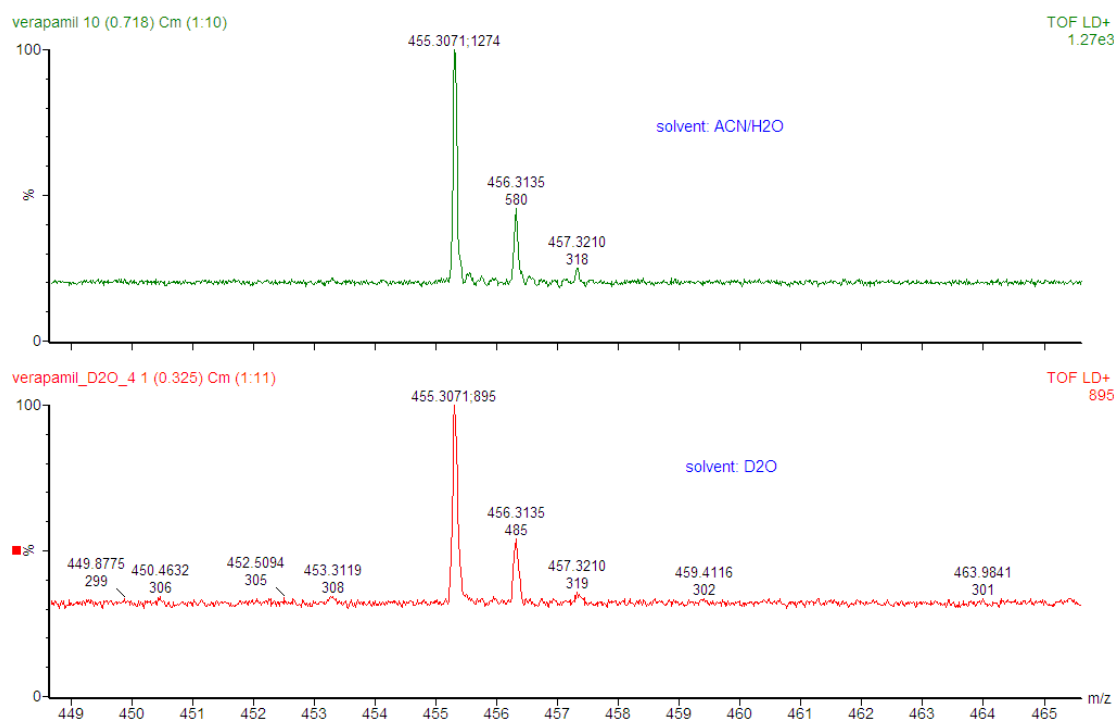


Figure 4-38 Spectra of verapamil deposited with H₂O and D₂O on plasma etched SALDI surface.

Figure 4-39 and Figure 4-40 show the spectra of dopamine and adenosine with and without the addition of acidic modifiers, respectively. These molecules are known to have high aqueous basicities. The results show that adding acidic buffer does not improve the ion yield and in fact, the intensity of the protonated molecules is lower.

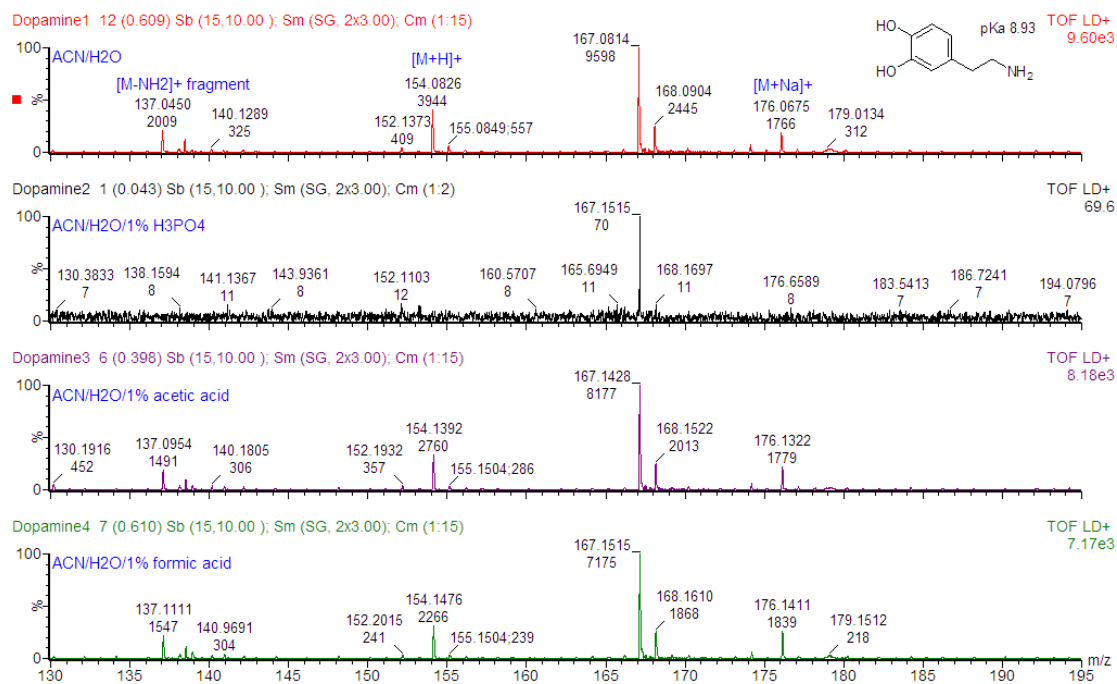


Figure 4-39 DIOS spectra of dopamine with and without addition of acidic modifiers. The spectra are presented normalised to peak m/z 167. Dopamine is an important neurotransmitter.

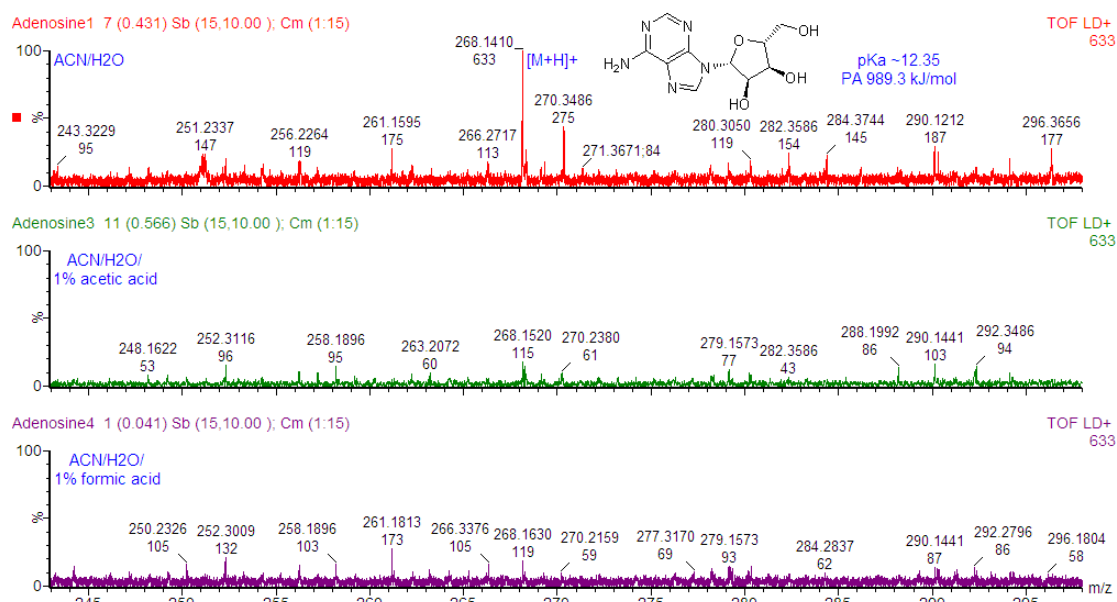


Figure 4-40 DIOS spectra of adenosine, with or without addition of acidic modifiers. The spectra are presented with the same vertical scale. Adenosine is a nucleoside.

Figure 4-41 shows the spectra of diphenhydramine prepared with and without the addition of different acid modifiers. The spectra are dominated by the major fragment ion at m/z 167. It is thought that the fragment is formed by hydrolysis occur at oxygen, (Figure 4-42) and yet the presence of acidic buffer did not lead to more intense fragment peak and similarly the total ion yield was in fact lower. This suggests protonation at oxygen may lead to fragmentation.

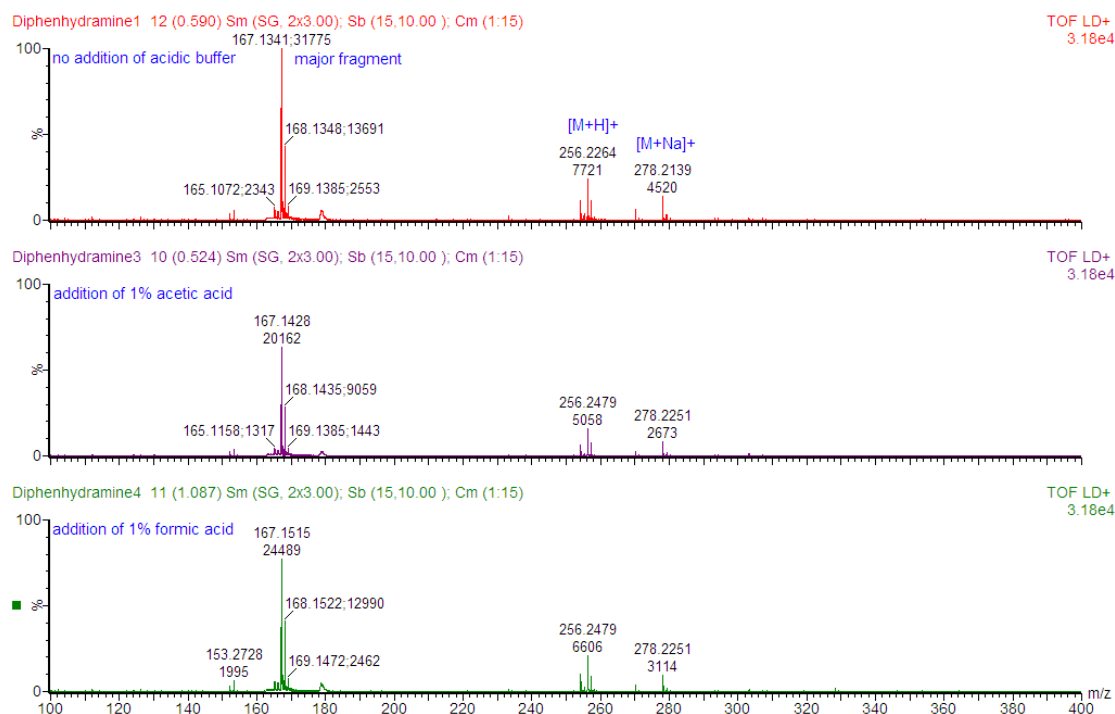


Figure 4-41 DIOS spectra of diphenhydramine, with or without addition of acidic modifiers. The spectra are presented with the same vertical scale. Diphenhydramine is an antihistamine.

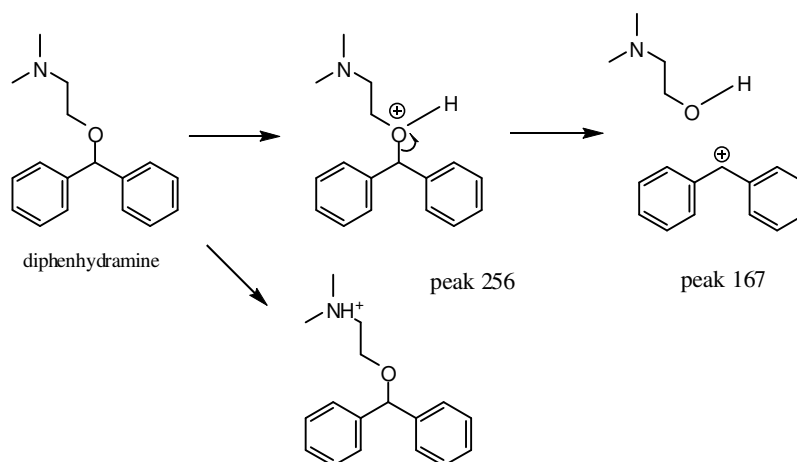


Figure 4-42 Proposed fragmentation pathways of diphenhydramine. Protonation occurs at the oxygen, unlike ESI, is energetically unfavourable and leads to fragmentation.

The results presented so far suggest that water or acid are less likely to be a major proton source and the presence of organic acid only results in lowering the ion yield due to ion-pairing effect. In particular, the addition of H_3PO_4 strongly suppresses ion formation. Exceptions occur if the acid functions to naturalise the excess charge, or to minimise the ion-pairing effect of salt, the addition of formic acid but not acetic acid or H_3PO_4 could result in a higher intensity of protonated molecules. (Figure 4-43)

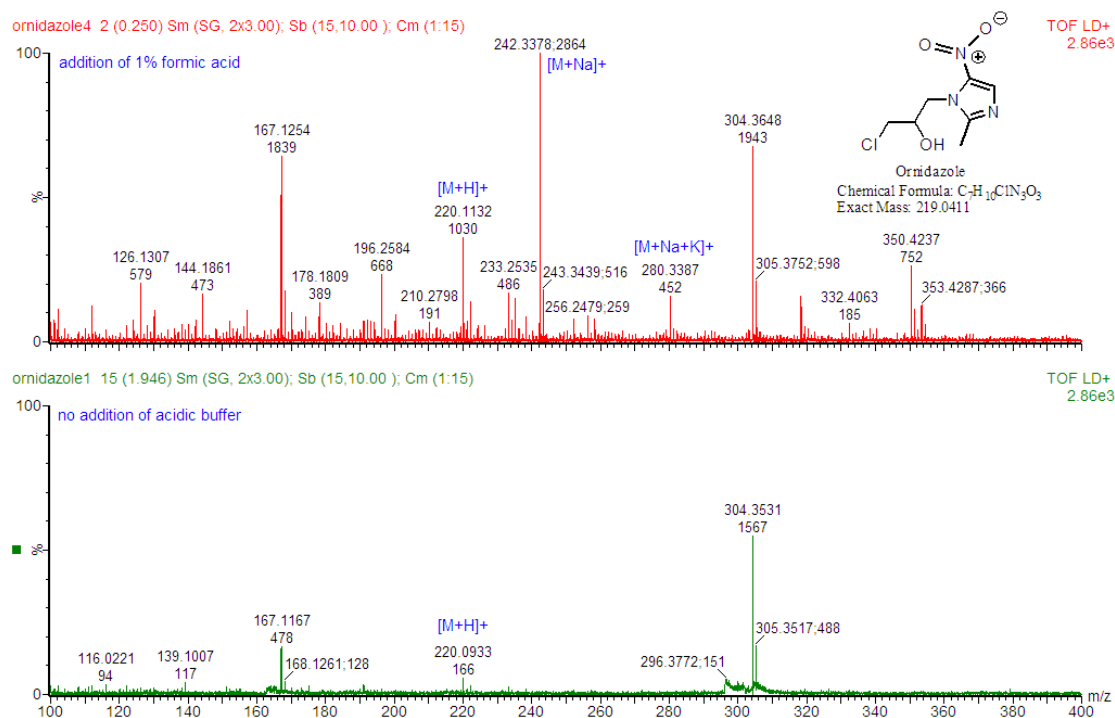


Figure 4-43 DIOS spectra of ornidazole with addition of 1% formic acid and no addition of acidic buffer. Spectra are presented with the same vertical scale. Ornidazole is an anti-protozoan drug, commonly used in poultry industry.

Generally, the highest sensitivity for small molecules is obtained with no addition of acidic modifier, but if addition of acidic modifier is required, such as for sample preparation, 0.1% of formic acid appears to be the best approach as this should have minimal effect toward the signal intensity for small molecules. A similar observation has also been reported in the thesis of Li,⁹ where addition 0.1% TFA, to an aged angiotensin I solution (*i.e.* with salt content) enhances the ion yield of $[\text{M}+\text{H}]^+$ ion, but higher amount, 0.5 and 1%, decreases the protonated molecule signal and increases background interferences.

4.2.9 Reduction of Metallic Ions

It has been reported that copper(II) and iron(III) are reduced to copper(I) and iron(II) during LDI,^{11, 12, 34, 37} and hence mass spectra of these metallic ions were acquired. (Figure 4-44) The spectra show that copper(II) is reduced to copper(I) and is desorbed as Cu^+ and $\text{Cu}(\text{H}_2\text{O})^+$ observed in the positive ion spectrum. This also implies the presence of hydrated state of copper ions. Furthermore, a mixture of copper(II) acetate and iron(III) chloride gives not only Cu(I/II) ionic clusters but also Fe(II)/(III) clusters in the negative ion spectrum.

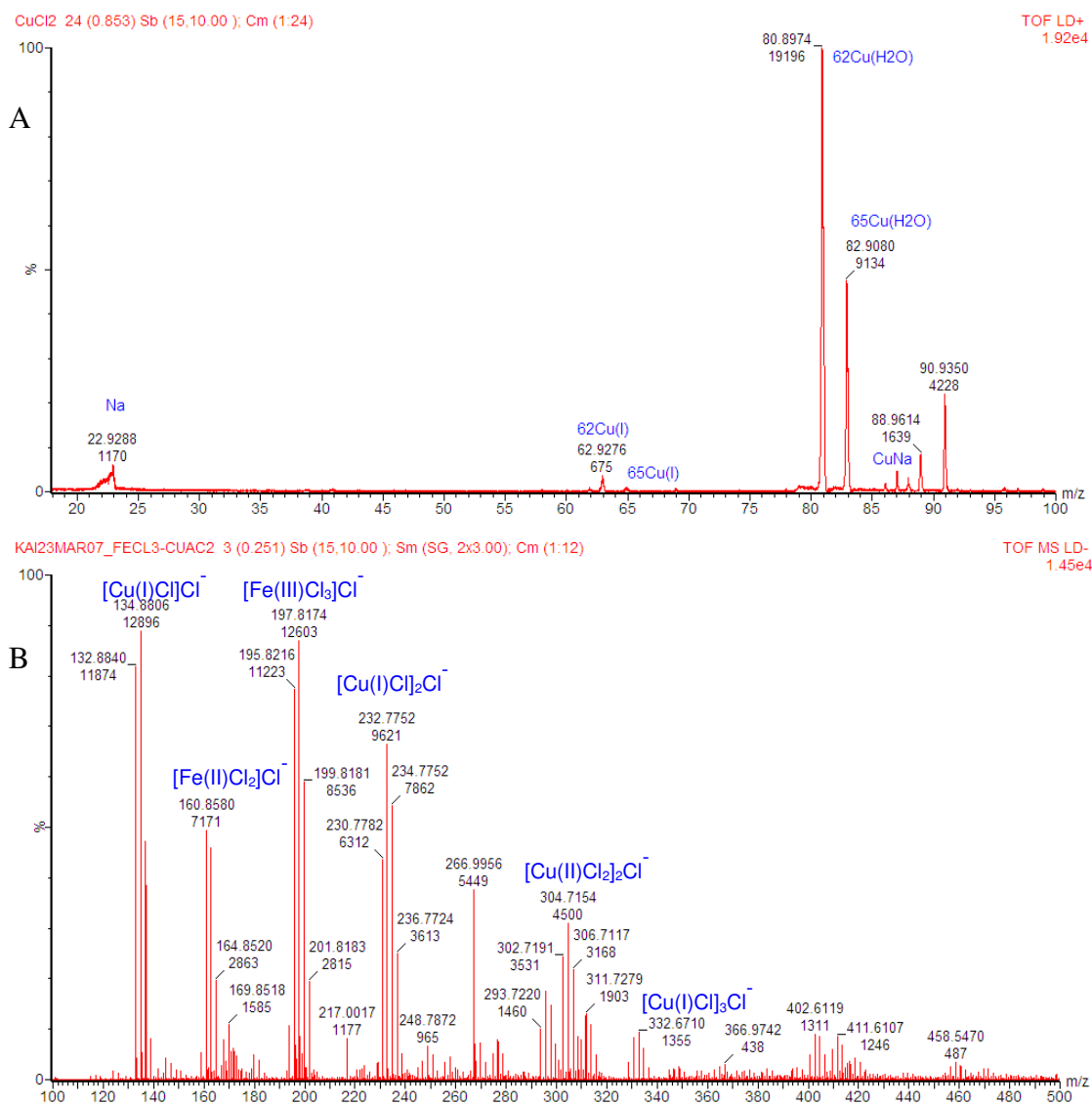


Figure 4-44 (A) Positive ion DIOS spectrum of a copper(II) acetate/sodium chloride mixture acquired on MALDI-ToF system. (B) Negative ion DIOS spectrum of a copper(II) acetate/iron(III) chloride mixture acquired on MALDI Q-ToF system.

4.2.10 Substrate Structural and Chemical Change After LDI Investigation

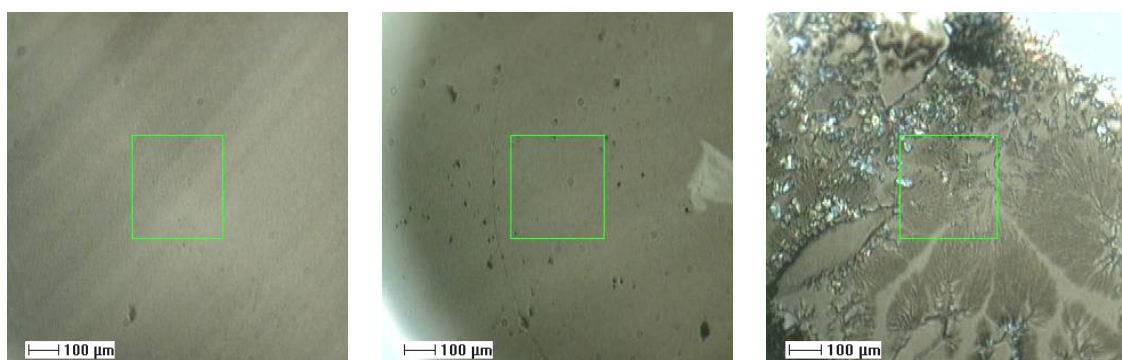
4.2.10.1 Porous Silicon DIOS Substrate

Observing the DIOS target before and after use for LDI investigation under a microscope revealed that a localised porous destruction (formation of bigger pores) had occurred on the surface and in an extreme case, the surface had melted. (Figure 4-45)

The effect was also observed by SEM. Figure 4-46 shows a SEM image of a DIOS surface after LDI investigation. Two pores are clearly seen on the images and are highlighted by circles. Additionally, in the surrounding area, particles are also observed on the surface. Initially, it was thought that those were remaining analyte (in a form of crystallites) adhered on the surface.

However, Figure 4-47 suggests a different picture. The SEM image on the left shows a sample well of DIOS target after LDI investigation. There are two distinct areas on the image; one is an area on a spiral burn-mark and the area outside this burn-mark. The spiral shape is due to the spiral stage movement of the MALDI instrument, where the laser scans different areas during data acquisition. This area shows a higher contrast relative to the area that has not been scanned or modified by laser.

The high magnification image (Figure 4-47 B) reveals that there are two types of particles, one has higher contrast than the other type (one is grey and the other is white). This may suggest the chemical nature of these two types of particles is not identical. Conversely, this is less evidenced on the image of the non-modified region (Figure 4-47 A). This suggests that these particles were not only the remaining deposited analyte but actually created during LDI. This led us to chemical imaging, by using XPS and SIMS, to investigate the chemical change due to laser modification or ablation.



Unused DIOS surface

Used for LDI investigation

Damaged by laser

Figure 4-45 Optical image of the surface that has not be used, used for LDI investigation, and damaged by laser.

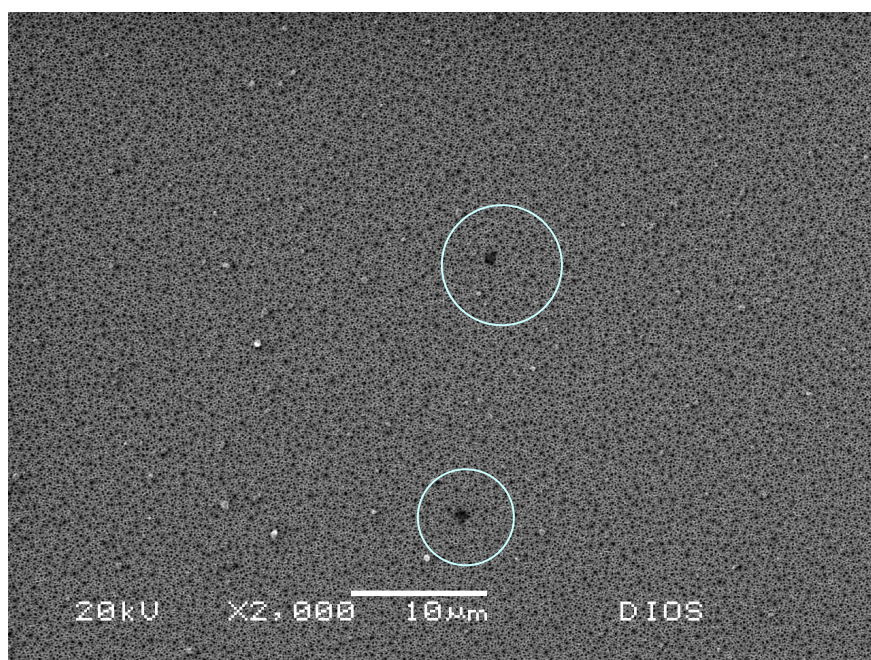


Figure 4-46 SEM image of DIOS substrate after use for LDI investigation. The surface had been subsequently washed and stored in propan-2-ol to remove deposited analyte after LDI investigation. The circles highlight the formation of big pores after the substrate was used for LDI investigation. The SEI also shows particles scattered on the surface.

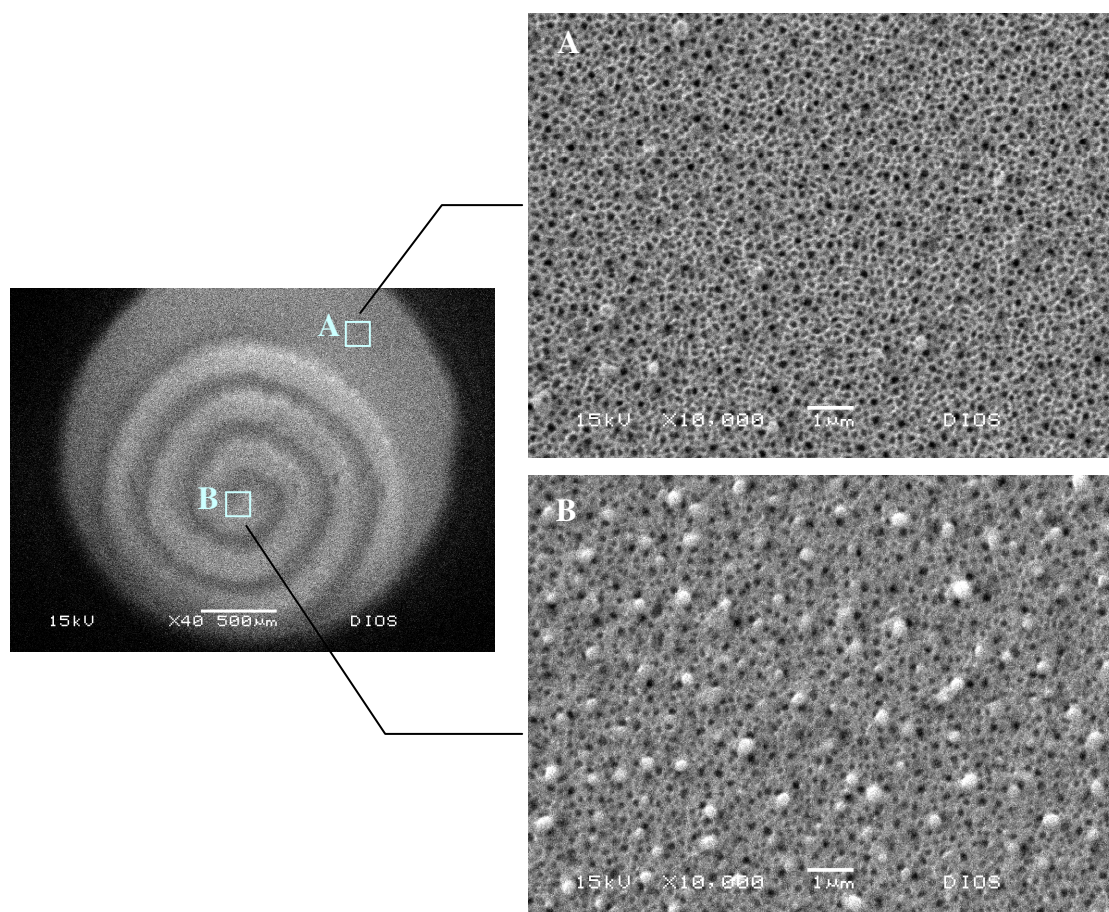


Figure 4-47 SEM images of DIOS substrate after LDI investigation. The surface had not been washed and stored in sealed container in freezer after use. The SEI on the left shows a lower magnification of a sample well. The spiral shape laser “burn mark” was formed as a result of spiral stage movement during data acquisition. Two areas were chosen with high magnification: (A) area that has not been modified by laser and (B) area that has been laser modified.

4.2.10.2 XPS and SIMS Imaging To Laser Modification of SALDI Substrate

The gas-phase SALDI-MS approach requires a chemical etched surface to be further “*subjecting... to optical radiation in water [vapour] environment at intensity lower than destruction threshold of [the] surface*”.³⁸ This laser etching carried out under vacuum inside the mass spectrometer ablates materials that have already been adsorbed onto the surface. The surface is said to be activated and highly susceptible to organic species adsorption and is essential for the function for gas-phase SALDI-MS. A sample solution is then introduced into the vacuum chamber of the mass spectrometer via a GC instrument. After laser etching, a visual alternation can be seen. Although no laser etching was performed in our LDI investigation, transformation in

surface chemistry is thought to occur. One question is what will occur to the surface because of laser excitation. The effect of prolonged laser etching on a silicon substrate had also been studied by Chen, *et al.*,³⁹ but was limited to morphological analysis by SEM. In here, SIMS and XPS chemical imaging was used to investigate the effects of laser etching or ablation of the SALDI substrates.

Some of the SALDI surfaces received had been used for gas-phase SALDI-MS testing and hence these surfaces are products of both laser etching and gas-phase SALDI processes. Typically, a laser beam is continuously fired onto the substrate inside the vacuum chamber of SALDI mass spectrometer, until the analyte signal is diminished. The relatively smooth SALDI surface morphology makes it a more suitable choice relative to porous surface for chemical imaging by XPS.

A laser modified surface was first investigated by SEM. (Figure 4-48) A ring is observed on the image. This ring was due to a circular movement of laser beam diverted by a rotating mirror during the gas-phase SALDI-MS investigation. This region has thus been laser modified under the gas-phase SALDI-MS condition and the surrounding area has not been modified by laser. One distinct difference here compared to the DIOS target is that, the laser-modified ring is darker relative to its surrounding area. Furthermore, because it was the mirror in rotation instead of the target stage transition, the laser incidence angle and spot size varied. Consequently, the thickness of the ring circumference varied and so would have been the localised laser intensity and temperature during the SALDI experiment.

The surface was further studied by XPS chemical imaging analysis. The applications of XPS in chemical mapping of germanium surface have been previously discussed by Smith, *et al.*⁴⁰ Multi-spectral datasets were acquired at 0.2 eV intervals. Images were taken from an area of interest, in this case $800 \times 800 \mu\text{m}^2$. Resolution was 256×256 pixels. The multi-spectral image data was then processed with SVD sorting and PCA. The method and instrumental settings have been outlined in Chapter 2, section 2.3.4.1 and 2.4.5.4. The final images were reconstructed from the first two principle components. Four images corresponding to silicon dioxide [Si 2p oxide], silicon element [Si 2p metal], carbon [C 1s] and oxygen [O 1s] are displaced. (Figure 4-49)

The XPS images of Si 2p oxide and C 1s show a very similar pattern and a higher intensity is observed on the right side of the image (laser modified region) than the left side of the image (non-modified region). This may suggest silicon dioxide and carbide complexes could be by-products created during the SALDI process. The XPS images of Si 2p element and O 1s show a higher Si element but lower oxygen signal on the laser-modified area relative to non-modified region. On the other hand, the pattern of O 1s signal is also a mirror image to that of Si 2p oxide and C 1s.

Si 2p core-level spectra are reconstructed by summing the multi-spectral datasets of the selected pixels of the Si 2p image, using the relative intensity of Si (element), which is corresponding to the laser modified and non-modified region of the surface. (Figure 4-50) The spectra are deconvoluted to elemental Si and silicon oxides. The change in elemental Si and oxides intensity between the laser modified and non-modified region indicate a thinning of oxides/hydroxides layer and the oxide thickness can be calculated by:

$$d_{oxides} = \lambda_{SiO_2} \sin \theta \ln(1 + R_{exp} / R_0)$$

as described in Chapter 2, section 2.4.5.4. The calculated SiO₂ thicknesses are 3.3 nm and 4.2 nm for modified and non-modified region respectively. The calculated values might have been over estimated as the surface roughness also influences the path of photoelectron.⁴¹ (Figure 4-52)

O 1s core-level spectra are also reconstructed and are deconvoluted to SiO₂ and SiOH components. (Figure 4-51) The reconstructed O 1s spectra show that the laser-irradiated region has a higher proportion of SiOH but lower proportion of SiO₂. This proportional change in the ratio of oxide and hydroxides is similar to that of argon plasma etching to the SALDI surface. However, there may be a contradiction to the Si 2p spectra.

For that reason, it would be an over generalisation to interpret these changes simply as thinning of oxides thickness due to laser ablation or surface melting, but a combination surface morphological rearrangement and chemical composition change.

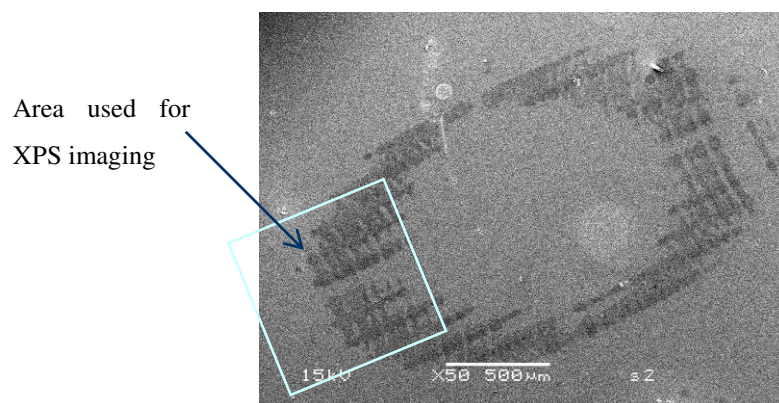


Figure 4-48 SEM image of the SALDI substrate s2 after SALDI-MS investigation showing a ring modified by laser etching. The substrate was stored in propan-2-ol until analysis.

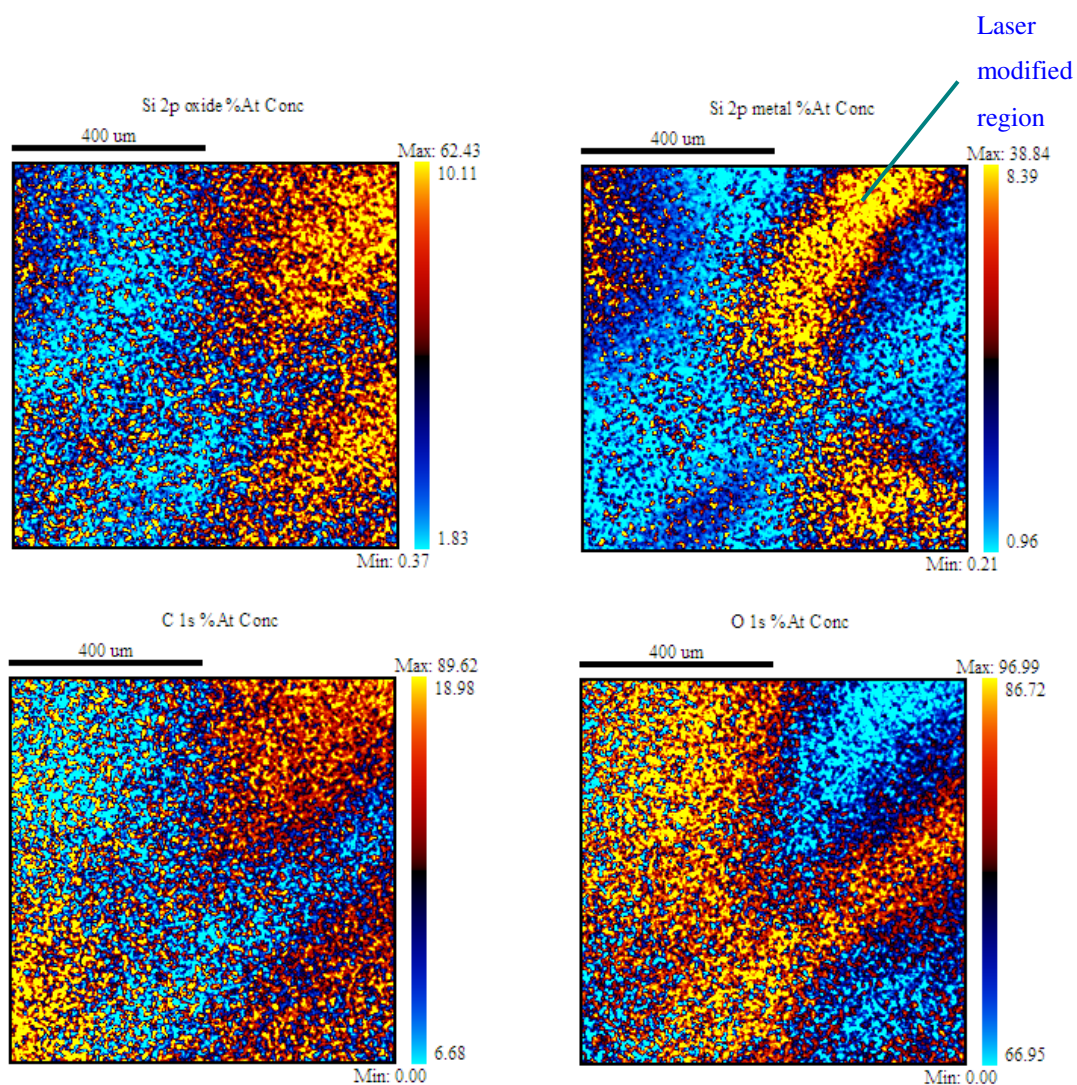


Figure 4-49 XPS imaging of the SALDI surface, s2, showing the ring that has been laser modified.

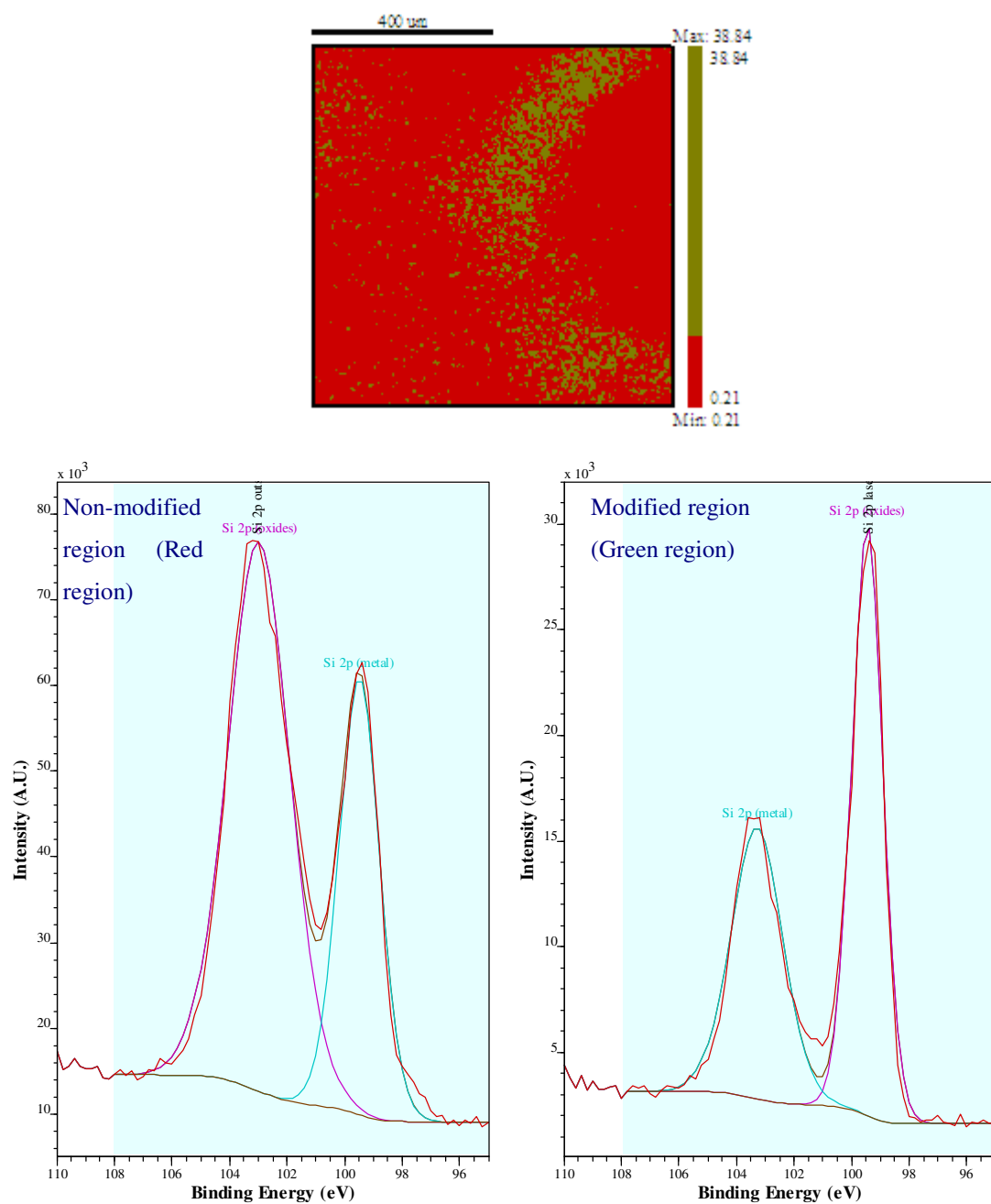


Figure 4-50 Reconstructed Si 2p spectra for each pixel generated from multi-spectral datasets summed for the regions that have been laser modified and without defined by reference to the bicolour image.

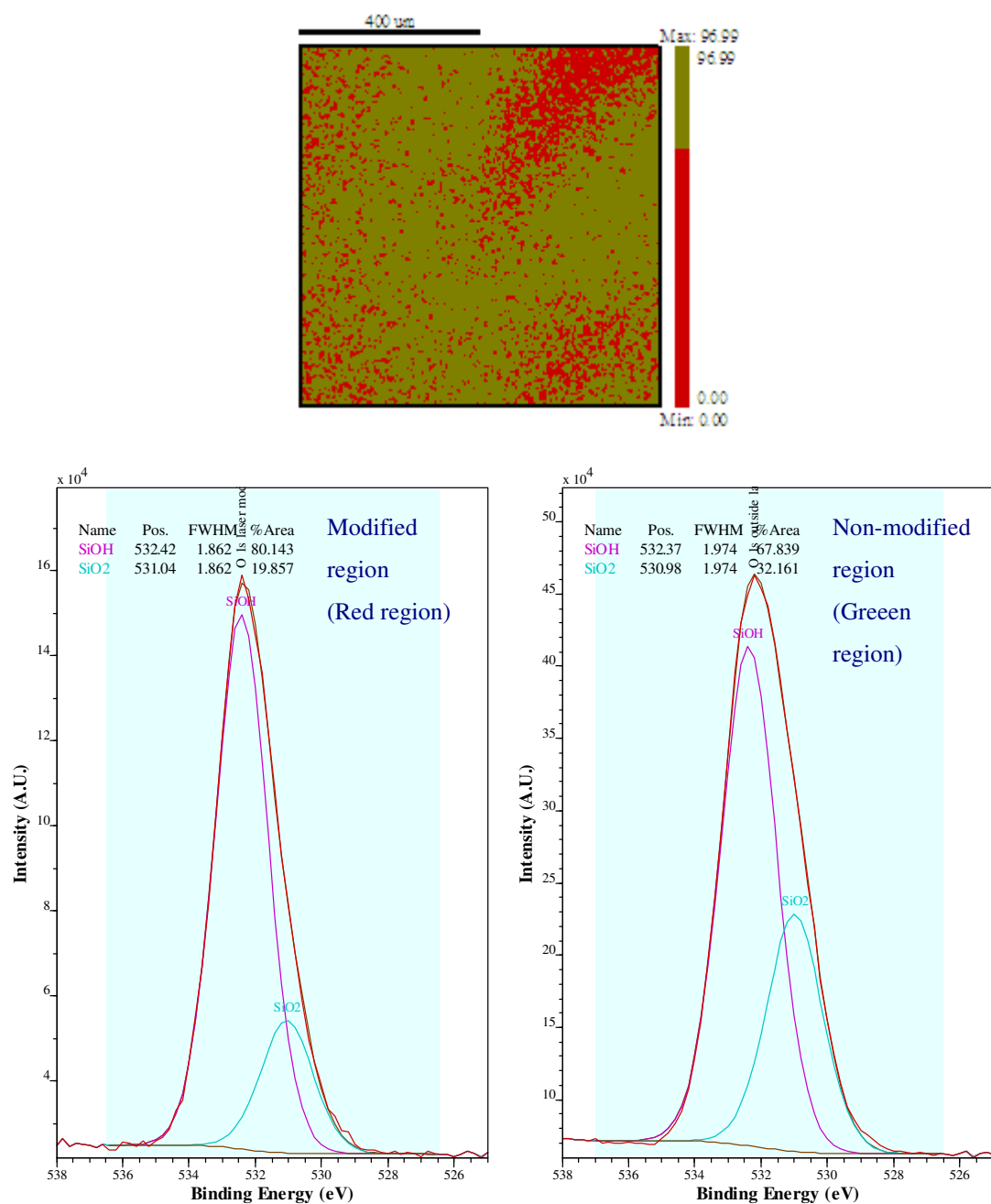


Figure 4-51 Reconstructed O 1s spectra for each pixel generated from multi-spectral datasets summed for the regions that has been laser modified and without defined by reference to the bicolour image. The deconvolution of SiO₂ and SiOH is calculated by constricting the peak width being identical.

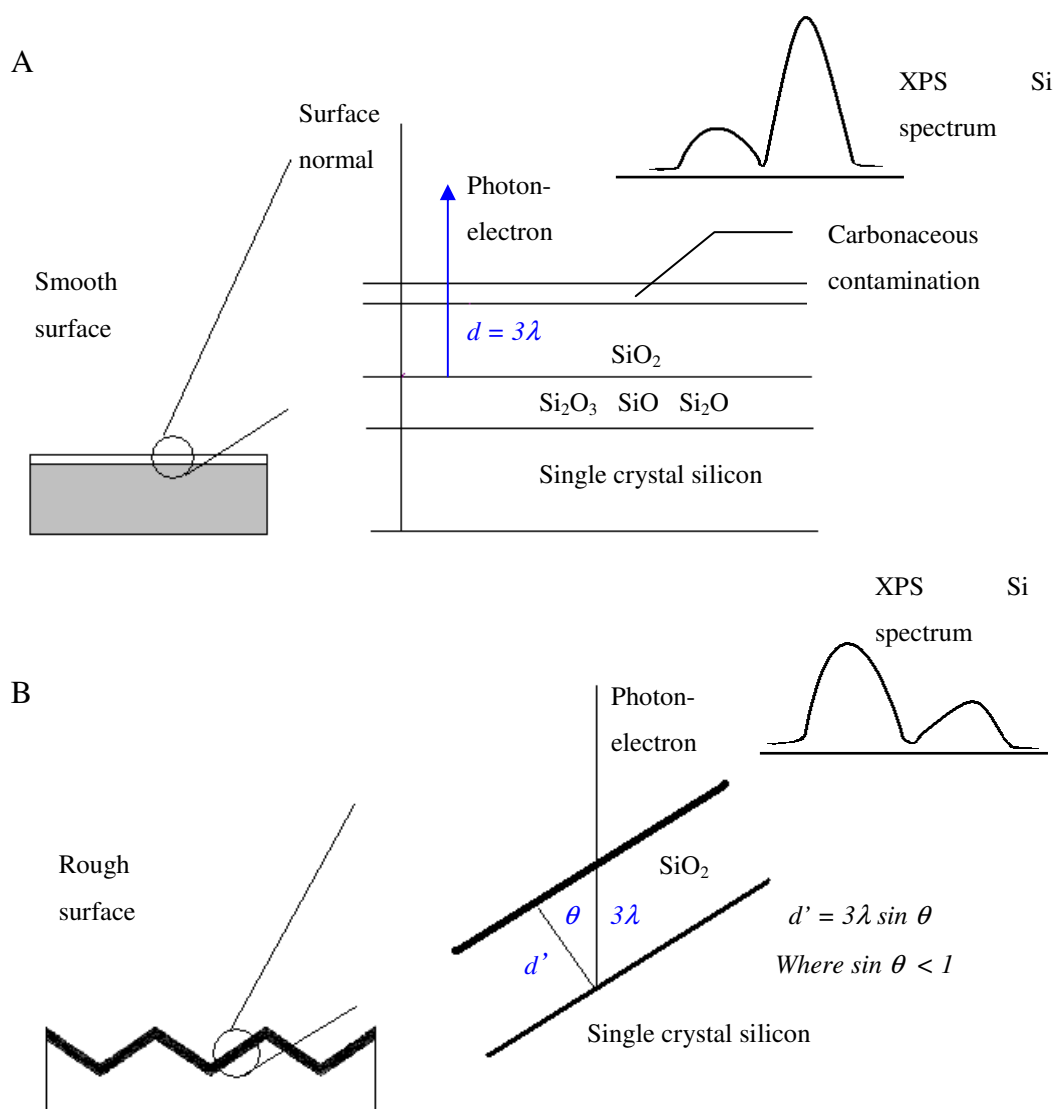


Figure 4-52 2D schematic of (A) smooth and (B) “triangular” rough silicon surface. On a smooth surface, the model of a silicon single-crystal substrate composed of an overlayer of silicon dioxide of thickness d , a contamination layer, and an intermediate oxides layer at the silicon dioxide/silicon interface. The photoelectrons emit at an angle normal to the surface and the thickness of dioxide $d = 3\lambda$, where λ is the attenuation length. On a simplified model of a rough surface, the surface is composed of a number of segments of smooth surface tilted according to the magnitude of the localised roughness, by an off-axis angle, θ , which is the angle between the central axis of the XPS analyser and the surface normal of the sample. Accordingly, the attenuation length measured is larger than the actual thickness of dioxide overlayer.

A laser modified SALDI surface was also examined by SIMS ion mapping, in which a wide variety of molecular species was accessed with an improved lateral resolution. However, SIMS is surface specific and only the topmost oxides layer was detected. Ion images were generated by a finely focused primary ion beam produced by Ga^+ liquid metal ion gun swept the sample in a raster pattern of an area $500 \times 500 \mu\text{m}^2$ and software saved secondary ion intensities as a function of beam position. Resolution was 512×512 pixels. Figure 4-53 shows an optical image of the surface used for imaging. Three areas, corresponding to laser modified region (Area A), non-modified region (Area B) and a particle (Area C), appeared as a purple dot, are highlighted. The SIMS images are shown at Figure 4-54 and the results are summarised in Table 4-7.

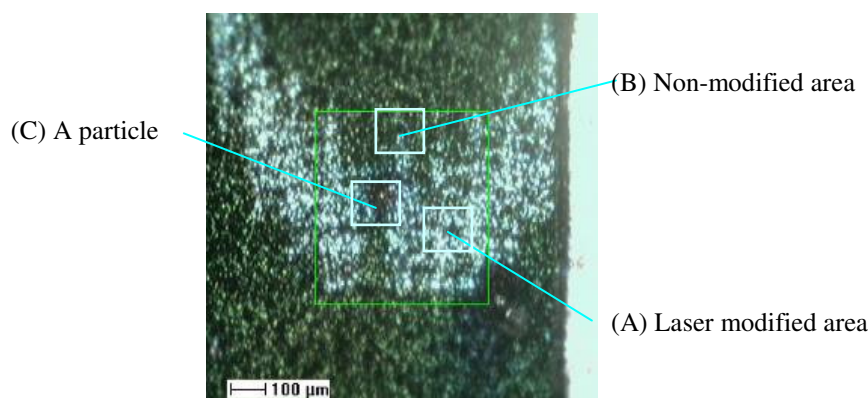
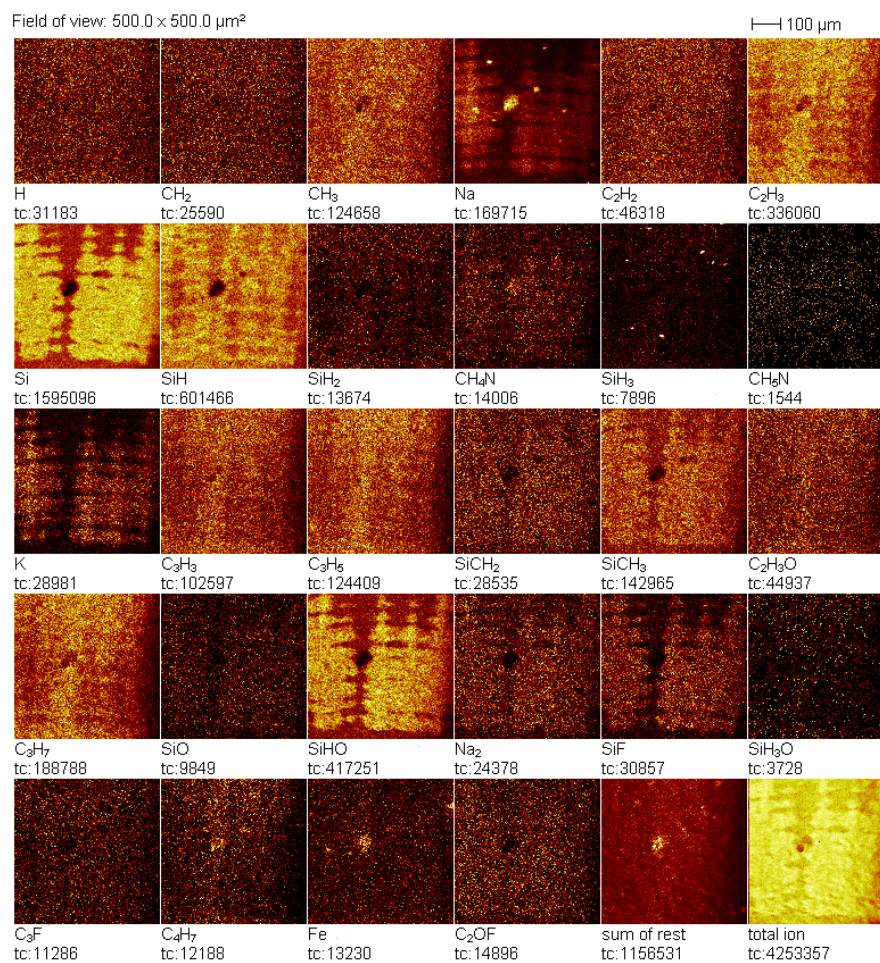


Figure 4-53 Optical image of SALDI substrate s1 after SALDI-MS investigation showing an arc caused by laser etching. The green square indicates the area used for SIMS imaging. The substrate was stored in propanol until analysis.

Table 4-7 Comparison of the elemental and molecular ions detected by ToF-SIMS at different region of the surface.

| Higher in Area A (modified region) | Higher in Area B (non-modified region) | Relative uniform between A and B | Higher in Area C (particle region) |
|---|--|---|---|
| Na^+ , Na_2^+ , K^+ , Si^+ , SiH^+ , SiF^+ , SiCH_2^+ , SiCH_3^+ , SiO^+ , SiHO^+ , CH_4N^+ , F^- , Cl^- , I^- , O_2^- , SiO_2^- , SiHO_2^- , SiO_3^- , SiHO_3^- , SiH_3S^- | SiH_2^+ , SiH_3^+ , CH_3^+ , C_2H_3^+ , C_3H_3^+ , C_3H_5^+ , C_3H_7^+ , C_4H_7^+ , H^- , C^- , CH^- , Si^- , SiH^- , SiH_2^- , SiHO^- , | H^+ , CH_2^+ , CH_3^+ , C_2H_2^+ , CH_5N^+ , $\text{C}_2\text{H}_3\text{O}^+$, SiH_3O^+ , C_3F^+ , C_2OF^+ , Fe^+ , O^- , OH^- , C_2^- , C_2H^- , C_2H^- , CN^- | Na^+ , Fe^+ , C_4H_7^+ , CH_4N^+ , C_2^- , CN^- |

Positive Ions



Negative Ions

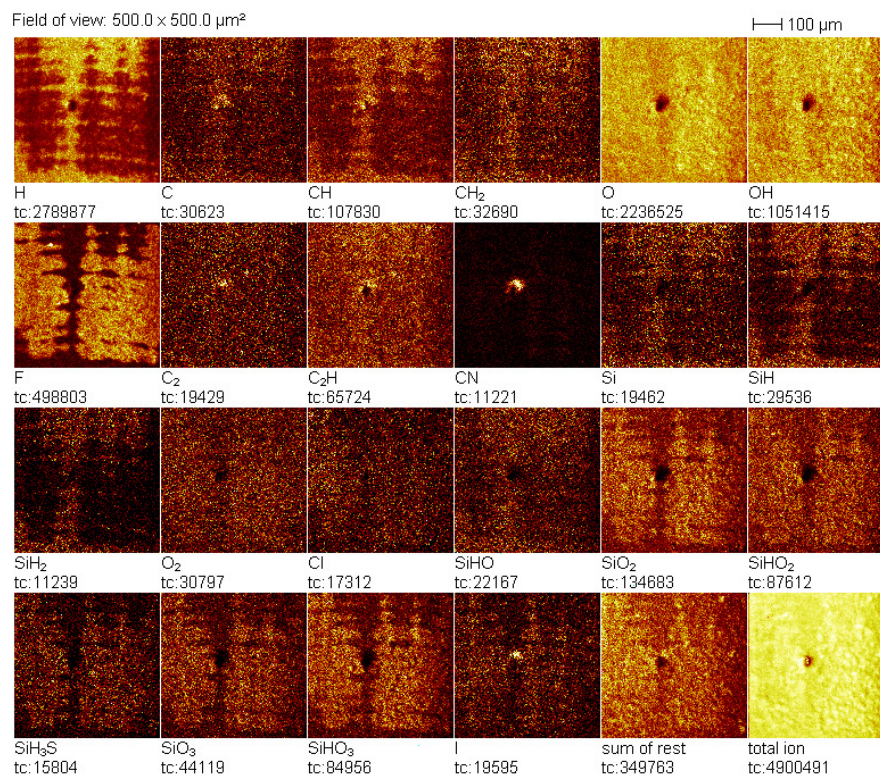


Figure 4-54 ToF-SIMS ion images of laser modified SALDI surface s1. Logarithmic scaling and Poisson correction is used to scale the contrast of the images.

The images of H^+ , CH_2^+ , CH_3^+ , O^- and OH^- ionic species are intense and are relatively uniform on the surface. This suggests they might have been formed from species subsequently adsorbed onto the surface after the gas-phase SALDI-MS testing. On the other hand, ionic species of silicon oxides (SiO^+ , SiO_2^- , SiO_3^-) and hydroxides (SiHO^+ , SiHO_2^- , SiHO_3^-) are observed on the laser-modified region with higher intensities relative to non-modified region. Silicon hydride ions (SiH_2^+ , SiH_3^+ , SiH^- , SiH_2^-) are lower on the laser-modified region relative to non-modified region. Similarly, Si^+ ion is intense and shows a higher intensity on the laser-modified region and yet the intensity of Si^- is lower on the same area. This observation points to the matrix effects caused by silicon oxides,⁴² and possibly involving other highly electronegative ions (F^- , Cl^- , I^- , O_2^-), which have a higher intensity on the modified region and favour the formation of Si^+ . In fact, the significant difference of F^- ion between these two regions is noteworthy. (*vide infra*) Overall, the surface was oxidised during the SALDI process.

Furthermore, conversely to the plasma etching, halogens/halides ion such as fluorides, chloride and iodide (F^- , Cl^- , I^-) are higher on the laser-modified area relative to non-modified area. The same is true for Na^+ and K^+ . This may be because laser has removed the surface contaminants and the deeper layer exposed to the surface. Then again, is there any relationship between sodium/potassium and halogens/halides signal? (See section 4.2.10.3) On the other hand, the particle observed may be an organic salt, as species such as Na^+ , Fe^+ , CN^- , and I^- are relatively stronger in its region.

The ion intensity of SiH^+ is also higher on the modified region. Even if matrix effects have a role in enhancing the intensity of Si^+ on the modified region, this still cannot explain the observed pattern of SiH^+ . A possible explanation is that, laser induces a further reaction with remaining etchant to the surface. This is supported by SiF^+ , F^- and I^- images. SIMS spectra are reconstructed using the relative intensity of Si^+ (positive) and F^- (negative), respectively, corresponding to modified and non-modified region of the surface. (Figure 4-55 and Figure 4-56) H^+ and O^- are uniform throughout the ion image and are chosen as a reference. The intensity ratio of SiH^+/H^+ increases from 17.7 to 20.0 (non-modified to modified region) and the intensity ratio of F^-/O^- also increases from 0.22 to 0.42 (non-modified to modified region). This implies that fluorine passivation as proposed may only occurs after laser etching.

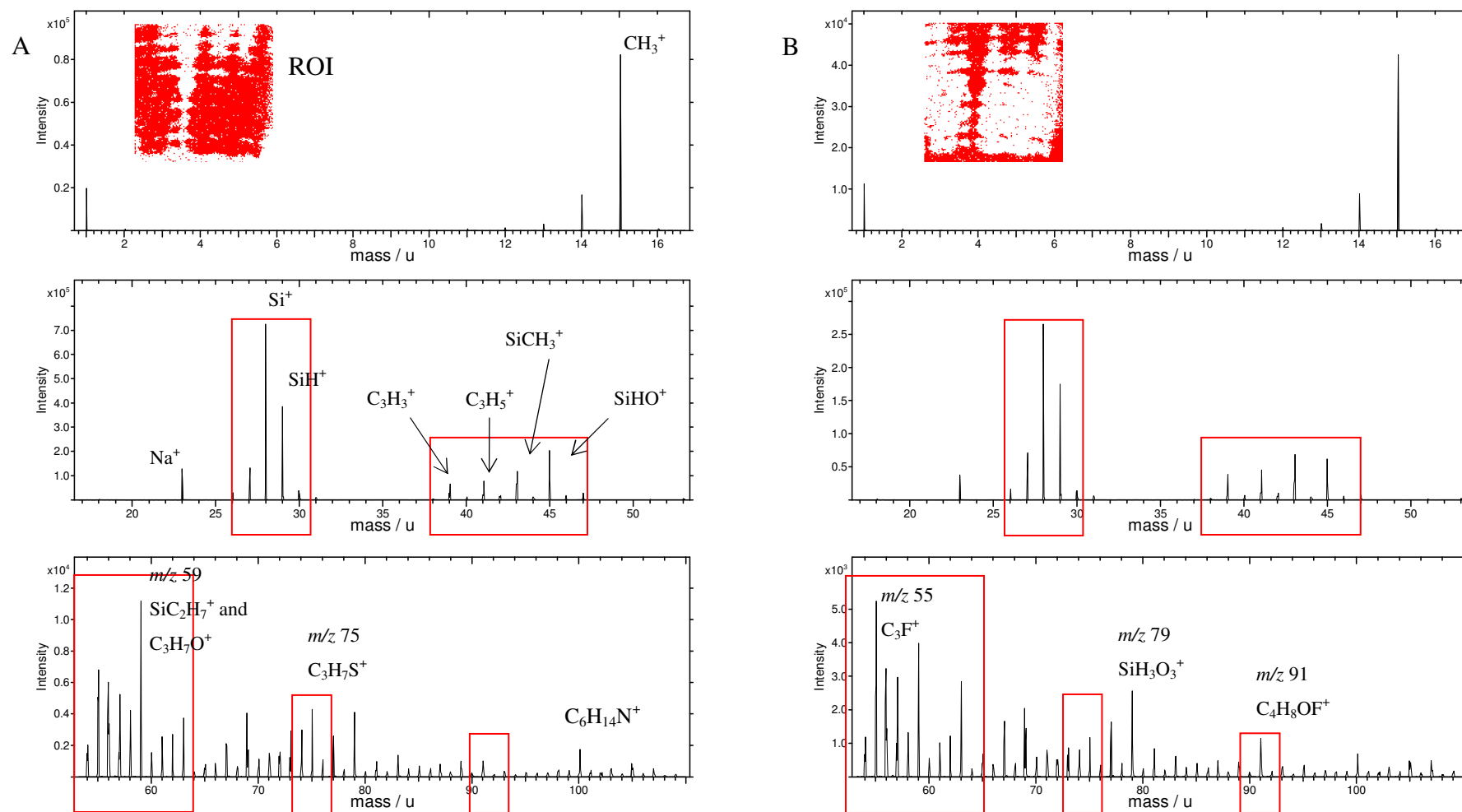


Figure 4-55 SIMS spectra of (A) modified region and (B) non-modified region under positive mode. The spectra are regenerated by summing the spectra collected at the selected region of interest (ROI), insert. Significant differences between the spectra are highlighted by red boxes.

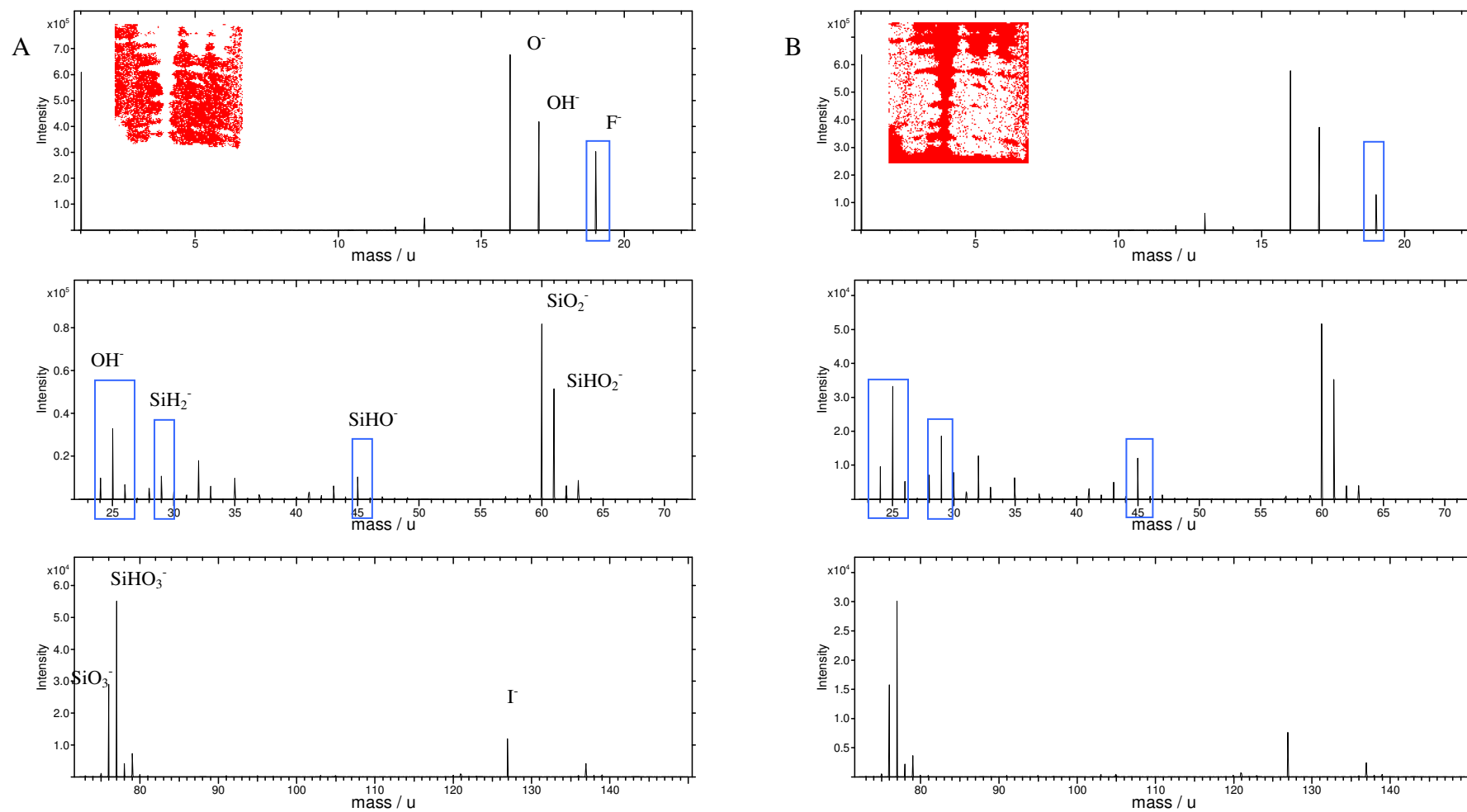


Figure 4-56 SIMS spectra of (A) modified region and (B) non-modified region under negative mode. The spectra are regenerated by summing the spectra collected at the selected region of interest (ROI), insert. Significant differences between the spectra are highlighted by blue boxes.

4.2.10.3 Observing Native Variation of SALDI Substrate by Using SIMS Imaging

According to the SALDI ionisation theory proposed, the SALDI surface is hydride, fluorine and/or iodine passivated.⁴³ Iodine on the surface is dissociated during the aforementioned laser etching, which then leads to the formation surface dangling bonds. Water is then dissociated adsorbed and incorporated onto the surface and forms Si-OH, which is believed to be the main proton source. This theory was based on the observation that during the laser etching, a high intensity of iodine ions is detected by the mass spectrometry under the negative ion mode. Apart from physical scratches and/or salt particles, the ToF-SIMS ion-imaging revealed that most of the SALDI substrates received are chemically uniform, but a few substrates have areas show some variations. This provides us an opportunity to look into the matter from another prospective.

Figure 4-57 shows an optical image of SALDI surface s4, which has a distinct upper and lower variation native to the surface. There is also a dot in the mid-lower region. This surface has also been investigated by SIMS imaging. (Figure 4-58) The SIMS images also reveal the presence of salt particles but are not clearly visible by the optical image. The results of SIMS imaging are summarised in Table 4-8.

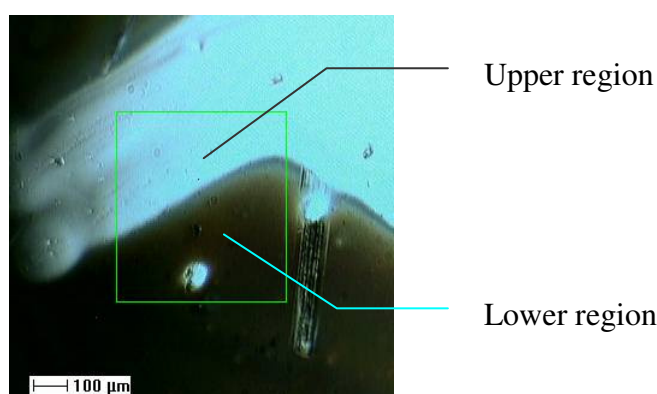
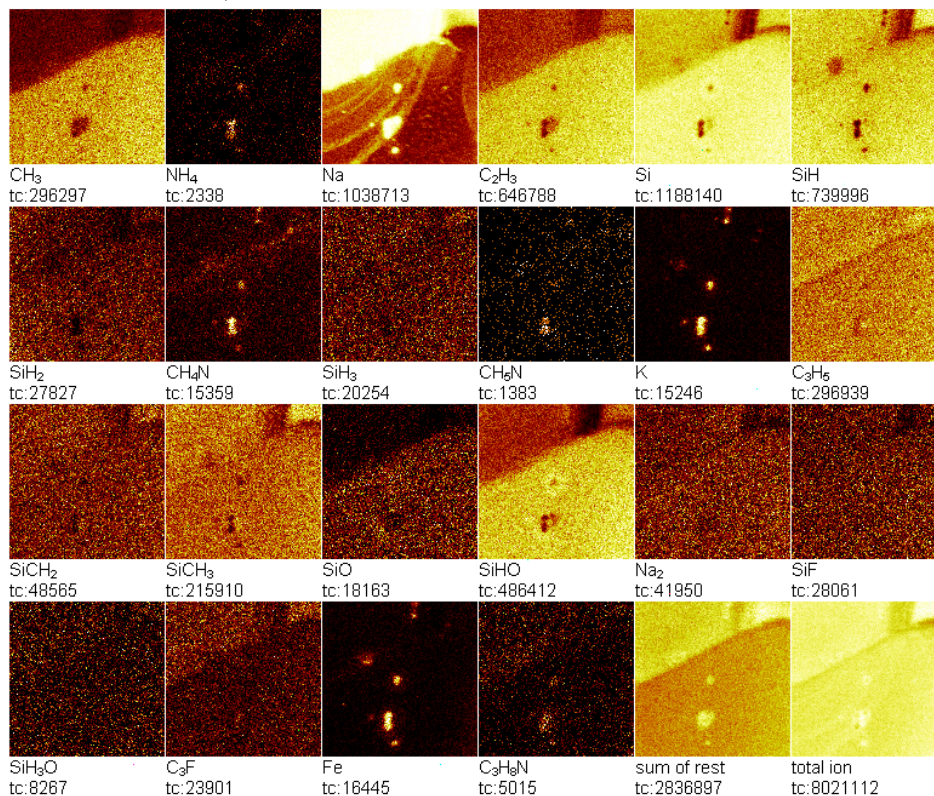


Figure 4-57 Optical image of the as-received SALDI substrate s4. The substrate was stored in propanol until analysis.

Positive Ions

Field of view: 500.0 × 500.0 μm²



Field of view: 500.0 × 500.0 μm²

Negative Ions

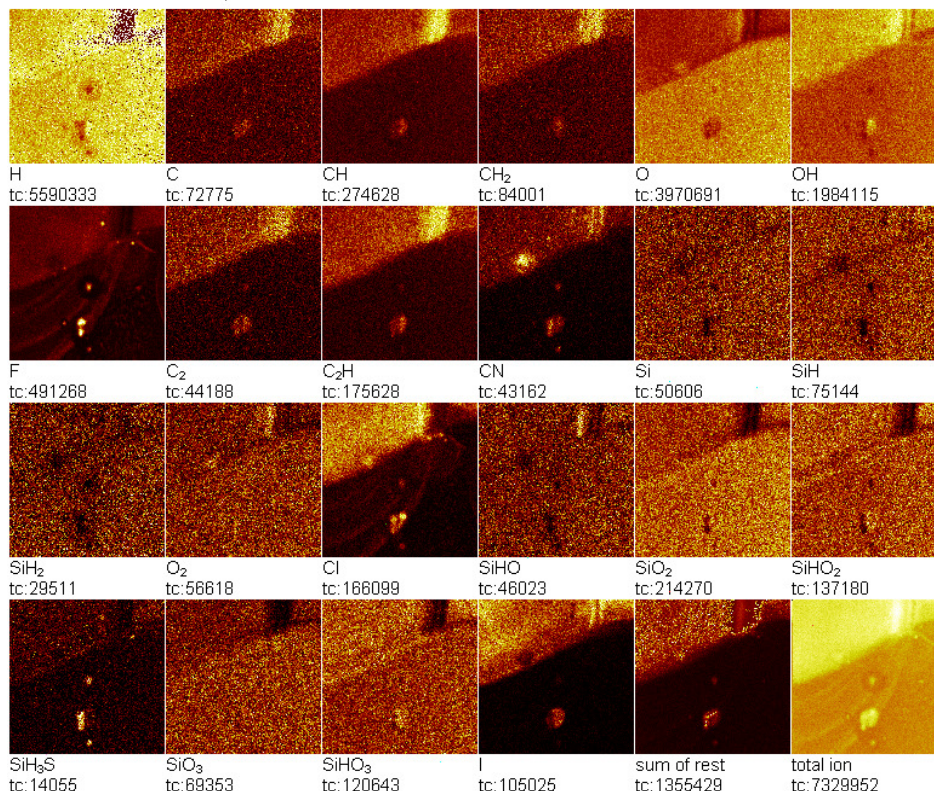


Figure 4-58 ToF-SIMS ion images of the as-received SALDI surface s4. The images suggest the SALDI substrates are not iodine passivated. Logarithmic scaling and/or Poisson correction is used to scale the contrast of the images.

Table 4-8 Comparison of the elemental and molecular ions detected by ToF-SIMS at upper and lower region of the surface.

| Higher in the upper region | Higher in the lower region | Relatively uniform | Particles |
|---|--|---|--|
| Na^+ , C_3F^+ , C^- , C_2^- , CH^- , CH_2^- , C_2H^- , CN^- , OH^- , F^- , Cl^- , I^- , SiHS^- , SiHO_3^- | CH_3^+ , C_2H_3^+ , Si^+ , SiO^+ , SiHO^+ , O^- , SiO_2^- , SiO_3^- | SiH^+ , SiH_2^+ , SiH_3^+ , SiCH_2^+ , SiCH_3^+ , SiF^+ , SiH_3O^+ , Si^- , SiH^- , SiH_2^- , O_2^- , SiHO^- | Na^+ , K^+ , Fe^+ , NH_4^+ , CH_4N^+ , CH_5N^+ , $\text{C}_3\text{H}_8\text{N}^+$ F^- , Cl^- , SiH_3S^- |

The highlight here is the pattern of Na^+ , OH^- , C_x^- , C_xH_y^- , CN^- , F^- , Cl^- , and I^- in the SIMS ion image shows a clear distinction between the upper part and the lower part of the image. The halide ions appear closely correlated to the Na^+ , water and hydrocarbons, but not silicon on this native SALDI surface. This suggests, the iodine ion observed by mass spectrometry may be in the form of sodium iodide, and may not be in the form of Si-I. Accordingly, iodine does not have any correlation to the SALDI ionisation mechanism as proposed and the formation of dangling bond due to iodine dissociation from the surface has to be rejected.

Model of Laser Modification of the SALDI Surface

A model is proposed to summarise the effects of laser modification to the SALDI surface. (Figure 4-59)

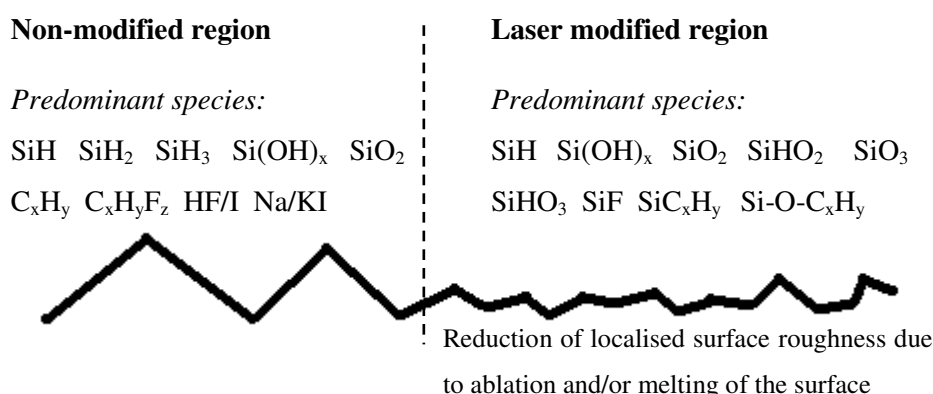


Figure 4-59 2D schematic of the effects of laser modification to the SALDI surface in SALDI-MS environment. Laser induces oxidation of the surface and leads to formation of Si-OH moiety.

4.3 Summary and Discussion

The simplest forms of ions generated by DIOS-MS are protonated and deprotonated ions. Nevertheless, fragment ions and various ionic products were observed in the DIOS mass spectra. There were also dissimilarities in spectral response among different instruments used. There are questions that arose from the results. The questions include the factors that govern the ionisation process, the process of proton transfer and the source of proton, the fragmentation reaction, the formation of molecular ions, the desorption of ions, the reduction of metallic ion such as copper (II) and iron (III), and the tendency of the formation of metallic aggregates of acidic compounds, etc. In here, the explanation to the experimental results observed is sought and a hypothesis on DIOS/SALDI activity is formulated.

4.3.1 Proton Affinities and Aqueous Basicities of the Analyte

It has been proposed that one of the determinants in gas-phase SALDI-MS is that, for the observation of protonated analytes, the pKa-value of the analyte must be larger than about 4.^{7, 43} The SALDI theory assumes that the basic compounds are ionised via metathesis reaction and are desorbed as pre-formed ions in a solvated state. An alternative view is that the detection of protonated ions depends on the PA value of the analyte molecules, as presented in the introduction section. PA is preferred over gas-phase basicity (GB) here because GB differs from PA with the inclusion of thermal and entropy corrections and yet the temperature of the LDI system is undeterminable.

Very early in this study, it was noted that the addition of acidic modifier did not improve ion yield, whether on the DIOS or the QuickMass targets, and for peptides or small molecules. This has already raised the question of whether pKa is a relevant factor, though the ion-pairing effect has to be considered concurrently. Interestingly, from our investigation of amino acids, only arginine, histidine and/or lysine could be effectively detected under positive ion mode – an observation opposite to that of ESI condition. The amino acid side chain functional group or their PA values are

important. The investigation of peptides also showed that the peptides which contain arginine, histidine and/or lysine residues, such as bradykinin (PA ~ 1025 kJ/mol) and angiotensin, could be effectively detected under positive ion mode. In contrast, the peak intensity of protonated species of synthetic peptides, such as polyglycine, polyalanine and polyphenylalanine, was relatively low, and the formation of salt adducts and salt-bridged cationised multimers were favoured. This observation is similar to that of organic acids observed under negative ion mode and cannot be explained comfortably by aqueous phase chemistry in bulk.⁴⁴ Increasing the chain length of synthetic peptides led to enhanced ionisation and such observation has to correlate to the increasing PA values of the peptides. Although the protonated ion of pentapeptide leucine enkephalin (PA ~ 998 kJ/mol) was detected under AP-MALDI condition, the DIOS spectra acquired under vacuum condition were dominated by its fragments and/or salt adducts. This observation may be explained by its amino acid chain (Tyr-Gly-Gly-Phe-Leu) lacking a high PA residue.

Insofar the results presented, albeit the pKa value of many basic compounds that can be detected under positive ion mode are high. On balancing the influence of the pKa and the PA values, the formation of protonated species from neutral molecules and their LDI sensitivity, the PA value is more influential than the pKa value by not just telling which substance is more likely to be detected as protonated species but also their relative sensitivity. Metathesis proton exchange reaction proposed previously could only be an ancillary process. Still, we cannot overlook the possibility that ion source pressure, temperature, laser beam divergence, ion guide design of the mass spectrometer, surface chemistry of the substrate, modifiers or salts and other instrumental factors will influence the relative distribution of $[M+H]^+$ ion and the ionic products of an analyte.

4.3.2 Formation of Ions

It is possible to rationalise the observations on ion formation in SALDI/DIOS by comparing the similarity with the MALDI ionisation mechanism. According to Knochenmuss,¹⁵⁻¹⁷ several possible ionisation reactions occur in MALDI, including multi-photon ionisation, disproportionation reactions, excited-state proton transfer,

energy pooling, thermal ionisation, desorption of preformed ions, and fragmentation of the sample into charged chunks and cluster, etc. These primary ionisation reactions produced the ions usually observed in MALDI mass spectra. Secondary ionisation reactions involve ion-molecule reaction, proton transfer, electron transfer, and cation attachment or transfer. It should be noted also the MALDI reactions are primarily governed by the principles of thermodynamics.¹⁶

On close examination of the LDI spectra obtained, there is a very close similarity between the MALDI and the matrix-free LDI reactions. For example, direct ionisation/desorption of molecules, which have a low IE value or are UV radiation sensitive or pre-charged ions. Disproportionation reactions that leads to the formation of quasi-molecular $[M-H]^+$ ion as well as protonated molecules $[M+H]^+$. Very often, the SALDI/DIOS mass spectra of amines display a tailing region of the molecular ion peak. This phenomenon is believed to be the metastable state of desorbed ions and such phenomenon is often seen in ToF-SIMS spectra. Metastable peaks are a result of fragmentations occurring in the field-free region of the spectrometer and means that fragmentation occurs after some initial acceleration (*i.e.* while passing down the flight tube). Indeed, the relatively controlled and specific fragmentation pattern and the application for post-source decay (PSD) in DIOS similar to that of MALDI without the need of collision induced dissociation (CID), is an usual capability of the DIOS technique we need to pay attention to.^{1, 45} These observations suggest the existence of excited-states of desorbed molecules/ions as in MALDI. The differences here is that the functions of the matrix are merely substituted by an active substrate. Gas-phase secondary ion-molecular reactions can also occur and give raise to products of cation attachment and alkylation.

If the observation of the excited states of desorbed ions and the influence of PA values of the analyte are correlated, it is possible to see that a fundamental protonation reaction is the excited-state proton transfer reaction and the reaction is in effect governed by the principles of thermodynamics identically to that of MALDI. This is further supported by the observation in relation to the instability of deprotonated molecules. How the neutral molecules are promoted to an excited state is not fully understood, since most of the compounds investigated do not absorb 337 nm UV radiation.

From the results we obtained in Chapter 3, the minimal requirement for LDI is the nanostructures of the surface. The capability of the surface coupling to laser radiation seems to be highly relevant in energy deposition. On the chemically etched surface, radiation absorption is highly efficient and the surface looks dark. The ability of absorbing UV radiation seems to be a key to the successful use of these substrates for the LDI-MS.

One possible scenario is that the laser energy is transferred via the substrate to the adsorbed molecules. Another possible scenario when highly concentrated sample droplet is added onto the surface, and hydrated micro-crystallites are formed, the laser excitation of the micro-crystallites via thermo-vibrational pathways ablates those micro-crystallites into gas-phase. Followed by disintegration of the micro-crystallites into the desorption plumb, ions are formed entirely in the gas-phase.

4.3.3 Proton Exchange on Silicon Substrates

Presumably, during laser excitation, the analyte molecules on the surface are promoted to an excited state, the next question is how the excited molecules obtain a proton. A number of possible proton sources have been considered throughout this investigation, such as organic contamination, residual water, acidic modified, water vapour in the residual gas of the vacuum system and hydroxide moieties on the surface.

Because of the high affinity of silicon surfaces to hydrocarbons, the adsorption of organic contaminants has been unavoidable in our experimental conditions. However, hydrocarbons somewhat provide a function of matrix and the desorption of the hydrocarbons carries the analyte molecules into the gas-phase and possibly behave as a low efficient proton donor.

On the other hand, though solvent decomposition is possible, the level of the residual water remained on the surface in UHV, even tightly bound water, is so low that residual water is less likely a major proton source. (Excepted in the AP-MALDI

system) As we have seen, the level of water did not contribute to the O 1s peak of the XPS spectra, and even if present, the concentration of water was below the detection limit of the instrument. Furthermore, the addition of D₂O did not produce a significant effect to the isotopic distribution of the spectra. Throughout our investigation, organic solvent systems have been applied onto the fluoro-silane modified silicon surfaces, and there has not been a problem in our laser mass spectrometry investigation. It appears that the solvent composition only effects to the aggregation and spreading of the sample droplet on the substrate. Similar observation has also been reported by Chen.³⁰ Organic acids added could be a proton source. Then again, additional energy is required to overcome the ion pairing effect and is energetically unfavourable.

It is very probable that the main proton source comes from the Si-OH moieties native on the surface and is partly supported by the results of XPS and SIMS imaging. The Si-OH moieties are converted to SiO₂ and releasing a proton as proposed by Alimpiev, *et al.* previously.⁴³ (Figure 1-19). Indeed, the SIMS and XPS spectra and WCA results have also shown that the SALDI substrates are passivated by an ultra-thin layer of oxides on the surface. The DIOS substrate though has been fluoro-silanised, its surface still has a high concentration of Si-OH moieties. Iodine, on the other hand, does not seem to have a role in the ionisation process and there is no evidence supporting the SALDI substrate has been passivated by iodine. Fluorine passivation to the SALDI substrates possibly occurs during the laser etching stage in the gas-phase SALDI-MS and no evidence supports that this is produced during the chemical etching procedure. Consequently, the formation of dangling bonds due to the iodine dissociation and subsequently reaction with adsorbed water as proposed previously cannot be considered a viable process and the involvement of Si-I, or its dissociation is not required.⁴³ If the proposed hydroxylation reaction occurs, the reaction may well be initiated by exciton, and/or thermal accelerated. (Figure 4-60) The availability of water vapour is dependent on the ion source pressure, and the proposed scheme may provide an insight accounting for the differences of the DIOS spectra obtained from AP and vacuum MALDI system. It should also note that the ablation of the oxide layer, surface melting and the further reaction of the surface with the remaining etchants could also occur as observed by XPS and SIMS imaging.

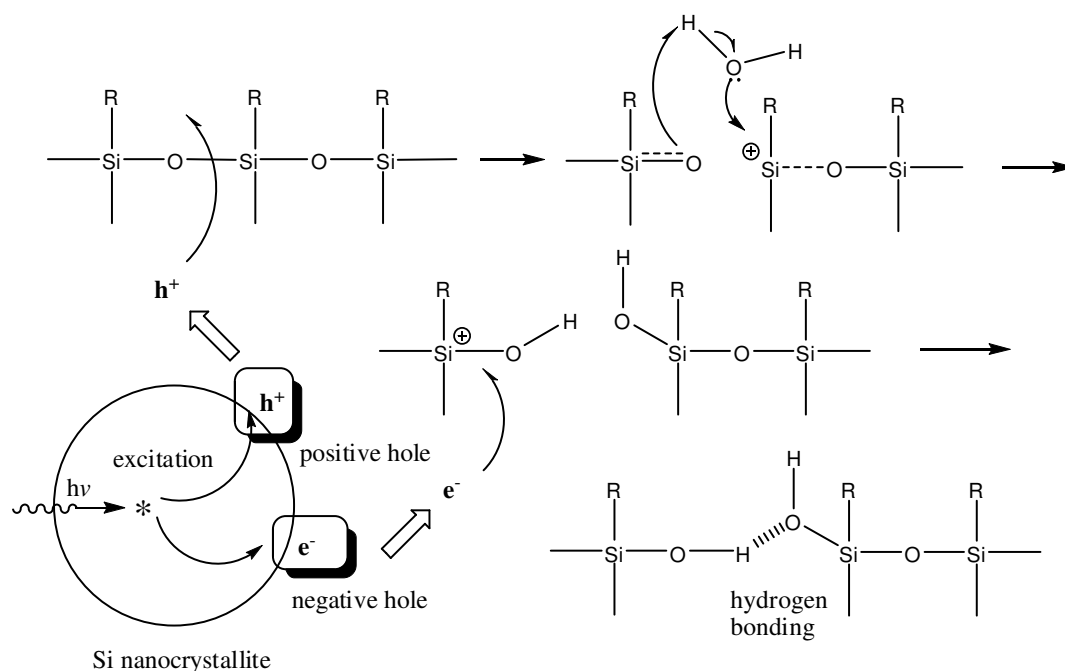


Figure 4-60 Proposed exciton-mediated hydroxylation reaction occurs during SALDI process. $R = H, OH, \text{ or } C_xH_y$. An unbound exciton produced by UV absorption leads to a surface-localised positive charge. This surface charge can then interact with an oxidising agent, or any nucleophile. In this case, where water is the nucleophile, Si-OH is formed. The abstract of an electron from exciton produces the final neutral species observed.

4.3.4 Surface Oxides, Halogen and Plasma Etching

If the Si-OH moieties were the main proton source, why would surface oxidation degrade the LDI performance since the plasma-etched SALDI surfaces requires significantly higher laser energy to obtain mass spectra. Firstly, only the Si-OH moieties are candidates for the main proton sources and not SiO_x where $x = 1-3$. Secondly, electrons can accumulate on the surface during LDI. (*vide infra*) The oxide layer and high electro-resistivity substrates may hide the charge neutralisation and thus an oxidised surface has a lower LDI performance. Furthermore, as Anderson has shown previously,²⁹ an oxidised surface is more reflective to UV radiation and hence has a much lower absorbance of UV radiation and hence less proportion of the laser energy will be deposited and transferred to the analyte molecules. (see Figure 3-6)

Furthermore, from the observations obtained in Chapter 3, the LDI performance can be enhanced either via chemical modification or via surface morphology. It is

evidenced that the fluoro-silane modified SALDI surfaces have a better SALDI performance relative to the as-received SALDI surfaces. The performance difference is contributed to the different interfacial reaction because of the fluoro-carbon termination on the surface. Halogens, as such fluorine, could well have an effect toward the proton exchange and have an important role in neutralisation the charge by withdrawing the electron density from the oxygen of the surface Si-OH moieties and hence stabilise the excited system and acidify the surface. In a system that halogens are absent, such as removing the halogens by plasma etching, it will be less energetically favourable for the protonation to occur. Indeed, the super-hydrophobicity introduced by fluorine not only enhances the desorption in DIOS, but also in DESI relative to non-modified silicon surface carried out in our laboratory.

4.3.5 Reducing Power and Electrostatic Field

It is known that the presence of electronic surface states at the surface of a semiconductor perturbs the local charge balance and the electronic structure inside the semiconductor material, leading to near-surface band bending.⁴⁶ Consequently, an additional negative charge is accumulated at the surface and the near-surface region is depleted of electrons and is hence positive. This is the origin of space-charge layer at the semiconductor interference.^{47, 48} (See section 4.3.6)

It is possible that because of the surface electronic configuration of a semiconductor surface, upon laser excitation electrons can be transferred from the surface to the analyte and this leads to redox reaction of metallic ions, such as copper (II),¹² iron (III),³⁷ and organ-metallic compounds.⁴⁹ It should also be noted that this is consistent with the reduction potential that can be provided by oxidation of silicon to its oxides. The charge accumulation could be amplified on nanostructures with sharp tips and lead to a large local electrostatic field and electron release.^{39, 50, 51} If this is the case, the release of electron plasma will undoubtedly lead to the formation of free radical in the desorption plumb and could lead to the onset of fragmentation and ion formation.

He, *et al.* proposed the electrostatic field is an (inverted) lightning-rod phenomenon.⁵² It is known that surface irregularities, such as sharp tips, produce a strong electrostatic

field upon irradiation with polarised light - an effect often associated with AFM technique and surface enhanced Raman spectroscopy (SERS). Nonetheless, while qualitatively plausible, quantitative calculation of the local field intensity show that it is too low for actual desorption/ionisation of natural molecules to occur.⁷ Secondly, the lightning rod effect, occurring when the particle is off-resonance, provides only a very small amplitude enhancement.⁵³ Then again, if the electrostatic effect was a resonance phenomenon, surface plasmon resonance was not observed by XPS on the substrate studied. The role of the sharp tips electrostatic field remains uncertain, and even if it does have a role, the effect is auxiliary or assists disintegration of ionic clusters and has to work collectively with the extraction field introduced by the mass spectrometer.⁷ The again, it is proposed that, though *electrostatic field* is less likely significant, *electronic transitions* are important.

4.3.6 Nanocrystalline Silicon Surfaces as Energy Transferring Media

Back to the time before MALDI was introduced, most species that was desorbed from the surface by direct laser desorption were neutrals at the laser fluences required to preserve molecular integrity (*i.e.* either fragment ions or no ions were obtained). Observations on how neutral molecules are desorbed from a surface concluded there are two main processes that contribute to the molecular desorption:

1. laser-induced *thermal* desorption (LITD)⁵⁴ and
2. *non-thermal* laser desorption induced by electronic transitions (DIET) [or more accurately, desorption induced by multiple electronic transition (DIMET)]⁴⁷

LITD occurs through excitation of the substrate by creation of electron-hole pairs that relax and causes phonon excitation. On the other hands, DIET is a non-thermal process that occurs by substrate excitation that leads to low energy electron transfer to the surface species. This charge-transfer on semiconductor surfaces is mainly governed by the band structure due to the presence of a space-charge layer. Indeed, the involvement of a thermal and a non-thermal electronic process perfectly fit the

experimental results, and the proposed gas-phase SALDI process.⁷ A question remains, what is the electron-hole pairs and space-charge layer?

Instead of forming a highly coordinated lattice structure like metals, semiconductors form structures in which the atoms are tetrahedrally coordinated. With these structures, the *ns* and *np* bands still overlap but the *ns/np* bands splits into upper and lower bands.⁵⁵ The upper band is the conduction band and the lower band is the valance band by analogy with the valence electrons of individual atoms. While in the conduction band, the electrons are free of their parent atoms and are conductive. There is an energy difference between the upper and lower band and is the band gap. The band gap is a forbidden zone and an electron cannot remain within this range of energy. In indirect bandgap semiconductors, such as silicon and germanium, the available energies for the electron also depend upon *k*, where *k* is the wavevector (resolved by the Schrödinger equation) and is related to the direction of motion of the electron in the crystal. (Figure 4-61)

(A) Silicon

(B) Germanium

Conduction
band

**Printed version includes figure(s) extracted
from the reference source describing
the indirect bandgap structure of bulk silicon and germanium.
Please refer to the cited reference for detail**

Valance band

Figure 4-61 Schematic of the band structure of indirect bandgap seiconductors: (A) silicon and (B) germanium. E_g is the bandgap energy.⁵⁶ In contrast to direct bandgap semiconductors, the minimum energy in the conduction band is shifted by a *k*-vector relative to the valence band. The *k*-vector difference represents a difference in momentum.

The electronic configuration of the atoms at the surface is different. All atoms in the bulk of a pure metal or elemental semiconductor are equivalent. The atoms at the

surface are different because they do not possess their full complement of bonding partners.⁴⁶ Consequently, a semiconductor surface usually possesses electronic surface states and such states are energetically located in the band gap.⁴⁷ These relatively localised states can result from dangling bonds on the surface, surface defects and impurities.⁴⁷ Depending on the type of surface state (donors or acceptors) and the position of the Fermi level (the highest energy level in the crystal that can remain populated by electrons at 0K) at the surface, the surface states may carry charge, which is screened by an opposite charge inside the semiconductor material.⁴⁷ Due to the low free-carrier concentration in semiconductors, the screen length is long and a space-charge layer is formed, giving rise to band bending.⁴⁷ (Figure 4-62)

A

B

**Printed version includes figure(s) extracted
from the reference source describing
the electronic structure of n-type silicon surfaces, which differs
from the bulk that there is an electric surface state and band
bending.**

C Please refer to the cited reference for detail

Electronic surface state

Figure 4-62 Schematic illustration of band bending near the surface of *n*-type semiconductor. (A) illustrates the disequilibrium between the bulk and the surface. (B) shows band at equilibrium. E_C and E_V are the conduction and valence-band edges, E_F the Fermi energy, E_D the energy of the bulk donor (*n*-type). $Q_{ss} = -Q_{sc}$ are the charges accumulated at the surface and in the space charge layer. $eV_s = e\psi(z=0)$ denotes the band bending. (C) Carrier excitation and transport near the surface during photo-excitation that lead to the formation of electron-hole pairs (e^- and h^+).^{47, 48} Non-radiative recombination of e^- and h^+ takes place only at the electronic surface state.

In fact, the unique features of charge transfer dynamic on the semiconductor surfaces are mainly governed by the band structure, particularly the presence of a space-charge layer. When photons with energy larger than the band gap are absorbed by the surface, electrons from the lower band can be promoted to the upper band and this creates energetic electron-hole pairs or excitons. Within the space-charge layer, electron-hole pairs are driven apart by the space charge field. For n-type semiconductors, electrons are driven into the bulk, while holes are transported toward the surface. This is because the charged carriers (electron and hole) are separated by the surface band bending and produce (UV radiation mediated) oxidation on the surface.⁵⁷ When such charge separation or exciton formation creates an electric field and when it is relaxed via carrier-phonon scattering, this causes an electronic perturbation and vibrational excitation to the surface and adsorbates. The relaxation of excitons eventually transfers the laser energy to the adsorbates and leads to a promotion of the adsorbates to an excited state. This is possibly followed by energy pooling as in MALDI. Without the band bending and the electronic surface state, the photoexcited electrons would quickly settle into the energy minimum of the conduction band. Because of the momentum difference between the energy minimum of the conduction band and the energy maximum of the valance band in indirect band gap semiconductors, non-radiative recombination of electrons and holes is prohibited and efficient excitation of the adsorbates is not happening.

The requirement of roughened or nanostructured surface for LDI appears to enhance the aforementioned energy transfer processes and leads to effective ion formation. Then again, substrates that consist of different surface morphology or use different bulk material may not share an identical excitation pathway and we cannot exclude that there are some differences in the ionisation mechanism. Graphite, for example, has a negative indirect bandgap, *i.e.* the energy maximum the valence band is higher than the energy minimum of the conduction band in energy, and thus would not share an identical excitation pathway.

We may consider a model that assumes only molecular species exist in the system, only protonation occurs in cation formation, and only deprotonation and metallic aggregates in anion formation. It should be noted that though the model presumes the deposited analyte molecules still to be in molecular state, it does not exclude the

possibility that the analyte molecules may also exist in hydrated states. Substances, which absorb UV radiation or exist as pre-charged ions are not applicable to this model.

After sample deposition, a thin film of solvent-analyte mixture is formed on the surface. Capillary condensation is believed to occur on porous surface. During the LDI, the laser pulses excite the surface, which in turn excites the adsorbed molecules. The physical parameter should accordingly be the activation energy (E_A). For positive ion system, as in MALDI, the excited system tends to lower its energy and return to chemical equilibrium that leads to the formation of protonated species (or in some cases, salt adducts). The physical parameter that governs the protonation reaction has to be another energy term, and that has to be the proton affinity (PA).^{4, 6} For that reason, protonation is therefore a thermodynamic consequence of lowering the energy of the system.

For a negative ion system, the analyte molecules are excited and then dissociate into M^{*-} ions and proton transfer occurs. The deprotonated species are unstable as they contain an extra negative charge and are excited. For larger molecules or molecules containing an aromatic system, the charge could be distributed throughout the whole molecular structure and would be relatively more stable, but for smaller molecules, this situation is unsustainable. One of the consequences is to form metallic aggregate where the excess charge could be distributed to the metallic ion. A possible solution to enhance the detection of these metastable species is that the ions must leave the ion source and reach the detector before its internal energy falls, for example, by using linear ToF. Figure 4-63 summarizes the reaction profile of this model. Consequently, it is the *entropy of the reaction ultimately determines which substance is detected by LDI and the rate of reaction determines the selectivity.*

The level of excited desorbed neutral molecules (neutral yield) may overwhelm the proton transfer process if the rate of desorption is higher than the rate of proton transfer, and the latter becomes inefficient. The internal energy of the excited molecules is redistributed via the intramolecular vibrational energy redistribution (IVR).⁵⁸ The energy randomly distributes over the molecule and becomes concentrated in particular fashions which in turn give rise to unimolecular

reconfiguration and dissociation in the acceleration and post-acceleration region of the mass spectrometer,⁵⁹ obeying the principles of quasi-equilibrium theory (QET).⁶⁰ This may explain the ordered fragmentation often observed.

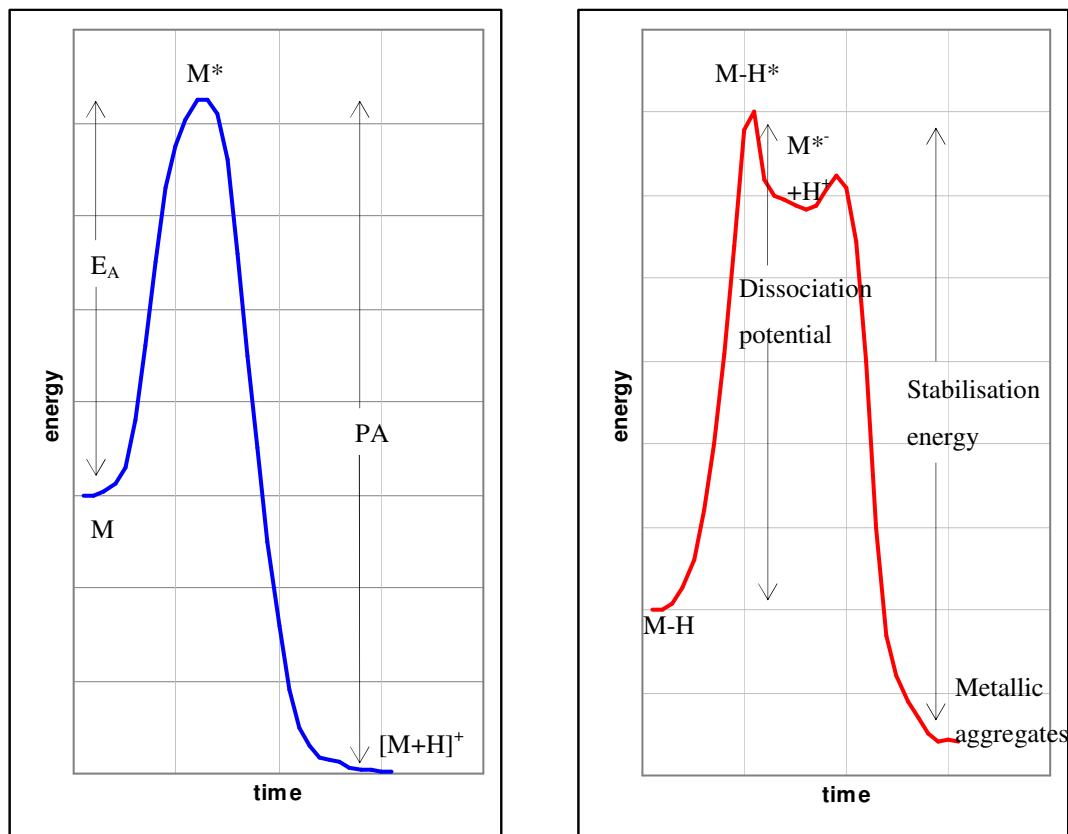


Figure 4-63 Proposed reaction profile of protonated ion formation (*left*) and deprotonated ion and metallic aggregate formation (*right*). “*” denotes excited state.

Although limited data has been presented relating PA and LDI sensitivity, to ascertain this theory, possibly we can adopt a similar approach of Ostman, *et al.*^{5, 6} by comparing the ion yield of many different compounds and with their known thermodynamic properties, such as PA values and dissociation constants. Unfortunately, very little experimental data is available and the thermodynamic properties are normally calculated based on quantum properties of the analyte molecules. Gaussian is often employed in the *ab initio* calculation, and it provides good speed and accuracy. However, a super computation power is required for the calculation. Although, the LDI spectral response of many compounds has been examined, in the absence of the support of computational chemistry, it is difficult to pursue further.

4.3.7 Possible Roles of the Pores

A consistent observation throughout this study and in data published in the literature is that the substrates composed of a thick porous layer, not only produce a higher ion yield than the non-porous surfaces in LDI, but also extends the effective detection range to larger molecules. Whether it is the rough surfaces such as the QuickMass target or the non-porous SALDI surfaces, in comparison to the porous surface, the non-porous surfaces are less effective in promoting the LDI activity and thus produce lower ion intensity.

In this investigation, structural change was observed after the target surface was used for LDI by optical imaging and SEM. One can assume that a sudden but localised thermal jump occurs during the laser excitation to the surface. The desorption plume cannot expand freely because of the confinement of the porous structure, a large pressure gradient relative to the vacuum chamber in the mass spectrometer is generated, bringing or ejecting the ions and analyte molecules into the vacuum (consider the similarity with gun barrel). The big pores could be formed due to the expansion of the desorbed plumb and/or the gas trapped inside the porous layer and led to a destruction of the porous structure. This result supports previous studies that the confinement introduced by the porous layer leads to explosive vaporisation and possibly generates a pressure gradient bringing the ions into vacuum.^{10, 39} Although the pores may not have a direct role in ionisation, but they do have a role in retaining the analyte, assisting the desorption process, increasing the sensitivity and extending the detection mass range.

Furthermore, it is possible that a thick porous layer increases the optical path length and enhances optical absorption and the longevity of analyte signals.⁶¹ Additionally, the molecules that are present within the pores should experience the strongest fluctuation of the electric field and this is an additional reason that surfaces which have a thick porous layer, among all the surfaces investigated, give the best LDI performance. Moreover, porous structure is an effective mean to increase the surface area of the matrix-free LDI substrates relative to roughening and yet pores are less

structural fragile than shape tips, and the pores provide a confined space to retain the analyte molecules and to enhance the ion yield (Figure 4-64).

When a fluid is confined to a very small cavity near to the size of molecules, such as nano-scale pores, its phase behaviour is altered. Long-range fluctuation and thermal-vibrational effects could be another energy transfer pathway. Unfortunately, molecular dynamics and interfacial interactions in a confined space remain less well understood and this area is normally studied by neutron scattering.⁶²⁻⁶⁵ At this time, one can only speculate that the molecules confined into the pores depending on the molecular size and shape may orientate themselves relative to the surface in a gel-like film and therefore are retained effectively. On the other hand, to investigate the desorption process, nanosecond time-resolved imaging and photoacoustic analysis, that has been employed in the investigation of the MALDI expanding and desorption process by the Laser Mass Spectrometry Group of the University of Münster could be of use.⁶⁶

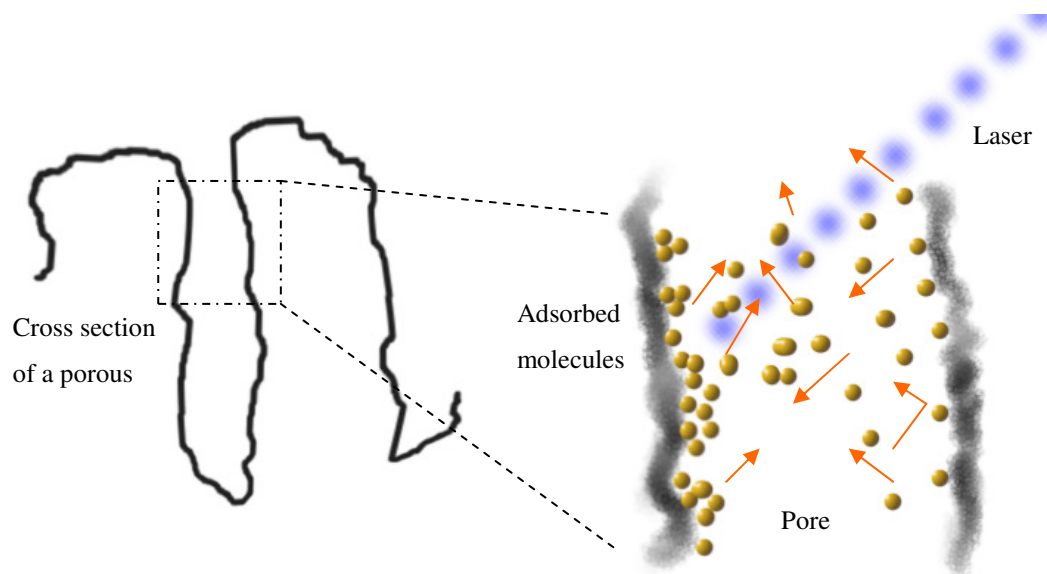


Figure 4-64 A proposed model of laser-induced desorption/ionisation on a porous surface. Two-dimension adsorbate on the wall of the pore is excited and desorbed into gas-phase. Unlike the adsorbate on a rough surface, the resulting plume cannot expand into all directions but into one dimension desorbed phase due to the confinement imposed by the porous structure. This generates a pressure gradient and ejects the ions into vacuum.

4.3.8 Differences to Gas-phase SALDI-MS

There have been inconsistent reports to the determinants of the LDI activity and the evidence collected suggests that there are differences between the gas-phase deposition approach and the common liquid-deposition approach. It should be noted that the first process of the gas-phase approach is gaseous adsorption of the analyte molecules onto the adsorbing surface. The proposed factors, such as reduced roughness (discussed in Chapter 3), the influence of aqueous basicities (pKa) of the analyte, acidifying the residual gas in the vacuum chamber by acetic acid, *etc.*, could relate to the rate of adsorption process, and/or the secondary ion-molecular reactions in the desorption plumb. Nevertheless, vacuum liquid-deposition approach is not positively influenced by those factors. Common processes though include laser excitation, thermo- and electronic effects and proton exchange via the surface Si-OH moieties.

4.4 Conclusions

We employed a wide range of pharmaceutical and biological related compounds, three different MALDI systems, and hence three different ion source pressures and ion optics to determine the DIOS capability. XPS and SIMS imaging were employed to reveal the laser induced surface reaction on the SALDI substrates. Evidence was produced and an ionisation theory was proposed based on the unique properties of semiconductor surfaces. Still, a lot of work is required to answer the questions fully. This study perhaps represents the most comprehensive and concrete understanding of the matrix-free LDI activity available to-date.

The matrix-free LDI ionic reaction is similar or identical to that of MALDI. However, the functions of the matrix are substituted by an active substrate. Comparison of two techniques, MALDI is still more sensitive than DIOS for peptide detection. The opposite is true for small molecules because of the removal of matrix-related ion suppression. Ion formation is not a simple acid-base reaction, but rather like any chemical reactions, is determined by the principle of thermodynamics. As such, the ions observed are contributed to the entropy of the reaction (ion stability) and the rate of reaction (selectivity), departing from the conventional view of pKa or PA dependence. Surface structural and chemical changes due to LDI modification are observed. The implications of such change may be significant, and relates to the ion formation and desorption. The results of surface chemical imaging using XPS and SIMS reinforce the previous investigation that the Si-OH moieties could be a major proton source.

The electronic structure of the semiconductor surface is believed to play a crucial role. It is believed the use of the nano-structured semiconductor surface affords an effective means for transferring laser energy to the adsorbate. The presence of surface hydroxyl groups provides an immediate proton source. The nano-sized pores can effectively retain the analyte and the confinement effect may produce a pressure gradient during LDI, assisting the ions desorption. The success of DIOS-MS is its fortuitous combination of its inter-related multi-reaction and leads to an effective ion desorption and formation and is different from early attempts of SALDI-MS approaches.

4.5 References

1. Wei, J., Buriak, J. & Siuzdak, G. Desorption/ionization mass spectrometry on porous silicon. *Nature* 399, 243-246 (1999).
2. Kitrinis, P., Sheeley, D. M. & Johnson, R. L. Desorption ionization on silicon (DIOS) for the analysis of small organic molecules. Proc. 48th ASMS Conf. Mass Spectrom. Allied Topics, (2000).
3. Credo, G. M., Hewitson, H. B., Fountain, K. J., Gilar, M., Finch, J. W., Stumpf, C. L., Benevides, C. C., Bouvier, E. S. P., Compton, B. J., Shen, Z. & Siuzdak, G. Desorption/ionization on silicon mass spectrometry (DIOS MS) of small molecules and peptide: sample handling, preparation and storage effects on performance. 51th Annual Conf. ASMS Montreal, Canada, 8-12 June, (2003).
4. Huikko, K., Ostman, P., Sauber, C., Mandel, F., Grigoras, K., Franssila, S., Kotiaho, T. & Kostiainen, R. Feasibility of atmospheric pressure desorption/ionization on silicon mass spectrometry in analysis of drugs. *Rapid Commun. Mass Spectrom.* 17, 1339-1343 (2003).
5. Östman, P., Pakarinen, J. M. H., Vainiotalo, P., Franssila, S., Kostiainen, R. & Kotiaho, T. Minimum proton affinity for efficient ionization with atmospheric pressure desorption/ionization on silicon mass spectrometry. *Rapid Commun. Mass Spectrom.* 20, 3669-3673 (2006).
6. Östman, P., Franssila, S., Kostiainen, R., Ketola, R. & Kotiaho, T. The effect of physical properties of selected molecules on desorption/ionization on porous silicon-mass spectrometry 53rd Annual Conf. ASMS, San Antonio, June 5-9, (2005).
7. Alimpiev, S., Nikiforov, S., Karavanskii, V., Miton, T. & Sunner, J. On the mechanism of laser-induced desorption-ionisation of organic compounds from etched silicon and carbon surfaces. *J. Chem. Phys.* 115, 1891-1901 (2001).
8. Budimir, N., Blais, J.-C., Fournier, F. & Tabet, J.-C. The use of desorption/ionization on porous silicon mass spectrometry for the detection of negative ions for fatty acids. *Rapid Commun. Mass Spectrom.* 20, 680-684 (2006).
9. Li, Q. Exploring desorption/ionization on porous silicon mass spectrometry and its applications. Ph.D. thesis, University of Florida, (2005).

10. Luo, G., Chen, Y., Siuzdak, G. & A., V. Surface Modification and Laser Pulse Length Effects on Internal Energy Transfer in DIOS. *J. Phys. Chem. B* 109, 24450-24456 (2005).
11. Okuno, S., Nakano, M., Matsubayashi, G.-e., Arakawa, R. & Wada, Y. Reduction of organic dyes in matrix-assisted laser desorption/ionization and desorption/ionization on porous silicon. *Rapid Commun. Mass Spectrom.* 18, 2811-2817 (2004).
12. Okuno, S., Arakawa, R. & Wada, Y. Reduction of Cu(II) and riboflavin in DIOS mass spectrometry. *J. Mass Spectrom. Soc. Jpn.* 52, 13-20 (2004).
13. Okuno, S., Oka, K. & Arakawa, R. Oxidation of Ferrocene Derivatives in Desorption/Ionization on Porous Silicon. *Anal. Sci.* 21, 1449-1451 (2005).
14. Gluckmann, M., Pfenninger, A., Kruger, R., Thierolf, M., Karasa, M., Horneffer, V., Hillenkamp, F. & Strupat, K. Mechanisms in MALDI analysis: surface interaction or incorporation of analytes? *Int. J. Mass Spectrom.* 210-211, 121-132 (2001).
15. Zenobi, R. & Knochenmuss, R. Ion formation in MALDI mass spectrometry. *Mass Spectrom. Rev.* 17, 337-366 (1998).
16. Breuker, K., Knochenmuss, R., Zhang, J., Stortelder, A. & Zenobi, R. Thermodynamic control of final ion distributions in MALDI: in-plume proton transfer reactions. *Int. J. Mass Spectrom.* 226, 211-222 (2003).
17. Knochenmuss, R. Ion formation mechanisms in UV-MALDI. *Analyst* 131, 966-986 (2006).
18. Knochenmuss, R. A quantitative model of ultraviolet matrix-assisted laser desorption/ionization. *J. Mass Spectrom.* 37, 867-877 (2002).
19. Dashtiev, M., Wafler, E., Rohling, U., Gorshkov, M., Hillenkamp, F. & Zenobi, R. Positive and negative analyte ion yield in matrix-assisted laser desorption/ionization *Int. J. Mass Spectrom.* (2007).
20. Vermillion-Salsbury, R. L. & Hercules, D. M. 9-Aminoacridine as a matrix for negative mode matrix-assisted laser desorption/ionization. *Rapid Commun. Mass Spectrom.* 16, 1575-1581 (2002).
21. Vaidyanathan, S. & Goodacre, R. Quantitative detection of metabolites using matrix-assisted laser desorption/ionization mass spectrometry with 9-aminoacridine as the matrix. *Rapid Commun. Mass Spectrom.* 21, 2072-2078 (2007).

22. Schneider, B. B., Lock, C. & Covey, T. R. AP and vacuum MALDI on a QqLIT instrument *J. Am. Soc. Mass Spectrom.* 16, 176-182 (2005).
23. Elsilá, J. E., deLeon, N. P. & Zare, R. N. Factors Affecting Quantitative Analysis in Laser Desorption/Laser Ionization Mass Spectrometry. *Anal. Chem.* 76, 2430-2437 (2004).
24. Thomas, J. J., Shen, Z., Crowell, J. E., Finn, M. G. & Siuzdak, G. Desorption/ionization on silicon (DIOS): A diverse mass spectrometry platform for protein characterization. In *Proc. Natl. Acad. Sci. USA.* , (2001). 98, 4932-4937.
25. Kinumi, T., Shimomae, Y., Arakawa, R., Tatsu, Y., Shigeri, Y., Yumoto, N. & Niki, E. Effective detection of peptides containing cysteine sulfonic acid using matrix-assisted laser desorption/ionization and laser desorption/ionization on porous silicon mass spectrometry. *J. Mass Spectrom.* 41, 103-112 (2006).
26. Sudhir, P.-R., Wu, H.-F. & Zhou, Z.-C. Identification of Peptides Using Gold Nanoparticle-Assisted Single-Drop Microextraction Coupled with AP-MALDI Mass Spectrometry. *Anal. Chem.* 77, 7380-7385 (2005).
27. Vaidyanathan, S., Jones, D. G., Ellis, J., Jenkins, T. E., Dunn, W., Hayes, A., Burton, N., Oliver, S., Kell, D. B. & Goodacre, R. A laser desorption ionisation mass spectrometry approach for high throughput metabolomics. *Metabolomics* 1, 1-8 (2005).
28. Go, E. P., Shen, Z., Harris, K. & Siuzdak, G. Quantitative analysis with desorption/ionization on silicon mass spectrometry using electrospray deposition. *Anal. Chem.* 75, 5475-5479 (2003).
29. Anderson, D. F. Mechanism and Application of Desorption/Ionization on Porous Silicon (DIOS). Ph.D. thesis, University of Florida, (2003).
30. Chen, Y. Analysis of Biological Molecules Using Stimulated Desorption Photoionization Mass Spectrometry. Ph.D. Dissertation, Georgia Institute of Technology, (2006).
31. Gross, J. H. Mass spectrometry : a textbook (Springer, Berlin, 2004).
32. Luo, G., Siuzdak, G. & Vertesa, A. Comparison of internal energy transfer in DIOS and in MALDI using small thermometer molecules. 52nd Annual Conf. ASMS, Nashville, TN, (2004).

33. Li, Q., Ricardo, A., Benner, S. A., Winefordner, J. D. & Powell, D. H. Desorption/Ionization on porous silicon mass spectrometry studies on pentose-borate complexes. *Anal. Chem.* (2005).
34. Budimir, N., Blais, J.-C., Fournier, F. & Tabet, J.-C. Desorption/ionization on porous silicon mass spectrometry (DIOS) of model cationized fatty acids. *J. Mass Spectrom.* 42, 42-48 (2007).
35. Luan, F., Ma, W., Zhang, H., Zhang, X., Liu, M., Hu, Z. & Fan, B. Prediction of pKa for Neutral and Basic Drugs Based on Radial Basis Function Neural Networks and the Heuristic Method. *Pharmaceutical Research* 22, 1454-1460 (2005).
36. Rousell, D. J., Dutta, S. M., Little, M. W. & Murray, K. K. Matrix-free infrared soft laser desorption/ionization. *J. Mass Spectrom.* 39, 1182-1189 (2004).
37. Budimir, N., Fournier, F., Blais, J.-C., Wind, F. & Tabet, J.-C. Study of fatty acids and sulfonic acids by desorption/ionization on silicon mass spectrometry. 51th Annual Conf. ASMS, Montreal, Canada, June 8-12, (2003).
38. Alimpiev, S. S., Nikiforov, S. M., Grechnikov, A. A., Karavanskii, V. A. & Sunner, J. A. Method of forming of rough surface of silicon substrates and electrolyte for anode etching of silicon substrate. (2003). *RU 2003-101425*. RU 2217840.
39. Chen, Y. & Vertes, A. Adjustable Fragmentation in Laser Desorption/Ionization from Laser-Induced Silicon Microcolumn Arrays. *Anal. Chem.* 78, 5835-5844 (2006).
40. Smith, E. F., Briggs, D. & Fairley, N. Further developments in quantitative X-ray photoelectron spectromicroscopy: preliminary results from the study of germanium corrosion. *Surf. Interface Anal.* 38, 69-75 (2006).
41. Gunter, P. L. J., Gijzeman, O. L. J. & Niemantsverdriet, J. W. Surface roughness effects in quantitative XPS: magic angle for determining overlayer thickness. *Appl. Surface Sci.* 115, 342-346 (1997).
42. Mann, K. & Yu, M. L. Effect of chemical bonding on positive secondary-ion yields in sputtering *Phy. Rev. B* 35, 6043-6050 (1987).
43. Alimpiev, S. S., Nikiforov, S. M., Karavansky, V. A., Grechnikov, A. A. & Sunner, J. A. Laser desorption of ions from microscopically rough surfaces: novel technique for ultrahigh sensitivity detection of organic and bioorganic compounds. In Libenson, M. N. *Proc. SPIE*, (2004). 5506 95-106.

44. Spoel, D. v. d. & Berendsen, H. J. C. Molecular Dynamics Simulations of Leu-Enkephalin in Water and DMSO. *Biophys. J.* 72, 2032-2041 (1997).
45. Shen, Z., Thomas, J. J., Averbuj, C., Broo, K. M., Engelhard, M., Crowell, J. E., Finn, M. G. & Siuzdak, G. Porous silicon as a versatile platform for laser desorption/ionization mass spectrometry. *Anal. Chem.* 73, 612-619 (2001).
46. Kolasinski, K. Surface science : foundations of catalysis and nanoscience (John Wiley & Sons, Chichester, UK, 2002).
47. Zhu, X. Surface Photochemistry. *Annu. Rev. Phys. Chem.* 45, 113-144 (1994).
48. Oura, K., Lifshits, V. G., Saranin, A. A., Zotov, A. V. & Katayama, M. Surface science : an introduction (Springer, Berlin ; London, 2003).
49. Okuno, S., Oka, K., Wada, Y. & Arakawa, R. Oxidation of ferrocene derivatives in Desorption/Ionization on Porous Silicon. 52nd MSSJ Annual Conf. Mass Spectrom., Nagoya, Japan, (2004).
50. Choi, H.-J. & Pyun, J.-C. Korea Inst. Science Technology. Nanowire Assisted Laser Desorption/Ionization Mass Spectrometric Analysis. (2005). *WO 2005KR00738 2005315*.
51. Gorecka-Drzazga, A., Dziuban, J., Drzazga, W., Kraj, A. & Silberring, J. Desorption/ionization mass spectrometry on array of silicon microtips. *J. Vac. Sci. Technol., B* 23, 819-823 (2005).
52. Finkel, N. H., Prevo, B. G., Velez, O. D. & He, L. Ordered silicon nanocavity arrays in surface-assisted desorption/ionization mass spectrometry. *Anal. Chem.* 77, 1088-1095 (2005).
53. Kottmann, J. P., Martin, O. J. F., Smith, D. R. & Schultz, S. Spectral response of plasmon resonant nanoparticles with a non-regular shape. *Opt. Express* 6, 213-219 (2000).
54. Hanley, L., Kornienko, O., Ada, E. T., Fuoco, E. & Trevor, J. L. Surface mass spectrometry of molecular species. *J. Mass Spectrom.* 34, 705-723 (1999).
55. Smart, L. & Moore, E. 146-151 (Stanley Thornes (Publishers) Ltd., 1996).
56. Singh, J. Semiconductor Devices: Basic Principles (John-Wiley, 2000).

57. Stewart, M. P. & Buriak, J. M. Exciton-mediated hydrosilylation on photoluminescent nanocrystalline silicon. *J. Am. Chem. Soc.* 123, 7821-7830 (2001).
58. King, A. K., Bellm, S. M., Hammond, C. J., Reid, K. L., Towrie, M. & Matousek, P. Picosecond time-resolved photoelectron spectroscopy as a means of elucidating mechanisms of intramolecular vibrational energy redistribution in electronically excited states of small aromatic molecules. *Mol. Phys.* 103, 1821-1827 (2005).
59. Budimir, N., Lesage, D., Naban-Maillet, J., Fournier, F., Blais, J.-C., Wind, F., Vékey, K. & Tabet, J.-C. Internal energy of ions produced by desorption/ionisation on porous silicon (DIOS). 52nd ASMS Conference on Mass Spectrometry and Allied Topics, Nashville, Tennessee, May 23 - 27, 2004, (2004).
60. Rosenstock, H. M., Wallenstein, M. B., Wahrhaftig, A. L. & Eyring, H. Absolute Rate Theory for Isolated Systems and the Mass Spectra of Polyatomic Molecules. *Proc. Natl. Acad. Sci. USA* 38, 667-678 (1952).
61. Fonash, S. J., Kalkan, A. K., Cuiffi, J. & Hayes, D. J. The Penn State Research Foundation. Matrix-free desorption ionization mass spectrometry using tailored morphology layer devices. (2002). US 20020187312 WO 02093170.
62. Huwe, A., Kremer, F., Behrens, P. & Schwieger, W. Molecular Dynamics in Confining Space: From the Single Molecule to the Liquid State. *Phys. Rev. Lett.* 82, 2338-2341 (1999).
63. Bellissent-Funel, M.-C., Lal, J. & Bosio, L. Structural study of water confined in porous glass by neutron scattering. *J. Chem. Phys.* 98, 4246-4252 (1993).
64. Bellissent-Funel, M.-C., Chen, S. H. & Zanolli, J.-M. Single-particle dynamics of water molecules in confined space. *Phys. Rev. E* 51, 4558-4569 (1995).
65. Guégan, R., Morineau, D., Loverdo, C. & Béziel, W. Evidence of anisotropic quenched disorder effects on a smectic liquid crystal confined in porous silicon. *Phys. Rev. E* 73, 011707 (2006).
66. Leisner, A., Rohlfing, A., Rohling, U., Dreisewerd, K. & Hillenkamp, F. Time-Resolved Imaging of the Plume Dynamics in Infrared Matrix-Assisted Laser Desorption/Ionization with a Glycerol Matrix. *J. Phys. Chem. B* 109, 11661-11666 (2005).

CHAPTER 5 ANALYTICAL CHARACTERISATION AND METABOLIC PROFILING USING DIOS-MS ON MALDI Q- TOF PREMIER

5.1 Introduction

5.1.1 Metabolomic Analysis: Emphasis on Biofluids

Metabolomics is a valuable platform for studies of complex diseases and the development of new therapies, both in non-clinical disease model characterisation and clinical settings.¹ The ultimate starting point of a metabolomic experiment is to quantify all of the metabolites in a cellular system (*i.e.* the cell or tissue in a given state at a given point in time).² However, for the past decade, mass spectrometric based metabolomic strategies emphasise quantification of a small subset of metabolites within representative biological matrices and these strategies are called target profiling.³ It is hypothesised that the matrix-free LDI approach can be effectively applied to global screening or profiling of metabolites, as is the NMR approach and is a focus of this chapter.

In metabolomic studies, the experiments are usually conducted on biological fluids or tissue extracts, which contain a rich collection of metabolites. Blood plasma, serum and urine are the most commonly encountered mammalian biofluids,⁴ whether in clinical diagnosis for the assessment of patient physiology or *in vivo* studies. These biofluids can be obtained non-invasively or relatively easily, making them easy to sample, thus affording opportunities to study the metabolites' change over time.⁴ However, intracellular fluids, excretes or secretes such as cerebrospinal fluid, bile, seminal fluid, tear and sweat, and other extracellular fluids develop as a result of a pathological process such as blister or cyst fluid and sputum can be also used. In contrast, the sampling of metabolites from biological tissue is invasive, one (usually animals) may have to be biopsied, sacrificed or destroyed. Tissue samples such as liver, kidney and brain are also often used in metabolomic studies.^{5,6} The selection of a biofluid or tissue for metabolite profiling can be linked to anomalies in a particular tissue or organ.⁷ For instance, urine is more likely to reflect renal diseases. Sputum is often associated with diseases of the respiratory tract and lungs. Serum or plasma analysis gives information relating the homeostatic levels of metabolites throughout the organism. Lipid metabolism and drug toxicity studies often involve liver tissue.

On the contrary, cells and culture media can be produced controllably or can be manipulated in *in vitro* conditions. Human and animal cell lines and single cell organisms, such as bacteria and yeasts,⁸⁻¹¹ are relatively easily cultured and the analysis involves the whole metabolome of an organism, which is an essential element to the development of functional genomics. However, before performing any biomedical analysis, a validation process has to be completed.

5.1.2 Validation Process

One of the objectives for any analytical procedure, including any biological and biomedical analysis, is to enable consistent and reliable data of the appropriate quality to be generated.¹² This is a vital step for method development and optimisation of an analytical method to ensure the information generated reflects the truth. Hence, an analytical procedure, including the analytical instruments used, must be properly characterised and validated to its designed specification. According to the US food and drug administration's (FDA) guidelines on General Principles of Validation (1987),¹³ a validation process is to *"[establish] documented evidence which provides a high degree of assurance that a specific process will consistently produce a product meeting its pre-determined specifications and quality attributes."*

A validation process consists of at least four distinct steps (Figure 5-1).

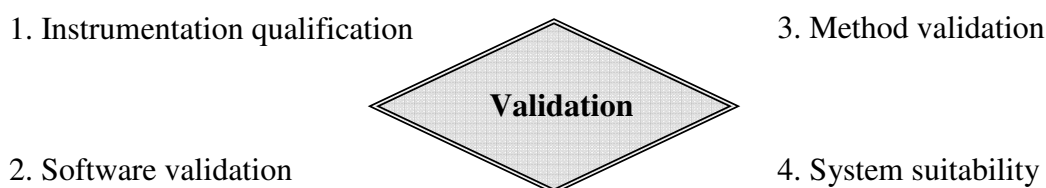


Figure 5-1 The validation process.

The first two steps are normally carried out by the equipment vendor (equipment qualification) and the process has 4 major steps: design qualification (DQ), installation qualification (IQ), operational qualification (OQ) and performance qualification (PQ). (Figure 5-2) The latter two are carried out by the instrument operators (method validation) and are discussed below.

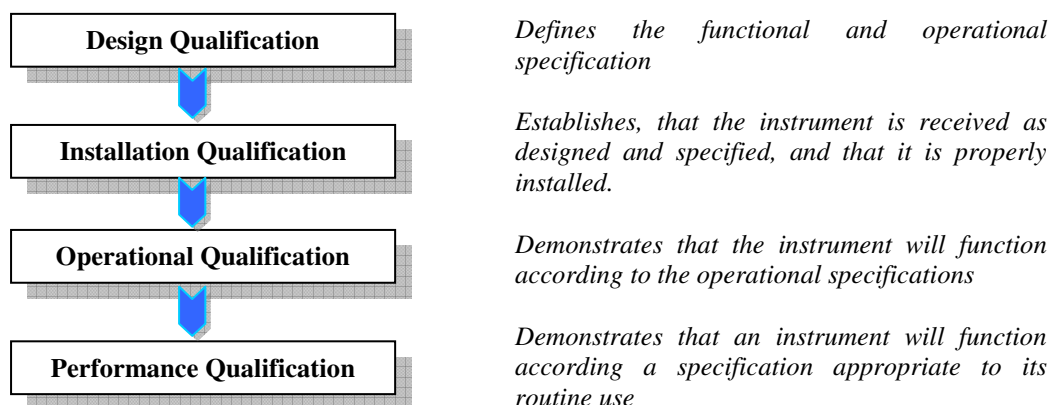


Figure 5-2 Equipment qualification (4Qs).¹⁴

5.1.3 Method Validation

Method validation is the process used to confirm that the analytical procedure employed for a specific test is suitable for its intended use. It assumes the analytical equipment used to acquire the experimental data is operating correctly and reliably.¹² The International Conference on Harmonisation of Technical Requirements for Registration of Pharmaceuticals for Human Use (ICH) divides the validation characteristics into nine parameters.¹⁵ (Figure 5-3) The definition of each parameter is available in the appendices.

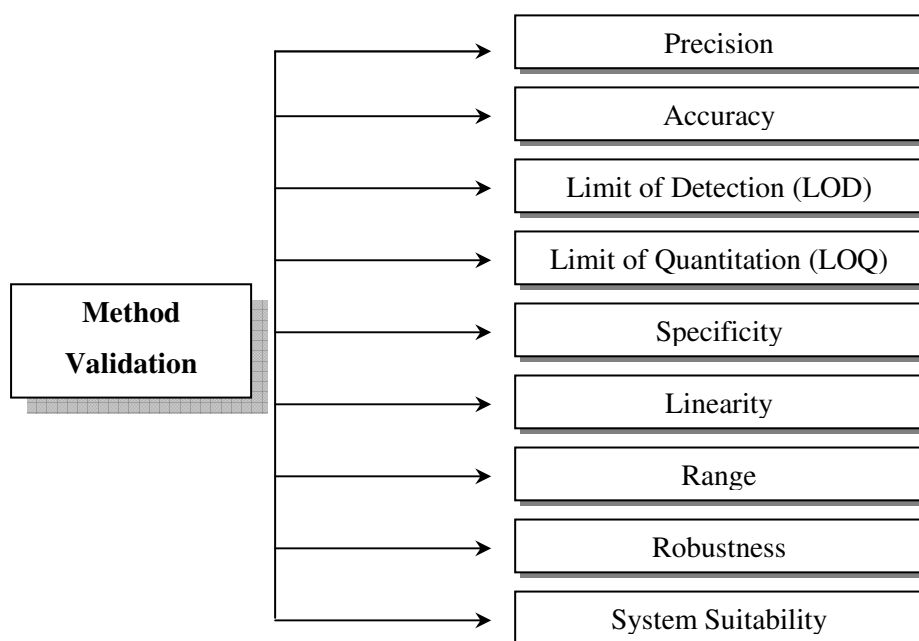


Figure 5-3 ICH method validation parameters.¹⁵

It should be noted that while it is ideal to evaluate every analytical performance parameter, practically, it is not necessary. The extent and scope of validation is also governed by the applicability of the method or “fitness for purpose”.¹² An example is the “bottom up” (tandem mass spectrometric analysis of fractionated enzymatic digested peptide mixtures) and “top down” (intact proteins) validation approaches employed in proteomics,¹⁶ and is different from the ICH approach.

5.1.4 Literature Data on Method Validation and Application of Biological Samples Using DIOS-MS

Analytical precision is probably one of the major concerns in developing DIOS-MS into a consistent quantitative analytical approach. It is because of the instability of a MALDI system that a relatively large variation of signal intensity is likely to occur. It is necessary to examine if DIOS suffers poor precision as in MALDI. To begin with, we shall observe the validation protocol and the experimental data reported by the manufacturer (Waters Corp.).

By comparing signal intensity of various pure organic compounds, Credo, *et al.* have reported that the DIOS “well-to-well” and “chip-to-chip” reproducibility is usually less than 50%.¹⁷ (Figure 5-4) Indeed, the precision varies considerably from analyte-to-analyte. RSD calculated varies from as little as 2% for lidocaine to as high as 73% for reserpine. There was also a relatively large chip-to-chip variation. The report has also mentioned instrument settings, such as laser power affecting the standard deviation (SD) of the intensity. Shion, *et al.* have also reported the SD of lysergic acid diethylamide (LSD), on 110 readings, is approximately $\pm 10\%$.¹⁸ (Figure 5-5)

The performance issue can be circumvented by using an internal standard. Credo, *et al.* have also reported that the linear response range was instrument-limited to two orders of magnitude when no internal standard was used, though LOD and LOQ were achieved below 10 ng/ml (17 fmol) for codeine.¹⁷ (Figure 5-6A) When a deuterated internal standard was used, the RSD fell below 10% and the linear range extended to the lower end of the calibration.¹⁷ (Figure 5-6B) Further examples using a similar approach are given in Figure 5-7.

**Printed version includes figure(s) extracted
from the reference source describing
the precision of the DIOS method.
Please refer to the cited reference for detail**

Figure 5-4 (A) Well-to-well signal intensity of 360 fmol of ranitidine on 16 wells of a DIOS chip. RSD = 12 % (no internal standard). (B) Chip-to-chip average intensities with standard deviation and %RSD. Each colour bar represents an individual DIOS target, three targets per analyte using a M@LDI R, Laser = 15 % of maximum, 100 shots. Each chip was spotted 16 times with the desired analyte (0.5 μ L of 250 ng/mL solution except for theophylline which was at 5000 ng/mL due to decreased DIOS performance). Procainamide exhibits detector saturation at 25500 counts. The SDs tend to be lower above 15000 counts.¹⁷

**Printed version includes figure(s) extracted
from the reference source describing
the precision of the DIOS method.
Please refer to the cited reference for detail**

Figure 5-5 DIOS-TOF-MS LSD reproducibility. The sample was applied to 96 wells DIOS plate. 110 data point were collected from those wells. The calculated standard deviation was about $\pm 10\%$.¹⁸

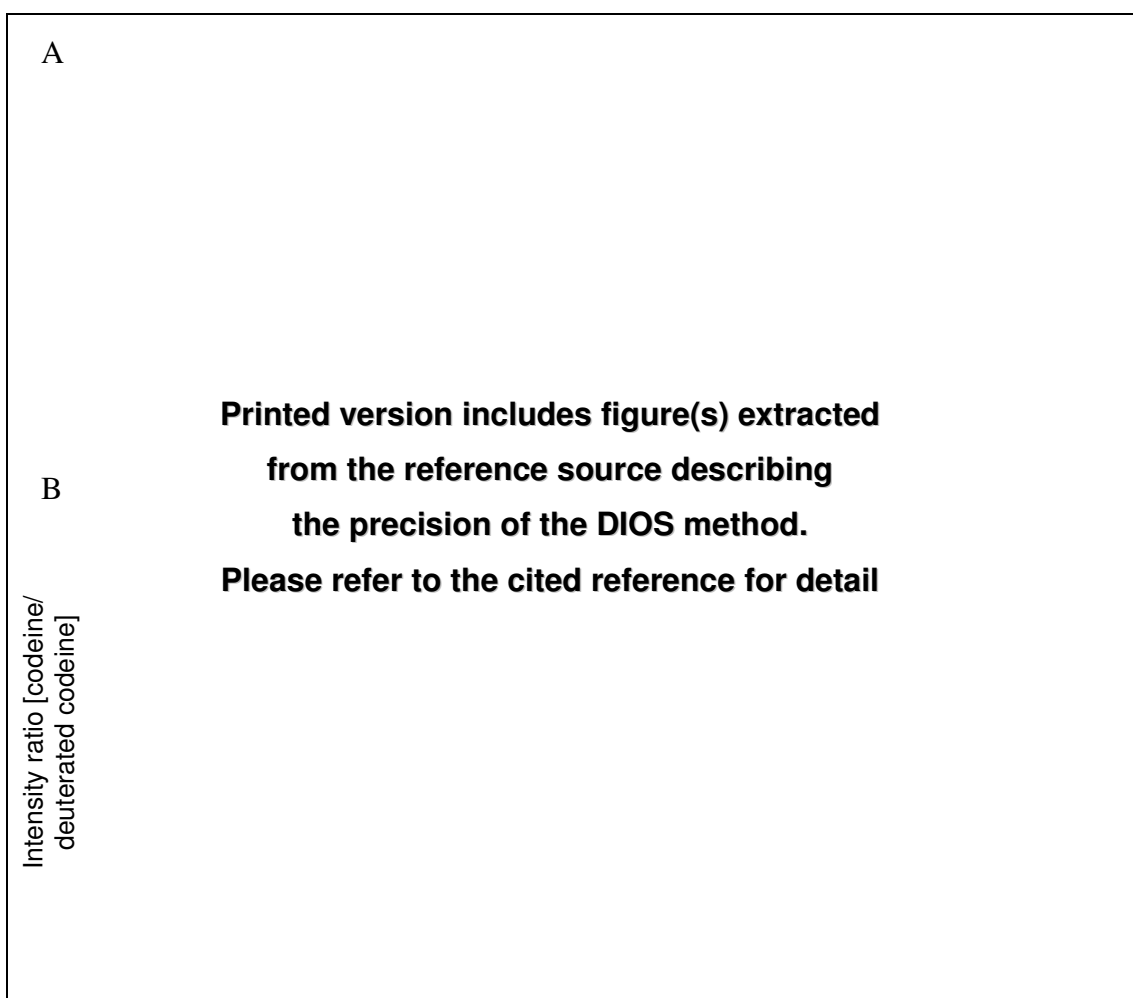


Figure 5-6 (A) Dynamic range for codeine detection. Insert shows the %RSDs without an internal standard. (B) Codeine response compared to deuterated codeine internal standard. Insert shows the %RSD with internal standard.¹⁷

A

B

**Printed version includes figure(s) extracted
from the reference source describing
the precision, linearity of the DIOS method using
isotopic dilution.
Please refer to the cited reference for detail**

C

Figure 5-7 (A) DIOS-ToF MS standard calibration curve for choline quantification correlating the intensity ratio of choline to the internal standard choline-d₉ with the concentration of choline. Each data point was run in triplet.¹⁹ (B) LSD calibration curve from 0.05 to 10.00 g/mL using LSD-d₃ IS and (C) Fentanyl calibration curve from 0.01 to 10.00 g/mL using Fentanyl-d₅ internal standard. Each data point was run in quadruplet.¹⁸

The data presented above is extracted from literature published by the manufacturer using reflector MALDI-ToF instruments. These results suggest that good reproducibility and linearity of small molecules is achievable by using a deuterated internal standard. It may be necessary to mention that even though an internal standard is used in the above examples, the improvement to the linear range only increases by 1 order of magnitude and does not extend much to the higher end of the calibration curve.^{18, 20} Furthermore, on comparing LC-MS with DIOS method, LC-MS still yields better accuracy, precision and wider dynamic range.²⁰

The data presented above was acquired in positive mode and on simple mixtures. It is questionable whether such a method would also be applicable to negative ions and/or complex biological mixtures. Independent studies have also adopted a similar approach by applying deuterated internal standard. Shen, *et al.* have long shown that quantitative analysis of small molecules by DIOS requires internal standards similar in chemical structure to the molecules of interest.²¹ Quantitation of sulphated pregnenolone in human urine by using a d₄ analogue was demonstrated. Comparable linearity was obtained with nanoelectrospray and DIOS in negative ion mode. (Figure 5-8) The authors also mentioned that sample purification was needed in such a case to get rid of the salts and other contaminants. The method employed a two-step procedure, 100 µl of urine was first extracted with 600 µl of diethyl ether/hexane (90:10 v/v). The aqueous phase was then further extracted by adding 600 µl of chloroform/butanol (50:50 v/v) and collecting the organic phase.²² The collected fraction was dried and reconstituted in 70/30 methanol/water with the addition of the testosterone-d₉ sulphate internal standard. On the basis that the extraction recovery was 83%, the calculated concentration of testosterone sulphate was 487 ng/ml in the male urine sample.²¹

Okuno and Wada have demonstrated that quantitation of salicylate in human serum by using deuterium-labelled d₆ isomer internal standard, in combining the advantage of solid-phase extraction (SPE), is achievable. (Figure 5-9) The serum salicylate level was accurately measured: 0.347 ± 0.028 mM (49.6 ± 3.4 mg/L) 2 hours after initial ingestion, and 0.645 ± 0.024 mM (92.2 ± 3.6 mg/L) 2 hours after the second dose from a volunteer.

**Printed version includes figure(s) extracted
from the reference source (A) comparing the linearity of nano-ESI-MS
and DIOS-MS methods, (B and C) negative ion DIOS spectra of urine
extract acquired using linear ToF mass spectrometer.
Please refer to the cited reference for detail**

Figure 5-8 (A) Calibration curve for sulphated pregnenolone using DIOS-MS and nano-ESI precursor ion scanning. (B and C) DIOS spectra of human urine extracts. The amount of the internal standard (pregnenolone-d₄) was 316 fmol of pregnenolone. The same amount of the same internal standard was used as in the calibration curve, and samples from males and females were found to contain different amounts of testosterone sulphate. Other conjugated steroids were assigned based upon their known masses or post source decay analysis.²¹

**Printed version includes figure(s) extracted
from the reference source describing
the linearity of the method in quantifying salicylic acid from blood
plasma extract using isotopic dilution.
Please refer to the cited reference for detail**

Figure 5-9 Peak intensity versus serum salicylic acid concentration in serum obtained by DIOS-MS measurements after SPE. (n = 5). Y-axis represents the ratio of unlabeled to deuterium-labelled species and x represents the mM concentration of salicylic acid. The curve showed a linear relationship in a serum range of 0.14 to 4.2 mM (20–600 mg/l).²³

The relatively high variation of signal intensity is mainly because the sample dried droplet method using pipette deposition often produces an inhomogeneous analyte distribution giving heterogeneous ion signals. In the conventional MALDI approach, the recrystallisation of matrix is a random nucleation process. In DIOS, aggregation in the dried droplet is associated with the chemical properties of analytes and the solvent used.²³ Although using an isotopically labelled internal standard could be an effective approach to minimise variability in analyte signal intensities and improve experimental reproducibility, deuterated isomer is not only costly and not always commercially available, but would not be suitable for global profiling of metabolite.

It has also been suggested that sample homogeneity can be enhanced by a specific method such as electrospray sample deposition (ESD). Hensel, *et al.*, have showed previously sample homogeneity can be improved in MALDI-MS by using ESD.²⁴ Go, *et al.* have also showed that ESD can be utilised to produce a more homogeneous sample spot in DIOS-MS.²⁵ Additionally, the method permits LC coupling.²⁶ Sensitivity and reproducibility investigation was conducted on DIOS-MS using a number of peptides at low μM levels, in which samples were spotted with a pipette versus those prepared by ESD. The results showed the RSD for the sample prepared by ESD was 1.8 to 7.1%, whereas analysis of the spotted sample ranged from 5.6 to 20.7%.²⁵ It is suggested this method significantly improves the signal reproductively in DIOS and is comparable to other quantitative ionisation techniques such as ESI.

5.1.5 *Pseudomonas aeruginosa* and Their Secondary Metabolites

Pseudomonas aeruginosa is a Gram-negative, aerobic, rod-shaped bacterium with unipolar motility. The bacterium is ubiquitous in soil and water. *P. aeruginosa* is an opportunistic pathogen of humans. The pathogenesis of *Pseudomonas* infections is multifactorial, as suggested by the number and wide array of virulence[†] determinants possessed by the bacterium. Multiple and diverse determinants of virulence are expected in the wide range of diseases caused, which include septicaemia, urinary

[†] Virulence is defined as the ability of a bacterium to cause infection. Virulence factors are molecules produced by a pathogen that specifically influence their host's function to allow the pathogen to thrive.

tract infections, pneumonia, chronic lung infections, endocarditis, dermatitis, and osteochondritis.²⁷

Pseudomonas infections are primary nosocomial.[‡] Most *Pseudomonas* infections are both invasive and toxinogenic. The disease process begins with some breakdown or circumvention of the host defences. Patients who suffer from cancer, cystic fibrosis, AIDS, severe burns or are immuno-compromised are particularly at risk of *Pseudomonas* infection. Traditional antibiotic therapy is usually not sufficient to eradicate these infections. One major reason for its resistance to antibiotics relates to its outer membrane barrier constituted of lipopolysaccharides (LPS). Moreover, the low antibiotic susceptibility is attributable to the multidrug efflux pumps with chromosomally-encoded antibiotic resistance genes. *P. aeruginosa* can easily develop acquired resistance either by mutation in chromosomally-encoded genes or by the horizontal gene transfer of antibiotic resistance determinants. In addition, mucoid strains of *P. aeruginosa* produce an exopolysaccharide envelope. The mucoid exopolysaccharide produced is a copolymer of β -1,4-linked D-mannuronic acid and L-guluronic acid residues referred to as alginate. Alginate slime forms the matrix of the *Pseudomonas* biofilm. Biofilm is a natural resistance to protect the bacterium from adverse environmental factors and aid colonising a surface. In medical situations, it protects the bacteria from the host defences such as lymphocytes, phagocytes, the ciliary action of the respiratory tract, antibodies and complement. This also makes the cells impervious to therapeutic concentrations of antibiotics. Furthermore, *P. aeruginosa* also has the ability to produce extracellular enzymes and toxins that break down physical barriers and damage host cells, as well as resistance to phagocytosis and the host immune defences. A few antibiotics are effective against *Pseudomonas*, including fluoroquinolones, gentamicin, carbenicillin, imipenem, tobramycin, amikacin, and colistin. However, even these antibiotics are not effective against all strains and resistant forms have developed.²⁷

A common characteristic of the *Pseudomonas* is the production of pigments and some of these pigments are fluorescent under ultraviolet light (254 nm). These pigments

[‡] Pertaining to or originating in the hospital, said of an infection not present or incubating prior to admittance to the hospital, but generally occurring 72 hours after admittance.

include pyocyanin[e] (blue-green, non-fluorescent), and fluorescein/pyoverdine (yellowish-green). Pyocyanin is an important virulence factor.²⁸ It impairs the normal function of human nasal cilia, disrupts the respiratory epithelium, and exerts a proinflammatory effect on phagocytes.^{29, 30} A derivative of pyocyanin, pyochelin is a siderophore produced under low-iron conditions to sequester iron from the environment for growth of the pathogen, and hence, production of these pigments is markedly enhanced under conditions of iron deficiency.³¹⁻³³ No role in virulence is known for the fluorescent pigments. Some strains also produce pyorubin (red-brown), pyomelanin (brown), two other red pigments (aeruginosin A and B) and various other pigments. (Figure 5-10) Fluorescence under ultraviolet light is therefore helpful in early identification of *P. aeruginosa* colonies. Fluorescence is also used to suggest the existence of *P. aeruginosa* in wounds.

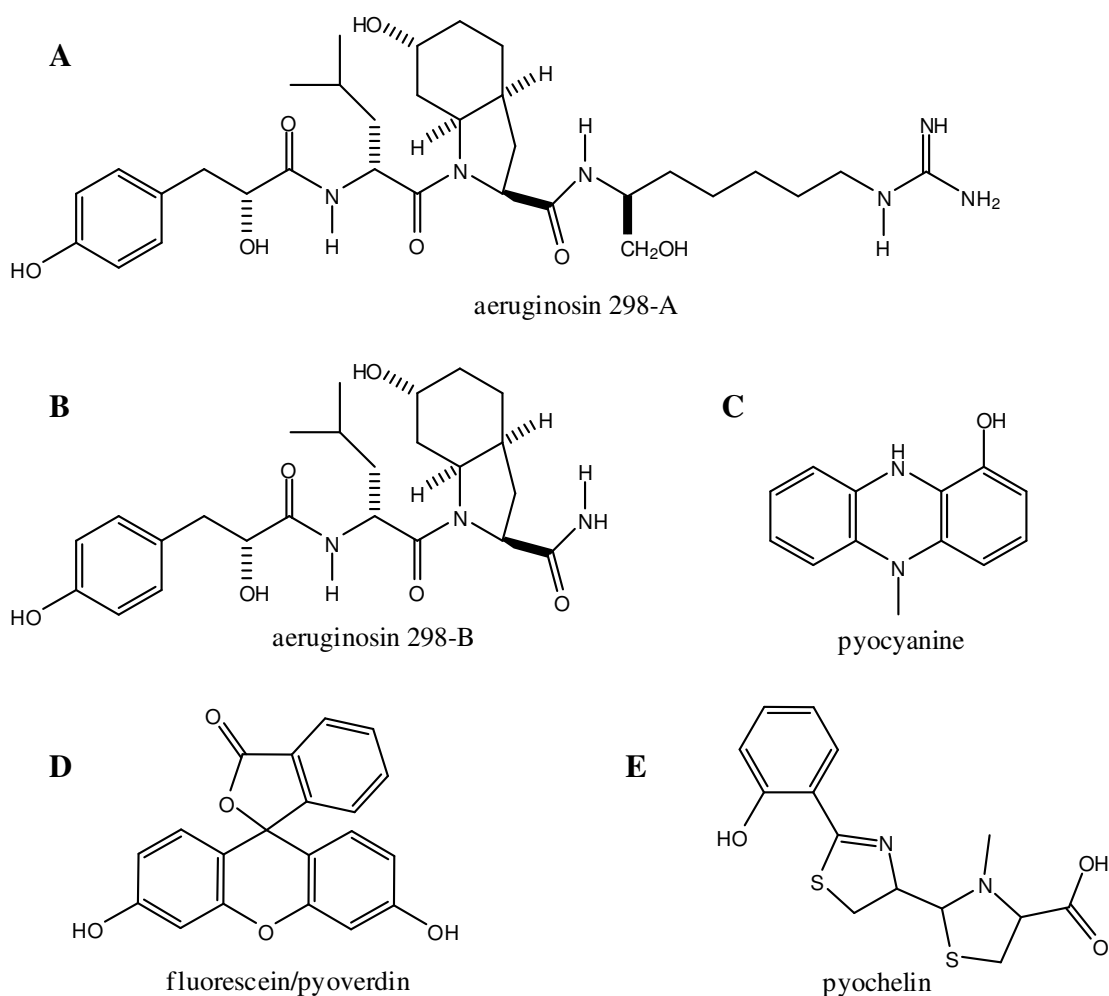


Figure 5-10 Chemical structure of (A and B) aeruginosine A and B,³⁴ (C) pyocyanine,³⁰ (D) fluorescein/pyoverdine and (E) pyochelin.³¹

It has only been recognised in the last decade that single-cell organisms such as bacteria also have the ability to coordinate themselves in order to adapt or modulate responses that are beneficial to survival.³⁵ In higher organisms, this is achieved by releasing a chemical or a pheromone, which triggers a natural response in another member. In contrast, the coordinated behaviour in single-cell organisms occurs through cell-cell communication or quorum sensing (QS).³⁶ QS is a process by which many bacteria coordinate gene expression according to the local density or population of bacteria. Regulation of gene expression can be via the production of small molecules called the autoinducers (AI) or quorum sensing signalling molecules (QSSM). Through this coordination, the bacterium coordinates their growth within a host without harming it, until they reach a certain population and their numbers become sufficient to overcome the host's immune system. In *P. aeruginosa*, QS is known to control expression of a number of virulence factors, such as biofilm development, exopolysaccharide production, and cell aggregation. Quorum-sensing systems involve at least two chemically distinct classes of signalling molecules, *N*-acyl-L-homoserine lactones (AHL) and alkyl quinolones (AQS). Another important QSSM is a boron containing autoinducer, AI-2, that may serve as a “universal” signal for communication between different bacterial species.³⁷ By attenuating or disrupting the signalling process (quorum quenching), it may be possible to down-regulate the genes that control the virulence factors and cause the pathogen to fail to adapt to the host environment and be readily cleared by the innate host defences.³⁸⁻⁴⁰ One known QS antagonists or inhibitors (QSI) are halogenated furanones,⁴¹ which are originally isolated from the Australian red macro-alga (seaweed), *Delisea pulchra*. (Figure 5-11)

On the other hand, the QSSM, in particular the *N*-(3-oxododecanoyl)-L-homoserine lactone (3-oxo-C₁₂-HSL) and 2-heptyl-3-hydroxy-4-quinolone (PQS, *Pseudomonas* Quinolone Signal), also have therapeutic value. These molecules suppress T-cell proliferation upstream and downstream of interleukin-2 (IL-2) secretion.⁴² 3-oxo-C₁₂-HSL also inhibits the JAK/STAT[§] signalling system and blocks proliferation and

[§] STAT proteins are a family of signal transducers that respond to extracellular cytokine signals and convert them into altered transcription of specific target genes. The STATs thus are key regulators of innate immunity and cell growth.

induces apoptosis in human BC cell lines.⁴³ It is possible that further development of these chemical entities may lead to new chemical agents for the treatment of immunological diseases.^{44, 45}

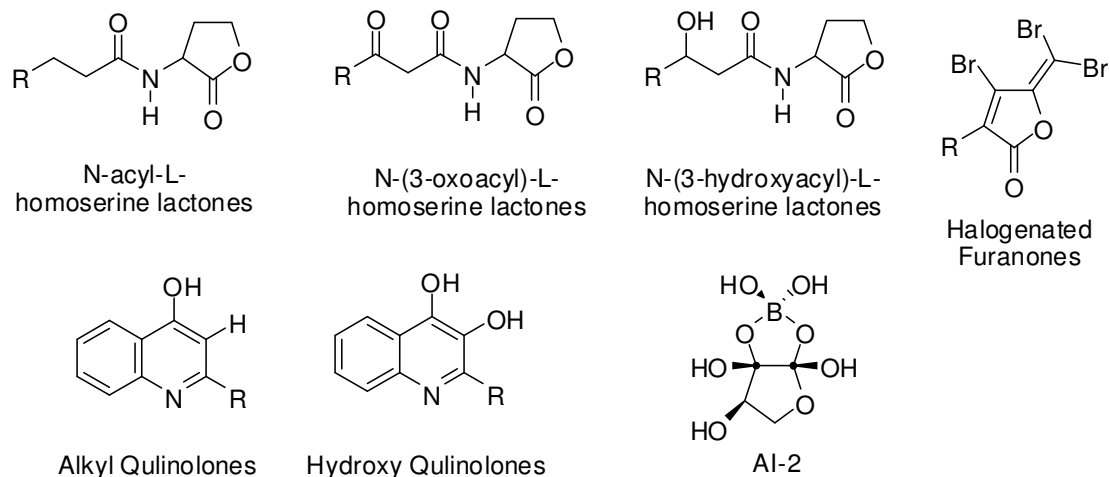


Figure 5-11 QSsMs and QSIs.

**Printed version includes figure(s) extracted
from the reference source describing
the conversion and relationship between HHQ, PQS and rhamnolipids.
Please refer to the cited reference for detail**

Figure 5-12 HHQ/PQS dual cell-to-cell communication system. HHQ is synthesised by a bacterial cell and released into the extracellular environment. HHQ is then taken up by neighbouring cells and converted by the action of PqsH into PQS. PQS is exported and used directly as a signal molecule by adjacent cells.⁴⁶

Another important class of compound produced by *P. aeruginosa* is rhamnolipids. Rhamnolipids are important biosurfactants, containing one or two 3-hydroxy fatty acids of various lengths, linked to a mono- or di-rhamnose moiety.^{47, 48} Their relationship with QSSMs and role in choric inflection has only been recently realised. (Figure 5-12) It is evidenced that the necrotic effect to the polymorphonuclear leukocytes is caused by QS-regulated secretion of cytotoxic amounts of rhamnolipids by *P. aeruginosa* and may be one of the reasons to the establishment and persistence of the infection.⁴⁹ Being biosurfactants, the production of rhamnolipids also increases the solubility of hydrophobic PQS which is a long hydrocarbon chain.⁴⁶

5.1.6 Approaches Used in this Study

In the previous chapters, the foundation of the matrix-free LDI approach has been established and its activity and ability has been examined. The DIOS technique has shown its promise and versatility toward analysing many pharmaceutically and biologically related small molecules and effectively overcomes the limitation of matrix related inferences in the low mass range of the MALDI approach. The exploration of the potential biomedical applications of the technique is still in its very early stage of development, examples of which have been discussed in Chapter 1, section 1.8. Successful applications of the technique will undoubtedly make an impact to the development of metabolomics and expedite our understanding to the biological systems. However, a number of questions remain as to whether the method is suitable for the global profiling of metabolites from complex biological matrices and how wide the coverage is in terms of the type and number of metabolites from the biological mixtures, as well as the possibility of identifying the ions detected. However, before any biomedical study, the method has to be validated.

The analytical characterisation and quantitative capability of the DIOS technique have been exhaustively explored and reported, and a selection of examples has been given in the previous section. Due to the instability of the laser desorption/ionisation system, the precision of the signal intensity varies greatly. The technique is thus less than ideal for quantitation. Improvements in quantitative capability can be achieved either by incorporation of an internal standard or by improved deposition approaches. Still,

the analytical dynamic range is still relatively narrow and is instrument-limited. A further question is that the ICH approaches may be too specific for food and pharmaceutical quantitative applications, and we may need to consider the bottom-up (cognitive) or the top-down (goal-oriented) validation approach used in qualitative studies. The strength of DIOS may lay on its throughput of data acquisition and uncomplicated method development and its sensitivity.

5.1.7 Aims of this Chapter

This chapter will investigate the analytical characteristic of DIOS-MS by using MALDI Q-ToF instrument. Precision, dynamic range, limit of detection, and robustness are evaluated using a number of simple analyte mixtures. The writer adopts “well-to-well” and “target-to-target” precision to describe the evaluation to the DIOS-MS performance. It is the first time this data has become available for this system.

Once the analytical characterisation is completed, the complexity of the samples is gradually increased. Complex biological matrices such as human urine, human blood plasma, and animal liver tissue extracts are chosen for the study to evaluate further the suitability of the method. These samples are clinically significant, and are in terms of their physical form, aqueous, semi-solid and solid mediums, respectively. Finally, and for the first time, comprehensive metabolite profiling of bacterial culture media and cells pellets of *Pseudomonas aeruginosa* are to be studied by DIOS-MS. The exoproducts of *P. aeruginosa* will be the focus of the research effort.

5.2 *Experimental*

5.2.1 Biological Sample Preparation

Human urine: urine sample was collected immediately before dilution or extraction. The extracts were stored in -20°C and were thawed at room temperature before analysis. Four extraction methods were compared:

Method 1: 3 ml of urine was extracted by 5 ml of 9:1 diethyl ether/hexane. The aqueous layer was further extracted by 5 ml of 1:1 chloroform/butanol. The organic fractions were collected and the remaining aqueous fraction was discarded. The organic extracts were reduced in volume by a centrifugal evaporator. The residue was reconstituted in ACN/H₂O.

The procedures were repeated with addition of 10 µl of HCl (*l*) or saturated NaOH (*aq.*) to the urine sample during the extraction.

Method 2: The procedures of method 1 were repeated with the exception that only 1:1 chloroform/butanol was used. The residue was reconstituted in ACN/H₂O.

Method 3: The procedures of method 1 were repeated with the exception that only 9:1 diethyl ether/hexane was used. The residue was reconstituted in ACN.

Method 4: The procedures of method 1 were repeated with ethyl acetate only. The residue was reconstituted in ACN.

Human blood plasma: blood plasma was obtained from blood bank and was extracted with methanol. 100 µl of plasma was first mixed with 1000 µl of methanol. Plasma proteins such as albumins were immediately precipitated out. The solution was then vortexed for ~5 mins and then pre-cooled to 4°C and centrifuged at 100000 RPM for ~10 mins. Clear supernatant was removed by a pipette. The extract was further diluted four or eight times using 1:1 ACN/H₂O. Further dilution was possible, but a higher

concentration might suppress ion desorption. Further sample clean-up, such as SPE, was not required. Serum extract was stored in -20°C and was thawed at room temperature before analysis.

Lambs' liver tissue: the lambs' liver was purchased from a supermarket and was stored in -20°C before extraction. After thawing, the tissue sample was first washed with ample of deionised water to remove blood and blood clot residue and was then homogenised. About 11g of homogenised sample was inserted into a 30 ml centrifuge tube and 16 ml of extraction solvent was added. Six different extract solvents were used in this experiment. Solvents used were HPLC grade. All except water were purchased from Fisher.

1. Ethyl acetate (ETA)
2. Propan-2-ol
3. Dimethyl sulfoxide (DMSO)
4. Methanol (MeOH)
5. Deionised water (H₂O)
6. Acetonitrile (ACN)

The samples were sonicated for 45 mins in a water-bath, and centrifuged for 10 mins (2000 RPM). The supernatant was taken out by a syringe and filtered (ETA extract was not filtered, because the filter was dissolved by ETA). (Figure 5-13) Each solution was further diluted 10 times using 1:1 ACN/H₂O. 1.2 µl of each solution was pipetted onto the DIOS target. Data was acquired by 2 minutes spiral scan. Eight replicas were acquired for each sample solution.

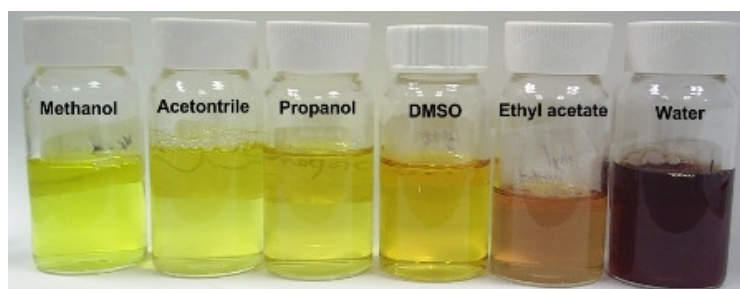


Figure 5-13 Solvent extract procedure. Water extract appears to be blood red, ethyl acetate extract appears to be greenish brown. Other extract are yellow in colour.

Rats' liver tissue: Sprague Dawley[®] Rats (Charles River Laboratory, UK) were killed by stunning followed by decapitation and dissection. The rats' liver tissue was stored at -80°C before extraction. The rats were housed grouped four per cage and were free to access food (standard rat "chow"), and tap water *ad libitum*, with 12 hours light/dark period. Similar procedures applied to the lambs' liver tissue were also applied here, with the exception that only 4g of homogenised rats' liver tissue was used for extraction. Other solvent combinations, such as methanol/chloroform, were also attempted.

Bacterial sample: *P. aeruginosa* culture and cell pellets were provided by the Quorum Sensing Research Group of the Institute of Infections, Immunity and Inflammation at the University of Nottingham. The bacterial samples were cultivated by a BIOSTAT B-plus fermentor system, (Satorius BBI system, Melsungen, Germany). The fermentor was connected to a feeding medium reservoir to resupply nourishments to the bacterial medium. The medium was constantly stirred and antifoam 204 (Sigma) was added to inhibit foam formation. Bacterial produces were harvested from the fermentor and was centrifuged to separate liquid supernatant and cell pellet. The cell pellet was further washed with phosphate buffered saline (PBS) solution. The samples were stored in -80°C before extraction and analysis.

After thawing, 3 ml of the bacterial culture medium and the feeding medium (control) were extracted by 3 ml ETA. The organic fraction was collected and the aqueous fraction was further extracted by either 1:1 chloroform/methanol or chloroform/butanol in PTFE tubes. The ETA and the chloroform fraction were combined as one single organic fraction. The aqueous fraction was then discarded. The organic fraction was placed into a centrifugal evaporator and was reduced volume to dryness. The residue of the organic fraction was reconstituted in 200 µl of 1:1 ACN/water. The cell pellet was first resuspended in 3 ml of water and transferred to a PTFE tube. The suspension was extracted by either 1:1 chloroform/methanol or chloroform/butanol and sonication. The organic fraction was collected and was reduced volume to dryness. The aqueous/slim fraction was then discarded. The residual of the organic fraction was reconstituted in 500 or 200 µl of propan-2-ol.

While chloroform/methanol is a standard extraction method, it can be seen from the Figure 5-14 that the use of chloroform/butanol has led to a larger extraction volume relative to chloroform/methanol, due to the partition coefficient of butanol between the aqueous and the organic fraction, and may produce higher extraction efficiency. A disadvantage is also the larger volume and the volatility of butanol. The extract required several hours to reduce to dryness by the vacuum evaporator.

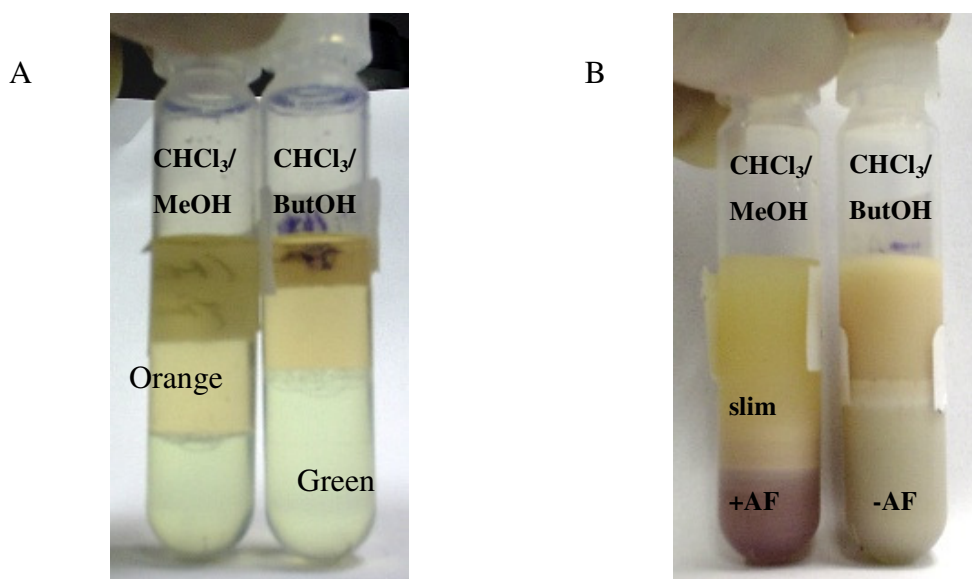


Figure 5-14 Extraction of (A) aqueous culture medium and (B) cell pellet by chloroform/methanol and chloroform/butanol. +AF and –AF denotes the bacteria was growth in a medium with the addition of antifoam and without, respectively.

5.2.2 Mass Spectrometry

The data presented in this chapter was acquired on Micromass MALDI Q-ToF Premier using Waters DIOS target (Manchester, UK). Samples solutions were spotted onto the target surface using a pipette. Target handling was carried out in a class I laminar flow hood to provide a clean air and sterile environment. The raw spectra were generated by summing all scans. The peak intensity was read directly from the spectra and was calculated by “auto peak detection” function available in MassLynx 4.1. Details of instrumental settings and target handling can be found in section 2.4.8. Two different scan modes, spiral and raster, were used.

5.2.3 Data Analysis by PCA

Raw spectra were smoothed and background subtracted within the platform of MassLynx version 4.1. The peak lists were exported to text files and imported to SpecAlign^{**} version 2.3.^{50, 51} The dataset obtained was then further “denoised” by wavelet soft thresholding and normalised to total ion counts (TIC) within the platform of SpecAlign and binned to 0.1 Th intervals before importing to SIMCA version 11. Spectral alignment was possible but was not necessary because the mass precision of Q-ToF was high. It should be noted that normalisation to TIC introduces dependencies between the variables that would not exist without this step and is required for data pre-processing for PCA.

Scaling is also an important step in PCA data processing. Previously, we have discussed this in the PCA investigation of SALDI substrates SIMS dataset. The PCA data presented in this chapter, variable j is centred and scaled to Pareto Variance. Pareto scaling gives the variable a variance numerically equal to its standard deviation (S) instead of unit variance and the base weight is computed as $1/\sqrt{S_j}$. Hence, Pareto scaling is intermediate between no scaling and UV-scaling. Pareto scaling gives the best possible result relative to UV and no scaling.

5.2.4 Metabolite Databases

Databases employed are listed in Table 5-1. A comprehensive list of databases can be found in the references⁵² and ⁵³.

Table 5-1 Metabolite databases.

| Database | URL | Comment |
|-----------|---|---|
| Metlin | http://metlin.scripps.edu/ | Metabolites primary from human biofluids |
| BioCyc | http://biocyc.org/ | PseudoCyc for <i>Pseudomonas aeruginosa</i> |
| LipidBank | http://lipidbank.jp/ | Natural lipids |
| LipidMaps | http://www.lipidmaps.org | Natural lipids |

^{**} Created by Jason Wong. Available at <<http://physchem.ox.ac.uk/~jwong/specalign/>>

5.3 Results and Discussion

5.3.1 Detection Characteristics (Laser Optimisation)

Previously, Cuiffi, *et al.* have demonstrated the detection characteristics of des-pro³,[ala^{2,6}]-bradykinin on a silicon nanostructured thin film produced by PE-CVD.⁵⁴ A similar investigation on DIOS system has only been reported recently and the ionisation process has also been found to be highly laser energy dependent.⁵⁵ We have briefly investigated this aspect on comparing DIOS and SALDI performance on a ToF instrument. We are revisiting this matter further to examine if the laser energy has any influence on signal precision as suggested by Credo, *et al.*¹⁷ Several compounds, including amines, peptides and a bile acid were chosen for the investigation.

Procainamide is used as an example here. The ion intensity of the protonated molecules and a major fragment ion as a function of laser settings are plotted to Figure 5-15. Representative spectra acquired at different laser settings are shown in Figure 5-16. As with MALDI, an analyte signal is obtained above a laser fluence threshold. The average ion intensity of the protonated molecules increases exponentially from laser setting 100 to 180, then drops from 190 to 220. Further increasing the laser setting beyond 300 reduces the ion intensity of the protonated molecules as well as the fragment ion due to the degradation of the analyte. The ratio of protonated molecules of procainamide to the fragment ion is insensitive to the laser energy and so is the ion signal precision reflected by the length of error bars. (Figure 5-15) High background due to surface destruction was not observed, even though the background level increased at 350. (Figure 5-16D) Cholic acid is used as a further example here, and it was detected in negative ion mode. The detection characteristic and representative spectra are shown at Figure 5-17 and Figure 5-18. Even though the ion intensity is lower for cholic acid, the detection characteristic is similar to that of procainamide. However, the highest ion yield was obtained at 250, and the intensities of background ions were high, indeed higher than the signal of cholic acid. Laser setting as high as 350 suffers intent background and the molecular ion intensity decreases.

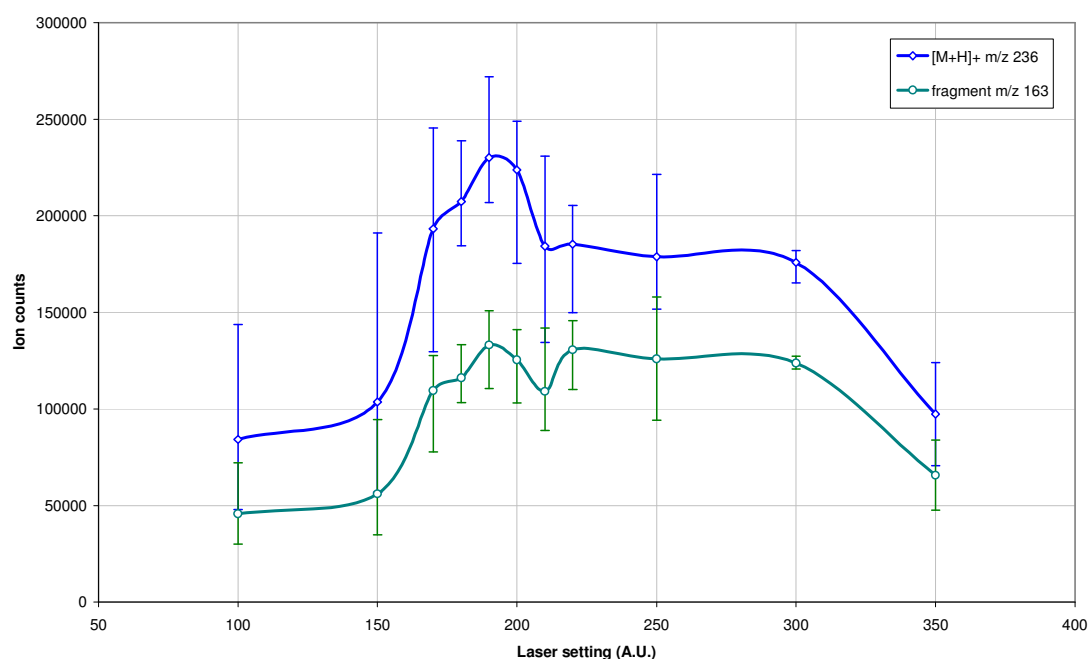


Figure 5-15 Ion intensity of 0.1 mM procainamide versus laser setting. Both the $[M+H]^+$ ion and its fragment at m/z 163 are shown on the plot. Each data point is an average of three replicas. The error bar indicates the highest and the lowest value obtained.

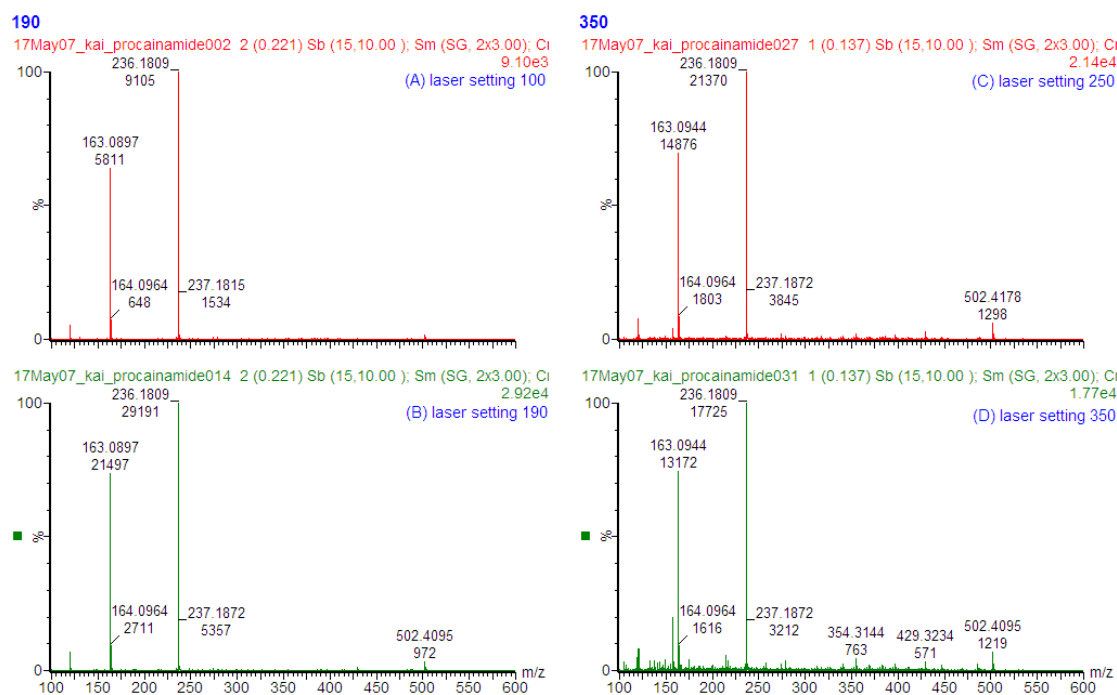


Figure 5-16 DIOS mass spectra of 0.1 mM procainamide at different laser setting: (A) laser setting at 100, (B) 190, (C) 250 and (D) 350. Data was acquired in positive mode with 1 μ l droplet of solution deposited onto each sample well, laser scanned across the well in 1 min. Raw spectra are smoothed, and background subtracted.

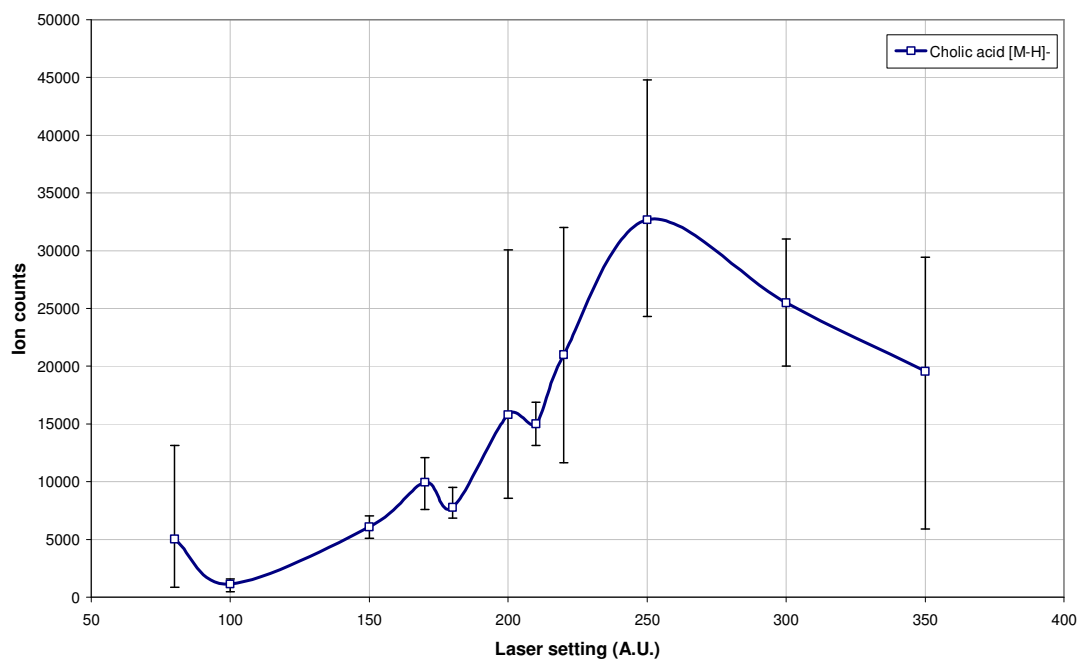


Figure 5-17 Ion intensity of 0.1 mM cholic acid $[M-H]^-$ versus laser setting. Each data point is an average of three replicas. The error bar indicates the highest and the lowest value obtained.

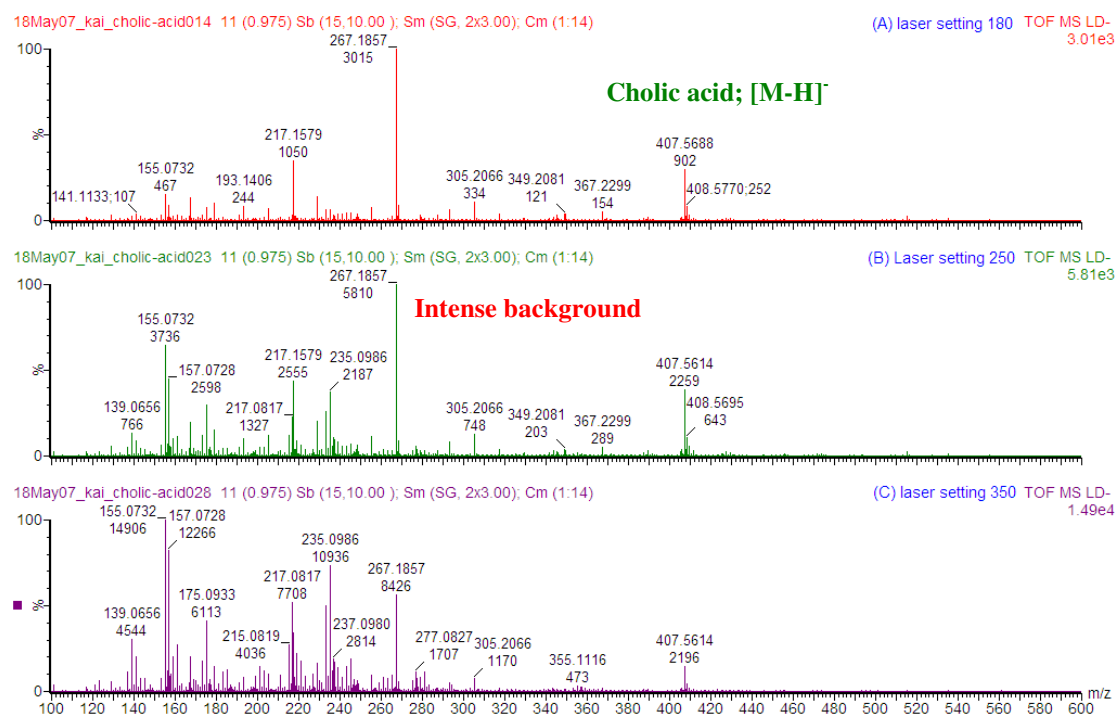


Figure 5-18 DIOS mass spectra of 0.1 mM cholic acid at different laser setting: (A) laser setting 180, (B) 250 and (C) 350. Data was acquired in negative mode with 2 μ l droplet of solution deposited onto each sample well, laser scanned across the well in 1 min. Raw spectra are smoothed, and background subtracted. Peak at m/z 267 is a phosphate contaminant.

Then again, a different observation was obtained on small peptides. Figure 5-19 and Figure 5-20 show the detection characteristic and representative spectra of HPLC peptide standard mixture. The mixture contains Gly-Tyr, Val-Tyr-Val, methionine enkephalin, leucine enkephalin, angiotensin II and a small quantity of salt (information was not provided by manufacturer). The signals of protonated methionine enkephalin and leucine enkephalin were low and they preferred to form salt adducts. This observation is consistent with those presented in the previous chapter. For the salt adduct of methionine and leucine enkephalin and protonated angiotensin II, the ion intensity increases as the laser energy is increased even if the energy has reached the surface destructive point (laser setting above 300), in contrast to the ion intensity of the protonated Gly-Tyr at the same region. Given that the unknown peak at m/z 465 exhibited a similar behaviour to the salt adduct of methionine and leucine enkephalin, it is possible the ion is a di-sodium adduct of Val-Tyr-Val, $[M+2Na-2H]^+$.

The reason for the above observation is not clear. Firstly, it may be because desorption of peptides require a higher laser energy relative to small organic compounds and this is related to the physicochemical properties of the peptides in the mixture. Secondly, the sample contained a small quantity of salt, which could cause ion suppression. The effect of suppression is compensated for by using higher laser energy. Thirdly, the complexity of the sample has increased from signal analyte with minor contaminants to essentially a protein digest. The available energy is divided among various ions and the profile obtained has shifted to the higher setting.

Overall, the detection characteristics obtained on Q-ToF system are similar to that obtained using ToF system, but differ in scale and laser range. The laser energy of the Q-ToF system is controlled by a density filter and the energy range is much wider than the ToF system used previously, in which an optical iris is used to control the laser energy and appears to have a relatively narrow energy range. This may further suggest that the laser system and/or other instrumental factors as discussed in the previous chapter, are significant in determining the analytical performance of DIOS, and possibly in other SALDI approaches.⁵⁶ Good quality spectra may have to be acquired at a suboptimal laser setting. Laser setting 180 to 220 appears to be suitable in positive as well as negative ion mode.

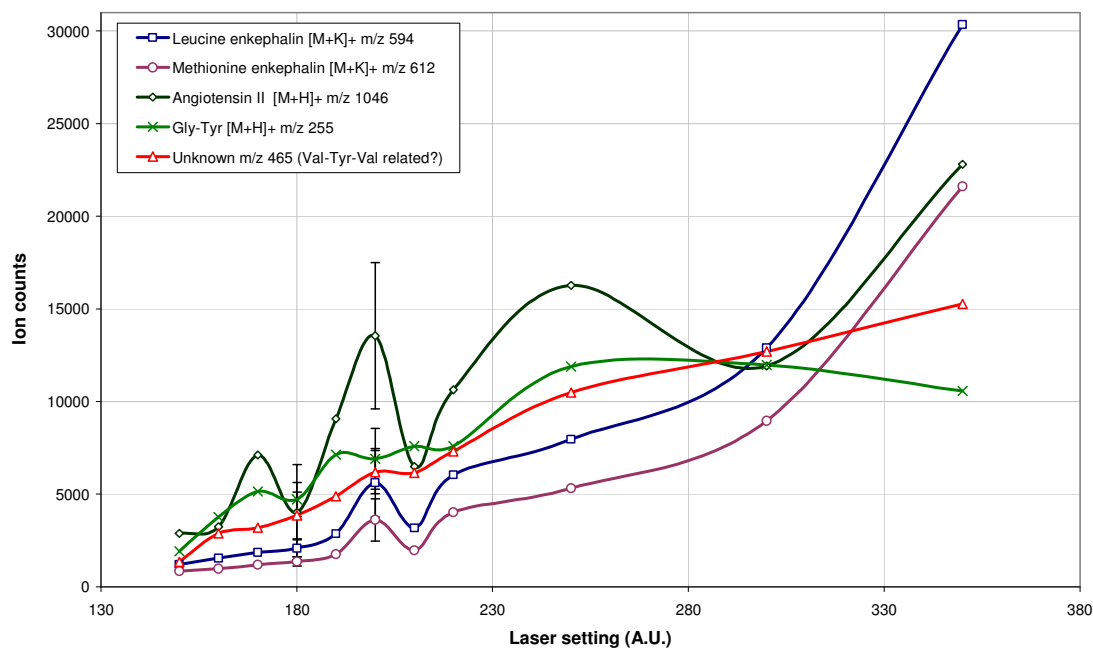


Figure 5-19 Ion intensity of HPLC peptide standard mixture versus laser setting. The peaks corresponding to potassiated methionine and leucine enkephalin and protonated Gly-Tyr and angiotensin II are chosen for plotting. An unknown peak, which is believed to be Val-Tyr-Val, is included. Each data point is the average value of two to eight replicas. The error bar indicates the standard deviation of the laser setting 180 and 200, where $n = 8$ and $n = 4$, respectively.

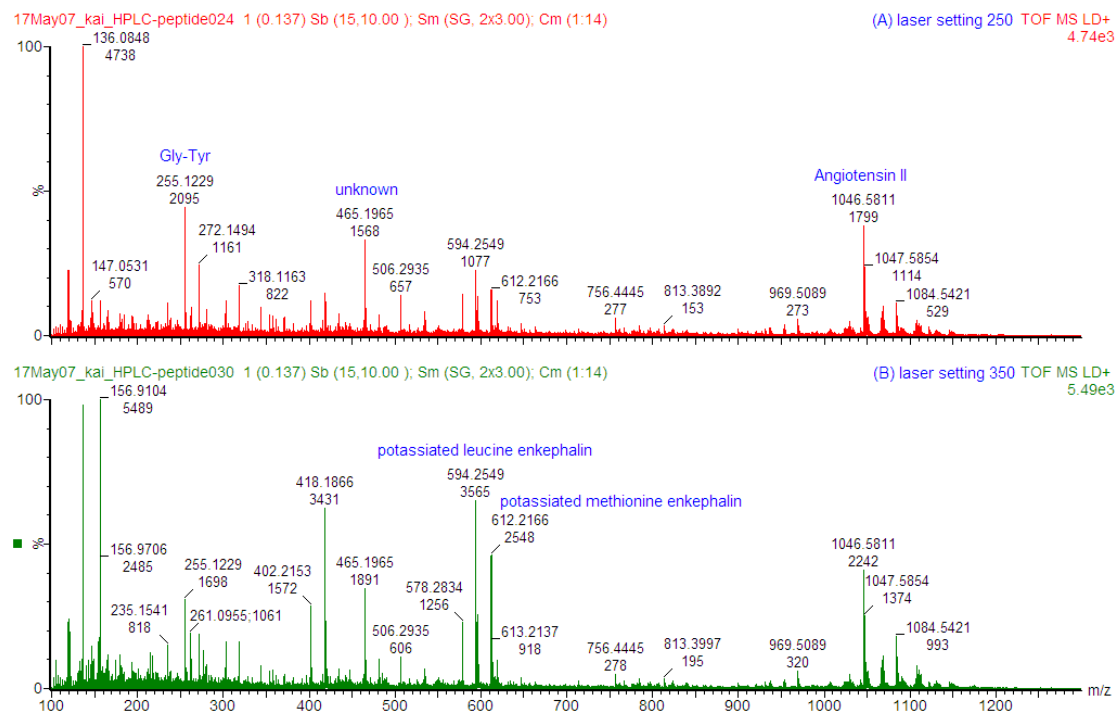


Figure 5-20 DIOS mass spectra of HPLC peptide standard mixture: (A) laser setting 250 and (B) 350. The concentration of the sample solution was not known. Data was acquired in positive mode with 1 μ l droplet of solution deposited onto each sample well, laser scanned across the well in 1 min. Raw spectra are smoothed, and background subtracted.

5.3.2 Dynamic range and Limit of Detection

Much of the data presented in the introductory section was concerned with the linearity and LOD. Here, we go beyond the upper limit of linearity and look into the dynamic range. Arginine, for instance, shows a typical calibration curve that we would expect for most quantitative analytical methods. (Figure 5-21) The ion intensity increases linearly up to 100 μM . Thereafter, the gradient of the curve reduces and the curve eventually smooths out. The linear range is about two orders of magnitude and the dynamic range is about three orders of magnitude. LOD was 1.6 μM .

Other compounds such as metoprolol and atenolol also show a similar analytical characteristic. (Figure 5-22 and Figure 5-23). An observed exception occurred with acetylcholine. (Figure 5-24) The ion intensity in the examples above levels off at higher concentration, while the intensity of acetylcholine M^+ ion decreases once the concentration reaches a maximum. This may be because of the ion pairing effect due to the concentration of chloride (acetylcholine was available as a chloride salt).

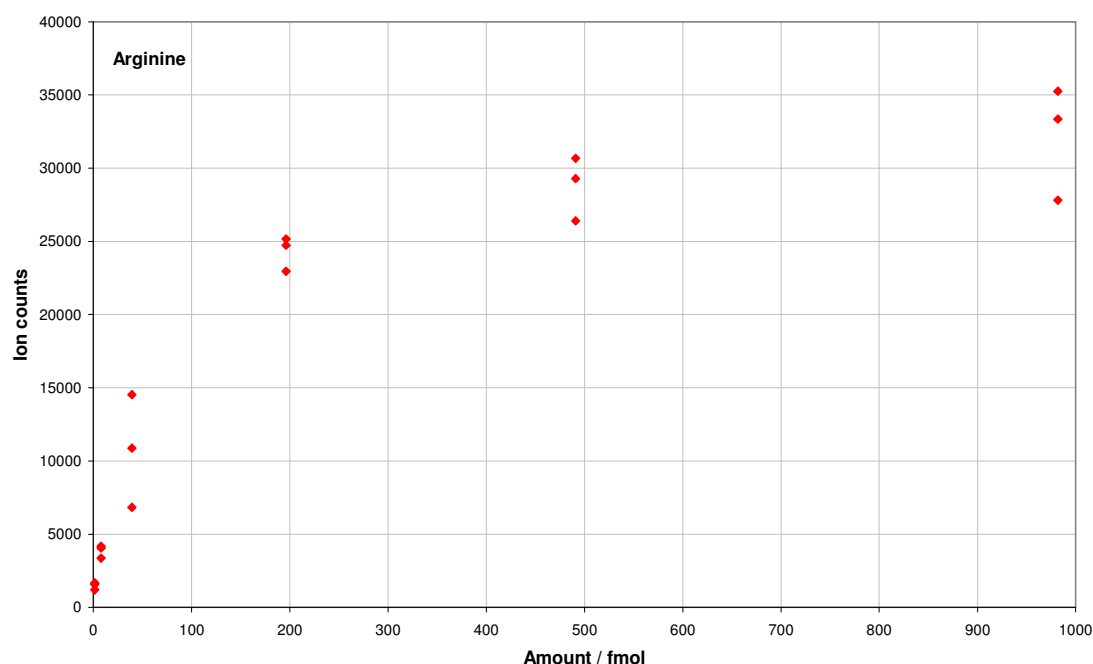


Figure 5-21 Calibration curve of arginine $[\text{M}+\text{H}]^+$. 1 μl of solution of concentration from 63 nM to 982 μM , was deposited onto the target. Data was acquired with 2 min spiral scan at laser setting 220. The LOD was 1.6 fmol. Linearity was 2 orders in magnetite.

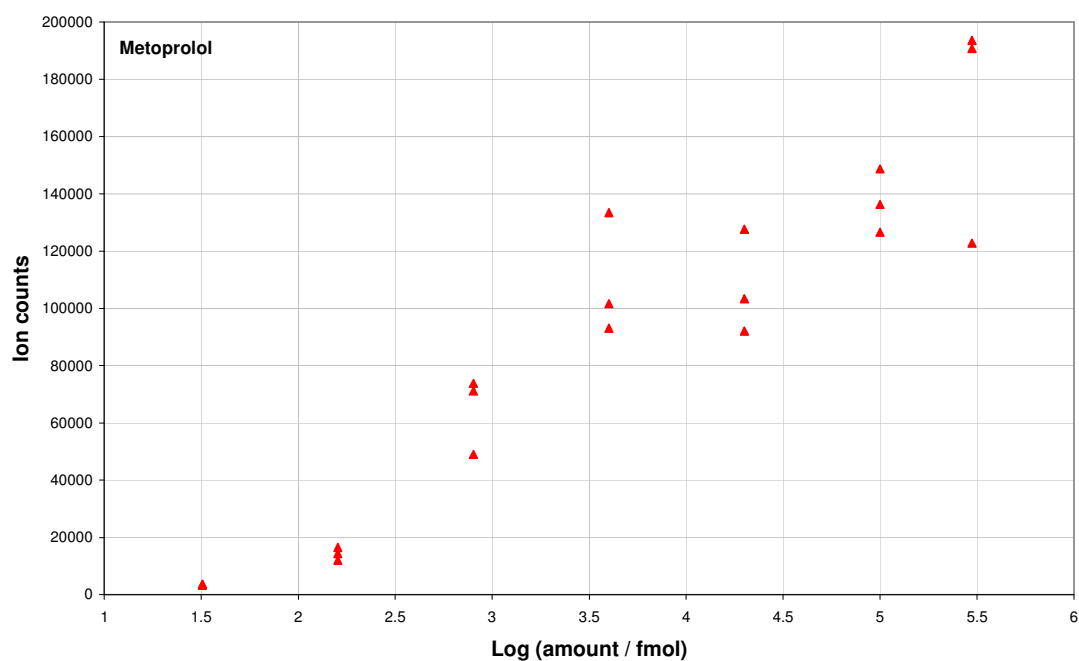


Figure 5-22 Calibration curve of metoprolol $[M+H]^+$. 1 μ l of solution of concentration from 6.4 nM to 298 μ M, was deposited onto the target. Data was acquired with 2 min spiral scan at laser setting 220. The LOD was 32 fmol. Linearity was 2 orders in magnetite.

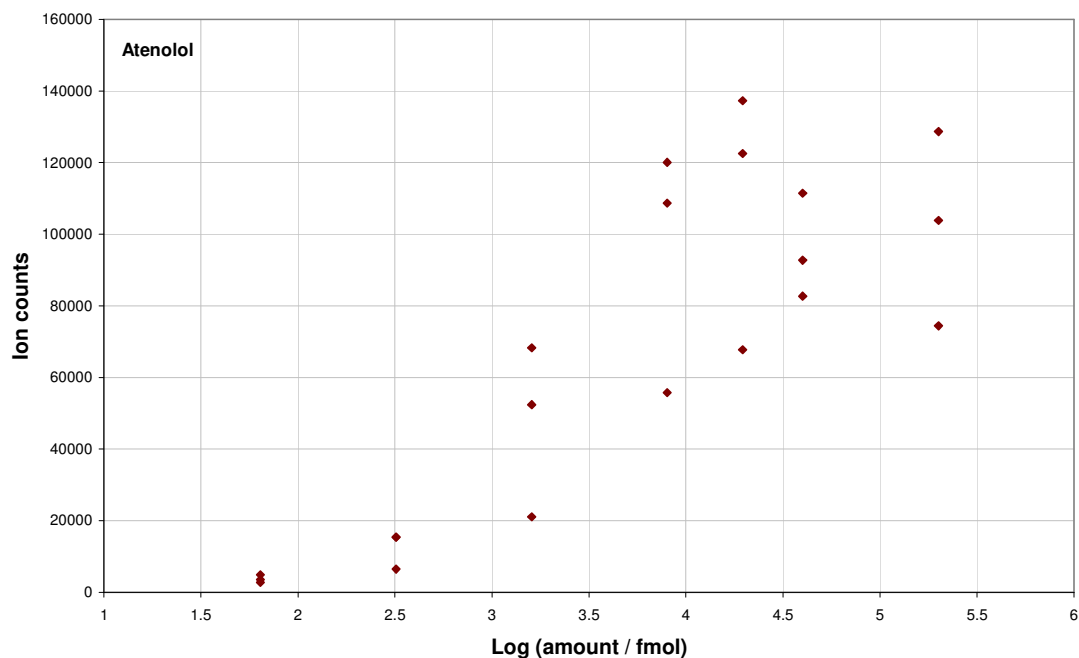


Figure 5-23 Calibration curve of atenolol $[M+H]^+$. 1 μ l of solution of concentration from 12.8 nM to 0.2 mM, was deposited onto the target. Data was acquired with 2 min spiral scan at laser setting 220. The LOD was 64 fmol. Linearity was 2.5 orders in magnetite.

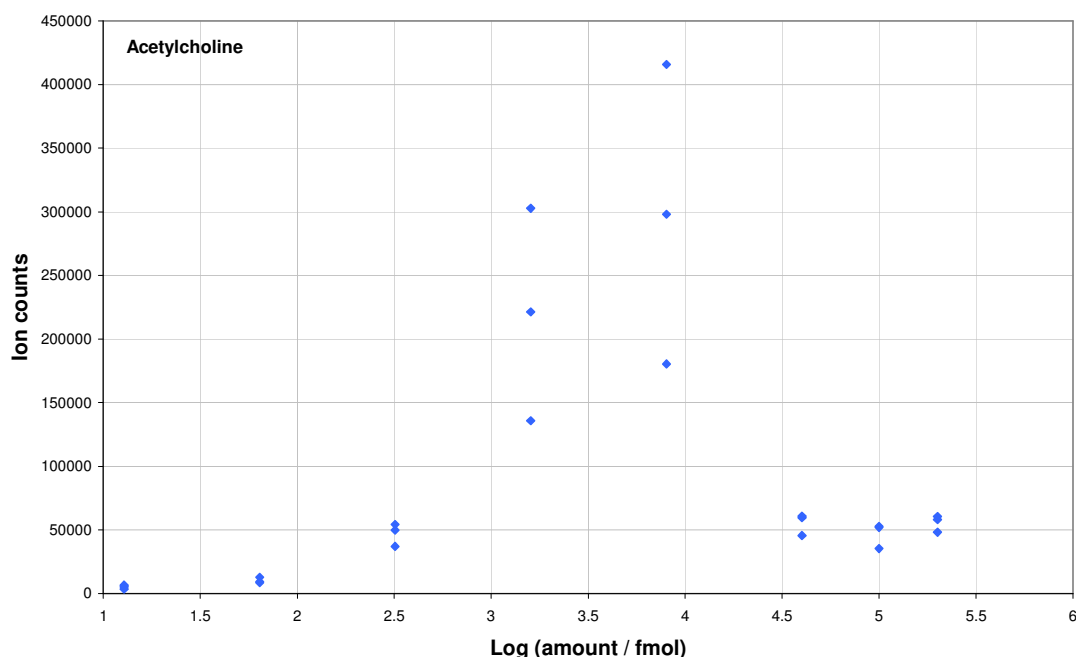


Figure 5-24 Calibration curve of acetylcholine M^+ . 1 μ l of solution of concentration from 12.8 nM to 0.2 mM, was deposited onto the target. Data was acquired with 2 min spiral scan at laser setting 220. The LOD was 12.8 fmol. Linearity was 2 orders in magnetite. The M^+ ion intensity decreased considerably after the concentration of the analyte (acetylcholine chloride) increased over 8 pmol. This was possibly because of the ion-pairing effect due to the increased concentration of chloride ion.

ToF instrument is characterised with a relatively narrow or inadequate linearity, because of the problem of detector saturation. Since MALDI is often coupled to ToF mass analyser, quantitation by MALDI is often instrument-limited. The Q-ToF Premier used in this study has therefore been equipped with a DRE lens system (see Figure 18, Chapter 2), which provides a function called programmable dynamic range enhancement (pDRE), and can extent the linearity by up to 4 orders of magnitude under the ESI or APCI mode. The again, the function is disabled in normal operation under the MALDI mode. The reason is not known, but is possibly because of the pulse nature of ion current in the MALDI system. No further improvement in linearity was therefore achieved. The issue of detector saturation may only partly explain to the linearity observed. Other possible factors, such as surface saturation may also be involved. Surface saturation occurs when multilayer of analyte is deposited on the surface impeding the ionisation or desorption processes. The linearity obtained could thus be about 2 to 3 orders of magnitude. Still, if we compare the dynamic range of other metabolomics tools, the dynamic range we obtained on DIOS is roughly the

same as NMR (see Table 1, Chapter1) and is a limitation of the technique to which we need to pay attention.

5.3.3 Precision and Robustness

In this section, the well-to-well and target-to-target precision are investigated. The results are summarised in Table 5-2 and Table 5-3. The precision was far from ideal, varying from ~10 to ~90%, and on average, the calculated values of RSD were less than 50%, concurring with Credo, *et al.*¹⁷ The repeatability and so possibly the robustness (in terms of ion intensity) were also far from ideal in most of the situations.

It is hypothesised that a simple data processing procedure, normalising to TIC, may be able to tackle the issue of reproducibility for data acquired by DIOS-MS.⁵⁷ We have also applied normalisation to SIMS dataset in the previous chapter in dealing with the signal precision and pre-processing the dataset for PCA. What if this approach could also be applied to the data acquired by DIOS-MS and become a simple solution to the poor precision here? To test this hypothesis, the datasets of two different mixtures were re-examined.

The detection characteristic and DIOS spectra of HPLC peptide standard mixture have been presented in Figure 5-19 and Figure 5-20. The precision of the ion intensity is calculated using data acquired at laser setting 180. Regrettably, the precision is poor. RSD varies from ~20% to ~60% even though the RSD of TIC is only 11%. (Table 5-4) We therefore apply normalisation to TIC to see if this leads to any improvement in the precision of the dataset. After the data processing, RSD varies from ~15% to ~50%. Relatively, there is an improvement to the precision. However, the improvement is relatively small (from ~4% to ~10%) and is still less than satisfactory.

Similar results are also obtained using a “metabonomics test mix”. (Table 5-5) The mixture contains nortriptyline, theophylline, caffeine, reserpine, 4-nitrobenzoic acid and hippuric acid. The final concentration of nortriptyline, theophylline, caffeine and reserpine was 20 µg/ml, and 4-nitrobenzoic acid, and hippuric acid was 200 µg/ml.

Table 5-2 Target-to-target precision. Three different targets were used and the experiments were carried over in three days. 1 μ solution deposited onto the target. Data was acquired with 2 min spiral scan, laser setting was 220. Six replicas were used for the calculation.

| | | | % RSD n = 6 | | |
|-------------------------|-------------|---------------------------|-------------|----------|----------|
| Substance | Conc. | Ions (<i>m/z</i>) | Target 1 | Target 2 | Target 3 |
| Acetylcholine | 1.6 μ M | M ⁺ 146 | 23 | 36 | 32 |
| Arginine | 982 μ M | [M+H] ⁺ 175 | 20 | 29 | 20 |
| Atenolol | 8 μ M | [M+H] ⁺ 267 | 9 | 17 | 17 |
| Fluorescein | 100 μ M | [M+H] ⁺ 333 | 56 | 54 | 90 |
| Procainamide | 100 μ M | [M+H] ⁺ 236 | 31 | 26 | 20 |
| Lidocaine | 100 μ M | [M+H] ⁺ 235 | 79 | 35 | 22 |
| Raffinose | 1 mM | [M+Na] ⁺ 527 | 34 | 54 | 61 |
| Cyclodextrin | 0.47 mM | [M+Na] ⁺ 1157 | 55 | 38 | 52 |
| Angiotensin I | 100 μ M | [M+H] ⁺ 1297 | 69 | 59 | 49 |
| Vitamin B ₁₂ | 100 μ M | [M+H] ⁺ 1355.5 | 29 | 55 | 47 |
| | | Fragment 1329.6 | 29 | 32 | 41 |
| | | fragment 971 | 26 | 36 | 31 |
| Metropol | 100 μ M | [M+H] ⁺ 268 | 30 | 47 | 11 |
| | 4 μ M | | 19 | 18 | 37 |
| Verapamil | 2000 ng/ml | [M+H] ⁺ 455 | 30 | 25 | 33 |
| | 500 ng/ml | | - | 26 | 19 |

Table 5-3 Precision and robustness. Except naproxen, the data was calculated using the ion intensity of [M+H]⁺ or [M-H]⁻ molecular ion. Data was only acquired at suboptimal conditions and was a design of the experiment (*i.e.* robustness). “Time” refers to acquisition time.

| Comments | Results | | Experimental condition | | | | | | Substance | |
|--|-----------|-------------|------------------------|------------------------|-----------------|----------------------|--------------------|------------------|---------------------|----------------------|
| | <i>SD</i> | <i>%RSD</i> | <i>Ave. intensity</i> | <i>No. of replicas</i> | <i>Polarity</i> | <i>Laser setting</i> | <i>Time (sec.)</i> | <i>Scan mode</i> | <i>Droplet (μl)</i> | <i>Concentration</i> |
| These two sets of data were acquired on the same target with different laser setting. The ion intensity was less sensitive to laser energy at the given experimental conditions and hence the average intensity was roughly the same. The calculated precision is also about 20%. | 28501 | 24 | 119823 | 6 | positive | 180 | 60 | raster | 1.0 | 0.1 mM |
| | 22096 | 18 | 124117 | 7 | positive | 200 | 60 | raster | 1.0 | 0.1 mM |
| | 109491 | 82 | 133686 | 6 | negative | 300 | 120 | spiral | 1.2 | 0.1 mM |
| | 67293 | 50 | 134416 | 5 | negative | 300 | 120 | spiral | 1.2 | 0.1 mM |
| | 39535 | 71 | 55745 | 6 | negative | 300 | 60 | spiral | 1.2 | 0.1 mM |
| | | | | | | | | | | |
| | | | | | | | | | | |
| | | | | | | | | | | |
| | | | | | | | | | | |
| | | | | | | | | | | |
| | | | | | | | | | | |
| | | | | | | | | | | |
| These three sets of data were acquired on the same target. The first two sets of data were acquired with an identical experimental condition. However, they differ by acquiring several hours apart. The first (and the third) set of data was acquired at the beginning of an experiment while the second was acquired near the end of the experiment. The average ion counts were similar even though the % RSD of the datasets varied considerably. While half the date acquisition time, ion count was half. | | | | | | | | | | |

| Verapamil | Reserpine | Cholic acid | | | |
|---|-----------|---|--|----------|----------|
| 500 ng/ml | 500 ng/ml | 20 µg/ml | 0.1 mM | 0.1 mM | 0.1 mM |
| 1.0 | 1.0 | 1.2 | 2 × 2 | 2 × 2 | 1.5 |
| raster | raster | raster | raster | raster | spiral |
| 60 | 60 | 120 | 60 | 60 | 120 |
| 220 | 180 | 220 | 200 | 210 | 210 |
| positive | positive | positive | negative | negative | negative |
| 12 | 6 | 5 | 6 | 6 | 8 |
| 137555 | 210749 | 92672 | 74296 | 87002 | 99954 |
| 159174 | | | | | |
| 19384 | 69862 | 48595 | 11473 | 13503 | 13107 |
| 26998 | | | | | |
| 14 | 33 | 52 | 15 | 15 | 13 |
| 17 | | | | | |
| Half the data acquisition time was used here. Compare to the similar data collected in Table 5-2. The average intensity was roughly the same. But on second occasion, a different result was obtained | | Similar to the literature data presented in the introduction, the precision of reserpine is around 50 to 60%. | These three sets of data were collected on the same target and the laser setting was gradually increased from 200 to 220. The average intensity gradually increased and the precision of these three sets of data was nearly the same. This relatively good precision may be related to the method of deposition. Each of the sample well was spotted twice and may therefore produce a more uniform analyte distribution. | | |

| Nalidoxic acid | | Flumequine | | Flufenamic acid | Diflunisal | Naproxen |
|---|----------|------------|----------|---|------------|-----------------|
| 0.2 mM | 0.2 mM | 0.5 mM | 0.5 mM | 0.9 mM | 1.0 mM | 1.0 mM |
| 1.2 | 1.2 | 1.2 | 1.2 | 1.2 | 1.2 | 1.2 |
| raster | spiral | raster | spiral | spiral | spiral | raster |
| 120 | 120 | 120 | 120 | 120 | 120 | 120 |
| 220 | 300 | 220 | 300 | 300 | 300 | 220 |
| positive | negative | positive | negative | negative | negative | positive |
| 6 | 5 | 5 | 6 | 6 | 6 | 6 |
| 21563 | 39357 | 36591 | 33351 | 11671 | 74120 | 9282 |
| 5448 | 25213 | 12664 | 6624 | 3349 | 49066 | 3380 |
| 25 | 64 | 35 | 20 | 29 | 66 | 36 |
| These two datasets were acquired on the same target. One was acquired in negative mode with laser setting 300 and the other was acquired in positive mode with laser setting 220. | | | | Substance could not be detected in position mode. | | Low sensitivity |

Table 5-4 The precision of ion intensity (IC) of individual peptide in a HPLC peptides standard mixture before and after normalisation to TIC. TIC is summation of all ion counts in the range between m/z 100-1500 in each spectrum. Data was acquired in positive mode, at laser setting 180, raster scan for 60s. Eight replicas are used for the calculation. The normalised values are calculated by $\frac{IC}{TIC} \times 100\%$ and are percentages of TIC. Two decimal points are used because the normalised values are small. SD denotes the standard deviation.

| Peptide | Gly-Tyr | Val-Tyr- Val | Leucine enkephalin | Methionine enkephalin | Angiotensin II | TIC |
|--|-----------|-----------------|-----------------------|--------------------------|-------------------|----------|
| Ion | $[M+H]^+$ | $[M+2Na-2H]^+$ | $[M+K]^+$ | $[M+K]^+$ | $[M+H]^+$ | |
| m/z | 255 | 455 | 594 | 612 | 1046 | 100-1500 |
| <i>Before normalisation</i> | | | | | | |
| %RSD | 26.84 | 23.85 | 22.05 | 18.12 | 64.23 | 11.38 |
| <i>After normalisation to TIC</i> | | | | | | |
| %RSD | 15.81 | 14.85 | 17.80 | 14.83 | 52.05 | - |

Table 5-5 The precision of ion intensity (IC) of individual substance in a metabonomics test mix. Data was acquired in positive mode, at laser setting 180, raster scan for 60s. 12 replicas were used for the calculation. 4-nitrobenzoic acid, hippuric acid, and theophylline were not detected under positive mode. Data processing is identical to the HPLC peptides standard mixture above.

| Compound | Caffeine | Nortriptyline | Reserpine | Reserpine fragment | TIC |
|--|-----------|---------------|-----------|-----------------------|----------|
| Ion | $[M+H]^+$ | $[M+H]^+$ | $[M-H]^+$ | | |
| m/z | 195 | 264 | 607 | 395 | 100-1000 |
| <i>Before normalisation</i> | | | | | |
| %RSD | 32.65 | 47.37 | 30.45 | 28.75 | 15.45 |
| <i>After normalisation to TIC</i> | | | | | |
| %RSD | 26.95 | 37.81 | 29.06 | 27.63 | - |

There are three major causes to the relatively large variation in signal intensity:⁵⁸

1. The instability of the N₂ laser and/or the mass spectrometer acquisition system
2. The native surface variation between the sample wells and target
3. Uneven distribution of the analyte due to sample preparation (Figure 5-25)

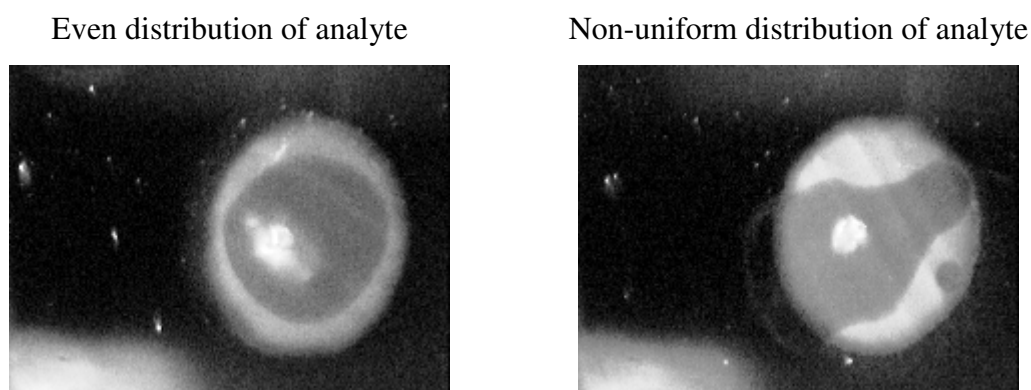


Figure 5-25 Optical micrographs of two spotted DIOS sample wells. The image on the left shows a relatively uniform distribution of the analyte and appears on the image as a circular “water mark” whereas the one on the right shows a non-uniform distribution and the analyte coverage was only ~60%. The white patch in the middle of the image is the laser spot. The images were taken during data acquisition.

The assumption of the normalising to TIC approach is that an individual ion varies proportionally to all other ions in the spectrum, and thus the intensity of an ion has a constant ratio to the TIC. Despite some improvements being obtained, this approach alone was obviously inadequate because the precision of TIC was less than half of that of any individual ion. While the normalisation approach does apply to surface analysis using SIMS technique in tackling the matrix effect or to minimise the variation due to instability of laser or surface variation between sample well, this assumption is unable to eliminate or minimise the intra (sample-to-sample) and inter (point-to-point) experimental variation.

Indeed, the main limiting factor in quantitation by LDI (either by MALDI or by DIOS) is the uneven distribution of the analyte on the surface. The precision becomes an issue largely surrounding how a sample droplet is added onto the surface and the droplet aggregation during drying.^{23, 25} The pipette deposition is relatively simple and fast, but it could not produce a reproducible result. Consequently, on considering the

linearity and the precision, DIOS-MS with pipette deposition is still a less than reliable method for quantitation and we may have to treat the method qualitatively.

While the analytical performance of DIOS has been evaluated based on the ICH parameters, those parameters are specific for quantitation of pharmaceutical products and food using chromatography and may not be applicable to laser mass spectrometry approaches. Possible alternatives are to use an internal standard to compensate for signal deviation, or improved deposition approaches such as ESD. Despite the data showing that the approach in its current form is not “fit” for quantitation, they do not answer the question of whether or not the method is suitable for global profiling of metabolites in complex biological matrices, nor can the method provide information about the identity of an unknown metabolite. It may have to stress that since the method is being used qualitatively, there is no need to test and validate the method’s LOQ, or the linearity. Validation only requires the measurement of LOD and specificity. These may also be reasons that the ICH approaches are rarely motioned in proteomics research, where MALDI is one of the most important tools. The approach was hence shifted to evaluate the method from a bottom-up approach and directly employed complex biological matrices.

5.3.4 Human Urine

Urine is a waste product, which is a readily collected, information-rich and can provide insight into the metabolic state of an organism. However, urine contains a high quantity of salts, which makes it difficult to analyse directly by mass spectrometry. Despite the high salt content, DIOS mass spectra could still be obtained, (Figure 5-26 and Figure 5-27) demonstrating its tolerance toward the presence of salts. However, the effects of ion suppression are noticeable. Desorption of ions was strongly suppressed by the relatively high content of salts, which also suppressed desorption of contaminants. As a result, background interferences were only observed in the blank spectra. In terms of the practicality of DIOS, the ubiquitous salt content in biological samples causes suppression to ion formation and/or leads to adduct formation. A sample clean-up procedure was thus developed to remove the salts and retain as many biological molecules as possible.

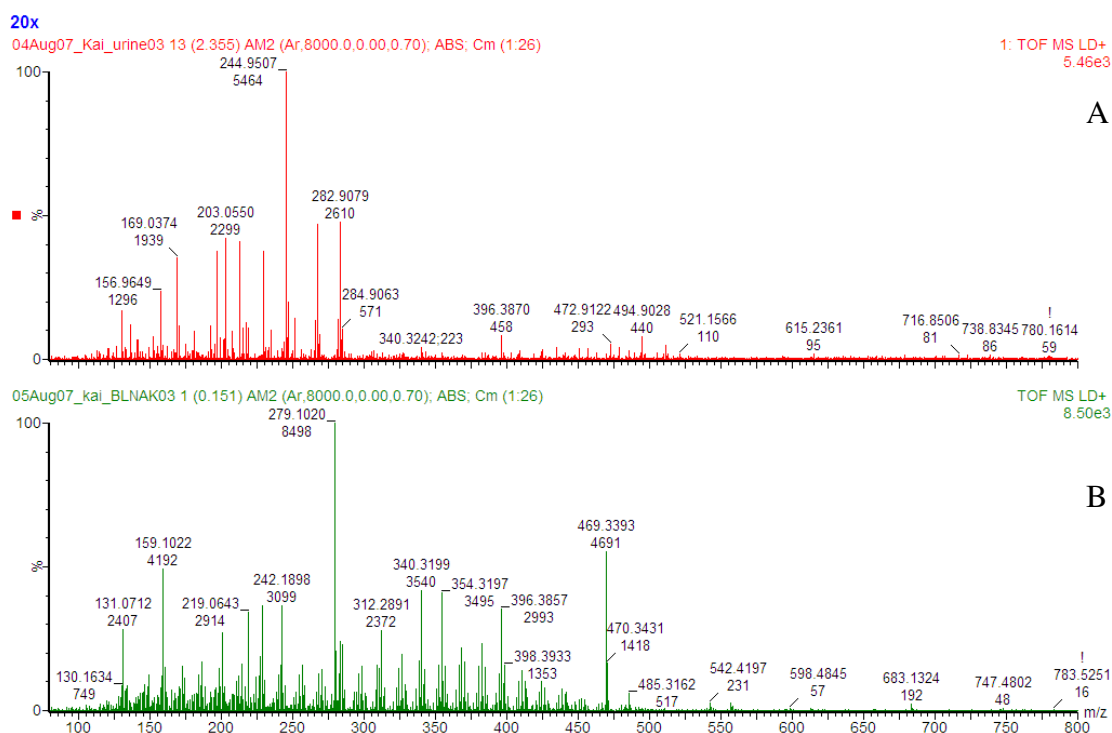


Figure 5-26 (A) Positive ion DIOS mass spectrum of human urine and (B) blank (ACN/H₂O). Urine was diluted in 1:1 ACN/H₂O for 20 times. Data was acquired with 120s spiral scan and the spectra were processed with adaptive background subtraction.

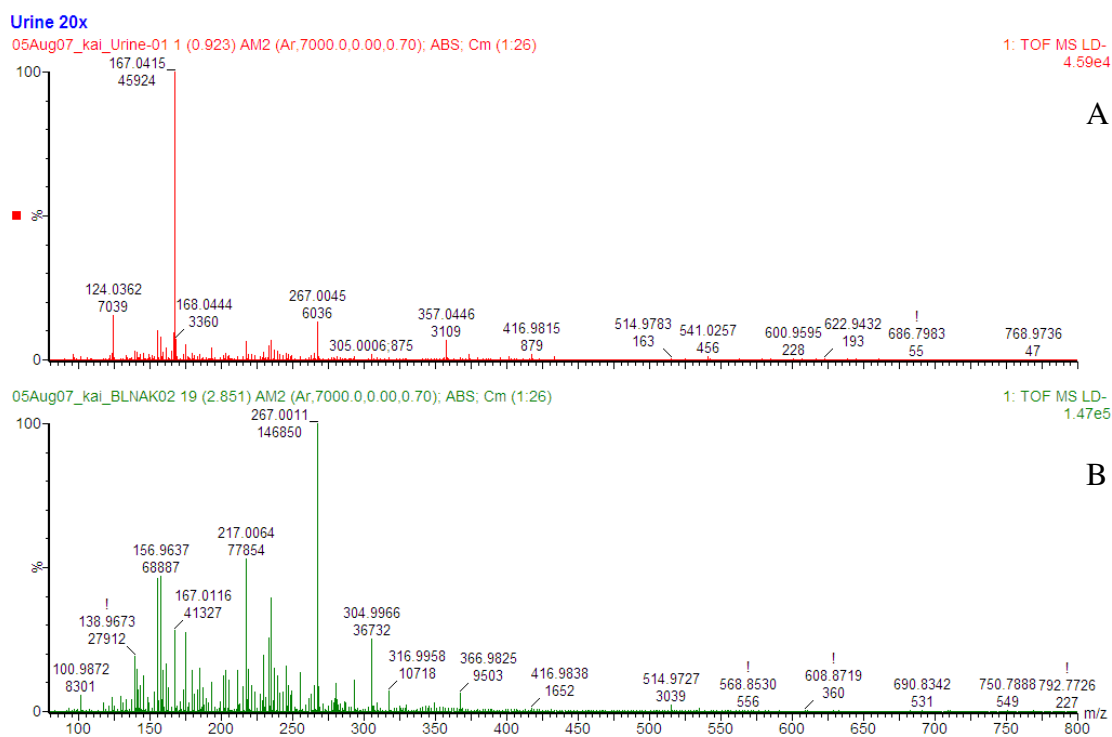


Figure 5-27 (A) Negative ion DIOS mass spectrum of human urine and (B) blank (ACN/H₂O). Urine was diluted in 1:1 ACN/H₂O for 20 times. Data was acquired with 120s spiral scan and the spectra were processed with adaptive background subtraction.

Four different extraction methods were attempted. The method which used diethyl ether/hexane and chloroform/butanol was adopted from Shen, *et al.*,²¹ and had been demonstrated as being suitable for DIOS-MS. (see Figure 5-8) Indeed, this method was also the most efficient extraction method in all four methods attempted. The method was modified from Shen, such as the volume of urine used and the residue was reconstituted in 50% ACN instead of 80% methanol. The analysis was performed in both positive and negative ion mode using MALDI Q-ToF instead of linear mode in ToF. The DIOS spectra of urine extracts are shown at Figure 5-28 and the spectra are information rich.

The foundation for the two-step extraction approach has been discussed by Chatman, *et al.*²² While the effort was focused on extracting steroid sulphates or removing the unconjugated steroids there, a further view is proposed here. On comparing the spectra of chloroform/butanol and diethyl ether/hexane urine extracts (Figure 5-29 to Figure 5-32), the species detected in positive spectra were extracted more efficiently by chloroform/butanol, whereas the species detected in negative spectra, especially those in between m/z 400 to 450, were extracted more efficiently by diethyl ether/hexane. The two-step extraction was thus ensuring a high recovery and extraction efficiency. On the other hand, ethyl acetate had a similar function as diethyl ether, likely because they have a similar polarity. (Figure 5-34)

We further evaluated the method by adding acidic or basic modifier during the sample extraction and we aimed to enhance the extraction efficiency. Although visual inspection of the HCl and NaOH extracts appeared to be denser than the extracts prepared by no addition of modifier, in no case did the addition of acidic or basic modifier improve the ion yield. (Figure 5-29 to Figure 5-34) The potential beneficial effects by alternating the pH of the urine extraction solution were outweighed by ion suppression effects in this case, and in most of the DIOS spectra obtained, the ion intensity was lower. The HCl extracts suffered suppression most strongly. NaOH extracts were subjected to a much lesser ion suppression effect and in certain situation where increasing the pH of the extraction solution would allow extraction of highly basic compounds. For example, an additional set of peaks, located at m/z 245 and shown in Figure 5-29B was detected in the positive spectrum. This compound was likely a nucleoside and was extracted by addition of alkaline modifier.

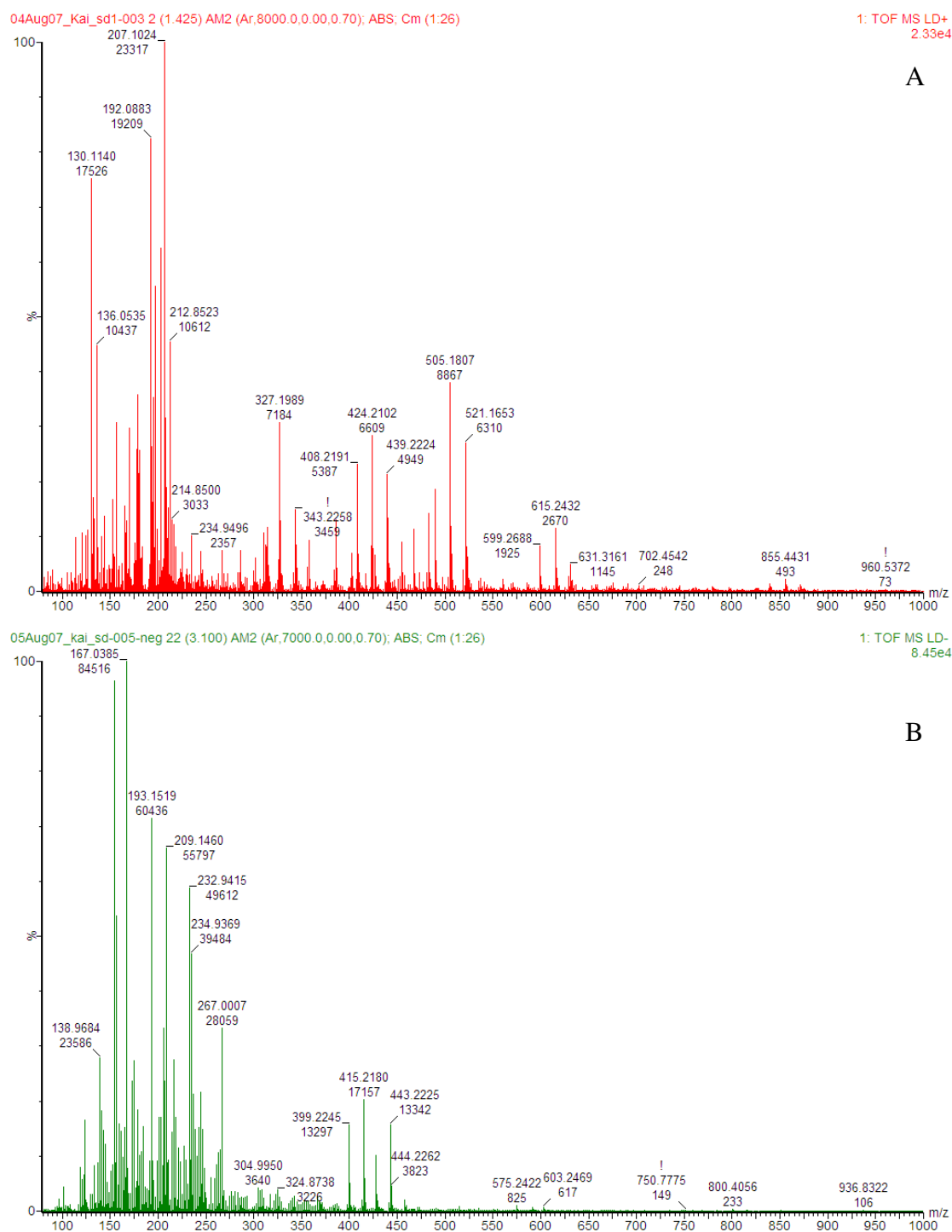


Figure 5-28 (A) Positive and (B) negative ion DIOS mass spectra of human urine donated by the writer. The writer suffers diabetic neuropathy. Glucose was detected as sodium adduct $[M+Na]^+$ at m/z 203. The sample was prepared by diethyl ether/hexane followed by chloroform/butanol. Addition of HCl or NaOH was not required and only suppressed the ion formation. 1 μ l of droplet was added onto the sample well. Data was acquired using 120s spiral scan. Laser setting for positive and negative mode was 220 and 200, respectively. Spectra were centroid and processed with adaptive background subtraction.

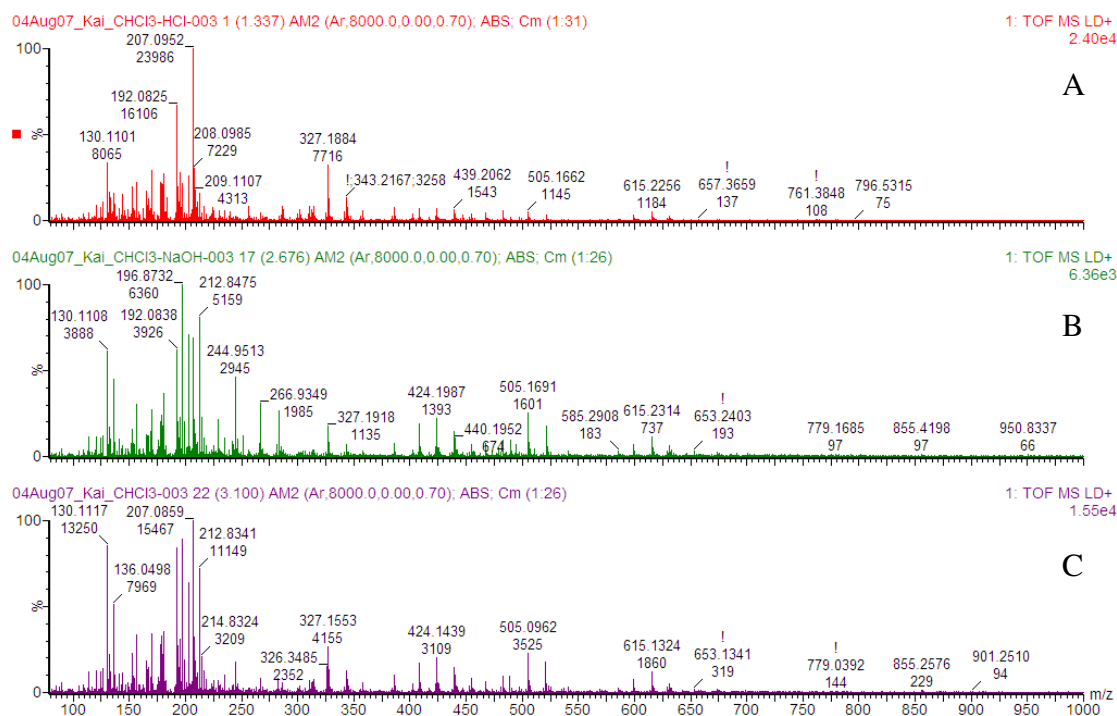


Figure 5-29 Positive ion DIOS mass spectra of chloroform/butanol extracts. (A) Addition of HCl, (B) addition of NaOH and (C) no addition of modifier. 1 μ l of droplet was added onto the sample well. Data was acquired using 120s spiral scan. Laser setting was 220. Spectra were centroid and processed with adaptive background subtraction.

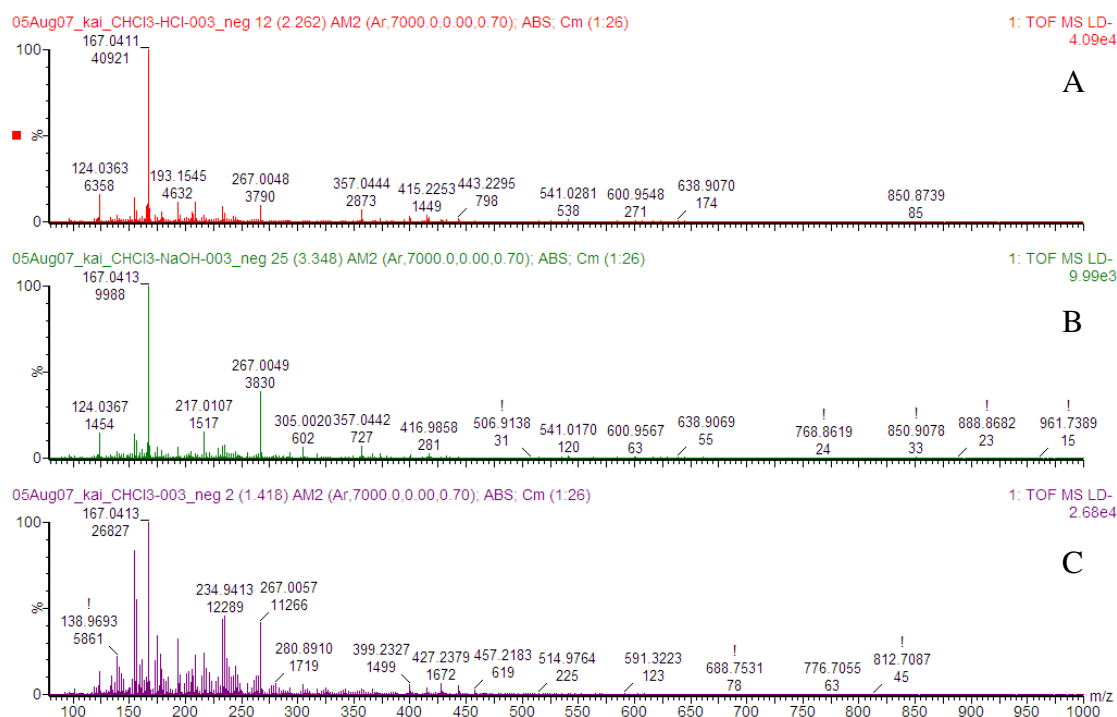


Figure 5-30 Negative ion DIOS mass spectra of chloroform/butanol extracts. (A) Addition of HCl, (B) addition of NaOH and (C) no addition of modifier. 1 μ l of droplet was added onto the sample well. Data was acquired using 120s spiral scan. Laser setting was 200. Spectra were centroid and processed with adaptive background subtraction.

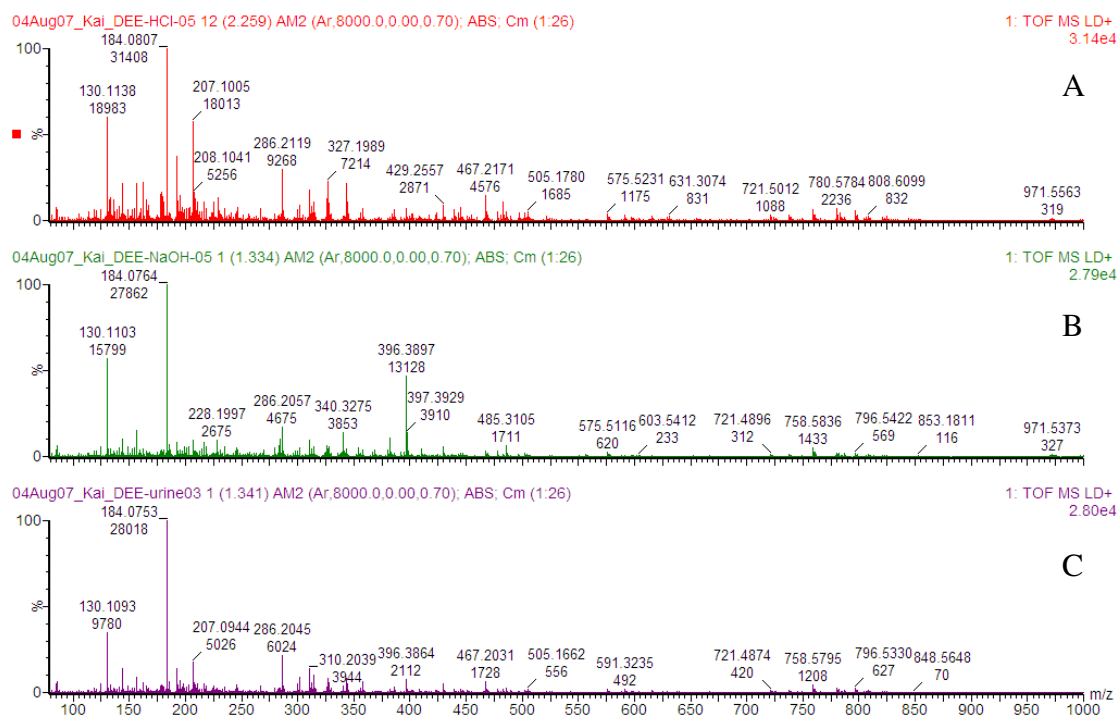


Figure 5-31 Positive ion DIOS mass spectra of diethyl ether extracts. (A) Addition of HCl, (B) addition of NaOH and (C) no addition of modifier. 1 μ l of droplet was added onto the sample well. Data was acquired using 120s spiral scan. Laser setting was 220, 230 and 210 respectively. Spectra were centroid and processed with adaptive background subtraction.

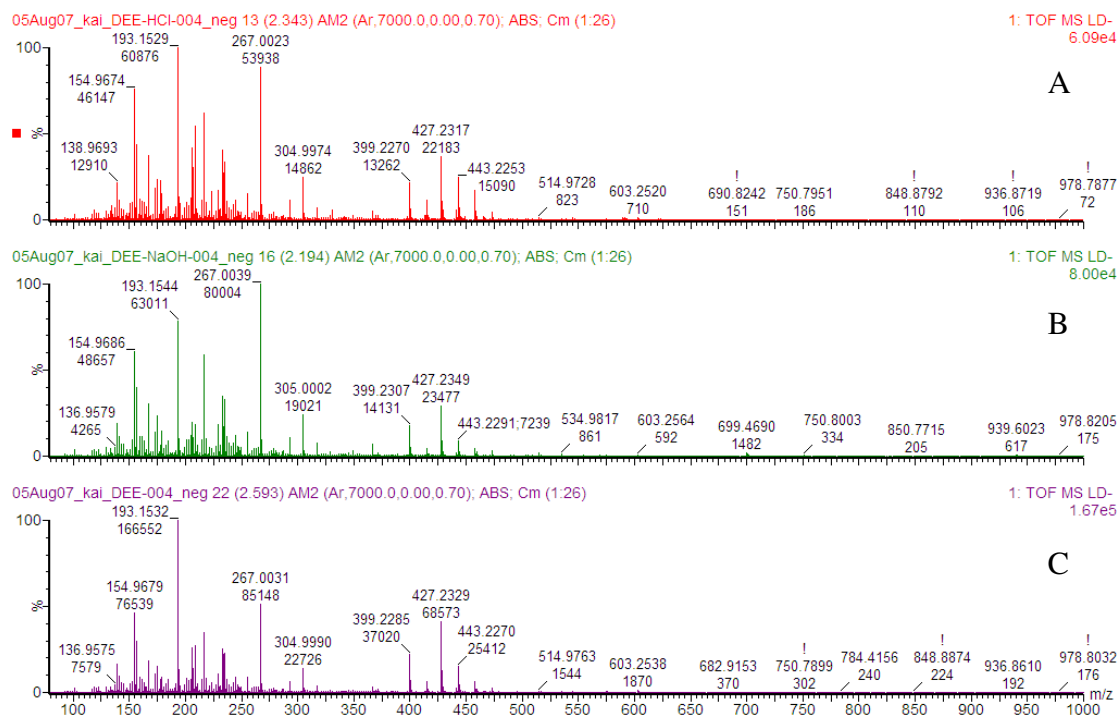


Figure 5-32 Negative ion DIOS mass spectra of diethyl ether extracts. (A) Addition of HCl, (B) addition of NaOH and (C) no addition of modifier. 1 μ l of droplet was added onto the sample well. Data was acquired using 120s spiral scan. Laser setting was 220. Spectra were centroid and processed with adaptive background subtraction.

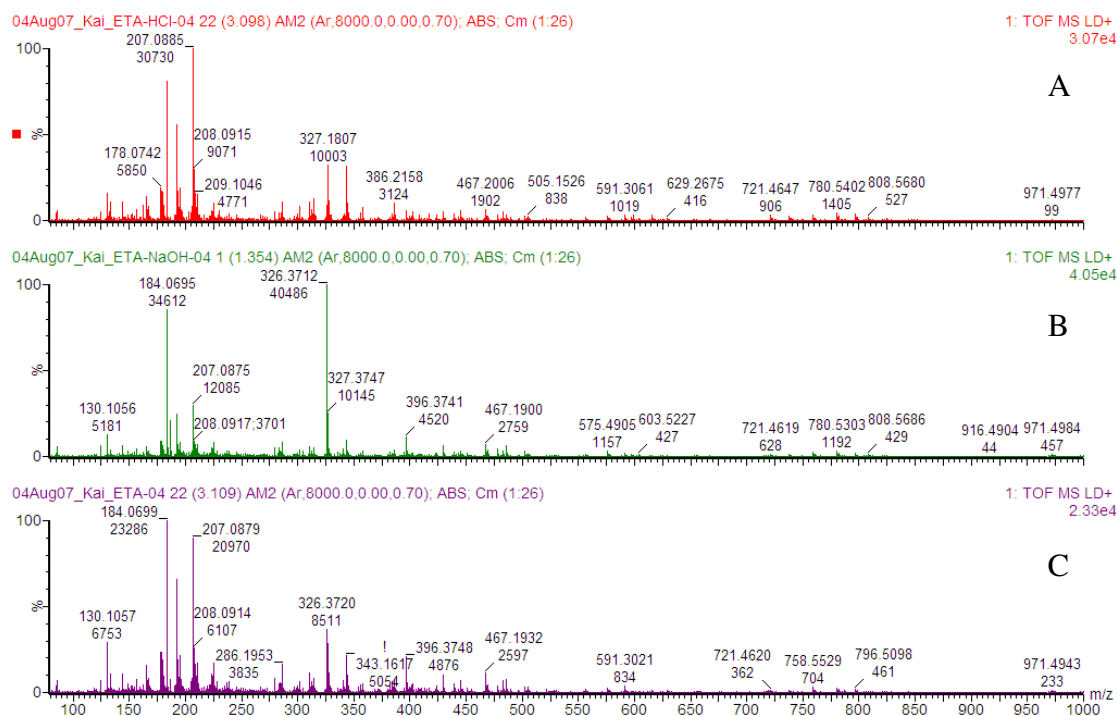


Figure 5-33 Positive ion DIOS spectra of ethyl acetate extracts. (A) Addition of HCl, (B) addition of NaOH and (C) no addition of modifier. 1 μ l of droplet was added onto the sample well. Data was acquired using 120s spiral scan. Laser setting was 220. Spectra were centroid and processed with adaptive background subtraction.

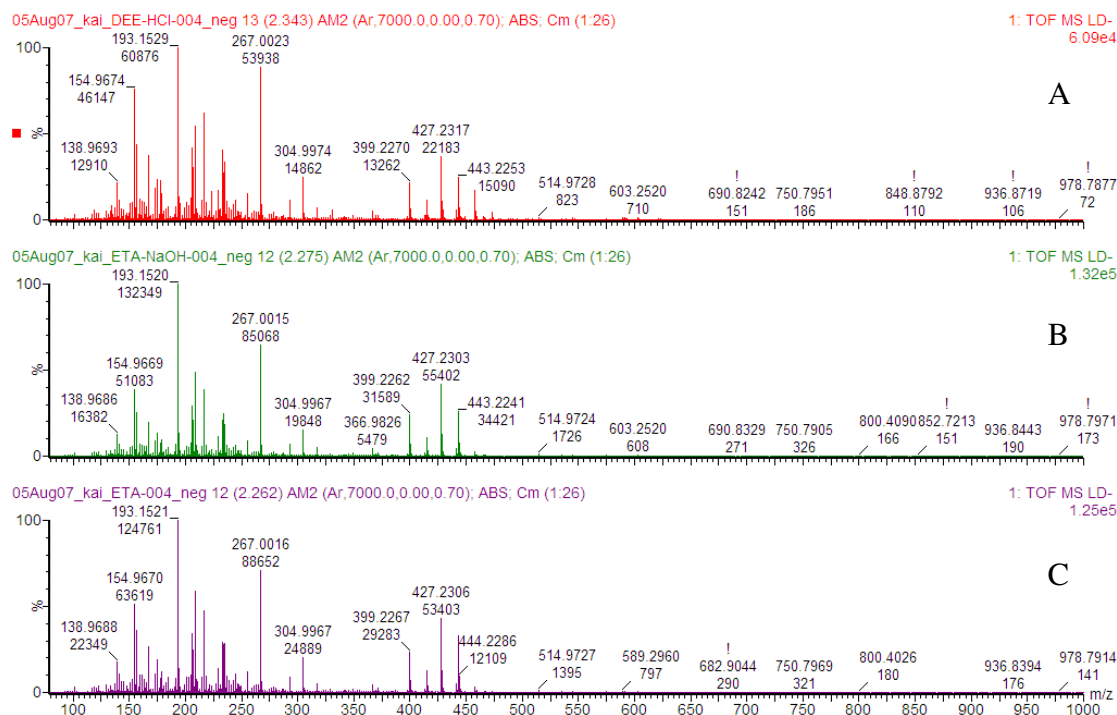


Figure 5-34 Negative ion DIOS spectra of ethyl acetate extracts. (A) Addition of HCl, (B) addition of NaOH and (C) no addition of modifier. 1 μ l of droplet was added onto the sample well. Data was acquired using 120s spiral scan. Laser setting was 220. Spectra were centroid and processed with adaptive background subtraction.

On examination of the negative spectra of the urine extracts, there were four different ions distinctively detected in between mass range m/z 400 to 450 on the spectra. While comparing the data with those available on the databases, *e.g.* Metlin, it is difficult to give the identity of those ions though it does give an impression that those are likely steroids/sterols, bile acids or related biomolecules. These ions detected under negative mode were therefore further analysed by MS/MS. The MS/MS spectra are shown at Figure 5-35. Two major product ions of m/z 193 and 209 were detected. Both of these fragment ions were also detected as shown in Figure 5-28B. The two product ions differ by 16 Th, *i.e.* an oxygen atom – or deoxy-analogous. Possibly this indicates that two of the precursor ions are steroids and the other two are related sterols.

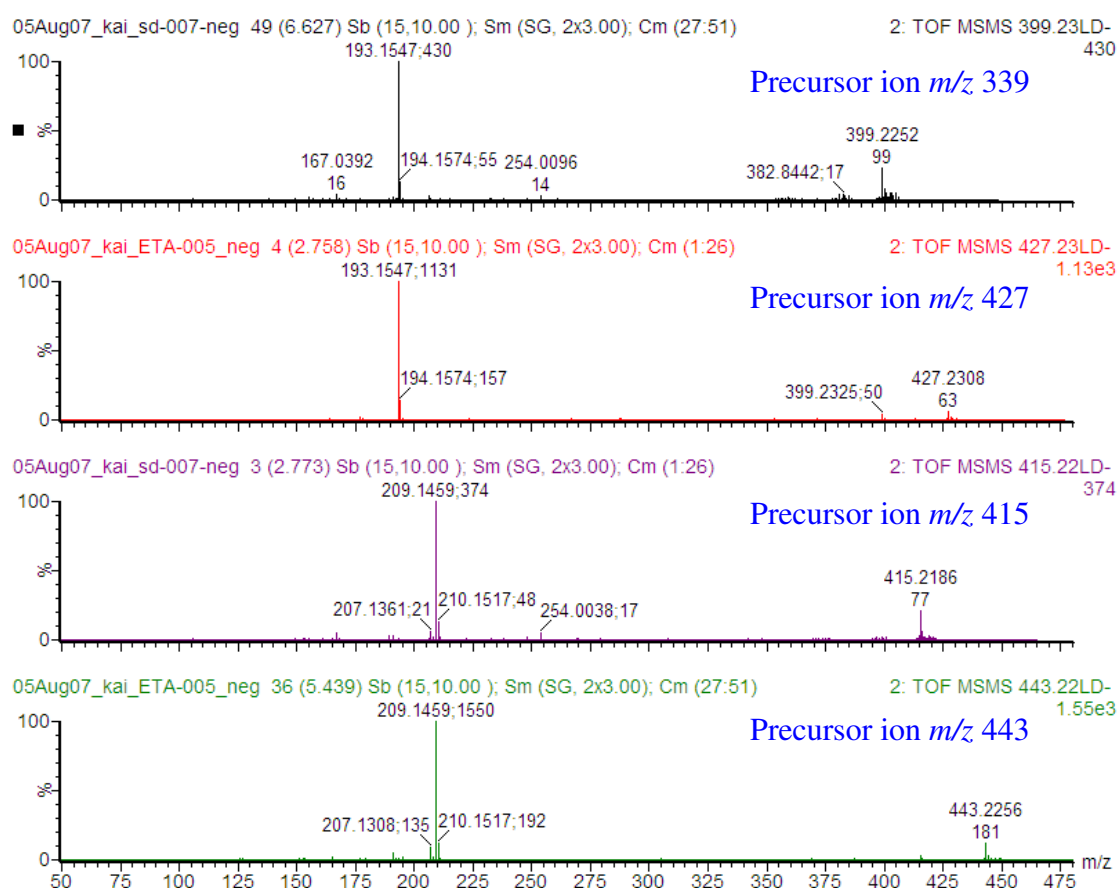


Figure 5-35 Negative ion DIOS MS/MS spectra of urine extract with precursor ions m/z 339, 427, 415 and 443. Two major fragment ions at m/z 193 and 209 were obtained.

To assist the determination of the possible identities of the ions detected, alternatively metabolite database search was carried out. A list of detected ions derived from Figure 5-28A of which the peak intensity above 5% of the base peak intensity (BPI) threshold value was inputted to the Metlin metabolite database search with a maximum of 5-ppm tolerance. The ions detected were assumed as molecular ions or sodium/potassium adducts of the metabolites present in the sample. The results are listed in Table 5-6. Although the search results are unconfirmed, the matching does reflect certain characteristics of the urine extract. For example, creatinine and creatine are known metabolites that present in high concentration in urine. Metformin is for the treatment of diabetes and concurs with the high concentration of glucose observed. N-(2-hydroxyethyl)-nicotinamide and cotinine are metabolites of cigarette smoking concurring with the life style of the donor.

Table 5-6 Result of the Metline database search for metabolites present in the urine extract derived from the data in Figure 5-28A. The spectrum was first internal “lockmassed” on the sodium adduct of glucose (m/z 203.0532). The name of the proposed metabolites, the formulae, the calculated exact masses and the mass differences (in ppm) are reported in the table. “-” denotes no match has been found within 5 ppm tolerance.

| Input ion (m/z) | Proposed metabolite (database match) [unconfirmed] | Formula | Calculated molecular Mass | Proposed ion | Mass difference (ppm) |
|------------------------|---|----------------|---------------------------------|-----------------|-----------------------------|
| 114.0666 | Creatinine | $C_4H_7N_3O$ | 113.0589 | $[M+H]^+$ | -0.9 |
| 121.0065 | - | | | | |
| 124.0867 | - | | | | |
| 126.0966 | - | | | | |
| 130.0657 | - | | | | |
| 130.1091 | Metformin | $C_4H_{11}N_5$ | 129.1014 | $[M+H]^+$ | -0.8 |
| 131.0167 | - | | | | |
| 132.0770 | Creatine | $C_4H_9N_3O_2$ | 131.0695 | $[M+H]^+$ | -2.3 |
| 132.9958 | - | | | | |
| 133.1016 | - | | | | |
| 136.0484 | Creatinine | $C_4H_7N_3O$ | 113.0589 | $[M+Na]^+$ | -2.7 |
| 137.0615 | - | | | | |
| 140.9673 | - | | | | |
| 144.1016 | - | | | | |
| 153.0664 | N-Methyl-pyridone-carboxamide | $C_7H_8N_2O_2$ | 152.0586 | $[M+H]^+$ | 0.0 |
| 154.0529 | - | | | | |

| | | | | | |
|----------|---|--|----------|---------------------|----------|
| 154.9837 | - | | | | |
| 156.9631 | - | | | | |
| 162.1125 | Carnitine | C ₇ H ₁₅ NO ₃ | 161.1052 | [M+H] ⁺ | -3.1 |
| 164.9219 | - | | | | |
| 165.0715 | - | | | | |
| 166.0781 | - | | | | |
| 166.9953 | α-ketoglutarate | C ₅ H ₄ O ₅ | 144.0059 | [M+Na] ⁺ | -2.8 |
| 167.0827 | N-(2-hydroxyethyl)-nicotinamide | C ₈ H ₁₀ N ₂ O ₂ | 166.0742 | [M+H] ⁺ | 4.2 |
| 170.0928 | Methylhistidine | C ₇ H ₁₁ N ₃ O ₂ | 169.0851 | [M+H] ⁺ | -0.6 |
| 174.9737 | - | | | | |
| 176.0481 | - | | | | |
| 177.1021 | Serotonin, Cotinine | C ₁₀ H ₁₂ N ₂ O | 176.095 | [M+H] ⁺ | -4.0 |
| 178.0781 | - | | | | |
| 179.0861 | - | | | | |
| 180.0866 | Glucosamine, Fructosamine | C ₆ H ₁₃ NO ₅ | 179.0794 | [M+H] ⁺ | -3.4 |
| 180.8964 | - | | | | |
| 181.0758 | - | | | | |
| 182.0857 | - | | | | |
| 182.9905 | - | | | | |
| 184.0755 | - | | | | |
| 192.0811 | - | | | | |
| 193.0862 | - | | | | |
| 194.0938 | - | | | | |
| 195.0889 | Caffeine | C ₈ H ₁₀ N ₄ O ₂ | 194.0804 | [M+H] ⁺ | 3.6 |
| 195.1501 | - | | | | |
| 196.0907 | - | | | | |
| 196.8699 | - | | | | |
| 198.8681 | - | | | | |
| 200.9378 | - | | | | |
| 203.0532 | Glucose (and/or other hexoses) | C ₆ H ₁₂ O ₆ | 180.0634 | [M+Na] ⁺ | LockMass |
| 206.0881 | - | | | | |
| 207.0946 | Pyrantel | C ₁₁ H ₁₄ N ₂ S | 206.0878 | [M+H] ⁺ | -4.9 |
| 208.0976 | Acetylphenylalanine, Phenylacetyl glycine methyl ester, Phenylpropionyl glycine | C ₁₁ H ₁₃ NO ₃ | 207.0895 | [M+H] ⁺ | 1.4 |
| 209.1083 | - | | | | |
| 210.1038 | - | | | | |
| 211.1343 | - | | | | |
| 212.8443 | - | | | | |
| 214.8419 | - | | | | |

| | | | | | |
|----------|--------------------------------------|---|----------|---------------------|-----|
| 216.9320 | - | | | | |
| 218.9433 | - | | | | |
| 225.1358 | - | | | | |
| 234.9407 | - | | | | |
| 244.9408 | - | | | | |
| 267.1529 | - | | | | |
| 286.2004 | - | | | | |
| 302.2334 | - | | | | |
| 310.2004 | L-Octanoylcarnitine | C ₁₅ H ₂₉ NO ₄ | 287.2097 | [M+Na] ⁺ | 3.1 |
| 312.1883 | - | | | | |
| 313.1613 | - | | | | |
| 314.2287 | - | | | | |
| 326.3787 | - | | | | |
| 327.1867 | - | | | | |
| 328.1914 | - | | | | |
| 328.2467 | - | | | | |
| 343.1623 | - | | | | |
| 343.2130 | 2,3-Dinor-TxB2 | C ₁₈ H ₃₀ O ₆ | 342.2042 | [M+H] ⁺ | 2.9 |
| 344.1994 | - | | | | |
| 358.2537 | - | | | | |
| 386.2229 | - | | | | |
| 402.2176 | - | | | | |
| 408.2038 | - | | | | |
| 409.2032 | 6-Hydroxydexamethasone | C ₂₂ H ₂₉ FO ₆ | 408.1948 | [M+H] ⁺ | 1.5 |
| 423.2131 | - | | | | |
| 424.1943 | - | | | | |
| 425.1957 | 1-tridecanoyl-sn-glycero-3-phosphate | C ₁₆ H ₃₇ NO ₇ P | 386.2308 | [M+K] ⁺ | 3.1 |
| 426.2056 | - | | | | |
| 439.2060 | - | | | | |
| 440.1914 | - | | | | |
| 441.2054 | Dehydrocholic acid | C ₂₄ H ₃₄ O ₅ | 402.2406 | [M+K] ⁺ | 2.7 |
| 455.1848 | - | | | | |
| 467.2047 | - | | | | |
| 483.1910 | - | | | | |
| 489.1809 | - | | | | |
| 490.1872 | - | | | | |
| 505.1617 | - | | | | |
| 506.1672 | - | | | | |
| 507.1620 | - | | | | |

| | | | | | |
|----------|---|--|--|--|--|
| 521.1458 | - | | | | |
| 522.1488 | - | | | | |
| 523.1503 | - | | | | |
| 599.2463 | - | | | | |
| 615.2202 | - | | | | |

5.3.5 Human Blood Plasma

Unlike urine, serum or plasma analysis accesses the homeostatic levels of metabolites throughout the organism. Sample preparation of blood plasma in comparison was relatively simple and only required precipitation of the albumin proteins. It should be noted that adjusting the ratio of plasma and methanol is a very important step to remove the proteins completely and leave only the serum. These large protein molecules are normally not desorbed and may clot up the surface.

The detection characteristic (laser optimisation) was first determined by acquiring a series of spectra under different laser setting. The TIC with respect to the laser setting is plotted to Figure 5-36. Representative DIOS spectra of plasma extract are shown in Figure 5-37 and Figure 5-38.

Note to the Figure 5-36, unlike the detection characteristic that obtained with simple mixtures discussed previously, the optimal setting shifts to 220. This suggests ion suppression has occurred and may well relate to the complexity of the sample as well as salts. Although the acquisition was only one minute, the ion intensity of the base peak fell below 2000 counts. (Figure 5-37) This may have an implication toward the application of MS/MS using Q-ToF.

The positive ion mass spectrum was information rich. S/N was good. (Figure 5-37) A number of lipids are located at the m/z 700-850 region. Sterol or fatty acids-like compounds are seen in the m/z 300-500 region. Glucose is detected as $[M+Na]^+$ at m/z 203. The spectrum also show a peak set at m/z 184.07 and 198.09 corresponds to $[C_5H_{15}NPO_4]^+$ and $[C_6H_{17}NPO_4]^+$, respectively and are likely headgroup fragment ion of phosphatidylcholines.

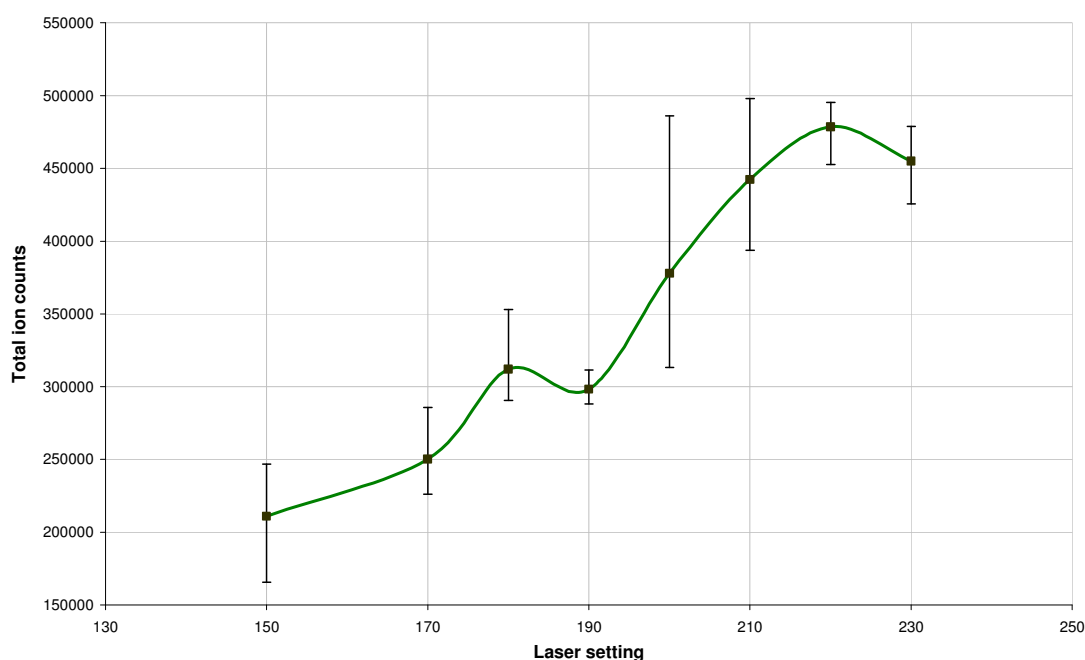


Figure 5-36 Detection characteristic of the plasma extract. Each data point represents the average value of three replicas. The error bar indicates the highest and the lowest value obtained.

However, the negative ion mass spectrum was not as information rich as the positive spectrum – in terms of the number of ions detected and the quality of the spectrum. (Figure 5-38) The spectrum was dominated by a phosphate-containing contaminant located at m/z 267 and a suboptimal laser setting and extended acquisition time was used to minimise the interference and to maintain sufficient ions were collected.

Despite the presence of salt would likely cause ion suppression, good quality MS/MS spectra could be obtained by extending the acquisition time to up to 5 minutes and increasing the amount of material added onto the target. (Figure 5-39) Common product ions at m/z 147 and 86.1 were detected in the MS/MS spectra. The fragment ion at m/z 147 has already been detected in Figure 5-37, but its identity remains unknown. The fragment ion at m/z 86.1 corresponds to $[C_5H_{12}N]^+$, a typical headgroup fragment of phosphocholine derivatives, supporting the observation above.

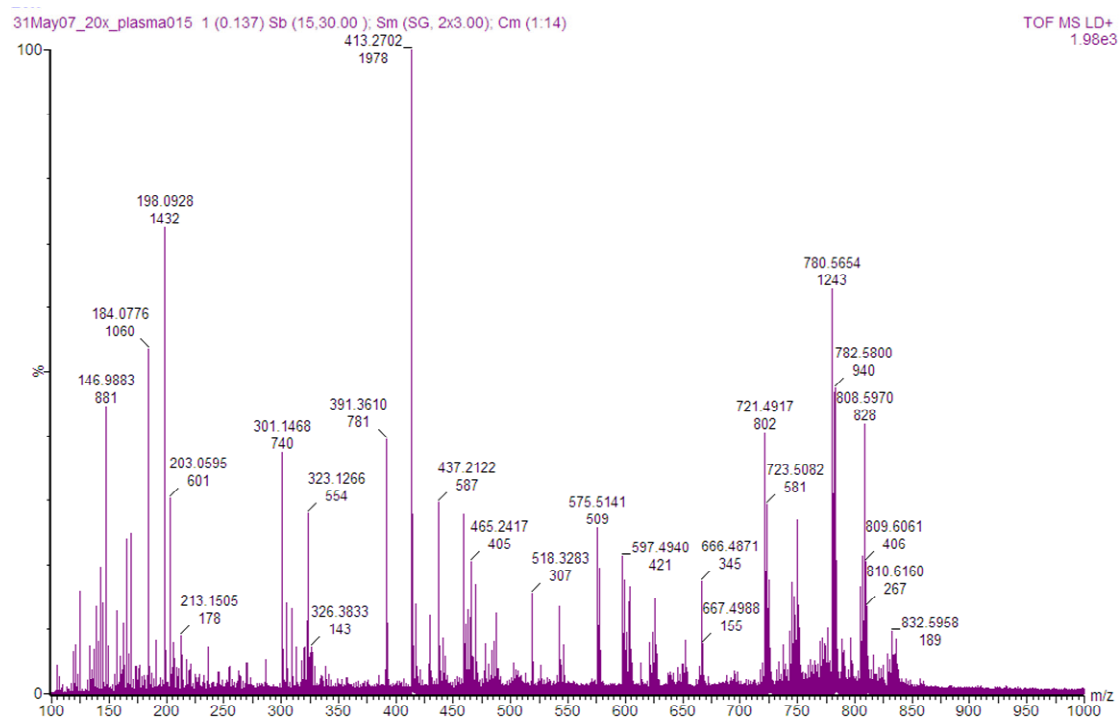


Figure 5-37 A representative positive ion DIOS mass spectrum of plasma extract. Data was acquired with 1 min raster scan. Laser setting was 220. The spectrum is smoothed and background subtracted.

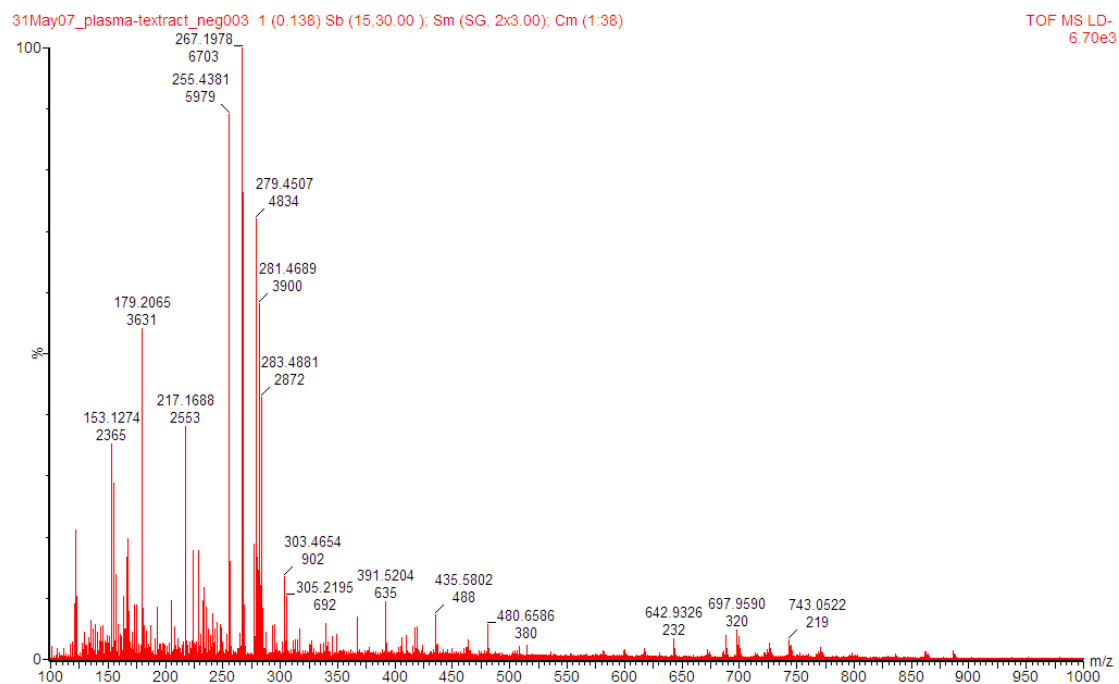
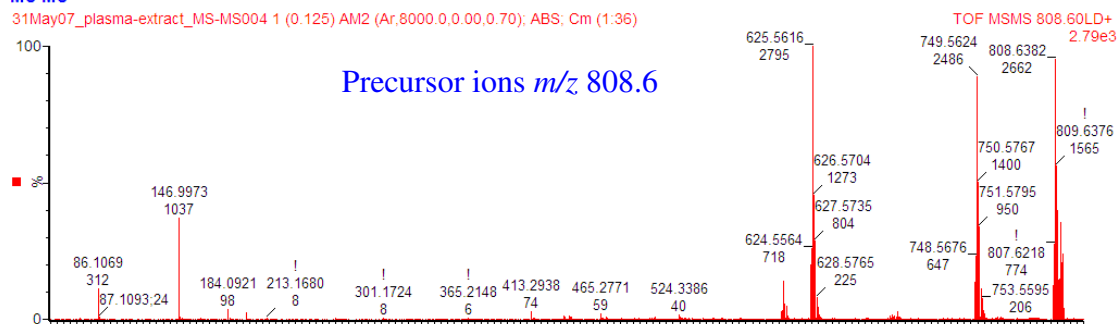


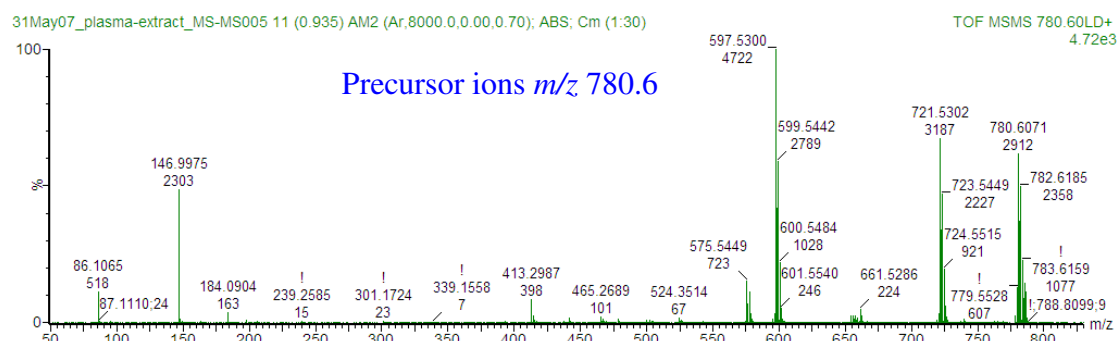
Figure 5-38 A representative negative ion DIOS mass spectrum of plasma extract. Data was acquired with 180s spiral scan. Laser setting was 170. The spectrum is smoothed and background subtracted.

MS-MS

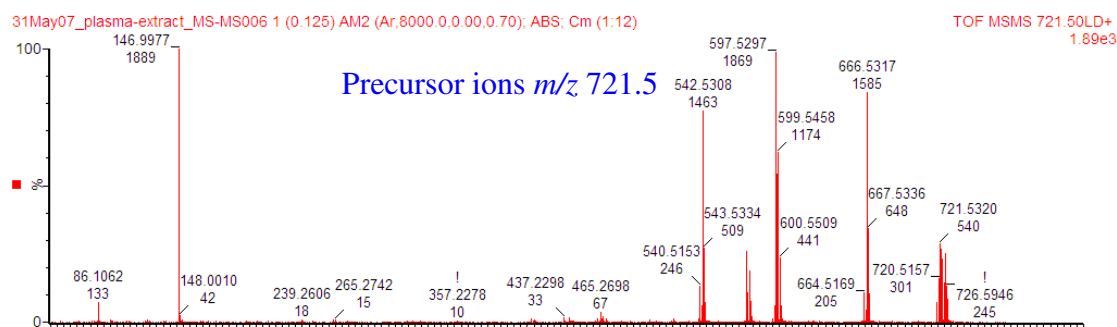
31May07_plasma-extract_MS-MS004 1 (0.125) AM2 (Ar.8000.0,0.00,0.70); ABS; Cm (1:36)



31May07_plasma-extract_MS-MS005 11 (0.935) AM2 (Ar.8000.0,0.00,0.70); ABS; Cm (1:30)



31May07_plasma-extract_MS-MS006 1 (0.125) AM2 (Ar.8000.0,0.00,0.70); ABS; Cm (1:12)



31May07_plasma-extract_MS-MS007 24 (2.100) AM2 (Ar.8000.0,0.00,0.70); ABS; Cm (1:48)

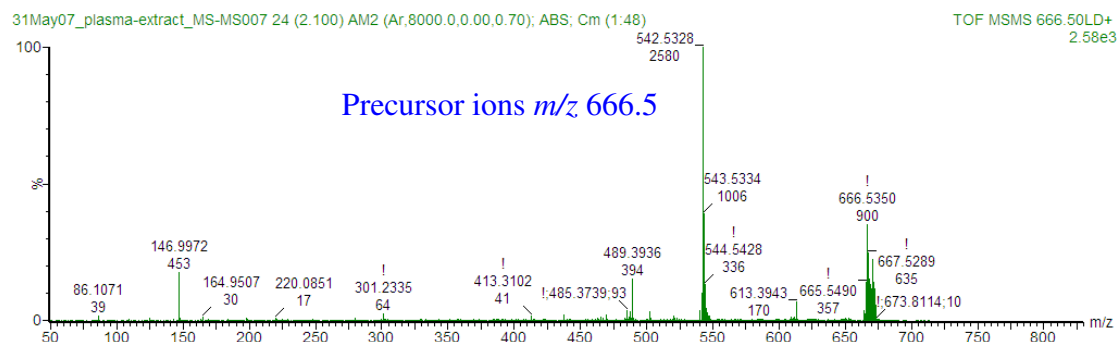


Figure 5-39 Positive DIOS MS/MS spectra of plasma exact. Precursor ions m/z 808.6, 780.6, 721.5 and 666.5 were selected and all these ions produce a product ion m/z 147 and 86. Precursor ions m/z 780.6, 721.5 and 666.5 may also be related as common product ions m/z 597.5 or 542.5 are observed.

Using the data acquired on the blood plasma extract, the analytical precision was assessed based on the variation of TIC of the DIOS mass spectra. Alternatively, an assessment was made based on the number of ions detected with ion intensity over a selected threshold value. Data was acquired successively from nine sample wells deposited with the blood plasma extract, in between the mass range from m/z 80 to 1000, either by spiral scan or by vertical scan mode. The peak lists were imported into Excel for further calculation. Since there is no standard in the selection of a threshold value to distinguish the significant ion peaks from those that are less significant, 5% of the BPI threshold value was chosen here arbitrarily. The data is plotted in Figure 5-40.

The results show that the total ion counts (TIC) of the spectra acquired by spiral or vertical scan mode were not significantly different. (Figure 5-40A) However, the data acquired by spiral scan mode was more consistent than that acquired by vertical scan mode. The RSD value calculated was 4.9% and 12.7% for spiral scan and vertical mode, respectively. In terms of the number of ions detected above the selected threshold value, the average number of ions detected in vertical scan mode was higher than that by spiral scan mode. (Figure 5-40B) Then again, the RSD value calculated was 4.8% and 7.7% for spiral scan and vertical mode, respectively.

The datasets were also further analysed by PCA. Figure 5-41 shows the PCA score plots. The spreading of the data point indicates the precision of the dataset – *i.e.* the wider the spreading, the lower the precision. The results indicate that the dataset acquired by spiral scan mode was more consistent than that acquired by vertical scan mode. In addition, the PC_1/PC_2 score plot identifies v3 (vertical scan, dataset3) is an outlier (Figure 5-41A) and agrees with the result of TIC. (Figure 5-40A)

On comparing the assessments of analytical precision based on the conventional univariate statistical approaches and on the multivariate statistical PCA approach, these two methods effectively lead to the same conclusion. The significance here is that by using PCA alone, it is already able to determine the precision of the data. The cluster analysis is able to distinguish the subtle differences between the datasets, which would otherwise be difficult to see using the conventional statistical approaches. The possibility of applying PCA to evaluate the mass spectrometric data produced by

DIOS-MS is further assessed and the data was preferably acquired by spiral scan mode.

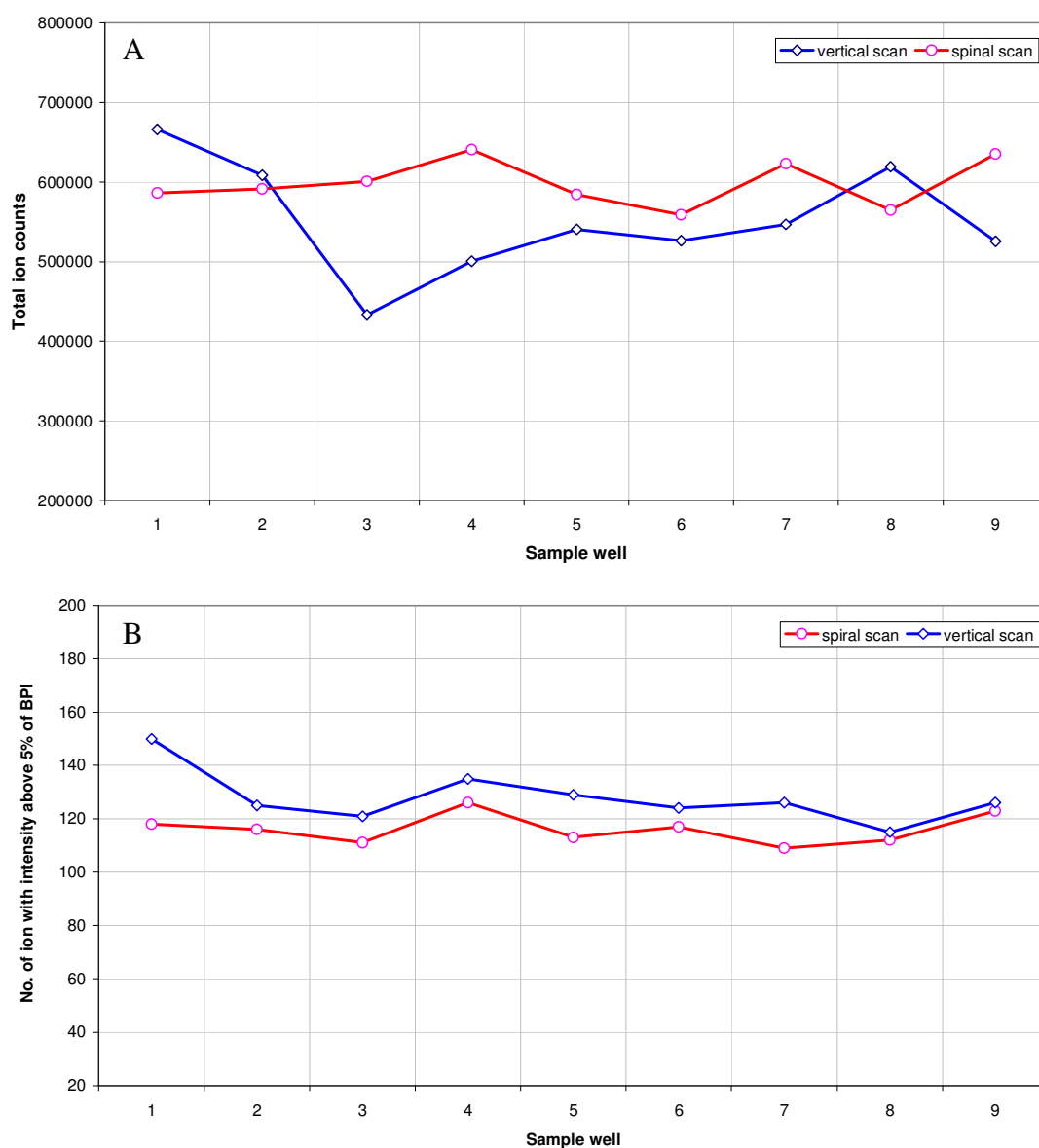


Figure 5-40 (A) The total ion counts, and (B) the number of ions detected over 5% of the BPI, of nine successive data acquired over nine sample wells, either by spiral scan mode or vertical scan mode. Raw data was first subject to Automatic Peak Detection function of the MassLynx software to remove electronic and chemical noise and the peak lists were then exported to Excel for calculation. Threshold value was set by using Data Threshold function of the MassLynx software to hide data of which the intensity below a set threshold value or in term of percentage scales of the base peak.

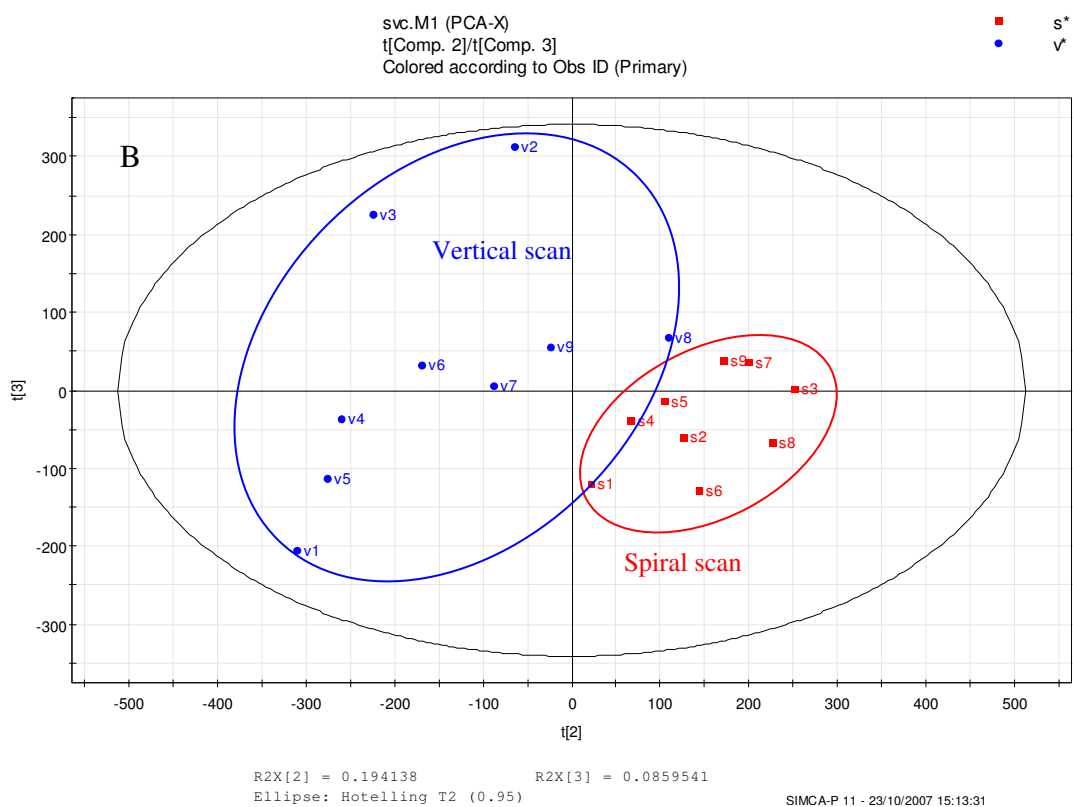
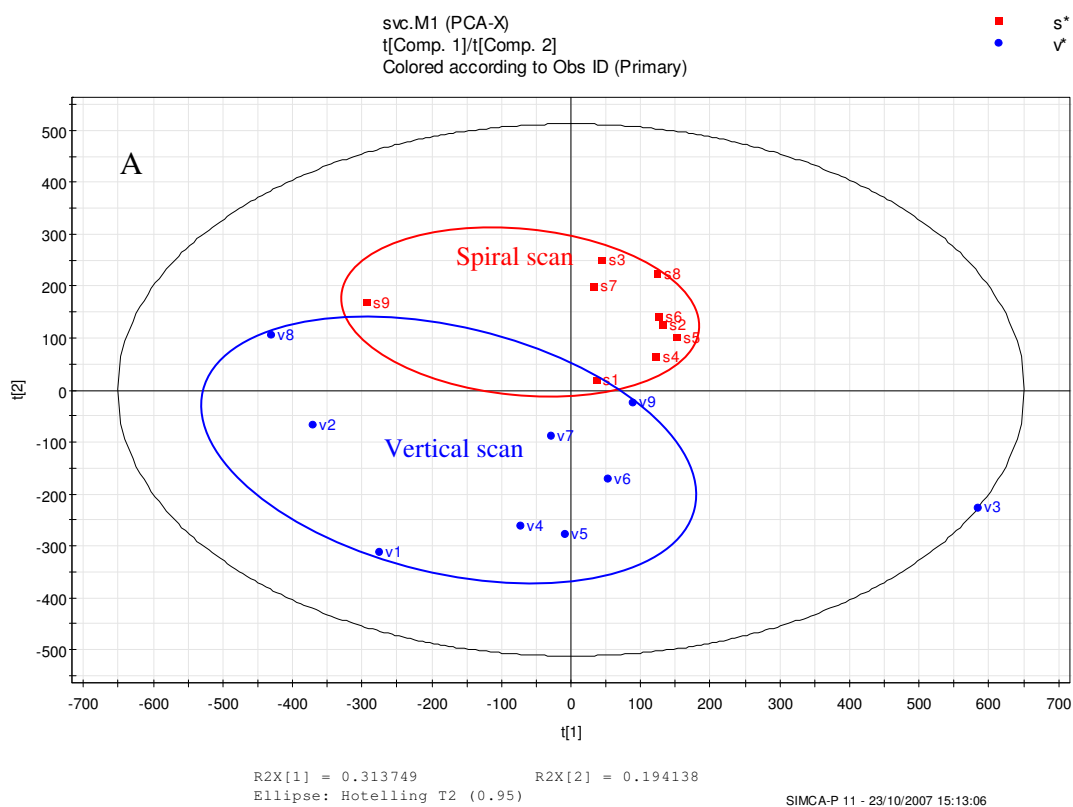


Figure 5-41 PCA score plot of (A) PC₁/PC₂ and (B) PC₂/PC₃. Data was acquired in successively over nine sample wells either by spiral scan mode or by vertical scan mode. PC₁, 2 and 3 represents 60% of the variability of the dataset.

5.3.6 Liver Tissue Extracts

Lambs' liver extracts were prepared by solvents of different polarity. The purpose of this approach was to create biological extracts, which had a global difference in terms of molecular distribution (*i.e.* a chemical model). Alternatively, an efficient extract protocol can be determined. Thus, we could then evaluate the possible effects of relatively poor precision of the DIOS-MS to PCA. The liver sample chosen here did not meet the criteria of metabolomic standards for mammalian experiments,⁵⁹ but was chosen because of the large sample size.

Similarly, to the study of blood plasma, the first step of an experiment is to optimise the laser-setting specific to the type of sample. The TIC vs. laser energy setting of liver methanolic extract under positive and negative ion mode is plotted to Figure 5-42 and Figure 5-43, respectively. The results show that the TIC varies linearly with the laser setting under positive ion mode in this range, whereas the data collected under negative mode increases exponentially and starts to level off with the laser setting at 230.

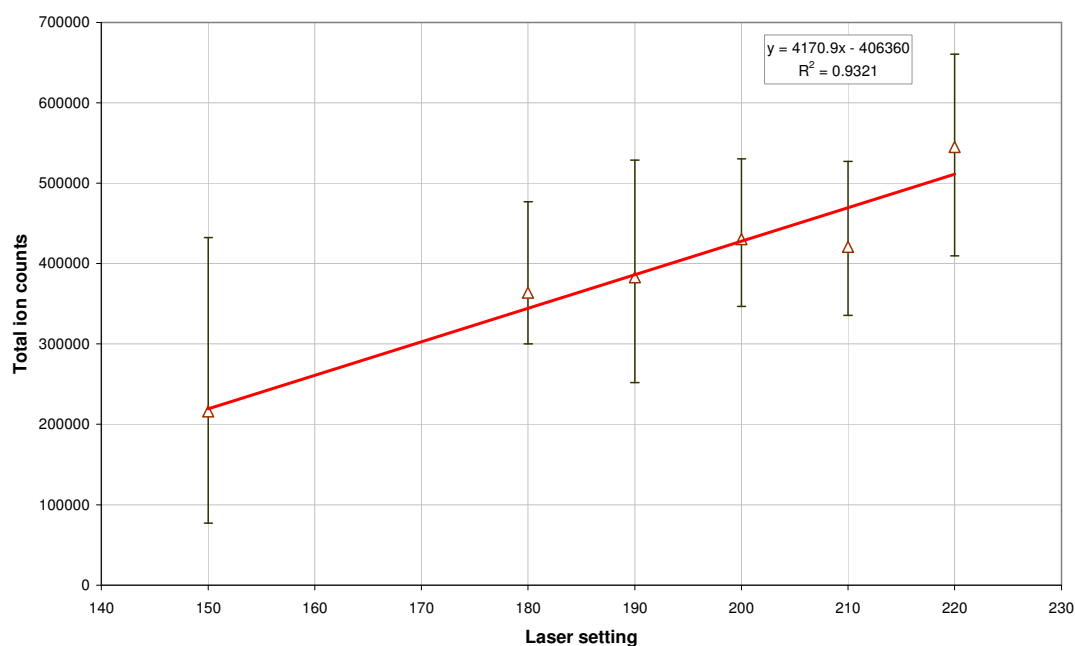


Figure 5-42 Detection characteristic of liver methanolic extract under positive ion mode. Each data point is the average value of three to five replicas. The error bar indicates the highest and the lowest value obtained.

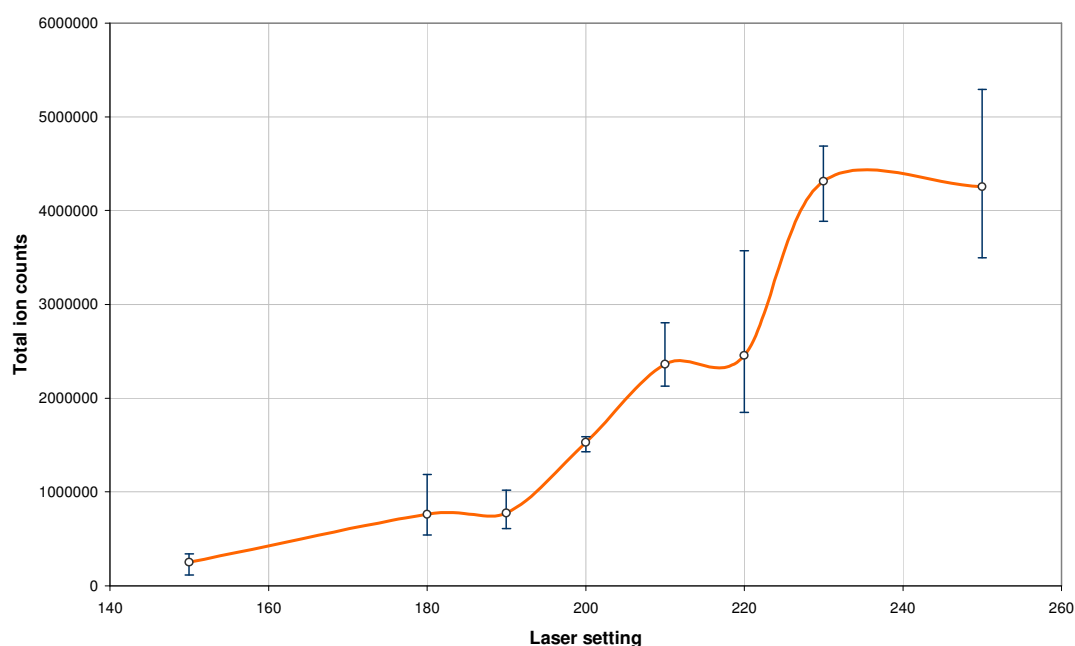


Figure 5-43 Detection characteristic of liver methanolic extract under negative ion mode. Each data point is the average value of three replicas. The error bar indicates the highest and the lowest value obtained.

We will first inspect the dataset obtained under positive ion mode. (Figure 5-44) Seven PCs were generated by SIMCA, where PC1, 2 and 3 accounts over 74% of the model, and PC1 and PC2 alone account over 60% of the model. All classes are well separated with no overlapping in the PCA score plot. The precision is in fact much better to be accessed by PCA. The spreading of ETA class is the largest in this case, and yet its variation in the PCA plot is less than 10 units. The PCA loading plot is also able to distinguish the differences between different classes; however, interpretation of the loading plot may be complicated. The actual differences between classes can be easily seen by visual inspection of the mass spectra (Figure 5-45) or with the aid of the contribution plots. A global difference was obtained. The results show that propan-2-ol and acetonitrile are very effective in extracting the lipids located at the m/z 700-900 region but are less effective in extracting sterol-like compounds located at the m/z 400-600 region and other small organics located at the m/z 100-300 region relative to DMSO and methanol. Then again, DMSO and methanol are not effective in extracting the lipids. Ethyl acetate on the other hand has a balanced extraction performance. The spectrum of water extract shows only one major peak at m/z 184 and a small peak at m/z 485.

The experiment was repeated under negative ion mode. Unfortunately, until now, we still have not found a suitable mass calibrant for negative ion mode and mass accuracy could only be corrected to the nominal mass by calibrating the instrument with one or two small organic acids. Mass accuracy could not be as accurate as in positive ion mode. Still, some information can be obtained. The detection characteristic is shown in Figure 5-43. Eight PCs were generated by SIMCA, where PC1, 2 and 3 accounts over 84% of the model and PC1 and PC2 alone account ~69% of the model. The PCA score plot shows some overlapping between classes. (Figure 5-46) Then again, this is not entirely due to the poor precision of the method, but similarity between the dataset of different classes. The spectra are shown in Figure 5-47. The spectra of water and DMSO extract are dominated by the peak located at m/z 155, followed by the peaks located at m/z 233 and 235. The spectra of methanol and propan-2-ol extract are dominated by the peak located at m/z 151 and 155. There are also peaks located at m/z 498 and 514 stood out in the spectra of methanol of acetonitrile extracts. The spectra of acetonitrile and ethyl acetate extracts are dominated by the peak located at m/z 281, whereas peaks m/z 135, 151, 498 and 514 are seen in the spectra of acetonitrile extract and a set of peaks located in the m/z 700-800 region is seen in the spectra of ethyl acetate extract.

The ions observed from the liver extracts (Figure 5-45) were also inputted to the Metline metabolite database with a maximum of 5-ppm tolerance. To reduce the complexity of the data, only ion peaks with an integrated area over 5000 counts threshold value were considered here. The ion intensity of the DMSO extract was relatively low and no ion was detected over 5000 counts. DMSO extract was thus excluded from the database search. The results are listed in Table 5-7. Furthermore, LipidBank was also employed because of the relatively low “hit” of lipid-like molecules from the Metline database. However, to make the database search more effective, a method that limited the search for di/triacylglycerols in between the mass range m/z 400-600, and glycerophospholipids, in between the mass range m/z 600-1000 was adopted. Tolerance was 0.01 amu – the smallest difference permitted by the database. The results are listed in Table 5-8 and Table 5-9. Given the chemistry of lipid molecules, as shown from the tables, the search returns a number of positional and/or structural isomers of the same subclass or different subclasses.

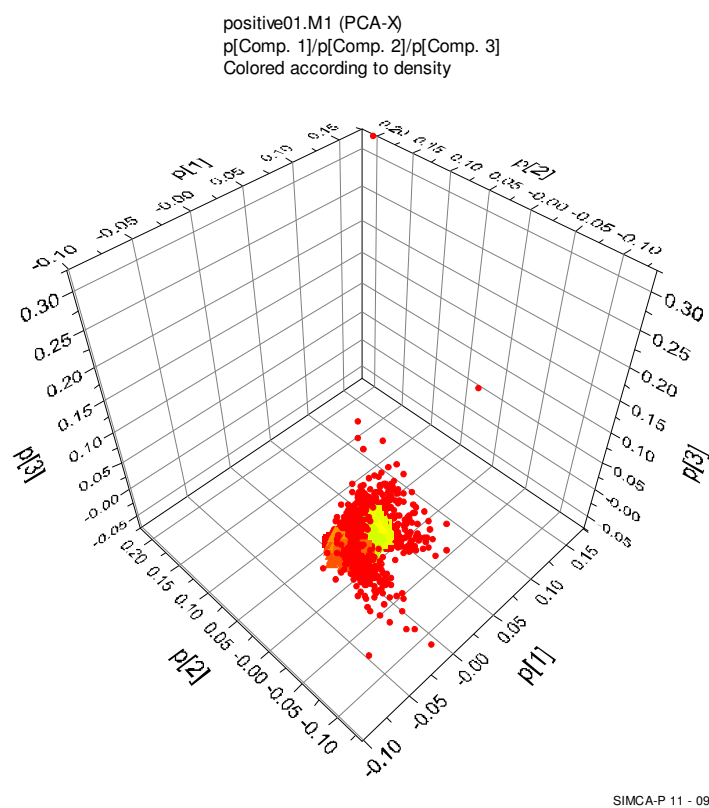
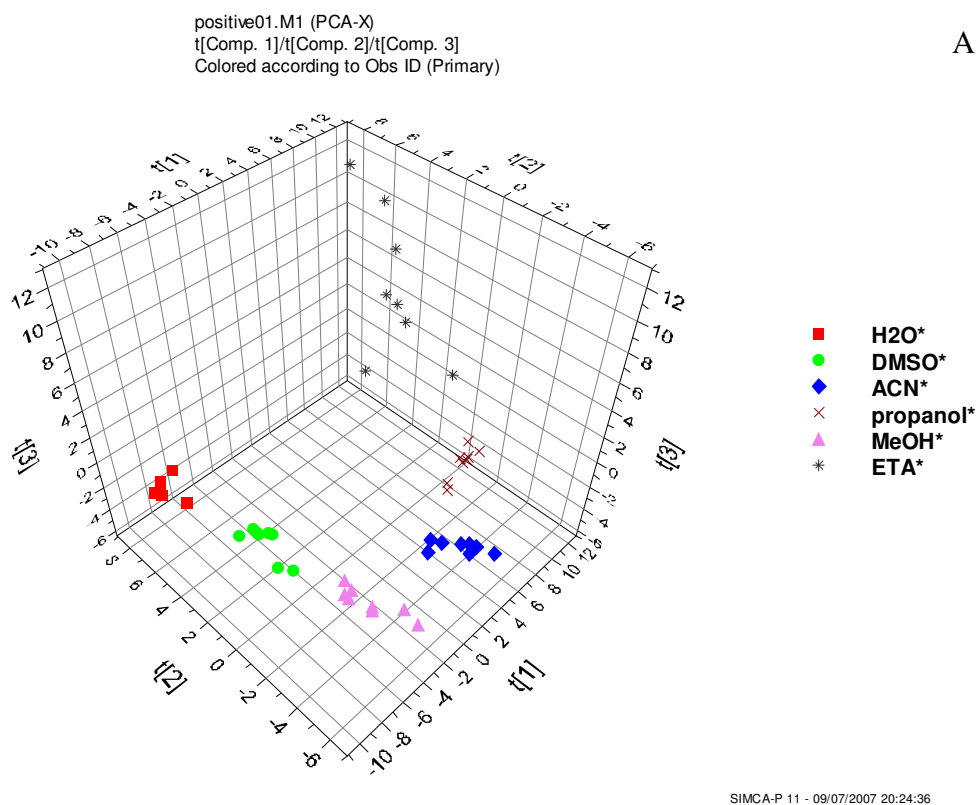
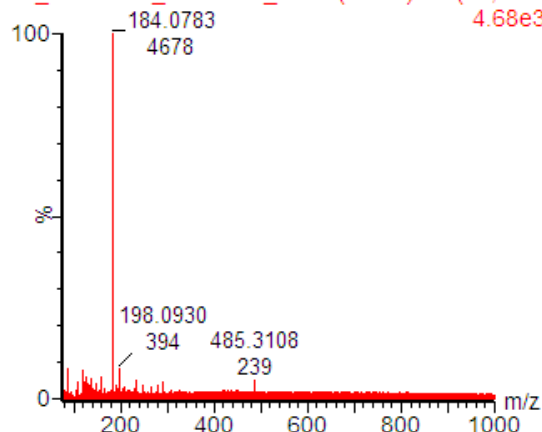


Figure 5-44 PCA $t_1/t_2/t_3$ score plot (A) and $p_1/p_2/p_3$ loading plot (B). Dataset was acquired in positive mode.

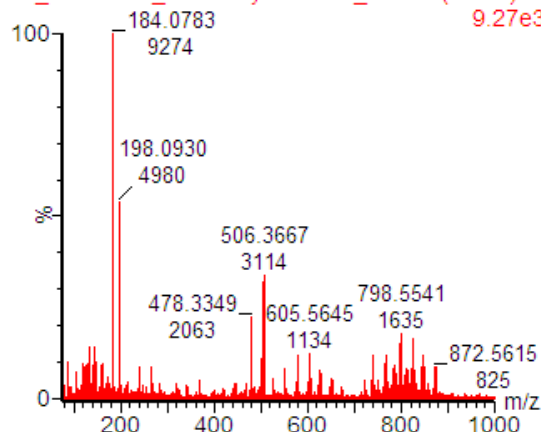
H2O

kai_13June07_liver-H2O_02 1 (0.831) Sb (15,10.0) 4.68e3



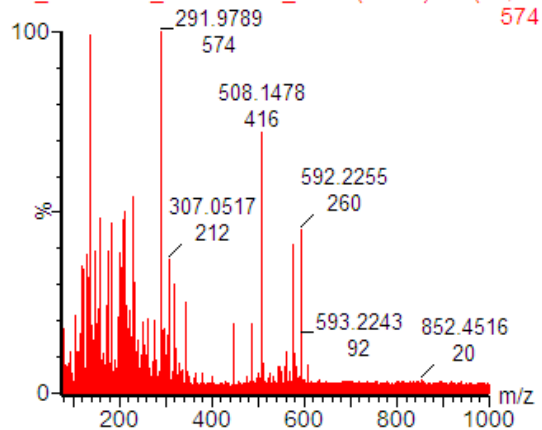
ethylacetate

kai_13June07_liver-ethyl-acetate_02 11 (1.768) St 9.27e3



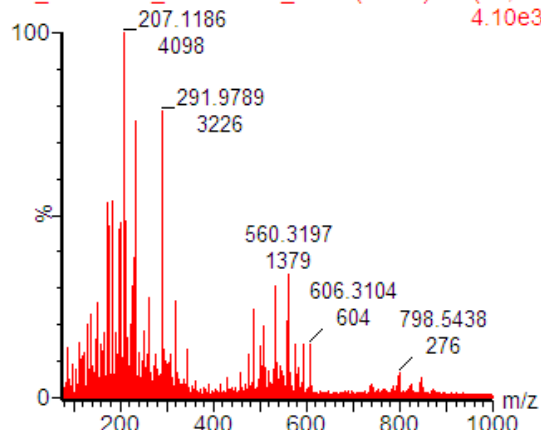
DMSO

kai_13June07_liver-DMSO_02 1 (0.881) Sb (15,10) 574



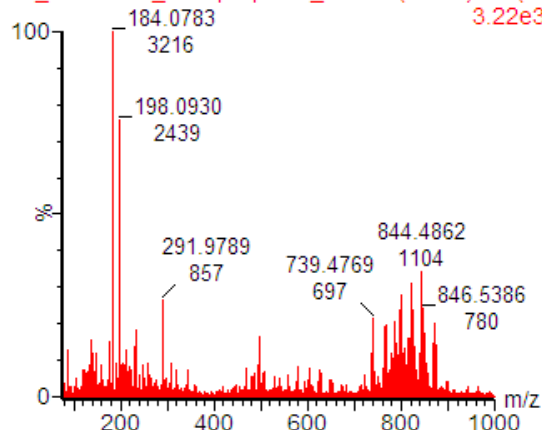
MeOH

kai_13June07_liver-MeOH_02 5 (1.252) Sb (15,10) 4.10e3



propanol

kai_13June07_liver-propanol_02 13 (1.922) Sb (15,10) 3.22e3



ACN

kai_13June07_liver-ACN_02 7 (1.349) Sb (15,10.0) 5.92e3

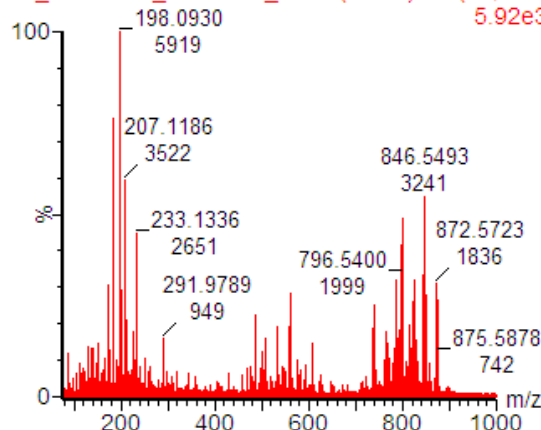


Figure 5-45 Positive ion DIOS mass spectra of liver extracts. Spectra are arranged in their similarity. Data was acquired with 120s spiral scan and laser setting was 220. The raw spectra are smoothed and background subtracted.

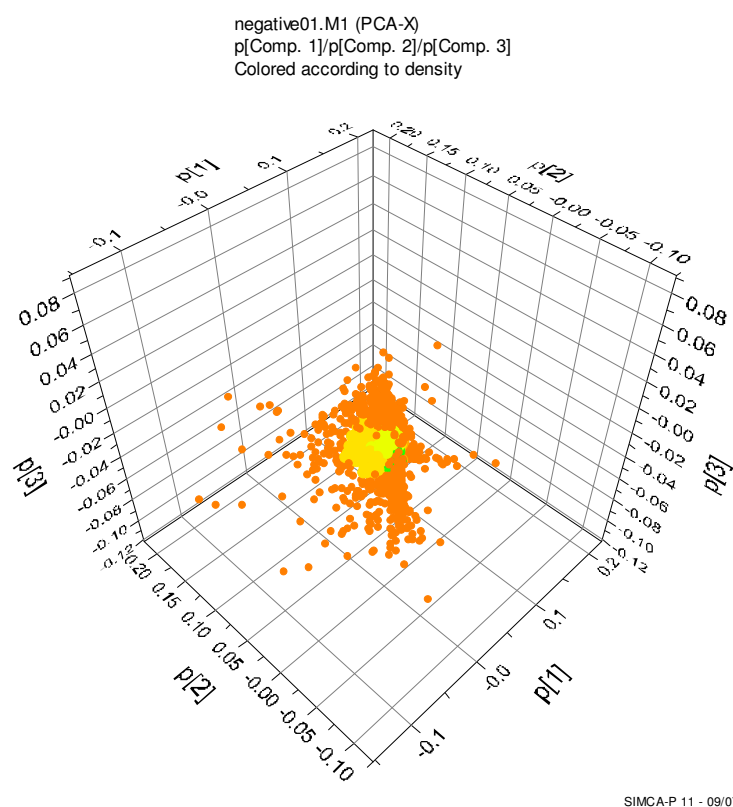
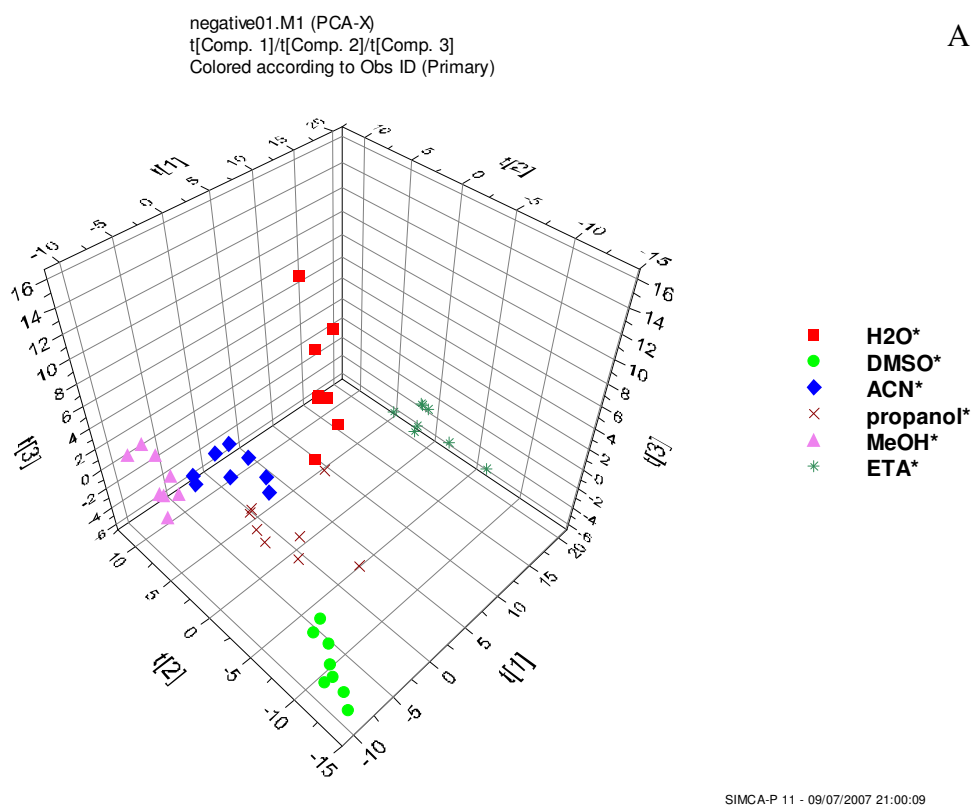
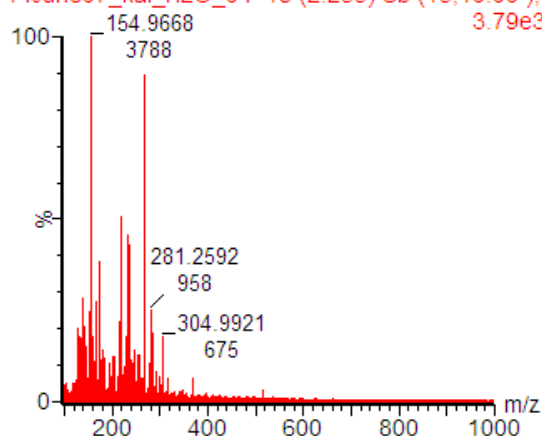


Figure 5-46 PCA $t_1/t_2/t_3$ score plot (A) and $p_1/p_2/p_3$ loading plot (B). Dataset was acquired in negative mode.

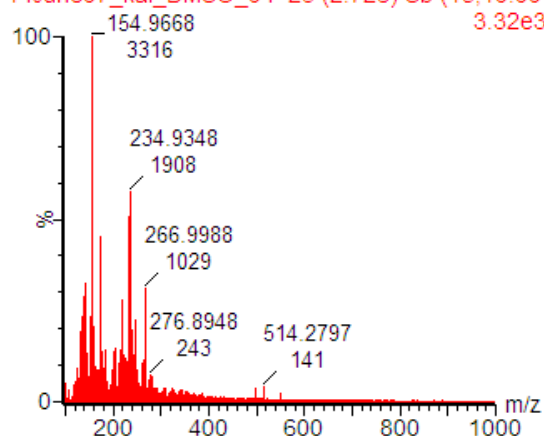
H2O

14June07_kai_H2O_04 18 (2.255) Sb (15,10.00); 3.79e3



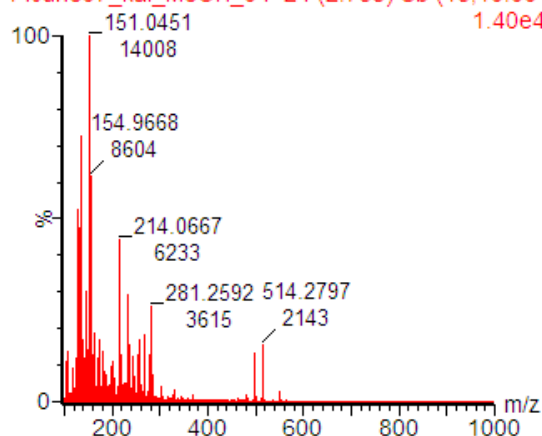
DMSO

14June07_kai_DMSO_04 23 (2.726) Sb (15,10.00) 3.32e3



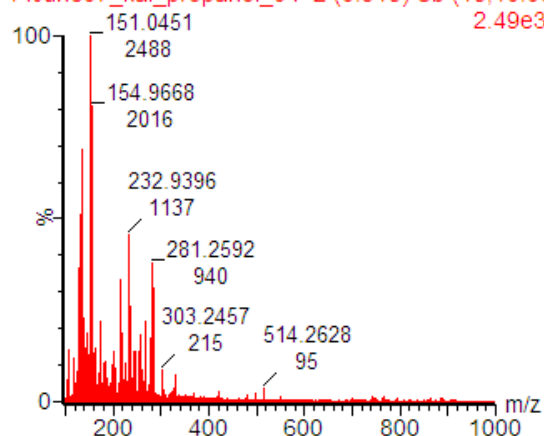
MeOH

14June07_kai_MeOH_04 24 (2.758) Sb (15,10.00) 1.40e4



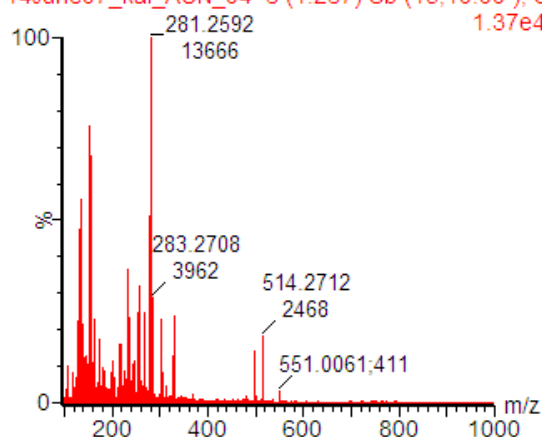
propanol

14June07_kai_propanol_04 2 (0.915) Sb (15,10.00) 2.49e3



ACN

14June07_kai_ACN_04 6 (1.267) Sb (15,10.00); S 1.37e4



ethyl acetate

14June07_kai_ethyl-acetate_04 24 (2.858) Sb (15, 2.23e4

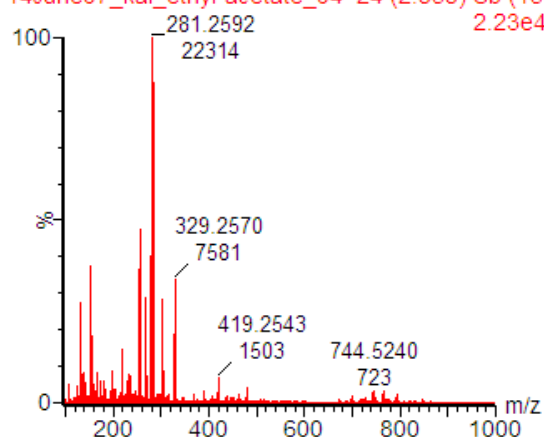


Figure 5-47 Negative ion DIOS mass spectra of liver extracts. Spectra are arranged in their similarity. The spectra were acquired with 2 mins spiral scan and laser setting 210. The raw spectra are smoothed and background subtracted.

Table 5-7 Result of the Metline database search for metabolites present in the lambs' liver extracts derived from the data in Figure 5-45. The spectra were first internal "lockmassed" on the fragment ion of phosphocholine (m/z 184.0739). The name of the proposed metabolites, the formulae, the calculated exact masses and the mass differences (in ppm) are reported in the table. "-" denotes no match has been found within 5 ppm tolerance.

| Input ion (m/z) | Proposed metabolite (database match) [unconfirmed] | Formula | Calculated molecular Mass | Proposed ion | Mass difference (ppm) | Ion observed in the spectrum of ... with integrated peak area over 5000 counts | | | | |
|------------------------|--|--|---------------------------------|---------------------|-----------------------------|---|----------|-----|------|------------------|
| | | | | | | ETA | Propanol | ACN | MeOH | H ₂ O |
| 119.0856 | - | C ₉ H ₁₁ NO | 149.084 | [M+H] ⁺ | 0.0 | + | | | | |
| 131.0858 | - | | | | | + | | | | |
| 133.1013 | - | | | | | + | | | | |
| 138.0923 | - | | | | | | | | + | |
| 139.0158 | - | | | | | + | | | | |
| 145.1016 | - | | | | | + | | | | |
| 147.1166 | - | | | | | + | | | | |
| 150.0919 | 2-Aminopropiophenone | | | | | | | | + | |
| 159.1166 | - | | | | | + | | | | |
| 163.0160 | - | | | | | + | | | | |
| 174.0919 | - | C ₅ H ₁₅ NO ₄ P | 184.0739 | M ⁺ | LM | | | + | + | |
| 174.8972 | - | | | | | | | | + | |
| 184.0739 | Phosphocholine, fragment of phosphocholine | | | | | + | + | + | + | + |
| 196.8687 | - | C ₁₁ H ₁₃ NO | 175.1 | [M+Na] ⁺ | -0.2 | | | + | + | |
| 198.0891 | N-Acetyltranlylcypramine | | | | | + | + | + | + | |
| 200.1077 | - | | | | | | | + | + | |

| | | | | | | | | | | |
|----------|--|--|---------|---------------------|------|---|---|---|---|--|
| 201.9350 | - | | | | | | | | + | |
| 207.1135 | Phenylethylmalonamide (PEMA) | C ₁₁ H ₁₄ N ₂ O ₂ | 206.106 | [M+H] ⁺ | 1.0 | | | + | + | |
| 212.8487 | - | | | | | | | + | + | |
| 212.9590 | - | | | | | | | | + | |
| 222.9954 | Acetazolamide | C ₄ H ₆ N ₄ O ₃ S ₂ | 221.988 | [M+H] ⁺ | -2.3 | | | | + | |
| 226.1237 | - | | | | | | | + | + | |
| 230.9234 | - | | | | | | | | + | |
| 233.1295 | N-Acetyl-5-methoxytryptamine | C ₁₃ H ₁₆ N ₂ O ₂ | 232.121 | [M+H] ⁺ | 2.2 | | | + | + | |
| 240.9614 | - | | | | | + | | | | |
| 250.9153 | - | | | | | | | | + | |
| 261.9290 | - | | | | | | | | + | |
| 264.2692 | - | | | | | + | | | | |
| 291.9753 | - | | | | | | + | + | + | |
| 320.0066 | - | | | | | | | | + | |
| 478.3274 | - | | | | | + | | | | |
| 485.2966 | - | | | | | | | + | + | |
| 501.2347 | - | | | | | | | + | | |
| 502.3260 | - | | | | | + | | | | |
| 504.3429 | 1-O-Hexadecyl-2-lyso-glycero-3-phosphorylcholine | C ₂₄ H ₅₂ NO ₆ P | 481.353 | [M+Na] ⁺ | -0.2 | + | | | | |
| 505.3470 | - | | | | | + | | | | |
| 506.3587 | - | | | | | + | | | | |
| 507.3622 | - | | | | | + | | | | |
| 508.1321 | - | | | | | | | + | + | |

| | | | | | | | | | | |
|----------|---|--|---------|---------------------|-----|---|---|---|---|--|
| 534.2953 | - | | | | | | | + | + | |
| 550.3271 | - | | | | | + | | | | |
| 552.3427 | - | | | | | + | | | | |
| 558.2757 | - | | | | | | | + | + | |
| 560.3068 | - | | | | | | | + | + | |
| 562.3223 | - | | | | | | | + | + | |
| 576.2148 | - | | | | | | | + | + | |
| 577.5177 | - | | | | | + | | | | |
| 592.2091 | - | | | | | | | | + | |
| 603.5331 | 1-O-hexadecyl-2-(9Z-octadecenoyl)-sn-glycerol | C ₃₇ H ₇₂ O ₄ | 580.543 | [M+Na] ⁺ | 0.3 | + | | | | |
| 605.5494 | - | | | | | + | | | | |
| 606.2928 | - | | | | | | | + | + | |
| 608.3071 | - | | | | | | | + | + | |
| 625.5172 | - | | | | | + | | | | |
| 627.5331 | - | | | | | + | | | | |
| 737.4493 | - | | | | | | | + | | |
| 739.4628 | - | | | | | + | + | + | | |
| 765.4792 | - | | | | | + | + | + | | |
| 767.4961 | - | | | | | + | | + | | |
| 782.5690 | - | | | | | + | | + | | |
| 785.4459 | - | | | | | | | + | | |
| 787.4615 | - | | | | | + | | + | | |
| 794.5116 | - | | | | | | | + | | |

| | | | | | | | | | | |
|----------|---|--|---------|---------------------|------|---|---|---|--|--|
| 796.5255 | - | | | | | | | + | | |
| 797.5260 | - | | | | | | | + | | |
| 798.5405 | - | | | | | + | + | + | | |
| 799.5399 | - | | | | | + | | + | | |
| 800.5529 | - | | | | | + | | + | | |
| 810.5990 | - | | | | | + | | | | |
| 813.4754 | - | | | | | | | + | | |
| 820.5172 | - | | | | | | + | + | | |
| 822.5191 | - | | | | | + | + | + | | |
| 824.5580 | - | | | | | + | + | + | | |
| 826.5690 | - | | | | | + | + | + | | |
| 827.5760 | - | | | | | + | | | | |
| 828.5431 | Galabiosylceramide (d18:1/12:0), Lactosylceramide (d18:1/12:0) | C ₄₂ H ₇₉ NO ₁₃ | 805.555 | [M+Na] ⁺ | -2.2 | + | | | | |
| 830.5652 | - | | | | | | | + | | |
| 842.4438 | - | | | | | | + | | | |
| 844.4899 | - | | | | | + | + | + | | |
| 845.5240 | - | | | | | | | + | | |
| 846.5319 | - | | | | | + | + | + | | |
| 847.5399 | - | | | | | | | + | | |
| 848.5493 | - | | | | | + | | + | | |
| 849.5551 | - | | | | | | | + | | |
| 870.5172 | - | | | | | | + | + | | |

| | | | | | | | | | | | |
|----------|---|--|--|--|--|--|---|---|---|--|--|
| 872.5483 | - | | | | | | + | + | + | | |
| 873.5563 | - | | | | | | | | + | | |
| 874.5661 | - | | | | | | + | | + | | |
| 875.5718 | - | | | | | | | | + | | |

Table 5-8 Results of LipidMap search in between the mass range m/z 400-600 for di/triacylglycerols (DG/TG) present in the lambs' liver extracts derived from the data in Figure 5-45. The spectra were first internal "lockmassed" on the fragment ion of phosphocholine (m/z 184.0739). The formulae, the calculated exact masses and the delta mass (in *amu*) of the proposed di/triacylglycerols are reported in the table. A maximum delta mass of ± 0.01 *amu* limit was applied to the search. Only the inputted ions returned a match are listed. C is the number of carbons and DB is the number of double bonds of the proposed di/triacylglycerol.

| Input ion (m/z) | Abbreviation of proposed di/triacylglycerol (unconfirmed) | C | DB | Formula | Calculated molecular mass | Delta mass (<i>amu</i>) | Ion | Ion observed in ... with an integrated peak area over 5000 counts | | | |
|------------------------|--|----|----|--------------------------|---------------------------------|---------------------------------|---------------------|--|----------|-----|------|
| | | | | | | | | ETA | Propanol | ACN | MeOH |
| 485.2966 | TG(18:4(6Z,9Z,12Z,15Z)/2:0/4:0) | 24 | 4 | C27H42O6 | 485.2879 | 0.0087 | [M+Na] ⁺ | | | + | + |
| | TG(18:4(6Z,9Z,12Z,15Z)/4:0/2:0) | 24 | 4 | C27H42O6 | 485.2879 | | [M+Na] ⁺ | | | | |
| | TG(20:4(5Z,8Z,11Z,14Z)/2:0/2:0) | 24 | 4 | C27H42O6 | 485.2879 | | [M+Na] ⁺ | | | | |
| | TG(2:0/18:4(6Z,9Z,12Z,15Z)/4:0) | 24 | 4 | C27H42O6 | 485.2879 | | [M+Na] ⁺ | | | | |
| | TG(2:0/4:0/18:4(6Z,9Z,12Z,15Z)) | 24 | 4 | C27H42O6 | 485.2879 | | [M+Na] ⁺ | | | | |
| | TG(4:0/18:4(6Z,9Z,12Z,15Z)/2:0) | 24 | 4 | C27H42O6 | 485.2879 | | [M+Na] ⁺ | | | | |
| | TG(4:0/2:0/18:4(6Z,9Z,12Z,15Z)) | 24 | 4 | C27H42O6 | 485.2879 | | [M+Na] ⁺ | | | | |
| 505.3470 | TG(17:1(9Z)/2:0/6:0) | 25 | 1 | C28H50O6 | 505.3505 | -0.0035 | [M+Na] ⁺ | + | | | |
| | TG(17:1(9Z)/4:0/4:0) | 25 | 1 | C28H50O6 | 505.3505 | | [M+Na] ⁺ | | | | |
| | TG(17:1(9Z)/6:0/2:0) | 25 | 1 | C28H50O6 | 505.3505 | | [M+Na] ⁺ | | | | |
| | TG(2:0/17:1(9Z)/6:0) | 25 | 1 | C28H50O6 | 505.3505 | | [M+Na] ⁺ | | | | |

| | | | | | | | | | | | |
|----------|--------------------------------------|----|---|--------------------------|----------|---------|---------------------|---|--|--|--|
| | TG(2:0/6:0/17:1(9Z)) | 25 | 1 | C28H50O6 | 505.3505 | | [M+Na] ⁺ | | | | |
| | TG(4:0/17:1(9Z)/4:0) | 25 | 1 | C28H50O6 | 505.3505 | | [M+Na] ⁺ | | | | |
| | TG(4:0/4:0/17:1(9Z)) | 25 | 1 | C28H50O6 | 505.3505 | | [M+Na] ⁺ | | | | |
| | TG(6:0/17:1(9Z)/2:0) | 25 | 1 | C28H50O6 | 505.3505 | | [M+Na] ⁺ | | | | |
| | TG(6:0/2:0/17:1(9Z)) | 25 | 1 | C28H50O6 | 505.3505 | | [M+Na] ⁺ | | | | |
| 507.3622 | TG(10:0/13:0/2:0) | 25 | 0 | C28H52O6 | 507.3662 | -0.0040 | [M+Na] ⁺ | + | | | |
| | TG(10:0/2:0/13:0) | 25 | 0 | C28H52O6 | 507.3662 | | [M+Na] ⁺ | | | | |
| | TG(13:0/10:0/2:0) | 25 | 0 | C28H52O6 | 507.3662 | | [M+Na] ⁺ | | | | |
| | TG(13:0/2:0/10:0) | 25 | 0 | C28H52O6 | 507.3662 | | [M+Na] ⁺ | | | | |
| | TG(13:0/4:0/8:0) | 25 | 0 | C28H52O6 | 507.3662 | | [M+Na] ⁺ | | | | |
| | TG(13:0/6:0/6:0) | 25 | 0 | C28H52O6 | 507.3662 | | [M+Na] ⁺ | | | | |
| | TG(13:0/8:0/4:0) | 25 | 0 | C28H52O6 | 507.3662 | | [M+Na] ⁺ | | | | |
| | TG(15:0/2:0/8:0) | 25 | 0 | C28H52O6 | 507.3662 | | [M+Na] ⁺ | | | | |
| | TG(15:0/4:0/6:0) | 25 | 0 | C28H52O6 | 507.3662 | | [M+Na] ⁺ | | | | |
| | TG(15:0/6:0/4:0) | 25 | 0 | C28H52O6 | 507.3662 | | [M+Na] ⁺ | | | | |
| | TG(15:0/8:0/2:0) | 25 | 0 | C28H52O6 | 507.3662 | | [M+Na] ⁺ | | | | |
| | TG(17:0/2:0/6:0) | 25 | 0 | C28H52O6 | 507.3662 | | [M+Na] ⁺ | | | | |
| | TG(17:0/4:0/4:0) | 25 | 0 | C28H52O6 | 507.3662 | | [M+Na] ⁺ | | | | |
| | TG(17:0/6:0/2:0) | 25 | 0 | C28H52O6 | 507.3662 | | [M+Na] ⁺ | | | | |
| | TG(19:0/2:0/4:0) | 25 | 0 | C28H52O6 | 507.3662 | | [M+Na] ⁺ | | | | |
| | TG(19:0/4:0/2:0) | 25 | 0 | C28H52O6 | 507.3662 | | [M+Na] ⁺ | | | | |
| | TG(21:0/2:0/2:0) | 25 | 0 | C28H52O6 | 507.3662 | | [M+Na] ⁺ | | | | |
| | TG(4:0/13:0/8:0) | 25 | 0 | C28H52O6 | 507.3662 | | [M+Na] ⁺ | | | | |

| | | | | | | | | | | | |
|----------|-------------------------------------|----|---|--------------------------|----------|--------|---------------------|---|--|--|--|
| | TG(4:0/15:0/6:0) | 25 | 0 | C28H52O6 | 507.3662 | | [M+Na] ⁺ | | | | |
| | TG(4:0/17:0/4:0) | 25 | 0 | C28H52O6 | 507.3662 | | [M+Na] ⁺ | | | | |
| | TG(4:0/19:0/2:0) | 25 | 0 | C28H52O6 | 507.3662 | | [M+Na] ⁺ | | | | |
| | TG(4:0/2:0/19:0) | 25 | 0 | C28H52O6 | 507.3662 | | [M+Na] ⁺ | | | | |
| | TG(4:0/4:0/17:0) | 25 | 0 | C28H52O6 | 507.3662 | | [M+Na] ⁺ | | | | |
| | TG(4:0/6:0/15:0) | 25 | 0 | C28H52O6 | 507.3662 | | [M+Na] ⁺ | | | | |
| | TG(4:0/8:0/13:0) | 25 | 0 | C28H52O6 | 507.3662 | | [M+Na] ⁺ | | | | |
| | TG(6:0/13:0/6:0) | 25 | 0 | C28H52O6 | 507.3662 | | [M+Na] ⁺ | | | | |
| | TG(6:0/15:0/4:0) | 25 | 0 | C28H52O6 | 507.3662 | | [M+Na] ⁺ | | | | |
| | TG(6:0/17:0/2:0) | 25 | 0 | C28H52O6 | 507.3662 | | [M+Na] ⁺ | | | | |
| | TG(6:0/2:0/17:0) | 25 | 0 | C28H52O6 | 507.3662 | | [M+Na] ⁺ | | | | |
| | TG(6:0/4:0/15:0) | 25 | 0 | C28H52O6 | 507.3662 | | [M+Na] ⁺ | | | | |
| | TG(6:0/6:0/13:0) | 25 | 0 | C28H52O6 | 507.3662 | | [M+Na] ⁺ | | | | |
| | TG(8:0/13:0/4:0) | 25 | 0 | C28H52O6 | 507.3662 | | [M+Na] ⁺ | | | | |
| | TG(8:0/15:0/2:0) | 25 | 0 | C28H52O6 | 507.3662 | | [M+Na] ⁺ | | | | |
| | TG(8:0/2:0/15:0) | 25 | 0 | C28H52O6 | 507.3662 | | [M+Na] ⁺ | | | | |
| | TG(8:0/4:0/13:0) | 25 | 0 | C28H52O6 | 507.3662 | | [M+Na] ⁺ | | | | |
| 577.5177 | TG(O-16:0/0:0/16:0) | 32 | 0 | C35H70O4 | 577.5172 | 0.0005 | [M+Na] ⁺ | + | | | |
| | DG(O-16:0/16:0/0:0) | 32 | 0 | C35H70O4 | 577.5172 | | [M+Na] ⁺ | | | | |
| | TG(O-18:0/0:0/14:0) | 32 | 0 | C35H70O4 | 577.5172 | | [M+Na] ⁺ | | | | |
| | DG(O-18:0/14:0/0:0) | 32 | 0 | C35H70O4 | 577.5172 | | [M+Na] ⁺ | | | | |
| | TG(O-20:0/0:0/12:0) | 32 | 0 | C35H70O4 | 577.5172 | | [M+Na] ⁺ | | | | |
| | DG(O-20:0/12:0/0:0) | 32 | 0 | C35H70O4 | 577.5172 | | [M+Na] ⁺ | | | | |

Table 5-9 Results of LipidMap search in between the mass range m/z 600-1000 for glycerophospholipids present in the lambs' liver extracts derived from the data in Figure 5-45. The spectra were first internal "lockmassed" on the fragment ion of phosphocholine (m/z 184.0739). The formulae, the calculated exact masses and the delta mass (in *amu*) of the proposed glycerophospholipids are reported in the table. Only the inputted ions returned a match are listed. A maximum delta mass of ± 0.01 *amu* limit was applied to the search. C is the number of carbons and DB is the number of double bonds of the proposed glycerophospholipid. Subclasses of glycerophospholipids include phosphocholine (PC), phosphatidylethanolamine (PE), protegrin (PG), phosphatidyl serine (PS), and phosphoinositide (PI).

| Input ion (m/z) | Abbreviation of proposed glycerophospholipid (unconfirmed) | Sub-class | C | DB | Formula | Calculated molecular mass | Delta mass (<i>amu</i>) | Ion | Ion observed in ... with integrated area over 5000 counts | | | |
|---------------------|--|-----------|----|----|----------------------------|---------------------------|---------------------------|---------------------|---|----------|-----|------|
| | | | | | | | | | ETA | Propanol | ACN | MeOH |
| 782.5690 | PC(12:0/22:1(13Z)) | PC | 34 | 1 | C42H82NO8P | 782.5676 | 0.0014 | [M+Na] ⁺ | + | | + | |
| 782.5690 | PC(14:0/20:1(11Z)) | PC | 34 | 1 | C42H82NO8P | 782.5676 | 0.0014 | [M+Na] ⁺ | | | | |
| 782.5690 | PC(17:0/17:1(9Z)) | PC | 34 | 1 | C42H82NO8P | 782.5676 | 0.0014 | [M+Na] ⁺ | | | | |
| 782.5690 | PC(17:1(9Z)/17:0) | PC | 34 | 1 | C42H82NO8P | 782.5676 | 0.0014 | [M+Na] ⁺ | | | | |
| 782.5690 | PC(14:1(9Z)/20:0) | PC | 34 | 1 | C42H82NO8P | 782.5676 | 0.0014 | [M+Na] ⁺ | | | | |
| 782.5690 | PC(20:0/14:1(9Z)) | PC | 34 | 1 | C42H82NO8P | 782.5676 | 0.0014 | [M+Na] ⁺ | | | | |
| 782.5690 | PC(22:1(13Z)/12:0) | PC | 34 | 1 | C42H82NO8P | 782.5676 | 0.0014 | [M+Na] ⁺ | | | | |
| 782.5690 | PC(20:1(11Z)/14:0) | PC | 34 | 1 | C42H82NO8P | 782.5676 | 0.0014 | [M+Na] ⁺ | | | | |
| 782.5690 | PC(18:1(9Z)/16:0) | PC | 34 | 1 | C42H82NO8P | 782.5676 | 0.0014 | [M+Na] ⁺ | | | | |
| 782.5690 | PC(18:0/16:1(9Z)) | PC | 34 | 1 | C42H82NO8P | 782.5676 | 0.0014 | [M+Na] ⁺ | | | | |
| 782.5690 | PC(16:1(9Z)/18:0) | PC | 34 | 1 | C42H82NO8P | 782.5676 | 0.0014 | [M+Na] ⁺ | | | | |
| 782.5690 | PC(16:0/18:1(9Z)) | PC | 34 | 1 | C42H82NO8P | 782.5676 | 0.0014 | [M+Na] ⁺ | | | | |

| | | | | | | | | | | | | |
|----------|--|----|----|---|----------------------------|----------|--------|---------------------|---|---|---|--|
| 782.5690 | PE(17:0/20:1(11Z)) | PE | 37 | 1 | C42H82NO8P | 782.5676 | 0.0014 | [M+Na] ⁺ | | | | |
| 782.5690 | PE(16:1(9Z)/21:0) | PE | 37 | 1 | C42H82NO8P | 782.5676 | 0.0014 | [M+Na] ⁺ | | | | |
| 782.5690 | PE(15:0/22:1(13Z)) | PE | 37 | 1 | C42H82NO8P | 782.5676 | 0.0014 | [M+Na] ⁺ | | | | |
| 782.5690 | PE(17:1(9Z)/20:0) | PE | 37 | 1 | C42H82NO8P | 782.5676 | 0.0014 | [M+Na] ⁺ | | | | |
| 782.5690 | PE(20:0/17:1(9Z)) | PE | 37 | 1 | C42H82NO8P | 782.5676 | 0.0014 | [M+Na] ⁺ | | | | |
| 782.5690 | PE(21:0/16:1(9Z)) | PE | 37 | 1 | C42H82NO8P | 782.5676 | 0.0014 | [M+Na] ⁺ | | | | |
| 782.5690 | PE(20:1(11Z)/17:0) | PE | 37 | 1 | C42H82NO8P | 782.5676 | 0.0014 | [M+Na] ⁺ | | | | |
| 782.5690 | PE(19:0/18:1(9Z)) | PE | 37 | 1 | C42H82NO8P | 782.5676 | 0.0014 | [M+Na] ⁺ | | | | |
| 782.5690 | PE(18:1(9Z)/19:0) | PE | 37 | 1 | C42H82NO8P | 782.5676 | 0.0014 | [M+Na] ⁺ | | | | |
| 782.5690 | PE(22:1(13Z)/15:0) | PE | 37 | 1 | C42H82NO8P | 782.5676 | 0.0014 | [M+Na] ⁺ | | | | |
| 797.5260 | PG(14:0/22:2(13Z,16Z)) | PG | 36 | 2 | C42H79O10P | 797.5309 | 0.0049 | [M+Na] ⁺ | | | + | |
| 797.5260 | PG(16:0/20:2(11Z,14Z)) | PG | 36 | 2 | C42H79O10P | 797.5309 | 0.0049 | [M+Na] ⁺ | | | | |
| 797.5260 | PG(16:1(9Z)/20:1(11Z)) | PG | 36 | 2 | C42H79O10P | 797.5309 | 0.0049 | [M+Na] ⁺ | | | | |
| 797.5260 | PG(17:2(9Z,12Z)/19:0) | PG | 36 | 2 | C42H79O10P | 797.5309 | 0.0049 | [M+Na] ⁺ | | | | |
| 797.5260 | PG(18:0/18:2(9Z,12Z)) | PG | 36 | 2 | C42H79O10P | 797.5309 | 0.0049 | [M+Na] ⁺ | | | | |
| 797.5260 | PG(22:2(13Z,16Z)/14:0) | PG | 36 | 2 | C42H79O10P | 797.5309 | 0.0049 | [M+Na] ⁺ | | | | |
| 797.5260 | PG(18:2(9Z,12Z)/18:0) | PG | 36 | 2 | C42H79O10P | 797.5309 | 0.0049 | [M+Na] ⁺ | | | | |
| 797.5260 | PG(19:0/17:2(9Z,12Z)) | PG | 36 | 2 | C42H79O10P | 797.5309 | 0.0049 | [M+Na] ⁺ | | | | |
| 797.5260 | PG(20:1(11Z)/16:1(9Z)) | PG | 36 | 2 | C42H79O10P | 797.5309 | 0.0049 | [M+Na] ⁺ | | | | |
| 797.5260 | PG(20:2(11Z,14Z)/16:0) | PG | 36 | 2 | C42H79O10P | 797.5309 | 0.0049 | [M+Na] ⁺ | | | | |
| 797.5260 | PG(18:1(9Z)/18:1(9Z)) | PG | 36 | 2 | C42H79O10P | 797.5309 | 0.0049 | [M+Na] ⁺ | | | | |
| 798.5405 | PE(O-18:1(1Z)/22:6(4Z,7Z,10Z,13Z,16Z,19Z)) | PE | 40 | 6 | C45H78NO7P | 798.5414 | 0.0009 | [M+Na] ⁺ | + | + | + | |
| 799.5399 | PG(14:0/22:1(13Z)) | PG | 36 | 1 | C42H81O10P | 799.5465 | 0.0066 | [M+Na] ⁺ | + | | + | |

| | | | | | | | | | | | | |
|----------|--|----|----|---|----------------------------|----------|--------|---------------------|---|--|---|--|
| 799.5399 | PG(16:0/20:1(11Z)) | PG | 36 | 1 | C42H81O10P | 799.5465 | 0.0066 | [M+Na] ⁺ | | | | |
| 799.5399 | PG(16:1(9Z)/20:0) | PG | 36 | 1 | C42H81O10P | 799.5465 | 0.0066 | [M+Na] ⁺ | | | | |
| 799.5399 | PG(18:0/18:1(9Z)) | PG | 36 | 1 | C42H81O10P | 799.5465 | 0.0066 | [M+Na] ⁺ | | | | |
| 799.5399 | PG(19:0/17:1(9Z)) | PG | 36 | 1 | C42H81O10P | 799.5465 | 0.0066 | [M+Na] ⁺ | | | | |
| 799.5399 | PG(20:0/16:1(9Z)) | PG | 36 | 1 | C42H81O10P | 799.5465 | 0.0066 | [M+Na] ⁺ | | | | |
| 799.5399 | PG(20:1(11Z)/16:0) | PG | 36 | 1 | C42H81O10P | 799.5465 | 0.0066 | [M+Na] ⁺ | | | | |
| 799.5399 | PG(22:1(13Z)/14:0) | PG | 36 | 1 | C42H81O10P | 799.5465 | 0.0066 | [M+Na] ⁺ | | | | |
| 799.5399 | PG(17:1(9Z)/19:0) | PG | 36 | 1 | C42H81O10P | 799.5465 | 0.0066 | [M+Na] ⁺ | | | | |
| 799.5399 | PG(18:1(9Z)/18:0) | PG | 36 | 1 | C42H81O10P | 799.5465 | 0.0066 | [M+Na] ⁺ | | | | |
| 800.5529 | PE(O-20:1(1Z)/20:5(5Z,8Z,11Z,14Z,17Z)) | PE | 40 | 5 | C45H80NO7P | 800.5570 | 0.0041 | [M+Na] ⁺ | + | | + | |
| 800.5529 | PE(O-18:0/22:6(4Z,7Z,10Z,13Z,16Z,19Z)) | PE | 40 | 6 | C45H80NO7P | 800.5570 | 0.0041 | [M+Na] ⁺ | | | | |
| 810.5990 | PC(14:0/22:1(13Z)) | PC | 36 | 1 | C44H86NO8P | 810.5989 | 0.0001 | [M+Na] ⁺ | + | | | |
| 810.5990 | PC(16:0/20:1(11Z)) | PC | 36 | 1 | C44H86NO8P | 810.5989 | 0.0001 | [M+Na] ⁺ | | | | |
| 810.5990 | PC(19:0/17:1(9Z)) | PC | 36 | 1 | C44H86NO8P | 810.5989 | 0.0001 | [M+Na] ⁺ | | | | |
| 810.5990 | PC(17:1(9Z)/19:0) | PC | 36 | 1 | C44H86NO8P | 810.5989 | 0.0001 | [M+Na] ⁺ | | | | |
| 810.5990 | PC(14:1(9Z)/22:0) | PC | 36 | 1 | C44H86NO8P | 810.5989 | 0.0001 | [M+Na] ⁺ | | | | |
| 810.5990 | PC(22:0/14:1(9Z)) | PC | 36 | 1 | C44H86NO8P | 810.5989 | 0.0001 | [M+Na] ⁺ | | | | |
| 810.5990 | PC(22:1(13Z)/14:0) | PC | 36 | 1 | C44H86NO8P | 810.5989 | 0.0001 | [M+Na] ⁺ | | | | |
| 810.5990 | PC(20:1(11Z)/16:0) | PC | 36 | 1 | C44H86NO8P | 810.5989 | 0.0001 | [M+Na] ⁺ | | | | |
| 810.5990 | PC(20:0/16:1(9Z)) | PC | 36 | 1 | C44H86NO8P | 810.5989 | 0.0001 | [M+Na] ⁺ | | | | |
| 810.5990 | PC(16:1(9Z)/20:0) | PC | 36 | 1 | C44H86NO8P | 810.5989 | 0.0001 | [M+Na] ⁺ | | | | |
| 810.5990 | PC(18:0/18:1(9Z)) | PC | 36 | 1 | C44H86NO8P | 810.5989 | 0.0001 | [M+Na] ⁺ | | | | |
| 810.5990 | PC(18:1(9Z)/18:0) | PC | 36 | 1 | C44H86NO8P | 810.5989 | 0.0001 | [M+Na] ⁺ | | | | |

| | | | | | | | | | | | | |
|----------|--|----|----|---|-----------------------------|----------|--------|---------------------|---|---|---|--|
| 810.5990 | PE(17:0/22:1(13Z)) | PE | 39 | 1 | C44H86NO8P | 810.5989 | 0.0001 | [M+Na] ⁺ | | | | |
| 810.5990 | PE(17:1(9Z)/22:0) | PE | 39 | 1 | C44H86NO8P | 810.5989 | 0.0001 | [M+Na] ⁺ | | | | |
| 810.5990 | PE(22:1(13Z)/17:0) | PE | 39 | 1 | C44H86NO8P | 810.5989 | 0.0001 | [M+Na] ⁺ | | | | |
| 810.5990 | PE(21:0/18:1(9Z)) | PE | 39 | 1 | C44H86NO8P | 810.5989 | 0.0001 | [M+Na] ⁺ | | | | |
| 810.5990 | PE(20:1(11Z)/19:0) | PE | 39 | 1 | C44H86NO8P | 810.5989 | 0.0001 | [M+Na] ⁺ | | | | |
| 810.5990 | PE(19:0/20:1(11Z)) | PE | 39 | 1 | C44H86NO8P | 810.5989 | 0.0001 | [M+Na] ⁺ | | | | |
| 810.5990 | PE(18:1(9Z)/21:0) | PE | 39 | 1 | C44H86NO8P | 810.5989 | 0.0001 | [M+Na] ⁺ | | | | |
| 810.5990 | PE(22:0/17:1(9Z)) | PE | 39 | 1 | C44H86NO8P | 810.5989 | 0.0001 | [M+Na] ⁺ | | | | |
| 813.4754 | PG(20:5(5Z,8Z,11Z,14Z,17Z)/18:3(9Z,12Z,15Z)) | PG | 38 | 8 | C44H71O10P | 813.4683 | 0.0071 | [M+Na] ⁺ | | | + | |
| 813.4754 | PG(18:3(9Z,12Z,15Z)/20:5(5Z,8Z,11Z,14Z,17Z)) | PG | 38 | 8 | C44H71O10P | 813.4683 | 0.0071 | [M+Na] ⁺ | | | | |
| 820.5172 | PS(15:0/22:4(7Z,10Z,13Z,16Z)) | PS | 37 | 4 | C43H76NO10P | 820.5105 | 0.0067 | [M+Na] ⁺ | | + | + | |
| 820.5172 | PS(17:0/20:4(5Z,8Z,11Z,14Z)) | PS | 37 | 4 | C43H76NO10P | 820.5105 | 0.0067 | [M+Na] ⁺ | | | | |
| 820.5172 | PS(17:2(9Z,12Z)/20:2(11Z,14Z)) | PS | 37 | 4 | C43H76NO10P | 820.5105 | 0.0067 | [M+Na] ⁺ | | | | |
| 820.5172 | PS(20:3(8Z,11Z,14Z)/17:1(9Z)) | PS | 37 | 4 | C43H76NO10P | 820.5105 | 0.0067 | [M+Na] ⁺ | | | | |
| 820.5172 | PS(20:4(5Z,8Z,11Z,14Z)/17:0) | PS | 37 | 4 | C43H76NO10P | 820.5105 | 0.0067 | [M+Na] ⁺ | | | | |
| 820.5172 | PS(22:4(7Z,10Z,13Z,16Z)/15:0) | PS | 37 | 4 | C43H76NO10P | 820.5105 | 0.0067 | [M+Na] ⁺ | | | | |
| 820.5172 | PS(17:1(9Z)/20:3(8Z,11Z,14Z)) | PS | 37 | 4 | C43H76NO10P | 820.5105 | 0.0067 | [M+Na] ⁺ | | | | |
| 820.5172 | PS(20:2(11Z,14Z)/17:2(9Z,12Z)) | PS | 37 | 4 | C43H76NO10P | 820.5105 | 0.0067 | [M+Na] ⁺ | | | | |
| 822.5191 | PS(17:0/20:3(8Z,11Z,14Z)) | PS | 37 | 3 | C43H78NO10P | 822.5261 | 0.0070 | [M+Na] ⁺ | + | + | + | |
| 822.5191 | PS(17:2(9Z,12Z)/20:1(11Z)) | PS | 37 | 3 | C43H78NO10P | 822.5261 | 0.0070 | [M+Na] ⁺ | | | | |
| 822.5191 | PS(18:3(9Z,12Z,15Z)/19:0) | PS | 37 | 3 | C43H78NO10P | 822.5261 | 0.0070 | [M+Na] ⁺ | | | | |
| 822.5191 | PS(20:2(11Z,14Z)/17:1(9Z)) | PS | 37 | 3 | C43H78NO10P | 822.5261 | 0.0070 | [M+Na] ⁺ | | | | |
| 822.5191 | PS(20:1(11Z)/17:2(9Z,12Z)) | PS | 37 | 3 | C43H78NO10P | 822.5261 | 0.0070 | [M+Na] ⁺ | | | | |

| | | | | | | | | | | | | |
|----------|--|----|----|---|-----------------------------|----------|--------|---------------------|---|---|---|--|
| 822.5191 | PS(20:3(8Z,11Z,14Z)/17:0) | PS | 37 | 3 | C43H78NO10P | 822.5261 | 0.0070 | [M+Na] ⁺ | | | | |
| 822.5191 | PS(17:1(9Z)/20:2(11Z,14Z)) | PS | 37 | 3 | C43H78NO10P | 822.5261 | 0.0070 | [M+Na] ⁺ | | | | |
| 822.5191 | PS(19:0/18:3(9Z,12Z,15Z)) | PS | 37 | 3 | C43H78NO10P | 822.5261 | 0.0070 | [M+Na] ⁺ | | | | |
| 826.5690 | PE(O-20:1(1Z)/22:6(4Z,7Z,10Z,13Z,16Z,19Z)) | PE | 42 | 6 | C47H82NO7P | 826.5727 | 0.0037 | [M+Na] ⁺ | + | + | + | |
| 827.5760 | PG(16:0/22:1(13Z)) | PG | 38 | 1 | C44H85O10P | 827.5778 | 0.0018 | [M+Na] ⁺ | + | | | |
| 827.5760 | PG(16:1(9Z)/22:0) | PG | 38 | 1 | C44H85O10P | 827.5778 | 0.0018 | [M+Na] ⁺ | | | | |
| 827.5760 | PG(18:0/20:1(11Z)) | PG | 38 | 1 | C44H85O10P | 827.5778 | 0.0018 | [M+Na] ⁺ | | | | |
| 827.5760 | PG(18:1(9Z)/20:0) | PG | 38 | 1 | C44H85O10P | 827.5778 | 0.0018 | [M+Na] ⁺ | | | | |
| 827.5760 | PG(21:0/17:1(9Z)) | PG | 38 | 1 | C44H85O10P | 827.5778 | 0.0018 | [M+Na] ⁺ | | | | |
| 827.5760 | PG(20:1(11Z)/18:0) | PG | 38 | 1 | C44H85O10P | 827.5778 | 0.0018 | [M+Na] ⁺ | | | | |
| 827.5760 | PG(22:0/16:1(9Z)) | PG | 38 | 1 | C44H85O10P | 827.5778 | 0.0018 | [M+Na] ⁺ | | | | |
| 827.5760 | PG(22:1(13Z)/16:0) | PG | 38 | 1 | C44H85O10P | 827.5778 | 0.0018 | [M+Na] ⁺ | | | | |
| 827.5760 | PG(17:1(9Z)/21:0) | PG | 38 | 1 | C44H85O10P | 827.5778 | 0.0018 | [M+Na] ⁺ | | | | |
| 827.5760 | PG(20:0/18:1(9Z)) | PG | 38 | 1 | C44H85O10P | 827.5778 | 0.0018 | [M+Na] ⁺ | | | | |
| 828.5431 | PC(16:0/22:6(4Z,7Z,10Z,13Z,16Z,19Z)) | PC | 38 | 6 | C46H80NO8P | 828.5520 | 0.0089 | [M+Na] ⁺ | + | | | |
| 828.5431 | PC(18:1(9Z)/20:5(5Z,8Z,11Z,14Z,17Z)) | PC | 38 | 6 | C46H80NO8P | 828.5520 | 0.0089 | [M+Na] ⁺ | | | | |
| 828.5431 | PC(18:2(9Z,12Z)/20:4(5Z,8Z,11Z,14Z)) | PC | 38 | 6 | C46H80NO8P | 828.5520 | 0.0089 | [M+Na] ⁺ | | | | |
| 828.5431 | PC(18:3(9Z,12Z,15Z)/20:3(8Z,11Z,14Z)) | PC | 38 | 6 | C46H80NO8P | 828.5520 | 0.0089 | [M+Na] ⁺ | | | | |
| 828.5431 | PC(20:3(8Z,11Z,14Z)/18:3(9Z,12Z,15Z)) | PC | 38 | 6 | C46H80NO8P | 828.5520 | 0.0089 | [M+Na] ⁺ | | | | |
| 828.5431 | PC(22:6(4Z,7Z,10Z,13Z,16Z,19Z)/16:0) | PC | 38 | 6 | C46H80NO8P | 828.5520 | 0.0089 | [M+Na] ⁺ | | | | |
| 828.5431 | PC(20:4(5Z,8Z,11Z,14Z)/18:2(9Z,12Z)) | PC | 38 | 6 | C46H80NO8P | 828.5520 | 0.0089 | [M+Na] ⁺ | | | | |
| 828.5431 | PC(20:5(5Z,8Z,11Z,14Z,17Z)/18:1(9Z)) | PC | 38 | 6 | C46H80NO8P | 828.5520 | 0.0089 | [M+Na] ⁺ | | | | |
| 828.5431 | PE(19:0/22:6(4Z,7Z,10Z,13Z,16Z,19Z)) | PE | 41 | 6 | C46H80NO8P | 828.5520 | 0.0089 | [M+Na] ⁺ | | | | |

| | | | | | | | | | | | | |
|----------|--|----|----|---|----------------------------|----------|--------|---------------------|--|--|---|--|
| 828.5431 | PE(22:6(4Z,7Z,10Z,13Z,16Z,19Z)/19:0) | PE | 41 | 6 | C46H80NO8P | 828.5520 | 0.0089 | [M+Na] ⁺ | | | | |
| 830.5652 | PC(16:1(9Z)/22:4(7Z,10Z,13Z,16Z)) | PC | 38 | 5 | C46H82NO8P | 830.5676 | 0.0024 | [M+Na] ⁺ | | | + | |
| 830.5652 | PC(18:0/20:5(5Z,8Z,11Z,14Z,17Z)) | PC | 38 | 5 | C46H82NO8P | 830.5676 | 0.0024 | [M+Na] ⁺ | | | | |
| 830.5652 | PC(18:1(9Z)/20:4(5Z,8Z,11Z,14Z)) | PC | 38 | 5 | C46H82NO8P | 830.5676 | 0.0024 | [M+Na] ⁺ | | | | |
| 830.5652 | PC(18:2(9Z,12Z)/20:3(8Z,11Z,14Z)) | PC | 38 | 5 | C46H82NO8P | 830.5676 | 0.0024 | [M+Na] ⁺ | | | | |
| 830.5652 | PC(18:3(9Z,12Z,15Z)/20:2(11Z,14Z)) | PC | 38 | 5 | C46H82NO8P | 830.5676 | 0.0024 | [M+Na] ⁺ | | | | |
| 830.5652 | PC(20:2(11Z,14Z)/18:3(9Z,12Z,15Z)) | PC | 38 | 5 | C46H82NO8P | 830.5676 | 0.0024 | [M+Na] ⁺ | | | | |
| 830.5652 | PC(22:4(7Z,10Z,13Z,16Z)/16:1(9Z)) | PC | 38 | 5 | C46H82NO8P | 830.5676 | 0.0024 | [M+Na] ⁺ | | | | |
| 830.5652 | PC(20:3(8Z,11Z,14Z)/18:2(9Z,12Z)) | PC | 38 | 5 | C46H82NO8P | 830.5676 | 0.0024 | [M+Na] ⁺ | | | | |
| 830.5652 | PC(20:4(5Z,8Z,11Z,14Z)/18:1(9Z)) | PC | 38 | 5 | C46H82NO8P | 830.5676 | 0.0024 | [M+Na] ⁺ | | | | |
| 830.5652 | PC(20:5(5Z,8Z,11Z,14Z,17Z)/18:0) | PC | 38 | 5 | C46H82NO8P | 830.5676 | 0.0024 | [M+Na] ⁺ | | | | |
| 830.5652 | PE(20:5(5Z,8Z,11Z,14Z,17Z)/21:0) | PE | 41 | 5 | C46H82NO8P | 830.5676 | 0.0024 | [M+Na] ⁺ | | | | |
| 830.5652 | PE(21:0/20:5(5Z,8Z,11Z,14Z,17Z)) | PE | 41 | 5 | C46H82NO8P | 830.5676 | 0.0024 | [M+Na] ⁺ | | | | |
| 845.5240 | PI(13:0/20:1(11Z)) | PI | 33 | 1 | C42H79O13P | 845.5156 | 0.0084 | [M+Na] ⁺ | | | + | |
| 845.5240 | PI(17:1(9Z)/16:0) | PI | 33 | 1 | C42H79O13P | 845.5156 | 0.0084 | [M+Na] ⁺ | | | | |
| 845.5240 | PI(14:1(9Z)/19:0) | PI | 33 | 1 | C42H79O13P | 845.5156 | 0.0084 | [M+Na] ⁺ | | | | |
| 845.5240 | PI(19:0/14:1(9Z)) | PI | 33 | 1 | C42H79O13P | 845.5156 | 0.0084 | [M+Na] ⁺ | | | | |
| 845.5240 | PI(20:1(11Z)/13:0) | PI | 33 | 1 | C42H79O13P | 845.5156 | 0.0084 | [M+Na] ⁺ | | | | |
| 845.5240 | PI(18:1(9Z)/15:0) | PI | 33 | 1 | C42H79O13P | 845.5156 | 0.0084 | [M+Na] ⁺ | | | | |
| 845.5240 | PI(17:0/16:1(9Z)) | PI | 33 | 1 | C42H79O13P | 845.5156 | 0.0084 | [M+Na] ⁺ | | | | |
| 845.5240 | PI(16:1(9Z)/17:0) | PI | 33 | 1 | C42H79O13P | 845.5156 | 0.0084 | [M+Na] ⁺ | | | | |
| 845.5240 | PI(15:0/18:1(9Z)) | PI | 33 | 1 | C42H79O13P | 845.5156 | 0.0084 | [M+Na] ⁺ | | | | |
| 845.5240 | PI(16:0/17:1(9Z)) | PI | 33 | 1 | C42H79O13P | 845.5156 | 0.0084 | [M+Na] ⁺ | | | | |

| | | | | | | | | | | | | |
|----------|---|----|----|---|-----------------------------|----------|--------|---------------------|---|---|---|--|
| 845.5240 | PG(22:6(4Z,7Z,10Z,13Z,16Z,19Z)/18:0) | PG | 40 | 6 | C46H79O10P | 845.5309 | 0.0069 | [M+Na] ⁺ | | | | |
| 845.5240 | PG(22:4(7Z,10Z,13Z,16Z)/18:2(9Z,12Z)) | PG | 40 | 6 | C46H79O10P | 845.5309 | 0.0069 | [M+Na] ⁺ | | | | |
| 845.5240 | PG(20:5(5Z,8Z,11Z,14Z,17Z)/20:1(11Z)) | PG | 40 | 6 | C46H79O10P | 845.5309 | 0.0069 | [M+Na] ⁺ | | | | |
| 845.5240 | PG(20:4(5Z,8Z,11Z,14Z)/20:2(11Z,14Z)) | PG | 40 | 6 | C46H79O10P | 845.5309 | 0.0069 | [M+Na] ⁺ | | | | |
| 845.5240 | PG(18:0/22:6(4Z,7Z,10Z,13Z,16Z,19Z)) | PG | 40 | 6 | C46H79O10P | 845.5309 | 0.0069 | [M+Na] ⁺ | | | | |
| 845.5240 | PG(20:2(11Z,14Z)/20:4(5Z,8Z,11Z,14Z)) | PG | 40 | 6 | C46H79O10P | 845.5309 | 0.0069 | [M+Na] ⁺ | | | | |
| 845.5240 | PG(20:1(11Z)/20:5(5Z,8Z,11Z,14Z,17Z)) | PG | 40 | 6 | C46H79O10P | 845.5309 | 0.0069 | [M+Na] ⁺ | | | | |
| 845.5240 | PG(18:2(9Z,12Z)/22:4(7Z,10Z,13Z,16Z)) | PG | 40 | 6 | C46H79O10P | 845.5309 | 0.0069 | [M+Na] ⁺ | | | | |
| 845.5240 | PG(20:3(8Z,11Z,14Z)/20:3(8Z,11Z,14Z)) | PG | 40 | 6 | C46H79O10P | 845.5309 | 0.0069 | [M+Na] ⁺ | | | | |
| 846.5319 | PS(19:0/20:5(5Z,8Z,11Z,14Z,17Z)) | PS | 39 | 5 | C45H78NO10P | 846.5261 | 0.0058 | [M+Na] ⁺ | + | + | + | |
| 846.5319 | PS(22:4(7Z,10Z,13Z,16Z)/17:1(9Z)) | PS | 39 | 5 | C45H78NO10P | 846.5261 | 0.0058 | [M+Na] ⁺ | | | | |
| 846.5319 | PS(17:1(9Z)/22:4(7Z,10Z,13Z,16Z)) | PS | 39 | 5 | C45H78NO10P | 846.5261 | 0.0058 | [M+Na] ⁺ | | | | |
| 846.5319 | PS(20:5(5Z,8Z,11Z,14Z,17Z)/19:0) | PS | 39 | 5 | C45H78NO10P | 846.5261 | 0.0058 | [M+Na] ⁺ | | | | |
| 847.5399 | PI(20:0/13:0) | PI | 33 | 0 | C42H81O13P | 847.5313 | 0.0086 | [M+Na] ⁺ | | | + | |
| 847.5399 | PI(19:0/14:0) | PI | 33 | 0 | C42H81O13P | 847.5313 | 0.0086 | [M+Na] ⁺ | | | | |
| 847.5399 | PI(18:0/15:0) | PI | 33 | 0 | C42H81O13P | 847.5313 | 0.0086 | [M+Na] ⁺ | | | | |
| 847.5399 | PI(17:0/16:0) | PI | 33 | 0 | C42H81O13P | 847.5313 | 0.0086 | [M+Na] ⁺ | | | | |
| 847.5399 | PI(21:0/12:0) | PI | 33 | 0 | C42H81O13P | 847.5313 | 0.0086 | [M+Na] ⁺ | | | | |
| 847.5399 | PI(15:0/18:0) | PI | 33 | 0 | C42H81O13P | 847.5313 | 0.0086 | [M+Na] ⁺ | | | | |
| 847.5399 | PI(14:0/19:0) | PI | 33 | 0 | C42H81O13P | 847.5313 | 0.0086 | [M+Na] ⁺ | | | | |
| 847.5399 | PI(13:0/20:0) | PI | 33 | 0 | C42H81O13P | 847.5313 | 0.0086 | [M+Na] ⁺ | | | | |
| 847.5399 | PI(12:0/21:0) | PI | 33 | 0 | C42H81O13P | 847.5313 | 0.0086 | [M+Na] ⁺ | | | | |
| 847.5399 | PI(16:0/17:0) | PI | 33 | 0 | C42H81O13P | 847.5313 | 0.0086 | [M+Na] ⁺ | | | | |

| | | | | | | | | | | | | |
|----------|--|----|----|---|-----------------------------|----------|--------|---------------------|---|--|---|--|
| 847.5399 | PG(22:4(7Z,10Z,13Z,16Z)/18:1(9Z)) | PG | 40 | 5 | C46H81O10P | 847.5465 | 0.0066 | [M+Na] ⁺ | | | | |
| 847.5399 | PG(22:2(13Z,16Z)/18:3(9Z,12Z,15Z)) | PG | 40 | 5 | C46H81O10P | 847.5465 | 0.0066 | [M+Na] ⁺ | | | | |
| 847.5399 | PG(20:5(5Z,8Z,11Z,14Z,17Z)/20:0) | PG | 40 | 5 | C46H81O10P | 847.5465 | 0.0066 | [M+Na] ⁺ | | | | |
| 847.5399 | PG(20:4(5Z,8Z,11Z,14Z)/20:1(11Z)) | PG | 40 | 5 | C46H81O10P | 847.5465 | 0.0066 | [M+Na] ⁺ | | | | |
| 847.5399 | PG(20:3(8Z,11Z,14Z)/20:2(11Z,14Z)) | PG | 40 | 5 | C46H81O10P | 847.5465 | 0.0066 | [M+Na] ⁺ | | | | |
| 847.5399 | PG(20:2(11Z,14Z)/20:3(8Z,11Z,14Z)) | PG | 40 | 5 | C46H81O10P | 847.5465 | 0.0066 | [M+Na] ⁺ | | | | |
| 847.5399 | PG(20:1(11Z)/20:4(5Z,8Z,11Z,14Z)) | PG | 40 | 5 | C46H81O10P | 847.5465 | 0.0066 | [M+Na] ⁺ | | | | |
| 847.5399 | PG(20:0/20:5(5Z,8Z,11Z,14Z,17Z)) | PG | 40 | 5 | C46H81O10P | 847.5465 | 0.0066 | [M+Na] ⁺ | | | | |
| 847.5399 | PG(18:1(9Z)/22:4(7Z,10Z,13Z,16Z)) | PG | 40 | 5 | C46H81O10P | 847.5465 | 0.0066 | [M+Na] ⁺ | | | | |
| 847.5399 | PG(18:3(9Z,12Z,15Z)/22:2(13Z,16Z)) | PG | 40 | 5 | C46H81O10P | 847.5465 | 0.0066 | [M+Na] ⁺ | | | | |
| 848.5493 | PS(17:0/22:4(7Z,10Z,13Z,16Z)) | PS | 39 | 4 | C45H80NO10P | 848.5418 | 0.0075 | [M+Na] ⁺ | + | | + | |
| 848.5493 | PS(17:2(9Z,12Z)/22:2(13Z,16Z)) | PS | 39 | 4 | C45H80NO10P | 848.5418 | 0.0075 | [M+Na] ⁺ | | | | |
| 848.5493 | PS(22:4(7Z,10Z,13Z,16Z)/17:0) | PS | 39 | 4 | C45H80NO10P | 848.5418 | 0.0075 | [M+Na] ⁺ | | | | |
| 848.5493 | PS(20:4(5Z,8Z,11Z,14Z)/19:0) | PS | 39 | 4 | C45H80NO10P | 848.5418 | 0.0075 | [M+Na] ⁺ | | | | |
| 848.5493 | PS(22:2(13Z,16Z)/17:2(9Z,12Z)) | PS | 39 | 4 | C45H80NO10P | 848.5418 | 0.0075 | [M+Na] ⁺ | | | | |
| 848.5493 | PS(19:0/20:4(5Z,8Z,11Z,14Z)) | PS | 39 | 4 | C45H80NO10P | 848.5418 | 0.0075 | [M+Na] ⁺ | | | | |
| 849.5551 | PG(18:0/22:4(7Z,10Z,13Z,16Z)) | PG | 40 | 4 | C46H83O10P | 849.5622 | 0.0071 | [M+Na] ⁺ | | | + | |
| 849.5551 | PG(18:2(9Z,12Z)/22:2(13Z,16Z)) | PG | 40 | 4 | C46H83O10P | 849.5622 | 0.0071 | [M+Na] ⁺ | | | | |
| 849.5551 | PG(18:3(9Z,12Z,15Z)/22:1(13Z)) | PG | 40 | 4 | C46H83O10P | 849.5622 | 0.0071 | [M+Na] ⁺ | | | | |
| 849.5551 | PG(20:0/20:4(5Z,8Z,11Z,14Z)) | PG | 40 | 4 | C46H83O10P | 849.5622 | 0.0071 | [M+Na] ⁺ | | | | |
| 849.5551 | PG(20:1(11Z)/20:3(8Z,11Z,14Z)) | PG | 40 | 4 | C46H83O10P | 849.5622 | 0.0071 | [M+Na] ⁺ | | | | |
| 849.5551 | PG(22:4(7Z,10Z,13Z,16Z)/18:0) | PG | 40 | 4 | C46H83O10P | 849.5622 | 0.0071 | [M+Na] ⁺ | | | | |
| 849.5551 | PG(20:3(8Z,11Z,14Z)/20:1(11Z)) | PG | 40 | 4 | C46H83O10P | 849.5622 | 0.0071 | [M+Na] ⁺ | | | | |

| | | | | | | | | | | | | |
|----------|--|----|----|---|-----------------------------|----------|--------|---------------------|---|---|---|--|
| 849.5551 | PG(20:4(5Z,8Z,11Z,14Z)/20:0) | PG | 40 | 4 | C46H83O10P | 849.5622 | 0.0071 | [M+Na] ⁺ | | | | |
| 849.5551 | PG(22:1(13Z)/18:3(9Z,12Z,15Z)) | PG | 40 | 4 | C46H83O10P | 849.5622 | 0.0071 | [M+Na] ⁺ | | | | |
| 849.5551 | PG(22:2(13Z,16Z)/18:2(9Z,12Z)) | PG | 40 | 4 | C46H83O10P | 849.5622 | 0.0071 | [M+Na] ⁺ | | | | |
| 849.5551 | PG(20:2(11Z,14Z)/20:2(11Z,14Z)) | PG | 40 | 4 | C46H83O10P | 849.5622 | 0.0071 | [M+Na] ⁺ | | | | |
| 872.5483 | PS(22:6(4Z,7Z,10Z,13Z,16Z,19Z)/19:0) | PS | 41 | 6 | C47H80NO10P | 872.5418 | 0.0065 | [M+Na] ⁺ | + | + | + | |
| 872.5483 | PS(19:0/22:6(4Z,7Z,10Z,13Z,16Z,19Z)) | PS | 41 | 6 | C47H80NO10P | 872.5418 | 0.0065 | [M+Na] ⁺ | | | + | |
| 873.5563 | PI(15:0/20:1(11Z)) | PI | 35 | 1 | C44H83O13P | 873.5469 | 0.0094 | [M+Na] ⁺ | | | | |
| 873.5563 | PI(17:1(9Z)/18:0) | PI | 35 | 1 | C44H83O13P | 873.5469 | 0.0094 | [M+Na] ⁺ | | | | |
| 873.5563 | PI(14:1(9Z)/21:0) | PI | 35 | 1 | C44H83O13P | 873.5469 | 0.0094 | [M+Na] ⁺ | | | | |
| 873.5563 | PI(21:0/14:1(9Z)) | PI | 35 | 1 | C44H83O13P | 873.5469 | 0.0094 | [M+Na] ⁺ | | | | |
| 873.5563 | PI(22:1(13Z)/13:0) | PI | 35 | 1 | C44H83O13P | 873.5469 | 0.0094 | [M+Na] ⁺ | | | | |
| 873.5563 | PI(20:1(11Z)/15:0) | PI | 35 | 1 | C44H83O13P | 873.5469 | 0.0094 | [M+Na] ⁺ | | | | |
| 873.5563 | PI(19:0/16:1(9Z)) | PI | 35 | 1 | C44H83O13P | 873.5469 | 0.0094 | [M+Na] ⁺ | | | | |
| 873.5563 | PI(18:1(9Z)/17:0) | PI | 35 | 1 | C44H83O13P | 873.5469 | 0.0094 | [M+Na] ⁺ | | | | |
| 873.5563 | PI(13:0/22:1(13Z)) | PI | 35 | 1 | C44H83O13P | 873.5469 | 0.0094 | [M+Na] ⁺ | | | | |
| 873.5563 | PI(18:0/17:1(9Z)) | PI | 35 | 1 | C44H83O13P | 873.5469 | 0.0094 | [M+Na] ⁺ | | | | |
| 873.5563 | PI(16:1(9Z)/19:0) | PI | 35 | 1 | C44H83O13P | 873.5469 | 0.0094 | [M+Na] ⁺ | | | | |
| 873.5563 | PI(17:0/18:1(9Z)) | PI | 35 | 1 | C44H83O13P | 873.5469 | 0.0094 | [M+Na] ⁺ | | | | |
| 873.5563 | PG(22:6(4Z,7Z,10Z,13Z,16Z,19Z)/20:0) | PG | 42 | 6 | C48H83O10P | 873.5622 | 0.0059 | [M+Na] ⁺ | | | | |
| 873.5563 | PG(22:4(7Z,10Z,13Z,16Z)/20:2(11Z,14Z)) | PG | 42 | 6 | C48H83O10P | 873.5622 | 0.0059 | [M+Na] ⁺ | | | | |
| 873.5563 | PG(22:2(13Z,16Z)/20:4(5Z,8Z,11Z,14Z)) | PG | 42 | 6 | C48H83O10P | 873.5622 | 0.0059 | [M+Na] ⁺ | | | | |
| 873.5563 | PG(22:1(13Z)/20:5(5Z,8Z,11Z,14Z,17Z)) | PG | 42 | 6 | C48H83O10P | 873.5622 | 0.0059 | [M+Na] ⁺ | | | | |
| 873.5563 | PG(20:5(5Z,8Z,11Z,14Z,17Z)/22:1(13Z)) | PG | 42 | 6 | C48H83O10P | 873.5622 | 0.0059 | [M+Na] ⁺ | | | | |

| | | | | | | | | | | | | |
|----------|--|----|----|---|-----------------------------|----------|--------|---------------------|---|--|---|--|
| 873.5563 | PG(20:4(5Z,8Z,11Z,14Z)/22:2(13Z,16Z)) | PG | 42 | 6 | C48H83O10P | 873.5622 | 0.0059 | [M+Na] ⁺ | | | | |
| 873.5563 | PG(20:2(11Z,14Z)/22:4(7Z,10Z,13Z,16Z)) | PG | 42 | 6 | C48H83O10P | 873.5622 | 0.0059 | [M+Na] ⁺ | | | | |
| 873.5563 | PG(20:0/22:6(4Z,7Z,10Z,13Z,16Z,19Z)) | PG | 42 | 6 | C48H83O10P | 873.5622 | 0.0059 | [M+Na] ⁺ | | | | |
| 874.5661 | PS(21:0/20:5(5Z,8Z,11Z,14Z,17Z)) | PS | 41 | 5 | C47H82NO10P | 874.5574 | 0.0087 | [M+Na] ⁺ | + | | + | |
| 874.5661 | PS(20:5(5Z,8Z,11Z,14Z,17Z)/21:0) | PS | 41 | 5 | C47H82NO10P | 874.5574 | 0.0087 | [M+Na] ⁺ | | | | |
| 875.5718 | PI(13:0/22:0) | PI | 35 | 0 | C44H85O13P | 875.5626 | 0.0092 | [M+Na] ⁺ | | | + | |
| 875.5718 | PI(21:0/14:0) | PI | 35 | 0 | C44H85O13P | 875.5626 | 0.0092 | [M+Na] ⁺ | | | | |
| 875.5718 | PI(20:0/15:0) | PI | 35 | 0 | C44H85O13P | 875.5626 | 0.0092 | [M+Na] ⁺ | | | | |
| 875.5718 | PI(19:0/16:0) | PI | 35 | 0 | C44H85O13P | 875.5626 | 0.0092 | [M+Na] ⁺ | | | | |
| 875.5718 | PI(18:0/17:0) | PI | 35 | 0 | C44H85O13P | 875.5626 | 0.0092 | [M+Na] ⁺ | | | | |
| 875.5718 | PI(17:0/18:0) | PI | 35 | 0 | C44H85O13P | 875.5626 | 0.0092 | [M+Na] ⁺ | | | | |
| 875.5718 | PI(16:0/19:0) | PI | 35 | 0 | C44H85O13P | 875.5626 | 0.0092 | [M+Na] ⁺ | | | | |
| 875.5718 | PI(15:0/20:0) | PI | 35 | 0 | C44H85O13P | 875.5626 | 0.0092 | [M+Na] ⁺ | | | | |
| 875.5718 | PI(22:0/13:0) | PI | 35 | 0 | C44H85O13P | 875.5626 | 0.0092 | [M+Na] ⁺ | | | | |
| 875.5718 | PI(14:0/21:0) | PI | 35 | 0 | C44H85O13P | 875.5626 | 0.0092 | [M+Na] ⁺ | | | | |
| 875.5718 | PG(22:4(7Z,10Z,13Z,16Z)/20:1(11Z)) | PG | 42 | 5 | C48H85O10P | 875.5778 | 0.0060 | [M+Na] ⁺ | | | | |
| 875.5718 | PG(22:2(13Z,16Z)/20:3(8Z,11Z,14Z)) | PG | 42 | 5 | C48H85O10P | 875.5778 | 0.0060 | [M+Na] ⁺ | | | | |
| 875.5718 | PG(22:1(13Z)/20:4(5Z,8Z,11Z,14Z)) | PG | 42 | 5 | C48H85O10P | 875.5778 | 0.0060 | [M+Na] ⁺ | | | | |
| 875.5718 | PG(22:0/20:5(5Z,8Z,11Z,14Z,17Z)) | PG | 42 | 5 | C48H85O10P | 875.5778 | 0.0060 | [M+Na] ⁺ | | | | |
| 875.5718 | PG(20:5(5Z,8Z,11Z,14Z,17Z)/22:0) | PG | 42 | 5 | C48H85O10P | 875.5778 | 0.0060 | [M+Na] ⁺ | | | | |
| 875.5718 | PG(20:4(5Z,8Z,11Z,14Z)/22:1(13Z)) | PG | 42 | 5 | C48H85O10P | 875.5778 | 0.0060 | [M+Na] ⁺ | | | | |
| 875.5718 | PG(20:3(8Z,11Z,14Z)/22:2(13Z,16Z)) | PG | 42 | 5 | C48H85O10P | 875.5778 | 0.0060 | [M+Na] ⁺ | | | | |
| 875.5718 | PG(20:1(11Z)/22:4(7Z,10Z,13Z,16Z)) | PG | 42 | 5 | C48H85O10P | 875.5778 | 0.0060 | [M+Na] ⁺ | | | | |

Overall, acetonitrile, ethyl acetate and propanol are all effective single solvent systems to extract the organic molecules here. One possible direction is to employ a mixed solvent system, such as acetonitrile-methanol or chloroform-methanol. These solvent systems have an additional advantage because they are miscible in all proportions. Alternatively, a two-step extraction approach similar to that employed in urine extraction may improve the extraction efficiency. To test this hypothesis, these solvent systems were employed for the extraction of rats' liver tissue. (Figure 5-48 and Figure 5-49)

The positive ion spectra show a distinctive peak at m/z 184.07 and 198.09 corresponds to $[\text{C}_5\text{H}_{15}\text{NPO}_4]^+$ and $[\text{C}_6\text{H}_{17}\text{NPO}_4]^+$, and a number of peaks in the region m/z 600-900. As discussed before, these ions are likely headgroup fragment ion and parent ions (sodium adducts) of phosphatidylcholines.

The negative ion spectra also show a number of distinct peaks in the region m/z 400 - 1000. While an ion at m/z 514 was detected in the negative ion spectra of the acetonitrile-methanol liver extracts, a different set of ions was observed from the negative spectrum of the chloroform-methanol extract.

However, while mass spectrometric profiles were successfully generated, an immediate challenge was a relatively small sample size. A comprehensive comparison between extraction methods could not be accomplished.

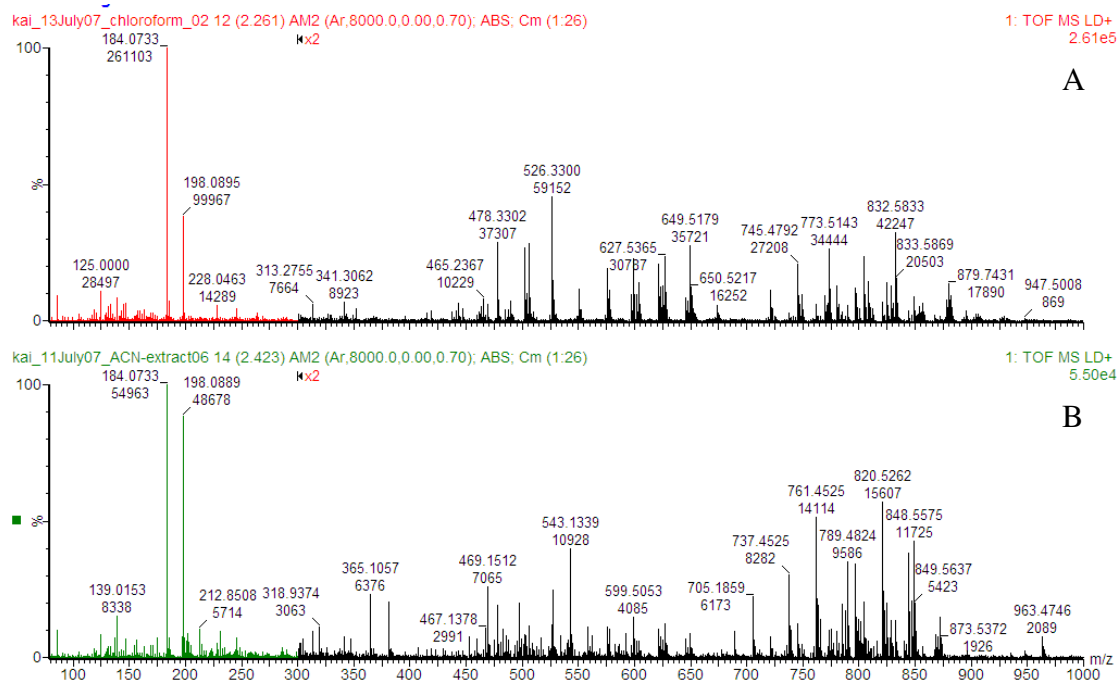


Figure 5-48 Positive ion DIOS mass spectra of 1:4 (A) methanol/chloroform and (B) methanol/acetonitrile rats' liver tissue extracts. Data was acquired with 120s spiral scan. Laser setting was 230. Raw spectra were centroid and processed with adaptive background subtraction. Region between m/z 300 to 1000 was magnified two times.

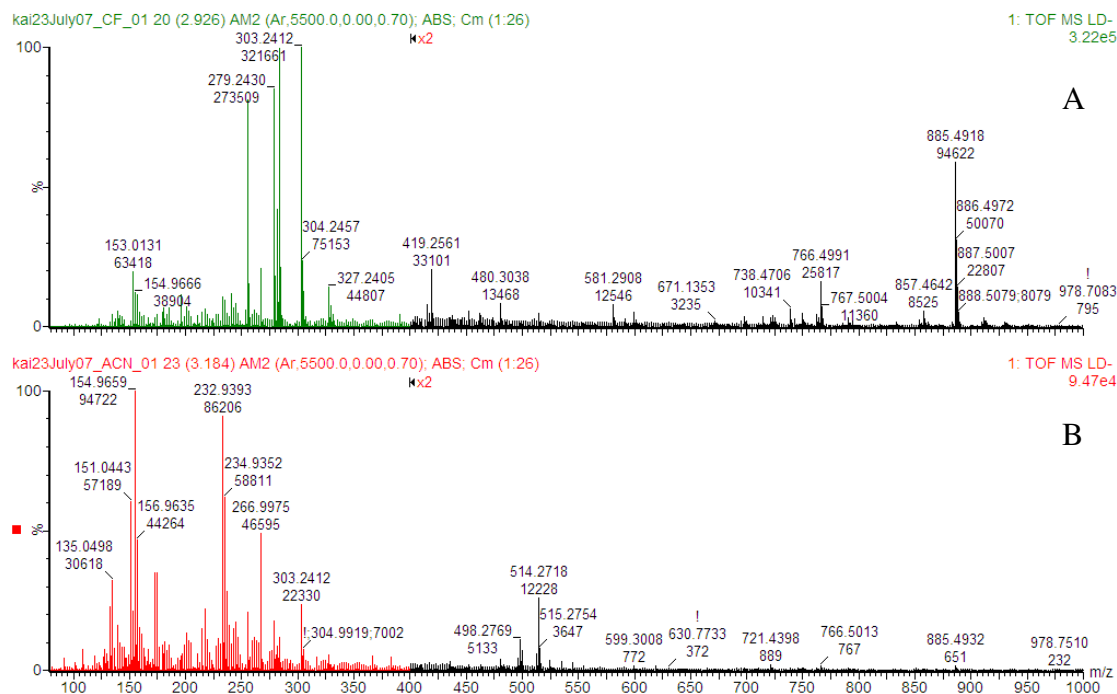


Figure 5-49 Negative ion DIOS mass spectra of 1:4 (A) methanol/chloroform and (B) methanol/acetonitrile rats' liver tissue extracts. Data was acquired with 120s spiral scan. Laser setting was 200. Raw spectra were centroid and processed with adaptive background subtraction. Region between m/z 400 to 1000 was magnified two times.

5.3.7 Detection of Quorum Sensing Signalling Molecules

Before analysis of the bacterial samples from *P. aeruginosa*, it is worthwhile to determine if the bacterial secondary metabolites or other exoproducts can be detected by the technique, as an essential post-experimental validation step to confirm the identity of unknown ions. The QSSMs were of most interest and had been a subject of research efforts in our laboratory. These molecules were thus available. The experiment was carried out in parallel with metabolite profiling of bacterial extracts but is presented here for the ease of subsequent discussion.

The DIOS spectral responses of N-acyl-L-homoserine lactones (AHL), N-(3-oxoacyl)-L-homoserine lactones (3-oxo-HSL), and N-(3-hydroxyacyl)-L-homoserine lactones (3-hydroxyl-HSL) were first investigated under both positive and negative ion mode. These molecules have been well characterised in our laboratory by LC-ESI couple to hybrid quadrupole linear ion trap mass spectrometer strictly under positive ion mode,⁶⁰ and the reference compounds were as provided in solution. However, the ionic species detected by DIOS may be, and in fact are, very different from those obtained by ESI. Under positive ion mode, these molecules were detected as salt adduct, rather than protonated species. (Figure 5-50) Nevertheless, C₈-AHL and 3-oxo-C₈-HSL were detected as deprotonated ions in negative ion mode, but was not for 3-hydroxyl-C₈-HSL. (Figure 5-51) As an additional note, though the as-provided reference solutions were intended for the use for HPLC, they had not been prepared to the standard ideally for DIOS and contained impurities or had degradation products. These problems were well tolerated.

Another intriguing aspect is the ionisation efficiency with respect to the acyl chain length. Previously, our group has reported that the relative response factor (RRF) of 3-oxo-HSLs increases with respect to the chain length.⁶⁰ This is believed to be the surface activity of the molecules (over the surface of droplets) as well as their volatility influencing the ionisation efficiency in ESI-MS. In DIOS, the ionisation efficiency of 3-hydroxyl-HSLs varies non-linearly with respect to the chain length. (Figure 5-52) 3-hydroxyl-C₄-HSL was detected as [M+H]⁺.

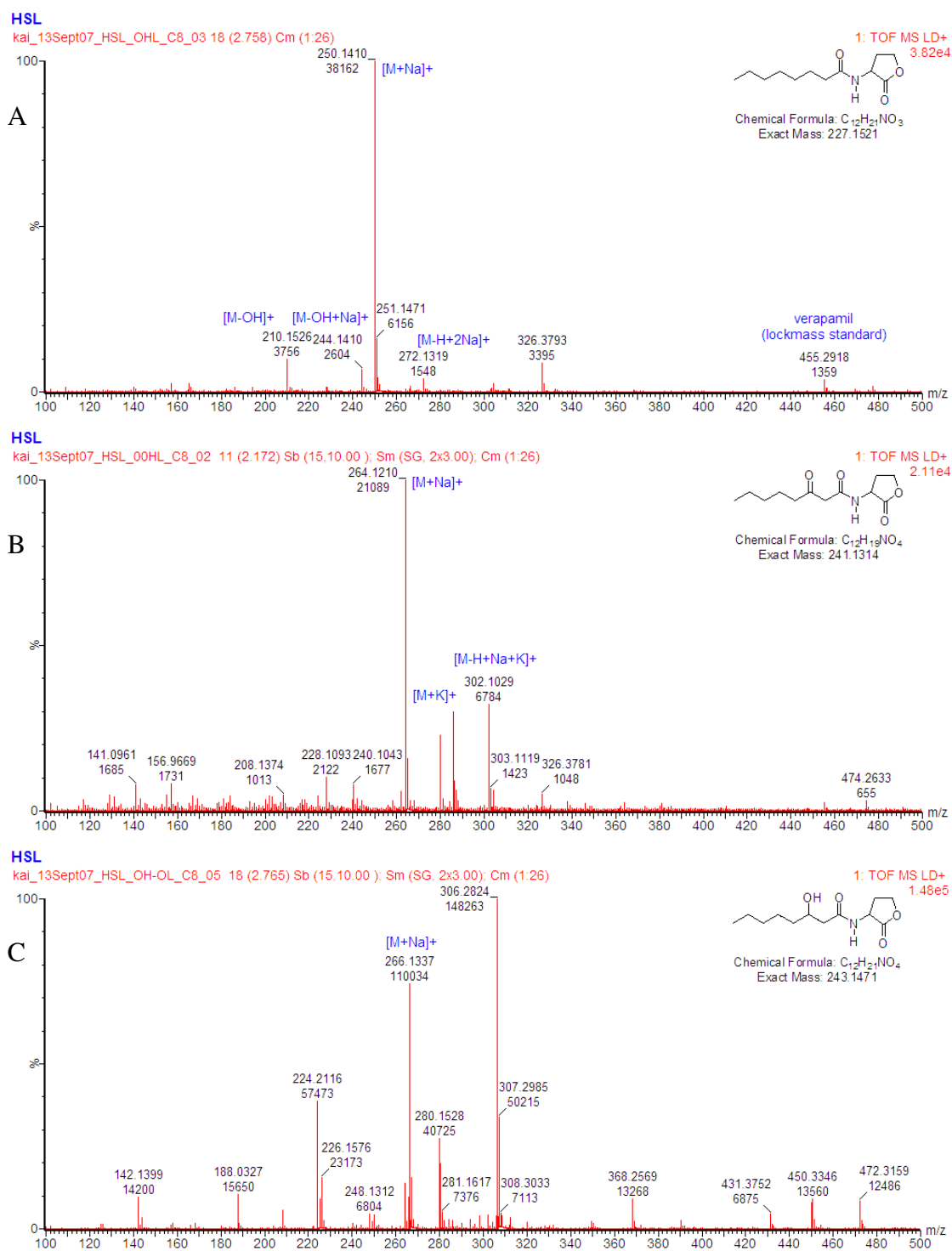


Figure 5-50 Positive ion DIOS mass spectra of (A) C₈-AHL, (B) 3-oxo-C₈-HSL and (C) 3-hydroxyl-C₈-HSL. The spectra are dominated by their [M+Na]⁺ ions. The ions located at *m/z* 306 and 224 in 3-hydroxyl-C₈-HSL spectrum are unknown contaminants from the sample. Inserts displace their structural and chemical formulae. Spectra were acquired by 120s spiral scan at laser setting 210.

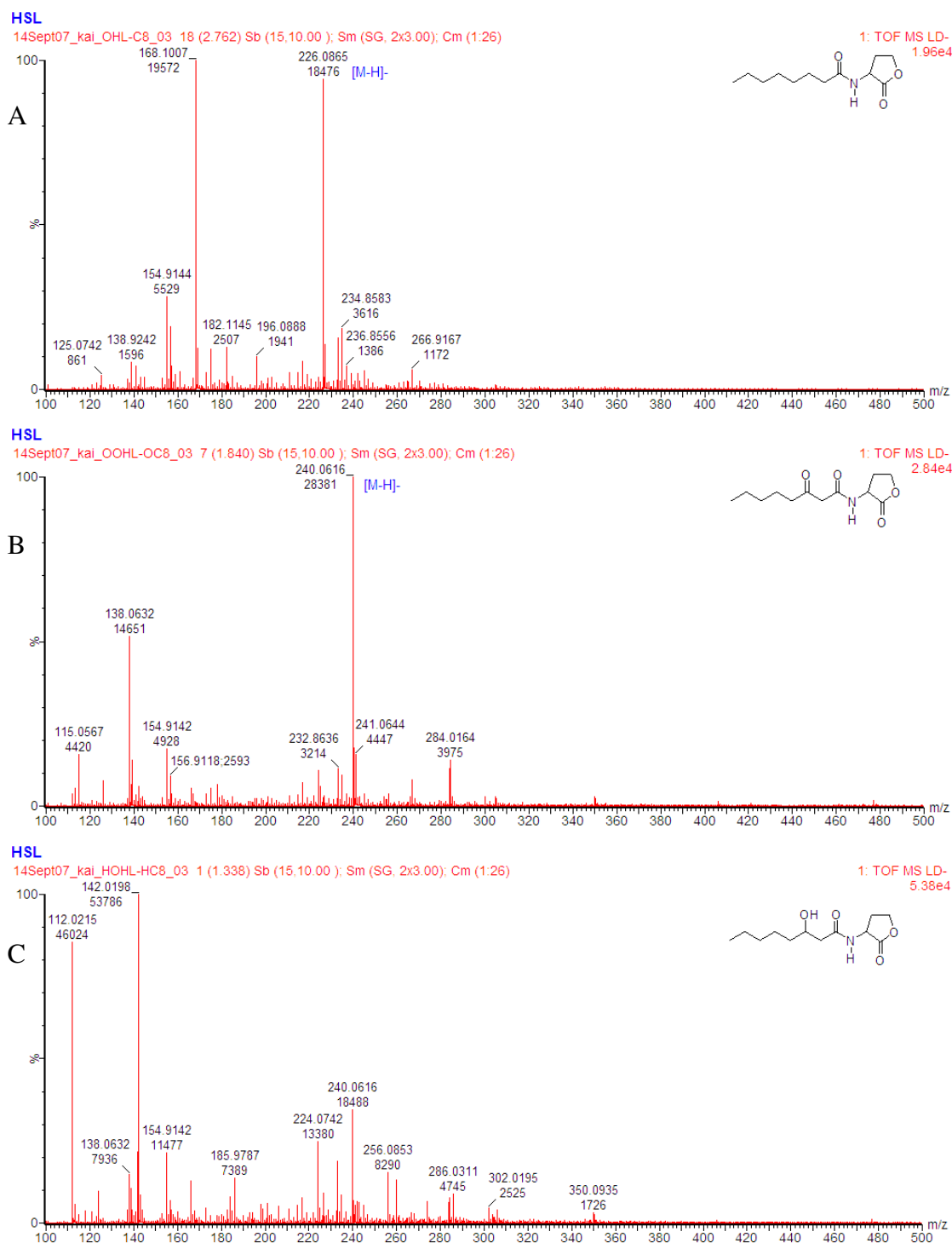


Figure 5-51 Negative ion DIOS mass spectra of (A) C₈-AHL, (B) 3-oxo-C₈-HSL and (C) 3-hydroxyl-C₈-HSL. The spectra of C₈-HSL and 3-oxo-C₈-HSL are dominated by their [M-H]⁻ ions. Ion peaks located at *m/z* 168 and 138 are unknown, which could be contaminants or degradation products. The deprotonated species of 3-hydroxyl-C₈-HSL is not seen, but the spectrum is dominated by ions located at *m/z* 122 and 142, which are contaminants from the sample. Inserts displace their structural formulae. Spectra were acquired by 120s spiral scan at laser setting 210.

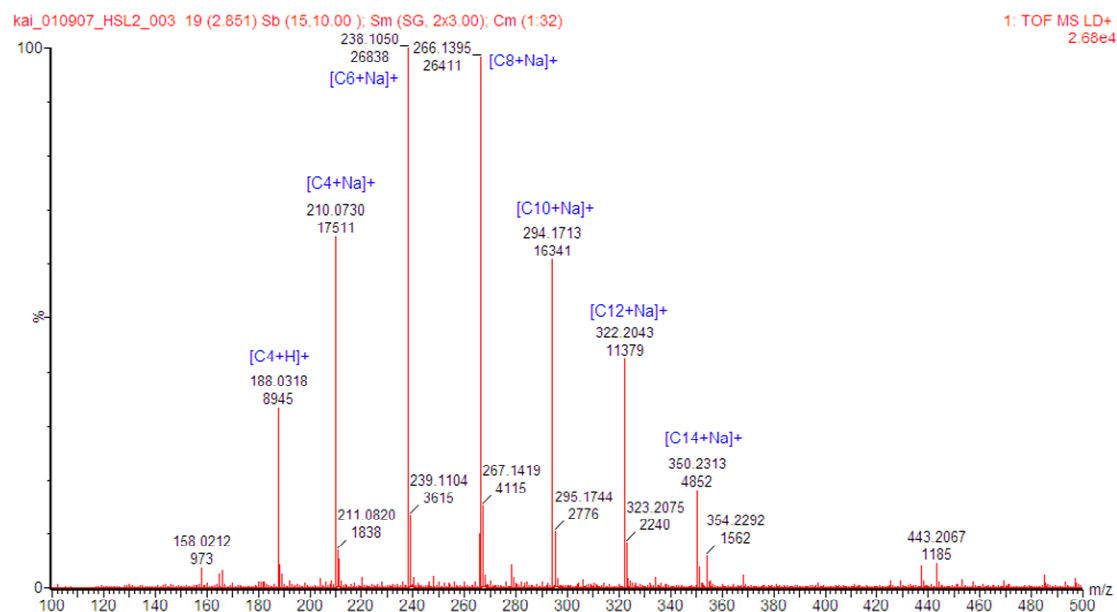


Figure 5-52 Positive ion DIOS mass spectrum of a mixture of equal molar 3-hydroxyl HSLs. The alkyl chain length of HSLs varies from C4 to C14. Ions detected are sodium adducts. Data was acquired with 120s spiral scan at laser setting 220.

Alkyl quinolones (AQSs) and 4-hydroxy-2-alkylquinolines (HAQs) have also been analysed. These molecules include 4-hydroxy-2-heptylquinoline (HHQ), 4-hydroxy-2-nonylquinoline (HNQ) and 3,4-dihydroxy-2-heptylquinoline (PQS). In chapter 3, section 3.4.3, the possibility of detecting AQSs by SALDI and non-etched silicon surface was briefly discussed. Hydroxy-quinolones have many interesting chemical properties. These molecules are hydrophobic. The hydroxyl group is dynamically interchanging to and from enone. Dihydroxy-quinolones have a high affinity to metallic ions (ligands). The aromatic heterocyclic system is also UV absorbing. These chemical properties make AQSs and HAQs among one of the most sensitive analytes to the matrix-free LDI platform. The spectra of AQSs and HAQs acquired under positive and negative ion mode are shown in Figure 5-53 and Figure 5-54. Protonated and deprotonated molecular ions were detected under positive and negative ion mode, respectively.

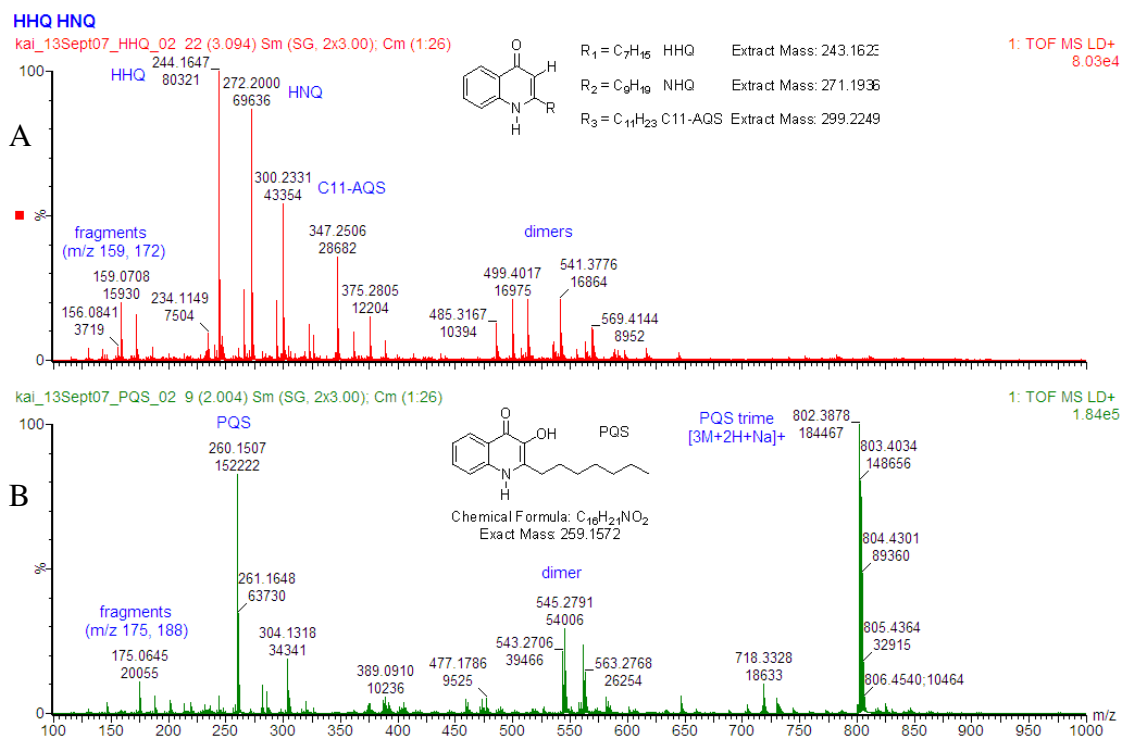


Figure 5-53 Positive ion DIOS mass spectra of (A) a mixture of AQSs and (B) PQS. The molecules are detected as $[M+H]^+$, dimers and trimers. Data was acquired with 120s spiral scan at laser setting 210.

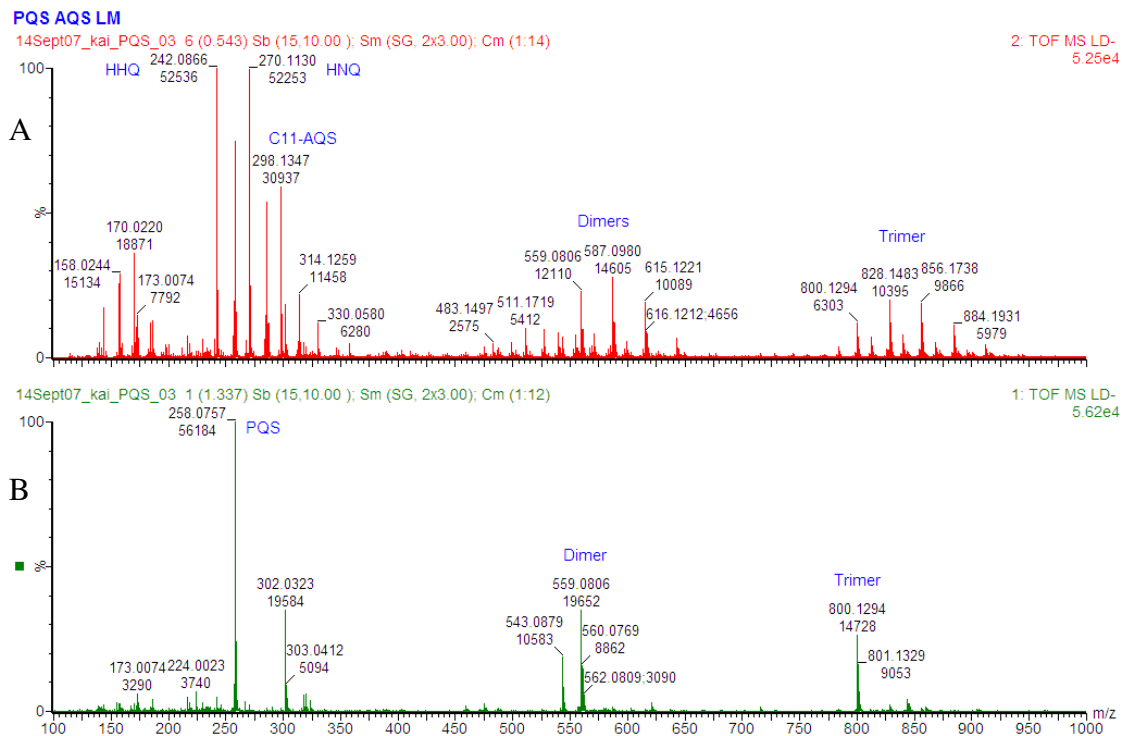


Figure 5-54 Negative ion DIOS mass spectra of (A) a mixture of AQS and HAQs and (B) PQS. The molecules are detected as $[M-H]^-$, dimers and trimers. Data was acquired with 60s spiral scan at laser setting 210.

5.3.8 Metabolite Profiling of *Pseudomonas aeruginosa*

The investigation of *Pseudomonas* exoproducts was not achieved without much difficulty. The initial attempt was complicated with the presence of antifoam (synthetic polymer molecules) in the sample, even through their concentration might be low. (Figure 5-55) While the addition of antifoam was necessary for bacterial culturing by fermentor and believed would not affect the growth of the *Pseudomonas*, the presence of the synthetic polymer obscured the mass spectra or suppressed the ion formation of other small molecules or metabolites. This problem also affected the analysis by ESI-MS in our laboratory. Subsequent investigations of the medium were therefore strictly on the sample without antifoam.

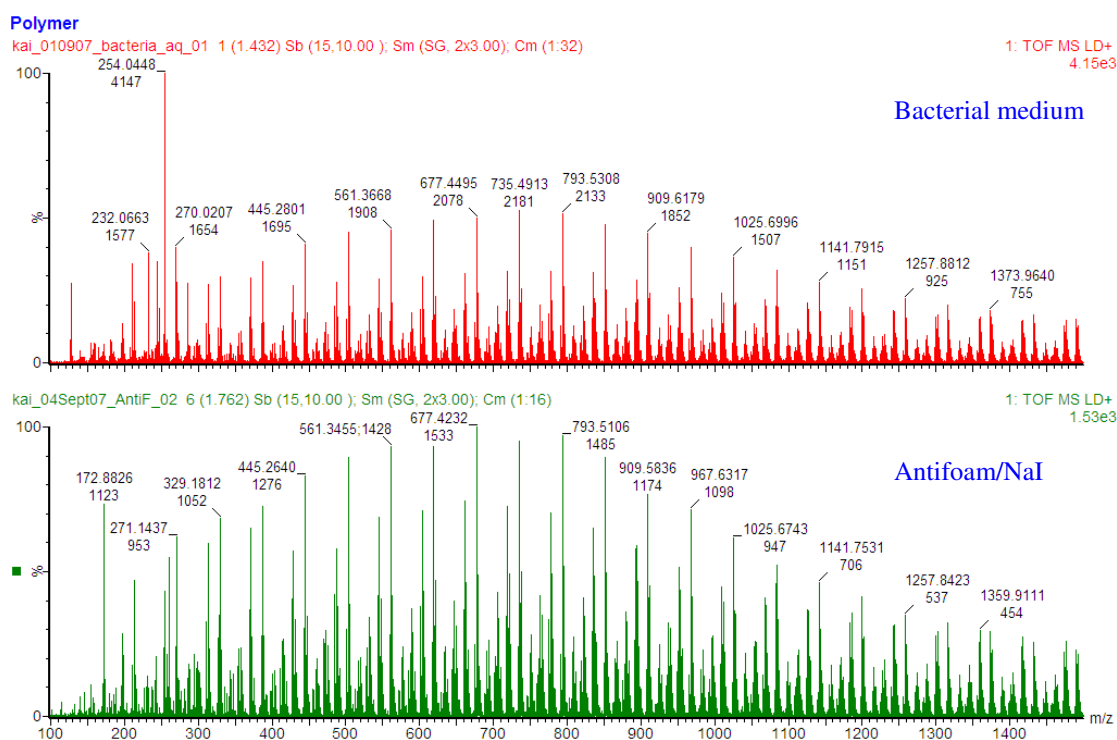


Figure 5-55 Positive ion DIOS mass spectra of bacterial medium and antifoam/NaI mixture.

Once the antifoam was removed, DIOS mass spectra of the bacterial media were successfully acquired. Positive ion spectra of the bacterial culture medium and feeding medium are shown at Figure 5-56 and Figure 5-57, respectively. The feeding medium was used as a control here. Spectra were successfully acquired on the as-received culture medium with no sample preparation. Enhancements were achieved

with a suitable extraction approach ensuring that the extraction recovery was high. As shown in the spectra, many secretory products of the *Pseudomonas* were detected from the culture medium. The ions detected were either absent or of low intensity from the control. Data was also acquired in negative ion mode. (Figure 5-58 and Figure 5-59) The major differences of the spectra of culture medium from the control were the ions m/z 180, 224, 663 and 900, while ions of m/z 208, 438 and 647 were common between them. Identification of these ions was difficult. However, AHLs were not seemingly detected in the spectra.

On the other hand, the bacterial cell pellets were not affected much by the antifoam because of the PBS washing procedure and the antifoam was thus removed. Mass spectra were successfully acquired in both positive and negative ion mode. (Figure 5-60 and Figure 5-61) AQSs and HAQs, such as HHQ, NHQ, and PQS, were detected. Lipids were not seen in the spectra. The bacterial samples used were harvested from the bioreactor at the same time and were cultured with addition of antifoam to the bioreactor. On inspecting the positive mass spectra of the extracts prepared either by chloroform/methanol or by chloroform/butanol, the pattern of detected ions is identical but differs only by the ion intensity. This was further confirmed by PCA. The differences between the negative spectra were obvious in the mass region m/z 500-900.

Another observation was possibly related to the dynamic of a biochemical system. The procedures were repeated on another set of bacterial cells pellet received. One of the samples was cultured without antifoam (denoted by -AF). Antifoam was added to the bioreactor subsequently and another set of bacterial cells was harvested (denoted by +AF). The -AF sample was extracted with chloroform/butanol and +AF with chloroform/methanol as shown in Figure 5-14B. The spectra are shown in Figure 5-62. The spectra produced by two methods did not contain the same set of ions and the ion pattern looked very different from that of Figure 5-60 and Figure 5-61. For example, while phospholipids (m/z 700-850) and an associated fragment ion at m/z 184 were not seen in Figure 5-60, these ions are detected in Figure 5-62 A and B. The data was also imported to SIMCA for further data analysis.

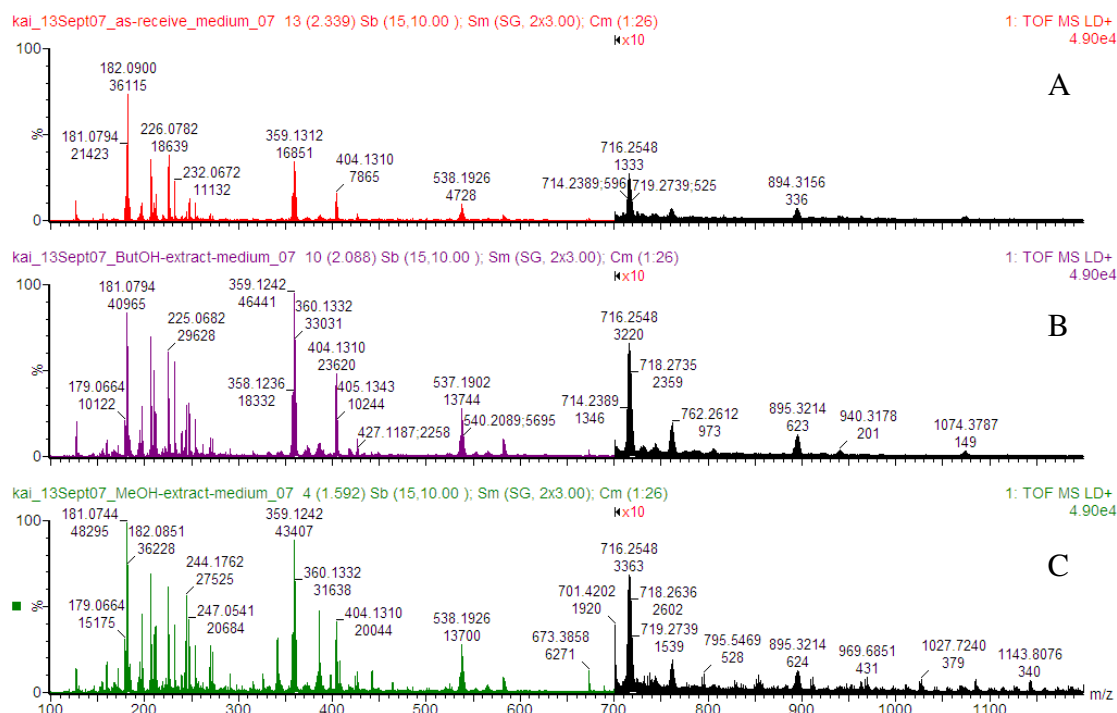


Figure 5-56 Positive ion DIOS mass spectra of bacterial culturing medium. (A) As-received (no sample preparation), (B) ETA-chloroform/butanol extract, and (C) ETA-chloroform/methanol extract. The spectra are presented in the same vertical scale. Region of m/z 700-1200 is magnified by 10 times. Data was acquired by 120s spiral scan at laser setting 220.

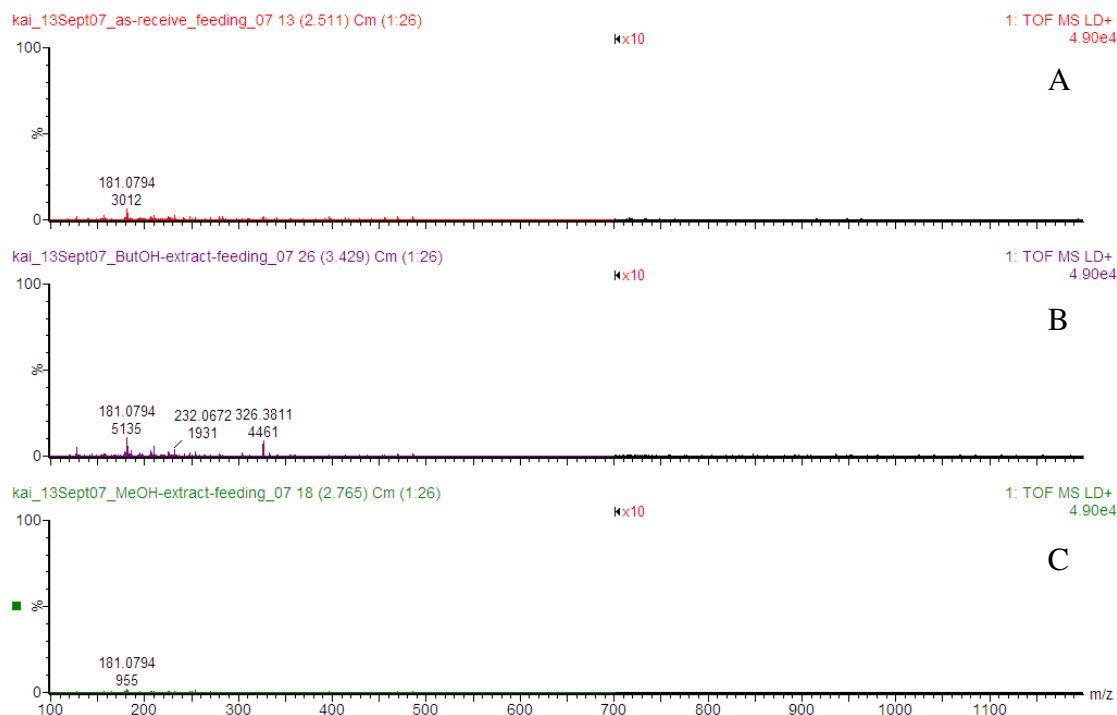


Figure 5-57 Positive ion DIOS mass spectra of bacterial feeding medium (control). (A) As-received (no sample preparation), (B) ETA-chloroform/butanol extract and (C) ETA-chloroform/methanol extract. The spectra are presented in the same vertical scale as in Figure 5-56. Data was acquired by 120s spiral scan at laser setting 220.

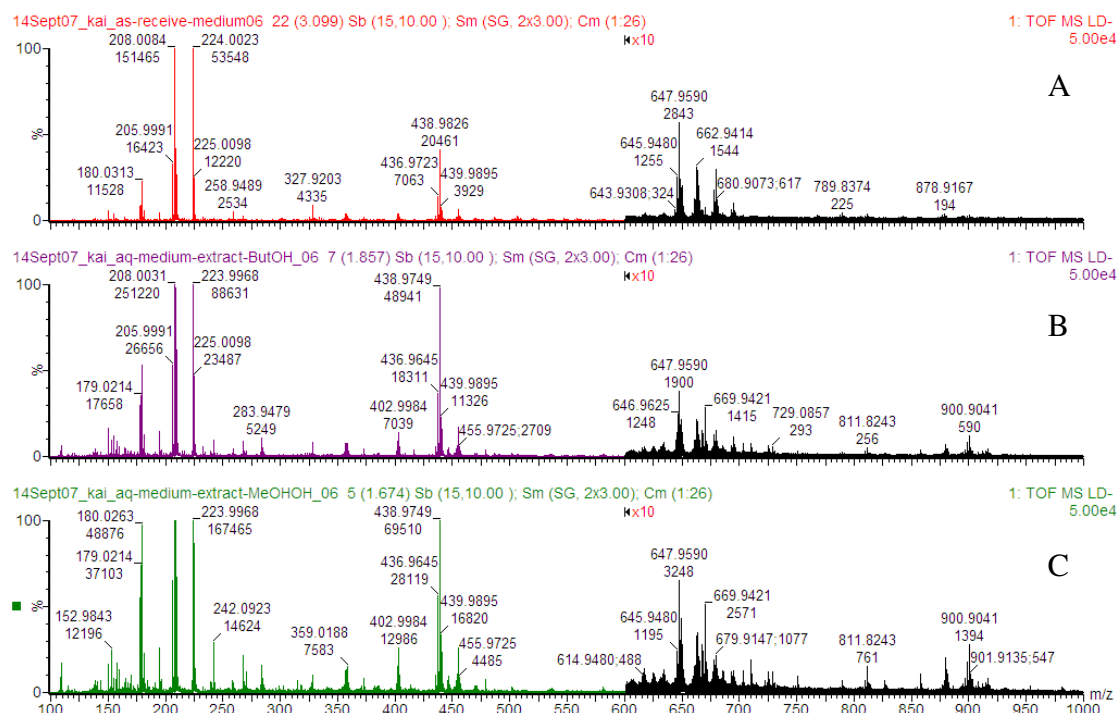


Figure 5-58 Negative ion DIOS mass spectra of bacterial culturing medium. (A) As-received (no sample preparation), (B) ETA-chloroform/butanol extract and (C) ETA-chloroform/methanol extract. The spectra are presented in the same vertical scale. Region of m/z 600-1000 is magnified by 10 times. Data was acquired by 120s spiral scan at laser setting 210.

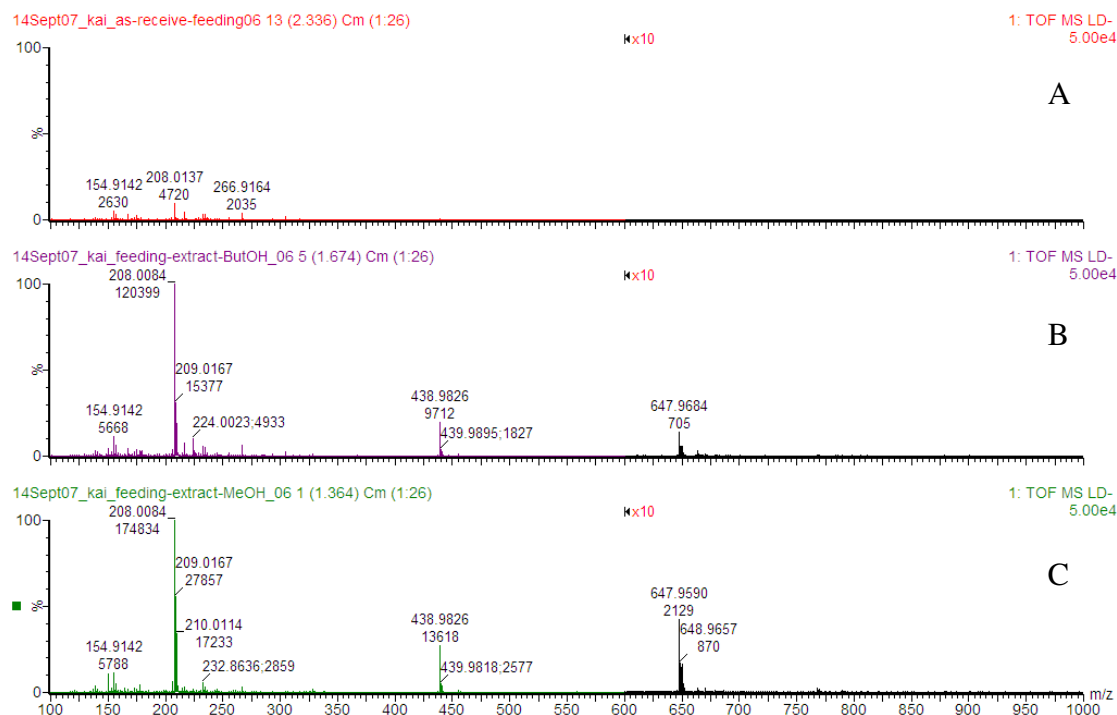


Figure 5-59 Negative ion DIOS mass spectra of bacterial feeding media. (A) As-received (no sample preparation), (B) ETA-chloroform/butanol extract and (C) ETA-chloroform/methanol extract. The spectra are presented in the same vertical scale as in Figure 5-58. Data was acquired by 120s spiral scan at laser setting 210.

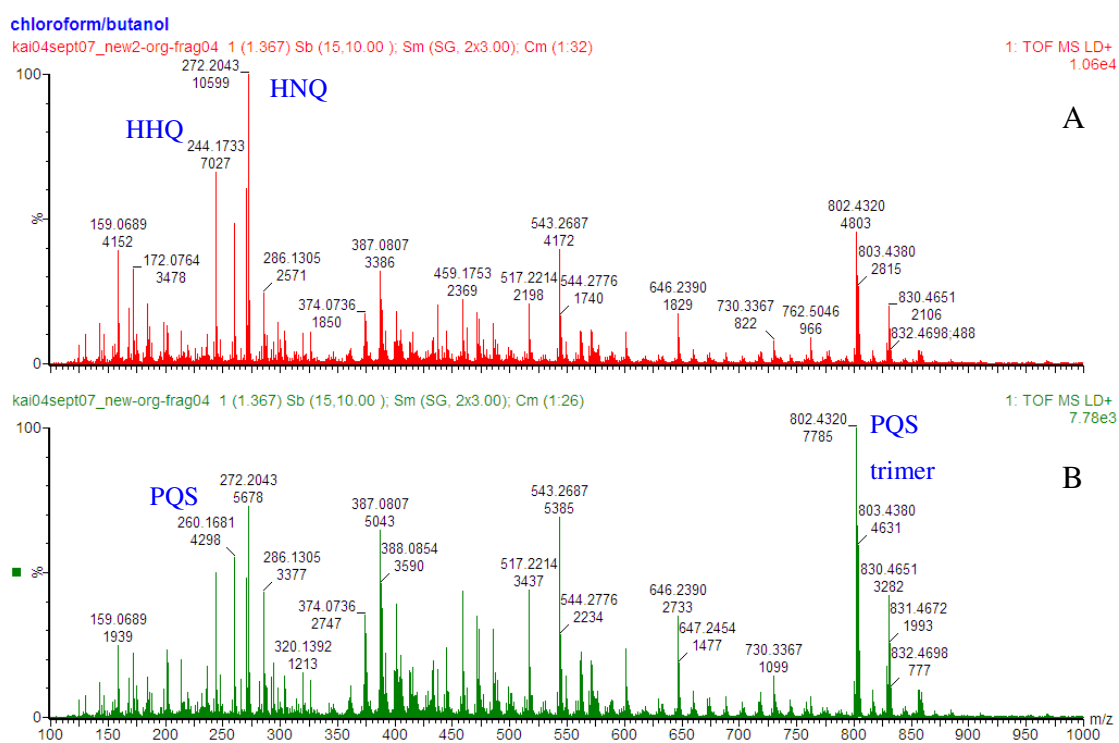


Figure 5-60 Positive ion DIOS mass spectra of *P. aeruginosa* bacterial cell pellets extracts: (A) chloroform/methanol and (B) chloroform/butanol. The spectra were acquired with 120s spiral scan at laser setting 220.

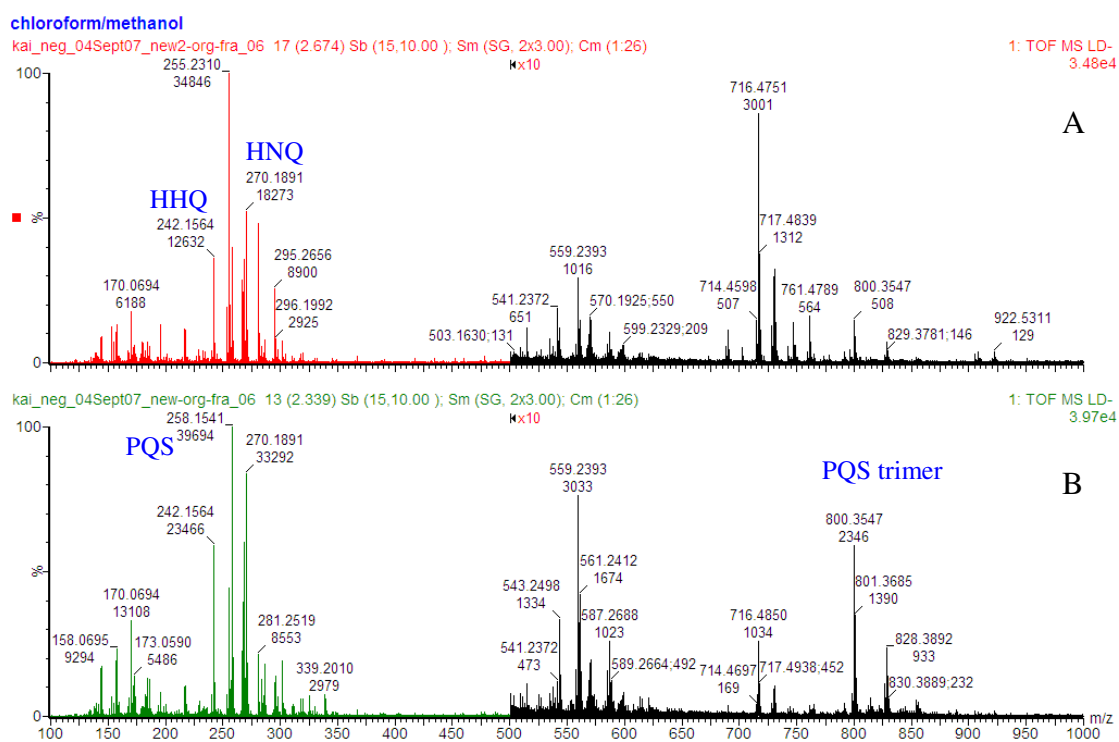


Figure 5-61 Negative ion DIOS mass spectra of *P. aeruginosa* bacterial cell pellets extracts: (A) chloroform/methanol and (B) chloroform/butanol. The spectra were acquired with 120s spiral scan at laser setting 230. The mass region m/z 500-1000 was magnified by 10 times.

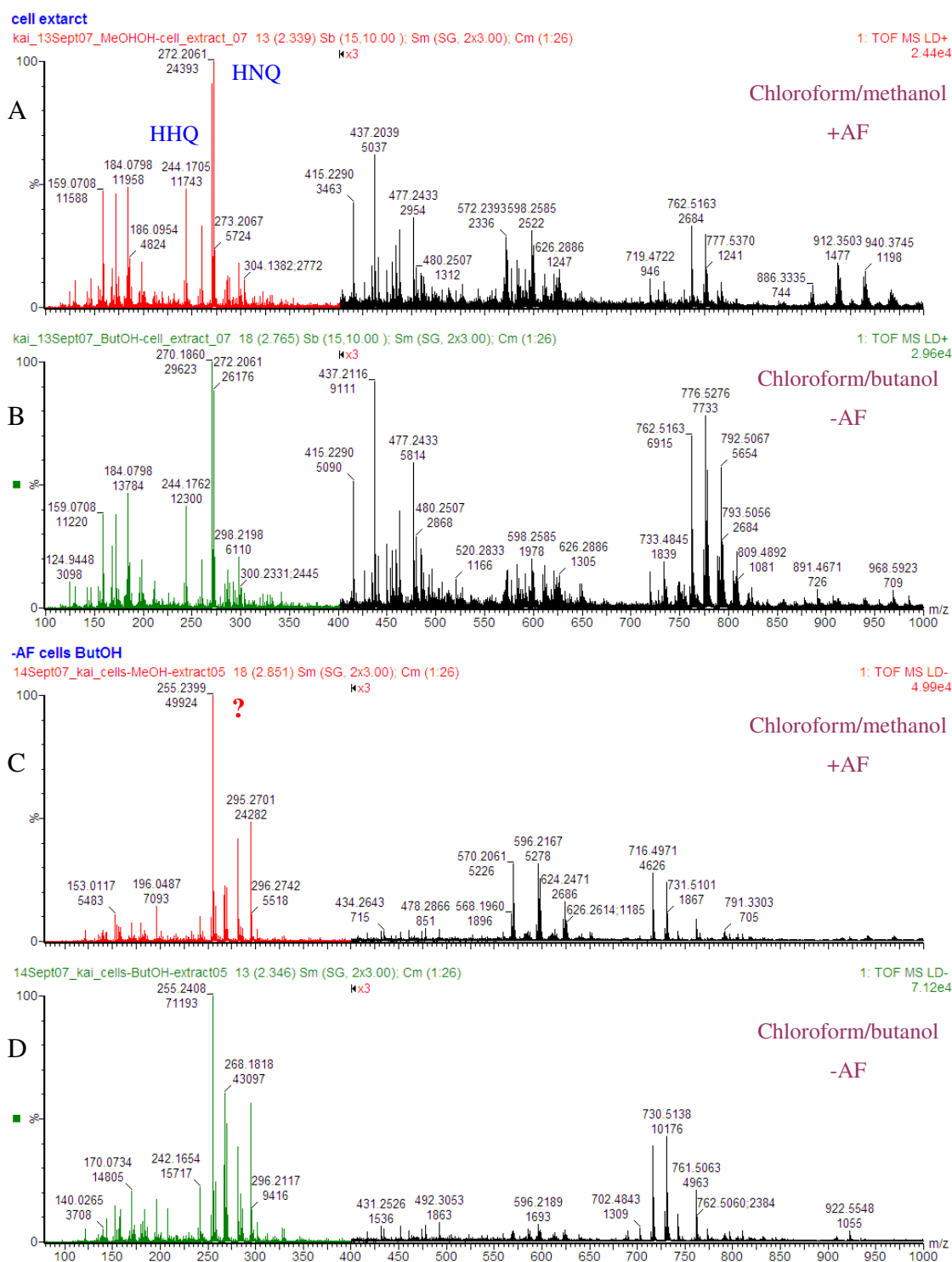


Figure 5-62 Positive and negative ion DIOS mass spectra of *P. aeruginosa* bacterial cell pellets extracts: (A) and (C) chloroform/methanol, and (B) and (D) chloroform/butanol. The bacterial cell pellet used for chloroform/butanol was cultured without addition of antifoam to the bioreactor whereas the cell pellet for chloroform/methanol was cultured with addition of antifoam and was harvested a day later. The spectra were acquired with 120s spiral scan at laser setting 220 and 210 for positive and negative ion mode, respectively.

Another major difference between the second set of bacterial cells and the first set of samples was the absence of molecular ion peaks corresponding to PQS [m/z 260 (positive) and m/z 258 (negative)] and its trimer [m/z 802 (positive) and m/z 800 (negative)]. Whether it was because of the harvesting time (*i.e.* exponential phase or stationary phase of the bacterium), or the presence or absence of antifoam, or any other environmental effects, it could not be determined at this stage. It is merely a speculation that at the time of harvesting, the bacterium had not reached to a point or density that the production of PQS was induced, while the production of HHQ and HNQ was still at early stage. (See Figure 5-12)

5.4 Summary and Remarks

5.4.1 Method Validation

Analytical validation is a routine procedure to ensure the performance of an instrument and the method employed is up to its specification and suitable for its applications. A control framework may be considered irksome and unnecessary by some analytical chemists. However, the successful deployment of a method or procedure relies heavily on a consistent and understandable approach.

Unfortunately, the consistency of the method was less than ideal and our results reconfirmed to those reported previously. There was point-to-point, well-to-well and target-to-target variation. RSD from approximately 10% to 90% were observed. There was no exception to MALDI Q-ToF comparing to MALDI-ToF. There were two major contributors to the poor precision obtained: one was the use of pipettes led to non-uniform distribution of the analyte over the surface and is a common problem in MALDI sample preparation. Secondly, the method was also affected by the matrix effects as shown in the detection characteristic. This was an inevitable consequence in the absence of a separation step, as in other high throughput approaches such as NMR and DiMS.⁶³

The traditional method of MALDI and DIOS sample preparation involves direct deposition of a sample droplet onto a sample well. The sample is then allowed to dry before analysis. While this method is fast and effective, there is a compromise in signal reproducibility due to non-uniform spatial distribution of the crystallised sample throughout the spot. An alternative approach, such as ESD, may produce more reproducible signal intensity.

Evaluation of the analytical performance of method or system suitability was carried out based on the bottom-up validation approach. The bottom-up approach stresses on building up from the foundations, rather like a *Lego* model. These *Lego* bricks are equivalent to the individual modules in any measurement system. Each brick is qualified or confirmed as suitable for use before the next layer is built. In this way, the integrity of the method is assured all the way to the top-most layer.¹⁴ Judgement is then made based on combining these individual modules. The modules involved in this investigation included the detection characteristics of the technique, evaluation of suitable sample preparation protocols, assessment on data or profiles generated, and the possibility of MVDA, identification of unknown metabolites, *etc.* In its essence, the ICH approaches can be considered a bottom-up approach. However, the conventional parameters were designed for quantitation and were not entirely suitable in the given circumstances. The technique is proven suitable for qualitative applications and it can be seen that the matrix-free LDI approach is promising for global metabolite profiling. However, in the current form of the technique, there is still a long development cycle required to make the technique reliable for the conventional metabolomic approaches, where experimental reproducibility and quantification of metabolites is critical.

5.4.2 Metabolite Profiling of Biological Matrices

A range of complex biological matrices, including human blood plasma extract, human urine extracts, animal liver tissue extracts and bacterial extracts were employed. Other types of sample such as plant leaves and rat brain had also been used, but the results were not included in this chapter. Metabolite profiles were successfully generated and a series of experiments ensured that global profiling was not an

exceptional case to a particular type of biological mixture, but a general capability of the technique and could be applied to a wide range of biological matrices. Certainly, the metabolite coverage is strongly dependent on the sample preparation step and the sample source or type. Still, the DIOS technique inherits the robustness of the MALDI technique and the time needed for method development was significantly reduced.

Investigation of urine was complicated by the large quantity of salt present in the sample. Even though mass spectra could be acquired, the metabolites converge and the sensitivity was poor. Nevertheless, a relatively simple liquid-liquid extraction procedure successfully extracted the organic molecules from the sample. Compared to NMR, which is employed for clinical metabolite profiling of urine^{64, 65} it does not require any sample preparation or a desalting procedure and addition of ionic buffer such as Na_2HPO_4 does not suppress signal intensity. NMR can therefore detect many water-soluble metabolites, such as urea, citrate, hippurate, and acetate, *etc.*, many of which may not even be amendable by DIOS. Compare with LC-MS method, online extraction with a trap column is still more efficient than liquid-liquid extraction though the most hydrophilic compounds will be lost in the washing step. Relatively, urine profiling by DIOS-MS is not as powerful and versatile as NMR and LC-MS, and the extraction procedure necessary has limited the number of metabolites to be detected or limited the method selectively for the hydrophobic compounds.

A metabolite database search was carried out based on the accurate mass of the ions detected and that gave the possible identity of the metabolites detected in the urine extract. Limitations of this approach are that the identity of the ions detected is still unconfirmed, the proposed identity of the metabolites is an educated guess based on the nature of the sample and a large proportion of ions detected do not even return a possible match, because many metabolites are still unknown, or are not available from the database employed. Ions detected may also be fragment ions, or adducts other than sodium or potassium (*e.g.* acetate), *etc.*

The DIOS spectra of blood plasma were information rich. The spectral quality and metabolite coverage was comparable to or might even exceed that acquired by DiMS.⁶⁶ Similarly, the most prominent molecules detected by DIOS-MS from the plasma extract were lipids and steroids. Phospholipids are a known biomarker for

diseases such as certain type of cancers and polycystic ovary syndrome. Indeed, lipids are among one the most sensitive compounds amendable by the DIOS technique and blood plasma is also possibly one the most suitable biological matrices for DIOS-MS.

Liver tissue required a relatively more complicated sample preparation procedure to extract the biomolecules from the tissue. Liver tissue normally stores a large blood volume, as it is one of the functions of the liver. Removal of the blood ensured successful analysis. While the liver tissue from lambs does not sufficiently meet the criteria of metabolomic standards, further investigation was therefore carried out on rats' liver tissue. Despite the use of rats' liver tissue deeming that the investigation adhere to the standards for mammalian/in vivo experiments,⁵⁹ there was an experimental limitation using tissue obtained from small laboratory animals - a relatively small sample size. The small size of the sample and the blood retained by the tissue presented a challenge in the investigation.

A database search using both the Metline and LipidBank database was carried out on the lambs' livers extracts. While the Metalin database returned a certain number of matches, the database did not contain the specific or specialised information about lipid and glycerol molecules as much the LipidBank database.

The metabolite profiling of the *P. aeruginosa* culture medium was initially complicated by the antifoam (a synthetic polymer) present in the culture medium. Other than the synthetic polymer itself, no metabolite was detected. It may be worth stressing that synthetic polymers are actually effectively detected by the DIOS approach and is an aspect of the technique receiving a great deal of attention recently.⁶⁷⁻⁷² However, with the throughput of the method, this problem was quickly ratified. Once the polymer was removed, mass spectrometric profiles of the bacterial exoproducts were obtained successfully. The DIOS mass spectra of the medium extracts contain a range of exoproducts. Then again, pathogenesis mediated signalling molecules AHLs or the iron salvager molecules such as pyocyanin were not seen in the spectra, though the detection of the standard compounds of AHLs was possible. Since AHLs were not even detected in as-received medium, this would not be because of the extraction method employed, but more likely due to their concentration present in the sample and/or their relatively low sensitivity in DIOS. Their signals could also

be suppressed due to the matrix effect. The most interesting finding was the detection of the QSSMs, AQSs and PQS, in the cell pellets.

5.4.3 Principle Component Analysis

A method was developed to transform the spectral data into a format that can be imported into SIMCA and the interpretation of the spectra was aided with PCA. By combining normalisation to TIC, mean centring and Pareto scaling, the dataset could be corrected and fit for PCA. Concurring with Vaidyanathan, *et al.* the precision of the data was best determined by PCA.⁵⁷ Concurrently, we may need to note that the relatively poor precision does not prevent the application of MVDA to MALDI proteomics and imaging data.⁷³ The measurement of the precision of the ion signal seemed irrelevant, and perhaps the relatively poor signal precision is a limitation of the technique we need to recognise. Perhaps to make sense of the observations so far, we need to be aware that the measurement of precision is an approximation to the absolute value of reproducibility of an analytical method. PCA plots the spectral profiles into a multi-dimensional space. The datasets are then evaluated in terms of the overall pattern or structure of the data, *i.e.* the presence or absence of ion peaks, and the significance or the weighting of an ion peak is determined statistically with respect to the mean value. The absolute value of ion peak intensity becomes less important here but the differences of the datasets are thus signified by their relativity.

5.5 Conclusions and Future Work

DIOS-MS has a number of advantages over other metabolomic tools, such as throughput and sensitivity and is very capable of analysing complex biological matrices. The interpretation of the spectra can be aided by PCA. Its advantage is also its drawback; there is no prior separation step in segregating individual molecules from a complex mixture. Although coupling to LC may be possible, this will also come with a price in reducing the data throughput. Detailed analysis has to be relied on the conventional approaches. Its strength lies in the situations where the speed and/or data throughput is the top priority as opposed to the cost.

A number of complex biological matrices have been analysed and they demonstrated the capability of the method. The question of reproducibility is vital in making the DIOS method not only suitable for quantitation but also able to distinguish the subtle differences between classes of samples, such as samples collected from the patients and the controls, or to distinguish the mutants from the wild type. The analytical variability is larger than the acceptable value for quantitation (maximum RSD 11% for 1 ppm), albeit the values of RSD calculated are usually less than 50%. This is contributed to the heterogeneous sample distribution related to pipette sample deposition. It is proposed that a better method is required in the future studies.

The matrix-free LDI platform is still in an early stage of development and the potential of DIOS in biomedical applications is waiting to be discovered. In a limited time, we have made so many steps towards this objective. The results have been promising. However, to make the DIOS technique a proven method, a lot of work is still required and is the future work proposed here.

5.6 References

1. Orešič, M., Vidal-Puig, A. & Hänninen, V. Metabolomic approaches to phenotype characterization and applications to complex diseases. *Expert Rev. Mol. Diagn.* 6, 575-585 (2006).
2. Goodacre, R., Vaidyanathan, S., Dunn, W. B., Harrigan, G. G. & Kell, D. B. Metabolomics by numbers: acquiring and understanding global metabolite data. *Trends Biotechnol.* 22, 245-252 (2004).
3. Saghatelian, A., Trauger, S. A., Want, E. J., Hawkins, E. G., Siuzdak, G. & Cravatt, B. F. Assignment of Endogenous Substrates to Enzymes by Global Metabolite Profiling. *Biochemistry* 43, 14332-14339 (2004).
4. Lindon, J. C., Holmes, E. & Nicholson, J. K. in *Metabonomics in Toxicity Assessment* (eds. Robertson, D. G. & Lindon, J.) 1-26 (Taylor & Francis, Boca Raton, Fla, 2005).
5. Waters, N. J., Holmes, E., Williams, A., Waterfield, C. J., Farrant, R. D. & Nicholson, J. K. NMR and Pattern Recognition Studies on the Time-Related Metabolic Effects of α -Naphthylisothiocyanate on Liver, Urine, and Plasma in the Rat: An Integrative Metabonomic Approach. *Chem. Res. Toxicol.* 14, 1401-1412 (2001).
6. Wang, Q., Jiang, Y., Wu, C., Zhao, J., Yu, S., Yuan, B., Yan, X. & Liao, M. Study of a novel indolin-2-ketone compound Z24 induced hepatotoxicity by NMR-spectroscopy-based metabonomics of rat urine, blood plasma, and liver extracts. *Toxicol. Appl. Pharmacol.* 215, 71-82 (2006).
7. Tolstikov, V. Biomarkers and Metabolomics: Practical Implication. 41st Western Regional Meeting of the American Chemical Society, San Diego, CA, US, 9-13 October, (2007).
8. Raamsdonk, L. M., Teusink, B., Broadhurst, D., Zhang, N., Hayes, A., Walsh, M. C., Berden, J. A., Brindle, K. M., Kell, D. B., Rowland, J. J., Westerhoff, H. V., Dam, K. v. & Oliver, S. G. A functional genomics strategy that uses metabolome data to reveal the phenotype of silent mutations. *Nat. Biotechnol.* 19, 45-50 (2001).
9. Castrillo, J., Zeef, L., Hoyle, D., Zhang, N., Hayes, A., Gardner, D., Cornell, M., Petty, J., Hakes, L., Wardleworth, L., Rash, B., Brown, M., Dunn, W., Broadhurst, D., O'Donoghue, K., Hester, S., Dunkley, T., Hart, S., Swainston, N., Li, P., Gaskell, S., Paton, N., Lilley, K., Kell,

- D. & Oliver, S. Growth control of the eukaryote cell: a systems biology study in yeast. *Journal of Biology* 6, 4 (2007).
10. Oliver, S. G. Functional genomics: lessons from yeast. *Phil. Trans. R. Soc. Lond. B* 357, 17-23 (2002).
 11. Kell, D. B., Brown, M., Davey, H. M., Dunn, W. B., Spasic, I. & Oliver, S. G. Metabolic footprinting and systems biology: the medium is the message. *Nat. Rev. Microbiol.* 3, 557-565 (2005).
 12. Burgess, C. Valid Analytical Methods and Procedures (Royal Society of Chemistry, Cambridge, 2000).
 13. General principles of validation, Rockville, MD, Center for Drug Evaluation and Research (CDER), May 1987, US FDA.
 14. Huber, L. Validation and Qualification in Analytical Laboratories (Informa Health Care/ CRC Press, Buffalo Grove, 1999).
 15. Ermer, J. in Method Validation in Pharmaceutical Analysis: A Guide to Best Practice (eds. Ermer, J. & Miller, J. H. M.) 21-120 (John Wiley & Sons, Weinheim, 2005).
 16. Guerrero, I. & Kleiner, O. Application of Mass Spectrometry in Proteomics. *Bioscience Reports* 25, 71-93 (2005).
 17. Credo, G. M., Hewitson, H. B., Fountain, K. J., Gilar, M., Finch, J. W., Stumpf, C. L., Benevides, C. C., Bouvier, E. S. P., Compton, B. J., Shen, Z. & Siuzdak, G. Desorption/ionization on silicon mass spectrometry (DIOS MS) of small molecules and peptide: sample handling, preparation and storage effects on performance. 51th Annual Conf. ASMS Montreal, Canada, 8-12 June, (2003).
 18. Shion, H., Kass, I. & Lund, A. High Throughput Screening of Small Molecular Weight New Chemical Entities and Non Covalent Binding of Small Molecules to Intact Proteins Using MALDI-TOF and DIOS Target Plates. 52nd Annual Conf. ASMS, Nashville, TN, May, (2004).
 19. Wall, D. B., Finch, J. W. & Cohen, S. A. Comparison of desorption/ionization on silicon (DIOS) time-of-flight and liquid chromatography/tandem mass spectrometry for assaying enzyme-inhibition reactions. *Rapid Commun. Mass Spectrom.* 18, 1482-1486 (2004).

20. Wall, D. B., Finch, J. W. & Cohen, S. A. Quantification of codeine by desorption/ionization on silicon time-of-flight mass spectrometry and comparisons with liquid chromatography/mass spectrometry. *Rapid Commun. Mass Spectrom.* 18, 1403-1406 (2004).
21. Shen, Z., Thomas, J. J., Averbuj, C., Broo, K. M., Engelhard, M., Crowell, J. E., Finn, M. G. & Siuzdak, G. Porous silicon as a versatile platform for laser desorption/ionization mass spectrometry. *Anal. Chem.* 73, 612-619 (2001).
22. Chatman, K., Hollenbeck, T., Hagey, L., Vallee, M., Purdy, R., Weiss, F. & Siuzdak, G. Nanoelectrospray Mass Spectrometry and Precursor Ion Monitoring for Quantitative Steroid Analysis and Attomole Sensitivity. *Anal. Chem.* 71, 2358-2363 (1999).
23. Okuno, S. & Wada, Y. Measurement of serum salicylate levels by solid-phase extraction and desorption/ionization on silicon mass spectrometry. *J. Mass Spectrom.* 40, 1000-1004 (2005).
24. Hensel, R. R., King, R. C. & Owens, K. G. Electrospray sample preparation for improved quantitation in matrix-assisted laser desorption/ionization time-of-flight mass spectrometry. *Rapid Commun. Mass Spectrom.* 11, 1785-1793 (1997).
25. Go, E. P., Shen, Z., Harris, K. & Siuzdak, G. Quantitative analysis with desorption/ionization on silicon mass spectrometry using electrospray deposition. *Anal. Chem.* 75, 5475-5479 (2003).
26. Prenni, J. E., Shen, Z., Trauger, S., Chen, W. & Siuzdak, G. Protein characterization using liquid chromatography desorption/ionization on silicon mass spectrometry (LC-DIOS-MS). *Spectroscopy* 17, 693-698 (2003).
27. Todar, K. *Pseudomonas aeruginosa*. Todar's Online Textbook of Bacteriology (2004).
28. Fothergill, J. L., Panagea, S., Hart, C. A., Walshaw, M. J., Pitt, T. L. & Winstanley, C. Widespread pyocyanin over-production among isolates of a cystic fibrosis epidemic strain. *BMC Microbiol.* 7 (2007).
29. O'Malley, Y. Q., Reszka, K. J., Rasmussen, G. T., Abdalla, M. Y., Denning, G. M. & Britigan, B. E. The *Pseudomonas* secretory product pyocyanin inhibits catalase activity in human lung epithelial cells. *Am. J. Physiol. Lung Cell Mol. Physiol.* 285, L1077-L1086 (2003).
30. O'Malley, Y. Q., Reszka, K. J., Spitz, D. R., Denning, G. M. & Britigan, B. E. *Pseudomonas aeruginosa* pyocyanin directly oxidizes glutathione and decreases its levels in airway epithelial cells *Am. J. Physiol. Lung Cell Mol. Physiol.* 287, L94-L103 (2004).

31. Cox, C. D., Rinehart, K. L., Moore, M. L. & Cook, J. C. Pyochelin: Novel Structure of an Iron-Chelating Growth Promoter for *Pseudomonas aeruginosa*. *Proc. NatL Acad. Sci. USA* 78, 4256-4260 (1981).
32. Cox, C. D. Effect of pyochelin on the virulence of *Pseudomonas aeruginosa*. *Infect Immun.* 36, 17-23 (1982).
33. Cox, C. D. Role of Pyocyanin in the Acquisition of Iron from Transferrin. *Infect Immun.* 52, 263-270 (1986).
34. Valls, N., López-Canet, M., Vallribera, M. & Bonjoch, J. First Total Syntheses of Aeruginosin 298-A and Aeruginosin 298-B, Based on a Stereocontrolled Route to the New Amino Acid 6-Hydroxyoctahydroindole-2-carboxylic Acid. *Chem. Eur. J.* 7, 3446-3460 (2001).
35. Lerat, E. & Moran, N. A. The Evolutionary History of Quorum-Sensing Systems in Bacteria. *Mol Biol Evol* 21, 903-913 (2004).
36. Williams, P., Winzer, K., Chan, W. C. & Cámara, M. Look who's talking: communication and quorum sensing in the bacterial world. *Philos. T. R. Soc. B* 362, 1119-1134 (2007).
37. Chen, X., Schauder, S., Potier, N., Van Dorsselaer, A., Pelczar, I., Bassler, B. L. & Hughson, F. M. Structural identification of a bacterial quorum-sensing signal containing boron. *Nature* 415, 545-549 (2002).
38. Williams, P. Quorum sensing: an emerging target for antibacterial chemotherapy? *Expert Opinion on Therapeutic Targets* 6, 257-274 (2002).
39. Winzer, K. & Williams, P. Quorum sensing and the regulation of virulence gene expression in pathogenic bacteria. *Int. J. Med. Microbiol.* 291, 131-143 (2001).
40. Sio, C. F., Otten, L. G., Cool, R. H., Diggle, S. P., Braun, P. G., Bos, R., Daykin, M., Cámara, M., Williams, P. & Quax, W. J. Quorum Quenching by an N-Acyl-Homoserine Lactone Acylase from *Pseudomonas aeruginosa* PAO1. *Infect. Immun.* 74, 1673-1682 (2006).
41. Hentzer, M., Wu, H., Andersen, J. B., Riedel, K., Rasmussen, T. B., Bagge, N., Kumar, N., Schembri, M. A., Song, Z., Kristoffersen, P., Manefield, M., Costerton, J. W., Molin, S., Eberl, L., Steinberg, P., Kjelleberg, S., Høiby, N. & Givskov, M. Attenuation of *Pseudomonas aeruginosa* virulence by quorum sensing inhibitors. *EMBO J.* 22, 3803-3815 (2003).

42. Hooi, D. S. W., Bycroft, B. W., Chhabra, S. R., Williams, P. & Pritchard, D. I. Differential Immune Modulatory Activity of *Pseudomonas aeruginosa* Quorum-Sensing Signal Molecules. *Infect Immun.* 72, 6463–6470 (2004).
43. Li, L., Hooi, D., Chhabra, S. R., Pritchard, D. & Shaw, P. E. Bacterial N-acylhomoserine lactone-induced apoptosis in breast carcinoma cells correlated with down-modulation of STAT3. *Oncogene* 23, 4897-4902 (2004).
44. Chhabra, S. R., Harty, C., Hooi, D. S. W., Daykin, M., Williams, P., Gary Telford, Pritchard, D. I. & Bycroft, B. W. Synthetic Analogues of the Bacterial Signal (Quorum Sensing) Molecule N-(3-Oxododecanoyl)-L-homoserine Lactone as Immune Modulators. *J. Med. Chem.* 46, 97-104 (2003).
45. Pritchard, D. I. Immune modulation by *Pseudomonas aeruginosa* quorum-sensing signal molecules *Int. J. Med. Microbiol.* 296, 111-116 (2006).
46. Diggle, S. P., Cornelis, P., Williams, P. & Cámara, M. 4-Quinolone signalling in *Pseudomonas aeruginosa*: Old molecules, new perspectives. *Int. J. Med. Microbiol.* 296, 83-91 (2006).
47. Déziel, E., Lépine, F., Dennie, D., Boismenu, D., Mamer, O. A. & Villemur, R. Liquid chromatography/mass spectrometry analysis of mixtures of rhamnolipids produced by *Pseudomonas aeruginosa* strain 57RP grown on mannitol or naphthalene. *Biochimica et Biophysica Acta (BBA) - Molecular and Cell Biology of Lipids* 1440, 244-252 (1999).
48. Déziel, E., Lepine, F., Milot, S. & Villemur, R. Mass spectrometry monitoring of rhamnolipids from a growing culture of *Pseudomonas aeruginosa* strain 57RP. *Biochimica et Biophysica Acta (BBA) - Molecular and Cell Biology of Lipids* 1485, 145-152 (2000).
49. Jensen, P. Ø., Bjarnsholt, T., Phipps, R., Rasmussen, T. B., Calum, H., Christoffersen, L., Moser, C., Williams, P., Pressler, T., Givskov, M. & Høiby, a. N. Rapid necrotic killing of polymorphonuclear leukocytes is caused by quorum-sensing controlled production of rhamnolipid by *Pseudomonas aeruginosa*. *Microbiology* 153, 1329-1338 (2007).
50. Wong, J. W. H., Cagney, G. & Cartwright, H. M. SpecAlign--processing and alignment of mass spectra datasets. *Bioinformatics* 21, 2088-2090 (2005).
51. Wong, J. W. H., Durante, C. & Cartwright, H. M. Application of Fast Fourier Transform Cross-Correlation for the Alignment of Large Chromatographic and Spectral Datasets. *Anal. Chem.* 77, 5655-5661 (2005).

52. Wishart, D. S. Bioinformatics in Drug Development and Assessment. *Drug Metab Rev.* 37, 279 - 310 (2005).
53. Want, E. J., Cravatt, B. F. & Siuzdak, G. The Expanding Role of Mass Spectrometry in Metabolite Profiling and Characterization. *ChemBioChem* 6, 1941-1951 (2005).
54. Cuiffi, J. D., Hayes, D. J., Fonash, S. J., Brown, K. N. & Jones, A. D. Desorption-ionization mass spectrometry using deposited nanostructured silicon films. *Anal. Chem.* 73, 1292-1295 (2001).
55. Northen, T. R., Woo, H. K., Northen, M. T., Nordström, A., Uritboonthail, W., Turner, K. L. & Siuzdak, G. High Surface Area of Porous Silicon Drives Desorption of Intact Molecules. *J. Am. Chem. Soc.* 129, 1945-1949 (2007).
56. Wada, Y., Yanagishita, T. & Masuda, H. Ordered Porous Alumina Geometries and Surface Metals for Surface-Assisted Laser Desorption/Ionization of Biomolecules: Possible Mechanistic Implications of Metal Surface Melting. *Anal. Chem.* (2007).
57. Vaidyanathan, S., Jones, D. G., Ellis, J., Jenkins, T. E., Dunn, W., Hayes, A., Burton, N., Oliver, S., Kell, D. B. & Goodacre, R. A laser desorption ionisation mass spectrometry approach for high throughput metabolomics. *Metabolomics* 1, 1-8 (2005).
58. Cohen, L. & Gusev, A. Small molecule analysis by MALDI mass spectrometry. *Anal. Bioanal. Chem.* 373, 571 (2002).
59. Griffin, J. L., Nicholls, A. W., Daykin, C. A., Heald, S., Keun, H. C., Schuppe-Koistinen, I., Griffiths, J. R., Cheng, L. L., Rocca-Serra, P., Rubtsov, D. V. & Robertson, D. Standard reporting requirements for biological samples in metabolomics experiments: mammalian/in vivo experiments. *Metabolomics* 3, 179-188 (2007).
60. Ortori, C., Atkinson, S., Chhabra, S., Cámara, M., Williams, P. & Barrett, D. Comprehensive profiling of N -acylhomoserine lactones produced by *Yersinia pseudotuberculosis* using liquid chromatography coupled to hybrid quadrupole-linear ion trap mass spectrometry. *Anal. Bioanal. Chem.* 387, 497-511 (2007).
61. Bedoux, G., Vallée-Réhel, K., Kooistra, O., Zähringer, U. & Haras, D. Lipid A components from *Pseudomonas aeruginosa* PAO1 (serotype O5) and mutant strains investigated by electrospray ionization ion-trap mass spectrometry. *J. Mass Spectrom.* 39, 505-513 (2004).

62. Silipo, A., Lanzetta, R., Amoresano, A., Parrilli, M. & Molinaro, A. Ammonium hydroxide hydrolysis: a valuable support in the MALDI-TOF mass spectrometry analysis of Lipid A fatty acid distribution. *J. Lipid Res.* 43, 2188-2195 (2002).
63. Peer, C. J., Shakleya, D. M., Younis, I. R., Kraner, J. & Callery, P. S. Direct-Injection Mass Spectrometric Method for the Rapid Identification of Fentanyl and Norfentanyl in Postmortem Urine of Six Drug-Overdose Cases *J. Anal. Toxicol.* 31, 515-521 (2007).
64. Ebbels, T. M. D., Holmes, E., Lindon, J. C. & Nicholson, J. K. Evaluation of metabolic variation in normal rat strains from a statistical analysis of ^1H NMR spectra of urine. *J. Pharmaceut. Biomed.* 36, 823–833 (2004).
65. Keun, H. C., Beckonert, O., Griffin, J. L., Richter, C., Moskau, D., Lindon, J. C. & Nicholson, J. K. Cryogenic Probe ^{13}C NMR Spectroscopy of Urine for Metabonomic Studies. *Anal. Chem.* 74, 4588-4593 (2002).
66. Wang, C., Yang, J., Gao, P., Lu, X. & Xu, G. Identification of phospholipid structures in human blood by direct-injection quadrupole-linear ion-trap mass spectrometry. *Rapid Commun. Mass Spectrom.* 19, 2443–2453 (2005).
67. Sato, H., Seino, T., Torimura, M., Shimada, K., Yamamoto, A. & Tao, H. Analysis of Polymer Additives by DIOS-MS. *J. Mass Spectrom. Soc. Jpn.* 53, 247-256 (2005).
68. Okuno, S., Fukuo, T. & Arakawa, R. Effects of Cationizing Agents on DIOS Mass Spectra of Poly(ethylene glycol)s. *J. Mass Spectrom. Soc. Jpn.* 53, 265-269 (2005).
69. Seino, T., Sato, H., Torimura, M., Shimada, K., Yamamoto, A. & Tao, H. Laser Desorption/Ionization on Porous Silicon Mass Spectrometry for Accurately Determining the Molecular Weight Distribution of Polymers Evaluated Using a Certified Polystyrene Standard. *Anal. Sci.* 21, 484-490 (2005).
70. Arakawa, R., Shimomae, Y., Morikawa, H., Ohara, K. & Okuno, S. Mass spectrometric analysis of low molecular mass polyesters by laser desorption/ionization on porous silicon. *J. Mass Spectrom.* 39, 961-965 (2004).
71. Okuno, S., Wada, Y. & Arakawa, R. Quantitative analysis of polypropyleneglycol mixtures by desorption/ionization on porous silicon mass spectrometry. *Int. J. Mass Spectrom.* 241, 43-48 (2005).

72. Arakawa, R., Miyake, N., Okuno, S. & Yamaoka, H. Signal enhancement on laser desorption/ionization using alkali dihydroxybenzoic acid salts as cationizing agents. *Rapid Commun. Mass Spectrom.* 20, 2063-2066 (2006).
73. Lapolla, A., Ragazzi, E., Andretta, B., Fedele, D., Tubaro, M., Seraglia, R., Molin, L. & Traldi, P. Multivariate Analysis of Matrix-Assisted Laser Desorption/Ionization Mass Spectrometric Data Related to Glycooxidation Products of Human Globins in Nephropathic Patients. *J. Am. Soc. Mass Spectrom.* 18, 1018-1023 (2007).

CHAPTER 6 CONCLUSIONS AND FUTURE WORK

6.1 *Introduction*

In this thesis, the foundations of the novel high-throughput mass spectrometric technique based on laser desorption/ionisation on nanostructured semiconductor substrates have been further established. The work has extended our knowledge and skills in successfully applying the method, addressed some of the issues presented in literature, proposed an alternative version of ionisation mechanism or phenomena and confirmed the suitability of the method in metabolite profiling of biological matrices. The achievements are summarised in this chapter. Possible future directions are also considered.

6.2 *Motive of the Research*

The importance of metabolomics lies on the integrated systems biology, which seeks to understand the biological systems at the molecular level. Currently, metabolomics relies on chromatographic techniques coupled to mass spectrometry and proton NMR approaches. These methods, though well characterised, reliable and versatile, do not cope with the increasing demand of today's research practices. The problems of those approaches either require a lengthy separation procedure before mass analysis or do not provide sufficient sensitivity. In today's research environment, good use of high-throughput techniques necessitates information generation. Surface mass spectrometry is a technique that fits our demand for such a need and is gaining interest in analytical and life sciences.

New high-throughput mass spectrometry techniques such as DIOS, DART, DESI and PADI are recently emerged examples permitting rapid mass analysis of small molecules. The purpose of this study was therefore to investigate the potential of the matrix-free LDI approach based on the nanostructured semiconductor surface and its potential biomedical applications. The fundamental question of matrix-free LDI-MS rests on the development of suitable substrates. Since the first report of DIOS-MS in 1999, several other substrates have been successfully developed and three different substrates were commercialised. The technological development has been an on-going

effort in producing a matrix-free LDI substrate, which is simple to make, homogeneous, structurally and chemically stable, and has high ionisation efficiency. The method aims to provide a rapid qualitative analytical tool, which yields only few background ions at the low mass region of the mass spectrum. Without matrix dependence and interference, the potential would have an immense impact on the metabolomics.

Then again, the determinants for successful applications of the method published in literature have been somewhat inconsistent and thus the information available may not be reliable or may contain omissions. These divergences could be due to the differences in the surface preparations and the MALDI instrument used. It is generally accepted that the most important factors that govern the LDI activity are the specific surface area, the absorption cross section at the irradiation wavelength and the thermal conductivity of the substrate. This led us to embark on a study of the substrate characteristics, in terms of their physicochemical properties, to the laser desorption/ionisation mass spectrometry performance.

6.3 *Fitness for Purpose: the Strengths and the Weaknesses*

The DIOS technique provides many advantages over other emerging high-throughput mass spectrometric techniques. The strength of DIOS and related approaches is its data generation throughput relative to the conventional techniques. Data throughput is generally 1 to 2 minutes per sample. This is achieved through a chip-based array format of the target surface. Once the instrumental settings are optimised, the data acquisition is fully automatic. It is foreseeable that by introducing robotic operation in the sample deposition procedure used in MALDI, it is possible to minimise the intervention of the operator and further increase the data throughput and improve the reproducibility in the sample disposition procedure. Compared to other emerging new mass spectrometric approaches, DIOS has a relatively high versatility in analysing complex biological matrices. Little or simplified sample preparation is sufficient for its successful application. Additionally, it does not require a modification to the existing MALDI instrument and does not require a specially designed interface. Operation is almost identical to the MALDI technique.

However, the technique also has its own limitations. One common problem in using PSi substrate is its high affinity toward hydrocarbons and other ambient species. The desorption of these species generates background interference in the low mass region of the mass spectrum. While any analytical technique suffers some degree of contamination problem, without a prior chromatographic separation step and given the sensitivity of the method, this problem may severely limit the application of the technique and/or reduce its sensitivity. This problem will no doubt put an extra burden and complication on operators who have limited skills and knowledge in dealing with clean-surfaces. In the course of our investigation, it was necessary that the surface handling to be performed in a clean air environment, such as in a laminar flow hood, to minimise the atmospheric contamination problem. Most proteomics laboratories are normally equipped with robotic systems set as stationary in a laminar flow hood and the availability of the facility should not be an issue.

A second problem is related to the nature of the ionisation mechanism. Many biomolecules that could be easily detected by ESI-MS and NMR are not even amenable to DIOS. This is because the method has a strong selectivity toward the compounds that have a high proton affinity, low ionisation energy and high stabilisation energy or are pre-charged ions. Additionally, they should be not too volatile or compatible with vacuum conditions. The situation is similar to that in the MALDI technique. One possible direction is to adjust the surface chemistry of the semiconductor surface by the SAM modification, such as by different type of silanes to “tailor” the chemical properties of the surface for the target compound, or to enhance the versatility. Indeed, our results have already shown that the commercial DIOS substrates are manufactured with fluoro-silanisation. Another possible direction is to add enhancer or initiator molecules to the surface. While addition of common acidic modifiers suppresses the ion formation in our study, fluorinated acidic surfactants and fluorinated siloxane compounds are reported to produce a marked difference toward the detection capability.^{1, 2}

The third problem of the method is its poor quantitative performance. Analytical characteristics of the DIOS target were examined on a MALDI Q-ToF instrument. The dynamic range of the method was only ~2 to 3 orders of magnitude. Spot-to-spot

precision was generally lower than 50% RSD. It is evidenced that to produce a uniform distribution of the analyte over the surface, pipette deposition is inadequate. Possible solutions reported in literature include the use of a deuterated internal standard and electrospray deposition. Consequently, it is not surprising that the Laser Diagnostics Laboratory has abrogated the conventional liquid deposition and devotes entirely to the gas-phase adsorption approach.

6.4 *The Development and Evaluation of SALDI Substrates*

The SALDI substrates received from the Laser Diagnostics Laboratory were analysed along with the two other types of substrates obtained from the commercial sources, DIOS and QuickMass. Unfortunately, the SALDI substrate is far from a finished product and the development has been optimised or designed for the gas-phase adsorption approach. Much effort has been spent on supporting its development.

The evaluation and the development of the SALDI substrates suffered severe organic contamination complications. The organic contamination had been difficult to remove. Intense backgrounds were observed by laser mass spectrometry. While the organic contamination could function as a conventional matrix, the ionisation efficiency of hydrocarbons was very high and the background interferences were not less than that of the organic matrices. Furthermore, it took weeks to months until a set of experiments was completed and it was unavoidable we suffered surface ageing in our investigation.

Argon plasma etching was found to be a suitable method in removing the carbonaceous contamination of SALDI substrates and the re-etched surface exhibited an improved SALDI performance relative to the aged surface. Removing the contaminants also improved the mass resolution. However, relative to the freshly prepared surface, the plasma-etched surface still had a lower LDI performance. The surface chemistry was examined by SIMS and XPS and reinforced that the removal of organic contaminant was achieved by plasma treatment and yet the thickness of oxides was increased. While a lightly oxidised surface could still generate spectra, the SALDI performance was not as strong as with the commercial products.

On understanding the surface chemistry, we then explored silanisation modification as it had been reported that silanisation could restore or even enhance the LDI performance of oxidised porous silicon DIOS substrate. Given that the SALDI substrates received were silicon in nature, plasma etching and fluoro-silanisation modification were performed and a solution to the SALDI substrate development was presented. The LDI performance of the SALDI substrate was substantially improved after modification and porous substrate had LDI performance approaching to that of the commercial product. Although a method was found to minimise the problems, a limited supply, unsuitable format and lack of input or control to substrate manufacturing hurdled the further development of the SALDI substrate. In future, it would be ideal that the SALDI substrates are fabricated in this laboratory.

Evidently, from our SIMS and XPS imaging, the post-etching treatment procedure, namely laser etching, is more important than the chemical etching of the SALDI substrate and its activity. It was evidenced that the surface chemistry was altered during the laser etching procedure. It was accompanied by surface melting and/or morphological changes due to intense localised thermal reactions. The resulting surface became partly fluorine passivated and had a thinner oxides layer but was hydroxyl-terminated. It is believed those factors are fundamental in assisting SALDI ionisation activity, supporting the view that fluorination increases the acidity of the surface Si-OH moieties and assists the ions desorption.

Provided that the laser etching is so vital here, the surface roughness or the nanostructures of SALDI substrates can be fabricated directly by using laser etching, or laser ablation alone, eliminating the chemical etching procedures.^{3, 4} In fact, one of the forefront developments relies on two-directional laser light interference ablation to generate sub-micro order (100 nm - 1 μ m) periodical groove structures and requires no chemical etching procedure.⁵

6.5 Recognition of the Ionisation Mechanism

While the SALDI substrates have been less suitable for the purpose of bimolecular mass spectrometry, the investigation into the SALDI substrates has led to a recognition of the surface properties or characteristics required for effective LDI. Understanding of the ionisation mechanism is essential to the substrate development, the optimisation of the method and the interpretation of biological mass spectrum.

While the effects of surface chemistry are important, the effects of surface morphology are equally significant, or perhaps dominant. The results have indicated that a roughened surface is required for LDI, but not all roughened surface can give an acceptable LDI performance. The relationship between the surface roughness and the LDI performance is not definite and no evidence substantiates that reduction in the characteristic size of the sharp tips or roughness enhances the LDI performance. In fact, to have a high ion yield and good quality mass spectra, the substrate must have a porous or nanostructured layer thicker than 100-150 nm and have a high density of nanostructures. The dimensions of the nanostructures should not be too small or the structures should not be too fragile. In comparing all the substrates that are effective for LDI in this study and the data available in literature, the common features are actually the surface nanostructures. It is speculative that the nanostructures do not only function to enhance the surface area, retain the analyte and reduce thermal conductivity, but also function in energy deposition and transfer. It is proposed that the nanostructured surface can be considered as an assembly of quasi-quantum particles, which function as energy absorber, energy pooling, and transferor, processing the analyte to an excited state and leads to the onset of ion formation.

A wide range of compounds has been analysed on the matrix-free LDI substrates, with and without addition of acidic modifier or buffer. In general, addition of modifier or buffer reduces ion yield. Along with the results observed in the study of substrate properties and the current understanding of MALDI ionisation mechanism, we proposed our model of the ionisation processes. One of the major differences from previous models proposed set on the concept of thermodynamics and quasi-equilibrium theory. Accordingly, it is the entropy of the reaction and rate of the

reaction ultimately determine the ions that actually observed. The excess energy of the desorbed molecules in the transition state leads to redistribution of its internal energy, resulting in unimolecular fragmentation. This proposition departs from the conventional view of aqueous or gas-phase basicities dependence. The silicon surface is also oxidised under the influence of UV proton, produces a reduction potential and has been probed by copper(II) and iron(III) metallic ions. Undoubtedly, the formation of preformed ions, photoionisation and other gas-phase processes cannot be ignored. Dissimilarities in the ion distribution were also observed between the vacuum and the atmospheric pressure MALDI systems.

Detection characteristics (influence of laser intensity to ion yield) have also been examined under the MALDI Q-ToF instrument. The ion yield follows an exponential increase with respect to the laser energy setting and once it reaches a maximum, the ion yield drops and then varies greatly. This suggests that under such conditions, the desorption system becomes unstable. This is followed by a second drop, where analyte degradation or surface destruction occurs. The detection characteristic also exhibited an analyte or sample dependence and the profile varied from sample to sample. Laser setting was optimised accordingly.

6.6 The Application of Complex Biological Matrices and MVDA

Various biological extracts were examined by the method. Blood plasma extract, urine extract, tissue extract and bacterial cell and culture were analysed and metabolite profiles were successfully generated. To evaluate the complicated spectral data, PCA was employed. PCA is an important tool in today's scientific researches, not limited in metabolomics, to reduce the complexity of a dataset, to search for patterns, to isolate the important factors and to generate hypothesis. Even though the DIOS-MS suffered poor signal precision, the application of PCA was still possible. In fact, the relatively poor signal precision of the MALDI technique has not prevented the application of PCA or other MVDA approaches into the evaluation of the MALDI dataset. A directive of future work should make use of this technique to estimate

changes in biological systems, such as mutation, disease diagnosis, and other environmental influences. Indeed, with the strength of the method based on its data throughput, it should be very valuable in clinical conditions where urgency is one of the demands. Consider the situation when a decision is needed to be made based on the results of a clinical chemical analysis, or consider the number of patients waiting for treatment in hospitals.

6.7 The Future Direction

A disadvantage of the MALDI Q-ToF relative to the MALDI-ToF mass spectrometer is the loss of ions due to its duty cycle. Where sufficient ions can be collected by the MALDI ToF in 1 minute, 2 minutes are required in the MALDI Q-ToF instead. Increasing the length of the ion optic also makes less stable ions undetectable. However, the Q-ToF instrument has a high mass resolution and mass accuracy. The detector is less likely saturated. MS/MS applications of the MALDI Q-ToF offer many opportunities, which would otherwise be difficult to achieve by post source decay alone. However, to apply MS/MS by the MALDI Q-ToF, a sufficiently high and possibly stable ion current is required. Extending the acquisition time and sacrificing the throughput may amend the problem. How to take advantage of the MALDI Q-ToF instrument is one of the future directives worth exploring.

On the other hand, being a surface mass spectrometric technique allows the DIOS technique and so the DESI technique to make their way towards molecular imaging of biological tissues. Relative to the DESI technique, the LDI imaging offers a higher spatial resolution. Relative to SIMS imaging, LDI imaging provides a larger field of view, but a lower spatial resolution.⁶ (Figure 6-1) The MALDI Q-ToF instrument used in this study has already been equipped with the imaging capability. However, the software development is still ongoing and we will have to wait until the next version is available.

One of the forefront developments in mass spectrometry technology is ion-mobility mass spectrometry. This development is a great stride towards biological mass spectrometry, specifically, in proteomics and metabolomics.^{7, 8} Separation of gas-

phase ions is achievable via the differential migration of ions through a homogeneous electric field. An instrument that couples ion-mobility to a MALDI interface is now commercially available and may prove useful to the matrix-free LDI approaches; particularly, it has no adverse effect to data throughput. (Figure 6-2) It is worth noting that the instrumental design of the MALDI ion-mobility mass spectrometer is closely similar to the MALDI Q-ToF used in this study, with the exception that the collision cell is replaced by an assembly of ion-trap and ion-mobility drift tube. In addition, ion-mobility mass spectrometry has also made its way into MALDI molecular imaging.^{9, 10}

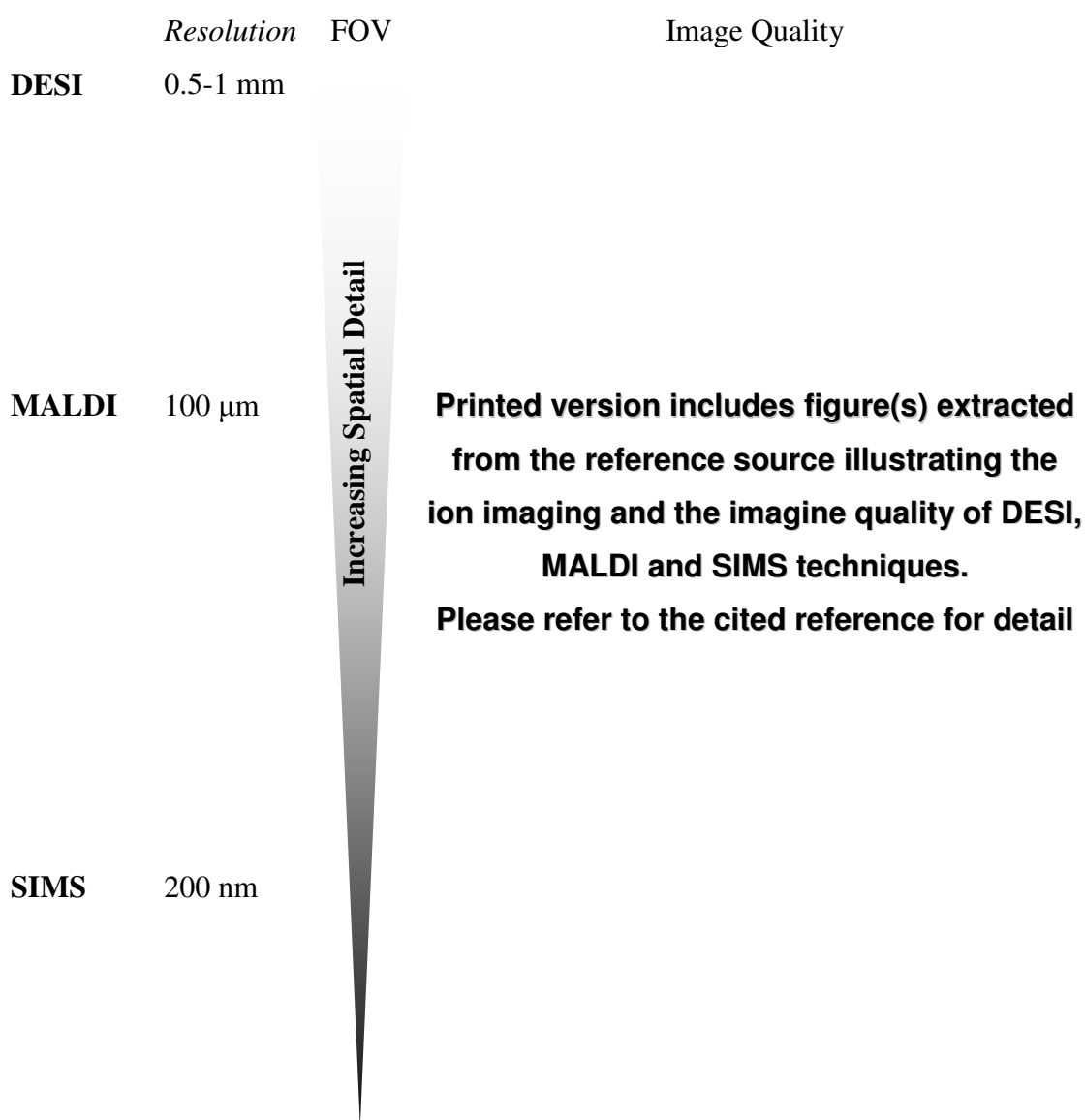


Figure 6-1 Molecular imaging of rat brain tissue by DESI, MALDI and SIMS.¹¹⁻¹⁴

**Printed version includes figure(s) extracted
from the manufacturer promotional material describing
the design and ion optic of Waters Synapt ion mobility mass
spectrometer coupled with a MALDI ion source.**

Figure 6-2 Schematic of Waters Synapt™ HDMS™ system, provided by the manufacturer.

6.8 *Final Thought*

Good scientific researches are to seek knowledge that will benefit to humans, animal welfare and the environment. It also presents a challenge as well as widens the horizon for those seeking this knowledge. On the road to seeking knowledge, whatever the research discipline, a large amount of data is required to generate relatively small amounts of information and even less information will become a human's knowledge. The bottleneck lies in data generation. The application of high-throughput approaches is therefore necessary or even imperative to drive the progression of science. Matrix-free LDI-MS has the potential to take part into the world of biomedical-analytical science, perhaps this is its true destiny. Nevertheless, for the time being, this marks an end of a beginning.

6.9 References

1. Nordstrom, A., Apon, J. V., Uritboonthai, W., Go, E. P. & Siuzdak, G. Surfactant-Enhanced Desorption/Ionization on Silicon Mass Spectrometry. *Anal. Chem.* 78, 272-278 (2006).
2. Northen, T. R., Yanes, O., Northen, M. T., Marrinucci, D., Uritboonthai, W., Apon, J., Golledge, S. L., Nordstrom, A. & Siuzdak, G. Clathrate nanostructures for mass spectrometry. *Nature* 449, 1033-1036 (2007).
3. Chen, Y. & Vertes, A. Adjustable Fragmentation in Laser Desorption/Ionization from Laser-Induced Silicon Microcolumn Arrays. *Anal. Chem.* 78, 5835-5844 (2006).
4. Chen, Y., Luo, G., Diao, J., Chornoguz, O., Reeves, M. & Vertes, A. Laser desorption/ionization from nanostructured surfaces: nanowires, nanoparticle films and silicon microcolumn arrays. *J. Phys: Conf. Ser.* 59, 548-554 (2007).
5. Ikeda, H., Shibamoto, K., Fujino, T. & Inaga, T. Tokyo Metropolitan University, Japan. Laser ablation ionizing method. (2007). *JP 2006-45691*. JP 2007225394.
6. McDonnell, L. A. & Heeren, R. M. A. Imaging Mass Spectrometry. *Mass Spectrom. Rev.* 26, 606-643 (2007).
7. Shockcor, J. SP1A Application of Ion Mobility Mass Spectrometry and Advanced Statistical Methods to Metabonomic/ Metabolomic Studies. *J. Biomol. Tech.* 18, 79-80 (2007).
8. Pringle, S. D., Giles, K., Wildgoose, J. L., Williams, J. P., Slade, S. E., Thalassinou, K., Bateman, R. H., Bowers, M. T. & Scrivens, J. H. An investigation of the mobility separation of some peptide and protein ions using a new hybrid quadrupole/travelling wave IMS/oa-ToF instrument. *Int. J. Mass Spectrom.* 261, 1-12 (2007).
9. Jackson, S. N., Ugarov, M., Egan, T., Post, J. D., Langlais, D., Schultz, J. A. & Woods, A. S. MALDI-ion mobility-TOFMS imaging of lipids in rat brain tissue. *J. Mass Spectrom.* 42, 1093-1098 (2007).
10. McLean, J. A., Ridenour, W. B. & Caprioli, R. M. Profiling and imaging of tissues by imaging ion mobility-mass spectrometry. *J. Mass Spectrom.* 42, 1099-1105 (2007).

11. Wiseman, J. M., Ifa, D. R., Song, Q. & Cooks, R. G. Tissue Imaging at Atmospheric Pressure Using Desorption Electrospray Ionization (DESI) Mass Spectrometry. *Angew. Chem. Int. Ed.* 45, 7188-7192 (2006).
12. Ifa, D. R., Wiseman, J. M., Song, Q. & Cooks, R. G. Development of capabilities for imaging mass spectrometry under ambient conditions with desorption electrospray ionization (DESI). *Int. J. Mass Spectrom.* 259, 8-15 (2007).
13. Garrett, T. J., Prieto-Conaway, M. C., Kovtoun, V., Bui, H., Izgarian, N., Stafford, G. & Yost, R. A. Imaging of small molecules in tissue sections with a new intermediate-pressure MALDI linear ion trap mass spectrometer. *Int. J. Mass Spectrom.* 260, 166-176 (2007).
14. Debois, D., Brunelle, A. & Laprévote, O. Attempts for molecular depth profiling directly on a rat brain tissue section using fullerene and bismuth cluster ion beams *Int. J. Mass Spectrom.* 260, 115-120 (2007).

Appendices

A1: Analytical Performance Parameters

Table A1: Analytical performance parameters.

| Parameters | Definition and description |
|--------------------------|---|
| Precision | <i>The closeness of agreement (degree of scatter) between a series of measurements obtained from multi sampling of the same homogeneous sample under the prescribed conditions. Precision may be considered at three levels; repeatability, intermediate precision and reproducibility. Repeatability is the results of the method operating over a short time interval under the same conditions (inter-assay precision). It should be determined from a minimum of nine determinations covering the specified range of the procedure (for example, three levels, three repetitions each) or from a minimum of six determinations at 100% of the test or target concentration. Intermediate precision is the results from within lab variations due to random events such as different days, analysts, equipment, etc. Reproducibility refers to the results of collaborative studies between laboratories. The data are reported in the standard deviation, the relative standard deviation (RSD) (coefficient of variation, CV) and the confidence interval.</i> |
| Accuracy | <i>The measure of exactness of an analytical method, or the closeness of agreement between the value which is accepted either as a conventional, true value or an accepted reference value and the value found. It is measured as the percent of analyte recovered by assay, by spiking samples in a blind study. For the assay of the drug substance, accuracy measurements are obtained by comparison of the results with the analysis of a standard reference material, or by comparison to a second, well-characterised method. For the assay of the drug product, accuracy is evaluated by analysing synthetic mixtures spiked with known quantities of components. For the quantitation of impurities, accuracy is determined by analysing samples (drug substance or drug product) spiked with known amounts of impurities.</i> |
| Limit of detection (LOD) | <i>The lowest concentration of an analyte in a sample that can be detected but not quantitated. It is a limit test that specifies whether or not an analyte is above or below a certain value. It is expressed as a concentration at a specified S/N ratio, usually 3.</i> |

| | |
|-----------------------------|---|
| Limit of quantitation (LOQ) | <i>The lowest concentration of an analyte in a sample that can be determined with acceptable precision and accuracy under the stated operational conditions of the method. Like LOD, LOQ is expressed as a concentration, with the precision and accuracy of the measurement also reported. Sometimes an S/N ratio of 10 is used to determine LOQ. This S/N ratio is a good rule of thumb, but it should be remembered that the determination of LOQ is a compromise between the concentration and the required precision and accuracy. That is, as the LOQ concentration level decreases, the precision increases. If better precision is required, a higher concentration must be reported for LOQ.</i> |
| Linearity | <i>The ability of the method to elicit test results that are directly proportional to analyte concentration within a given range. Linearity is generally reported as the variance of the slope of the regression line.</i> |
| Range | <i>the interval between the upper and lower levels of analyte (inclusive) that have been demonstrated to be determined with precision, accuracy and linearity using the method as written. The range is normally expressed in the same units as the test results obtained by the method. The ICH guidelines specify a minimum of five concentration levels, along with certain minimum specified ranges.</i> |
| Specificity | <i>The ability to measure accurately and specifically the analyte of interest in the presence of other components that may be expected to be present in the sample matrix. It is actually referring to selectivity.</i> |
| Robustness | <i>Robustness is the capacity of a method to remain unaffected by small deliberate variations in method parameters. The robustness of a method is evaluated by varying method parameters such as percent organic, pH, ionic strength, temperature, etc., and determining the effect (if any) on the results of the method. As documented in the ICH guidelines, robustness should be considered early in the development of a method. In addition, if the results of a method or other measurements are susceptible to variations in method parameters, these parameters should be adequately controlled and a precautionary statement included in the method documentation.</i> |
| System suitability | <i>An integral system that is evaluated as a whole to verify that the system are adequate for the analysis to be performed.</i> |

A2: Conferences and Publications

1. **Small Molecule Analysis Using Matrix-less Laser Desorption/Ionisation Mass Spectrometry**, poster presented at the BMSS annual conference, 2005.
2. **Metabolomic Applications of Matrix-free Desorption/Ionisation Mass Spectrometry on Porous Substrates: Theory and Applications**, oral presentation at the RSC Analytical Research Forum, 2006.
3. **DIOS Coupled to MALDI Q-ToF Primer Shows Promise As a High-Throughput Method Applied to Profile Metabolites in Bacterial Extracts from *Pseudomonas aeruginosa***, poster presented at the 3rd CBCB Annual Symposium, 2007.

A3: Selected Presentations

- *Poster:* **DIOS Coupled to MALDI Q-ToF Primer Shows Promise As a High-Throughput Method Applied to Profile Metabolites in Bacterial Extracts from *Pseudomonas aeruginosa***, poster presented at the 3rd CBCB Annual Symposium, 2007.
- *Presentation:* **High Throughput Analysis by Matrix-Free Laser Mass Spectrometry Approach.**

DIOS Coupled to MALDI Q-ToF Primer Shows Promise As a High-Throughput Method Applied to Profile Metabolites in Bacterial Extracts from *Pseudomonas aeruginosa*

Kai P. Law,¹ Sergey N. Nikiforov,³ Vladimir A. Karavanskii,³ Michael W. George,² Morgan R. Alexander,¹ Dave A. Barrett¹

¹School of Pharmacy, and ²School of Chemistry, University of Nottingham, University Park, Nottingham, NG7 2RD, UK

³A.M.Prokhorov General Physics Institute of Russian Academy of Sciences, Vavilov str.38, 119991, Moscow, Russia



The University of Nottingham

1. Introduction

Pseudomonas aeruginosa is an opportunistic pathogen of humans. Most *Pseudomonas* infections are both invasive and toxinogenic. Patients who suffer cancer, cystic fibrosis, AIDS, severe burns or are immunocompromised are particularly at risk of *Pseudomonas* infection. Traditional antibiotic therapy is usually not sufficient to eradicate these infections.[1] It has only been recognised recently that single-cell organisms such as bacteria also have ability to coordinate themselves in order to adapt or modulate responses that are beneficial to survival.[2] This coordinated behaviour in single-cell organisms occurs through cell-cell communication or quorum sensing (QS).[3]

QS is a process by which many bacteria coordinate gene expression according to the local density or population of bacteria. Regulation of gene expression can via the production of small molecules called the quorum sensing signalling molecules (QSSM). Through this coordination, the bacterium coordinates their growth within a host without harming it, until they reach a certain population and their numbers become sufficient to overcome the host's immune system. In *P. aeruginosa*, QS is known to control expression of a number of virulence factors. QS systems involve at least two chemically distinct classes of signalling molecules, *N*-acyl-L-homoserine lactones (AHL) and alkyl quinolones (AQS). By attenuation or disrupting the signalling process (quorum quenching), it may be possible to down-regulate the genes that control the virulence factors and the pathogen fails to adapt to the host environment and is readily cleared by the innate host defences.[4-6] Alternatively, early detection of the QSSM enables us to determine the disease cause and provide appropriate treatments.

Desorption/ionisation on silicon mass spectrometry (DIOS-MS) is a newly emerged high-throughput qualitative analytical technique, capable of analysing complex biological matrices.[7] Data throughput is 1 to 2 mins per sample. The approach employs nanostructured silicon surface to retain and assist the desorption and ionisation of the analyte (fig.1) and permits rapid mass analysis of small molecules and mixtures of metabolites.[8] In here, we further demonstrate the suitability of the method for global metabolite profiling of *P. aeruginosa* cells and culture extracts.

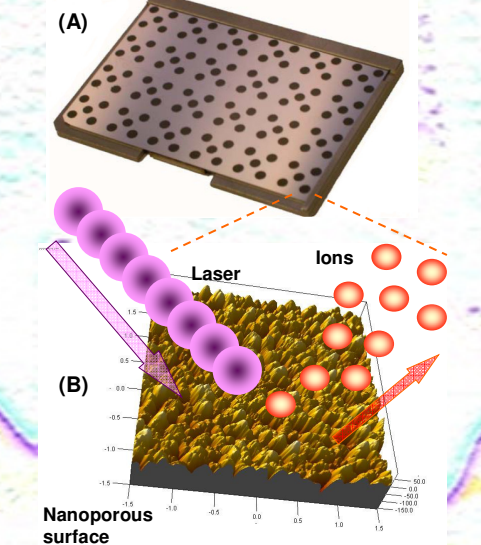


Fig. 1 (A) The DIOS target. The target is made in standard 98 array format. (B) AFM image of the nanostructured surface. Added visual effects ascribes the LDI process.

References
[1]. Todar, K. *Pseudomonas aeruginosa*. Today's Online Textbook of Bacteriology (2004).
[2]. Lerat, E. & Moran, N. A. The Evolutionary History of Quorum-Sensing Systems in Bacteria. *Mol Biol Evol* 21, 903-913 (2004).
[3]. Williams, P., Winzer, K., Chan, W. C. & Cámara, M. Look who's talking: communication and quorum sensing in the bacterial world. *Philos. T. R. Soc. B* 362, 1119-1134 (2007).
[4]. Williams, P. Quorum sensing: an emerging target for antibacterial chemotherapy? *Expert Opin on Therapeutic Targets* 6, 257-274 (2002).
[5]. Winzer, K. & Williams, P. Quorum sensing and the regulation of virulence gene expression in pathogenic bacteria. *Int. J. Med. Microbiol.* 291, 131-143 (2001).
[6]. Sio, C. F., Otten, L. G., Cool, R. H., Diggie, S. P., Braun, P. G., Bos, R., Daykin, M., Cámara, M., Williams, P. & Quorum Quenching by an N-Acyl-Homoserine Lactone Acylase from *Pseudomonas aeruginosa* PAO1. *Infect. Immun.* 74, 1673-1682 (2006).
[7]. Wei, J., Burnak, J. & Sluzadka, G. Desorption/ionization mass spectrometry on porous silicon. *Nature* 399, 243-246 (1999).
[8]. Shen, Z., Thomas, J. J., Averbuk, C., Broo, K. M., Engelhard, M., Crowell, J. E., Finn, M. G. & Sluzadka, G. Porous silicon as a versatile platform for laser desorption/ionization mass spectrometry. *Anal. Chem.* 73, 612-619 (2001).

2. Experimental

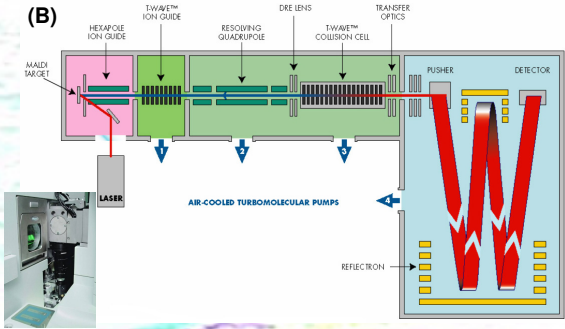
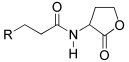
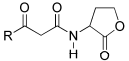
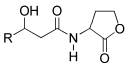


Fig. 2 (A) The *Pseudomonas* samples were cultivated by a BIostat B-plus fermentor system, (Satorius BBI system, Melsungen, Germany). Bacterial produces were harvested from the fermentor and was centrifuged to separate liquid supernatant and cell pellet. The cell pellet was further washed with BPS solution. Data was acquired on a Micromass MALDI Q-ToF Premier using Waters DIOS target (Manchester, UK). Samples solutions were spotted onto the target surface using a pipette. Target handling was carried out in a class I laminar flow hood to provide a clean air and sterile environment. (B) and (C) shows the schematic and the instrument itself, respectively.

3. Detection Capability of DIOS-MS to QSSM (Synthetic Compounds)

| HSL QSSM | Structural formula | Chain length | Molecular weight (Da) | Spectral respond | |
|----------------|--|--|-----------------------|--|--------------------|
| | | | | Positive | Negative |
| HSLs |  | R = CH ₃ | 171 | × | - |
| | | | 199 | [M+Na] ⁺ | - |
| | | | 227 | [M+Na] ⁺ | [M-H] ⁻ |
| | | | 255 | [M+Na] ⁺ | - |
| | | | 283 | [M+Na] ⁺ | - |
| | | | 311 | [M+Na] ⁺ | - |
| 3-oxo HSLs |  | R = C ₂ H ₅ CH ₃ R = C ₄ H ₉ CH ₃ R = C ₆ H ₁₃ CH ₃ R = C ₈ H ₁₇ CH ₃ | 185 | [M+Na] ⁺ | - |
| | | | 213 | [M+Na] ⁺ | - |
| | | | 241 | [M+Na] ⁺ | [M-H] ⁻ |
| | | | 269 | [M+Na] ⁺ | - |
| | | | 297 | [M+Na] ⁺ | - |
| | | | 325 | [M+Na] ⁺ | - |
| 3-hydroxy HSLs |  | R = C ₁₀ H ₂₁ CH ₃ | 187 | [M+H] ⁺ & [M+Na] ⁺ | [M-H] ⁻ |
| | | | 215 | [M+Na] ⁺ | × |
| | | | 243 | [M+Na] ⁺ | × |
| | | | 271 | [M+Na] ⁺ | × |
| | | | 299 | [M+Na] ⁺ | × |
| | | | 327 | [M+Na] ⁺ | × |

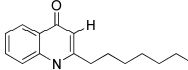
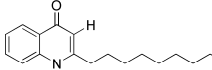
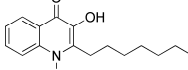
| AQS QSSM | Structural formula | Molecular weight (Da) | Spectral respond | |
|----------|---|-----------------------|---|--|
| | | | Positive | Negative |
| HHQ |  | 243 | [M+H] ⁺ , cationised dimer & trimer | [M-H] ⁻ , cationised dimer & trimer |
| HNQ |  | 271 | [M+H] ⁺ , cationised dimer & trimer | [M-H] ⁻ , cationised dimer & trimer |
| PQS |  | 259 | [M+H] ⁺ , cationised dimer & trimer | [M-H] ⁻ , cationised dimer & trimer |

Table 1. The DIOS-MS detection capability of *N*-acyl-L-homoserine lactones with respect to the chain length under MALDI Q-ToF conditions. The QSSM molecules are detected mostly as sodium adduct under position ion mode and deprotonated ion in negative ion mode. However, not all molecules are detected. The signal-to-noise of C4-HSL is low or distinguishable from the background. On the other hand, only C4-3-hydroxy HSL is detected in negative mode. "X" denotes corresponding ion is not detectable or its S/N < 3

Table 2. The DIOS-MS detection capability of 4-hydroxy-2-heptylquinoline (HHQ), 4-hydroxy-2-nonylquinoline (HNQ) and 3,4-dihydroxy-2-heptylquinoline (PQS). Hydroxy quinolones have many interesting chemical properties. These molecules are hydrophobic. The hydroxyl group is dynamically interchanging to and from enone. Dihydroxy-quinolones have a high affinity to metallic ions (ligands). The aromatic heterocyclic system is also UV absorbing. These chemical properties make AQSs and HAQs among one of the most sensitive analytes to the DIOS platform.

4. Qualitative Metabolite Profile of Bacterial Culture and Cell Pellet

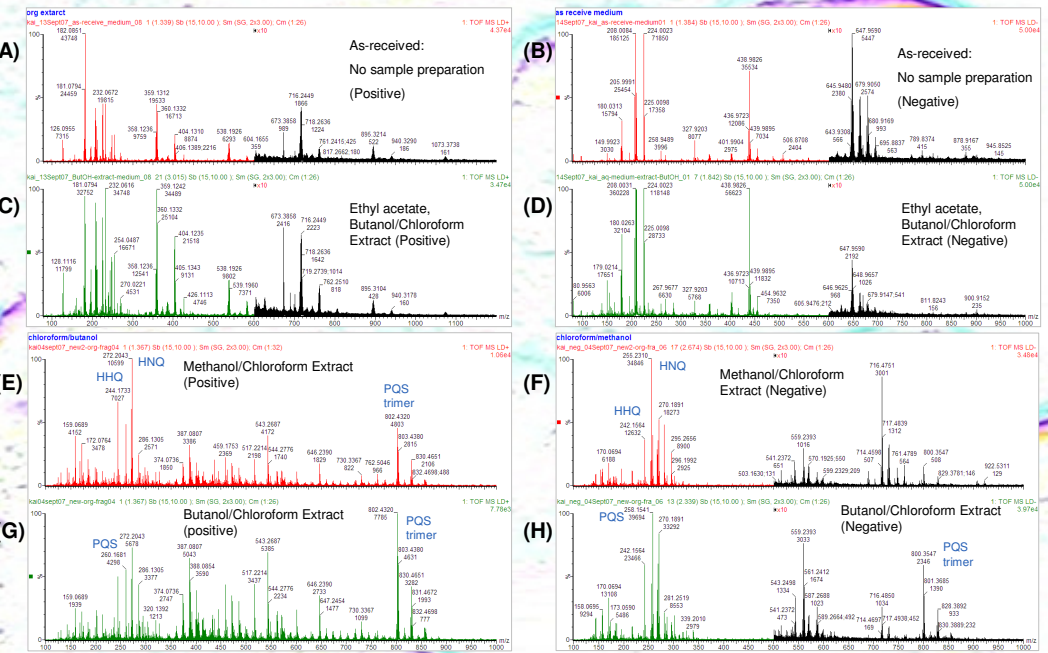


Fig. 3 (A and B) DIOS spectrum of *P. aeruginosa* culture supernatant, with no sample preparation under positive and negative ion respectively. The culture contains a spectrum of secretory products and some enhancement is achieved with suitable extraction method. (C and D) This implies under certain circumstances, biological matrices can be directly analysed without a complicated sample preparation procedure. Cell pellets are extracted with either methanol/chloroform (E and F) or butanol/chloroform (G and H). The ASQ QSSMs are detected as protonated and deprotonated species in positive and negative ion mode, respectively. Relatively, the ion yield of PQS is higher in the butanol/chloroform extract than the methanol/chloroform extract due to the high hydrophobicity of PQS.

High Throughput Analysis by Matrix-Free Laser Mass Spectrometry Approach

Kai P. Law
School of Pharmacy
University of Nottingham

19 December 2007

Overview

Introduction

A brief introduction of matrix-free LDI approach based on nanostructured semiconductor substrate

Summary of the Research Work

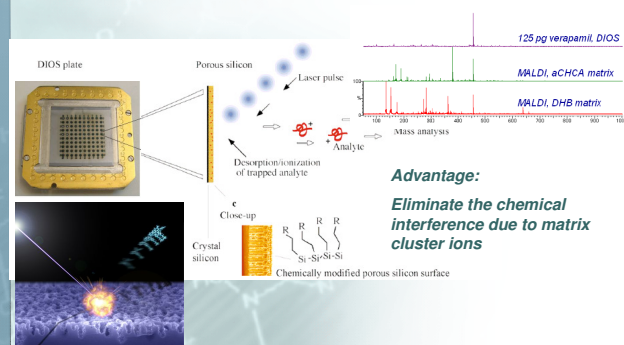
Surface characterisation and modification
Evaluation of the LDI performance
Investigation of the ionisation mechanism
Application in metabolite profiling in polycystic ovary syndrome

Others Experience Gained During My PhD Study

DIOS-MS

- DIOS is a matrix-free method that uses pulsed laser desorption/ionisation on porous silicon.
- Porous silicon is a nanostructured UV-absorbing semiconductor produced through anodisation, electrochemical or photochemical etching procedure of crystalline silicon in the presence of HF.
- For its application to LDI-MS, the structure of porous silicon provides a scaffold for retaining solvent and analyte molecules, and the UV absorptivity affords a mechanism for the transfer of the laser energy to the analyte.
- DIOS has been shown useful for a large variety of biomolecules of various types.
- Unlike other direct, matrix-free desorption techniques, DIOS enables desorption/ionization with little or no analyte degradation.

Desorption/Ionisation on Porous Silicon (DIOS)



Project Objectives

- What are these substrates?

- Physical
- Chemical

Approaches



Surface characterisation/
substrate development
-AFM, SEM, XPS, SIMS, WCA

- What can this method do?
- How does this method do?
- What are they not doing?



Mechanistic study

- Can complex biological matrix be applicable?
- How can it help the development of system biology?

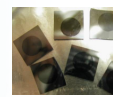
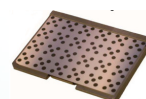


Biological studies

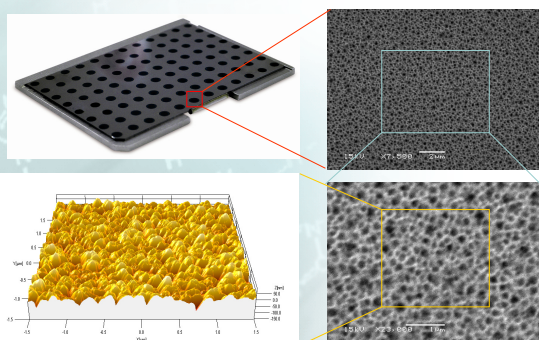
Substrates Studied

Substrate materials studied:

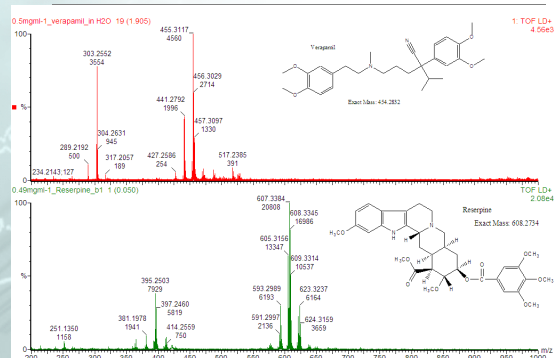
- DIOS (aqueous electrolyte)
- QuickMass (Ge thin film prepared by CVD)
- SALDI (I₂ etching additive – oxidising electrolyte)



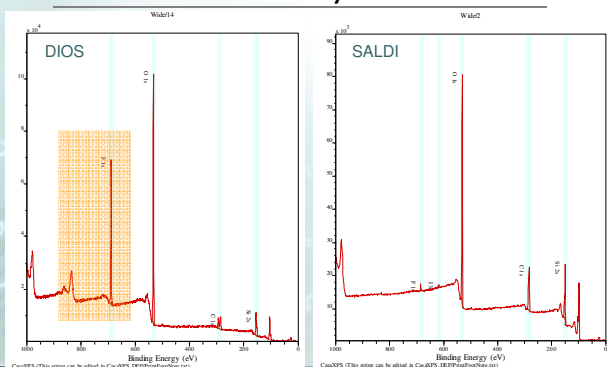
Microscopic images of porous silicon DIOS substrate



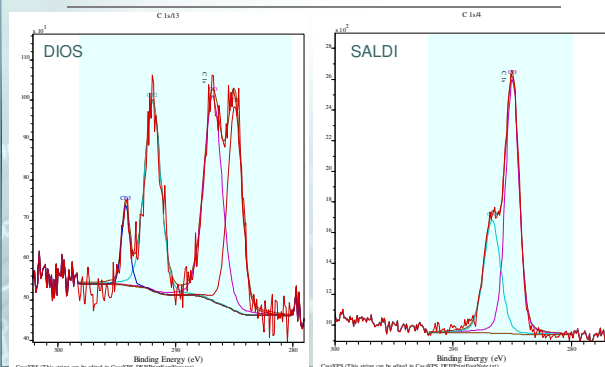
Mass spectra of reserpine and verapamil



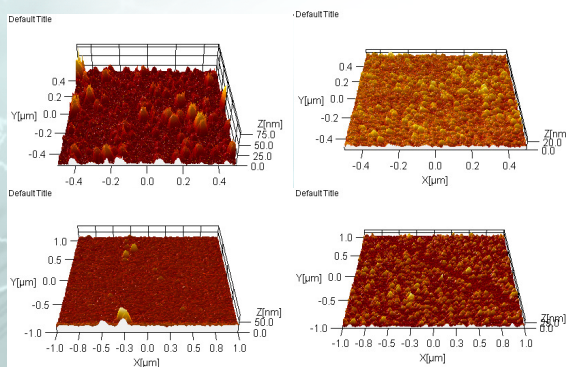
XPS Survey Scan



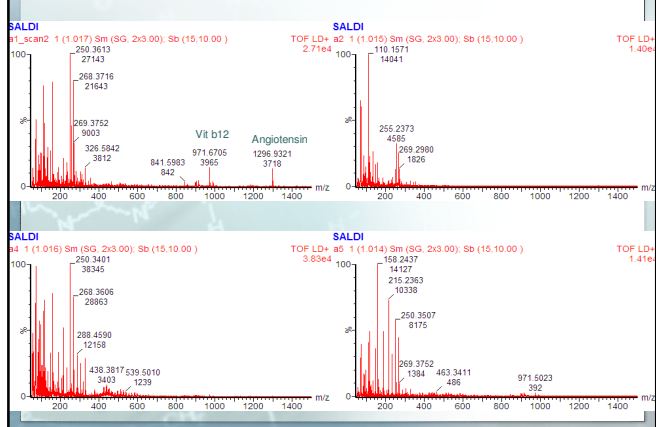
XPS C 1s Core Scan



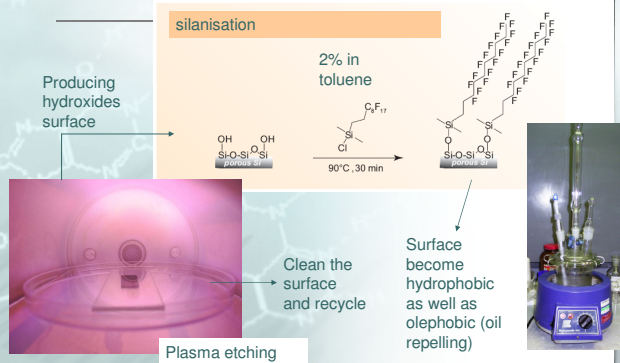
SALDI substrates: non-porous, thin roughened nanostructured layer



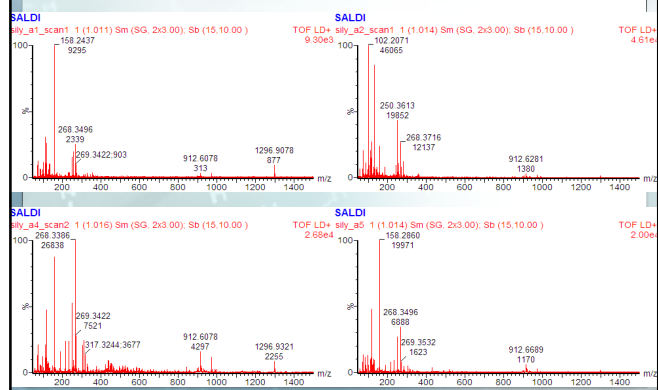
SALDI spectra: no surface modification



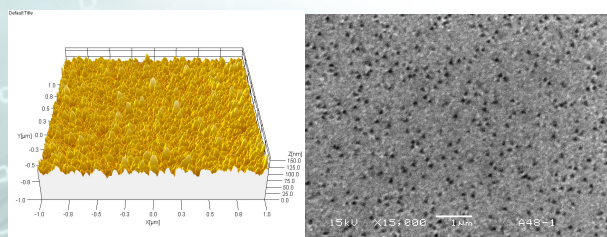
Silanisation Surface Modification



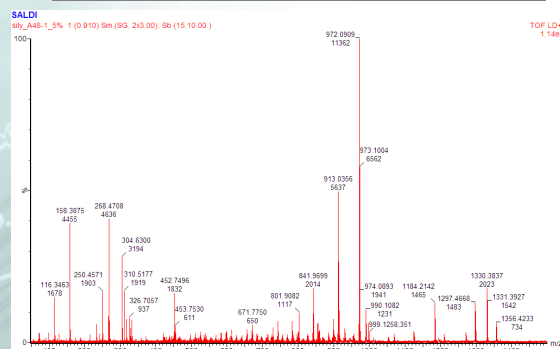
Some Improvement After modification



Suitable Substrate: Porous



The porous SALDI substrate after modification



Results Highlight

- Nano-size pores is not absolutely essential in ion generation
- However, it is believed the nano-size pores provides many functions that enhances the ion yields e.g.
 - Increase the surface area effectively
 - Retain the analyte more effectively
 - Reduce thermo-conductivity
 - Gun-barrel effect
 - Surface chemistry is essential
 - F and Si-OH

Surface Reaction

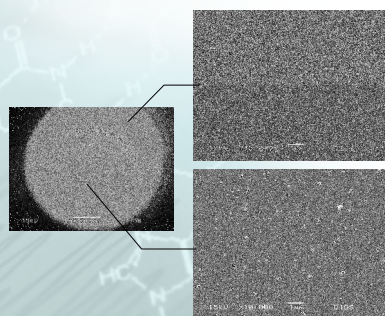
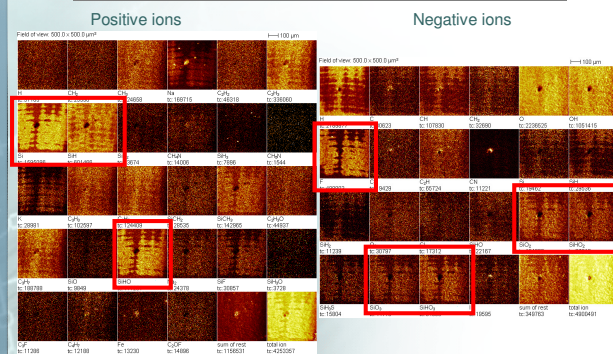


Figure 1 consists of three parts. The top left is an SEM image of the epoxy resin surface, showing a rough, granular texture. The top right is an XRD pattern of the epoxy resin, showing a broad peak at $2\theta \approx 20^\circ$. The bottom part shows two intensity profiles (Intensity vs. 2θ) for the non-modified (red) and modified (green) regions. The non-modified region shows a broad peak at $2\theta \approx 20^\circ$, while the modified region shows a sharp peak at $2\theta \approx 20^\circ$ and a smaller peak at $2\theta \approx 10^\circ$.

[illegible]

| Positive ions | Negative ions |
|--------------------------------|------------------------------------|
| Na^+ | Cl^- |
| Ca^{2+} | SO_4^{2-} |
| Mg^{2+} | NO_3^- |
| K^+ | F^- |
| Al^{3+} | O^{2-} |
| Fe^{2+} | CO_3^{2-} |
| Zn^{2+} | HCO_3^- |
| Cu^{2+} | S^{2-} |
| Ag^+ | PO_4^{3-} |
| Ba^{2+} | CH_3COO^- |
| Li^+ | NH_4^+ |
| Pb^{2+} | $\text{C}_6\text{H}_5\text{COO}^-$ |
| Sn^{2+} | HSO_4^- |
| Ni^{2+} | H_2PO_4^- |
| Co^{2+} | HPO_4^{2-} |
| Mn^{2+} | H_2PO_4^- |
| Cr^{3+} | H_2PO_4^- |
| V^{3+} | H_2PO_4^- |
| UO_2^{2+} | H_2PO_4^- |
| VO_2^+ | H_2PO_4^- |
| MoO_4^{2-} | H_2PO_4^- |
| $\text{W}_6\text{O}_{21}^{6-}$ | H_2PO_4^- |
| AsO_4^{3-} | H_2PO_4^- |
| SbO_4^{3-} | H_2PO_4^- |
| BiO_3^- | H_2PO_4^- |
| TeO_4^{2-} | H_2PO_4^- |
| PoO_4^{2-} | H_2PO_4^- |
| AtO_4^- | H_2PO_4^- |
| NhO_4^- | H_2PO_4^- |
| FlO_4^- | H_2PO_4^- |
| McO_4^- | H_2PO_4^- |
| LvO_4^- | H_2PO_4^- |
| Tl^+ | H_2PO_4^- |
| Pb^{2+} | H_2PO_4^- |
| Bi^{3+} | H_2PO_4^- |
| Po^{4+} | H_2PO_4^- |
| At^{7+} | H_2PO_4^- |
| Nh^{8+} | H_2PO_4^- |
| Fl^{9+} | H_2PO_4^- |
| Mc^{10+} | H_2PO_4^- |
| Lv^{11+} | H_2PO_4^- |
| Ts^{12+} | H_2PO_4^- |
| Og^{13+} | H_2PO_4^- |
| Lr^{3+} | H_2PO_4^- |
| Th^{4+} | H_2PO_4^- |
| Pa^{5+} | H_2PO_4^- |
| U^{6+} | H_2PO_4^- |
| Np^{7+} | H_2PO_4^- |
| Pu^{8+} | H_2PO_4^- |
| Am^{9+} | H_2PO_4^- |
| Cm^{10+} | H_2PO_4^- |
| Bk^{11+} | H_2PO_4^- |
| Cf^{12+} | H_2PO_4^- |
| Es^{13+} | H_2PO_4^- |
| Fm^{14+} | H_2PO_4^- |
| Md^{15+} | H_2PO_4^- |
| No^{16+} | H_2PO_4^- |
| Lw^{17+} | H_2PO_4^- |
| Uub^{18+} | H_2PO_4^- |
| Uut^{19+} | H_2PO_4^- |
| Uuq^{20+} | H_2PO_4^- |
| Uuh^{21+} | H_2PO_4^- |
| Uus^{22+} | H_2PO_4^- |
| Uuo^{23+} | H_2PO_4^- |
| Uuhs^{24+} | H_2PO_4^- |
| Uuhx^{25+} | H_2PO_4^- |
| Uueh^{26+} | H_2PO_4^- |
| Uuek^{27+} | H_2PO_4^- |
| Uuev^{28+} | H_2PO_4^- |
| Uuew^{29+} | H_2PO_4^- |
| Uuey^{30+} | H_2PO_4^- |
| Uuej^{31+} | H_2PO_4^- |
| Uuek^{32+} | H_2PO_4^- |
| Uuev^{33+} | H_2PO_4^- |
| Uuew^{34+} | H_2PO_4^- |
| Uuey^{35+} | H_2PO_4^- |
| Uuej^{36+} | H_2PO_4^- |
| Uuek^{37+} | H_2PO_4^- |
| Uuev^{38+} | H_2PO_4^- |
| Uuew^{39+} | H_2PO_4^- |
| Uuey^{40+} | H_2PO_4^- |
| Uuej^{41+} | H_2PO_4^- |
| Uuek^{42+} | H_2PO_4^- |
| Uuev^{43+} | H_2PO_4^- |
| Uuew^{44+} | H_2PO_4^- |
| Uuey^{45+} | H_2PO_4^- |
| Uuej^{46+} | H_2PO_4^- |



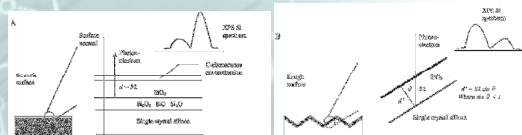
Non-modified region : Laser modified region

| | |
|---|--|
| <p><i>Predominant species:</i></p> <p>SiH SiH₂ SiH₃ Si(OH)_x SiO₂ C₂H₄ C₂H₂F₂ HF/H₂ Na/KI</p> | <p><i>Predominant species:</i></p> <p>SiH Si(OH)_x SiO₂ SiHO₂ SiO₃ SiHO₂ SiF SiC₂H₅ Si-O-C₂H₅</p> |
|---|--|

Predominant species:

SiH Si(OH)₃ SiO₂ SiHO₂ SiO₃
SiHO₂ SiF SiC₂H₅ Si-O-C₂H₅

Figure 62 2D schematic of the effects of laser modification to the SALDI surface in SALDI-MS environment. Laser induces oxidation of the surface and leads to formation of Si-OH moiety.



1. Surface melting – reduce roughness (see figs below)
2. Surface oxidation
3. Laser ablation (particular oxides layer)
4. Reaction with etchants / adsorbates

EDS spectrum of the sample, showing intensity versus energy (keV). The spectrum displays characteristic peaks for Cu, Fe, and Cl. The x-axis ranges from 0 to 500 keV, and the y-axis represents intensity. Peaks are labeled with their corresponding chemical species and energy values.

| Chemical Species | Energy (keV) |
|-----------------------------|--|
| [Cu(I)Cl]Cl | 132.8940, 11874 |
| [Fe(III)Cl ₂]Cl | 134.8906, 12996, 197.8174, 12903, 195.8216, 11223 |
| [Fe(II)Cl ₂]Cl | 160.8580, 7171 |
| [Cu(I)Cl ₂]Cl | 232.7752, 9621, 234.7752, 1982, 230.7782, 6312, 236.7752, 3613, 248.7872, 965 |
| [Cu(II)Cl ₂]Cl | 256.9556, 5449, 304.7154, 4500, 302.7191, 3531, 306.7117, 317.7220, 1460, 311.7279, 1907, 332.6710, 1355, 366.9742, 438, 482.6119, 1311, 411.6107, 1246, 458.5470, 487 |

Reduction potential (electrons transfer from the Si surface)

Weblelements

Standard reduction potentials (E°/V)

| | | | |
|-----------------|------------------------|----------------|---------------------------------|
| +4 | +2 | 0 | -4 |
| -0.909 | | | |
| acidic solution | | | |
| SiO_2 | $\xrightarrow{-0.967}$ | SiO^- | $\xrightarrow[-0.80]{\text{H}}$ |
| | | Si | $\xrightarrow{-0.143}$ |
| basic solution | | | |
| SiO_2 | $\xrightarrow{-1.69}$ | Si | |

© 2006 Webley Science Pty Ltd. All rights reserved.

Weblelements

Standard reduction potentials (E°/V)

| | | | |
|-----------------------------|------------------------|------------------|---------------------------------|
| +4 | +2 | 0 | -4 |
| 0.124 | | | |
| acidic solution | | | |
| Ge^{4+} | $\xrightarrow{0.00}$ | Ge^{2+} | $\xrightarrow{0.247}$ |
| GeO_2 | $\xrightarrow{-0.370}$ | GeO | $\xrightarrow[0.295]{\text{H}}$ |
| | | Ge | $\xrightarrow{-0.29}$ |
| basic solution | | | |
| $\text{Ge(OH)}_2\text{O}_2$ | $\xrightarrow{-0.89}$ | Ge | |

© 2006 Webley Science Pty Ltd. All rights reserved.

E°/V

+0.77

+0.16

Human Blood Plasma

3114ay07_20n_plasma015 1 (0.137) 30 (15.30.00) 1 Sm (63 243.00) Cm (1.14)

TOF MS L20
1.05e3

Mass spectrum showing relative intensity (%) versus m/z. The base peak is at m/z 413.2702. Other significant peaks are labeled with their m/z values.

| m/z | Relative Intensity (%) |
|----------|------------------------|
| 154.0778 | 100 |
| 154.0808 | 100 |
| 154.0812 | 100 |
| 154.0816 | 100 |
| 154.0820 | 100 |
| 154.0824 | 100 |
| 154.0828 | 100 |
| 154.0832 | 100 |
| 154.0836 | 100 |
| 154.0840 | 100 |
| 154.0844 | 100 |
| 154.0848 | 100 |
| 154.0852 | 100 |
| 154.0856 | 100 |
| 154.0860 | 100 |
| 154.0864 | 100 |
| 154.0868 | 100 |
| 154.0872 | 100 |
| 154.0876 | 100 |
| 154.0880 | 100 |
| 154.0884 | 100 |
| 154.0888 | 100 |
| 154.0892 | 100 |
| 154.0896 | 100 |
| 154.0900 | 100 |
| 154.0904 | 100 |
| 154.0908 | 100 |
| 154.0912 | 100 |
| 154.0916 | 100 |
| 154.0920 | 100 |
| 154.0924 | 100 |
| 154.0928 | 100 |
| 154.0932 | 100 |
| 154.0936 | 100 |
| 154.0940 | 100 |
| 154.0944 | 100 |
| 154.0948 | 100 |
| 154.0952 | 100 |
| 154.0956 | 100 |
| 154.0960 | 100 |
| 154.0964 | 100 |
| 154.0968 | 100 |
| 154.0972 | 100 |
| 154.0976 | 100 |
| 154.0980 | 100 |
| 154.0984 | 100 |
| 154.0988 | 100 |
| 154.0992 | 100 |
| 154.0996 | 100 |
| 154.1000 | 100 |
| 154.1004 | 100 |
| 154.1008 | 100 |
| 154.1012 | 100 |
| 154.1016 | 100 |
| 154.1020 | 100 |
| 154.1024 | 100 |
| 154.1028 | 100 |
| 154.1032 | 100 |
| 154.1036 | 100 |
| 154.1040 | 100 |
| 154.1044 | 100 |
| 154.1048 | 100 |
| 154.1052 | 100 |
| 154.1056 | 100 |
| 154.1060 | 100 |
| 154.1064 | 100 |
| 154.1068 | 100 |
| 154.1072 | 100 |
| 154.1076 | 100 |
| 154.1080 | 100 |
| 154.1084 | 100 |
| 154.1088 | 100 |
| 154.1092 | 100 |
| 154.1096 | 100 |
| 154.1100 | 100 |
| 154.1104 | 100 |
| 154.1108 | 100 |
| 154.1112 | 100 |
| 154.1116 | 100 |
| 154.1120 | 100 |
| 154.1124 | 100 |
| 154.1128 | 100 |
| 154.1132 | 100 |
| 154.1136 | 100 |
| 154.1140 | 100 |
| 154.1144 | 100 |
| 154.1148 | 100 |
| 154.1152 | 100 |
| 154.1156 | 100 |
| 154.1160 | 100 |
| 154.1164 | 100 |
| 154.1168 | 100 |
| 154.1172 | 100 |
| 154.1176 | 100 |
| 154.1180 | 100 |
| 154.1184 | 100 |
| 154.1188 | 100 |
| 154.1192 | 100 |
| 154.1196 | 100 |
| 154.1200 | 100 |
| 154.1204 | 100 |
| 154.1208 | 100 |
| 154.1212 | 100 |
| 154.1216 | 100 |
| 154.1220 | 100 |
| 154.1224 | 100 |
| 154.1228 | 100 |
| 154.1232 | 100 |
| 154.1236 | 100 |
| 154.1240 | 100 |
| 154.1244 | 100 |
| 154.1248 | 100 |
| 154.1252 | 100 |
| 154.1256 | 100 |
| 154.1260 | 100 |
| 154.1264 | 100 |
| 154.1268 | 100 |
| 154.1272 | 100 |
| 154.1276 | 100 |
| 154.1280 | 100 |
| 154.1284 | 100 |
| 154.1288 | 100 |
| 154.1292 | 100 |
| 154.1296 | 100 |
| 154.1300 | 100 |
| 154.1304 | 100 |
| 154.1308 | 100 |
| 154.1312 | 100 |
| 154.1316 | 100 |
| 154.1320 | 100 |
| 154.1324 | 100 |
| 154.1328 | 100 |
| 154.1332 | 100 |
| 154.1336 | 100 |
| 154.1340 | 100 |
| 154.1344 | 100 |
| 154.1348 | 100 |
| 154.1352 | 100 |
| 154.1356 | 100 |
| 154.1360 | 100 |
| 154.1364 | 100 |
| 154.1368 | 100 |
| 154.1372 | 100 |
| 154.1376 | 100 |
| 154.1380 | 100 |
| 154.1384 | 100 |
| 154.1388 | 100 |
| 154.1392 | 100 |
| 154.1396 | 100 |
| 154.1400 | 100 |
| 154.1404 | 100 |
| 154.1408 | 100 |
| 154.1412 | 100 |
| 154.1416 | 100 |
| 154.1420 | 100 |
| 154.142 | |

Polycystic ovary syndrome (PCOS)

- is an endocrine disorder that affects approximately one in ten women and most common hormonal disorder among women of reproductive age
- The principal features are weight problems, lack of regular ovulation and/or menstruation
- The exact cause is not totally clear.
- Diagnosis can be difficult, particularly because of the wide range of symptoms and the variability in presentation.
- Blood plasma of patients vs. control (method/chloroform extraction)
- Spectra are complicated and PCA is used to aid the interpretation and avoid false positive due to relatively large biological variation

PCA Score Plot

p015.M1 (PCA-X)
t(Comp. 1)/t(Comp. 2)
Colored according to Cls. ID (Primary)

Legend: ● c' ● p'

PC1 (X-axis) vs PC2 (Y-axis)

Key compounds labeled: c11a, c17, c12b, c10a, c10b, c10c, c10d, c10e, c10f, c10g, c10h, c10i, c10j, c10k, c10l, c10m, c10n, c10o, c10p, c10q, c10r, c10s, c10t, c10u, c10v, c10w, c10x, c10y, c10z, c10aa, c10ab, c10ac, c10ad, c10ae, c10af, c10ag, c10ah, c10ai, c10aj, c10ak, c10al, c10am, c10an, c10ao, c10ap, c10aq, c10ar, c10as, c10at, c10au, c10av, c10aw, c10ax, c10ay, c10az, c10ba, c10bb, c10bc, c10bd, c10be, c10bf, c10bg, c10bh, c10bi, c10bj, c10bk, c10bl, c10bm, c10bn, c10bo, c10bp, c10bq, c10br, c10bs, c10bt, c10bu, c10bv, c10bw, c10bx, c10by, c10bz, c10ca, c10cb, c10cc, c10cd, c10ce, c10cf, c10cg, c10ch, c10ci, c10cj, c10ck, c10cl, c10cm, c10cn, c10co, c10cp, c10cq, c10cr, c10cs, c10ct, c10cu, c10cv, c10cw, c10cx, c10cy, c10cz, c10da, c10db, c10dc, c10dd, c10de, c10df, c10dg, c10dh, c10di, c10dj, c10dk, c10dl, c10dm, c10dn, c10do, c10dp, c10dq, c10dr, c10ds, c10dt, c10du, c10dv, c10dw, c10dx, c10dy, c10dz, c10ea, c10eb, c10ec, c10ed, c10ee, c10ef, c10eg, c10eh, c10ei, c10ej, c10ek, c10el, c10em, c10en, c10eo, c10ep, c10eq, c10er, c10es, c10et, c10eu, c10ev, c10ew, c10ex, c10ey, c10ez, c10fa, c10fb, c10fc, c10fd, c10fe, c10ff, c10fg, c10fh, c10fi, c10fj, c10fk, c10fl, c10fm, c10fn, c10fo, c10fp, c10fq, c10fr, c10fs, c10ft, c10fu, c10fv, c10fw, c10fx, c10fy, c10fz, c10ga, c10gb, c10gc, c10gd, c10ge, c10gf, c10gg, c10gh, c10gi, c10gj, c10gk, c10gl, c10gm, c10gn, c10go, c10gp, c10gq, c10gr, c10gs, c10gt, c10gu, c10gv, c10gw, c10gx, c10gy, c10gz, c10ha, c10hb, c10hc, c10hd, c10he, c10hf, c10hg, c10hh, c10hi, c10hj, c10hk, c10hl, c10hm, c10hn, c10ho, c10hp, c10hq, c10hr, c10hs, c10ht, c10hu, c10hv, c10hw, c10hx, c10hy, c10hz, c10ia, c10ib, c10ic, c10id, c10ie, c10if, c10ig, c10ih, c10ii, c10ij, c10ik, c10il, c10im, c10in, c10io, c10ip, c10iq, c10ir, c10is, c10it, c10iu, c10iv, c10iw, c10ix, c10iy, c10iz, c10ja, c10jb, c10jc, c10jd, c10je, c10jf, c10jg, c10jh, c10ji, c10jj, c10jk, c10jl, c10jm, c10jn, c10jo, c10jp, c10jq, c10jr, c10js, c10jt, c10ju, c10jv, c10jw, c10jx, c10jy, c10jz, c10ka, c10kb, c10kc, c10kd, c10ke, c10kf, c10kg, c10kh, c10ki, c10kj, c10kk, c10kl, c10km, c10kn, c10ko, c10kp, c10kq, c10kr, c10ks, c10kt, c10ku, c10kv, c10kw, c10kx, c10ky, c10kz, c10la, c10lb, c10lc, c10ld, c10le, c10lf, c10lg, c10lh, c10li, c10lj, c10lk, c10ll, c10lm, c10ln, c10lo, c10lp, c10lq, c10lr, c10ls, c10lt, c10lu, c10lv, c10lw, c10lx, c10ly, c10lz, c10ma, c10mb, c10mc, c10md, c10me, c10mf, c10mg, c10mh, c10mi, c10mj, c10mk, c10ml, c10mm, c10mn, c10mo, c10mp, c10mq, c10mr, c10ms, c10mt, c10mu, c10mv, c10mw, c10mx, c10my, c10mz, c10na, c10nb, c10nc, c10nd, c10ne, c10nf, c10ng, c10nh, c10ni, c10nj, c10nk, c10nl, c10nm, c10nn, c10no, c10np, c10nq, c10nr, c10ns, c10nt, c10nu, c10nv, c10nw, c10nx, c10ny, c10nz, c10oa, c10ob, c10oc, c10od, c10oe, c10of, c10og, c10oh, c10oi, c10oj, c10ok, c10ol, c10om, c10on, c10oo, c10op, c10oq, c10or, c10os, c10ot, c10ou, c10ov, c10ow, c10ox, c10oy, c10oz, c10pa, c10pb, c10pc, c10pd, c10pe, c10pf, c10pg, c10ph, c10pi, c10pj, c10pk, c10pl, c10pm, c10pn, c10po, c10pp, c10pq, c10pr, c10ps, c10pt, c10pu, c10pv, c10pw, c10px, c10py, c10pz, c10qa, c10qb, c10qc, c10qd, c10qe, c10qf, c10qg, c10qh, c10qi, c10qj, c10qk, c10ql, c10qm, c10qn, c10qo, c10qp, c10qq, c10qr, c10qs, c10qt, c10qu, c10qv, c10qw, c10qx, c10qy, c10qz, c10ra, c10rb, c10rc, c10rd, c10re, c10rf, c10rg, c10rh, c10ri, c10rj, c10rk, c10rl, c10rm, c10rn, c10ro, c10rp, c10rq, c10rr, c10rs, c10rt, c10ru, c10rv, c10rw, c10rx, c10ry, c10rz, c10sa, c10sb, c10sc, c10sd, c10se, c10sf, c10sg, c10sh, c10si, c10sj, c10sk, c10sl, c10sm, c10sn, c10so, c10sp, c10sq, c10sr, c10ss, c10st, c10su, c10sv, c10sw, c10sx, c10sy, c10sz, c10ta, c10tb, c10tc, c10td, c10te, c10tf, c10tg, c10th, c10ti, c10tj, c10tk, c10tl, c10tm, c10tn, c10to, c10tp, c10tq, c10tr, c10ts, c10tt, c10tu, c10tv, c10tw, c10tx, c10ty, c10tz, c10ua, c10ub, c10uc, c10ud, c10ue, c10uf, c10ug, c10uh, c10ui, c10uj, c10uk, c10ul, c10um, c10un, c10uo, c10up, c10uq, c10ur, c10us, c10ut, c10uu, c10uv, c10uw, c10ux, c10uy, c10uz, c10va, c10vb, c10vc, c10vd, c10ve, c10vf, c10vg, c10vh, c10vi, c10vj, c10vk, c10vl, c10vm, c10vn, c10vo, c10vp, c10vq, c10vr, c10vs, c10vt, c10vu, c10vv, c10vw, c10vx, c10vy, c10vz, c10wa, c10wb, c10wc, c10wd, c10we, c10wf, c10wg, c10wh, c10wi, c10wj, c10wk, c10wl, c10wm, c10wn, c10wo, c10wp, c10wq, c10wr, c10ws, c10wt, c10wu, c10wv, c10ww, c10wx, c10wy, c10wz, c10xa, c10xb, c10xc, c10xd, c10xe, c10xf, c10xg, c10xh, c10xi, c10xj, c10xk, c10xl, c10xm, c10xn, c10xo, c10xp, c10xq, c10xr, c10xs, c10xt, c10xu, c10xv, c10xw, c10xx, c10xy, c10xz, c10ya, c10yb, c10yc, c10yd, c10ye, c10yf, c10yg, c10yh, c10yi, c10yj, c10yk, c10yl, c10ym, c10yn, c10yo, c10yp, c10yq, c10yr, c10ys, c10yt, c10yu, c10yv, c10yw, c10yx, c10yy, c10yz, c10za, c10zb, c10zc, c10zd, c10ze, c10zf, c10zg, c10zh, c10zi, c10zj, c10zk, c10zl, c10zm, c10zn, c10zo, c10zp, c10zq, c10zr, c10zs, c10zt, c10zu, c10zv, c10zw, c10zx, c10zy, c10zz

R[2][1] = 0.351318 R[2][2] = 0.161463
Ellipse: Rotating 22 (9.35)

SMCA-P 11 - 13010007 10.00.10

PCA Loading Plot

pc[15],M1 (PCA-X)
p[Comp. 1]p[Comp. 2]
Colored according to Var 1 (Primary)

Var 1

Var 2

Var 3

Var 4

Var 5

Var 6

Var 7

Var 8

Var 9

Var 10

Var 11

Var 12

Var 13

Var 14

Var 15

Var 16

Var 17

Var 18

Var 19

Var 20

Var 21

Var 22

Var 23

Var 24

Var 25

Var 26

Var 27

Var 28

Var 29

Var 30

Var 31

Var 32

Var 33

Var 34

Var 35

Var 36

Var 37

Var 38

Var 39

Var 40

Var 41

Var 42

Var 43

Var 44

Var 45

Var 46

Var 47

Var 48

Var 49

Var 50

Var 51

Var 52

Var 53

Var 54

Var 55

Var 56

Var 57

Var 58

Var 59

Var 60

Var 61

Var 62

Var 63

Var 64

Var 65

Var 66

Var 67

Var 68

Var 69

Var 70

Var 71

Var 72

Var 73

Var 74

Var 75

Var 76

Var 77

Var 78

Var 79

Var 80

Var 81

Var 82

Var 83

Var 84

Var 85

Var 86

Var 87

Var 88

Var 89

Var 90

Var 91

Var 92

Var 93

Var 94

Var 95

Var 96

Var 97

Var 98

Var 99

Var 100

Var 101

Var 102

Var 103

Var 104

Var 105

Var 106

Var 107

Var 108

Var 109

Var 110

Var 111

Var 112

Var 113

Var 114

Var 115

Var 116

Var 117

Var 118

Var 119

Var 120

Var 121

Var 122

Var 123

Var 124

Var 125

Var 126

Var 127

Var 128

Var 129

Var 130

Var 131

Var 132

Var 133

Var 134

Var 135

Var 136

Var 137

Var 138

Var 139

Var 140

Var 141

Var 142

Var 143

Var 144

Var 145

Var 146

Var 147

Var 148

Var 149

Var 150

Var 151

Var 152

Var 153

Var 154

Var 155

Var 156

Var 157

Var 158

Var 159

Var 160

Var 161

Var 162

Var 163

Var 164

Var 165

Var 166

Var 167

Var 168

Var 169

Var 170

Var 171

Var 172

Var 173

Var 174

Var 175

Var 176

Var 177

Var 178

Var 179

Var 180

Var 181

Var 182

Var 183

Var 184

Var 185

Var 186

Var 187

Var 188

Var 189

Var 190

Var 191

Var 192

Var 193

Var 194

Var 195

Var 196

Var 197

Var 198

Var 199

Var 200

Var 201

Var 202

Var 203

Var 204

Var 205

Var 206

Var 207

Var 208

Var 209

Var 210

Var 211

Var 212

Var 213

Var 214

Var 215

Var 216

Var 217

Var 218

Var 219

Var 220

Var 221

Var 222

Var 223

Var 224

Var 225

Var 226

Var 227

Var 228

Var 229

Var 230

Var 231

Var 232

Var 233

Var 234

Var 235

Var 236

Var 237

Var 238

Var 239

Var 240

Var 241

Var 242

Var 243

Var 244

Var 245

Var 246

Var 247

Var 248

Var 249

Var 250

Var 251

Var 252

Var 253

Var 254

Var 255

Var 256

Var 257

Var 258

Var 259

Var 260

Var 261

Var 262

Var 263

Var 264

Var 265

Var 266

Var 267

Var 268

Var 269

Var 270

Var 271

Var 272

Var 273

Var 274

Var 275

Var 276

Var 277

Var 278

Var 279

Var 280

Var 281

Var 282

Var 283

Var 284

Var 285

Var 286

Var 287

Var 288

Var 289

Var 290

Var 291

Var 292

Var 293

Var 294

Var 295

Var 296

Var 297

Var 298

Var 299

Var 300

Var 301

Var 302

Var 303

Var 304

Var 305

Var 306

Var 307

Var 308

Var 309

Var 310

Var 311

Var 312

Var 313

Var 314

Var 315

Var 316

Var 317

Var 318

Var 319

Var 320

Var 321

Var 322

Var 323

Var 324

Var 325

Var 326

Var 327

Var 328

Var 329

Var 330

Var 331

Var 332

Var 333

Var 334

Var 335

Var 336

Var 337

Var 338

Var 339

Var 340

Var 341

Var 342

Var 343

Var 344

Var 345

Var 346

Var 347

Var 348

Var 349

Var 350

Var 351

Var 352

Var 353

Var 354

Var 355

Var 356

Var 357

Var 358

Var 359

Var 360

Var 361

Var 362

Var 363

Var 364

Var 365

Var 366

Var 367

Var 368

Var 369

Var 370

Var 371

Var 372

Var 373

Var 374

Var 375

Var 376

Var 377

Var 378

Var 379

Var 380

Var 381

Var 382

Var 383

Var 384

Var 385

Var 386

Var 387

Var 388

Var 389

Var 390

Var 391

Var 392

Var 393

Var 394

Var 395

Var 396

Var 397

Var 398

Var 399

Var 400

Var 401

Var 402

Var 403

Var 404

Var 405

Var 406

Var 407

Var 408

Var 409

Var 410

Var 411

Mass spectra

patient

control

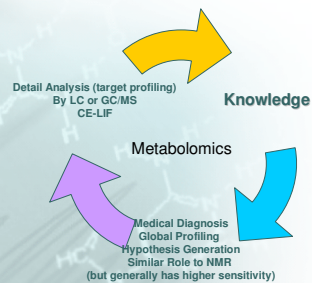
Conclusions

- Surface morphology is important or perhaps dominant in affecting the LDI performance / ion yield
- Surface chemistry is also important (which has not been investigated in detailed previously)
 - Laser leads to change in surface chemistry and morphology
 - The method has a high potential for clinical diagnostic purpose

However, a lot of work is still required to make it a proven method.

Idea → possibility → Promising → validated → Proven method

The Possible Role of DIOS-MS in Metabolomics



Acknowledgement

Special thank to supervisors and collaborator

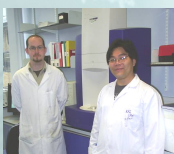
- Dr Dave Barrett (School of Pharmacy)
- Prof. Michael George (School of Chemistry)
- Dr Morgan Alexander (School of Pharmacy)
- Dr Sergey Nikiforov (General Physics Institute, Moscow)

Frank Rutten for assistance of ToF-SIMS work,

Emily Smith for assistance of XPS work,

Mathew Carlisle for MALDI-MS instrument assistance.

RSC/EPSRC for funding



Franz Hillenkamp

